Optique atomique quantique sur des nuages ultra-froids d'hélium métastable

Denis Boiron

To cite this version:

Denis Boiron. Optique atomique quantique sur des nuages ultra-froids d'hélium métastable. Physique Atomique [physics.atom-ph]. Université Paris Sud - Paris XI, 2009. tel-00472841

HAL Id: tel-00472841
https://theses.hal.science/tel-00472841

Submitted on 13 Apr 2010

Institut d'Optique - Graduate School
Laboratoire Charles Fabry de l'Institut d'Optique
Université Paris-Sud

HABILITATION A DIRIGER DES RECHERCHES
présentée par
Denis Boiron

Optique atomique quantique sur des nuages ultra-froids d'hélium métastable

Soutenue le 23 février 2009 devant le jury composé de :

M. Gerhard Birkl	Rapporteur
M. David Guéry-Odelin	Rapporteur
M. Jean-François Roch	Rapporteur
Mme Michèle Leduc	Présidente
M. Pierre Pillet	Examinateur
M. Christoph Westbrook	Examinateur

Remerciements

J'ai eu l'opportunité de rejoindre le groupe d'optique atomique après ma thèse et je tiens en premier lieu à remercier Alain Aspect et Chris Westbrook pour m'avoir fait confiance et soutenu pour le poste de maître de conférence qui était ouvert à l'Institut d'Optique, ainsi que les membres du laboratoire et son directeur pour m'y avoir accueilli. J'avais souhaité rejoindre l'équipe "hélium métastable" co-encadrée par Chris et Alain. L'hélium avait une "saveur" différente du césium sur lequel j'avais travaillé pendant ma thèse par l'existence du refroidissement sub-recul VSCPT mais surtout par sa grande énergie interne, conduisant par exemple à une détection électronique et non pas optique. Bien que l'hélium métastable était un atome réputé difficile, ce montage ouvrait des perspectives enthousiasmantes, que j'avais envie de vivre. Cela m'a permis de travailler avec Chris tout au long de ces années et de bénéficier de ses connaissances en physique bien plus étendues que les miennes et de son approche "avec les mains", qui conduisent à des discussions très stimulantes. De part ses activités multiples, j'interagis moins avec Alain mais les réunions communes, autour soit de la rédaction d'un article ou de perspectives sur la manip ont toujours été instructives. Son obstination à rechercher la meilleure mise en perspective de notre travail, la clarté et les images physiques simples a toujours fini par être bénéfique. En tant que figure de proue avec Chris de la manip hélium, il nous permet également de continuer à faire de la recherche en trouvant des financements et en attirant nombre d'étudiants et de post-doctorants. Le groupe optique atomique fort de ses dix chercheurs/enseignants-chercheurs permanents, de ses deux électroniciens et de sa vingtaine d'étudiants/post-doctorants forme un ensemble impressionnant de compétences qui permet une auto-émulation et un transfert de savoir-faire entre équipes qui nous est très bénéfique. Il est ainsi fréquent qu'un problème résolu sur un montage serve à un autre ou qu'un outil développé chez l'un diffuse chez l'autre. C'est en particulier vrai pour l'électronique. Le travail de Frédéric Moron et d'André Villing nous permet de disposer d'une électronique dédiée et parfaitement adaptée à nos expériences, et c'est une véritable force de notre groupe. Je citerai comme exemple sur notre montage, le séquenceur pour le contrôle de l'expérience, l'électronique autour des galettes de micro-canaux et, en cours de réalisation, l'alimentation RF des cellules d'absorption saturée, en plus des "traditionnels" alimentations de diode laser et systèmes d'asservissement. Merci donc à tous deux et plus généralement à tous les autres membres du groupe d'optique atomique.

Travailler sur le montage "hélium métastable" fut et reste une aventure avec ces hauts et ces bas. Les équipes d'étudiants qui se sont succédées ont permis à chaque fois de rebondir et d'obtenir de très beaux résultats. Je tiens ainsi à les remercier tous et à souhaiter à ceux qui sont encore en thèse ou en séjour post-doctoral de réussir leur vie professionnelle, *qu'elle soit dans la science ou ailleurs. Julie Poupard, Alice Robert et Martijn Schellekens travaillent maintenant dans l'industrie, Olivier Sirjean et Rodolphe Hoppeler dans l'enseignement, Antoine Browaeys, Signe Seidelin et Jose Viana Gomes dans la recherche académique. A l'heure actuelle Aurélien Perrin est en séjour post-doctoral à Vienne et finalement Valentina Krachmalnicoff, Jean-Christophe Jaskula et Marie Bonneau sont encore en thèse.*

Antoine et Julie étaient en deuxième année de thèse quand je suis arrivé ; ils ont formé une équipe redoutable que des problèmes techniques (vide pas assez poussé) ont empêché d'aller plus loin vers la condensation. Je retiendrai d'Antoine ses capacités de travail, sa compréhension profonde de la physique mais aussi sa relative impatience. En parfaite ingénieure de l'Ecole Supérieure d'Optique, Julie gérait la partie optique très efficacement et son langage "fleuri" égaillait la salle de manip. Je suis arrivé en même temps qu'Alice et nous avons appris ensemble comment marchait l'expérience. Il n'était pas facile de succéder à Antoine, mais, de nouveau, sa complémentarité avec Olivier arrivé l'année suivante a permis de franchir un cap important et d'apporter sa pierre à l'expérience. Olivier a été un étudiant clé ; il avait une rigueur et une vision claire de ce qu'il voulait faire sur la manip et c'est sa persévérance qui nous a permis d'observer le premier condensat de Bose-Einstein en février 2001. J'ai regretté qu'il ait décidé d'arrêter la recherche en choisissant un poste de professeur en classe préparatoire. Ont suivi Signe et Jose. Si chaque étudiant est différent de part sa personnalité, le système éducatif français les forme dans un moule que l'on connaît bien. Signe et José en tant que danoise et portugais étaient "exotiques" et j'avoue avoir eu une petite appréhension au départ. Signe était déjà dans le groupe depuis un an pour un stage théorique ; elle n'était donc pas une inconnue pour nous mais elle n'avait jamais mis la main dans le cambouis d'une manip. Elle s'y est fait assez rapidement, aider en cela par sa farouche volonté de continuer dans la recherche. José était un étudiant non conventionnel, un peu plus âgé que la moyenne, avec déjà une expérience expérimentale en optique, mais relativement moins de connaissances théoriques que nos étudiants français standards. Ses qualités expérimentales étaient évidentes et je fus rassuré en moins d'une semaine. Son esprit bouillonnant est d'autre part capable de sortir des dizaines d'idées par jour. Certes il faut faire le tri, mais j'ai particulièrement aimé le faire avec lui. Ce fut et cela reste très stimulant pour moi et j'espère que la collaboration que nous maintenons depuis la fin de sa thèse va se poursuivre et qu'il arrivera à développer une activité expérimentale en atomes froids dans son université au Portugal. Rodolphe a eu un rôle un peu ingrat car c'est lors de sa thèse que se sont opérées les modifications du montage expérimental pour installer la galette de micro-canaux sensible en position. Je crains que les difficultés que nous avons rencontrées pour réobtenir un condensat et la lourdeur de ce changement n'aient contribué à son choix de quitter le monde de la recherche pour enseigner dans le secondaire. J'espère qu'il s'y épanouit pleinement. Martijn fut un autre étudiant clé. Si Rodolphe s'était occupé de la partie "gros oeuvre", Martijn fut seul maître à bord pour la partie informatique (le désormais célèbre "Heevman" pour helium event manager) et électronique autour de ce nouveau détecteur. Même si j'ai toujours quelques petites craintes sur la pérennité de la partie informatique (la notion de commentaires de codes informatiques lui étant à peu près inconnue...), je ne peux que constater le succès et la richesse des outils qu'il a développés. C'est sous son ère qu'ont débuté les expériences de corrélations Hanbury Brown et Twiss. Son côté entrepreneurial ressortait déjà et c'est sans grande surprise qu'il a choisi de *travailler dans l'industrie après sa thèse. J'ai peu de doutes quant à son succès dans cette voie.Si Martijn avait le verbe haut, Aurélien, qui prenait la suite, était par comparaison très discret et plus enclin à se plonger dans des calculs théoriques obscurs. Nous nous y sommes attelés ensemble pour approfondir tout le méli-mélo autour de l'expérience de création de paires atomiques. J'ai beaucoup apprécié cette collaboration étroite entre nous. La thèse des autres étudiants, Valentina, Jean-Christophe et Marie n'est pas encore terminée. Le déménagement d'Orsay à Palaiseau puis les problèmes de haute tension autour du détecteur nous ont arrêté pendant près d'un an et demi et cela a évidemment pénalisé l'obtention de tous les résultats que nous espérions. Je ne peux que souhaiter pour eux, mais évidemment pour moi aussi que les quelques mois ou années qu'il leur reste à travailler sur l'expérience soient pleins. Je retiendrai de Valentina sa force de travail et sa motivation, avec en point d'orgue l'expérience faite à Amsterdam où ils avaient instauré un 3X8 voire un 2X12 heures pendant quasiment deux mois. C'est une expérience qui restera gravée en elle, je pense. Il n'est pas courant qu'une collaboration expérimentale de durée aussi courte, sur un montage aussi complexe, soit une telle réussite. Je ne peux que la féliciter d'avoir géré cela, avec les autres, aussi efficacement. Quant à Jean-Christophe et à Marie, j'espère qu'ils tireront les bénéfices de leurs investissements présents et je conseillerai au premier d'augmenter le volume de sa voix, cela lui évitera d'avoir à se répéter tout le temps et à la seconde de ralentir son débit ; elle parle tellement vite que j'ai des fois du mal à la comprendre !*

J'ai également eu l'opportunité de travailler avec quatre post-doctorants, Stephan Nowak, Hong Chang, Vanessa Leung et Guthrie Partridge. En allemand qui se respecte Stephan a conçu une partie du bâti qui soutenait la partie ultra-vide de l'enceinte et a participé au premier piégeage magnétique de l'hélium métastable. Son inébranlable bonne humeur et son amour de la France en ont fait un collaborateur apprécié. Hong, arrivé de Chine après sa thèse, et qui a travaillé sur les expériences HBT fermion et paires atomiques, était un opticien hors pair ; un réglage de Hong ne pouvait se mettre en doute ! Il est dommage que la barrière de la langue est ralentie son insertion dans le groupe. Pour Vanessa, néozélandaise, ce problème ne se posait évidemment pas, c'est plutôt notre anglais qui devait lui faire mal aux oreilles. Elle est venue nous rejoindre sachant que nous devions déménager d'Orsay à Palaiseau. Cette période difficile s'est prolongée et cela l'a malheureusement empêché de participer à une compagne de données victorieuse. Des articles théoriques lui ont quand même permis de capitaliser sa période chez nous et j'espère que son nouveau post-doc dans le groupe de Cass Sackett de l'université de Virginie lui sera profitable. Finalement Guthrie nous a rejoint depuis un an. Ses qualités et son savoir-faire expérimental nous apportent déjà beaucoup et je l'en remercie.

Je remercie Michèle Leduc, Pierre Pillet, David Guéry-Odelin, Jean-François Roch et Gerhard Birkl pour avoir accepté de faire partie de mon jury d'habilitation et particulièrement les trois derniers pour y avoir contribuer en tant que rapporteurs. Je tiens finalement à remercier Gilbert Grynberg qui m'encadra pendant les débuts de ma thèse. Son enthousiasme pour la recherche, son imagination pour trouver une réponse possible à tous les résultats parfois délirants que nous obtenions, sa jubilation quand il parlait de science m'ont profondément marqué. Gilbert fut et restera pour moi un modèle.

Table des matières

Chapitre 1

Travaux de recherche

1.1 Thèmes de recherche :

Toutes mes activités de recherche se situent dans le domaine des “atomes froids”. Ce domaine de la physique atomique, dont les premières expériences datent de la fin des années 1980 explore les propriétés quantiques des atomes et de l’interaction lumière-matière. Ceci met en avant les aspects ondulatoires de la matière, d’où le terme d’optique atomique. Mes travaux de thèse, que je résumerai dans la section 1.2, portaient sur un mécanisme de refroidissement spécifique à certaines transitions atomiques et pouvaient être vus comme une nouvelle voie vers la condensation de Bose-Einstein. Celle-ci a été observée pendant ma thèse par une approche très différente où le refroidissement laser est abandonné au profit du refroidissement évaporatif.

C’est cette méthode que nous avons utilisé après mon arrivée en tant que maître de conférence dans le groupe d’optique atomique du laboratoire Charles Fabry de l’Institut d’Optique pour d’une part étudier ce nouvel état de la matière (partie “matière condensée” de mes recherches) et pour d’autre part utiliser ces propriétés de cohérence (partie “optique atomique quantique”). Plus précisément j’ai co-encadré avec Christoph Westbrook et Alain Aspect l’expérience *“hélium métastable"*. Nos recherches sont pour une grande part expérimentales, mais j’ai développé, seul ou avec un étudiant, un modèle théorique pour quasiment toutes les expériences que nous avons réalisées. Un résumé de ces recherches est donné en section 1.3.

1.2 Résumé de mes travaux de recherche doctoraux

Le refroidissement laser est une méthode extrêmement performante et permet de refroidir un échantillon gazeux à des températures proches du zéro absolu en une fraction de seconde [1, 2]. La température Doppler et la température sub-recul définissent trois régimes de température, correspondant à des mécanismes de refroidissement différents. La température Doppler est donnée par la largeur naturelle du niveau excité par le laser (40 μK pour l’hélium métastable et 120 μK pour le césium) et la température sub-recul par l’énergie minimale donnée par un photon spontané (4 μK pour l’hélium métastable et 0.2 μK pour le césium). Ces mécanismes de refroidissement standards ne sont efficaces qu’à faible densité atomique, quand la diffusion multiple de photons peut être négligée [1].

Or le seuil de condensation de Bose-Einstein n'est franchi qu'à des densités atomiques relativement fortes, de l'ordre de 10^{13} at/cm^3. L'épaisseur optique et donc la diffusion multiple sont alors très importantes. L'idée à la base de ma thèse était de démontrer un mécanisme de refroidissement où le taux de diffusion de photons est très faible, diminuant ainsi, pensait-on, le phénomène de diffusion multiple.

Le refroidissement laser traditionnel nécessite de travailler sur une transition atomique du type $J_f \rightarrow J_e = J_f+1$ avec un laser sur le rouge (fréquence plus faible que la fréquence de résonance atomique). Dans ce cas l'atome effectue en permanence des cycles d'absorption-émission spontanée. Par contre si on utilise une transition du type $J_f \rightarrow J_e = J_f - 1$ ou $J_f \rightarrow J_e = J_f$ avec un laser sur le bleu, on peut montrer que les atomes sont pompés et refroidis dans un état *gris* où le taux d'émission spontanée est très faible. Ma thèse a consisté à étudier ces mélasses grises sur la transition $6\ S_{\frac{1}{2}}\ F = 3 \rightarrow 6\ P_{\frac{3}{2}}\ F = 2$ de l'atome de césium. Les premières vérifications de l'efficacité de ce refroidissement ont été effectuées dans un réseau optique dissipatif à quatre faisceaux [6, 7]. Dans une mélasse optique à six faisceaux, la température limite de 1 μK est plus faible d'un facteur 3 qu'avec le refroidissement usuel sur le rouge, mais malheureusement le taux de chauffage par diffusion multiple est sensiblement le même [8]. La raison principale vient du fait que bien que le taux de diffusion de photons est de deux ordres de grandeur plus faible dans une mélasse grise, le temps de thermalisation est de deux ordres de grandeur plus long : il y a moins de photons spontanés mais leur effet est plus dévastateur.

Nous avons combiné ce refroidissement dans deux types de piège dipolaire utilisant un laser YAG : Nd^{3+} à 1064 nm. Dans le premier cas, il s'agissait d'un faisceau gaussien focalisé où nous avons mis en évidence que l'anisotropie élevée du piégeage diminuait fortement la réabsorption de photons et, dans le deuxième cas, un réseau holographique bi-dimensionnel réalisant par effet Talbot un piégeage tri-dimensionnel [9]. Nous avons obtenu une densité dans l'espace des phases de l'ordre de 10^{-3}, ce qui constituait à l'époque un record pour du refroidissement purement optique. Ce chiffre aurait sans doute pu être amélioré si le vide avait été de meilleure qualité ; la durée de vie pour ces expériences était de l'ordre de la seconde. L'image des atomes piégés dans le réseau optique a été utilisée comme première de couverture pour la revue des Comptes-rendus de l'Académie des Sciences pendant l'année 1998.

1.3 Travaux de recherche post-doctoraux

Dès mon arrivée à l'Institut d'Optique, nous avions décidé de nous lancer dans la course de la condensation de Bose-Einstein de l'hélium métastable. Cet atome a en effet un atout : sa métastabilité. Son énergie interne de 20 eV est suffisamment grande pour que cet atome puisse être détecté électroniquement de façon très efficace par une galette de micro-canaux ; il est ainsi possible de faire du comptage d'atomes uniques, d'où la thématique optique atomique quantique. De plus, la probabilité d'avoir une ionisation lors d'une collision entre deux ou trois atomes d'hélium métastable est assez importante aux densités atomiques

---

[1] Le refroidissement Doppler dans un piège magnétique [3, 4] ou le refroidissement dit "festina lente" [5] n'a pas cet inconvénient.

auxquelles nous travaillons. Les ions produits, détectables par la même galette permettent d'avoir un diagnostic in situ original de la densité atomique.

On peut chronologiquement distinguer trois périodes. De 1998 à 2004 nous avons obtenu le condensat et étudié ces propriétés collisionnelles. Ceci sera décrit dans le chapitre 2. De 2004 à 2007 nous avons mesuré les propriétés de corrélation à deux corps des nuages au-dessus ou en dessous de la dégénérescence quantique, suite à une amélioration de notre système de détection (chapitre 3). Depuis 2006, nous avons commencé une nouvelle thématique portant sur l'optique atomique quantique et une première expérience sur la création de paires d'atomes a déjà eu lieu. Ceci sera décrit dans le chapitre 4.

Je donne un bref résumé ci-dessous des principaux résultats de nos travaux de recherche.

1.3.1 Condensation de Bose-Einstein de l'hélium métastable

Condensation de Bose-Einstein de l'hélium métastable : L'obtention d'un condensat de Bose-Einstein passe par une étape de refroidissement évaporatif qui nécessite d'avoir de "bons" paramètres collisionnels. Cela signifie qu'il faut beaucoup de collisions élastiques et peu de collisions inélastiques. Les constantes de collisions utiles n'avaient jamais été mesurées et il était notoirement connu que dans un piège magnéto-optique d'hélium métastable les collisions inélastiques sont très importantes [10]. De plus les nuages d'hélium métastable étaient peu denses et relativement chauds. En conclusion, le succès d'une telle expérience n'était pas du tout garanti.

Après de nombreuses modifications du montage expérimental, nous avons entrepris d'estimer l'importance des collisions élastiques. J'ai établi un modèle simulant une expérience originale de thermalisation que nous avons menée au laboratoire. L'analyse des résultats montrait que la condensation de Bose-Einstein pouvait être obtenue avec le nuage atomique et le piège dont nous disposions [11]. La condensation a effectivement été observée quelques mois plus tard [12, 13].

Propriétés collisionnelles d'un gaz dégénéré d'hélium métastable : L'obtention d'un condensat, ou d'un nuage froid très dense, permet en principe de mesurer les constantes de collisions élastiques et inélastiques. Ces dernières sont généralement considérées comme néfastes car elles limitent les densités atomiques accessibles. Dans le cas de l'hélium métastable, elles ouvrent, au contraire, des perspectives extrêmement intéressantes car elles conduisent majoritairement à l'ionisation d'un atome d'hélium. Ces ions pouvant être détectés avec une efficacité proche de 100%, ils constituent un outil de mesure très précieux. C'est dans cette optique qu'une série d'expériences a d'abord été menée sur des condensats [14, 15] puis sur des nuages proches du seuil de condensation [16, 17]. La longueur de diffusion, paramètre des collisions élastiques, et les constantes de collisions inélastiques à deux et trois corps ont pu être extraites de ces mesures.

1.3.2 Corrélation Hanbury Brown et Twiss sur des gaz ultra-froids de ^{4}He* et ^{3}He*

La détection par galette de micro-canaux des expériences précédentes ne permettait que de remonter au flux d'atomes d'hélium métastable tombant sur notre détecteur. L'ajout de lignes à retard sous la galette [18] rend ce détecteur sensible en position. On peut alors considérer que nous disposons d'un détecteur 3D (deux positions et un temps d'arrivée) qui ouvre la voie à de nombreuses expériences, dont les mesures de fonction de corrélation.

L'expérience conceptuellement la plus simple, mais expérimentalement très exigeante, est la mesure de la fonction de corrélation à deux particules, autrement appelée corrélation d'intensité ou corrélation Hanbury Brown et Twiss [19, 20]. La probabilité de trouver une particule bosonique en $\mathbf{r}$ sachant qu'une autre a été mesurée en $\mathbf{r}'$ est plus importante pour $|\mathbf{r} - \mathbf{r}'|$ petit, ceci même s'il n'existe aucune interaction entre particules. En optique, on parle de groupement de photons. Bien qu'il existe une interprétation totalement classique de ce phénomène, celui-ci prend tout son sens en mécanique quantique en terme d'interférence constructive entre chemins indiscernables. La mécanique quantique prévoit que le groupement se produit pour des bosons alors qu'il s'agit d'"anti-groupement" pour des fermions (principe d'exclusion de Pauli). Nous avons réalisé cette mesure sur un nuage très froid de bosons et sur un condensat. Comme en première approximation un condensat est un état pur, la fonction de corrélation attendue est plate, ce que nous avons effectivement observé, en parallèle de l'observation du groupement pour un nuage "chaud" [21]. J'ai développé avec J. Viana Gomes un calcul analytique de la fonction de corrélation sur un nuage en expansion libre sous l'effet de la gravité afin de comparer théorie et expérience [22]. L'accord était très satisfaisant.

Nous avons mené au cours de l'été 2006 une collaboration avec l'équipe de W. Vassen à l'université libre d'Amsterdam sur des nuages fermioniques d'Hélium 3 métastable. Nous avons effectivement observé une diminution de la fonction de corrélation à courte distance [23].

1.3.3 Création de paires d'atomes corrélés

Il s'agit d'une étape supplémentaire par rapport à l'expérience précédente. Les corrélations HBT que nous avions étudiées étaient une conséquence de la statistique quantique de nuages à l'équilibre thermodynamique. Dans cette nouvelle thématique, nous avons cherché à créer des sources non classiques. Dans ce premier exemple nous avons créé des paires d'atomes corrélés. Il s'agit de la brique élémentaire pour faire de l'optique atomique quantique, comme une mesure EPR par exemple ou du squeezing. L'idée de base pour la création de paires d'atomes corrélés est de créer par faisceaux Raman deux condensats qui ont une vitesse relative suffisamment importante pour qu'il y ait des collisions élastiques entre eux. La distribution de vitesse d'un condensat étant très faible par rapport à cette vitesse relative, les vitesses de deux atomes ayant subis une collision sont fortement corrélées [24, 25]. On peut voir ce mécanisme comme un mélange à quatre ondes spontané.

Chapitre 2

Condensation de Bose-Einstein de l'hélium métastable

2.1 Introduction

Depuis 1995 et la naissance des condensats de Bose-Einstein gazeux sur le sodium, rubidium et lithium [26, 27, 28], la physique atomique et plus particulièrement l'optique atomique se devait d'évoluer pour étudier et utiliser ces sources atomiques cohérentes. Le groupe optique atomique du LCFIO a ainsi démarré une expérience de condensation de rubidium en 1996 et observé un condensat en 1998 [29] peu avant mon arrivée dans le groupe. Nous avons entrepris de "condenser" un autre atome, l'hélium métastable. On peut se demander pourquoi il est nécessaire ou utile d'avoir des condensats d'atomes différents [1]. La réponse est multiple. Comme en optique, même si tous les lasers ont en gros les mêmes propriétés, l'interaction avec la matière dépend elle fortement de la longueur d'onde et donc permet de mener des études sur des matériaux différents et donc augmente considérablement leur intérêt. Pour les atomes c'est identique ; chaque atome a une structure interne particulière, des propriétés collisionnelles différentes et des méthodes de détection différentes. Il est donc important de choisir tout nouveau candidat à la condensation de Bose-Einstein dans cette perspective.

L'hélium métastable répond parfaitement à ce cahier des charges : il n'a pas de structure hyperfine, les processus collisionnels inélastiques sont très différents de ceux des alcalins (cf section 2.5.1) et permettent un diagnostic original (section 2.3). De plus ayant une grande énergie interne, *il se détecte très facilement et très efficacement* (section 2.3). Ce dernier point est le point clé de la plupart des expériences que je décrirai et est l'argument principal pour tenter l'aventure de la condensation de l'hélium métastable.

Après les premières observations de la condensation en 1995, de très nombreux groupes ont démarré une activité de recherche dans ce domaine. Parmi les premières travaux expérimentaux, on peut citer l'étude des excitations élémentaires [30, 31, 32], des propriétés de cohérence des condensats [33], l'observation d'un laser à atomes [34, 35], de condensats dans plusieurs états internes ("spinor condensate") [36]. Je renvoie aux articles de

---

[1] La très grande majorité des équipes a choisi l'atome de rubidium pour sa "facilité" à se condenser.

revue [37, 38, 39, 40] et aux ouvrages [41, 42] pour une bibliographie plus détaillée. Je reviendrai dans la section 2.6 sur les principaux travaux dans ce domaine de recherche après 2001 en général et sur les condensats d'hélium métastable en particulier.

Ce chapitre commence par une description de l'hélium métastable avant d'aborder la méthode de détection électronique que nous utilisons. Je décrirai ensuite l'expérience qui nous a permis d'observer la condensation et poursuivrai par les propriétés collisionnelles, élastiques et inélastiques. Je terminerai par quelques perspectives de recherche dans la section 2.7.

Cette partie décrit les expériences effectuées durant la période 1998-2004 et correspond au travail de thèse d'Antoine Browaeys [43], d'Alice Robert [13], d'Olivier Sirjean [15], de Signe Seidelin [16], de Rodolphe Hoppeler [19] et de Jose C. Viana Gomes [44].

2.2 Description de l'hélium métastable

L'hélium est un atome étudié/utilisé tant en matière condensée avec l'hélium liquide qu'en astrophysique puisque c'est un atome abondant dans les étoiles. C'est également un atome dont la structure interne est relativement simple à décrire car il n'a que deux électrons et quatre nucléons. Des mesures spectroscopiques, sur ^{3}He et ^{4}He, sont d'ailleurs toujours menées pour en déduire des mesures de la constante de structure fine [45, 46, 47] ou de tailles nucléaires [48].

Un diagramme d'énergie simplifié se trouve figure 2.1. Les deux états $2\ ^1S_0$ et $2\ ^3S_1$ sont métastables mais la durée de vie de l'état singulet n'est que de 19.5 ms (transition dipolaire électrique à deux photons [49]) alors qu'elle vaut de l'ordre de 2 h pour l'état triplet (transition dipolaire magnétique au premier ordre [50, 49]) du fait de la violation de la conservation du spin. La conservation au premier ordre du spin implique également que tous les états triplets excités vont se désexciter préférentiellement vers l'état $2\ ^3S_1$ et non vers $1\ ^1S_0$ ou $2\ ^1S_0$. L'état $2\ ^3S_1$ peut ainsi être considéré comme un état fondamental à l'échelle de la durée des expériences. C'est l'état que nous utilisons dans nos expériences et je le noterai He* dans la suite. Je reviendrai brièvement sur la méthode de production de ces atomes dans la section 2.4.

En réalité, il existe une petite probabilité que les états triplets se désexcitent vers l'état fondamental en émettant des photons UV ($\lambda \sim 62$ nm) [51]. Une partie de la thèse de Julie Poupard consistait à étudier les deux transitions $2\,^3P_1 \rightarrow 1\ ^1S_0$ (transition dipolaire électrique via un couplage avec l'état singulet $2\ ^1P_1$, de taux de départ ~ 177 s^{-1}) et $2\,^3P_2 \rightarrow 1\ ^1S_0$ (transition quadrupolaire électrique, ~ 0.33 s^{-1}) en détectant directement les photons UV émis sur la galette de micro-canaux (cf 2.3). Nous avons pu mesurer la durée de vie et le diagramme de rayonnement de ces deux transitions. L'accord avec la théorie n'était pas trop satisfaisant sur la transition $2\,^3P_1 \rightarrow 1\ ^1S_0$ (facteur 3 sur la durée de vie) et nous estimons après coup que cela était dû à une mauvaise calibration du nombre d'atomes.

Le refroidissement laser s'effectue sur la transition $2\ ^3S_1 \rightarrow 2\ ^3P_2$ mais nous avons également utilisé la transition $2\ ^3S_1 \rightarrow 2\ ^3P_0$ pour effectuer des transitions Raman (cf chapitre 4 sur la création de paires d'atomes corrélés). Ces deux transitions sont à une

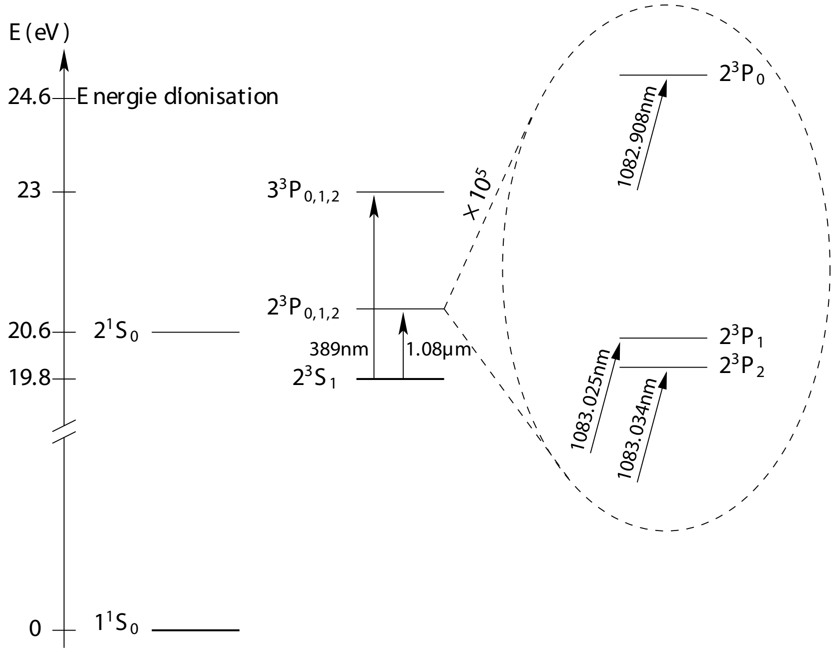

FIG. 2.1 – *Diagramme d'énergie simplifié de l'atome d'hélium. L'état 2* $^3S_1$*, noté He* dans la suite, est un état métastable de grande durée de vie. La transition vers l'état 2* $^3P_2$ *est quasi-fermée et accessible expérimentalement avec une diode laser à 1083 nm. Cette transition est utilisée pour le refroidissement laser.*

longueur d'onde de 1083 nm, la largeur naturelle des états excités est de $\Gamma/2\pi = 1.6$ MHz et l'intensité de saturation 0.16 mW/cm^2. Il existe des diodes DBR (50-70 mW) et depuis quelques années des lasers à fibre (jusqu'à 10 W !) à cette longueur d'onde.

2.3 Méthode de détection

2.3.1 Méthode optique

La détection optique est *la* méthode utilisée en atomes froids. Cela peut être une mesure de fluorescence, d'absorption voire d'indice (par contraste de phase par exemple). Malheureusement 1.08 μm se trouve à l'extrême limite du gap du silicium et les meilleures détectivités sont de l'ordre de 2% sur une caméra CCD, donc bien faibles [2]. Les caméras en InGaAs sont plus sensibles, $\sim$ 60%, mais ont trop de bruit pour donner de résultats meilleurs que les CCD au silicium. Un autre point délicat quand on veut faire une imagerie optique sur He* est la vitesse de recul de 9.2 cm/s. Cette vitesse élevée fait qu'un

---

[2] Les caméras bas bruit sont généralement refroidis. Comme le gap du silicium augmente quand la température diminue, la détectivité à notre longueur d'onde est significativement plus faible à basse température et nous avons constaté une baisse d'un facteur deux entre 20°C et -60°C lors d'un test sur une caméra Hamamatsu.

atome sort très vite de résonance au fur et à mesure qu'il absorbe des photons ; une mesure quantitative du nombre d'atomes est donc délicate [3].

Malgré ces inconvénients, il faut reconnaître que la facilité d'exploitation des images, la qualité des détecteurs CCD en terme de bruit, de linéarité et de résolution spatiale et la possibilité de choisir le moment où on veut observer le nuage pendant le temps de vol ou in situ, en font une méthode de détection précieuse et très utile, que nous avons regrettée à plusieurs moments de ne pas avoir. Notre choix, en effet, s'est porté dès le départ sur une détection électronique.

2.3.2 Méthode électronique

Généralités : L'énergie interne d'He* est suffisamment grande pour pouvoir extraire des électrons lors de son impact sur une surface solide [52]. Sur une surface métallique, il s'agit d'un mécanisme d'ionisation résonante $He^* + A \rightarrow He^+ + A^-$ suivi d'une neutralisation Auger $He^+ + A^- \rightarrow He + A^+ + e^-$ et des détectivités de l'ordre de 60% ont été mesurées [53, 54, 55]. Cette production efficace d'électrons permet d'envisager la détection de particules uniques d'He*. Pour cela il faut amplifier ce signal électronique. C'est le rôle d'une galette de micro-canaux (microchannel plate en anglais que je noterai MCP dans la suite) [4] [56]. Ce schéma de détection (plaque métallique et galette de micro-canaux) a été employé, par exemple par Shimizu [57], mais généralement on place directement la galette sous le flux d'He*.

Jusqu'en 2004 la douche d'électrons à la sortie du MCP était détectée sur une anode de la taille de la galette. Depuis, l'utilisation d'une anode composée de lignes à retard permet de connaître la position de l'impact des He* sur la surface de la galette. Comme ce détecteur est l'atout principal de notre expérience, je vais détailler un peu son fonctionnement et ses performances.

Description d'une galette de microcanaux : On peut se référer aux thèses d'Olivier Sirjean [15] et de Martijn Schellekens [20] pour une étude détaillée.

Une galette de micro-canaux se compose d'un ensemble de fibres creuses collées entre elles. Leur face interne est traitée pour maximiser l'éjection d'électrons par les particules incidentes (ions, photons UV, X, gaz rare métastable) et les faces avant et arrière sont métallisées pour imposer une différence de potentiel de l'ordre de 1 kV afin d'accélérer ces électrons et de provoquer un mécanisme d'avalanches. Une galette a un gain de l'ordre de 10^4 mais la distribution du gain est quasi-exponentielle et il n'est donc pas possible d'utiliser ce système en comptage. Par contre deux galettes en série ont un gain de l'ordre de 10^7 et surtout la distribution du gain est piquée [56] ; il est alors possible de fixer un discriminateur sous le gain moyen pour éliminer le bruit électronique et de détecter la quasi-totalité des impulsions électriques. Ce régime de fonctionnement permet donc de faire du comptage. Nous n'avons pas de mesures précises de détectivité mais une estimation de

---

[3] La solution généralement adoptée est de rétroréfléchir le faisceau d'imagerie pour minimiser cet effet.

[4] Une autre solution est le channeltron, version "macroscopique" moins onéreuse d'une galette de micro-canaux.

10 % basée sur une comparaison entre notre détecteur et une mesure optique [5].

Ce type de détecteur est très linéaire tant que le flux d'He* n'est pas trop fort. Il n'existe pas de chiffres absolus dans la littérature, car cela dépend du type exact de galettes (constructeur, traitement des faces internes, densité des fibres ...), de la taille du nuage d'He*, mais un ordre de grandeur est 10^5 coups/s/cm^2. Expérimentalement les temps de vol des condensats de Bose-Einstein sont fortement perturbés par cette saturation car trop dense. C'est pourquoi ce régime de comptage n'a pas été utilisé avant 2004 pour les temps de vol mais uniquement pour la détection des ions He^+ (cf. 2.5.1). Pour les temps de vol nous travaillions à haute tension plus faible et faisions une détection analogique des nuages (filtre passe-bas sur l'anode). Depuis 2004, nous travaillons en comptage et devons donc vivre avec la saturation sur les nuages atomiques trop denses car l'information spatiale n'est accessible que dans ce régime de fonctionnement.

Détection des ions : Comme nous le verrons dans la section 2.5.1, un nuage d'He* produit des ions He$^+$ et des électrons. Ces particules sont chargées donc peuvent être attirées et accélérées suffisamment pour pouvoir déclencher une avalanche dans une galette de micro-canaux. Une efficacité de détection de 60% est atteinte pour He$^+$ si la tension accélératrice dépasse 1 kV [58]. Ce pourcentage correspond en fait au rapport de la surface ouverte formée par les trous des fibres par la surface totale du MCP. Il est en principe possible d'améliorer encore ce pourcentage en ajoutant une grille au-dessus du détecteur pour permettre aux électrons éjectées depuis sa surface métallique d'être réinjectés dans une fibre creuse ; cette méthode a été validée par l'équipe de B. Deconihout dans un contexte différent et une détectivité de l'ordre de 80% a été mesurée [59].

Comme nous le verrons dans la suite de ce chapitre, cette détection des ions constitue une mesure in situ non invasive de la densité atomique d'un nuage ultra-froid d'He*. Le temps de transit de la zone de production des ions au détecteur est inférieure à la microseconde ; ce temps est donc court devant les temps caractéristiques de la dynamique dans des nuages ultra-froids. Il s'agit donc d'un diagnostic original, permettant de faire des mesures en temps réel, que nous avons mis à profit pendant la période 2001–2004 [13, 15, 60, 17], pour observer le seuil de la condensation de Bose-Einstein et mesurer les constantes de collisions (cf. 2.5).

Détection des atomes par temps de vol : Une fois le nuage atomique créé, le piège est coupé et les atomes tombent sous l'effet de la gravité. Après un temps de chute t, une "image" du nuage est réalisée. Comme annoncé précédemment, cette image est traditionnellement obtenue par absorption d'un faisceau laser résonnant. Notre méthode consiste à laisser tomber le nuage jusqu'au détecteur et mesurer le flux $\phi(t)$ ou $\phi(x, y, t)$. Quelque soit la méthode d'imagerie, l'analyse d'un temps de vol nécessite de connaître l'évolution du nuage pendant la chute. Lorsque les interactions peuvent y être négligées, ceci ne pose pas de problème et des solutions analytiques existent dans les cas simples. Par exemple, si t est suffisamment grand, la distribution des positions dans l'image correspond à la distribution des vitesses dans le piège. Les choses se compliquent singulièrement si les

---

[5] Cette mesure a été faite lors de notre séjour à Amsterdam dans le cadre d'une collaboration sur la mesure de l'effet Hanbury Brown et Twiss sur des fermions que je décrirai au chapitre 3.

interactions doivent être prises en compte. A ma connaissance, seul le cas d'un condensat de Bose-Einstein pur ($T = 0$) piégé dans un potentiel harmonique [61, 62] est connu analytiquement.

La figure 2.2 illustre la forme du flux d'ions pour différentes températures. Pour un détecteur de taille finie D placé à une distance h sous le piège, deux régimes apparaissent suivant l'importance relative de l'énergie cinétique $k_B T$ et de l'énergie potentiel mgh. Si l'énergie cinétique domine, les trajectoires atomiques sont des lignes droites, le temps d'arrivée typique est donné par $h/\sqrt{k_B T/m}$ et le nombre d'atomes détecté varie comme D^2/h^2. Plus la température baisse, plus les trajectoires sont courbées et plus la détectivité est grande. Quand l'énergie potentielle domine, le temps d'arrivée moyen vaut $\sqrt{2g/h}$ et la largeur temporelle du flux, $\sqrt{k_B T/m}/g$, diminue avec la température.

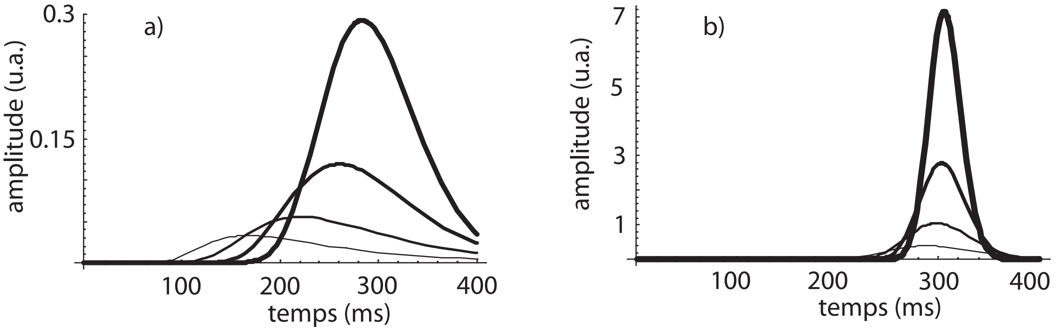

FIG. 2.2 – *Flux atomique au niveau du détecteur positionné à* $h = 46.6$ *cm de la zone de piégeage pour différentes températures du nuage. Sur le graphe a) les températures sont* $T = 1, 0.5, 0.25$ *et 0.125 mK de la courbe la plus claire à la plus foncée. Sur le graphe b) les températures sont* $T = 100, 50, 25$ *et* 12.5 μK *de la courbe la plus claire à la plus foncée. Le nombre d'atomes est identique pour toutes les courbes. La taille finie du détecteur (8 cm de diamètre) fait que le nombre d'atomes détectés croît quand la température baisse. Tous les atomes sont détectés pour une température de* 1 μK *alors que pour* 12.5 μK *seuls 30 % sont détectés ; ce nombre chute à 0.6 % à 1 mK. La taille finie du détecteur est aussi responsable du temps moyen d'arrivée. A haute température, ce temps* $\approx h/\sqrt{k_B T/m}$ *augmente quand la température baisse ; à basse température ce temps se fige à la valeur donnée par la gravité,* $\sqrt{2g/h}$.

Plus généralement, pour des nuages ultra-froids, on s'attend à ce que le flux soit de forme gaussienne, sa largeur permettant de mesurer la température et son aire le nombre d'atomes. Pour un condensat de Bose-Einstein dans le régime Thomas-Fermi [37, 61, 62], la forme est une parabole inversée dont la largeur est reliée au potentiel chimique car les interactions entre atomes prédominent sur leur énergie cinétique.

Résolution temporelle : Le phénomène d'avalanche dans une galette de micro-canaux est très rapide, de l'ordre de quelques centaines de picosecondes. Il faut cependant tenir compte du fait que la chaîne électronique peut avoir des temps morts, que l'adaptation des impédances n'est jamais parfaite, etc. Cela nous a conduit a imposé un temps mort dans le traitement des données de typiquement 300 ns (le temps mort minimal atteignable est de l'ordre de 20 ns). Ces échelles de temps sont bien inférieures à toutes les constantes de temps que l'on peut trouver dans des expériences sur des condensats. On peut ainsi considérer que la résolution est infiniment bonne.

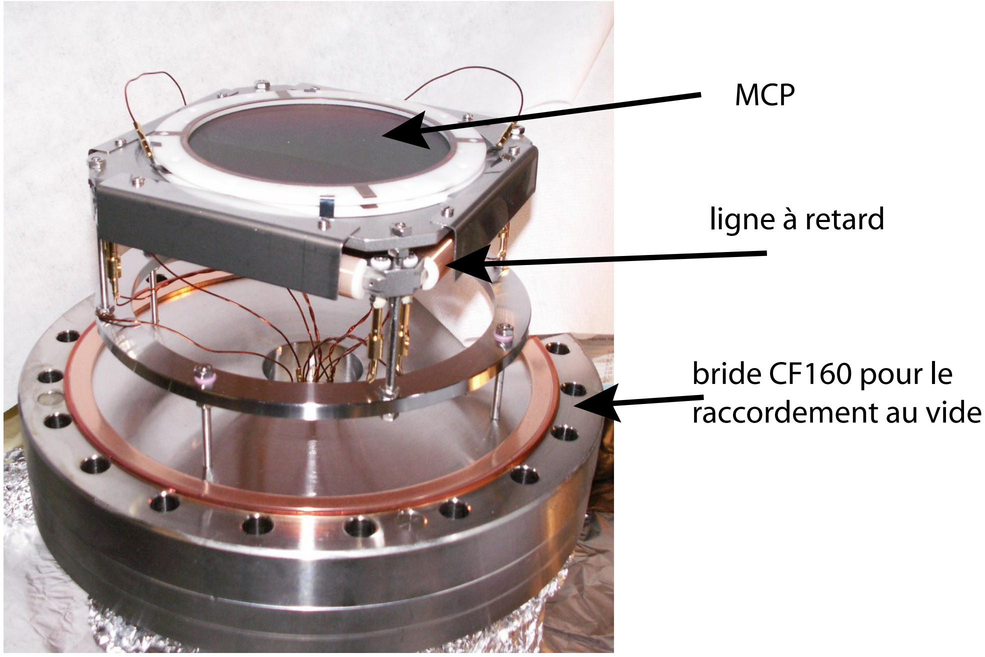

FIG. 2.3 – *Photo du détecteur. En premier plan ce trouve la galette de micro-canaux Hamamatsu de 8 cm de diamètre ; on entre-aperçoit l'enroulement des lignes à retard sous un cache métallique en forme de L.*

Résolution spatiale avec anode à lignes à retard : La figure 2.3 montre une photo du détecteur et le schéma sur la figure 2.4 illustre le principe de fonctionnement. L'idée est de coder la position par une mesure de différence de temps d'arrivée de l'impulsion électrique aux deux bouts de la ligne [18]. Les lignes à retard sont en fait des lignes de transmission pour minimiser la dispersion au cours de la propagation. On détecte avec notre électronique des impulsions de 20 ns de large que l'on parvient à pointer à 700 ps près. Si on compare avec des montages similaires (très souvent utilisés pour l'étude de collisions entre ions par exemple), on devrait être capable de faire mieux et être limité par la pas de codage, qui est de 275 ps actuellement. Notre résolution spatiale actuelle de 300 μm rms pourrait donc devenir de l'ordre de $100 - 150$ μm en travaillant sur l'électronique. Ceci serait une amélioration importante car les expériences présentées aux chapitres 3 et 4 ont un rapport signal à bruit et une résolution limités par cette résolution.

Il faut noter qu'il existe de très nombreux types d'anodes/systèmes de mesure comme un réseau d'anodes discrètes [63], des mesures par division de charge (anode résistive [6] [64],

---

[6] C'est ce type d'anode qui fut utilisé à l'ENS dans les expériences de refroidissement sub-recul VSCPT.

anode Vernier [65], ...), etc... Certaines méthodes permettent d'obtenir des résolutions spatiales bien meilleures, 10 μm rms ayant par exemple été démontrée dans Ref. [65] mais le détecteur "parfait" n'existe pas encore. En particulier la plupart des dispositifs ne fonctionnent qu'à des flux de particules bien plus faibles (quelques 10^3 coups/s) que ceux des temps de vol typiques de notre expérience (jusqu'à 10^6 coups/s). Mais des progrès constants sont réalisés [66] et on peut raisonnablement être optimiste pour l'avenir.

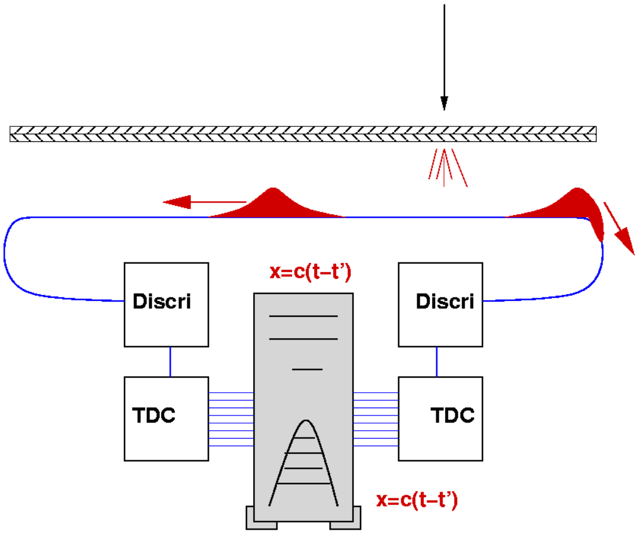

FIG. 2.4 – *Schéma de principe de fonctionnement d'un détecteur composé de galettes de micro-canaux et de lignes à retard pour la mesure de la position. Le point d'impact de la douche électronique à la sortie de la galette est déterminé par la mesure de la différence de temps d'arrivée aux deux bouts de la ligne à retard.*

Limitations actuelles : J'ai déjà énoncé plus haut deux limitations de notre détecteur : la saturation à haut flux et la résolution spatiale. Il reste une dernière limitation non due au détecteur en lui-même mais à notre montage expérimental : nous ne détectons pas tous les atomes à la coupure du piège magnétique (cf. 2.4). Une mesure de la composante du champ magnétique parallèle au biais est reportée sur la figure 2.5 [13]. On y observe une décroissance très rapide du champ, une inversion, puis un retour lent à zéro. On attribue la décroissance rapide à la coupure des alimentations de courant et la lente à des courants de Foucault, difficilement évitables dans une enceinte métallique. On a pu montrer, par effet Stern et Gerlach, que la plupart des atomes suivent le retournement du champ et donc restent dans l'état piégeant $m = 1$. Une faible partie passe dans $m = 0$ par transfert non adiabatique [7]. Notre enceinte n'a pas de blindage magnétique et la distance du piège au détecteur est très grande (47 cm dans la version actuelle). En conséquence, le nuage d'atomes dans $m = 1$ subit une décompression lente de son confinement et sera très, trop sensible, au champ magnétique parasite pendant la chute. En conséquence, ces atomes sont inutilisables. Par contre les atomes dans $m = 0$ sont insensibles au champ et toutes nos

---

[7] Une fraction encore plus faible passe dans $m = -1$.

expériences sont basées sur des mesures faites sur cet état interne. Le taux de transfert est cependant faible, estimé à ≈ 10%, n'est pas totalement maîtrisé et varie suivant les caractéristiques du nuage d'atomes [60]. Cela nous empêche d'avoir une mesure fiable du nombre d'atomes dans le piège à partir du nombre d'atomes que nous détectons sur la galette. Je reviendrai sur ce problème dans la section 2.5.2.

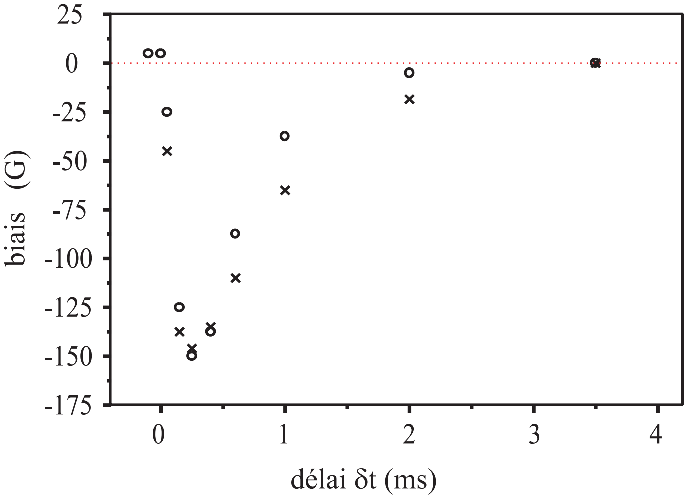

FIG. 2.5 – *Valeur du champ magnétique sur l'axe du biais en fonction du temps. Le piège est coupé à $t = 0$. On observe que le champ se retourne très rapidement puis décroît lentement vers 0. Une expérience complémentaire, décrite dans la thèse d'A. Robert [13] montre que la composante transverse du champ ne s'annule pas en même temps et donc que la plupart des atomes suivent adiabatiquement l'état $m = 1$ pendant la coupure. Une partie des atomes effectue néanmoins une transition non adiabatique vers $m = 0$ et ce sont ces atomes et uniquement ceux-ci que nous détectons avec la galette de micro-canaux.*

Conclusion : Notre système de détection électronique permet de connaître le temps et la position d'arrivée des atomes d'hélium métastable sur la galette. On peut donc considérer que c'est un détecteur 3D. De plus nous sommes capables de compter les atomes. Il s'agit donc d'un outil extrêmement performant encore unique dans la communauté atomes froids, qui trouvera toute son utilité dans les expériences de corrélation que je décrirai dans les chapitres 3 et 4. J'aurai l'occasion de revenir sur une autre méthode de détection de particules uniques basée sur une cavité optique en couplage fort dans le chapitre 3. On peut également signaler que le groupe de C. Zimmermann développe une méthode de détection par ionisation d'atomes de rubidium [67, 68] et celui de H. Ott [69, 70] par ionisation par un faisceau électronique de taille sub-micronique.

2.4 Condensation de Bose-Einstein

Outils nécessaires pour obtenir un condensat : Le phénomène de condensation se produit quand la distance typique entre atomes est de l'ordre de grandeur de la longueur d'onde thermique de de Broglie. Comme les densités atomiques maximales sont de l'ordre de 10^{15} at/cm^3 (limitation due aux processus inélastiques à deux et/ou trois corps, cf. section 2.5.1), la température du nuage doit être de l'ordre du microKelvin. Compte tenu de la taille des nuages atomiques confinés dans un potentiel localement harmonique [8], le nombre d'atomes minimum est de l'ordre de 10^3 à la température de transition.

On caractérise la proximité au seuil de condensation par le paramètre de dégénérescence $n\lambda_{th}^3$ où n est la densité pic et $\lambda_{th} = h/\sqrt{2\pi m k_B T}$ la longueur d'onde thermique de de Broglie. Dans une enceinte ultra-vide (nécessaire pour limiter les collisions inélastiques) à température ambiante, ce paramètre est de l'ordre de 10^{-20}. Il faut donc gagner 20 ordres de grandeur pour aboutir à la condensation ! Je vais décrire rapidement, et en utilisant les chiffres de notre expérience, les différentes étapes à franchir.

Montage expérimental : Quand je suis arrivé dans l'équipe "hélium métastable" (composée à l'époque d'A. Browaeys, J. Poupard et C. I. Westbrook) celle-ci étudiait les collisions Penning assistées par la lumière dans un piège magnéto-optique (cf. section 2.5.1). La durée de vie mesurée sur les atomes n'était que de quelques centaines de milliseconde et donc inadaptée pour des expériences de condensation. Une modification du montage expérimental avait déjà été décidée (enceinte ultra-vide, montage d'un MCP sous vide, etc...) et j'ai finalisé avec eux le dessin de la nouvelle enceinte à vide. Antoine Browaeys a été le principal artisan de ces changements [43].

Source et piège magnéto-optique : Dans notre montage la source est un jet supersonique d'hélium, refroidi à l'azote liquide, et excité dans l'état métastable par une décharge sous vide de 2 kV [43]. Ce jet, refroidi transversalement et longitudinalement par laser, charge un piège magnéto-optique. On obtient typiquement quelques 10^8 atomes à une température de 1 mK. Le paramètre de dégénérescence vaut de l'ordre de 10^{-7}. Le refroidissement laser est donc très efficace et absolument nécessaire à l'heure actuelle [9]. L'étape suivante est de transférer ce nuage dans un piège magnétique et de faire du refroidissement évaporatif.

Piège magnétique : Nous avons débuté en 1999 par un piégeage magnétique quadrupolaire [75] dont le succès nous a amené vers un piège Ioffe-Pritchard de type "clover-leaf" [76]. Contrairement au premier, celui-ci ne souffre pas des transitions de Majorana [77] car son biais (minimum du module du champ) est non nul. Nous travaillons avec des biais entre 150 et 300 mG ; cela conduit à des fréquences d'oscillation le long de l'axe du biais de l'ordre de

---

[8] En excluant le cas particulier des réseaux optiques dont je reparlerai brièvement, je ne connais qu'une seule expérience où le confinement n'est par harmonique : l'équipe de M. Raizen a créé par un ensemble de quatre faisceaux dont deux faisceaux TEM$_{01}$ un piège qui, dans une direction, est proche d'une boite [71].

[9] Le refroidissement laser étant peu efficace pour des molécules, des approches alternatives ont été utilisées comme les décélérateurs Stark [72], le refroidissement par gaz tampon [73, 74] mais les températures atteintes sont encore élevées, dans la gamme de la dizaine de mK.

50 Hz et de 1000 à 2000 Hz transversalement. De plus ce piège a l'avantage de n'avoir des bobines que dans deux plans parallèles (un agencement des bobines est représenté sur la figure 2.6). L'enceinte est métallique et non en verre pour deux raisons. Tout d'abord une enceinte métallique est beaucoup plus flexible pour d'éventuelles modifications ultérieures. Enfin le métal est aussi une immense masse électrique, ce qui garanti un comportement sain quand on applique plusieurs kV pour le fonctionnement des galettes de microcanaux (le verre a tendance à se charger et modifie donc la carte de champ électrique). Cela a cependant comme inconvénient que les bobines de champ magnétique sont assez éloignées de la zone du piège [10] et donc que les performances de celui-ci sont modestes.

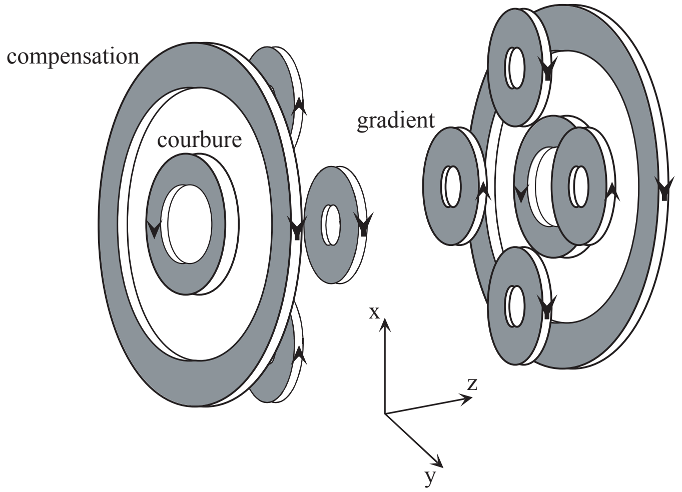

FIG. 2.6 – *Piège magnétique de type clover-leaf. Avec un courant de 200 A, on obtient un gradient transverse* $B' = 80$ *G/cm et une courbure longitudinale* $B'' = 20$ *G/cm*^{2}.

Refroidissement évaporatif : Une fois dans le piège magnétique il faut utiliser le refroidissement évaporatif [11] [79, 80]. L'idée de ce refroidissement est d'expulser du piège les atomes les plus énergétiques par une onde RF effectuant une transition dipolaire magnétique vers un état non piégeant et laisser les atomes restants se thermaliser par collision élastiques. En diminuant petit à petit la fréquence de l'onde RF, on diminue la température et, si la perte d'atomes n'est pas trop importante, on augmente la densité et la densité dans l'espace des phases jusqu'à l'obtention du condensat. Ce refroidissement n'est efficace que si le taux de collisions élastiques est bien supérieur au taux de collisions inélastiques. Je reviendrai sur les mesures de ces collisions dans la section 2.5.

---

[10] L'option "bobines dans l'enceinte à vide" est évidemment intéressante du point du vue du champ magnétique mais plus risquée du point du vue de la qualité du vide. En pratique, cette option n'est utilisée que dans les montages à puce atomique [78] pour lesquels les contraintes de vide sont relâchées du fait de la rapidité d'obtention d'un condensat (quelques secondes).

[11] Depuis 2005 nous appliquons au préalable une phase de refroidissement Doppler dans le piège magnétique [4] permettant de diminuer la température d'un facteur deux avec une perte d'atomes de ~ 10 % [24].

Condensats : Je présente figure 2.7 les premières données qui montraient l'obtention du condensat dans la nuit du 12 février 2001. On retrouve bien le type de courbes présentées sur la figure 2.2 mais avec une différence notable : le signal détecté diminue ici fortement avec la température. Ceci est évidemment dû à la perte d'atomes pendant le refroidissement évaporatif. Expérimentalement cela veut dire que le signal diminue pendant le refroidissement pour être quasiment indétectable pour une gamme de température vers les $20-50$ μK. Nous n'arrivions jamais à avoir un signal dans cette gamme de température. Ce n'est qu'en poursuivant la rampe "dans le noir" que nous avons fini par retrouver un signal quand la température était inférieure à ~ 5 μK.

La courbe la plus foncée de la figure 2.7 n'est pas une gaussienne car trop pointue ; elle correspond à un nuage sous la température critique et a donc une double structure : une gaussienne caractérisant le nuage thermique et une parabole inversée, plus fine, caractérisant le condensat. Une telle courbe permet donc en principe de déterminer, la température et le nombre d'atomes du nuage thermique ainsi que le potentiel chimique et le nombre d'atomes du condensat. Comme expliqué précédemment, il nous est difficile d'utiliser de façon fiable l'amplitude des signaux et donc de connaître les nombres d'atomes.

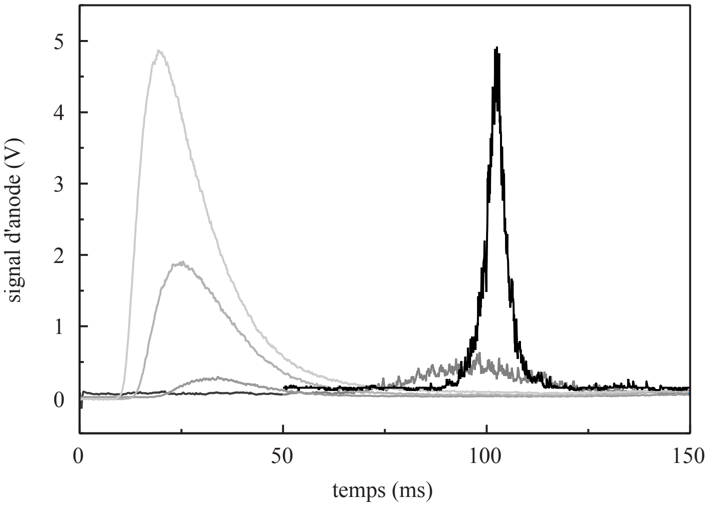

FIG. 2.7 – *Temps de vol "historiques" correspondant à différents moments au cours du refroidissement évaporatif. Les températures sont de* 850 μ*K,* 550 μ*K,* 350 μ*K pour les courbes de temps d'arrivée inférieur à 50 ms. La courbe grise de temps moyen d'arrivée de 100 ms correspond à* 10 μ*K, la dernière courbe correspond quant à elle à un nuage sous le seuil de condensation. Ces deux derniers temps de vol ont été multipliés par un facteur 20 sur cette figure. Le détecteur étant positionné à 5 cm en 2001, un atome de vitesse nulle est détecté 100 ms après la coupure du piège.*

Avec nos paramètres expérimentaux, la température de transition se situe entre 0.5 et 2.5 μK. Le nombre d'atomes est alors de l'ordre de 10^6. Le potentiel chimique typique est de 0.3 μK, ce qui correspond à 10^5 atomes dans un condensat pur. Durant les périodes "fastes" la durée d'un cycle complet de production d'un condensat est de 20-25 s. Une durée plus typique est 40 s.

2.5 Propriétés collisionnelles

Comme décrit plus haut, le succès du refroidissement évaporatif nécessite d'avoir beaucoup de collisions élastiques par rapport aux collisions inélastiques. D'autre part, les propriétés des condensats sont paramétrées par l'interaction répulsive entre atomes. Il est donc important de connaître les constantes de ces différentes collisions. Aucune de ces grandeurs n'avaient été mesurées quand nous avons démarré la projet condensation de l'hélium métastable.

2.5.1 Collisions inélastiques

Généralités : Les collisions inélastiques majoritaires dans le cas d'He* sont des collisions dites Penning où un atome d'He* retourne dans l'état fondamental et un ion est créé. Dans le cas de collisions à deux corps les réactions sont [81] :

$$\begin{cases} \mathrm{He}^* + \mathrm{He}^* \rightarrow \mathrm{He}^+ + \mathrm{He} + \mathrm{e}^- \\ \mathrm{He}^* + \mathrm{He}^* \rightarrow \mathrm{He}_2^+ + \mathrm{e}^- \end{cases}$$

La constante de collision associée, notée traditionnellement β, est assez importante, de l'ordre de 10^{-10} cm^3/s [82, 83, 84, 85, 86, 87, 88, 89]. Cependant cette constante est encore plus importante dans un piège magnéto-optique car la collision est beaucoup plus favorable quand l'un des atomes est dans l'état excité. Une première mesure faite à l'ENS indiquait une valeur de l'ordre de 10^{-7} cm^3/s [10]. Une nouvelle série de mesures a été menée dans notre groupe [90] ainsi que dans les autres groupes He* [88, 87, 91] suite à la publication par P. van der Straten d'une mesure beaucoup plus favorable [85]. Toutes ces nouvelles expériences ont cependant confirmé le résultat initial.

On minimise ces collisions inélastiques en travaillant à grand désaccord, $\sim$ 40 MHz, pour diminuer la population de l'état excité et ainsi maximiser le nombre d'atomes (dans la gamme $10^8 - 10^9$) [12].

Même sans lumière la constante de collision $\beta \approx 10^{-10}$ cm^3/s est beaucoup trop grande pour espérer obtenir la condensation. En utilisant le potentiel moléculaire de Stärk et Meyer [92], G. V. Shlyapnikov et ses collègues ont prédit que si les atomes étaient polarisés dans l'état de m maximum ($m = 1$) alors les collisions précédentes étaient fortement inhibées car elles ne conservaient pas le spin [93, 94]. Une valeur de l'ordre de 10^{-14} cm^3/s étaient annoncée (voir aussi Refs. [95, 96]). Cette valeur conjointement avec leur prédiction d'une longueur de diffusion de l'ordre de 8 nm (cf. section suivante) devait permettre l'observation de la condensation de Bose-Einstein de l'hélium métastable. Toutefois, le calcul ab initio des potentiels moléculaires est souvent trop approximatif pour en déduire des valeurs fiables des processus collisionnels à basse température et des mesures expérimentales sont nécessaires.

---

[12] Les processus sub-Doppler n'étant pas efficaces sur He*, sans doute à cause de la trop faible différence entre la limite Doppler et la limite sub-recul (40 μK et 4 μK respectivement), la température est bien décrite par un refroidissement Doppler et est de l'ordre de 1 mK.

A haute densité, les collisions à trois corps entrent aussi en jeu, et représentent le facteur limitant sur l'atome de rubidium par exemple. Des calculs théoriques prédisent que la constante de collisions, notée traditionnellement L, varie comme la longueur de diffusion à la puissance quatre [97, 98]. Dans le cas d'He*, la molécule formée par ce processus va finir par s'ioniser suivant un processus Penning :

$\mathrm{He^* + He^* + He^* \rightarrow He^*_2 + He^*_{chaud} \rightarrow He^+ + He + e^- + He^*_{chaud}}$

Mesure des constantes de collisions : Nous venons de voir que les processus inélastiques prépondérant à haute densité conduisent à l'ionisation d'un atome d'hélium métastable. Le taux d'ions, que nous sommes capables de mesurer avec la galette de microcanaux (cf. 2.3) est donc relié aux constantes de collision et à la densité atomique. Plus précisément, le taux d'ions ϕ est donné par :

$$\begin{cases} \phi = N/\tau' + \frac{1}{2}\kappa_2\beta \int \mathbf{dr}\, n^2(\mathbf{r}) + \frac{1}{3}\kappa_3 L \int \mathbf{dr}\, n^3(\mathbf{r}) \\ \text{avec : } dN/dt = -N/\tau - \kappa_2\beta \int \mathbf{dr}\, n^2(\mathbf{r}) - \kappa_3 L \int \mathbf{dr}\, n^3(\mathbf{r}) \end{cases}$$

où τ est la durée de vie, $\tau' > \tau$ la contribution des collisions à un corps qui conduisent à une ionisation, N le nombre d'atomes et n la densité atomique. Les facteurs $1/2$ et $1/3$ viennent du fait qu'il n'y a qu'un ion produit par réaction alors qu'il y a perte de 2 ou 3 atomes d'hélium métastable. Les coefficients κ_2 et κ_3 sont les facteurs de dégénérescence quantique. Ils valent 1 pour un nuage thermique et respectivement $1/2!$ et $1/3!$ pour un condensat [13] [14] [99].

Cette analyse montre aussi que, si les constantes de collision sont connues, mesurer le taux d'ions permet de mesurer la densité atomique, et cela en temps réel. Ce fut une motivation supplémentaire pour mener une campagne de mesure de ces constantes. Cette mesure est décrite dans la référence [14] dont la figure 2.8 est extraite.

Un inconvénient de cette mesure est que, comme je l'ai mentionné dans la section 2.3, nous ne sommes capables d'extraire d'un temps de vol de condensat que sa largeur, c'est-à-dire que mesurer son potentiel chimique μ. Cependant, dans l'approximation de Thomas-Fermi [37], le nombre d'atomes et la densité peuvent se déduire de μ et de la longueur de diffusion a [15]. On montre alors que la mesure du taux d'ions en fonction de la densité pic permet de mesurer β/a^2 et L/a^3 [14].

En utilisant les résultats effectués au seuil de condensation [17], que je décris dans la prochaine section, nos mesures donnent :

$$\beta = 0.9^{+1.7}_{-0.8}\ 10^{-14}\ \mathrm{cm^3/s} \text{ et } L = 2.5^{+4.5}_{-1.7}\ 10^{-27}\ \mathrm{cm^6/s}$$

---

[13] Ces coefficients sont différents pour un nuage thermique et un condensat car ils sont liés aux fonctions de corrélation à deux et trois corps qui sont différentes pour ces deux types de nuages. Nous reviendrons sur des mesures de ces fonctions de corrélation dans le chapitre 3.

[14] Dans le cas de gaz avec interaction ces coefficients doivent être corrigés par un facteur en $\sqrt{na^3}$ avec a la longueur de diffusion [14, 15].

[15] On a les relations suivantes : $\mu = \frac{4\pi\hbar^2 a}{m} n_0$ avec n_0 est la densité pic et $\mu = \frac{\hbar\omega}{2}(Na/\sigma)^{2/5}$ où ω est la moyenne géométrique des pulsations du piège et σ la moyenne géométrique des tailles de l'état fondamental du piège.

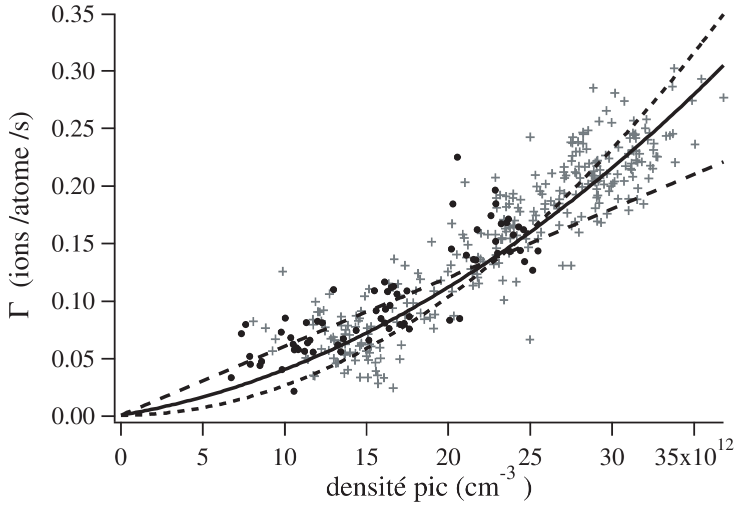

FIG. 2.8 – *Taux d'ions normalisé par le nombre d'atome en fonction de la densité pic. Ces mesures sont réalisées sur des condensats de Bose-Einstein d'hélium métastable. La non-linéarité de la courbe indique que les processus à trois corps ne sont pas négligeables aux densités accessibles expérimentalement. Figure extraite de Ref. [14].*

Des résultats similaires ont été obtenus sur les montages de l'ENS [100] et d'Amsterdam [101]. Dans le cas des alcalins, la constante de collisions à deux corps est généralement très faible et le taux de pertes correspondant est négligeable par rapport à celui du trois corps ; la constante de collisions à trois corps est typiquement 10 fois plus faible pour les alcalins [102]. L'hélium métastable a donc des propriétés collisionnelles inélastiques plus défavorables que ces derniers.

2.5.2 Collisions élastiques

Généralités : A basse température les collisions s'effectuent uniquement dans l'onde s et sont donc isotropes. Les ondes d'ordres supérieurs ne contribuent pas à cause de leur barrière centrifuge correspondante. On peut estimer que sur He* les collisions sont en onde s quand la température est inférieure à 8 mK [81]. La section efficace de collision vaut alors $8\pi a^2$ où a est la longueur de diffusion.

Plusieurs méthodes sont disponibles pour mesurer a : expérience de thermalisation (cf. ci-dessous), mesure sur des condensats (par la mesure du nombre d'atomes et du potentiel chimique), mesure spectroscopique sur le potentiel moléculaire par photoassociation (cf. ci-dessous). En 2000, il n'y avait pas encore de condensats et c'est donc par une méthode de thermalisation que nous avons fait notre première mesure de la longueur de diffusion.

Expérience de thermalisation : La méthode traditionnelle est de mettre le nuage hors équilibre en appliquant un couteau radio-fréquence et en étudiant le retour à l'équilibre à travers le rapport d'anisotropie du nuage atomique [103, 104, 105]. Ne disposant pas de caméra, nous ne pouvions utiliser cette méthode. Nous avons donc développé une méthode originale qui consiste à appliquer, après un délai variable, un deuxième couteau. Celui-ci vient mesurer le nombre d'atomes, qui après thermalisation repeuple les états d'énergie élevée. La figure 2.9 reproduit les résultats expérimentaux [11]. J'ai développé un modèle théorique, que l'on peut partiellement trouvé dans la thèse d'A. Robert [13], qui permet de relier analytiquement la constante de temps associée à cette expérience au taux de collisions élastiques. Je n'ai malheureusement jamais pris le temps d'écrire un article complet sur ce modèle. La conclusion de cette étude était encourageante et laissait penser que le refroidissement évaporatif devrait conduire à la condensation de Bose-Einstein dans nos conditions expérimentales [16].

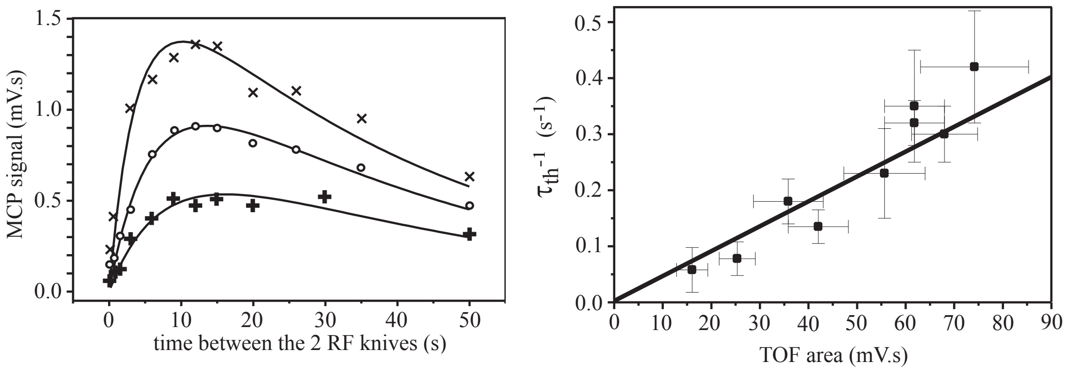

FIG. 2.9 – *Expérience de thermalisation. Un couteau RF expulse les atomes d'énergie élevée. Un deuxième couteau, à la même fréquence, est appliqué après un délai variable et sonde le repeuplement des niveaux d'énergies élevées. La constante de temps de retour à l'équilibre thermodynamique est d'autant plus courte que le taux de collisions est grand. La chute à temps long est due à la durée de vie des atomes. La figure de droite montre que le temps de thermalisation est bien relié au nombre d'atomes et donc aux collisions élastiques. Figures extraites de Ref. [11].*

Mesure à la température critique : Nous avons vu que le taux d'ions était lié aux constantes de collisions et à la densité atomique. Celle-ci dépend du nombre d'atomes et du potentiel chimique pour un condensat pur alors qu'elle dépend du nombre d'atomes et de la température pour un nuage thermique. Donc si on était capable de mesurer ces deux derniers paramètres dans un nuage thermique nous pourrions faire une deuxième mesure, indépendante, des constantes de collision. La confrontation de ces deux mesures permettrait alors de mesurer la seule inconnue restante, la longueur de diffusion. Le problème est que nous ne sommes pas capables de mesurer le nombre d'atomes expérimentalement(cf. 2.3). Sauf au seuil de condensation où *ce nombre est relié thermodynamiquement à la température critique*. Ainsi l'étude du taux d'ions de nuages au seuil de condensation en fonction de leur température critique permet de mesurer la longueur de diffusion et également les constantes de collisions inélastiques. C'est le principe de la mesure décrite dans la thèse de Signe Seidelin [16] et dans la référence [17].

---

[16] Cette expérience mesurait donc le taux de collisions élastiques et non la longueur de diffusion. Passer de l'un à l'autre nécessite de connaître la densité et donc le nombre d'atomes qui, comme je l'ai déjà dit, est une quantité mal connue dans notre expérience.

C'est grâce au signal d'ions que nous pouvons détecter des nuages au seuil de condensation. La figure 2.10 présente le taux d'ions pendant un laps de temps où le seuil de la condensation est franchi ; il se produit une brusque augmentation de densité et donc une augmentation du taux d'ions (bien que la constante de collision soit plus faible). On peut donc a priori utiliser le taux d'ions comme indicateur du seuil de condensation et ainsi produire des nuages "exactement" au seuil [60, 44]. Cependant l'instabilité du biais de ±50 kHz nécessite de confirmer ce diagnostic par une étude de la forme du temps de vol.

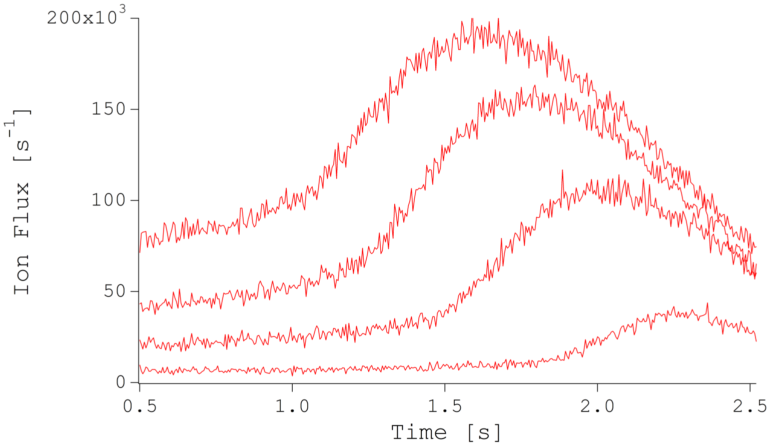

FIG. 2.10 – *Evolution du taux d'ions produit dans les dernières secondes de la rampe radiofréquence pour différents nombres d'atomes initiaux. On observe clairement l'apparition du seuil de condensation par la brusque augmentation du taux d'ions. Le seuil est atteint d'autant plus tard (et donc la température critique est d'autant plus faible) que le nombre initial d'atomes est faible.*

La figure 2.11 montre nos résultats. Nous obtenons ainsi,

$$a = 11.3^{+2.5}_{-1.0} \text{ nm}$$

Cette valeur est légèrement plus grande que celle prévue par G. V. Shlyapnikov, mais en bon accord avec un calcul moléculaire effectué par Gadéa, Dickinson et Leininger [106, 107]. Postérieurement à notre mesure, un nouveau calcul théorique conduisait à $a = 7.5 \pm 0.2$ nm [108] et une mesure faite dans le groupe de M. Leduc était en très bon accord avec cette dernière valeur.

Mesure par photoassociation du LKB : Bien que nous n'ayons pas du tout participé à cette expérience, il m'a semblé nécessaire de résumer ici les résultats obtenus dans le groupe de M. Leduc [109, 110]. La longueur de diffusion caractérise la section efficace de collision élastique à basse température, mais caractérise aussi l'énergie du dernier niveau lié du potentiel moléculaire ${}^5\Sigma_g^+$ qui est relié asymptotiquement à deux atomes dans le niveau $m = 1$. Une mesure de l'énergie de ce niveau par rapport au continuum permet donc d'en déduire très précisément la longueur de diffusion. C'est ce qui a été effectué dans cette équipe par différentes techniques de photoassociation. Il est peu vraisemblable que cette

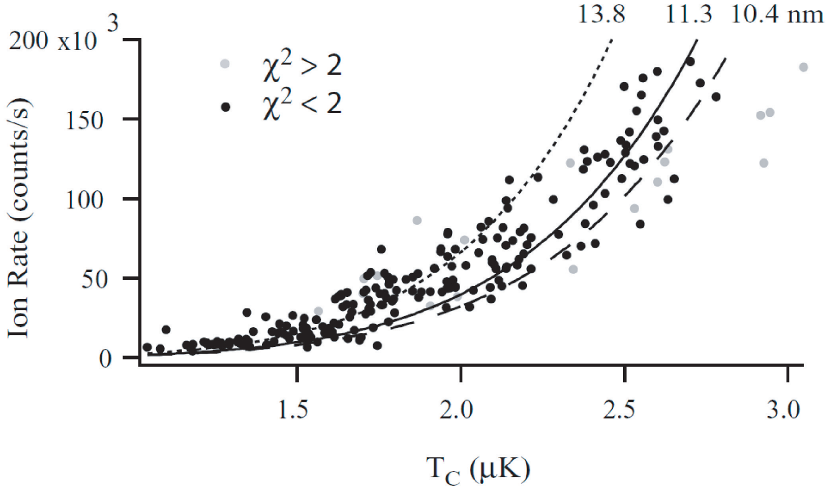

FIG. 2.11 – *Mesure du taux d'ions de nuages au seuil de condensation en fonction de la température critique. Les courbes correspondent aux résultats théoriques pour différentes valeurs de la longueur de diffusion. Figure extraite de Ref. [16].*

mesure soit fausse, d'autant que deux méthodes différentes ont donné le même résultat. La valeur obtenue est :

$$a = 7.512 \pm 0.005 \text{ nm}$$

Notre résultat est donc très vraisemblablement erroné. José Viana Gomes est revenu sur ce point dans sa thèse [44]. Il a entrepris une analyse critique des mesures et testé une méthode différente de celle de S. Seidelin pour le traitement des données ; il a étudié tous les nuages, même ceux qui ne sont pas au seuil et a affiné le critère permettant de s'assurer que les nuages sont au seuil. Son analyse a permis de fortement diminuer les barres d'erreurs statistiques sur notre valeur publiée, mais la valeur moyenne est restée la même : $a = 11.2 \pm 0.4$ nm ! La figure 2.12 traduit sa nouvelle analyse.

On doit en conclure qu'une erreur systématique entache nos résultats. Faute de tests fiables sur l'expérience, il n'a pu émettre que des hypothèses. La plus plausible est une erreur sur la mesure du potentiel chimique. Dans l'analyse des données sur les condensats [14, 17], nous supposions que la partie du nuage ($\sim 10\%$) qui a effectué un transfert non adiabatique dans $m = 0$ évolue en temps de vol avec le potentiel chimique des atomes piégés. En effet, lors des premiers instants après la coupure, les atomes dans $m = 0$ sont encore baignés dans le nuage $m = 1$. Les deux nuages s'étalent et transforment leur énergie d'interaction (i.e. μ) en énergie cinétique. Comme le nuage $m = 1$ est plus dense nous pensions que c'est lui qui gouverne, par collisions élastiques entre les deux nuages, l'expansion du nuage $m = 0$. Cette hypothèse est sans doute trop forte.

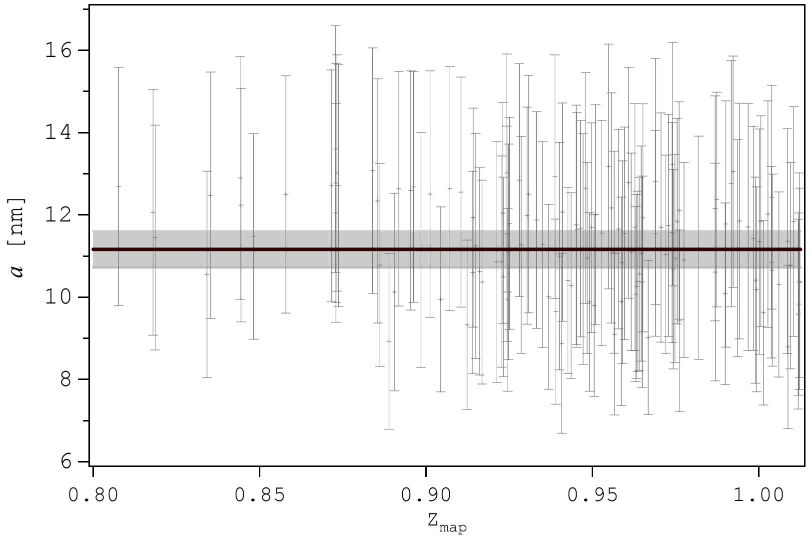

FIG. 2.12 – *Longueur de diffusion obtenue sur des nuages au-dessus ou proche du seuil de condensation. Chaque point sur la figure représente la valeur de la longueur de diffusion (et sa barre d'erreur) déduite d'une mesure sur un nuage thermique de fugacité Z_{map} ($Z_{map} = 1$ pour un nuage au seuil de condensation). Aucun effet systématique n'est observé en fonction de la fugacité et la valeur moyenne est la même que celle trouvée précédemment [17] mais avec des barres d'erreur bien plus faibles (la partie grisée correspond à ± la valeur rms de l'erreur).*

2.6 Etat de l'art en 2007

Condensat, ce qui a été fait depuis 2001 : Depuis le démarrage de notre projet et l'obtention de notre premier condensat en 2001, divers types de condensats ont été observés et étudiés. Je renvoie aux articles de revue [37, 39, 40] pour une bibliographie complète. Je liste ci-dessous une petite sélection :

- Vortex [111, 112] - réseau de vortex [113]. L'existence de vortex est une caractéristique fondamentale d'un superfluide en rotation [111]. Le moment cinétique associé est quantifié par unité de $\hbar$ [112]. Pour une vitesse de rotation importante, il est énergétiquement moins couteux de créer un réseau ordonné de vortex de charge unité (réseau d'Abrikosov) plutôt qu'un seul vortex de charge élevée [113].
- Soliton [114, 115, 116]. Un soliton est une excitation qui se propage sans déformation et nécessite une non-linéarité. Dans le cas d'interaction répulsive entre atomes il s'agit d'un soliton noir ("trou" dans le profil de densité) [114]. La propagation d'un soliton brillant ("bosse" dans le profil de densité) a aussi été observée pour des interactions attractives. Le soliton n'est cependant stable que pour une propagation dans un guide 1D [115, 116].
- Condensat moléculaire [117, 118, 119]. En utilisant des résonances de Feshbach, on peut créer un condensat moléculaire à partir d'un nuage ultra-froid de fermions [17].

---

[17] A cause du principe d'exclusion de Pauli les molécules formées de fermions sont beaucoup plus stables

- Quasi-condensat [121]. Si le nuage est très anisotrope, il existe une gamme de température pour laquelle la longueur de cohérence du nuage est inférieure à sa taille du fait de fluctuations de phase le long de l'axe long.
- Gaz 1D, régime de Tonks [122]. Un nuage bosonique 1D en interaction forte (ce qui signifie paradoxalement faible densité en 1D), a certaines caractéristiques d'un nuage fermionique. En particulier, les atomes n'ont plus tendance à être groupés (cf. chapitre 3).
- Gaz 2D : transition de Berezinskii-Kosterlitz-Thouless [123].
- Transition superfluide - isolant de Mott dans un réseau optique [124]. Dans un potentiel périodique, l'état fondamental d'un nuage à température nulle dépend de l'importance relative de l'énergie d'interaction à l'intérieur d'un puits et de l'énergie tunnel. Si cette dernière est plus importante, l'état fondamental sera superfluide et le nombre d'atomes par puits est très fluctuant. Dans le cas contraire, la population de chaque puits a une valeur fixe et identique d'un puits à l'autre ; c'est l'isolant de Mott.
- Mélange à quatre ondes d'ondes de matière [125]. Le terme d'interaction est un terme non linéaire et conduit donc à des phénomènes d'optique atomique non linéaire. Je reviendrai sur ce type d'expérience dans le chapitre 4.
- Amplification cohérente d'une onde de matière [126]. Phénomène relié au précédent mais avec deux ondes de matière et deux ondes lumineuses et également relié à la superradiance dont je parlerai dans la section 4.5.
- La condensation a été obtenue avec les atomes de ^{85}Rb [127], césium [128], chrome [129] (fort moment magnétique de 6 μ_B, interaction dipôle-dipôle longue portée importante), ytterbium [130] (niveau fondamental non dégénéré) et potassium [131].

Condensat, ce qui reste à faire : Je cite en vrac une liste, *non exhaustive*, de situations où je trouve qu'il serait intéressant de produire des condensats :

- Laser à atomes continu/Condensat en régime stationnaire. Une expérience initiée à l'ENS se poursuit à Toulouse dans le groupe de D. Guéry-Odelin [132, 133]. Le processus de formation du condensat en pompage/refroidissement continu où la stimulation bosonique serait importante est une problématique encore largement ouverte.
- Interaction forte en 3D pour se rapprocher de la matière condensée et en particulier de l'hélium liquide où la déplétion quantique n'est pas du tout perturbative.
- Condensat homogène : cela éliminerait le champ moyen (ou plutôt son inhomogénéité) et donc permettrait observer plus facilement les effets N corps (quasi-particules de Bogoliubov, effet sur la température critique...).

Fermions : Depuis quelques années, beaucoup de progrès ont été faits sur l'étude de gaz dégénérés fermioniques. Ces atomes ayant une section efficace de collisions très faibles à basse température, il est nécessaire de faire du refroidissement évaporatif avec un bo-

---

que celles formées de bosons [120].

son [18] [19] [135, 136]. Depuis l'obtention de la première mer de Fermi [135, 137], on peut citer l'observation de la transition BCS [138, 139], le régime unitaire (longueur de diffusion infinie) [140, 141].

Les condensats He* : Les équipes de Michèle Leduc à Paris, de Wim Vassen à Amsterdam et d'Andrew Truscott à Canberra ont obtenu un condensat respectivement en 2001 [100], 2005 [101] et 2006 [142].

L'équipe de M. Leduc s'est principalement focalisée sur la mesure de la longueur de diffusion [109, 110] et la création de molécules froides d'hélium métastable [143, 144, 145]. Cette équipe a récemment décidé de déplacer son activité vers l'étude de condensats d'He* dans un réseau optique. L'équipe de W. Vassen s'est elle concentrée sur le refroidissement de l'isotope fermionique ^{3}He* [146] et l'obtention d'une mer de Fermi [147]. Nous avons d'ailleurs collaboré avec cette équipe sur une expérience que je décrirai dans la section 3.5 sur l'observation "directe" du blocage de Pauli [23]. La première expérience de l'équipe de A. Truscott porte sur les lasers à atomes [148].

Toutes ces expériences utilisent une détection optique. Les équipes hollandaise et australienne disposent aussi de galettes de micro-canaux, mais seuls les australiens en tirent une information spatiale en imageant un écran de phosphore à la sortie du MCP. Ces trois expériences ont en commun un nombre d'atomes de quelques 10^9 dans le piège magnéto-optique, de $10^5 - 10^6$ dans un condensat pur obtenu en $10 - 20$ s. Ces performances sont donc bien supérieures aux nôtres et on peut, en partie au moins, l'imputer à une puissance optique disponible bien plus importante que dans notre montage ainsi qu'au fait qu'ils utilisent des sources laser de largeur spectrale faible par rapport à la largeur de raie, ce qui n'est pas notre cas avec les diodes DBR. Nous sommes en train de remédier à ces deux problèmes.

2.7 Perspectives

Je liste ci-dessous des expériences que nous pourrions mener dans l'avenir pour caractériser un condensat de Bose-Einstein moyennant des améliorations du dispositif expérimental ou l'ajout de nouveaux outils.

2.7.1 Mesure de la densité atomique de nuages froids

Notre détecteur est capable de mesurer les coordonnées des atomes détectés. il s'agit donc d'un détecteur 3D. Cependant l'inhomogénéité du gain observée ainsi que les possibles problèmes de saturation de ce détecteur font qu'il n'est pas encore possible d'avoir une parfaite confiance en cette reconstruction 3D pour des nuages denses. Si l'on parvient à maîtriser ces aspects dans le futur, nous pourrions étudier la forme des temps de vol en détail, en particulier pour des nuages proches du seuil de condensation. La plupart des

---

[18] En fait il suffit d'avoir deux espèces différentes c'est-à-dire que deux niveaux Zeeman du même atome fermionique conviennent également.

[19] En utilisant une résonance de Feshbach il est théoriquement possible de condenser avec des collisions en onde p [134].

équipes ajustent les images obtenues par une gaussienne plus une parabole inversée en dessous du seuil et une gaussienne au-dessus. C'est évidemment une grossière approximation, et il serait intéressant d'étudier de façon plus précise la forme de la densité atomique dans un temps de vol. En particulier le coeur du nuage atomique (donc la densité pic) est l'endroit où la densité est la plus forte et où les effets des interactions seront les plus forts. Par exemple, un calcul semi-classique standard donne une densité pic au seuil de condensation de $2.612/\lambda_{th}^3$ où λ_{th} est la longueur d'onde de de Broglie. Cela n'a jamais été vérifié sur des nuages d'atomes froids. En étudiant une situation plus simple, gaz sans interaction dans un piège harmonique, nous nous sommes aperçus que ce résultat n'allait pas de soi et qu'on s'attendrait plutôt à avoir une densité pic au seuil de $6.24/\lambda_{th}^3$ car le confinement spatiale dans un piège harmonique fait que la densité de l'état fondamental augmente considérablement plus vite que sa population [149]. Par contre, la fraction condensée, elle, est bien décrite par un calcul semi-classique. Ce petit exemple montre bien que des mesures globales (comme le nombre d'atomes) sont moins sensibles que des mesures locales. Nous avons un outil unique pour faire ces mesures locales. Or, une image par absorption ne permet pas de mesurer la densité mais uniquement la densité intégrée le long de l'axe de propagation du laser. Notre détection est donc beaucoup plus adaptée pour ces études.

Ces études pourraient être conduites sur des nuages 3D, 2D et 1D, ces deux derniers exemples étant réalisables avec des pièges optiques que j'évoque dans le prochain paragraphe. Il faut encore une fois souligner que l'analyse théorique reste à faire car nos mesures ne seraient pas in situ mais en temps de vol et l'effet des interactions sur la forme des nuages sera sans doute plus faible que dans le piège.

2.7.2 Piège optique

Les sections précédentes ont montré que l'He* permet d'avoir des diagnostics originaux, mais que les propriétés collisionnelles sont peu favorables pour des études nécessitant des densités atomiques importantes. Un piège optique pourrait permettre d'améliorer ce point. Nous reviendrons également sur d'autres attraits de ce type de piège dans la section 3.6.

Nuage uni ou bidimensionnel : Un piège optique ou encore mieux un réseau optique permet un confinement très fort, inaccessible avec un piège magnétique (sauf puce atomique [78]). Si la fréquence d'oscillation est plus grande que le potentiel chimique et la température du nuage, aucune excitation n'est possible sur cet axe. Si cette propriété est réalisée sur un axe le nuage peut être décrit par une physique à deux dimensions, et à une dimension si cela est réalisé sur deux axes.

Résonance de Feshbach : Dans un piège magnétique les atomes d'He* sont piégés dans le niveau $m = 1$ et comme cet atome n'a pas de structure hyperfine, c'est le niveau de l'état $2\ ^3S_1$ d'énergie maximale ; il ne peut donc pas y avoir de résonances de Feshbach [40]. Ce type de résonance permet de modifier les propriétés collisionnelles aussi bien élastiques [150, 151] qu'inélastiques [152, 102, 98, 153] même si ce dernier effet n'a pas à ma connaissance été encore observée [20].

---

[20] Une observation expérimentale de ce phénomène a peut être été faite dans le groupe de R. Grimm [154].

Il peut ainsi être judicieux de piéger He* dans un piège optique pour pouvoir travailler sur le niveau $m = 0$ ou $m = -1$ et chercher des résonances de Feshbach. Il n'existe actuellement pas de données théoriques sur ces résonances, mais comme les puits de potentiel sont particulièrement profonds pour He* [92], on peut craindre que les champs magnétiques utiles ne soient élevés.

On peut noter que ^{3}He*, l'isotope fermionique, possède une structure hyperfine, donc les résonances de Feshbach sont plus nombreuses et sans doute plus facilement accessibles expérimentalement.

Finalement, on peut noter que des résonances de Feshbach peuvent aussi être induites par laser soit à un ou deux photons [155, 156, 157]. Il y a déjà eu quelques vérifications expérimentales [158, 159, 160, 161] mais en général le changement de longueur de diffusion s'accompagne d'une forte augmentation de processus inélastiques et cette méthode n'est donc pas vraiment utilisée jusqu'à présent. A noter un article qui traite explicitement le cas de l'hélium métastable bosonique [162] avec la même conclusion quant aux collisions inélastiques.

Propriétés collisionnelles : Si le confinement est très fort (fréquence d'oscillation dans la gamme du MHz), les propriétés collisionnelles élastiques et inélastiques peuvent être considérablement modifiées [163, 164] ; en particulier il est prédit que pour certaines valeurs discrètes la constante de collisions inélastiques est très fortement réduite. Il faut travailler dans un réseau optique pour atteindre cette gamme de fréquence.

Imagerie ionique : Un autre avantage du piège optique est qu'il pourrait être envisageable de faire une imagerie ionique in situ des atomes piégés. Il semble en effet difficile de le faire dans un piège magnétique à cause des aberrations dues au champ magnétique inhomogène. La longueur d'onde des ions pouvant être très petite si on les accélère, on peut en principe faire des mesures très fines. Il faut cependant faire attention que le nombre d'ions produits n'est pas très grand, de l'ordre de 10^5/s au seuil de condensation. Il semble donc difficile de vouloir à la fois faire une étude en dynamique et avoir une bonne résolution spatiale. Cependant le gros avantage est que la non-linéarité de la production d'ions (processus à deux ou trois corps) fait qu'on privilégie le coeur du nuage, là où la densité est la plus forte et donc là où les effets N corps sont les plus importants.

2.8 Conclusion

Cette activité de recherche qui recouvre les années 1998-2004, nous a permis d'obtenir un condensat de Bose-Einstein composé, pour la première fois, d'atomes qui n'étaient pas dans leur état interne fondamental. Dans notre article sur la condensation de l'hélium métastable [12] nous faisions remarquer que ces atomes ont une énergie interne 11 ordres de grandeur plus grande que leur énergie externe. Même si cet argument a un petit côté publicitaire, il montre bien que l'obtention d'un gaz dégénéré d'hélium métastable n'allait pas de soi. Cette étape franchie, de nombreuses études où l'existence d'ions et la détectivité individuelle d'atomes d'He* s'offraient à nous. J'ai évoqué dans ce chapitre certaines d'entre elles et en ai évoqué d'autres dans la partie 2.7, dans un domaine que je qualifierai de matière condensée. Les deux chapitres suivants décrivent des expériences où nous avons mis à profit les atouts de l'hélium métastable dans le domaine de l'optique atomique quantique.

Chapitre 3

Corrélation d'intensité : effet Hanbury Brown et Twiss

3.1 Introduction

Une source lumineuse ou matérielle est d'abord définie par sa taille, sa brillance, sa divergence, le nombre d'atomes qu'elle contient, etc... Mais cela ne la définit évidemment pas totalement. Utilisée comme source dans un interféromètre, on en déduira les longueurs de cohérence transverse et longitudinale. Dans ce type de mesure, la physique mise en jeu n'est qu'à une particule. Par contre savoir si la probabilité de détecter une particule influence la détection des autres particules nécessite de connaître les propriétés à N corps de la source via ses fonctions de corrélation d'ordre $n = 1, ..., \infty$ (voir plus bas pour une définition précise).

Une source n'est donc a priori totalement définie que si ces dernières sont connues. Il se trouve que les sources "naturelles" telles que les sources cohérentes (laser, laser à atomes idéal) ou chaotiques (lampe à décharge, nuage atomique thermique) sont totalement décrites par la fonction de corrélation d'ordre 1. Cependant, des phénomènes tels que la supraconductivité haute température, l'hélium superfluide sont décrits par des sources fortement corrélées. Si la précision de mesure d'un déphasage dans un interféromètre (atomique ou optique) est généralement limitée par le bruit de projection quantique ($\propto 1/\sqrt{N}$ où N est le nombre de particules utilisées pour la mesure), l'utilisation de sources fortement corrélées permet en principe d'être plus précis. Il est alors possible d'atteindre la limite d'Heisenberg ($\propto 1/N$) [165]. Si le déphasage dans l'interféromètre est dû à un effet à p-corps, il est même prédit que le bruit minimal sur la constante de couplage associée est en $1/N^p$ [166, 167]. Pour un gaz en interaction la longueur de diffusion pourrait par exemple être mesurée avec une précision en $1/N^2$ [168, 169]. Dans un autre domaine, un ordinateur quantique nécessite également d'utiliser de telles sources. En conclusion, il est clair que l'un des thèmes actuels majeurs de la physique est de créer des sources fortement corrélées, et de les étudier.

Il est plus que probable que les fonctions de corrélation d'ordre $n \geq 2$ seront des outils de mesure majeurs. C'est le thème de ce chapitre, qui repose sur deux séries d'expériences que nous avons menées pendant la période 2004–2007 sur des nuages ultra-froids de bosons et de fermions (section 3.5). Je commencerai ce chapitre par décrire l'expérience de Hanbury

Brown et Twiss (3.2) qui représente l'analogue optique de nos expériences et qui est sans doute l'expérience fondatrice de l'optique quantique moderne. Je décrirai ensuite, de façon plus formelle, les fonctions de corrélation et leurs propriétés dans la section 3.3. Notons tout de suite que nos expériences n'ont pas montré d'effets à N-corps et que les nuages sondés sont, à notre rapport signal sur bruit près, bien décrits par des sources cohérentes (condensat de Bose-Einstein) ou chaotiques (nuages thermiques de fermions ou de bosons). Ces expériences montrent la faisabilité de mesures de fonction de corrélation. J'évoquerai en perspective (section 3.6) d'autres études qu'il serait intéressant de mener sur des nuages à l'équilibre thermodynamique où des effets N corps sont attendus [40]. La création d'une source spécifique, source de paires d'atomes corrélés, fera l'objet du chapitre 4.

Je ne discuterai donc pas des expériences exploitant la fonction de corrélation du premier ordre, c'est-à-dire de l'interférométrie atomique. Il faut noter qu'il s'agit de l'une des principales applications des atomes froids à travers des horloges, gyromètres, gravimètres, etc car ceux-ci sont aujourd'hui très précis et concurrentiels par rapport aux interféromètres optiques, et leur marge de progression est encore très grande. Ils utilisent soit des jets atomiques froids transversalement soit des atomes froids. Notons également que la première observation de la cohérence du premier ordre d'un condensat a été faite par l'équipe de W. Ketterle en 1997 par la visualisation de franges résultant de l'interférence de deux condensats [33].

Ce chapitre reprend le travail de thèse de Rodolphe Hoppeler [19] pour la partie préparatoire, de Martijn Schellekens [20] en étudiant clé, d'Aurélien Perrin [24] et, pour la partie fermion, de Valentina Krachmalnicoff.

3.2 Expérience de R. Hanbury Brown et R. Twiss

La question posée en introduction (*"est-ce que la probabilité de détecter une particule influence la détection des autres particules ?"*) peut être vue légèrement différemment en optique car il est plus traditionnel de parler d'ondes que de particules. Détecter des particules revenant à mesurer une intensité, cette question se résume à comparer $\langle I(x)I(x')\rangle$, valeur moyenne de la probabilité de détection d'une particule en x et une autre en x', à $\langle I(x)\rangle \langle I(x')\rangle$. L'intensité I est une fonction fluctuante autour de sa valeur moyenne. Si le bruit est totalement aléatoire, c'est-à-dire s'il n'existe aucune influence, aucune corrélation entre $I(x)$ et $I(x')$, la valeur moyenne (au sens statistique) du produit des intensités doit être égale au produit des valeurs moyennes et cela quelque soit le paramètre x qui peut représenter ici le temps ou la position relative des détecteurs. Toutefois on conçoit que pour toute source réelle, le bruit a un spectre fini et si $|x - x'| \to \infty$, on doit trouver

$$\langle I(x)I(x')\rangle = \langle I(x)\rangle \langle I(x')\rangle \;\; \text{si} \;\; |x - x'| \to \infty$$

Si I est une fonction (et non un opérateur), on peut également démontrer les relations suivantes en utilisant des inégalités de Cauchy-Schwarz [170],

$$\langle I^2(x)\rangle \geq \langle I(x)\rangle^2 \;\; \text{et} \;\; \langle I^2(x)\rangle \geq \langle I(x)I(x')\rangle \tag{3.1}$$

La fonction $\langle I(x)I(x')\rangle/\langle I(x)\rangle\ \langle I(x')\rangle$, qui sera appelé fonction de corrélation d'ordre deux normalisée dans le prochain paragraphe est donc maximale pour $x = x'$ et tend vers 1 pour $|x - x'| \rightarrow \infty$. La largeur caractéristique de cette fonction est la longueur de corrélation.

Si la source lumineuse est une source chaotique, la lumière émise présente des tavelures en temps comme en position. Un calcul [170] conduit alors à :

$$\langle I^2(x)\rangle = 2\ \langle I(x)\rangle^2$$

Ce résultat que tout un chacun peut démontrer et comprendre en terme d'excès de bruit à $x = x'$ est un peu choquant quand on y pense. Revenant à notre question initiale, cela revient à dire que, oui, dans le cas d'une source chaotique, la probabilité de détection d'un photon dépend de la détection d'un premier photon et la probabilité de détecter deux photons est deux fois plus grande si les photons sont proches que séparés. Cela évidemment n'a pas manqué de susciter la polémique car il n'existe strictement aucune force entre les photons qui pourraient contraindre ceux-ci à se grouper.

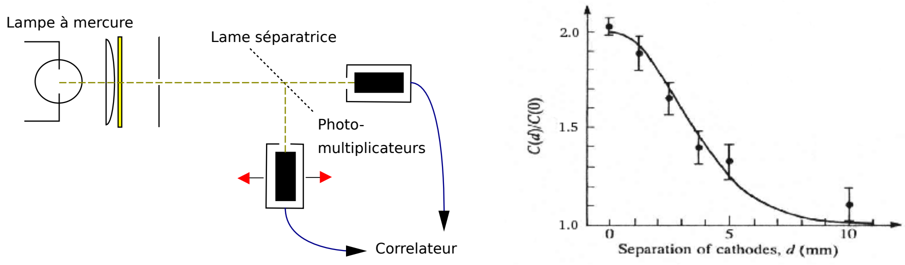

Fig. 3.1 – *(a) Dispositif expérimental de Hanbury Brown et Twiss pour la mesure de la fonction de corrélation à deux corps d'une source chaotique. (b) Résultat expérimental montrant le groupement des photons. Figure extraite de Ref [171].*

Les premiers à pointer cette situation sont R. Hanbury Brown et R. Q. Twiss deux radio-astronomes qui cherchaient à mesurer des diamètres angulaires d'étoiles sans être génés par les fluctuations atmosphériques qui brouillaient les franges d'un interféromètre de Michelson classique. Après leur expérience de principe sur une lampe à mercure (cf figure 3.1) [171], ils ont effectivement utilisé cette technique, dite aussi d'interférence en intensité, pour mesurer le diamètre angulaire de Sirius A [172]. Ce que l'histoire a surtout retenu est l'interprétation quantique de ce phénomène, due non pas à une quelconque attraction entre photons mais comme une conséquence directe de la statistique quantique de cette source bosonique. C'est le phénomène de groupement ou bunching en anglais. L'interprétation de ces expériences et de ce qu'elles impliquaient est due en particulier à Fano [173] et Glauber [174, 175, 176] et a valu à ce dernier le prix Nobel en 2005 [177]. En un certain sens, l'optique quantique est née de cette expérience.

Le traitement quantique prédit qu'il est possible de violer les inégalités classiques données par Eq.(3.1). Un exemple simple est un atome unique excité par un laser pulsé de telle sorte qu'un seul photon de fluorescence au maximum est émis par pulse. Dans ce cas la lumière de fluorescence se compose de photons séparés par la période des impulsions et en particulier $\langle I^2(t)\rangle = 0$. On parle alors de dégroupement ou d'antibunching. La première observation a été réalisée dans le groupe de H. J. Kimble en 1977 [178]. Je reviendrai sur la violation de ces inégalités classiques dans le chapitre 4.

3.3 Fonctions de corrélation

3.3.1 Définitions

De manière formelle on définit les fonctions de corrélation d'ordre n par,

$$G^{(n)}(\mathbf{x}_1, ..., \mathbf{x}_{2n}) = \mathrm{tr}\left[\widehat{\rho}\widehat{\Psi}^{(-)}(\mathbf{x}_1)...\widehat{\Psi}^{(-)}(\mathbf{x}_n)\widehat{\Psi}^{(+)}(\mathbf{x}_{n+1})...\widehat{\Psi}^{(+)}(\mathbf{x}_{2n})\right]$$

avec la notation $\mathbf{x}_i = (\mathbf{r}_i, t_i)$. Dans cette expression $\widehat{\rho}$ correspond à la matrice densité du système quantique considéré, $\widehat{\Psi}$ le champ électrique ou l'opérateur champ suivant la nature photonique ou matérielle des particules. Il est souvent plus commode d'utiliser la forme normalisée des fonctions de corrélation, qui permet de comparer les propriétés de cohérence de deux sources de particules

$$g^{(n)}(\mathbf{x}_1, ..., \mathbf{x}_{2n}) = G^{(n)}(\mathbf{x}_1, ..., \mathbf{x}_{2n}) / \prod_{j=1}^{2n} \left[G^{(1)}(\mathbf{x}_j, \mathbf{x}_j)\right]^{1/2}$$

Si $\mathbf{x}_{n+i} = \mathbf{x}_i$ pour tout i, on peut interpréter la fonction de corrélation $G^{(n)}$ comme une mesure de la probabilité qu'une particule soit détectée à chaque position $\mathbf{r}_i$ et instant t_i. Par exemple, $G^{(1)}(\mathbf{x}_1, \mathbf{x}_1)$ correspond à une mesure de l'intensité moyenne de la source, tandis que $G^{(2)}(\mathbf{x}_1, \mathbf{x}_2, \mathbf{x}_2, \mathbf{x}_1)$ correspond à la mesure du taux de coïncidences de détection aux positions $\mathbf{r}_1$ et $\mathbf{r}_2$ aux temps t_1 et t_2. Dans la suite nous nous focaliserons sur les fonctions de corrélation d'ordre 1 et 2 puisque ce sont celles qui interviendront dans nos expériences et que nous avons mesurées.

Notons que, de manière générale, il est très difficile de mesurer une fonction de corrélation d'ordre élevé. Regarder des coïncidences entre détecteurs nécessite qu'ils soient de taille inférieure à la largeur de cohérence de la source et qu'ils aient des positions relatives définies à mieux que cette largeur de cohérence. Finalement leur résolution temporelle doit être meilleure que le temps de cohérence de la source. La probabilité de faire une mesure de n coïncidences varie donc comme ϵ^n où ϵ décrit la cohérence de la source (densité fois volume de cohérence ou population dans une cellule élémentaire de l'espace des phases dans nos expériences). Pour une source non cohérente, $\epsilon < 1$ ce qui rend ces mesures d'autant plus dures que n est grand.

3.3.2 Fonction de corrélation du premier ordre

Théorèmes de Zernike-van Cittert et de Wiener-Kinchine : Par simple transformation de Fourier on montre que

$$\iiint d\mathbf{R}\; G^{(1)}(\mathbf{R}-\frac{\mathbf{r}}{2},\mathbf{R}+\frac{\mathbf{r}}{2};t,t) = \iiint d\mathbf{K}\; G^{(1)}(\mathbf{K},\mathbf{K};t,t)e^{-i\mathbf{K}.\mathbf{r}} \tag{3.2}$$

$$\iiint d\mathbf{K}\; G^{(1)}(\mathbf{K}-\frac{\mathbf{k}}{2},\mathbf{K}+\frac{\mathbf{k}}{2};t,t) = \iiint d\mathbf{R}\; G^{(1)}(\mathbf{R},\mathbf{R};t,t)e^{-i\mathbf{k}.\mathbf{R}} \tag{3.3}$$

Ces équations relient la corrélation d'ordre un en vecteur d'onde avec la densité de la source (intensité en optique photonique) et réciproquement la corrélation spatiale d'ordre un avec la distribution en vecteur d'onde de la source. Ces équations traduisent le théorème de Zernike-van Cittert [1] [179]. Dans le cas d'un nuage atomique à l'équilibre thermodynamique de taille s et de température T, cela signifie que la longueur de cohérence vaut $\hbar/\sqrt{mk_BT}$ (longueur d'onde thermique de de Broglie) et que la largeur de la corrélation en impulsion vaut $\hbar/s$.

Des relations équivalentes existent entre les espaces temps et fréquence. Dans le cas d'une source stationnaire et uniquement dans ce cas là, on obtient le théorème de Wiener-Kinchine [179] qui indique que la corrélation temporelle d'ordre un est la transformée de Fourier de la densité spectrale de puissance. Par exemple dans un nuage atomique à température T le temps de cohérence est $\hbar/k_BT$.

Il n'existe pas dans le cas général de relations similaires aux Eqs.(3.2) et (3.3) pour les ordres plus élevés.

Cas d'une source pulsée : Dans notre expérience, nous étudions des nuages initialement à l'équilibre thermodynamique mais dont le confinement est coupé brutalement à $t = 0$. La mesure de la corrélation s'effectue après un temps de vol de ~ 300 ms. La corrélation temporelle n'est donc plus reliée au spectre de la source mais à la distribution des vitesses suivant l'axe vertical et obéit donc au théorème de Zernike-van Cittert. On peut comprendre cela en disant que dans une source continue, deux atomes détectés en même temps au même endroit peuvent avoir des vitesses quelconques, alors qu'avec une source pulsée ils doivent avoir la même vitesse (à la taille du nuage initial près).

3.3.3 Fonction de corrélation en optique atomique

Il y a a priori une parfaite analogie entre les ondes lumineuses et les ondes de matière. Mathématiquement on remplace les opérateurs création et annihilation par les opérateurs champs et la longueur d'onde par la longueur d'onde de de Broglie. Il existe cependant quelques différences : les atomes ont une masse, sont sensibles à la gravité et ont une relation de dispersion non linéaire. D'autre part les photons sont des bosons alors que les atomes peuvent aussi être fermioniques. Finalement, les atomes interagissent naturellement alors que l'observation de phénomènes non-linéaires avec la lumière nécessite l'ajout d'un cristal non-linéaire. En corollaire les non-linéarités atomiques sont également plus importantes que les photoniques [180]. Ces différences et donc cette richesse de situations différentes font des atomes des candidats excitants pour des mesures de corrélation. Nous verrons dans la

---

[1] Ces équations ne sont pas définies dans le cas d'une source homogène et il faut alors prendre quelques précautions d'usage (calcul dans une boite dont on fait tendre la taille à l'infini en fin de calcul).

suite que la première catégorie de différences (masse, accélération, relation de dispersion) ne modifie pas les mesures que nous avons effectuées mais peuvent modifier les caractéristiques des corrélations dans d'autres situations, comme dans le cas d'un flux continu. Une étude théorique est en cours sur ce point mais n'est pas encore achevée et je ne reviendrai pas dessus dans ce manuscrit.

3.3.4 Résultat à l'équilibre thermodynamique

Gaz sans interaction : Les calculs sont ici équivalents à ceux sur la lumière chaotique et peuvent être menés de manière analytique dans le cas d'un confinement harmonique [181, 22]. Si la fréquence d'oscillation dans la direction α vaut ω_α, on obtient par exemple :

$$\begin{aligned} G^{(1)}(\mathbf{r},\mathbf{r}') &= \frac{1}{\pi^{3/2}} \sum_{l=1}^{\infty} e^{\beta l \tilde{\mu}} \prod_\alpha \frac{1}{\sigma_\alpha \sqrt{1-e^{-2\tau_\alpha l}}} \\ &\times \exp\left[-\tanh(\frac{\tau_\alpha l}{2}) \left(\frac{r_\alpha + r'_\alpha}{2\sigma_\alpha} \right)^2 - \coth(\frac{\tau_\alpha l}{2}) \left(\frac{r_\alpha - r'_\alpha}{2\sigma_\alpha} \right)^2 \right]. \end{aligned}$$

où $\tilde{\mu} = \mu - \frac{\hbar}{2} \sum\limits_\alpha \omega_\alpha$, $\beta = 1/k_B T$, $\sigma_\alpha = \sqrt{\frac{\hbar}{m\omega_\alpha}}$ et $\tau_\alpha = \frac{\hbar\omega_\alpha}{k_B T}$. On a noté k_B la constante de Boltzmann et μ le potentiel chimique, déterminé par la condition de normalisation $\iiint d\mathbf{r}\; G^{(1)}(\mathbf{r},\mathbf{r}) = N$, le nombre d'atomes.

Cette expression, particulièrement indigeste, est valable quelque soit la température et montre la richesse de la corrélation même pour un gaz sans interaction :

- Très au-dessus de la température critique, $\mu < 0$ et $|\mu| \gg k_B T$ et donc,

  $$G^{(1)}(\mathbf{r},\mathbf{r}') = \frac{N}{\lambda_{\mathrm{t}h}^3} \prod_\alpha \tau_\alpha e^{-\frac{\tau_\alpha}{2}(\frac{\mathbf{r}_\alpha + \mathbf{r}'_\alpha}{2\sigma_\alpha})^2} e^{-\pi(\frac{\mathbf{r}_\alpha - \mathbf{r}'_\alpha}{\lambda_{\mathrm{t}h}})^2}$$

  et

  $$g^{(2)}(\mathbf{r},\mathbf{r}') = 1 + e^{-2\pi(\frac{\mathbf{r}-\mathbf{r}'}{\lambda_{\mathrm{t}h}})^2}$$

  où $\lambda_{\mathrm{t}h} = \hbar\sqrt{\frac{2\pi}{m k_B T}}$ est la longueur d'onde thermique de de Broglie. Celle-ci est donc la longueur de corrélation d'un nuage thermique chaud. Elle est isotrope car la distribution de vitesse l'est (cf. Eq.(3.2)). Cette longueur est aussi homogène (même valeur dans tout le nuage).
- En se rapprochant de la température critique, la corrélation devient inhomogène. La longueur de corrélation est toujours la longueur de de Broglie loin du centre du piège, mais proche du centre, il faut considérer de plus en plus de termes dans la somme sur l, ce qui augmente la longueur de corrélation.
- Au seuil de condensation et au centre du nuage, la longueur de corrélation diverge.
- A température très en dessous du seuil, les atomes sont tous dans le même état (l'état fondamental), $G^{(1)}(\mathbf{r},\mathbf{r}') = \sqrt{\rho_0(\mathbf{r})\rho_0(\mathbf{r}')}$ avec ρ_0 la densité de l'état fondamental du piège. Le nuage est alors cohérent et la fonction de corrélation normalisée ne présente plus de groupement mais est plate, $g^{(2)}(\mathbf{r},\mathbf{r}') = 1$.

Gaz avec interaction : Dans un nuage ultra-froid les interactions sont en général en onde s et sont donc caractérisées par un seul paramètre, la longueur de diffusion a. Il est légitime dans les situations explorées jusqu'à présent de remplacer le vrai potentiel moléculaire d'interaction par un potentiel de contact [37]. La résolution exacte du problème n'est plus possible, mais les interactions étant généralement faibles, on peut faire une théorie de champ moyen [2] [37]. Dans cette approximation et à température nulle, le condensat de Bose-Einstein est toujours un état cohérent, tous les atomes dans la même fonction d'onde, mais cette fonction d'onde n'est plus l'état fondamental à une particule du piège. Cette approche s'est révélée très fructueuse et est largement satisfaisante pour la très grande majorité des expériences. Mais il s'agit d'une approximation. L'approche de Bogoliubov [37, 38] montre que même à température nulle, tous les atomes ne sont pas dans l'état fondamental donné par le champ moyen et on appelle déplétion quantique la partie des atomes qui se trouvent en dehors. La fonction de corrélation normalisée n'est donc pas plate et égale à 1. Intuitivement c'est évident à cause de l'interaction répulsive entre atomes qui provoque un “creux” à séparation spatiale faible [181, 182]. Une observation expérimentale de la déplétion quantique a été effectuée sur des atomes confinés dans un réseau optique dans l'équipe de W. Ketterle [183].

L'effet des interactions sur le nuage thermique est très faible car la densité de ces nuages est faible. On pourrait donc penser que ces effets sont négligeables ou à tout le moins qu'une approche de type champ moyen est suffisante. Ceci ne semble pas vrai. Dans un article récent [184], T. Esslinger et ses collègues ont montré que proche du seuil de condensation, la longueur de corrélation spatiale était sensible aux interactions et que leur résultat est plus en accord avec une théorie de Bogoliubov qu'avec une théorie de champ moyen.

3.3.5 Dans un temps de vol

Gaz sans interaction : La longueur de corrélation typique dans un piège est de 1 μm voire moins. Faire une mesure in situ est donc une gageure. Par contre on sait bien que durant la chute libre d'un nuage, sa taille augmente linéairement à temps long, $s_i(t) = s_i \omega_i t$ [3]. On peut se demander ce qu'il en est pour la longueur de corrélation. C'est pour répondre à cette question, de façon quantitative, que nous avons mené une étude théorique dans un cas simple : un gaz sans interaction, confiné initialement dans un piège harmonique, et qui s'étend en chute libre sous l'effet de la gravité. L'analyse détaillée se trouve dans la thèse de José Carlos Viana Gomes [44] et est retranscrite dans l'article Ref. [22]. Un calcul analytique exacte est possible et dans le cas limite qui nous intéresse (temps de chute long devant la période d'oscillation dans le piège et vitesse acquise par la gravité grande devant la largeur de la distribution de vitesse) on trouve que la fonction de corrélation pendant la chute est identiquement égale à celle à l'équilibre thermodynamique si on applique un changement d'échelle sur les longueurs $x \rightarrow x/\omega_x t$, $y \rightarrow y/\omega_y t$ et $z \rightarrow (H - gt^2/2)/\omega_z t$ où

---

[2] Je ne traiterai dans ce manuscrit que du cas des interactions répulsives, $a > 0$.

[3] Pour un gaz sans intéraction, la taille à l'instant t est reliée à la taille initiale par $s_i(t) = s_i\sqrt{1 + (\omega_i t)^2}$ avec $s_i = \sqrt{k_B T / m\omega_i^2}$. A temps long on trouve donc $s(t) \approx \sqrt{k_B T/m}\, t$. Comme attendu, la taille est alors donnée par la distribution de vitesse.

H est la hauteur de chute. Donc la longueur de corrélation pendant la chute vaut :

$$l_i^{(chute)} = \lambda_{\rm th}\,\omega_i t \;\; avec \;\; i = x, y, z \tag{3.4}$$

On obtient la même dilatation que la taille du nuage.On peut en donner une interprétation simple. Nous avons déjà vu dans la section précédente que la fonction de corrélation à un corps était la transformée de Fourier de la distribution d'impulsion (d'où $\lambda_{th} = h/\Delta p$). De manière symétrique, Eq.(3.3) montre que la fonction de corrélation à un corps en impulsion est la transformée de Fourier de la distribution de position. Cette formulation n'est pas toujours connue car on travaille souvent en matière condensée avec des systèmes homogènes où la largeur de corrélation en impulsion est donc nulle. Ce n'est plus le cas ici. La longueur de corrélation en impulsion est donc,

$$l_{p;i} = h/s_i$$

Dans un piège harmonique de pulsation $\{\omega_i\}$ cela devient :

$$l_{p;i} = h/s_i = m\omega_i\lambda_{th}$$

Or la mesure de la position d'un atome sur le détecteur est en très grande partie reliée à sa vitesse transverse et non pas à sa position transverse dans le piège. Donc une corrélation en position sur le détecteur revient à une corrélation en impulsion. On réobtient bien Eq.(3.4) avec $x_i = p_i t/m$.

Les relations précédentes permettent aussi d'écrire que

$$l_i^{(chute)} = \hbar t/m s_i$$

où s_i est la taille du nuage dans la direction i. Sous cette forme, on peut faire l'analogie optique avec les tavelures dont la longueur de corrélation est $\lambda L/s$ où s est la taille de la source lumineuse, λ la longueur d'onde et L la distance d'observation. Il suffit d'identifier λ à $\hbar/mv$ et $L = vt$ avec v la vitesse moyenne des atomes.

Il faut souligner que le calcul conduit à la même formule pour la corrélation spatiale suivant l'axe de propagation (axe vertical). Ceci vient du fait que *notre source n'est pas continue mais pulsée*. Comme je l'ai déjà souligné, on ne retrouve donc pas la relation de Wiener Kinchine qui relie la corrélation le long de l'axe de propagation à la largeur spectrale de la source. Cela signifie aussi que la gravité ne modifie pas les propriétés de corrélation.

Gaz avec interaction : Je n'ai pas connaissance de calculs dans le cas de gaz avec interactions. Le seul article que je connaisse traite de la cohérence d'ordre un et montre par une simulation numérique que les interactions peuvent avoir un effet non négligeable en élargissant les pics de diffraction d'un condensat se réfléchissant sur un potentiel périodique [185]. Les articles théoriques se placent généralement dans le cas où *les interactions sont supprimées pendant la chute en annulant la longueur de diffusion par résonance de Feshbach...* Un pauvre expérimentateur n'a pas toujours la possibilité de réaliser cela aussi simplement qu'écrire une ligne dans un article théorique. On peut cependant émettre l'idée qu'après la coupure du piège, la conversion de l'énergie d'interactions en énergie cinétique est suffisamment lente pour que l'état du système évolue en grande partie de manière adiabatique vers un état sans interaction. La "trace" laissée par les interactions pourrait donc être assez faible.

3.4 Résultats expérimentaux sur des particules massives

Etat des lieux : Des mesures des fonctions de corrélation ont été menées dans des domaines très divers de la physique comme sur des électrons dans un conducteur [186, 187], des électrons libres [188], des neutrons [189], des particules de haute énergie [190, 191, 192, 193]. Dans le domaine des atomes froids, l'expérience pionnière est celle de Yasuda et Shimizu en 1996 [57] sur un jet continu de néon métastable extrait d'un piège magnéto-optique. Cette expérience de principe a été suivie par des expériences sur des quasi-condensats (longueur de cohérence de phase, effet des interactions en géométrie quasi 1D) [194, 195], sur des atomes initialement confinés dans un réseau optique (transition superfluide-isolant, observation du dégroupement pour un nuage fermionique) [196, 197, 198], sur un laser à atomes (fonction de corrélation plate) [199], sur un nuage au seuil de condensation (divergence de la longueur de corrélation au seuil) [184], ainsi que nos propres expériences [21, 23]. Il faut aussi noter une autre série d'expériences qui ont mesuré la valeur de la fonction de corrélation à séparation nulle (spatiale et temporelle) par la mesure du taux de collisions inélastiques à deux et trois corps dans des nuages d'atomes froids (comparaison nuage thermique-condensat, voir discussion à la section 2.5.1) [200, 201, 202].

Méthodes de détection avec des atomes froids : Se posent toujours la question de la mesure de ces corrélations. Plusieurs types de mesures ont déjà été démontrés :

- Mesure des pertes inélastiques à deux et trois corps : mesure de $g^{(2)}(0)$ et $g^{(3)}(0)$. Théorie : [99]. Expérience : [200, 201, 202].
- Etude du bruit sur des images en absorption : mesure des corrélations transverses d'un nuage, intégrées le long de l'axe d'illumination. Théorie : [203, 204]. Expérience : [205, 196, 197].
- Utilisation d'un détecteur résolu en temps et en position. Expérience [199, 21, 23, 184].

Dans toute les expériences citées plus haut, la fonction de corrélation d'ordre 2 n'a été mesurée que sur une variable (temps pour les sources stationnaires ou spatiale pour les sources pulsées). Aucune expérience n'utilise un détecteur dont la taille (taille physique et temps de réponse) soit inférieure à la longueur de corrélation. Les situations les plus pures sont celles nommées "détecteur résolu en temps et en position". Le groupe de Tilman Esslinger [199, 184] utilise une cavité optique de finesse suffisante pour que le passage d'un unique atome change significativement la transmission d'un faisceau sonde (interaction atome-cavité en couplage fort). Le "détecteur" a donc une surface donnée par la longueur de la cavité et la taille du mode optique ($\sim 120 \times 30\ \mu\mathrm{m}^2$) et une résolution temporelle donnée par le temps de passage dans la cavité et par son électronique de comptage. Cette surface relativement importante, vu la distance détecteur-source de 36 mm, fait que ce détecteur n'est pas bien adapté à des nuages larges et de corrélation spatiale faible. D'autre part il ne mesure que des corrélations temporelles. L'avantage et l'originalité de notre détecteur est qu'il a une très grande surface, 50 cm^2, et qu'il s'agit en fait de $\sim 10^5$ détecteurs en parallèle, ce qui permet de mesurer la fonction de corrélation dans les trois directions de l'espace. Par contre sa résolution spatiale est moins bonne, 300 μm rms.

Mesures effectuées sur notre montage : J'ai déjà décrit brièvement notre système de détection dans le chapitre 2. Pour des raisons de rapport signal sur bruit, nous n'avons pas mesuré la fonction de corrélation $g^{(2)}(x, x')$ mais plutôt une fonction de corrélation moyenne (moyennage sur un des deux points à séparation fixe) :

$$g_m^{(2)}(\mathbf{r}) = \frac{\int d\mathbf{R}\, G^{(2)}(\mathbf{R}, \mathbf{R}+\mathbf{r})}{\int d\mathbf{R}\, \rho(\mathbf{R})\rho(\mathbf{R}+\mathbf{r})} \tag{3.5}$$

où ρ est la densité atomique.

3.5 Nos résultats expérimentaux

Deux séries d'expériences ont été menées : nuage bosonique d'^{4}He* (thermique et condensat) et nuage fermionique d'^{3}He*. Cette dernière expérience est le fruit d'une collaboration avec le groupe de W. Vassen-W. Hogervorst de l'université d'Amsterdam qui dispose d'une source froide de cette isotope [147]. V. Krachmalnicoff assistée de M. Schellekens, H. Chang et A. Perrin est partie en juillet-août 2006 à Amsterdam avec notre détecteur et toute l'électronique de pilotage pour effectuer l'expérience [4].

Nuages thermiques de bosons L'expérience est conceptuellement très simple. On crée un nuage de température donnée, on coupe le piège et on détecte les particules sur notre détecteur sensible en position. Le reste n'est qu'un traitement informatique des données pour calculer le nombre moyen de paires d'atomes séparés d'une distance donnée et donc en déduire la corrélation d'ordre 2. J'ai rappelé dans la section 3.3.5 que les longueurs de corrélation sont en $\hbar t / m s_\alpha$ dans la direction α. Comme $s_\alpha \propto \sqrt{T}$, changer la température permet de changer la longueur de corrélation détectée. Avec un temps de chute de 308 ms, des fréquences d'oscillation de 50 et 1200 Hz, le volume de corrélation au niveau du détecteur est de l'ordre de $30 \times 800 \times 800$ μm^3. Notre détecteur est donc capable de résoudre deux des trois directions [5]. Comme notre résolution n'est pas suffisante sur l'axe long des nuages, notre détecteur moyenne sur une zone grande devant la longueur de corrélation et donc la hauteur de la fonction de corrélation $g_m^{(2)}$ sera de l'ordre de $l_x/2d$ et non pas 2 [22]. Dans cette formule l_x est la longueur de corrélation théorique dans le temps de vol sur l'axe long et d la résolution à une particule du détecteur.

La figure 3.2 présente nos résultats expérimentaux et montrent sans ambiguïté l'observation du groupement bosonique et ceci dans les trois directions de l'espace. L'analyse des largeurs et des hauteurs de corrélation en fonction de la température permet de montrer,

---

[4] En tout 9 m^3 de matériel tout de même !

[5] En fait, si l'axe long des nuages (axe du biais) était sur la verticale, nous serions capable de résoudre les trois directions.

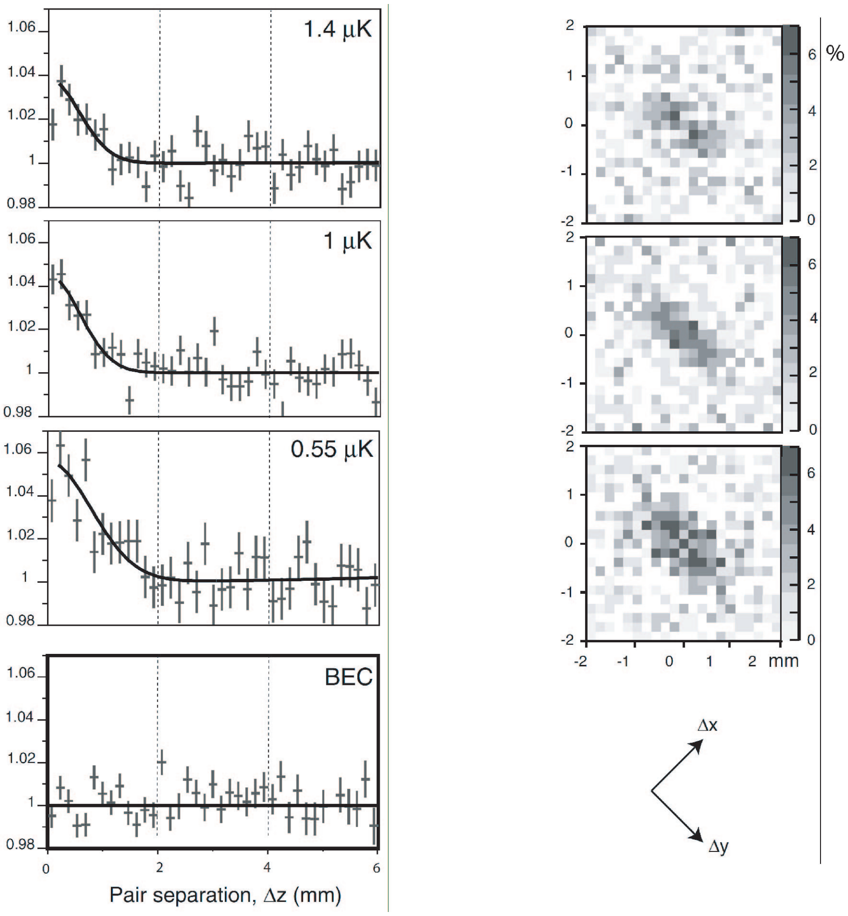

FIG. 3.2 – *Fonction de corrélation pour des nuages thermiques et pour un condensat d'* $^4He^*$*. Les courbes de gauche montrent la fonction de corrélation suivant l'axe vertical, celles de droite la corrélation dans le plan du détecteur. L'anisotropie observée est plus faible qu'attendue théoriquement du fait de la résolution de notre détecteur. Courbe extraite de Ref [21].*

qu'à notre rapport signal sur bruit près, un modèle de gaz sans interaction suffit à expliquer nos mesures. Ces données ont nécessité un moyennage sur plus de 1000 différentes réalisations de l'expérience.

Condensat de Bose-Einstein J'ai déjà évoqué le fait que dans l'approche de Bogoliubov la fonction de corrélation spatiale du condensat présente un dégroupement alors que le calcul en champ moyen prédit une fonction de corrélation plate.

A quoi peut-on s'attendre dans un temps de vol ? Comme dit plus haut, la réponse n'est pas évidente car lors des premiers instants après la coupure du piège, l'énergie d'interaction se transforme en énergie cinétique de façon douce et l'état fondamental N corps de Bogoliubov se transforme sans doute en l'état cohérent du champ moyen. La vraie interaction répulsive existe toujours mais est à trop courte portée pour pouvoir être visible expérimentalement. On s'attend donc à trouver en bonne approximation une fonction de corrélation plate. C'est bien ce que nous avons observé (cf fig 3.2). Les données expérimentales ont nécessité un traitement informatique un peu complexe à cause des problèmes de saturation du détecteur évoqués dans le chapitre 2. Je renvoie le lecteur au manuscrit de thèse de M. Schellekens [20] pour plus de détails. Il faut signaler qu'une mesure dans le cas d'un laser à atome (flux continu et non pulsé comme dans nos expériences) a été faite dans le groupe de T. Esslinger et donne également une fonction de corrélation plate [199].

Nuages thermiques de fermions L'expérience est en tout point identique à la précédente. La seule différence provient de la méthode pour refroidir des fermions. L'équipe hollandaise utilise le refroidissement sympathique entre ^{3}He* et ^{4}He* : les deux espèces sont confinées dans le piège magnétique dans l'état de moment magnétique maximal ($m_J = 1$ pour ^{4}He* et $F = 3/2$ $m_F = 3/2$ pour ^{3}He*) et sont donc soumises au même potentiel magnétique. A la fin du refroidissement évaporatif sur l'isotope bosonique, un couplage dipolaire magnétique par radio-fréquence permet d'extraire du piège tous les bosons sans affecter les fermions [6]. Pour vérifier la cohérence de nos résultats, nous avons également répété la mesure sur le nuage de bosons [7]. Comme la taille spatiale est la même pour les deux isotopes à même température, les longueurs de corrélation ne diffèrent que par le facteur de masse. Ceci conduit donc à une largeur plus grande de 4/3 pour le fermion et une hauteur également plus grande (en valeur absolue) de 4/3. Evidemment, avec des fermions la fonction de corrélation ne présente pas de groupement mais un dégroupement dû au principe d'exclusion de Pauli. La figure 3.3 illustre nos résultats. L'accord est bon sur la largeur, mais pas vraiment sur la hauteur, celle du boson étant pour une raison inconnue trop faible. La coupure du champ magnétique étant plus lente à Amsterdam qu'à Orsay, l'expansion des nuages, le bosonique avec interaction, le fermionique sans interaction pourrait être différente et donc influer sur la fonction de corrélation.

Conclusions : Le cas des gaz sans interaction est bien connu et faire une mesure de corrélation n'apporte rien sur la physique. Cependant, les interactions sont bien présentes et montrer qu'elles ne jouent aucun rôle dans nos expériences est un résultat en soi. D'autre part, ces expériences ont un caractère pédagogique indéniable. Si on peut comprendre le groupement des bosons par un raisonnement purement classique (cf section 3.2), il n'en est pas du tout de même pour les fermions. On est obligé d'utiliser une analyse quantique. Finalement, ces expériences montrent la maturité de systèmes de détection extrêmement performants dans le domaine des atomes ultra-froids et le savoir-faire développé au sein de notre groupe [8].

3.6 Perspectives

---

[6] La fréquence RF pour extraire les bosons est 3/2 fois plus grande que celle qui extrairait les fermions. La température de ces derniers est suffisamment basse pour que le nombre de fermions extraits est quasi-nul.

[7] Dans ce cas, on ne chargeait même pas les fermions dans le piège.

[8] Mis bout à bout, le temps passé pour "apprivoiser" le détecteur dépasserait la durée d'une thèse si une seule personne avait travaillé dessus.

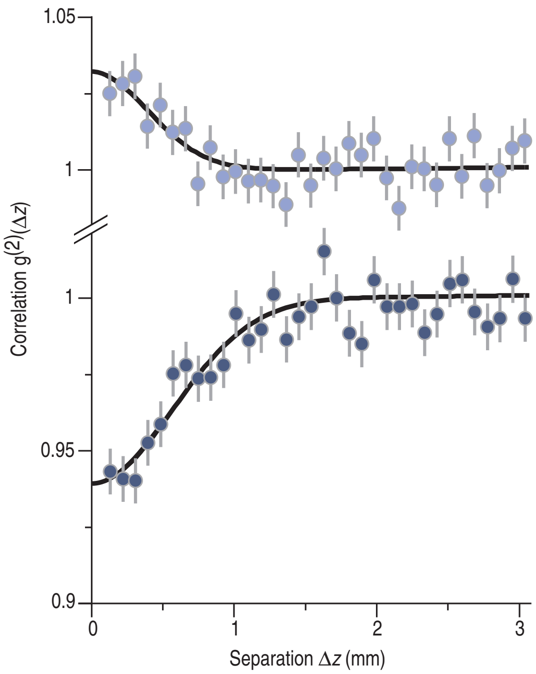

FIG. 3.3 – *Comparaison entre la corrélation d'un nuage bosonique (points clairs) et à celle d'un nuage fermionique (points foncés) de même température. On observe bien un groupement pour les bosons et un dégroupement pour les fermions. Figure extraite de ref. [23].*

Corrélations dans des structures complexes : Comme le montre les parties précédentes, les interactions ont un effet faible dans nos expériences. Cependant, il est bien connu que plus la dimensionnalité du nuage est faible plus les interactions auront une influence sur les propriétés de corrélation. L'article de revue Ref. [40] présente un panorama assez exhaustif des différentes situations envisageables. En basse dimensionnalité les états sont vraiment N corps et donc très loin des situations classiques que l'on peut sonder sur des nuages 3D. Ce domaine de recherche est en pleine expansion actuellement tant théoriquement qu'expérimentalement. Voici une liste, non exhaustive, des situations physiques où il serait intéressant d'étudier la corrélation d'ordre 2 :

- 1D : La physique 1D est particulière en ce sens qu'il existe dans certaines situations des résultats théoriques exactes du problème à N corps [206, 207, 208]. Suivant le régime des interactions et de la température on peut obtenir un gaz thermique, un quasi-condensat, un gaz de Tonks. Aucune fonction de corrélation n'a encore été mesurée mais des valeurs moyennes [195] et à séparation nulle [201, 202] ont récemment été établies.
- 2D : La transition de phase à deux dimensions d'un gaz homogène en interaction est la transition Berezinskii-Kosterlitz-Thouless récemment observée sur des atomes froids [123].
- Réseau 1D, 2D et 3D : Le fait d'avoir plusieurs puits peut modifier la thermodynamique des systèmes si l'effet tunnel n'est pas négligeable. Je ne peux manquer de mentionner la transition superfluide – isolant de Mott et son observation expé-

rimentale dans le groupe de T. W. Hänsch [124]. Comme exemple de perspective plus lointaine, les réseaux semblent aussi de bons candidats pour observer l'effet Hall quantique fractionnaire [209, 210].

Mesures de corrélation locales : Si l'on revient sur notre expérience, nous n'avons pas été capable d'extraire toute l'information souhaitée. En effet pour des problèmes de rapport signal à bruit, nous ne pouvons que faire une mesure d'une fonction de corrélation moyenne (cf. 3.4) alors que le coeur du nuage, où la densité est la plus forte et où le condensat "pousse", pourrait apporter des informations précieuses. Comme nous l'avons souligné dans la section 3.3.4, la forme de la fonction de corrélation s'écarte d'une gaussienne au centre du nuage quand la température approche la température critique. J'ai déjà signalé l'expérience de T. Esslinger [184] qui semble montré que l'exposant critique associé à la largeur de corrélation est plus en accord avec une théorie Bogoliubov N corps qu'avec une théorie de champ moyen dans un nuage 3D standard. Il serait évidemment très intéressant de refaire une telle étude avec si possible un meilleur rapport signal à bruit.

On pourrait aussi s'intéresser au $g^{(2)}$ sous le seuil de condensation, à la fois dans la partie condensée et dans la partie thermique. Il faut rappeler toutefois que la relation entre la corrélation en position à temps de chute long et la corrélation en vitesse ou position dans le piège n'est pas connue dans le cas général d'un nuage avec interaction et il n'est donc pas garanti que des effets d'interaction sur la fonction de corrélation soient accessibles par cette méthode.

Mesures de corrélation d'ordres supérieures à deux : Très récemment, dans le groupe de J. Schmiedmayer, une expérience d'interférence entre deux quasi-condensats 1D a montré que la statistique du contraste des franges contenait une information très riche et serait sensible à des fonctions de corrélation d'ordres élevés [204]. Cette nouvelle approche est prometteuse et mérite sans doute un développement. Sur notre montage expérimental, une fois les atomes détectés rien ne nous empêche a priori de calculer des fonctions de corrélation d'ordre 3, 4... Comme indiqué précédemment la limitation ne vient que d'un problème de rapport signal à bruit.

Chapitre 4

Création et détection de paires atomiques corrélées

Dans le chapitre précédent j'ai décrit des expériences de corrélation d'intensité sur des nuages bosoniques et fermioniques qui mettaient en avant la statistique quantique des particules. La section 3.6 montrait quelques exemples où il serait intéressant de mesurer ces effets dans des systèmes plus complexes où le nuage atomique doit être considéré comme un vrai système à N corps.

La thématique développée dans ce chapitre est différente et se rapproche plus des problématiques actuelles de l'optique quantique et de l'information quantique. Nous désirons *créer* des corrélations entre particules, et à plus long terme créer des intrications. L'expérience décrite dans ce chapitre concerne la création de paires d'atomes corrélés lors de la collision de deux condensats de Bose-Einstein [25]. Ce point de vue corpusculaire s'appellerait plutôt processus à quatre ondes spontané dans le langage de l'optique quantique. Cette forte analogie sera soulignée dans les sections 4.1 et 4.2. Je décrirai ensuite l'expérience et les principaux résultats dans la section 4.3. Différents contacts avec des groupes de théoriciens ont enrichi notre point de vue et des articles théoriques ont été publiés en commun ou sont en préparation (K. Mølmer [211], K. V. Kheruntsyan [212], M. Trippenbach [213]) ; je décrirai qualitativement notre compréhension actuelle de ces expériences. Comme dans les chapitres précédents je terminerai par les perspectives qu'offrent cette première expérience (section 4.5).

L'acteur clé de ce travail est Aurélien Perrin. On trouvera des informations détaillées dans sa thèse [24]. Martijn Schellekens et Valentina Krachmalnicoff ont aussi contribué à ce travail. Notre activité expérimentale est encore centrée sur cette thématique.

4.1 Fluorescence paramétrique

Si les bases théoriques de l'optique quantique moderne sont nées des expériences de Hanbury Brown et Twiss [171], c'est la création de sources non classiques qui a lancé ce domaine de recherche. En particulier la création de photons jumeaux dans les expériences de fluorescence paramétrique ("spontaneous parametric down conversion") a été une étape décisive. L'expérience pionnière est celle de D. C. Burnham et D. L. Weinberg qui ont montré en 1970 que les photons étaient bien créés par paires [214, 215]. Parmi les expériences clé qui ont suivi on peut noter l'intrication [216], la violation des inégalités de Bell [1] [221], le phénomène d'interférence sur une séparatrice, dit effet HOM [222].

La figure 4.1 présente le dispositif expérimental qu'ont utilisé Burnham et Weinberg. Un cristal non linéaire d'ordre 2 permet de créer à partir d'un laser à 347 nm deux faisceaux lumineux en forme de cône de longueurs d'onde 633 nm et 668 nm. Les angles des deux cônes et les longueurs d'onde respectent l'accord de phase du processus d'amplification paramétrique. La vérification que les photons émis sont bien corrélés est effectuée par une mesure de coïncidence sur deux détecteurs en comptage de photons : un détecteur est fixe et centré sur le cône des photons à 668 nm et l'autre se déplace dans un plan perpendiculaire à l'axe du cône à 633 nm. Ils ont alors vérifié que le taux de coïncidence est maximal quand les détecteurs sont positionnés sur des modes de photons jumeaux.

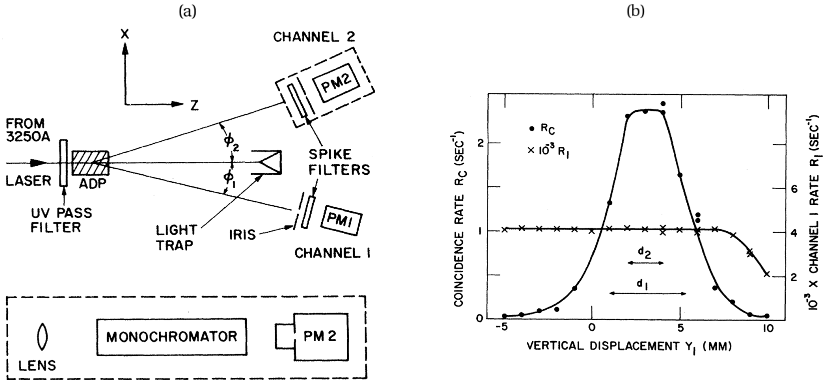

FIG. 4.1 – *Montage expérimental et résultat de l'expérience de Burnham et Weinberg pour la démonstration de la production de paires de photons corrélés dans un processus d'amplification paramétrique. La figure de droite montre que le taux de coïncidence entre les deux détecteurs est maximal quand ceux-ci sont positionnés sur deux modes vérifiant l'accord de phase. Figures extraites de Ref. [214].*

Dans le cas d'un processus d'amplification paramétrique, un photon pompe est absorbé et deux photons de fluorescence sont émis. L'usage les appelle photons signal et complémentaire (*idler* en anglais). Si la pompe est intense, on peut se contenter de quantifier les modes de fluorescence. Dans ces conditions, une décomposition en onde plane du Hamiltonien d'interaction donne

$$\hat{H}(t) = \chi^{(2)} \iint d\mathbf{k_i} d\mathbf{k_s} \iiint d\mathbf{r}\ E_p(\mathbf{r},t) e^{-i(\mathbf{k_s}+\mathbf{k_i}).\mathbf{r}+i(\omega_i+\omega_s)t} \hat{a}^\dagger_{\mathbf{k_i}} \hat{a}^\dagger_{\mathbf{k_s}} \tag{4.1}$$

où $E_p(\mathbf{r},t)$ décrit le champ électrique de la pompe. Si la fluorescence est peu intense, on peut linéariser l'opérateur d'évolution $\exp[-i\hbar \int d\tau \hat{H}(\tau)] \approx 1 - i\hbar \int d\tau \hat{H}(\tau)$ pour obtenir l'état quantique des modes de fluorescence, $|\Psi\rangle \propto \int d\tau \hat{H}(\tau)|vide\rangle$. On peut alors mettre

---

[1] Les premières expériences d'inégalités de Bell [217, 218, 219, 220] ont été réalisées sur une cascade radiative et non pas sur une amplification paramétrique. L'intrication est alors en polarisation.

cet état sous la forme

$$|\Psi\rangle \propto \iint d\mathbf{k_i} d\mathbf{k_s}\ \phi(\mathbf{k_i}, \mathbf{k_s}) |\mathbf{k_i}, \mathbf{k_s}\rangle \tag{4.2}$$

où la fonction $\phi(\mathbf{k_i}, \mathbf{k_s})$ se calcule par intégration spatiale sur le volume du cristal doubleur et par intégration temporelle [223, 224]. Dans le cas idéalisé d'une onde plane et continue ainsi qu'un cristal de longueur d et de section infinie, on trouve par exemple

$$\phi(\mathbf{k_i}, \mathbf{k_s}) \propto \int d\omega_p\ f(\omega_p)\, \delta(\omega_i + \omega_s - \omega_p)\, \delta(k_{i\perp} + k_{s\perp})\, \mathrm{sinc}[(k_{iz} + k_{sz} - k_{pz})\frac{d}{2}]$$

où f décrit le spectre de la pompe [2]. De manière générale, les conditions d'accord de phase font que la fonction $\phi(\mathbf{k_i}, \mathbf{k_s})$ est non séparable. L'état $|\Psi\rangle$ est ainsi un état intriqué correspondant à une somme cohérente de paires individuelles de photons. Les caractéristiques de corrélation de la lumière spontanée dépendent de la largeur du spectre de la pompe, de sa durée (dans le cas d'une pompe pulsée), de la taille de son mode spatial, du volume du cristal [3].

La situation décrite ici correspond à la fluorescence paramétrique dans des cristaux où l'accord de phase est de type I ; les photons jumeaux ont alors la même polarisation et l'état $|\Psi\rangle$ correspond à une intrication à variables continues. Il est donc nécessaire pour démontrer l'intrication d'utiliser deux paires différentes de photons [221, 216]. On peut d'ailleurs signalé que c'est ce type de source (création en un point donné de deux particules de vitesses corrélées) qu'ont considéré Einstein, Podolski et Rosen dans leur fameux papier sur l'effet EPR [225].

Avec un accord de phase de type II, les photons jumeaux ont des polarisations orthogonales. L'intrication peut alors être démontrée sur un montage comportant un seul couple de modes $(\mathbf{k}, \mathbf{k}')$ pour les paires de photons jumeaux et des polariseurs.

Régime stimulé : On peut parvenir au régime stimulé de deux façons. Soit on injecte en plus de la pompe un signal faible à la bonne fréquence et le bon angle pour l'accord de phase (amplificateur paramétrique optique ou OPA), soit on place le cristal dans une cavité résonnante sur deux modes jumeaux (oscillateur paramétrique optique ou OPO). La situation théorique est alors un peu plus complexe [226, 224], en particulier s'il faut tenir compte de plus de deux modes [227, 228]. De manière qualitative on peut comprendre que comme les photons sont créés par paires, l'intensité des deux modes peut fluctuer (shot noise) mais la différence d'intensité doit être très faible (sub shot noise) [229].

4.2 Optique atomique quantique et atomes jumeaux

Introduction : Des phénomènes quantiques équivalents peuvent être étudiés avec d'autres types de sources et de particules. Dans la section précédente j'ai évoqué des états intriqués de photons. On peut aussi s'intéresser à des états photon-atome ou atome-atome. C'est ce dernier type d'états que nous avons commencé à étudier. De plus les sources peuvent

---

[2] Dans cette expression ce sont les vecteurs d'onde à l'intérieur du cristal qui interviennent.

[3] Comme souvent, la vérification expérimentale de l'intrication dépend de la méthode de détection et en particulier des propriétés en taille et réponse spectrale des détecteurs.

être macroscopiques (en taille et nombre de particules) ou microscopiques. Il se trouve que les techniques d'intrication et leur observation sont assez différentes suivant les caractéristiques de ces sources et conduisent à deux domaines de la physique encore assez disjoints à l'heure actuelle. On peut citer les expériences sur des ions piégés (voir ci-dessous) ou sur des atomes dans des cavités optiques [230, 231] pour des sources microscopiques. Une expérience pionnière d'états photon-atome sur des sources macroscopiques, mais où seule la corrélation et non l'intrication a été montrée, a été effectuée dans le groupe de J. Mlynek [232]. Dans la suite je me limite à des états atome-atome.

Corrélations-intrication avec sources microscopiques : De très nombreuses expériences d'optique atomique quantique ont été réalisées sur des sources contenant quelques particules. Ces expériences utilisent pour la plupart des ions ultra-froids [233, 234] et ont été en partie initiées par une proposition d'ordinateur quantique avec des ions par I. Cirac et P. Zoller [235]. La porte quantique proposée dans cet article a été réalisée dans le groupe de R. Blatt [236]. Un des derniers faits d'arme est la création d'un chat de Schrödinger à 6 ions dans le groupe de D. Wineland [237]. Les ions sont utilisés car il est très facile de les piéger, de les refroidir et les temps de confinement sont bien supérieurs à ceux que l'on trouve pour des atomes car la profondeur des pièges est gigantesque. De plus l'interaction entre ions étant très forte par rapport à des atomes, il est "plus simple" de faire des portes quantiques. Des expériences sur la manipulation quantique d'atomes ou molécules uniques ont déjà été réalisées et des intrications/violations d'inégalité de Bell entre atomes ont été démontrées via des intrications atome-photon [238, 239, 240, 241]. Signalons également quelques expériences de violation d'inégalité de Bell en physique des particules [242, 243, 244].

atomes jumeaux avec sources macroscopiques – Expériences et modélisation : En atomes froids, les deux expériences faites avec des ondes de matière qui ont démontré l'existence de corrélation, celle de D. S. Jin [205] et la notre [25], sont très liées au processus de fluorescence paramétrique. Dans l'expérience de D. Jin, des molécules ultra-froides sont dissociées par résonance de Feshbach en deux atomes fermioniques de potassium. La conservation de l'énergie et de la quantité de mouvement conduisent à ce que les atomes soient sur une sphère dans l'espace des vitesses et que les deux atomes issus de la même molécule aient des vitesses opposées ; ils forment une paire d'atomes corrélés, comme les photons jumeaux précédemment décrits. Une étude du bruit sur les images en absorption de cette sphère de diffusion [203] a permis d'observer cette corrélation. Cependant, aucune étude quantitative sur la largeur de la corrélation ou sur son amplitude n'a été menée.

Notre expérience consiste à faire collisionner deux condensats de Bose-Einstein et, comme précédemment, les atomes diffusés se trouvent sur une sphère dans l'espace des vitesses. Le détecteur 3D permet alors de mesurer la corrélation. Je décrirai plus en détail l'expérience dans la section 4.3 suivante.

Formellement, dans l'amplification paramétrique et dans l'expérience de Jin, il s'agit d'un effet à trois particules (un photon pompe et deux photons jumeaux, ou une molécule et deux atomes diffusés), alors que dans notre cas il y a quatre particules (deux atomes du condensat et deux atomes diffusés). Cependant le traitement théorique confond toutes ses approches car les sources sont supposées suffisamment intenses pour que les opérateurs des champs sources soient traités classiquement. Le Hamiltonien final est donc formellement identique à Eq.(4.1) et ne contient que les champs des particules diffusées et, dans l'approximation considérée, est quadratique en ces champs [245, 246, 247, 248, 249, 250, 251, 252]. Par exemple dans notre situation il suffit de remplacer $E_p(\mathbf{r},t)$ par $\psi_+(\mathbf{r},t)\psi_-(\mathbf{r},t)$ où $\psi_\pm$ représente les fonctions d'onde des deux condensats en collision et $\chi^{(2)}$ par le couplage en onde s, $4\pi\hbar^2 a/m$.

Mélange à quatre ondes : Bien que notre expérience devrait être considérée comme un mélange à quatre ondes, ce terme est plus couramment employé dans le cas où trois ondes intenses donnent naissance à une quatrième onde. On se trouve alors dans le régime stimulé que j'ai brièvement décrit dans la section 4.1. L'amplification d'une onde de matière a été observée, avec un facteur d'amplification de l'ordre de 1.5 dans le groupe de W. D. Philipps [125] ; une série d'expériences plus récentes dans le groupe de W. Ketterle a conduit à un facteur d'amplification de 20 [126, 253]. Aucune mesure de corrélations ou de réduction de fluctuations d'intensité sub shot noise n'a cependant été effectuée.

4.3 Notre expérience

Montage expérimental : Nous avons cherché à créer deux condensats de Bose-Einstein de vitesse relative suffisante pour qu'ils collisionnent comme des particules libres [4]. Comme nous ne détectons que les atomes dans $m = 0$ (cf section 2.3), il faut aussi que les atomes des condensats soient dans cet état. Tout ceci est réalisé dans notre montage par trois faisceaux qui effectuent deux transitions Raman $m = 1 \to m = 0$ avec deux transferts de vitesse différents. Le schéma du transfert est expliqué sur la figure 4.2. Les faisceaux sont proches de la transition $2\,^3S_1 \to 2\,^3P_0$. La transition vers $2\,^3P_2$ serait moins efficace car on ne pourrait éviter un peuplement de l'état $m = -1$, et la transition vers $2\,^3P_1$ est peu favorable à cause de l'apparition du phénomène de superradiance Raman (cf section 4.5). Comme les atomes diffusés sont dans l'état $m = 0$ il n'est pas nécessaire de couper le champ magnétique après les impulsions Raman.

Dès que le transfert est effectué les collisions se produisent jusqu'à un temps où le taux de collision devient négligeable. Dans notre cas, ce temps n'est pas donné par la séparation physique des deux condensats mais par leur expansion radiale car la vitesse relative des condensats est dirigée suivant l'axe long des condensats [5]. Un calcul semi-classique du taux de collisions montre que celui-ci chute d'un facteur 2 après typiquement 140 μs.

Observation de la sphère de collision : Il suffit ensuite de mesurer la position et le temps d'arrivée des atomes sur le détecteur puis de faire le calcul des corrélations atomiques dans la sphère de diffusion. Bien que l'on observe un certain nombre d'effets parasites, la

---

[4] Cela signifie que la vitesse relative doit être grande devant la vitesse du son [254]. Le rapport des deux vaut en gros 8 dans notre cas.

[5] Ces temps sont alors de l'ordre de $r_{||}/2v_{rec}$ et $1/\omega_\perp$. Leur rapport est donc $\frac{\omega_\perp}{\omega_{||}}\sqrt{\frac{\mu}{E_{rec}}}$ où $\omega_\perp$ et $\omega_{||}$ sont les fréquences d'oscillation transverse et longitudinale, μ le potentiel chimique et E_{rec} l'énergie de recul.

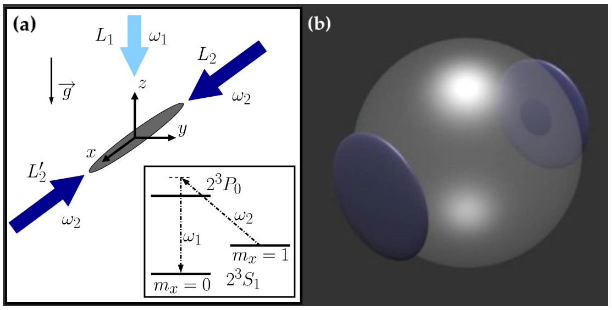

FIG. 4.2 – *Dispositif expérimental pour le transfert Raman. Les faisceaux L_2 et L_1 induisent une transition Raman vers l'état $m = 0$ avec un transfert de vitesse de $v_{rec}(\mathbf{e_x} - \mathbf{e_z})$. De même les faisceaux L_2' et L_1 induisent une transition Raman vers l'état $m = 0$ avec un transfert de vitesse de $v_{rec}(-\mathbf{e_x} - \mathbf{e_z})$. Les deux transitions sont effectuées en même temps et durent 500 ns. La figure de droite représente la sphère de collision et les deux condensats après un temps de vol long. Figure extraite de Ref. [25].*

sphère de diffusion est bien visible comme le montre la figure 4.3. Le nombre d'atomes détectés sur la sphère est en moyenne de 100. La détectivité étant estimée à 10%, cela correspond donc à 1000 atomes et représente ainsi environ 5% des atomes du condensat initial.

Observation d'une corrélation opposée et locale : La figure 4.4 présente les résultats sur la corrélation. Tout d'abord, comme pour les corrélations vues dans le chapitre précédent, nous avons été obligé de moyenner sur tous les couples d'atomes ayant la même différence de position, cf Eq. (3.5) [6]. Ensuite, pour plus de clarté, les courbes tracées sont des projections de la fonction de corrélation 3D. Les axes sont les axes propres du condensat initial. Finalement, nous avons également tracé ces projections pour des atomes proches (corrélation locale) en plus de celles des atomes de vitesses relatives opposées.

Nous observons bien une corrélation, preuve que les atomes sont émis par paires. La corrélation est anisotrope, et les tailles mesurées sont proches des largeurs en vitesse de la fonction d'onde initiale du condensat. Comme pour le chapitre précédent, la résolution spatiale du détecteur est trop élevée pour résoudre la vraie corrélation sur l'axe long du condensat (axe x) et limite donc aussi la hauteur de la corrélation. Nous observons également une corrélation locale, qu'un modèle corpusculaire classique est totalement incapable de reproduire. Les largeurs de la fonction de corrélation sont très proches de celles en opposé, mais la hauteur est notablement plus faible.

---

[6] Comme dans le cas du chapitre précédent, ce moyennage fait perdre des informations ; je reviendrai sur ce point dans la partie analyse.

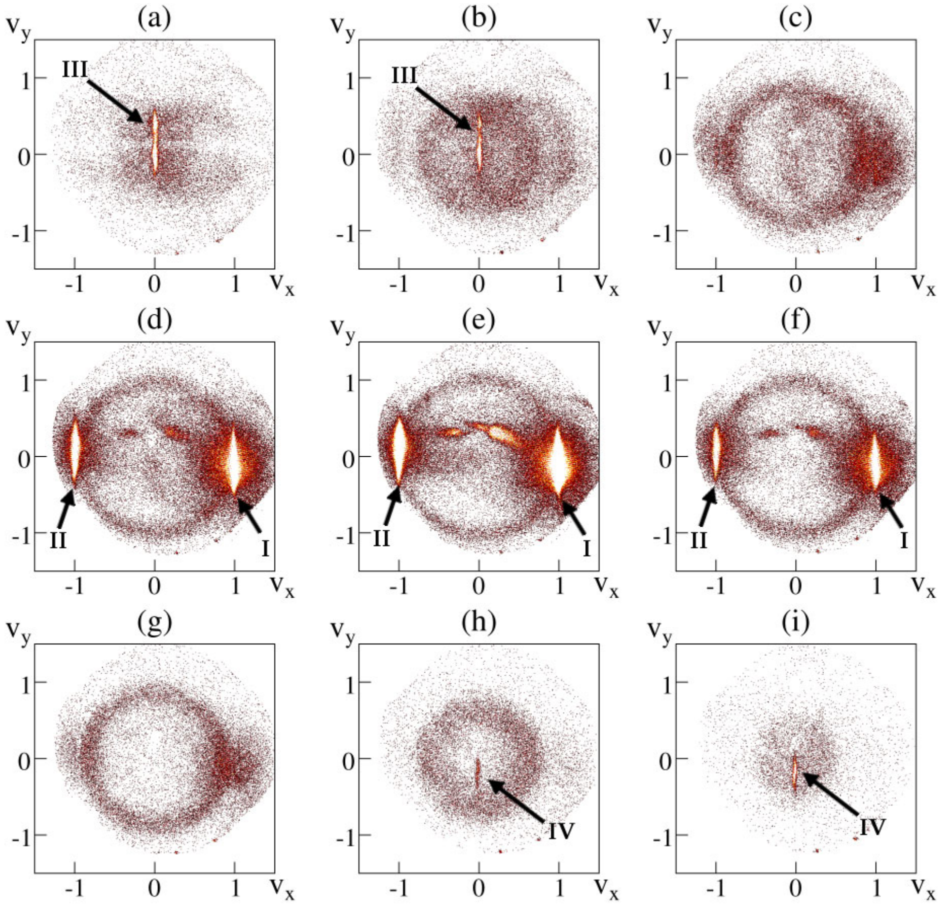

FIG. 4.3 – *Tranche en temps de la sphère de collision sur le détecteur. Les nuages I et II correspondent à la partie restante des deux condensats qui ont collisionné. Il est probable que le nuage III corresponde à un condensat extrait par un processus Raman non résonant à un faisceau et que le nuage IV soit son conjugué par mélange à quatre ondes stimulé. Les vitesses sont normalisées par la vitesse de recul. Voir Ref. [24] pour plus de détails. Figure extraite de Ref. [25].*

4.4 Analyse et interprétation

Approches-informations souhaitées : De très nombreux articles théoriques discutent de la corrélation de particules par collision entre deux condensats. Si l'on rajoute les articles sur la dissociation moléculaire, qui correspond au même Hamiltonien, la liste se rallonge encore plus. Je vais dans la suite utiliser plusieurs approches et donner les résultats auxquels elles conduisent. Le but de cette section est dans l'idéal de comparer nos résultats expérimentaux à un calcul théorique. Je serai dans la plupart des cas moins ambitieux. D'une part, la compréhension théorique des phénomènes mis en jeu s'est révélée plus compliquée que prévu et des études complémentaires sont nécessaires. D'autre part, les données expérimentales ne sont pas assez précises et diversifiées pour être sûr de l'interprétation.

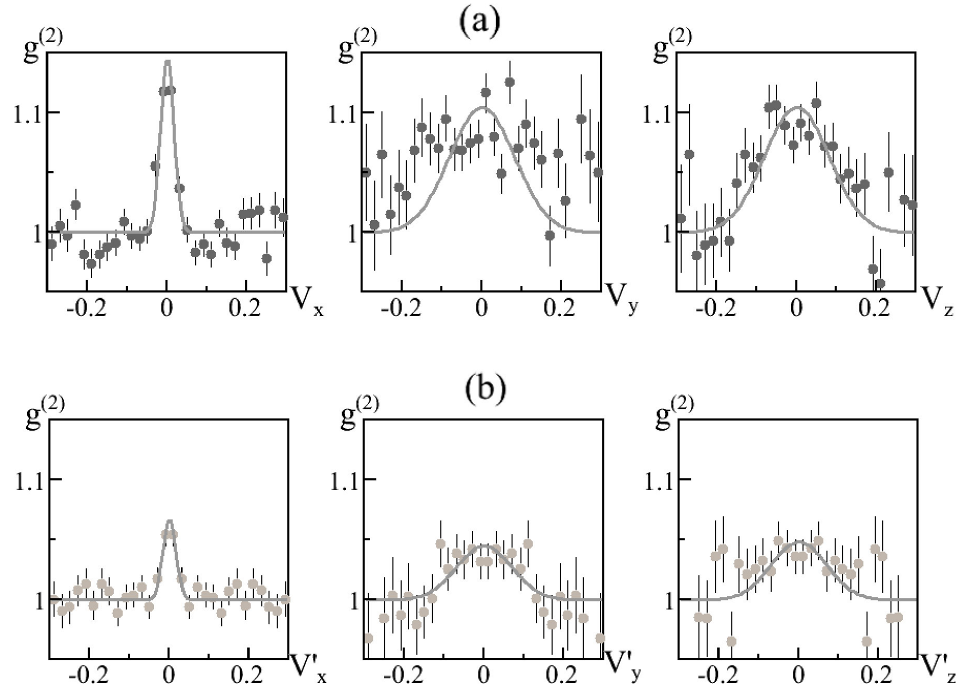

Fig. 4.4 – *Projection de la fonction de corrélation 3D sur les axes propres du condensat initial. a) Corrélation opposée. b) Corrélation locale. On note l'anisotropie des projections, les largeurs similaires en local et en opposé et l'amplitude plus élevée pour la corrélation opposée. Figure extraite de Ref. [25].*

Approche classique : Si l'on adopte le point de vue corpusculaire, notre expérience se résume à une expérience de choc entre deux particules ; les particules incidentes sont des atomes des deux condensats et les particules après le choc sont les atomes diffusés. On s'attend donc à une conservation de l'impulsion et de l'énergie. Le condensat initial ayant une dispersion de vitesses très faible, on peut considérer en première approximation que l'impulsion incidente totale est nulle et que l'énergie incidente totale est de deux énergies de recul. Il en sera donc de même pour les atomes diffusés, d'où la sphère de collision de rayon la vitesse de recul et des paires d'atomes de vitesse opposée. La densité du condensat et la section efficace de collision vont donner le nombre d'atomes diffusés. La taille finie de la fonction d'onde du condensat va se refléter sur une sphère d'épaisseur finie et sur une largeur en vitesse de la fonction de corrélation ($\delta v^{(corr)}$) donnée par la largeur en vitesse (V) de la fonction d'onde des condensats,

$$\delta v_i^{(corr)} \propto V_i \text{ pour } i = x, y, z \tag{4.3}$$

Nous allons, dans une certaine mesure, retrouver ces conclusions dans les modèles suivants. Par contre, cette approche corpusculaire ne peut prédire la corrélation locale observée expérimentalement, ni en conséquence sa largeur. Une approche ondulatoire l'aurait au contraire prédit immédiatement ; les ondes émises de manière spontanée par la source (ici les condensats en collision) ont les propriétés de corrélation d'une source thermique vues au chapitre précédent. On attend donc un effet Hanbury Brown et Twiss, c'est-à-dire un groupement pour des atomes de vitesses proches, d'où une corrélation locale [211]. Comme d'habitude une approche quantique contient automatiquement ces deux points de vue et prédira donc les deux effets.

Calcul onde plane : Si le nombre d'atomes diffusés est négligeable devant le nombre initial dans le condensat et si on peut considérer celui-ci comme étant uniforme, un calcul analytique non perturbatif [7] peut être effectué [255]. En utilisant une base ondes planes pour les modes des atomes diffusés, un atome dans le mode $\mathbf{k}$ est alors exclusivement couplé au mode $-\mathbf{k}$. Les équations de Heisenberg des opérateurs champs $\hat{a}_{\mathbf{k}}$ et $\hat{a}_{-\mathbf{k}}$ sont couplées et peuvent être intégrées analytiquement. On obtient alors les résultats suivants :

$$g^{(2)}(\mathbf{k},\mathbf{k},t) = 2 \tag{4.4}$$

$$g^{(2)}(\mathbf{k},-\mathbf{k},t) = 2 + 1/n_{\mathbf{k}}(t) \tag{4.5}$$

$$g^{(2)}(\mathbf{k},\mathbf{k}',t) = 1 \text{ si } k' \neq k \text{ ou } k' \neq -k \tag{4.6}$$

où $n_{\mathbf{k}} = \langle \hat{a}^{\dagger}_{\mathbf{k}} \hat{a}_{\mathbf{k}} \rangle$ est la population du mode $\mathbf{k}$. Celle-ci est une fonction en $\sinh^2(\gamma t)$ avec γ un taux dépendant du terme de couplage de création des paires et de l'énergie des atomes diffusés. Ce modèle prédit bien l'effet HBT et la corrélation en opposé ainsi que l'influence de la population sur la hauteur de la corrélation en opposé. Remarquons que les facteur 2 de la corrélation locale et opposée ne sont pas reliés et rien n'assure qu'il en sera de même dans le cas d'un condensat inhomogène. De plus, utilisant un condensat homogène, ce modèle prédit des largeurs des fonctions de corrélation infiniment fines.

Calcul perturbatif : Un calcul analytique est possible en régime perturbatif, c'est-à-dire quand le nombre d'atomes extraits est faible devant le nombre d'atomes dans le condensat initial et quand la population des modes diffusés est faible devant un (régime spontané). Cette approche a été suivie par M. Trippenbach dans une série d'articles [249, 250, 256] et par V. A. Yurovsky [247]. Dans le cas d'un piège isotrope, cette approche peut être comparé avec un calcul numérique, valide même dans le régime stimulé (modes de population supérieure à un) [250, 256].

Une collaboration avec M. Trippenbach et ses collègues est en cours pour étudier le cas de la collision entre deux condensats anisotropes, la collision se produisant suivant l'axe long (Ox dans la suite) des condensats [213]. Même si tous les calculs ne sont pas finis, on retrouve que les longueurs de corrélation en opposé sont reliées aux tailles V_i de la distribution en vitesse du condensat initial. On retrouve également une hauteur de la corrélation inversement proportionnelle à la population des modes de la sphère.

La corrélation locale conduit bien à $g^{(2)}(\mathbf{k},\mathbf{k}) = 2$ [211] mais la largeur de la fonction de corrélation apporte quelques surprises à première vue. On trouve que la largeur de la fonction de corrélation $g^{(2)}(\mathbf{k}+\delta\mathbf{k},\mathbf{k}-\delta\mathbf{k})$ est certes anisotrope (dépend de la direction de $\delta\mathbf{k}$) mais est aussi inhomogène (dépend de la direction de $\mathbf{k}$). On retrouve un résultat

---

[7] Un mode $\mathbf{k}$ peut avoir une population grande devant 1, mais la somme des populations de tous les modes doit rester faible devant le nombre d'atomes des condensats initiaux.

équivalent à Eq.(4.3) uniquement quand $\mathbf{k}\perp\delta\mathbf{k}$. Dans les autres situations la corrélation en locale aura une largeur proche de V_x quelque soit la direction de $\delta\mathbf{k}$. Ce résultat est un peu difficile à comprendre mais on peut tenter quelques hypothèses. L'équation (4.3) provient uniquement de la conservation de la quantité de mouvement. Cependant il y a aussi conservation de l'énergie. Cette équation est une équation qui mélange toutes les directions ; or l'énergie cinétique initiale dépend au premier ordre uniquement de la vitesse suivant x des atomes car la collision se produit suivant x. Comme dans notre situation expérimentale $V_x \ll V_y = V_z$, il n'est pas aberrant que la corrélation locale soit dominée par V_x.

Quoiqu'il en soit on ne peut que constater que ce modèle n'explique pas parfaitement nos résultats expérimentaux où corrélation locale et opposée ont des largeurs semblables. Il est probable que ceci soit relié au fait que dans ce modèle on ne prend pas en compte le champ moyen i.e. que les atomes diffusés sont créés sur une colline de potentiel inhomogène. Ceci va nécessairement élargir les corrélations. Une simulation de cet effet classique est en cours.

Approche “Positive-P” : Il existe des méthodes numériques pouvant s'appliquer dans le régime stimulé. On peut citer la méthode *truncated Wigner* [251, 257] mais je vais détailler un peu plus la méthode *Positive P* puisque nous avons une collaboration avec K. Kheruntsyan [212]. Cette méthode [258] consiste à remplacer les opérateurs champ dans le Hamiltonien N corps par des champs classiques en ajoutant des termes de bruits. Les équations d'évolution de ces champs sont ensuite calculer numériquement. Cette méthode est très puissante car on peut démontrer l'exacte équivalence entre les résultats quantiques et ceux donnés par cette méthode après moyennage sur différentes réalisations du bruit. Cependant cette méthode a deux talons d'Achille. Tout d'abord elle est très exigeante numériquement ; les calculs qu'Aurélien Perrin a effectués en Australie nécessitaient typiquement 100 heures de calculs sur 7 CPU en parallèle ! Deuxièmement, une instabilité numérique fait que les résultats deviennent aberrants à partir d'un certain temps d'évolution temporelle (amplification exponentielle du bruit [259]). Le temps maximal d'applicabilité est de 25 μs dans nos conditions expérimentales alors que le temps de collision est de l'ordre de 140 μs. La simulation complète de notre expérience est donc impossible.

Les résultats obtenus sont cependant en très bon accord avec les données expérimentales (à 20% près). En conséquence ils le sont moins avec le calcul perturbatif. Ceci pourrait s'expliquer par le fait que la méthode *Positive P* étant restreinte à des temps très courts, la conservation de l'énergie est moins stricte et il est donc logique d'obtenir un résultat conforme à la conservation de la quantité de mouvement.

Cette simulation montre aussi que des effets de stimulation bosonique devraient être observables expérimentalement si nous sommes capables d'avoir des condensats ayant un nombre d'atomes d'un ordre de grandeur plus grand. Deux articles théoriques se sont intéressés à cette situation. Même si l'approche de Pu et Meystre [246] semble incorrecte [248, 260], Vardi et Moore [248] prédisent le même type d'effet : dans certaines situations, l'anisotropie du condensat peut conduire à ce que les atomes ne soient diffusés que dans des modes se propageant suivant l'axe long du condensat. Cette situation est analogue au phénomène de superradiance [261] (cf section suivante) où les photons diffusés d'un condensat anisotrope ne sont plus émis isotropiquement mais sont dirigés suivant l'axe long du condensat (*end-fire modes*). Cependant, le critère d'apparition de la directionnalité dans Ref. [248] est difficilement "chiffrable" et nécessiterait une étude plus approfondie.

4.5 Perspectives

Calculateur quantique : On associe de plus en plus les termes optique (atomique) quantique et information quantique. J'ai déjà mentionné au 4.2 les expériences sur des ions piégés. L'un des systèmes envisagés sur les atomes neutres est le piégeage d'atomes dans un réseau optique dans le régime de Mott (exactement un atome par puits). Dans ce cadre l'hélium métastable ne semble pas être un bon candidat car son atout réside dans sa détection en temps de vol alors qu'il est vraisemblable que les opérations entre qubits et la lecture de ces derniers nécessiteront des méthodes in situ ayant en plus une efficacité de détection proche de 100%. Si on ote de la problématique ce dernier point, l'hélium métastable pourrait être un atome intéressant si on utilise plutôt une approche équivalentes aux "variables continues" de l'optique quantique en opposition aux photons uniques. L'information quantique sera ainsi partagée par plusieurs atomes et pourrait être codée sur l'impulsion et non sur le spin d'atomes localisés. Une telle approche est envisagée par exemple dans Ref. [262]. Ce thème de recherche semble cependant difficile à aborder, d'autant plus quand on ajoute le problème de détectivité.

Densité anisotrope : J'ai mentionné précédemment qu'il existe encore peu d'études théoriques dans le cas où la population des modes sur la sphère est proche ou supérieure à un. Le premier effet devant apparaître serait une augmentation de la population des modes dans l'axe long du condensat [248, 260]. Comme dans notre situation expérimentale les condensats collisionnent dans cette direction, ces zones de la sphère de collision sont occupées par les deux condensats et aucune mesure n'est possible (cf. fig. 4.2). Il faudrait donc faire se collisionner les condensats suivant leur axe court. Cependant la direction longue est celle qui maximisait le nombre de collisions ; le nombre d'atomes diffusés serait donc plus faible et pourrait rendre l'expérience difficile à mener à son terme.

Classique ou quantique, telle est la question : On peut se demander ce qui est quantique dans une collision entre deux condensats. Si on utilise un point de vue ondulatoire, la corrélation en opposée, la stimulation bosonique éventuelle sont quantiques, alors que la corrélation locale est classique. D'un point de vue corpusculaire, plus naturel pour des atomes, la corrélation en opposée est classique et la stimulation ainsi que la corrélation locale sont quantiques. Ce type d'expériences touche donc intimement à la dualité onde-corpuscule. On pourrait aller un peu plus loin dans ce sens en s'intéressant au squeezing (réduction de fluctuations) de la différence de populations entre modes diamétralement opposées et à la violation d'inégalités de Cauchy-Schwartz [224, 263, 264, 212, 265].

Si le détecteur a une efficacité de 100%, d'un point de vue corpusculaire on s'attend donc à ce que la différence de population entre deux modes diamétralement opposées soit strictement nulle et donc que le squeezing soit parfait (variance de la différence de populations nulle). Ce résultat n'est pas du tout évident avec une approche ondulatoire. Le calcul quantique dans le cas de la collision entre deux ondes planes de matière conduit également à un squeezing parfait, mais le résultat n'est pas connu dans le cas plus réaliste d'ondes de matière de taille finie. Des effets de champ moyen, de collisions multiples pourraient également limiter la valeur du squeezing.

Avec un détecteur d'efficacité $\eta < 1$, l'observation de squeezing est plus délicate. Si on considère une sphère de collision contenant N atomes, seuls ηN atomes seront détectés. Considérons deux hémisphères. S'il n'existe aucun processus de création de paires, le bruit sur la mesure du nombre détecté sur chaque hémisphère ainsi que de la différence de population entre les hémisphères sera en $\sim \sqrt{\eta N}$. Si au contraire la sphère ne contient que des paires, le bruit sur la différence de population devrait être en $\sim \sqrt{(1-\eta)\eta N}$. Pour démontrer une réduction de fluctuations sur la différence de population, il faut donc que le bruit sur la mesure du bruit soit faible. Avec une efficacité estimée de l'ordre de $\eta \approx 0.1$, il faut que la mesure de la largeur de la distribution de différence de population entre les hémisphères soit précise au % près, ce qui n'est pas simple. Bien que l'analyse des résultats de cette expérience [24] semble faire croire que nous avons effectivement observé une réduction des fluctuations, le traitement informatique n'est pas assez robuste pour l'affirmer. Cette mesure semble toutefois envisageable si l'on parvient à accumuler plus de données (deux à trois fois plus que pour l'expérience décrite dans ce chapitre).

Intrication - Inégalité de Bell : L'état que nous créons par cette collision est un état à N corps, Eq.(4.2). Il s'agit donc d'un état intriqué. Si on utilise l'approche perturbative vue plus haut, ainsi que les approximations de Ref. [213] on trouve, à temps long,

$$|\Psi\rangle \approx \iint d\mathbf{q} d\mathbf{k}\, e^{-(\frac{q_\perp \sigma_\perp}{2})^2 - (\frac{q_x \sigma_x}{2})^2} h(\zeta)\, |\mathbf{k}+\mathbf{q}/2, -\mathbf{k}+\mathbf{q}/2\rangle$$

avec $\zeta = \frac{\sigma_Q}{4Q}(2Q^2 - 2k^2 - q^2)$ et $h(\zeta) = e^{-\zeta^2}[\mathrm{Erfi}(\zeta) + i]$. Dans ces expressions $\sigma_x, \sigma_\perp$ et σ_Q sont respectivement les largeurs des condensats initiaux suivant les axes long, court et suivant la direction de la collision. Les condensats ont dans ce modèle une vitesse relative de $\pm \hbar Q/m$. La fonction h étant complexe, chaque couple d'atomes jumeaux a une phase propre.

Il serait évidemment très intéressant de démontrer cette intrication et de violer des inégalités de Bell correspondantes. En optique, les inégalités de Bell ont été testées d'abord sur des états intriqués en polarisation [217, 218, 219, 220]. Ce n'est qu'en 1990 que J. G. Rarity et P. R. Tapster montre l'intrication en impulsion [221, 216]. L'idée était de considérer deux paires de photons et de les mélanger sur des séparatrices. La mesure de taux de coïncidences entre les différents détecteurs à la sortie des deux séparatrices leur a permis de démontrer l'intrication.

Nous pourrions utiliser une méthode analogue où la séparatrice est remplacée par une impulsion Bragg $\pi/2$ (voir Ref. [266] pour une autre proposition). La difficulté réside dans le très faible nombre de paires que nous créons par nuage. La statistique sera donc très mauvaise, ce qui rend cette expérience difficile voire impossible sauf si on parvient à obtenir des condensats plus gros [8].

---

[8] Comme le processus de création de paires varie en N^α où $\alpha \approx 1.4$, un condensat contenant 10 fois plus d'atomes produira 25 fois plus de paires. De tels condensats ont déjà été produits dans les autres groupes ayant des condensats d'hélium métastable.

Une autre façon de démontrer l'intrication est d'utiliser le critère d'inséparabilité de Duan, Gieldke, Cirac et Zoller [267]. En désignant par $j = 1, 2$ la particule de la paire et en définissant $\hat{X} = \hat{x}_1 + \hat{x}_2$ et $\hat{k} = \hat{k}_1 - \hat{k}_2$, ils ont montré que si $(\Delta \hat{X})(\Delta \hat{K}) \leq 2$, alors l'état était intriqué [9]. Dans ces équations les positions sont les positions initiales, au moment de la création de la paire. Cette méthode se rapproche de ce qu'on appelle "ghost interference", mis en avant dans le groupe de Y. Shih [268, 269]. Une mesure directe in situ de la corrélation spatiale est inenvisageable mais une mesure sur une image du nuage suffirait. Cependant, la réalisation d'une lentille atomique, de qualité et ayant la bonne focale n'est sans doute pas triviale.

Photoassociation comme méthode alternative de création de paires : Il faudra peut être considérer d'autres propositions pour créer des paires, comme par exemple en utilisant la photoassociation [270]. Une méthode similaire a été proposée par F. Masnou-Seeuws [271, 272] et je vais la détailler un peu. L'idée est d'illuminer un condensat avec un laser accordé sur une résonance moléculaire. Deux atomes à la bonne distance vont former une molécule qui va se désexciter pour former soit une molécule dans l'état fondamental soit deux atomes libres. Comme ce processus est symétrique pour les atomes, ces atomes libres sont corrélés. L'optimisation de ce processus de formation de paires consiste à avoir un taux de production important, une distribution d'énergie faible (on couple vers un continuum donc toutes les paires n'auront pas la même énergie cinétique) et des processus parasites faibles, comme l'émission spontanée atomique si le niveau moléculaire est peu désaccordé par rapport à la transition atomique. Des calculs sont en cours sur l'hélium métastable (F. Masnou-Seeuws, P. Naidon, J. Mur Petit).

Mélange à quatre ondes stimulé : Les premières observations expérimentales d'un mélange à quatre ondes stimulé ont été obtenues dans le groupe de W. Ketterle et W. D. Phillips [125, 126, 273]. Dans ces expériences, les atomes dans le mode du "germe" et ceux du mode conjugué doivent également conduire à un squeezing. L'inconvénient expérimental est la possible saturation du détecteur si ces condensats sont trop denses (cf 2.3). Evidemment ces sources sont aussi de bons candidats pour de l'intrication car il n'y a que deux modes à considérer et non pas tous ceux de la sphère de collision dans le processus spontané. On peut noter toutefois que dans un réseau optique, comme la relation de dispersion est modifiée, il y a une grande flexibilité dans les modes qui peuvent être stimulés [274, 275]. Cela pourrait être plus intéressant d'un point de vue pratique.

Superradiance : Si la diffusion de la lumière par un atome est simple à décrire, la situation se complique très vite dans le cas de la diffusion par un grand nombre d'atomes. En particulier il peut apparaître un phénomène de superradiance dans le cas d'un nuage de taille faible devant la longueur d'onde optique ou dans le cas d'un nuage allongé [276, 277, 261]. Dans ce dernier cas, la lumière de fluorescence n'est plus isotrope mais se concentre sur l'axe long du nuage. Suivant le nombre d'atomes et l'anisotropie du nuage, plusieurs régimes différents apparaissent et leurs compréhensions théoriques restent délicates. La su-

---

[9] Chacune des particules vérifie bien sûr $[\hat{x}_j, \hat{k}_j] = i$ et donc $(\Delta \hat{x}_j)(\Delta \hat{k}_j) \geq 1$, mais les opérateurs $\hat{X}$ et $\hat{K}$ commutent et donc $(\Delta \hat{X})(\Delta \hat{K}) = 0$ est possible en théorie.

perradiance a été observée et étudiée depuis les années 1970 [261] et elle a été observée depuis sur des condensats de Bose-Einstein [278, 273, 279] ainsi que sur des nuages thermiques froids [280]. Comme dans ces situations la largeur de la distribution de vitesses est faible ou de l'ordre de la vitesse de recul, les atomes ayant subi un (ou plusieurs) cycle de fluorescence se distinguent très facilement des autres dans un temps de vol. Des propriété de corrélation ont été prédites (corrélation atome-lumière et atome-atome) [260] mais il n'existe pas encore de mesure. Ce mécanisme a d'ailleurs été utilisé pour amplifier des ondes de matière [281, 282]. La figure 4.5 présente des exemples de superradiance observée sur notre montage expérimental quand un faisceau laser est proche du niveau 2 $^3P_1$.

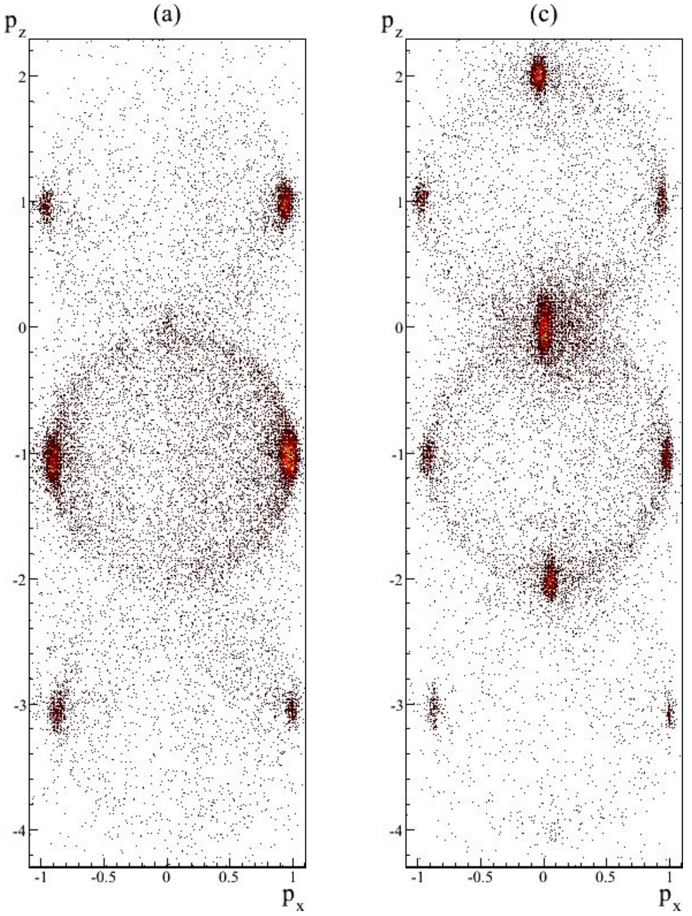

FIG. 4.5 – *Exemples de superradiance observés dans notre montage expérimental avec un faisceau pompe polarisé linéairement se propageant suivant l'axe Oz. Dans la courbe de gauche la polarisation est suivant Ox et dans celle de droite, suivant Oy. Outre les condensats ayant des vitesses de* $nk_z + pk_x$ *avec* (n, p) *entiers relatifs, on remarque également des sphères de collision. Voir la thèse d'A. Perrin [24] pour plus de détails.*

Chapitre 5

Conclusion

Ce manuscrit traduit 10 ans de recherche sur le montage “hélium métastable” du laboratoire Charles Fabry de l’Institut d’Optique. Débutant avec une source d’atomes froids, nous sommes parvenus à atteindre la dégénérescence quantique et utiliser les atouts de cet atome pour entrer dans le régime de l’optique atomique quantique. Les premières expériences sur la corrélation d’intensité de nuages thermiques ou dégénérés nous ont montré que notre dispositif expérimental était très performant. L’étude de situations plus exotiques a commencé avec la création de paires d’atomes, mais clairement nous sommes au début d’une longue histoire : corrélation de nuages à basse dimensionnalité, confinés dans un réseau optique, inégalités de Bell pour ne citer que quelques exemples. L’analyse de la plupart de ces expériences est de nature statistique. Le nombre d’atomes participant à l’expérience et l’efficacité de détection seront ainsi deux paramètres importants qui aiguillonneront nos choix expérimentaux.

Annexe A

Partie administrative

A.1 Curriculum vitae

- Ancien élève de l'Ecole Normale Supérieure de Lyon (1990 – 1995).
- Agrégé de physique option physique (1993, $17^{\text{ème}}$).
- Thèse au laboratoire Kastler Brossel (1994 – 1998) sous la direction de Christophe Salomon (DR CNRS).
  Thèse soutenue le 16 janvier 1998 à l'université Paris VI avec pour titre : *Etude du refroidissement et du piégeage d'atomes de césium dans des structures lumineuses à faible taux de diffusion.*
  Allocataire couplé de l'université Paris VI (1995–1998)
- Maître de conférence à l'Institut d'Optique - Graduate School depuis septembre 1998.
  Travail de recherche au sein du laboratoire Charles Fabry de l'Institut d'Optique dans le groupe "optique atomique" dirigé par Alain Aspect.

A.2 Responsabilités administratives

Liste de mes principales activités administratives depuis 1998 :

- Enseignement :
  - Examinateur TP d'optique du concours d'entrée Centrale-SupElec depuis 1999.
  - Responsable pédagogique du CFA SupOptique (centre de formation par l'apprentissage, dispense de 24 h. eq. TD) depuis 2002.
  - Membre du conseil de la formation de l'Institut d'Optique-Graduate School depuis 2004.
  - Responsable de la partie physique pour l'admission sur titre à l'Institut d'Optique-Graduate School depuis 2006.
- Recherche :
  - Membre de la commission de spécialiste CS30 de l'université Paris-Sud depuis 2000.
  - Membre du jury de thèse d'Olivier Sirjean (27/06/2003) et de Rodolphe Hoppeler (28/10/2005).
  - Membre invité du jury de thèse de Jose Carlos Viana Gomes (09/02/2007) et d'Aurélien Perrin (29/11/2007).

- Contrat Pessoa (*Puce à atomes et corrélations spatiales de condensats de Bose-Einstein*) avec Prof. M. Belsley (université de Minho, Portugal) de 2004 à 2006.
- Contrat Pessoa (*Propriétés de cohérence d'un faisceau d'atomes ultra-froids*) avec Prof. J. Viana Gomes (université de Minho, Portugal) en 2008.

A.3 Encadrement d'étudiants

A.3.1 Etudiants en DEA et M2

J'ai encadré 5 étudiants en stage de DEA ou M2 :

- 2000 : Olivier Sirjean, DEA laser et matières, *Piégeage magnétique de l'hélium métastable.*
- 2001 : Jérome de Vasconcelos, DEA physique théorique, *Etude théorique de la thermalisation d'un gaz d'atomes piégés.*
- 2002 : Rodolphe Hoppeler, DEA physique théorique rhône-alpin, *Condensation de Bose-Einstein de l'hélium métastable : mise en oeuvre d'une transition Raman stimulée pour la détection du condensat.*
- 2004 : Aurélien Perrin, DEA physique quantique, *Transfert adiabatique de population par utilisation d'états non couplés.*
- 2007 : Jean-Christophe Jaskula, M2 physique du solide *Condensation de Bose-Einstein de l'hélium métastable - Diode laser en cavité étendue.*

A.3.2 Etudiants en thèse

Co-encadrement : J'estime mon pourcentage d'encadrement entre 50 et 70% suivant les étudiants. Le directeur de thèse est soit Alain Aspect soit Christoph Westbrook à l'exception de Jean-Christophe Jaskula dont je suis officiellement le directeur de thèse. Je donnerai leurs contributions respectives à la fin de l'introduction de chacun des chapitres du manuscrit.

Thèses déjà soutenues :

- 2000 : Julie Poupard : *Mesure de deux caractéristiques de l'hélium métastable importantes pour le refroidissement radiatif.*
- 2000 : Antoine Browaeys : *Piégeage magnétique d'un gaz d'hélium métastable : vers la condensation de Bose-Einstein.*
- 2001 : Alice Robert : *Réalisation d'un condensat de Bose-Einstein d'atomes d'hélium métastable.*
- 2003 : Olivier Sirjean : *Collisions ionisantes : un nouveau diagnostic pour les condensats de Bose-Einstein d'hélium métastable.*
- 2004 : Signe Seidelin : *Collisions dans un gaz d'hélium métastable au voisinage de la dégénérescence quantique.*
- 2005 : Rodolphe Hoppeler : *De la condensation de Bose-Einstein à l'effet Hanbury Brown et Twiss atomique de l'hélium métastable.*
- 2007 : Jose Carlos Viana Gomes : *Thermométrie et propriétés de cohérence d'un gaz quantique ultra-froid d'hélium métastable.*

- 2007 : Martijn Schellekens : *L'effet Hanbury Brown et Twiss pour les atomes froids.*
- 2007 : Aurélien Perrin : *Observation de paires d'atomes corrélés au travers de la collision de deux condensats de Bose-Einstein.*

Thèses en cours : Valentina Krachmalnicoff (soutenance prévue en 2009), Jean-Christophe Jaskula (soutenance prévue en 2010), Marie Bonneau (soutenance prévue en 2011).

Premier emploi en CDI des anciens thésards : université/CNRS : 3, industrie : 3, enseignement dans le secondaire : 2.

A.3.3 Docteurs en séjour post-doctoral

Pour être complet, l'équipe a aussi accueilli des docteurs en séjour post-doctoral : Stephan Nowak en 1999-2000, Hong Chang en 2006-2007, Vanessa Leung en 2007-2008 et Guthrie Partridge en 2008-2009.

Annexe B

Publications

B.1 Publications depuis 1998

B.1.1 Publications dans des revues à comité de lecture

1. **Pair correlations of scattered atoms from two colliding Bose-Einstein Condensates : Perturbative Approach**
   J. Chwedeńczuk, P. Ziń, M. Trippenbach, A. Perrin, V. Leung, D. Boiron and C. I. Westbrook,
   Physical Review A **78**, 053605 (2008)
2. **Atomic four-wave mixing via condensate collisions**
   A. Perrin, C. M. Savage, D. Boiron, V. Krachmalnicoff, C. I. Westbrook and K.V. Kheruntsyan,
   New Journal of Physics **10**, 045021 (2008)
3. **Hanbury Brown and Twiss correlations in atoms scattered from colliding condensates**
   K. Mølmer, A. Perrin, V. Krachmalnicoff, V. Leung, D. Boiron, A. Aspect and C. I. Westbrook,
   Physical Review A **77**, 033601 (2008)
4. **Comment on "Quantum time-of-flight distribution for cold trapped atoms"**
   J. Viana Gomes, M. Belsley, D. Boiron,
   Physical Review A **77**, 026101 (2008)
5. **Observation of atom pairs in spontaneous four wave mixing of two colliding Bose-Einstein Condensates**
   A. Perrin, H. Chang, V. Krachmalnicoff, M. Schellekens, D. Boiron, A. Aspect and C. I. Westbrook,
   Physical Review Letters **99**, 150405 (2007)
6. **Comparison of the Hanbury Brown-Twiss effect for bosons and fermions**
   T. Jeltes, J. M. McNamara, W. Hogervorst, W. Vassen, V. Krachmalnicoff, M. Schellekens, A. Perrin, H. Chang, D. Boiron, A. Aspect, C. I. Westbrook
   Nature **445**, 402 (2007)

7. **Atomic density of a harmonically trapped ideal gas near Bose-Einstein transition temperature**
R. Hoppeler, J. Viana Gomes, D. Boiron
European Physical Journal D **41**, 157 (2007)
8. **Theory for a Hanbury Brown Twiss experiment with a ballistically expanding cloud of cold atoms**
J. Viana Gomes, A. Perrin, M. Schellekens, D. Boiron, C. I. Westbrook and M. Belsley
Physical Review A **74**, 053607 (2006)
9. **Hanbury Brown Twiss effect for ultracold quantum gases**
M. Schellekens, R. Hoppeler, A. Perrin, J. Viana Gomes, D. Boiron, A. Aspect, and C. I. Westbrook
Science **310**, 648 (2005)
Sciencexpress, 10.1126/science.1118024 le 15/09/2005
10. **Getting the Elastic Scattering Length by Observing Inelastic Collisions in Ultracold Metastable Helium Atoms**
S. Seidelin, J. Viana Gomes, R. Hoppeler, O. Sirjean, D. Boiron, A. Aspect, and C. I. Westbrook
Physical Review Letters **93**, 090409 (2004)
11. **Using ion production to monitor the birth and death of a metastable helium Bose-Einstein condensate**
S. Seidelin, O. Sirjean, J. Viana Gomes, D. Boiron, C. I. Westbrook, and A. Aspect
Journal of Optics B **5**, S112 (2003)
12. **Ionization rates in a Bose-Einstein condensate of metastable Helium**
O. Sirjean, S. Seidelin, J. Gomes, D. Boiron, C. I. Westbrook, A. Aspect, G. Shlyapnikov
Physical Review Letters **89**, 220406 (2002)
13. **A Bose-Einstein condensate of metastable atoms**
A. Robert, O. Sirjean, A. Browaeys, J. Poupard, S. Nowak, D. Boiron, C. I. Westbrook, A. Aspect
Science **292**, 461 (2001)
Sciencexpress, 10.1126/science.1060622 le 22/03/2001
14. **Thermalization of magnetically trapped metastable helium**
A. Browaeys, A. Robert, O. Sirjean, D. Boiron, C. I. Westbrook, A. Aspect
Physical Review A **64**, 034703 (2001)
15. **Magnetic trapping of metastable helium atoms**
S. Nowak, A. Browaeys, J. Poupard, A. Robert, D. Boiron, C. I. Westbrook, A. Aspect
Applied Physics B **70**, 455 (2000)
16. **Two body loss rate in a magneto-optical trap of metastable He**
A. Browaeys, J. Poupard, A. Robert, S. Nowak, W. Rooijakkers, E. Arimondo, L. Marcassa, D. Boiron, C. I. Westbrook, A. Aspect
European Physical Journal D **8**, 199 (2000)

B.1.2 Contributions à un ouvrage collectif

1. **Density correlations of an ultra-cold quantum gas in the vicinity of Bose-Einstein condensation**
   J. Viana Gomes, D. Boiron, M. Belsley
   Strongly correlated systems, coherence and entanglement, edts. J. M. P. Carmelo, P. D. Sacramento, J. M. B. Lopes dos Santos and V. Rocha Vieira, World Scientific (Singapore 2007), p.335-384.

2. **Producing and Detecting Correlated atoms**
   C. I. Westbrook, M. Schellekens, A. Perrin, V. Krachmalnicoff, J. Viana Gomes, J.-B. Trebbia, J. Estève, H. Chang, I. Bouchoule, D. Boiron, A. Aspect, T. Jeltes, J. McNamara, W. Hogervorst, W. Vassen.
   Atomic Physics 20, Proceedings of the International Conference on Atomic Physics, Innsbruck, Austria 16-21 July 2006, Am. Inst. Phys. (USA, 2006), edts. C. Roos, H. Haffner and R. Blatt, p. 181-187.

3. **The Hanbury Brown Twiss Effect for Atoms**
   C. I. Westbrook, M. Schellekens, A. Perrin, R. Hoppeler, J. Viana Gomes, D. Boiron, A. Aspect.
   Laser Spectroscopy, Proceedings of the XVII International Conference on Laser Spectroscopy, Aviemore, Scotland 19-24 June 2005, World Scientific (Singapore, 2005), edts. E. Hinds, A. Ferguson and E. Riis, p. 299-306.

4. **Bose-Einstein condensation of metastable helium : some experimental aspects**
   C. I. Westbrook, A. Robert, O. Sirjean, A. Browaeys, D. Boiron, A. Aspect
   15th International Conference on LASER Spectroscopy, World Scientific, Singapore (2002), edts. S. Chu, V. Vuletic, A.J. Kerman, C. Chin, p. 12-20.

5. **Condensation of metastable helium**
   S. Seidelin, O. Sirjean, A. Robert, A. Browaeys, J. Poupard, D. Boiron, C.I. Westbrook, A. Aspect
   Journal de physique IV **12**, 135 (2002)

6. **Development of a magnetic trap for metastable helium atoms**
   A. Robert, A. Browaeys, J. Poupard, S. Nowak, D. Boiron, C. I. Westbrook, A. Aspect
   Journal de physique IV **10**, 137 (2000)

B.1.3 Articles de vulgarisation

1. **Quantum atom optics with bosons and fermions**
   A. Aspect, D. Boiron, C. I. Westbrook
   Europhysicsnews **39**, p.25–29 (2008)

2. **L'optique atomique quantique : après les bosons, les fermions**
   A. Aspect, D. Boiron, C. I. Westbrook
   Reflets de la physique **4**, p.10–14 (2007)

B.1.4 Contributions à des conférences internationales

Je n'indique que les conférences auxquelles j'ai personnellement participé.

1. **Noise and correlation measurements using single atom detection**
   A. Perrin, H. Chang, V. Krachmalnicoff, M. Schellekens, J.-C. Jaskula, V. Leung, D. Boiron, A. Aspect, C. I. Westbrook
   21st International Conference on Atomic Physics, Storrs (USA), juillet 2008
2. **Quantum degenerate gases of metastable helium atoms**
   D. Boiron, A. Perrin, V. Krachmalnicoff, M. Schellekens, H. Chang, V. Leung, A. Aspect, C. I. Westbrook, S. Moal, M. Portier, J. Dugué, M. Leduc, C. Cohen-Tannoudji, T. Jeltes, J. McNamara, W. Hogervorst, W. Vassen
   EuroQuam Inaugural Conference, Barcelone (Espagne), avril 2008
3. **Production and detection of correlated atom pairs**
   D. Boiron, A. Perrin, H. Chang, V. Krachmalnicoff, M. Schellekens, A. Aspect, C. I. Westbrook
   Workshop on Quantum Engineering based on Atoms and Photons, Hannovre (Allemagne), février 2007
4. **Cold atoms, BEC and atomic Hanbury Brown and Twiss experiment with He***
   D. Boiron, M. Schellekens, A. Perrin, J. Viana Gomes, A. Aspect, C. I. Westbrook
   CBES 2005 – Complex Behavior in Electronic Systems, Braga (Portugal), septembre 2005
   conférence invitée
5. **Correlation properties of an ideal cloud near quantum degeneracy**
   D. Boiron, J. Viana Gomes, R. Hoppeler, M. Schellekens, A. Perrin, A. Aspect, C. I. Westbrook
   BEC 2005, San Feliu de Guixols (Espagne), septembre 2005
6. **Cold atoms and Bose-Einstein condensation**
   D. Boiron
   First Russian - French Laser Physics Workshop for Young Scientists, St. Petersbourg, Russie, juillet 2004
7. **Bose-Einstein Condensation of metastable helium**
   D. Boiron
   RFLS 2003 – Third Russian-French Laser Symposium, Moscou (Russie), octobre 2003
8. **BEC of metastable helium**
   D. Boiron, S. Seidelin, J. Viana Gomes, R. Hoppeler, M. Schellekens, O. Sirjean, C. I. Westbrook, A. Aspect
   BEC 2003, San Feliu de Guixols (Espagne), septembre 2003
9. **Ionization rates in a Bose-Einstein condensate of metastable helium**
   O. Sirjean, D. Boiron, J. Viana Gomes, S. Seidelin, C. I. Westbrook, A. Aspect
   7th Internat. Workshop on Atom Optics and Interferometry, Lunteren (Pays-Bas), octobre 2002

10. **Losses in a metastable helium BEC – preliminary results**
    D. Boiron, A. Robert, O. Sirjean, C. I. Westbrook, A. Aspect
    BEC 2001, San Feliu de Guixols (Espagne), septembre 2001
11. **Bose-Einstein condensation of metastable helium**
    D. Boiron, O. Sirjean, S. Seidelin, J. Viana Gomes, C. I. Wesbrook, A. Aspect
    17th Interdisciplinary Laser Science Conference, Long Beach (USA), octobre 2001
    conférence invitée
12. **Towards Bose-Einstein condensation with metastable helium atoms**
    S. Nowak, A. Browaeys, J. Poupard, A. Robert, D. Boiron, C. I. Westbrook, A. Aspect
    European Quantum Electronics Conference (Nice (Fr), sept. 2000)

B.1.5 Contributions à des conférences nationales

Je n'indique que les conférences auxquelles j'ai personnellement participées.

1. **La vie sociale des bosons et des fermions**
   D. Boiron, V. Krachmalnicoff, M. Schellekens, A. Perrin, H. Chang, A. Aspect, C. I. Westbrook
   Congrès général de la SFP (Grenoble (France), juilllet 2006)
   conférence invitée
2. **Magnetic trapping of metastable helium atoms**
   D. Boiron
   Conférence Lasertag (Hanovre (Allemagne), décembre 2000)
3. **Piégeage et refroidissement d'un gaz d'hélium métastable**
   D. Boiron, A. Browaeys, J. Grosperrin, A. Robert, S. Nowak, C. Westbrook, A. Aspect
   Colloque Alain Bouyssy (Orsay (France), mars 1999) (conférence nationale à comité de sélection)

B.1.6 Séminaires

Liste des séminaires présentés par moi-même.

1. **Création d'atomes corrélés par mélange à quatre ondes spontané**
   Journée C'nano, université Paris-Sud (France), mai 2007.
2. **Effet Hanbury Brown Twiss pour des Gaz Ultra-Froids**
   Laboratoire Aime Cotton, université Paris-Sud (France), novembre 2005.
3. **Bose-Einstein condensation of dilute trapped gases**
   Université de Minho, Braga (Portugal), octobre 2002.
4. **Bose-Einstein condensation of metastable helium**
   Université de Goettingen (Allemagne), mai 2001.
5. **Themalisation d'un gaz froid d'helium metastable**
   Laboratoire Aime Cotton, université Paris-Sud (France), février 2001.

B.2 Publications correspondant au travail doctoral

Les deux articles les plus récents correspondent à un mini post-doc effectué dans le groupe de Gilbert Grynberg de février à juillet 1998.

B.2.1 Publications dans des revues à comité de lecture

1. **Trapping and cooling of cesium atoms in a speckled light**
   D. Boiron, C. Mennerat-Robilliard, L. Guidoni, J.M. Fournier, C. Salomon, G. Grynberg
   European Physical Journal D **7**, 373 (1999)
2. **Cooling cesium atoms in a Talbot lattice**
   C. Mennerat-Robilliard, D. Boiron, J.M. Fournier, A. Aradian, P. Horak, G. Grynberg
   Europhysic Letters **44**, 442 (1998)
3. **Cold and dense cesium clouds in far detuned dipole traps**
   D. Boiron, A. Michaud, J.M. Fournier, L. Simard, M. Sprenger, G. Grynberg, C. Salomon
   Physical Review A, **57**, R4106 (1998)
4. **Laser cooling of cesium atoms in gray optical molasses down to 1.1μK**
   D. Boiron, A. Michaud, P. Lemonde, Y. Castin, C. Salomon, S. Weyers, K. Szymaniec, L. Cognet, A. Clairon
   Physical Review A **53**, R3734 (1996)
5. **Cesium atoms in grey optical lattices. Study of temperature and capture efficiency**
   C. Triché, D. Boiron, S. Guibal, D.R. Meacher, P. Verkerk, G. Grynberg
   Optics Communication **126**, 49 (1996)
6. **Three-dimensional laser cooling of cesium atoms in a four-beam gray optical lattices**
   D. Boiron, C. Triché, D.R. Meacher, S. Guibal, P. Verkerk, G. Grynberg
   Physical Review A **52**, R3425 (1995)
7. **Four-wave mixing and Bragg scaterring in two and three-dimensional optical lattices**
   G. Grynberg, D. Boiron, J.-Y. Courtois, B. Lounis, D.R. Meacher, C. Salomon, P. Verkerk
   Nonlinear-Optics,-Principles,-Materials,-Phenomena-and-Devices **12**, 353 (1995)
8. **Method for velocimetry of cold atoms**
   D.R. Meacher, D. Boiron, H. Metcalf, C. Salomon, G. Grynberg
   Physical Review A **50**, R1992 (1994)

B.2.2 Contributions à un ouvrage collectif

1. **Atoms in three-dimensional optical lattices**
   P. Verkerk, D. Boiron, J.-Y. Courtois, S. Guibal, D.R. Meacher, C. Triché, G. Grynberg

12th International Conference on Laser Spectroscopy,
p. 35–8, ed. M. Inguscio, M. Allegrini, A. Sasso, World Scientific (1996)

2. **Temperature of cesium atoms in gray optical molasses**
   D. Boiron, A. Michaud, P. Lemonde, C. Salomon, S. Weyers, K. Szymaniec, A. Clairon
   Proc. of the 5th Symposium on frequency Standards and Metrology,
   p. 499–502, ed. J.C. Berquist, World Scientific (1996)

B.2.3 Contributions à des conférences internationales

Les présentations ont été effectuées par les auteurs dont le nom est inscrit en gras.

1. **Cold and dense cesium clouds in far-detuned dipole traps**
   D. Boiron, A. Michaud, J.M. Fournier, L. Simard, M. Sprenger, G. Grynberg, C. Salomon
   European Quantum Electronics Conference (Glasgow (GB), sept. 1998)
2. **Two-dimensional tight confinement of cold cesium atoms in a far-detuned dipole trap**
   D. Boiron, A. Michaud, J.M. Fournier, L. Simard, M. Sprenger, G. Grynberg, C. Salomon
   Quantum Electronics and Laser Science Conference (Baltimore (USA), 1997)
3. **Temperature of cesium atoms in gray optical molasses**
   D. Boiron, A. Michaud, P. Lemonde, C. Salomon, S. Weyers, K. Szymaniec, L. Cognet, A. Clairon
   European Quantum Electronics Conference (Hambourg (Allemagne), 1996)
4. **Temperature of cesium atoms in gray optical molasses**
   D. Boiron, A. Michaud, P. Lemonde, C. Salomon, S. Weyers, K. Szymaniec, L. Cognet, A. Clairon
   Int. workshop on quantum effects in cold atomic gases (Les Houches (France), 1996)
5. **Velocimetry of cold atoms using stimulated optical scattering**
   D.R. Meacher, D. Boiron, H. Metcalf, C. Salomon, G. Grynberg
   International Conference on Atomic Physics (Boulder (USA), 1994)

B.2.4 Contributions à des conférences nationales

Les présentations ont été effectuées par les auteurs dont le nom est inscrit en gras.

1. **Résonances induites par le recul**
   D. Boiron, D.R. Meacher, H. Metcalf, C. Salomon, G. Grynberg
   Séminaire sur la Manipulation d'Atomes par Laser et Applications (Lille (France), 1996)

Annexe C

Articles

Les pages suivantes reproduisent le texte des articles correspondant à mon travail au laboratoire Charles Fabry de l'Institut d'Optique.

Eur. Phys. J. D **8**, 199–203 (2000)

THE EUROPEAN PHYSICAL JOURNAL D
EDP Sciences

Two body loss rate in a magneto-optical trap of metastable He

A. Browaeys[1], J. Poupard[1], A. Robert[1], S. Nowak[1,a], W. Rooijakkers[1,b], E. Arimondo[2], L. Marcassa[3], D. Boiron[1], C.I. Westbrook[1], and A. Aspect[1]

[1] Laboratoire Charles Fabry de l'Institut d'Optique[c], B.P. 147, 91403 Orsay Cedex, France
[2] INFM and Dipartimento di Fisica, Università di Pisa, Piazza Torricelli 2, 56126 Pisa, Italy
[3] IFSC, Universidad of São Paulo, Caixa Postal 369, 13560-970, São Carlos S.P., Brazil

Received 20 April 1999 and Received in final form 12 July 1999

Abstract. We have measured the two body loss rate in a magneto-optical trap containing triplet metastable He atoms. We find a rate constant $\beta = 3 \times 10^{-8}$ cm^3/s at a -8 MHz detuning, with an uncertainty of a factor 2. This measurement is in disagreement with a recent experiment which measures the absolute, ion-producing collision rate, but agrees with several other published measurements.

PACS. 32.80.Pj Optical cooling of atoms; trapping – 34.50.Rk Laser-modified scattering and reactions

Metastable helium (He*) is an interesting and unusual atom for laser cooling and trapping studies. It has a very well understood structure and is thus of interest for precision measurements [1]. Its large recoil velocity poses unusual problems for producing laser cooled samples, and also provides an interesting testing ground for the theory of laser cooling when the recoil velocity is large [2]. It has also been suggested as a promising candidate for evaporative cooling [3]. Dense, cold samples would clearly be useful for furthering these studies. Already in the first magneto-optical trap (MOT) for He* however, it was reported that light assisted collisions lead to large two body loss rates and severely limit the density [4]. On the other hand, a recent experiment reported a very much lower loss rate constant [5]. It is obviously of great importance to resolve this discrepancy in order to understand the loss processes.

The loss rate measured in reference [4] was attributed to the following processes:

$$\mathrm{He}^*(2^3\mathrm{S}, 2^3\mathrm{P}) + \mathrm{He}^*(2^3\mathrm{S}) \rightarrow \begin{cases} \mathrm{He}(1^1\mathrm{S}) + \mathrm{He}^+(1^2\mathrm{S}) + e^- \\ \mathrm{He}_2^+ + e^- \end{cases} .$$

This rate was measured by monitoring all the ions produced by the trap and observing the non-exponential decay of the ion signal. By contrast, the work of reference [5] reports an absolute measurement of the He^+ and He_2^+ ion production rate and found a rate 40 times smaller than that of reference [4]. This new rate appeared to be in good agreement with a theoretical calculation made by the authors. Since the technique of reference [4] is sensitive to the total two body loss rate while that of reference [5] observes only the ion production rate, this discrepancy may point to some other light-assisted collision process that does not produce ions.

In order to help clarify this issue, we have undertaken a new experiment to measure the two body loss rate paying close attention to several possible sources of systematic errors including the measurement of the density. We use the trapped atom fluorescence to observe the non-exponential decay of the trap. Our experiments confirm the measurements of reference [4] and seem to indicate that the two body loss rate is much higher than the rate measured by [5]. In addition, even more recent experiments, one measuring the trap loss [6] and one measuring the absolute ion production rate [7], appear to agree with our results. Thus, the preponderance of experimental data indicate that the two body loss rate from the trap is higher than measured in [5] and is largely due to ionizing collisions.

Our starting point is the phenomenological equation for the evolution of the number $N(t)$ of trapped atoms during the loading of the MOT

$$\frac{\mathrm{d}}{\mathrm{d}t}N(t) = R - \frac{N(t)}{\tau} - \beta \int n^2(\mathbf{r}, t)\mathrm{d}^3r \,. \qquad (1)$$

In this equation R is the flux of atoms captured by the trap during the loading. It depends on various parameters of the MOT, particularly on the detuning and intensity of the trapping laser. The lifetime τ of the trap is due to collisions of He* with background gas molecules. Our measurements indicate that τ is independent of the MOT parameters to within 20%. The last term of the equation describes the two body losses resulting from collisions between trapped atoms. Our definition of β is the same

---

[a] e-mail: `stephan.nowak@iota.u-psud.fr`

[b] *Present address:* Sussex Center for Optical and Atomic Physics, University of Sussex, Brighton BN1 9QH, UK.

[c] Unité Mixte du CNRS No. 8501

as that of references [4–6], and we have assumed that the quantity β is independent of position.

If one assumes that the spatial distribution is independent of the number of atoms in the trap, one can write $n(\mathbf{r},t)$ as a product $n_0(\mathbf{r})f(t)$ where $n_0(\mathbf{r})$ describes the shape of the trapped atom distribution. In this case the last term in equation (1) can be expressed as $-\beta N^2(t)/V_{\mathrm{eff}}$, where V_{eff} is an effective volume of the trap. Our measurements indicate that V_{eff} is indeed independent of the number of trapped atoms and, during the trap decay, independent of time. As the trap has a Gaussian profile in 3 dimensions $V_{\mathrm{eff}} = \pi^{\frac{3}{2}}(2\sigma_x)(2\sigma_y)(2\sigma_z)$, where σ is the rms size.

The decay of N is given by integrating equation (1) with respect to time in the absence of loading ($R = 0$) and assuming that the initial number of atoms is equal to the steady state value $N(0) = N_{\mathrm{S}}$. This leads to

$$N(t) = \frac{N_{\mathrm{S}}}{\left(1 + \frac{\beta N_{\mathrm{S}}\tau}{V_{\mathrm{eff}}}\right)\mathrm{e}^{\frac{t}{\tau}} - \frac{\beta N_{\mathrm{S}}\tau}{V_{\mathrm{eff}}}} \cdot \qquad (2)$$

In the presence of a loading rate ($R \neq 0$) the solution for equation (1) with $N(0) = 0$ is

$$N(t) = N_{\mathrm{S}}\frac{1 - \mathrm{e}^{-\frac{t}{\tau_0}}}{1 + \frac{N_{\mathrm{S}}^2\beta}{V_{\mathrm{eff}}R}\mathrm{e}^{-\frac{t}{\tau_0}}} \qquad (3)$$

where

$$\tau_0 = \frac{\tau}{\sqrt{1 + \frac{4\beta R\tau^2}{V_{\mathrm{eff}}}}} \cdot \qquad (4)$$

Equation (3) describes the number of trapped atoms during the loading phase. The steady state solution for equation (1) gives a simple relation between β and N_{S}

$$\beta = \frac{R - \frac{N_{\mathrm{S}}}{\tau}}{N_{\mathrm{S}}^2}V_{\mathrm{eff}} \cdot \qquad (5)$$

The above equations all offer different, though related routes to get β. Taking for example equation (5), one can measure V_{eff} using camera observations, τ using the exponential decay of the trap when the density is low, and N_{S} from the number of trapped atoms observed in steady state. The quantity R can also be measured by observing the initial slope of the loading curve $R = \mathrm{d}N/\mathrm{d}t(t = 0)$. Note that the uncertainty with which one measures R is highly correlated with that of N_{S}. If τ is very large, N_{S}/τ can be neglected compared to R and thus τ is unimportant in determining β. Equations (2, 3) permit the determination of β by fitting the decay and loading curves. However, the fitting parameters contain combinations of the quantities β, N_{S} and V_{eff}, so that it is still necessary to make independent measurements of N_{S} and V_{eff} to extract β. Our strategy is to use all three methods to check the consistency of our approach while making the best measurements we can of N_{S} and V_{eff}.

Our LN_2 cooled helium source is similar to the one described in references [8,9]: a high voltage DC discharge produces metastable atoms. The flux of metastable atoms is 10^{12} s^{-1} (luminosity of 4×10^{14} $\mathrm{sr}^{-1}\mathrm{s}^{-1}$). The mean longitudinal velocity is 1300 m/s and the FWHM of the velocity distribution is 300 m/s. We optically manipulate the atomic beam with laser light using the closed transition $2^3\mathrm{S}_1$–$2^3\mathrm{P}_2$ at a wavelength of 1083 nm. The natural linewidth is $\Gamma/2\pi = 1.6$ MHz. The light is emitted by 50 mW DBR laser diodes. Their frequency width Γ_{diode} is estimated from the measured beat note between two identical diodes. The measured width was 4 ± 0.5 MHz, FWHM from which we deduce $\Gamma_{\mathrm{diode}}/2\pi = 2 \pm 0.3$ MHz, assuming Lorentzian line shapes. They are locked on the transition $^3\mathrm{S}_1$–$^3\mathrm{P}_2$ using saturated absorption in a He RF discharge cell. The detuning of the laser trapping beams is controlled with an adjustable Zeeman shift produced by Helmholtz magnetic coils around the He cell.

We collimate the atomic beam using a transverse molasses with curved wave fronts [9–11]. Under normal trapping conditions, we observe an increase in the number of trapped atoms of a factor 6. This molasses also allows us to bend the atomic beam by an angle of 1° so as to reduce the flux of ground state atoms as well as ions and UV photons produced in the discharge. The atoms are then slowed down in a Zeeman slower to a velocity less than 50 m/s. The Zeeman field passes through zero partway along the slowing path so as to allow us to detune the slowing laser by −400 MHz from the $^3\mathrm{S}_1$–$^3\mathrm{P}_2$ resonance. The total slowing length is 2.4 m.

The resulting slow atomic beam then loads a MOT consisting of three retroreflected laser beams. The center intensity per beam is 4 $\mathrm{mW/cm^2}$, and the waist diameter of the order of 2 cm. The magnetic field gradients were 10, 6 and 4 G/cm in the different directions. The lack of symmetry is due to the presence of the Zeeman slower and a compensation coil which remained on during the experiment. A typical background pressure of 4×10^{-8} mbar results in a lifetime τ of the trap of 150 ms. This lifetime is unchanged when either the atomic beam or the cooling laser is blocked by a mechanical shutter. The temperature of the trap was roughly measured by an absorption technique to be 1.5 mK at a detuning of the trapping laser of −20 MHz.

The measurement of β proceeds in two steps. First one fits the data to one of the equations (2, 3) or (5). For example typical decay curves of the trap fluorescence at 1.083 μm when cutting off the slowing laser beam at time $t = 0$ are shown in Figure 1 for two detunings of the trapping laser. For a –16 MHz detuning the decay is purely exponential whereas at –6.4 MHz the decay is exponential only for times bigger than 150 ms. Before that the influence of the non linear terms of equation (1) is clearly visible. Fitting this nonlinearity leads generally to a measurement of $\beta N_{\mathrm{S}}/V_{\mathrm{eff}}$. The next step is to measure N_{S} and V_{eff} to extract the rate constant β. We discuss these steps below.

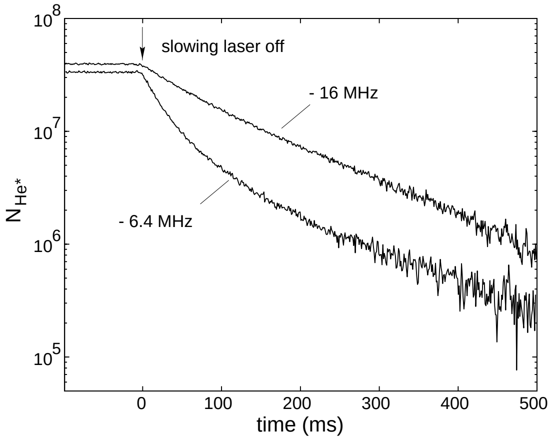

Fig. 1. Time dependence of the trap fluorescence for two different detunings. The vertical axis is logarithmic, and the curvature is due to two body loss processes

To analyse curves such as in Figure 1 we use the analytical solution (2) with $\beta N_S/V_{\rm eff}$ and the lifetime τ as fitting parameters. We checked that the value of τ is the one deduced from a fit of the exponential part of the decay, reached when the number of trapped atoms is low enough for the two body collisions between He* atoms to be negligible. We measured $V_{\rm eff}$ as a function of the number of atoms in the trap. We did this both by changing the loading rate and observing the size in steady state as well as by taking pictures during the decay of the trap. In both cases we see a 30% increase in the size as the number of atoms increases from 3×10^6 to 3×10^7. This change in size only has a small effect on the resulting value of β ($\sim$ 10%). We estimate the uncertainty in the fitted parameters to be approximately 10% by examining dispersion in the results when we fit the same data over different time intervals. Fits to data taken under nominally the same conditions within several hours show a statistical dispersion of 15%.

To confirm the results we get from the decay curves, we also performed a fit of the loading of the trap to the function in equation (3). Our fits give a value of $\beta N_S/V_{\rm eff}$ that is a factor of 2 smaller than the one we get using the decay data from the same run. We also used equation (5) to get β by measuring R/N_S from the initial slope of the loading curve (and using the value of τ from the fit of the decay curve). This method also gives a β that is 2 times smaller than the decay curve. This disagreement is surprising because although the absolute uncertainties with which we measure N_S, $V_{\rm eff}$, and β are of order a factor of two, most of the uncertainties should be common to the three methods.

To explain this discrepancy we first checked that it is not due to the presence of the slowing laser or the atomic beam. We found that decay data give the same value of β and τ regardless of the presence of the slowing laser and the atomic beam. We also checked that the value of β derived from the loading curve did not change when we blocked that part of the slowing laser beam which intersected the MOT by an absorber, thus making a dark spot slower [12].

We also made measurements of the trap size and shape during loading. In the first 10 ms of loading the trap is not Gaussian but rather appears to have a slight halo in the direction from which the atomic beam arrives. It appears that in the early phases of loading the atoms are not immediately captured in the steady state volume of the trap. Thus the effective volume of the trap is slightly bigger than is assumed in equation (3). This may account for the discrepancy. It is difficult to quantitatively estimate the influence of this effect on the value of β deduced from the loading curve because the temporal resolution with which we were able to observe the loading trap was only of order 5 ms. At the start of the loading the number of atoms in the trap varies rapidly on this time scale. We conclude that the loading curves are probably not as reliable for extracting β as the decay data. On the other hand, in view of our overall uncertainty, this discrepancy is not large and thus the loading curves do confirm our results at the factor of two level. In what follows we will only show data derived from the decay curves.

In order to determine the number of trapped atoms N_S we monitor the total power P scattered by the trapped atoms into a solid angle Ω with a photodiode. This power is given by $P = \hbar\omega\Gamma(\Omega/4\pi)\pi_P N_S$, where ω and Γ are the frequency and natural linewidth of the MOT transition and π_P is the fraction of atoms in the excited state. We use the following formula to calculate π_P [13]

$$\pi_P = \frac{1}{2}\frac{C\dfrac{I}{I_0}}{1 + C\dfrac{I}{I_0} + \left(\dfrac{2\Delta}{\Gamma_{\rm diode}+\Gamma}\right)^2} \qquad (6)$$

where Δ is the laser detuning from resonance and I is the total laser intensity of all 6 beams taken at the center of the Gaussian profile. I_0 is the saturation intensity of the transition taking into account the width of the lasers, that is $I_0 = (\Gamma_{\rm diode}+\Gamma)I_{\rm sat}/\Gamma = 0.37$ mW/cm^2, where $I_{\rm sat} = 0.16$ mW/cm^2 for the transition $m_J = 1 \longleftrightarrow m_J = 2$. The phenomenological parameter C would be equal to unity if a single, circularly polarized beam were present and all atoms were in $m_J = 1$ ground state. However, since 6 differently polarized beams are present at the center of the trap, C should be smaller. In reference [13] it was found empirically for a Cs MOT that C is somewhat larger than the average of the squares of the Clebsch-Gordan coefficients over all possible transitions. For the $J = 1 \longleftrightarrow J = 2$ transition this average is 0.56. We will assume here $C = 0.8\pm0.2$. Because of the high saturation of our MOT, the uncertainty we have assumed for C amounts to only a 5% uncertainty in π_P for small detunings and 10% for large detunings. The high saturation also means that we are not very sensitive to the effect of the linewidth of the lasers.

We have roughly confirmed the value of π_P by measuring the absorption of a weak resonant probe beam through

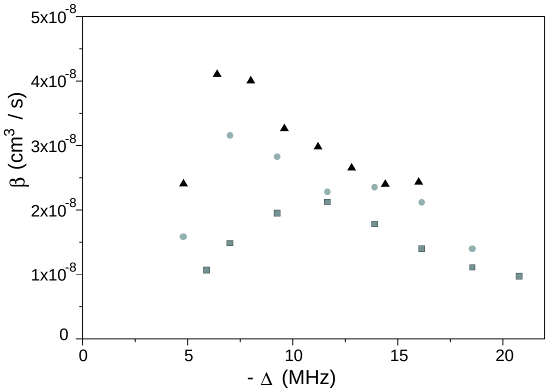

Fig. 2. Fitted two body loss rate coefficient β as a function of detuning at total intensity $I/I_{\mathrm{sat}} = 160$. Different symbols refer to different runs taken on different days.

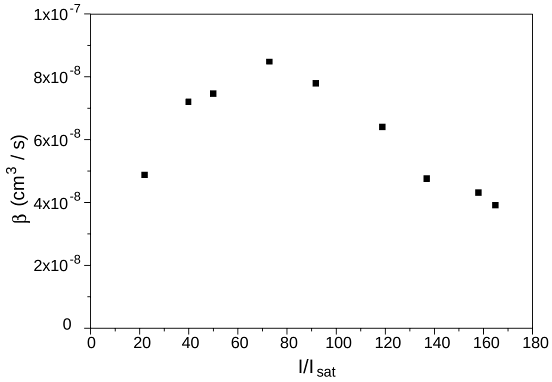

Fig. 3. Fitted two body loss rate coefficient β as a function of total intensity at detuning $\Delta = -6$ MHz.

the atomic cloud after the MOT laser beams had been turned off. Our observation of 30% absorption on resonance confirms the measurement of the number of trapped atoms to within a factor of two. Note also that the observed absorption indicates that, at typical MOT detunings, the optical thickness of the cloud is negligible. The calibration of our photodiode is known to the order of 10%. The major source of uncertainty in N_{S} is the solid angle which we can only estimate to within a factor of 1.5. We estimate the uncertainty in our detected power measurement (P) to be about 20%.

The volume V_{eff} is measured by observing the size of the trap along three orthogonal axes in the steady state regime using a calibrated CCD camera. The Zeeman shift due to the magnetic field gradient is negligible compared to our detuning and therefore does not affect our estimate of the volume. Similarly the Doppler shift at 1.5 mK, about 2 MHz, is negligible as well. We estimate the uncertainty in V_{eff} to be about 20%.

Our final uncertainty in the absolute value of β is the quadrature sum of the contributions described above and is dominated by the statistical fluctuations in $\beta N_{\mathrm{S}}/V_{\mathrm{eff}}$ and by the uncertainty in the solid angle, both of order 50%. The total uncertainty is a little less than a factor of two. Therefore our conclusion that $\beta = 3\times10^{-8}$ cm^3/s at a –8 MHz detuning of the trapping laser is to be understood as 1.5×10^{-8} cm^3/s $< \beta < 6 \times 10^{-8}$ cm^3/s.

We performed the measurement of β for various detunings of the trapping beams, from -5 MHz to -16 MHz, and various intensities corresponding to I/I_{sat} varying from 10 to 160. We found that in steady state, the shape of the trap is always Gaussian. The volume V_{eff} varies between 30 mm^3 and 200 mm^3. The number of trapped atoms slightly increases with the detuning of the trapping beams from 3×10^7 up to 4×10^7 while the density at the center decreases from 3×10^9 cm^{-3} to 6×10^8 cm^{-3}. The dependence of β with the detuning and the intensity is shown in Figures 2 and 3. Figure 2 presents the measured values for β *versus* the detuning of the trapping laser for experiments carried out on 3 different days at nominally the same conditions. There are clearly some conditions in the MOT that are not very reproducible. The uncertainty in the solid angle is common to all measurements, therefore the trends shown in Figures 2 and 3 are weak but statistically significant. The detuning dependence shows the same general behavior as the data of reference [5] although it was taken over a much smaller range of detunings. This behavior can be understood in terms of a model similar to reference [14] in which one assumes that a competition between incident flux and survival give a maximum collision rate at some value of the detuning.

In order to compare our results to other measurements, we note that our results are consistent with those of reference [4], which found 2×10^{-8} cm^3/s $< \beta <$ 3×10^{-7} cm^3/s for a detuning of -5 MHz and approximately the same intensity. Our results also agree with two recent experiments done with MOT parameters similar to ours: reference [6] used the decaying trap signal to find $\beta = 1 \times 10^{-8}$ cm^3/s and reference [7] reports a measurement $\beta = 4 \times 10^{-8}$ cm^3/s using the absolute ion signal. All these results disagree with that of [5], who measured $\beta = 2 \times 10^{-9}$ cm^3/s at -5 MHz detuning and about the same intensity. The experiment of reference [7] is very important in ruling out the possibility that a decay mechanism producing no ions can account for the result of reference [5]. Note also that the work of reference [6] also includes measurements of trap loss processes resulting in metastables escaping from the trap (radiative escape). This also lends credence to the view that ionizing collisions are indeed the primary trap loss mechanism.

S.N. acknowledges support from the EU under grant ERBFMRX CT96-0002 and from the DFG under grant No. 392/1-1. This work was supported by the Région Ile de France. We thank P. Tol for helpful comments and for communicating his results before publication.

References

1. F. Minardi, G. Bianchini, P. Cancio Pastor, G. Giusfredi, F.S. Pavone, M. Inguscio, Phys. Rev. Lett. **82**, 1112 (1999).
2. B. Saubaméa, T.W. Hijmans, S. Kulin, E. Rasel, E. Peik, M. Leduc, C. Cohen-Tannoudji, Phys. Rev. Lett. **79**, 3146 (1997).
3. P. Fedichev, M. Reynolds, U. Rahmanov, G. Shlyapnikov, Phys. Rev. A **53**, 1447 (1996).
4. F. Bardou, O. Emile, J.-M. Courty, C.I. Westbrook, A. Aspect, Europhys. Lett. **20**, 681 (1992).
5. H.C. Mastwijk, J.W. Thomsen, P. van der Straten, A. Niehaus, Phys. Rev. Lett. **80**, 5516 (1998).
6. P.J.J. Tol, N. Herschbach, E.A. Hessels, W. Hogervorst, W. Vassen, Phys. Rev A. **60**, 761 (1999).
7. M. Kumakura, N. Morita, Phys. Rev. Lett. **82**, 2849 (1999).
8. W. Rooijakkers, W. Hogervorst, W. Vassen, Opt. Commun. **123**, 321 (1996).
9. G. Labeyrie, Ph.D. thesis, University Paris-Sud, 1998.
10. J. Nellessen, J. Müller, K. Sengstock, W. Ertmer, J. Opt. Soc. Am. B **6**, 2149 (1989).
11. N. Vansteenkiste *et al.,* J. Phys. II France **1**, 1407 (1991).
12. S. Miranda, S.R. Muniz, G.D. Telles, L.G. Marcassa, K. Helmerson, V.S. Bagnato, Phys. Rev. A **59**, 882 (1999).
13. C.G. Townsend, N. Edwards, C. Cooper, K. Zetie, C. Foot, A. Steane, P. Szriftgiser, H. Perrin, J. Dalibard, Phys. Rev. A **52**, 1423 (1995).
14. A. Gallagher, D.E. Pritchard, Phys. Rev. Lett. **63**, 957 (1989).

Appl. Phys. B 70, 455–457 (2000) / Digital Object Identifier (DOI) 10.1007/s003400000246

Applied Physics B
Lasers
and Optics

Rapid communication

Magnetic trapping of metastable helium atoms

S. Nowak, A. Browaeys, J. Poupard, A. Robert, D. Boiron, C. Westbrook, A. Aspect

Laboratoire Charles Fabry de l'Institut d'Optique, Unité Mixte du CNRS n° 8501, BP 147, 91403 Orsay Cedex, France

Received: 18 October 1999/Revised version: 13 January 2000/Published online: 23 February 2000 – © Springer-Verlag 2000

Abstract. Metastable helium atoms were efficiently transferred from a magneto-optical trap (MOT) to a magnetic quadrupole trap, producing samples of up to 3×10^7 magnetically trapped atoms at a temperature of about 1 mK. We observe purely exponential decay of the samples with time constants of 9–10 s and derive an upper bound for the rate coefficient of inelastic Penning collisions.

PACS: 32.80.Pj; 42.50.Vk; 34.50.RK

The breakthrough achievement of Bose–Einstein condensation (BEC) [1, 2] in dilute atomic vapors was largely due to the successful combination of laser cooling, magnetic trapping and evaporative cooling. But, although cooling and trapping techniques have been applied to many different atomic species, BEC in dilute gases has been achieved for only a few elements. Metastable helium (He*) is an interesting and challenging candidate for extending the list of Bose condensed gases beyond the first column of the periodic table [3]. Cold, dense samples of He* could possibly have many applications in precision measurements [4] and in surface potential studies [5]. Metastable helium, however, poses particularly difficult problems for experiments. One of the worst of these is the severe limit for the particle density in a magneto-optical trap (MOT) due to light-assisted Penning ionizing collisions [6–10]. The rate of Penning ionization can be greatly suppressed in magnetic traps, first because of the absence of resonant light, and secondly because in a magnetic trap, Penning ionizing collisions are highly forbidden by spin conservation when the sample is spin polarized in the magnetic trap. A suppression of five orders of magnitude is estimated in theory [11]. In addition, an elastic collision rate in the spin polarized sample large enough that evaporative cooling should be possible is estimated in [11]. In this paper we report the efficient transfer of He*-atoms from a MOT to a magnetic trap. The observed magnetic trap lifetime allows us to put an upper limit on the inelastic collision rate coefficient for spin-polarized atoms.

An atom with magnetic moment $\boldsymbol{\mu}$, adiabatically following a magnetic field $\boldsymbol{B}(\boldsymbol{r})$, experiences a potential

$$W_{\text{mag}} = -\boldsymbol{\mu} \cdot \boldsymbol{B}(\boldsymbol{r}) = g_J m_J \, \mu_{\text{B}} \, B(\boldsymbol{r}) \ . \tag{1}$$

Here, μ_{B} is the Bohr magneton and for He* $m_J = -1, 0, +1$ and $g_J = 2$. For $m_J = +1$, this potential is confining at a local minimum of the magnitude of the magnetic field, $B(\boldsymbol{r})$. In our experiment we use a simple magnetic quadrupole potential produced by two parallel coils with opposite currents, which has already proven useful in BEC experiments [2]. This potential has the advantage of having a nonzero gradient close to the center, thus confining more tightly than a parabolic trap [12, 13], and producing an exponentially peaked density distribution.

We use a DC-gas discharge source [14] to produce a beam of metastable helium atoms (intensity $10^{14}\,\text{s}^{-1}\text{sr}^{-1}$), which is transversely collimated with a molasses, and slowed with a Zeeman slower to a velocity of 10–30 m/s to load an MOT in the standard 6-beam σ^+/σ^- configuration. There we have 10^8 atoms (based on absolute fluorescence measurements) at a central density of $10^9\,\text{cm}^{-3}$ (limited by Penning collisions), at temperatures between 0.6 and 1.5 mK, depending on laser detuning. Laser light resonant with the atomic transition $2\,^3S_1 - 2\,^3P_2$ (1083 nm) is provided by DBR laser diodes (Spectra Diode Labs) locked to this transition, with fine tuning by acousto–optical modulators. We transfer the atomic sample from the MOT to the magnetic quadrupole trap by shutting off the laser light and ramping up the magnetic field at the same time. This scheme ensures a good alignment of the magnetic trap with respect to the MOT, as at typical working parameters the atomic cloud is quite large compared to any displacement induced by gravity or laser radiation imbalances.

We detect the atoms with a multichannel plate (MCP) stack (HAMAMATSU 4655) with a detector anode, mounted 5 cm below the trap. Its upper side is set to -2 kV, with the lower side on ground potential. The detector anode is set to a small positive voltage to help extract the electrons from the MCP. Two fine grids are mounted above the detector. The first is at ground potential and used to shield the trap region from the high electric fields produced around the MCP stack. The second one is biased so as to repel positive ions. In the absence of metastables hitting the detector we detect negligible anode current. We calibrated this He*-detector and tested its linearity by comparing its signal to fluorescence and absorption measurements of particle numbers in the MOT.

Figure 1a shows the timing in the experiment. During the loading phase all lasers are on, as well as the atom beam and the magnetic field B_{Zeem} of the Zeeman slower. The gradient of the quadrupole field B_{quad} for the MOT is low (typically $5\,\mathrm{G/cm}$ in the radial direction). At $t = 0$, after typically 1 s of loading, the laser and magnetic field of the Zeeman slower are switched off, the atom beam is blocked with a mechanical shutter, and the MOT lasers are switched off. The MOT lasers are switched using an acousto–optical modulator in series with a mechanical shutter. The field gradient of the quadrupole is raised in about 3 ms to 50–80 G/cm (radial direction) to produce the magnetic trap. After a delay t_D the magnetic trap is switched off with a time constant of $\sim 500\,\mu\mathrm{s}$ and we observe the arrival of the atoms on the MCP. The quadrupole magnetic fields of the MOT and the magnetic trap are produced by the same pair of coils. They have a diameter of 11 cm and are placed at a separation of 7 cm outside the vacuum. The pressure is around 10^{-9} mbar when the atom beam is on, as was measured with an ion gauge and somewhat lower when the atom beam is shut off after loading the MOT.

Figure 1b shows the time-of-flight (TOF) signals of the metastable atoms detected by the MCP detector. The first peak is due to those atoms in the MOT which could not be transferred to the magnetic trap, the second peak is produced by atoms released from the magnetic trap. Detailed inspection of the first peak reveals a double structure, corresponding to atoms in the $m_J = -1$ state, which are repelled from the magnetic field minimum, and in the $m_J = 0$ state, which are insensitive to the magnetic field. By integrating the area of these signals, taking into account a geometrical correction factor accounting for atoms that do not hit the detector, we derive a transfer efficiency from the MOT to the magnetic trap of typically 30%, showing that atoms in a MOT are unpolarized on average.

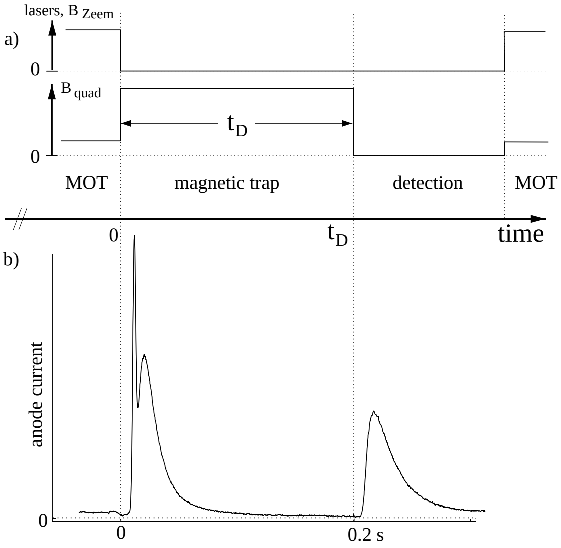

Fig. 1. Timing of a typical experimental run, together with some typical TOF data. The nonzero offset during the MOT phase is due to detection of not trapped atoms, and UV photons coming from the atom source. The two peaks just after turning on the magnetic trap correspond to untrapped atoms in the $m_J = -1$ state (expelled) and in the $m_J = 0$ state (insensitive to the magnetic field)

For further analysis we fit calculated TOF signals to our data, assuming Maxwell–Boltzmann velocity distribution in the trap and taking into account gravity. We neglect the size of the trap, because for trap diameters up to 10 mm, which is the largest trap diameter we used, its size has only a small influence on the detected signal. The only parameters for the fit are the temperature T of the sample and a scaling factor proportional to the number of atoms. We found that the value of the gradient of the magnetic trap does not dramatically affect the transfer efficiency nor the change of mean energy of the atomic cloud.

By repeating measurements with different delay times t_D and evaluating the number of particles in the detected TOF peak we measured the lifetime of the magnetic trap. The data set in Fig. 2 is fitted very well by a purely exponential decay, revealing a decay constant of $\alpha^{-1} = 9\,\mathrm{s}$. We varied the pressure in the chamber by a factor of 3 by reducing the rotation rate of our turbo pumps and found that this lifetime is approximately inversely proportional to the residual gas pressure. Besides collisions with residual gas particles, Majorana spin flips can contribute to losses from a quadrupolar magnetic trap at a rate [13] $\Gamma_M \sim \hbar/m \times 1/l^2$, where l is the typical length scale of the radius of the trapped atomic cloud. Evaluating l from the temperature and the magnetic field gradient of the trap, we find that Majorana spin flips occur at time constants of about $\Gamma_M^{-1} \sim 60\,\mathrm{s}$. Therefore, we do not expect this to be a lifetime-limiting factor for the trap, in agreement with the observation of the pressure dependence of the lifetime.

It is interesting to attempt to derive an upper limit for the rate coefficient β of inelastic collisions of polarized atoms

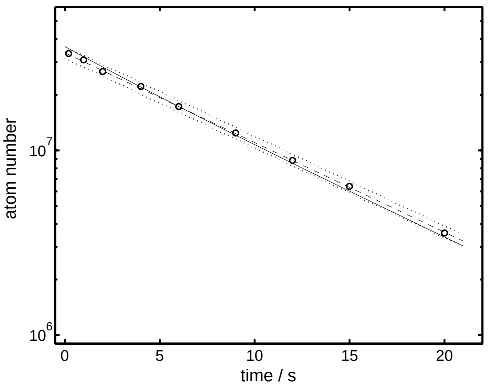

Fig. 2. Particle number in the magnetic trap as a function of time. *Circles* are measured data, the *dashed line* is a fitted linear curve in the semilog plot showing a trap lifetime of 9 s and the *dotted lines* indicate the uncertainty in particle number produced by the fit. The *thin solid line* is what we would expect in the presence of inelastic two-body collisions with a rate coefficient of $8 \times 10^{-11}\,\mathrm{cm^3\,s^{-1}}$

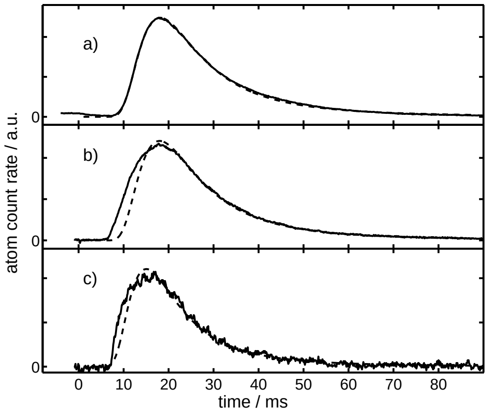

Fig. 3. Typical TOF data of atoms from the magneto-optical trap (**a**) and from the magnetic trap after storing times of 0.5 s (**b**) and 20 s (**c**). *Solid curves* are experimental data, *dashed lines* show the respective best fits to TOF signals as expected from a Maxwell–Boltzmann distribution, corresponding to about 1.0 mK in **a** and **b** and 1.3 mK in **c**. The data in **c** deviate somewhat less from the Maxwell–Boltzmann case than the data curve in **b**. This may be interpreted as an effect of the onset of thermalization due to elastic collisions. It is, however, not possible to deduce a time constant for thermalization from these data

inside the trap. To do so, we need to determine the particle density in the trap, i. e. the shape of the atomic cloud. As a working hypothesis we assume that the atoms in the trap are in thermal equilibrium. The TOF characteristics (see Fig. 3) of the atoms released from the trap show that this is not exactly the case, but the deviation from a Maxwell–Boltzmann distribution is small enough that this hypothesis is reasonable. This permits us to estimate the diameter of the cloud inside the magnetic trap and so determine the density. Using the measured particle number in the magnetic trap we find a peak density of $3 \times 10^8\,\mathrm{cm}^{-3}$ in the trap, from which we deduce an effective density [15] inside the trap of $n_{\mathrm{eff}} = 4 \times 10^7\,\mathrm{cm}^{-3}$. Experimentally we found that the statistical scatter of our measurements of particle numbers is at most 5%, so the statistical scatter of the density amounts to the same value.

To the data in Fig. 2 we fit the solution of the equation $\dot{N}/N = -\alpha - \beta n_{\mathrm{eff}}$ which describes one- and two-body losses from the trap [6–10]. Using the same fitting function as in [6, 8, 10], with n_{eff} adapted to our case, we find that β is negligible. To derive the most conservative upper limit for this coefficient we proceed as follows: A linear fit to the data in the linear-logarithmic plot (dashed line in Fig. 2) provides us with the decay coefficient α. We find that the uncertainty in this fit (indicated by dotted lines) is practically identical to the uncertainty of the fitted initial number of atoms. We then superpose the experimental data with tentative fit functions with different values of β, keeping α fixed. With this method we can determine $8 \times 10^{-11}\,\mathrm{cm}^3\,\mathrm{s}^{-1}$ as an upper limit for this rate coefficient. Figure 2 shows a decay curve using this coefficient (straight line). This value is consistent with calculations presented by Mastwijk et al. [7] for an unpolarized sample of metastable helium $2\,^3S_1$ and compatible with the suppression factor measured by Hill et al. [16] for a polarized sample. The uncertainty in this coefficient is mainly due to the statistical scatter in the number of atoms in the trap and due to the deviation of the velocity distribution from a Maxwell–Boltzmann distribution, which affects the value of n_{eff}.

To summarize, we have set up a magnetic trap for metastable helium and demonstrated the efficient transfer of atoms from the MOT ($\sim 30\%$), atom numbers as high as 3×10^7 and background-gas limited lifetimes of more than 9 s in the magnetic trap. From this lifetime we deduce an upper limit of $8 \times 10^{-11}\,\mathrm{cm}^3\,\mathrm{s}^{-1}$ for the inelastic collisional rate coefficient with polarized atoms. Application of a stronger field gradient and improved vacuum will bring us into a good starting position for evaporative cooling experiments to increase the phase space density of our sample and to more precisely measure collision rate coefficients as well as the scattering length for ultra cold elastic $\mathrm{He}^* - \mathrm{He}^*$ collisions.

Acknowledgements. The work of SN is funded by the Deutsche Forschungsgemeinschaft (grant no. NO 392/1-1). This work was supported by the Région Ile de France and the CNRS.

References

1. C.J. Anderson, J.R. Ensher, M.R. Matthews, C.E. Wieman, E.A. Cornell: Science **269**, 198 (1995); C.C. Bradley, C.A. Sackett, J.J. Tollett, R.G. Hulet: Phys. Rev. Lett. **75**, 1687 (1995)
2. K.B. Davis, M.O. Mewes, M.R. Andrews, N.J. van Druten, D.S. Durfee, D.M. Kurn, W. Ketterle: Phys. Rev. Lett. **75**, 3969 (1995)
3. W. Vassen: OSA TOPS on Ultracold Atoms and BEC **7**, 20 (1997)
4. F. Minardi, G. Bianchini, P. Cancio-Pastor, G. Giusfredi, F.S. Pavone, M. Inguscio: Phys. Rev. Lett. **82**, 1112 (1999)
5. B. Segev, R. Côté, M. Raizen: Phys. Rev. A **56**, R3350 (1997); R. Marani, L. Cognet, V. Savalli, N. Westbrook, C. Westbrook, A. Aspect: Phys. Rev. A (2000), in press
6. F. Bardou, O. Emile, J.M. Courty, C.I. Westbrook, A. Aspect: Eur. Phys. Lett. **20**, 681 (1992)
7. H.C. Mastwijk, J.W. Thomsen, P. van der Straten, A. Niehaus: Phys. Rev. Lett. **80**, 5516 (1998)
8. P.J.J. Tol, N. Herschbach, E.A. Hessels, W. Hogervorst, W. Vassen: Phys. Rev A **60**, 761 (1999)
9. M. Kumakura, N. Morita: Phys. Rev. Lett. **82**, 2848 (1999)
10. A. Browaeys, J. Poupard, A. Robert, S. Nowak, W. Rooijakkers, E. Arimondo, L. Marcassa, D. Boiron, C.I. Westbrook, A. Aspect: Eur. Phys. J. D **8**, 199 (1999)
11. G. Shlyapnikov, J. Walraven, U. Rahmanov, M. Reynolds: Phys. Rev. Lett. **73**, 3247 (1994); P. Fedichev, M. Reynolds, U. Rahmanov, G. Shlyapnikov: Phys. Rev. A **53**, 1447 (1996)
12. T. Bergeman, E. Erez, H. Metcalf: Phys. Rev. A **35**, 1535 (1987)
13. W. Petrich, M. Anderson, J. Ensher, E. Cornell: Phys. Rev. Lett. **74**, 3352 (1995)
14. G. Labeyrie, A. Browaeys, W. Rooijakkers, D. Voelker, J. Grosperrin, B. Wanner, C.I. Westbrook, A. Aspect: Eur. Phys. J. D **7**, 341 (1999); J. Grosperrin, W. Rooijakkers, A. Browaeys, G. Labeyrie, B. Wanner, C.I. Westbrook, A. Aspect: Ann. Phys. **23**, 207 (1998)
15. K.B. Davis, M.O. Mewes, M.A. Joffe, M.R. Andrews, W. Ketterle: Phys. Rev. Lett. **74**, 5202 (1995)
16. J.C. Hill, L.L. Hatfield, N.D. Stockwell, G.K. Walters: Phys. Rev. A **5**, 189 (1972)

A Bose-Einstein Condensate of Metastable Atoms

A. Robert, O. Sirjean, A. Browaeys,* J. Poupard,† S. Nowak,‡ D. Boiron, C. I. Westbrook, A. Aspect§

We report the realization of a Bose-Einstein condensate of metastable atoms (helium in the lowest triplet state). The excitation energy of each atom with respect to the ground state is 20 electron volts, but inelastic processes that would destroy the sample are suppressed strongly enough in a spin-polarized sample to allow condensation. Our detection scheme takes advantage of the metastability to achieve detection of individual atoms as well as of the decay products of inelastic processes. This detection opens the way toward new studies in mesoscopic quantum statistical physics, as well as in atomic quantum optics.

Bose-Einstein condensation (BEC) of helium in its ground electronic state has been known for decades and is responsible for many extraordinary properties of liquid helium. The more recently observed BEC of weakly interacting atomic gases exhibits a rich variety of phenomena at the interface between condensed matter and statistical physics on the one hand and atomic, molecular, and quantum optical physics on the other (*1*). The phenomenon has thus far been observed in four different atomic species: H, Li, Na, and Rb (*2*–*5*). We now report the observation of BEC in a fifth species: metastable triplet He (He*). This result is important in itself because not all atoms lend themselves to condensation with present technology and, as was demonstrated in the case of Cs (*6*), sometimes only in attempting to form a BEC can one obtain accurate enough information to conclude whether it is possible or not. In the case of He*, it was in fact predicted that elastic collision rates were sufficiently large and inelastic collision rates were sufficiently low to permit BEC (*7*), and this prediction has stimulated experimental efforts in several labs (*8*–*10*). Our work verifies these predictions, and helium is now the only atom that exhibits BEC in two phases with vastly different densities, corresponding to different electronic states.

A BEC of He* is remarkable in that the constituent atoms contain a large internal energy: the 2 $^3S_1$ state is 20 eV above the electronic ground state, and this energy is huge compared to the thermal energy of our sample (10^{-10} eV per atom at 1 μK). Only a complete decoupling of the internal and external degrees of freedom prevents conversion of the internal electronic atomic energy into ionization and kinetic energy that would lead to an immediate destruction of the condensate. An unpolarized sample of metastable helium at such a large density (about 10^{13} cm^{-3}) would be destroyed in less than a millisecond (*11*–*13*). The reason this does not happen is the complete spin polarization of a magnetically trapped gas. When all spins are aligned along the same direction, Penning ionizing collisions that could release the internal potential energy are suppressed by spin conservation (*14*). Theoretical studies (*7*, *15*, *16*) that take into account spin relaxation predict a suppression factor as large as 10^5 (*17*).

The large energy content of each atom opens the ultimate possibility of detecting individual atoms with nanosecond time resolution, an extremely challenging task when using optical detection. When the atoms hit a detector such as a microchannel plate (MCP) with a velocity of 1 m/s as in our experiment, the time resolution translates into nanometer position resolution. With such sensitive detection, it will become possible to study mesoscopic statistical physics, with a number of particles ranging from 10^5 or larger to a few, thereby allowing the study of finite number effects in an unusual range (*18*). Individual atom detection will also allow one to perform new quantum atom optics experiments. For instance, the celebrated experiments of spatial interference between two independent condensates (*19*) could be done with a time- and position-resolved detector, so that the emergence of a relative phase between the two condensates, as predicted in several theoretical papers (*20*), could be followed in real time.

Our experiment begins with a magneto-optical trap of He* (*21*). After optical molasses cooling, optical pumping, and magnetic compression, the magnetic trap contains about 2 × 10^8 atoms at 1 mK. Metastable helium in the 2 $^3S_1$ state has a (purely electronic) spin of 1, and only the $m = +1$ magnetic sublevel can be trapped. The $m = -1$ sublevel is antitrapped, and $m = 0$ is insensitive to the magnetic field. The magnetic trap is of a "cloverleaf" design (*22*) with $B' = 85$ G/cm, $B'' = 20$ G/cm^2, and a bias field $B_0 = 0.3$ G at the end of the compression. The corresponding axial and radial oscillation frequencies in the harmonic trapping potential are about 50 and 1300 Hz, respectively. The atomic cloud is elongated along the coils' axial direction (Fig. 1), and its lifetime is 50 to 60 s.

After the compression stage, thermalization is rapid enough for evaporative cooling (*21*), and we begin a radio frequency (RF) evaporation ramp at a frequency of 135 MHz. The ramp lasts about 60 s and goes down to a value around 1 MHz, which is about 150 kHz above the minimum of the trapping potential. After the ramp, the trap holds the remaining atoms for 100 ms or more. We then turn off the currents producing the magnetic trap, and atoms falling under the influence of gravity are detected by a MCP placed 5 cm below the trap center. We show in Fig. 2 the signal from the MCP as a function of time after the atoms' release and for various values for the final frequency of the ramp. The time-of-flight (TOF) spectra show the arrival time distribution for a cloud of atoms falling on the detector. The mean arrival time corresponds to the time it takes for the atoms, initially nearly at rest, to fall 5 cm.

Because the width of the distribution is small compared to the mean arrival time, all of the atoms hit the detector with nearly the same final velocity of 1 m/s. The TOF spectra are then proportional to the spatial distribution along the vertical x direction, integrated over y and z.

Figure 2 thus shows the behavior characteristic of most other BEC experiments using atoms in a harmonic trapping potential: At a high final ramp frequency (that is, above the condensation temperature), the spatial distribution is well approximated by a Maxwell-Boltzmann distribution, whereas when the ramp goes low enough and reduces the temperature sufficiently, the distribution exhibits a narrow peak on top of a broad one. The fraction of atoms in the narrow peak increases as the final ramp frequency is lowered, and we interpret this peak as a BEC. The signal disappears altogether when the ramp is allowed to go even lower and to completely empty the trap.

Laboratoire Charles Fabry de l'Institut d'Optique, UMR 8501 du CNRS, Bâtiment 503, Campus Universitaire d'Orsay, Boîte Postale 147, F-91403 Orsay Cedex, France.

*Present address: Laser Cooling and Trapping Group, National Institute of Standards and Technology (NIST), Gaithersburg, MD 20899, USA.
†Present address: R&D Laboratory, GN NETTEST Photonics, Boîte Postale 39, F-78160, Marly le Roi, France.
‡Present address: Bayer Central Research Laboratory, D-51368 Leverkusen, Germany.
§To whom correspondence should be addressed. E-mail: alain.aspect@iota.u-psud.fr

The spectra shown in Fig. 2 correspond to approximately 5×10^3 atoms falling on the MCP. They correspond to freely falling atoms released from the trap immediately after the currents in the coils are turned off. Stray magnetic field gradients are present during the atoms' fall, and therefore we conclude that these atoms are in the field-insensitive $m = 0$ state. We have confirmed this interpretation by deliberately applying a field gradient of 0.1 to 1 G/cm along the vertical direction during the 100-ms fall time. We observed no change in the arrival time nor in the height of the observed peak in the presence of these gradients. We thus interpret the spectra as a sample of the cold, trapped cloud in $m = +1$ (including both the condensed and the uncondensed fractions) that was rapidly transferred to the $m = 0$ state during the switch-off of the current. We know from previous in situ magnetic field measurements that when the current is switched off, eddy currents in the vacuum chamber cause the bias magnetic field at the position of the atoms, originally 0.3 G, to reverse and attain values above 100 G. This reversal takes place in about 100 μs, after which time the magnetic field decays with a time constant of about 1 ms. We presume that during this fast reversal, most of the atomic spins adiabatically follow the magnetic field, but a small fraction ends up in the $m = 0$ state. Such a nonadiabatic transition must take place while the field is close to zero; that is, in a time short compared to the 100-μs reversal time (*23*).

This scenario is supported by two additional observations. First, when applying the vertical gradient mentioned above, we observed a second peak in the TOF spectrum. This peak arrived earlier by an amount consistent with the acceleration caused by the applied gradient and therefore corresponded to atoms in one of the field-sensitive states. This peak had an area as much as seven times greater than that of the $m = 0$ peak, indicating that many more atoms were in the trap than were observed in the TOF spectrum. In a second experiment, we used an RF knife ramping through the trap at 1 kHz/ms to couple the atoms out of the condensate rather than turning off the magnetic field. In this way, we also observed as many as seven times more atoms as in the curves in Fig. 2.

We can confirm the idea that many more atoms are trapped than are observed in Fig. 2 by an independent analysis leading to the number $N_{\rm th}$ of atoms in the thermal cloud below the critical temperature. By fitting the wings of the TOF spectra, we are able to determine the temperature T of the trapped atomic cloud and, using the Bose distribution, to infer $N_{\rm th}$. As discussed in (*18*) and experimentally demonstrated in (*22*, *24*, *25*), this number should be given by: $N_{\rm th} = 1.202\,(kT/\hbar\tilde{\omega})^3$, where k is Boltzmann's constant, $\hbar$ is Planck's constant divided by 2π, and $\tilde{\omega}$ denotes the geometric mean of the trap oscillation frequencies. This relation gives an absolute thermodynamic measurement of the number of atoms. It is greater by a factor $f = 8 \pm 4$ than the value from the MCP. The uncertainty given for f is the standard deviation of 28 measurements. Taking this correction into account, the largest condensate we have observed contained about 10^5 atoms.

We have also examined the behavior of the condensate for different atom numbers. Figure 3 shows the results of a series of runs for which the number of atoms in the condensate was varied. We plot the width corresponding to the Thomas-Fermi radius of the condensate after expansion, as a function of the number N_0 of atoms in the condensed fraction. We obtained good fits to an inverted parabola squared for numbers of detected atoms as low as 400. The size w_i of the condensate in the direction i, in the Thomas-Fermi approximation, and for a scattering length a is given by

$$w_i = \sigma_i \sqrt{\frac{\tilde{\omega}}{\omega_i}} \left(15\frac{N_0 a}{\tilde{\sigma}}\right)^{1/5}$$

where $\sigma_i = \sqrt{\{\hbar/m\omega_i\}}$ is the size of the ground state harmonic oscillator wavefunction along the ith direction, and $\tilde{\sigma}$ denotes the geometric mean of the three sizes. To obtain the size of the condensate in the trap from the measured size after the expansion of duration $(t) = 100$ ms, we use the analysis of (*26*) according to which, for a sudden switch-off of the trapping potential, the spatial distribution of the condensate along an initially tightly confined direction i is simply dilated by a factor $\omega_i t$ during expansion. Thus, the condensate size should vary as the 1/5 power of the number of atoms, as is confirmed by a fit to a log-log plot (slope 0.19) and Fig. 3.

Knowing the size as a function of the number of atoms in the condensate allows

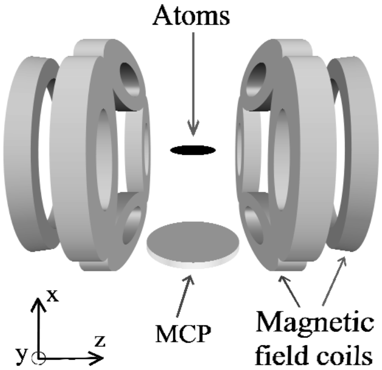

Fig. 1. Schematic diagram of the apparatus (not to scale). The coils that form the magnetic trap are outside the vacuum in reentrant flanges. The microchannel plate is 5 cm below the center of the trap. The incoming He* beam propagates along the *y* axis (horizontally). The three pairs of magneto-optical trap laser beams (not shown) propagate along the *z* axis and at 45° to the *x* and *y* axes.

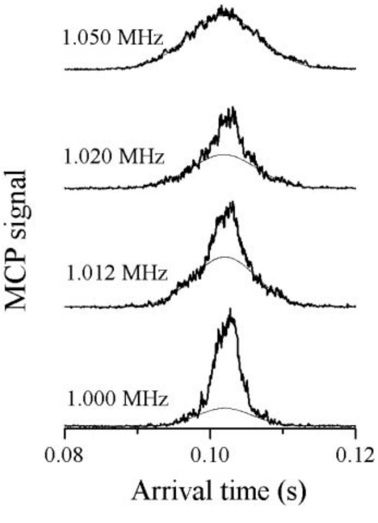

Fig. 2. TOF spectra for different final frequencies of the RF ramp (values are shown at the left of each curve). The solid lines show Gaussian fits to the wings. This series of spectra shows the BEC transition as the RF ramp lowers the temperature further and further. The temperature at the transition is 0.7 μK. Each spectrum is a single-shot acquisition containing about 5×10^3 atoms, although the actual number in the condensate is higher by a factor of about 8.

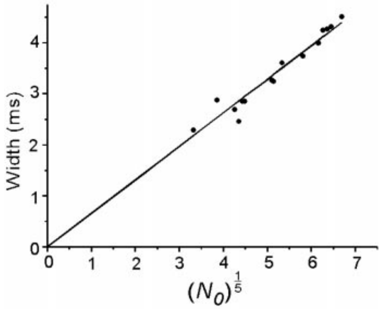

Fig. 3. Observed width of the condensate peak after expansion, as a function of the number of atoms in the peak to the 1/5 power. The width is derived from the TOF spectrum and is given in milliseconds. After correcting the number of atoms for the fraction we do not observe (see text), the slope of the straight line gives an estimate of the scattering length of 20 ± 10 nm.

us also to get an estimate of the scattering length a. We used the data in Fig. 3, and correcting the number of atoms by the correction factor f we obtained $a = 20 \pm 10$ nm. This result is consistent with our elastic rate constant measurements at 1 mK (*21*). The validity of the above analysis relies on two important assumptions. First, the release of the atoms from the trapping potential must be rapid as compared to the inverse of the angular frequency ω_i. If this were not the case, the expansion would not be as fast as expected, and this discrepancy would lead to an underestimate of the size of the condensate and therefore of a. According to the discussion of the rapid transfer to $m = 0$ above, it is reasonable to believe that the condition is fulfilled in our case, but its violation can lead to large errors. The second assumption is that the interaction energy between the atoms in the various m sublevels is described by a single scattering length a (*27*, *28*) and that they all expand freely (*29*).

We have also observed the ions produced by the trapped condensate by negatively biasing a grid above the MCP (Fig. 4). These ions are due to Penning ionization of residual gases, two-body Penning collisions within the condensate, or possibly to other, more complicated processes. We observed a factor of 4 to 5 more ions from the condensate than from a thermal cloud at 1 μK, and we attribute this increase to the larger density in the condensate. The lifetime of the condensate, estimated by observing the decay of the ion rate, is on the order of a few seconds. This is true both with and without an RF knife to evacuate hot atoms (*22*, *30*), although the lifetime is slightly longer with the knife present. The density of the condensate, deduced from its vertical size measurement and its known aspect ratio, is on the order of 10^{13} cm^{-3}, so from the lifetime we can place an upper limit of 10^{-13} cm^3 s^{-1} on the relaxation-induced Penning ionization rate constant.

The observation of BEC in He*, together with our MCP detector, offers many new possibilities for the investigation of BECs. The ion detection described in the previous paragraph allows continuous nondestructive monitoring of the trapped condensate. Our ability to count individual He* atoms falling out of the trap can be combined with several outcoupling schemes releasing the atoms in the field-insensitive $m = 0$ state: A laser-induced Raman transition (*31*) can provide an even faster and more flexible scheme than the fast reversal of the magnetic field presented here; on the other hand, like an RF outcoupler, it can also produce a quasi–continuous-wave atom laser (*32*, *33*), and the RF experiment presented above is a crude version of it. Fast dumping of atoms, with numbers ranging from over 10^5 to a few, can offer new opportunities for studies in statistical physics with low numbers of particles, such as investigations of corrections far from the thermodynamical limit (*18*). Slow outcoupling combined with space- and time-resolved detection of individual atoms should allow one to perform accurate comparisons of correlation functions (*30*) for a thermal beam of ultracold atoms (*34*) and for an atom laser, realizing the quantum atom optics counterpart of one of the fundamental experiments of quantum optics. Experiments that are still unrealized in quantum photon optics may also become possible with a system such as that reported here.

It has already been shown that the laser and vacuum apparatus necessary to manipulate ^{4}He is readily adapted to the fermionic isotope ^{3}He (*12*). Thus we expect that it will soon be possible to study a degenerate gas of fermions using sympathetic cooling (*35*–*37*). Finally, the upper-lying levels of triplet metastable helium are radiatively coupled to the electronic $1\,^1S_0$ ground state, so that a laser excitation of the condensate toward one of these levels would create a population inversion with the ground state. This excitation could lead to superradiance, and even lasing beyond 20 eV. It might also yield a dilute degenerate sample of ground-state helium, giving yet a third phase of quantum degenerate helium.

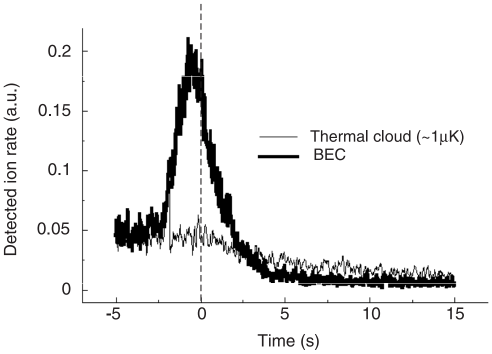

Fig. 4. Ions detected by the MCP during the magnetic trap phase. The vertical dashed line at $t = 0$ corresponds to the end of the RF ramp. The thin line corresponds to a final RF frequency of 1.2 MHz (Fig. 2) [that is, a thermal cloud ($T = 1$ μK)], whereas for 0.97 MHz (thick line) the cloud is almost a pure BEC. The lifetime is smaller in the latter case, indicating a higher loss rate for a BEC.

References and Notes

1. *Proceedings of the International School of Physics "Enrico Fermi," Course CXL*, M. Inguscio, S. Stringari, C. E. Wieman, Eds. (IOS Press, Amsterdam, 1999).
2. M. H. Anderson, J. R. Ensher, M. R. Matthews, C. E. Wieman, E. A. Cornell, *Science* **269**, 198 (1995).
3. K. B. Davis *et al.*, *Phys. Rev. Lett.* **75**, 3969 (1995).
4. C. C. Bradley, C. A. Sackett, J. J. Tollet, R. G. Hulet, *Phys. Rev. Lett.* **75**, 1687 (1995).
5. D. G. Fried *et al.*, *Phys. Rev. Lett.* **81**, 3811 (1998).
6. D. Guéry-Odelin, J. Söding, P. Desbiolles, J. Dalibard, *Europhys. Lett.* **44**, 25 (1998).
7. G. V. Shlyapnikov, T. M. Walraven, U. M. Rahmanov, M. W. Reynolds, *Phys. Rev. Lett* **73**, 3247 (1994).
8. W. Vassen, *OSA TOPS on Ultracold Atoms and BEC* **7**, 20, K. Burnett, Ed. (Optical Society of America, Washington, DC, 1996).
9. F. Pereira Dos Santos *et al.*, *Euro. Phys. J. D.* **14**, 15 (2001).
10. H. C. W. Beijerinck, E. J. D. Vredenbregt, R. J. W. Stas, M. R. Doery, J. G. C. Tempelaars, *Phys. Rev. A* **61**, 023607 (2000).
11. H. C. Mastwijk, J. W. Thomsen, P. van der Straten, A. Niehaus, *Phys. Rev. Lett.* **80**, 5516 (1999).
12. M. Kumakura, N. Morita, *Phys. Rev. Lett.* **82**, 2848 (1999).
13. P. J. J. Tol, N. Herschbach, E. A. Hessels, W. Hogervorst, W. Vassen, *Phys. Rev. A* **60**, R761 (1999).
14. For two colliding spin-polarized atoms, the initial value of the total spin is 2, whereas the final value cannot be larger than 1 for the products of Penning ionization, a ground-state helium atom with zero spin, a He$^+$ ion with spin 1/2, and an electron with spin 1/2.
15. P. O. Fedichev, M. W. Reynolds, U. M. Rahmanov, G. V. Shlyapnikov, *Phys. Rev. A* **53**, 1447 (1996).
16. V. Venturi, I. B. Whittingham, P. J. Leo, G. Peach, *Phys. Rev. A* **60**, 4635 (1999).
17. This suppression is particularly remarkable in He*. For instance, it has not been observed in Xe* [C. Orzel, M. Walhout, U. Sterr, P. S. Julienne, S. L. Rolston, *Phys. Rev. A* **59**, 1926 (1999)].
18. F. Dafolvo, S. Giorgini, L. P. Pitaevskii, S. Stringari, *Rev. Mod. Phys.* **71**, 463 (1999) and references therein.
19. M. R. Andrews *et al.*, *Science* **275**, 637 (1997).
20. See, for example, P. Horak, S. M. Barnett, *J. Phys. B* **32**, 3421 (1999) and references therein.
21. A. Browaeys *et al.*, in preparation.
22. M.-O. Mewes *et al.*, *Phys. Rev. Lett.* **77**, 416 (1996).
23. If the field passes almost exactly through zero during reversal, most of the atoms would become anti-aligned with the field, but also in this case a small fraction would end up in the $m = 0$ state, and this transfer would again take place in significantly less than the total reversal time.
24. L. V. Hau *et al.*, *Phys. Rev. A* **58**, R54 (1998).
25. J. R. Ensher, D. S. Jin, M. R. Matthews, C. E. Wieman, E. A. Cornell, *Phys. Rev. Lett.* **77**, 4984 (1996).
26. Y. Castin, R. Dum *Phys. Rev. Lett.* **77**, 5315 (1996).
27. Theoretical arguments support this assumption [P. Leo, E. Tiesinga, personal communication].
28. P. J. Leo, V. Venturi, I. B. Whittingham, J. F. Babb, in preparation.
29. This is a reasonable assumption because, in a cloverleaf trap, an increase of the bias field results in a dramatic decrease of the stiffness of the potential, so that a few microseconds after the partial transfer to $m = 0$, atoms in $m = \pm 1$ can also be considered free at the scale of the interaction energy. Otherwise, one would have to take into account a correction factor not larger than 2 [see reference 20 in (*31*)].
30. E. A. Burt *et al.*, *Phys. Rev. Lett.* **79**, 337 (1997).
31. E. Hagley *et al.*, *Science* **283**, 1706 (1999).
32. I. Bloch, T. W. Hänsch, T. Esslinger, *Nature* **403**, 166 (2000).
33. F. Gerbier, P. Bouyer, A. Aspect, *Phys. Rev. Lett.*, in press (and references therein).
34. Y. Yasuda, F. Shimizu, *Phys. Rev. Lett.* **77**, 3090 (1996).

35. B. DeMarco, D. S. Jin, *Science* **285**, 1703 (1999).
36. F. Schreck *et al.*, in preparation.
37. A. G. Truscott, K. E. Strecker, W. I. McAlexander, G. B. Partridge, R. G. Hulet, *Science* 1 March 2001 (10.1126/science.1059318).
38. During the preparation of this manuscript, we learned that the He* group at the Ecole Normale Supérieure, Paris, also observed BEC [F. Pereira Dos Santos *et al.*, *Phys. Rev. Lett* **86**, 3459 (2001)]. We thank the NIST Laser Cooling and Trapping and Quantum Processes groups and G. Shlyapnikov for helpful discussions and A. Villing and F. Moron for invaluable assistance. Supported by the European Union under grants IST-1999-11055 and HPRN-CT-2000-00125, and by the Direction Générale de l'Armement grant 99.34.050.

12 March 2001; accepted 16 March 2001
Published online 22 March 2001;
10.1126/science.1060622
Include this information when citing this paper.

PHYSICAL REVIEW A, VOLUME 64, 034703

Thermalization of magnetically trapped metastable helium

A. Browaeys, A. Robert, O. Sirjean, J. Poupard, S. Nowak, D. Boiron, C. I. Westbrook, and A. Aspect
Laboratoire Charles Fabry de l'Institut d'Optique, UMR 8501 du CNRS, Boite Postale 147, F-91403 Orsay Cedex, France

(Received 21 February 2001; published 10 August 2001)

We have observed thermalization by elastic collisions of magnetically trapped metastable helium atoms. Our method directly samples the reconstruction of a thermal energy distribution after the application of a RF knife. The relaxation time of our sample toward equilibrium gives an elastic collision rate constant of $\alpha \sim 5 \times 10^{-9}\ \mathrm{cm}^3/\mathrm{s}$ at a temperature of 1 mK. This value is close to the unitarity limit.

DOI: 10.1103/PhysRevA.64.034703 PACS number(s): 34.50.−s, 32.80.Pj, 51.10.+y, 67.65.+z

Bose-Einstein condensation (BEC) of dilute atomic vapors has been observed in Rb [1], Na [2], Li [3], and H [4]. Atoms in these gases are in their electronic ground states. Metastable helium in the 2^3S_1 state (He*), which has long been of interest to the laser cooling community, is by contrast in a state 20 eV above the ground state. This situation presents additional possibilities for the study of cold dilute atomic gases. First, the large internal energy permits efficient detection by ionization of other atoms and surfaces: it is possible to study very small samples. Second, Penning ionization both by the background gas and between trapped atoms offers a high time resolution monitor of the number and density of trapped atoms. Third, the possibility of using the large internal energy of He* for atomic lithography has already been demonstrated [5], and this application as well as atom holography [6] may benefit from highly coherent sources. Finally, much theoretical work has already been devoted to estimation of the elastic collision cross sections on the one hand and Penning ionizing rates on the other [7,8]. Experiments such as the one reported here can test this work.

BEC is achieved in dilute gases by evaporative cooling of a magnetically trapped sample [9]. In He*, it is hampered by the fact that in a magneto-optical trap, the typical starting point of magnetic trapping, the achievable atomic density is limited by a large light-assisted Penning ionization rate [10–15]. On the other hand, the scattering length for low energy elastic collisions is predicted to be quite large, and the Penning ionization rate highly suppressed in a spin polarized sample [7,8]. He* in a magnetic trap necessarily constitutes a spin polarized sample and experiments have already demonstrated a suppression of more than one order of magnitude [16–18]. If the theoretical estimates are right, efficient evaporative cooling may still be possible in spite of the low initial trap density. We report here the observation of the thermalization of He* due to elastic collisions which appears to roughly bear out the predictions.

To perform a thermalization experiment, a trapped cloud is deliberately placed out of equilibrium and its relaxation due to the elastic collisions between trapped particles is observed. Usually the observations are made by imaging the spatial distribution as a function of time [19–21]. In our experiment the relaxation is observed directly in the energy distribution of the atoms in the magnetic trap. First this distribution is truncated above $E_{\mathrm{RF}} = h\nu$ by a radio frequency pulse (or RF knife) of frequency ν. The cloud rethermalizes by elastic collisions and the population of the states of energy higher than E_{RF} increases from zero; for large times compared to the thermalization time τ_{th} the distribution reaches a thermal distribution [22]. With the help of an analytical model and numerical simulations, we deduce τ_{th} from the time dependence of the number of atoms with energy above E_{RF}. We measure this time dependence by applying a second RF knife after a delay time *t*, and with a frequency slightly above that of the first one. Our model also allows us to relate τ_{th} to the elastic collision rate per atom in the trap.

Much of our setup has been described previously [14,17]. Briefly, we use a liquid N_2 cooled dc discharge source to produce a beam of metastable He atoms. The beam is slowed down to $\sim$100 m/s using Zeeman slowing and loads a magneto-optical trap (MOT). Typically, 3×10^8 atoms are trapped at a peak density of 3×10^9 at./cm^3, limited by light-induced Penning ionization. The temperature of the cloud is about 1 mK and the cloud is roughly spherical with a rms size of 2.5 mm. We then apply a 5 ms Doppler molasses to cool the atoms down to 300 μK. This is achieved by switching off the magnetic field, decreasing the detuning close to resonance, and lowering the intensity to 10% of its value in the MOT. An optical pumping step allows us to trap up to 1.5×10^8 atoms in a Ioffe-Pritchard trap. We use a "cloverleaf" configuration [23] with $B' = 85$ G/cm, $B'' = 25$ G/cm^2, and a bias field $B_0 = 200$ G. The two sets of coils are outside the vacuum, separated by 4 cm. After lowering the bias field to 4 G, the temperature of the compressed atomic sample reaches 1 mK. The lifetime of the trap is 60 s.

We use a two stage microchannel plate (MCP) to detect the atoms. The MCP is placed 5 cm below the trapping region and has an active area of 1.4 cm diameter. Two grids above the MCP allow us to repel all charged particles and detect only the He*. After turning off the magnetic trap, the MCP signal corresponds to a time of flight (TOF) spectrum that gives the temperature of the atoms. The area of this spectrum is proportional to the number of atoms in the trap at the time it was turned off. The collection and detection efficiency of the MCP varies by roughly a factor of 2 depending on the magnetic field configuration we use, and so one must take care to use only data corresponding to the same magnetic field when making comparisons. We also use the MCP to monitor the atoms falling out of the trap while applying a RF knife. The area of the MCP signal in this case measures the number of atoms with an energy above that of the RF knife. Finally, when we bias the grids so as to attract positive

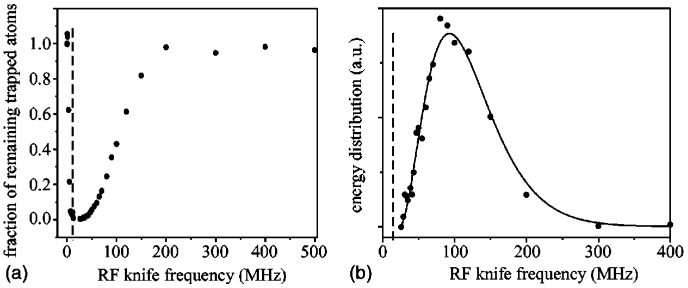

FIG. 1. RF spectrum of atoms in the magnetic trap. (a) Fraction of remaining trapped atoms after the RF pulse as a function of the RF frequency ν. (b) Derivative of these data, i.e., the energy distribution in the magnetic trap. The solid line is the prediction for a cloud at a temperature of 1.1 mK, the temperature measured by time of flight (TOF). The dashed line indicates the frequency corresponding to the bias field.

ions, the MCP signal can be used to observe the products of Penning ionization with the background gas while the trap is on. This signal is proportional to the number of trapped atoms. We observe an exponential decay, indicating that two body loss $(\mathrm{He}^*+\mathrm{He}^*)$ is negligible.

Two parallel coils in the vacuum system produce a RF magnetic field perpendicular to the bias field and constitute the RF knife. To understand the effect of the RF knife on the trapped cloud and to assure that our sample is at thermal equilibrium, we first performed a RF spectroscopy measurement of the energy of the atoms in the trap [24]. We apply a RF pulse at a frequency $h\nu$ which changes the Zeeman sublevel of the atoms from the trapped $M=+1$ state to $M=0$. The duration of the knife is 3 s, which is necessary to expel all the atoms with energy above $h\nu$ over the entire range that we explore. We then turn off the magnetic trap to measure the number of remaining atoms. Observation of the atoms falling onto the MCP during the RF knife shows that the flux of atoms expelled is negligible at the end of the pulse.

An example of the RF spectrum is shown in Fig. 1(a). The derivative of the data gives the energy distribution. In Fig. 1(b) we compare this distribution with a thermal one at 1.1 mK, the temperature measured by an independent TOF measurement. We conclude that our atomic sample is close to thermal equilibrium.

We begin the thermalization experiment with a 2 s RF knife of frequency $\nu_1=135$ MHz [corresponding to $\eta=(h\nu-2\mu_\mathrm{B}B_0)/k_\mathrm{B}T\sim 6$]. Next we measure the number of atoms falling onto the MCP during a second RF knife at a slightly higher frequency ($\nu_2=138$ MHz) and delayed by a time *t*. Assuming that the angular distribution of the atoms expelled by the second RF knife is constant during the thermalization process, the MCP signal is proportional to the number of expelled atoms. Furthermore, we have checked that the difference of the TOF areas before and after application of the RF knife agrees to within 20% with the number of atoms that should be expelled by the knife, given our temperature and the position of the knife. This gives us confidence that at the end of the RF knife the energy distribution is a truncated Maxwell-Boltzmann distribution, and that the sufficient ergodicity hypothesis we make below is reasonable.

Plots of the number of expelled atoms as a function of *t* are shown in Fig. 2 for samples having different numbers of atoms but the same temperature to within 10%. Figure 2 shows that the number of atoms above the RF knife increases rapidly and then falls again with a time constant close to the trap lifetime as atoms are lost. If the initial increase is indeed due to thermalizing collisions, the initial slope of each curve should be proportional to the square of the number of atoms. Our data roughly confirm this dependence.

To be more quantitative, and to determine the thermalization time τ_th, we use a model based on the Boltzmann equation under the sufficient ergodicity hypothesis and inspired by [25]. We divide the sample into two energy regions $\mathcal{E}_-$ and $\mathcal{E}_+$ with energies below and above $\eta k_\mathrm{B}T$, respectively, and denote by N_- and N_+ the number of atoms belonging to the two regions. We assume that $\eta\gg 1$. Immediately after truncation, $N_+=0$, and we seek a differential equation governing the time dependence of N_+. Since $\eta\gg 1$, we take into account only collisions of the type $(\mathcal{E}_-)+(\mathcal{E}_-)\leftrightarrow(\mathcal{E}_-)+(\mathcal{E}_+)$, and neglect all collisions involving two atoms in $\mathcal{E}_+$ in either the final or initial state. The corresponding flux $\dot{N}_+$ is thus of the form

$$\dot{N}_+=\Delta_1 N_-^2-\Delta_2 N_- N_+ . \tag{1}$$

The coefficients Δ_1 and Δ_2 are calculated using Boltzmann equation [27]. In particular, $\Delta_1 N_-$ is exactly the evaporation rate in an evaporative cooling process [25]. If we make the further approximations that the atoms in $\mathcal{E}_-$ and $\mathcal{E}_+$ have thermal distributions [26], neglect variations of the temperature during thermalization, and assume that the collision cross section σ is independent of velocity, Δ_1 and Δ_2 are analytic functions of the trap parameters, atomic mass *m*, σ,

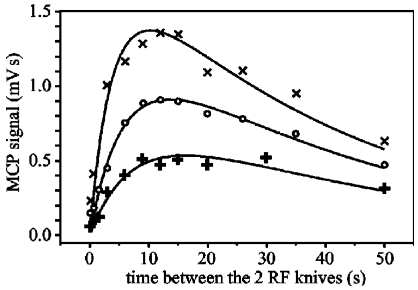

FIG. 2. Integrated MCP signal during the RF probe pulse as a function of the delay between the truncation and probe pulses. The three curves correspond to 5×10^7, 7×10^7, and 10×10^7 atoms in the trap, varied by changing the power in the Zeeman slowing laser. The lifetime of the trap is 38 ± 4 s, and the temperature is 0.9 ± 0.1 mK.

η, and $\mu_B B_0/k_B T$. This last parameter appears because our trap cannot be approximated by a harmonic trap; we use the semilinear form [25]. It is straightforward to take into account the finite lifetime τ of the atomic sample since $N_-(t)+N_+(t)=N_-(0)\exp(-t/\tau)$. The solution of the resulting differential equation is

$$N_+(t)=N_{\text{th}}e^{-t/\tau}\left[1+\frac{q}{1-q-\exp[(\tau/\tau_{\text{th}})(1-e^{-t/\tau})]}\right], \tag{2}$$

where $\tau_{\text{th}}^{-1}=(\gamma_{\text{el}}/\sqrt{2})[q/(1-q)](e^{-\eta}V_{\text{ev}}/V_{\text{e}})$ and $N_{\text{th}}=(1-q)N_-(0)$. The elastic collision rate is $\gamma_{\text{el}}=n\sigma\overline{v}$ with n defined at the center of the trap and $\overline{v}=4\sqrt{k_B T/\pi m}$. The quantities V_{ev}, V_{e}, and q are defined as in [25,27]; they are analytic functions of η and $\mu_B B_0/k_B T$. The quantity q is the ratio of the number of atoms below the RF knife to the total for a thermal distribution (about 0.9 under our conditions), and N_{th} is the asymptotic value of N_+ for infinite trap lifetime. Numerical simulations of the energy form of the Boltzmann equation are in good agreement with our model for $\eta>10$; for $\eta=6$ the quantity $\gamma_{\text{el}}\tau_{\text{th}}$ is 1.8 times larger, meaning that our assumption about the distribution function fails for small η [27]. We take this factor into account in calculating γ_{el}.

To fit the data of Fig. 2 with Eq. (2), we fix the lifetime τ at its measured value and use τ_{th} and N_{th} as adjustable parameters. The uncertainty in τ_{th} is estimated by varying the lifetime of the trap within its uncertainty range and looking at the resulting dispersion in τ_{th}. The uncertainty in the number of trapped atoms is estimated from the dispersion of the TOF area measurements before and after taking a curve as in Fig. 2. The exact value of q has little influence on the fit.

We made several tests to check the consistency of our results. First, we checked that the fitted value of N_{th} corresponds to the expected fraction of atoms above the knife for our temperature. Second, Fig. 3 shows that τ_{th}^{-1} is proportional to the number of trapped atoms, as it must be if the process of refilling of the upper energy class is due to two body collisions. We can exclude any effect independent of the number of atoms. The line passing through the origin uses the slope as a fit parameter and has $\chi^2=5$ for eight degrees of freedom. Third, we have done an additional experiment that confirms the presence of elastic collisions: in a trap decay rate experiment, *in the presence* of the RF knife, the ion signal exhibits a clear nonexponential behavior at short times. This effect can be satisfactorily interpreted as elastic collisions bringing atoms above the RF knife and hence allows a measurement of the evaporation rate. This rate is consistent with the results obtained in our thermalization experiment. Fourth, we have checked that heating cannot explain the repopulation of the upper energy classes. With the trap undisturbed, we can place an upper limit on the heating rate of 25 μK in 60 s. This limit is two orders of magnitude too low to explain our data. Lastly, we have performed the thermalization experiment for different lifetimes of the magnetic trap (20, 40, and 60 s) and found consistent results.

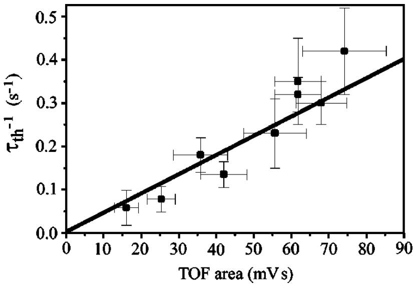

FIG. 3. Thermalization rate τ_{th}^{-1} versus the area of the corresponding TOF spectrum (proportional to the number of trapped atoms). The solid line shows a linear fit constrained to pass through the origin.

From our data in Fig. 3, we can deduce an accurate measurement of the thermalization time; the fit gives $\tau_{\text{th}}=3.0\pm0.3$ s for the densest sample. Using the measured temperature and bias field, this value of τ_{th} leads to $\gamma_{\text{el}}=6\pm1$ s^{-1}; this result depends on the accuracy of our thermalization model. To find the rate constant $\alpha=\gamma_{\text{el}}/n$, we must estimate the density. Since the data show that our sample is close to thermal equilibrium, we can calculate the volume of the trap knowing the trap parameters. The absolute measurement of the number of atoms is performed by measuring the total power absorbed from a saturating laser beam, similar to [15]. A TOF area of 75 mV s corresponds to 10^8 atoms in the magnetic trap with an uncertainty of a factor of 2. This leads to $\alpha=5\times10^{-9}$ cm^3/s to within a factor of 3 at $T=1\pm0.1$ mK. Leduc *et al.* have obtained a similar result with a different measurement [28]. The unitarity limit at that temperature is $\alpha\sim10^{-8}$ cm^3/s. This means that it is probably not valid to use a constant elastic cross section in our model and some deviation might appear in the quantity $\gamma_{\text{el}}\tau_{\text{th}}$. The results shown here are very encouraging for evaporative cooling of He* in search of BEC.

We thank P. Leo and P. Julienne and the ENS helium group for helpful discussions. This work was partially supported by the EC under Contract No. IST-1999-11055 and No. HPRN-CT-2000-00125, and DGA Grant No. 99.34.050.

---

[1] C.J. Anderson, J.R. Ensher, M.R. Matthews, C.E. Wieman, and E.A. Cornell, Science **269**, 198 (1995).
[2] K.B. Davis, M.O. Mewes, M.R. Andrews, N.J. van Druten, D.S. Durfee, D.M. Kurn, and W. Ketterle, Phys. Rev. Lett. **75**, 3969 (1995).
[3] C.C. Bradley, C.A. Sackett, J.J. Tollett, and R.G. Hulet, Phys. Rev. Lett. **75**, 1687 (1995).
[4] D.G. Fried, T.C. Killian, L. Willmann, D. Landhuis, S.C. Moss, D. Kleppner, and T.J. Greytak, Phys. Rev. Lett. **81**, 3811 (1998).

[5] S. Nowak, T. Pfau, and J. Mlynek, Appl. Phys. B: Lasers Opt. **63**, 203 (1996); A. Bard *et al.*, J. Vac. Sci. Technol. B **15**, 1805 (1997).
[6] J. Fujita, M. Morinaga, T. Kishimoto, M. Yasuda, S. Matsui, and F. Shimizu, Nature (London) **380**, 691 (1996).
[7] G. Shlyapnikov, J. Walraven, U. Rahmanov, and M. Reynolds, Phys. Rev. Lett. **73**, 3247 (1994); P. Fedichev, M. Reynolds, U. Rahmanov, and G. Shlyapnikov, Phys. Rev. A **53**, 1447 (1996).
[8] V. Venturi, I.B. Whittingham, P.J. Leo, and G. Peach, Phys. Rev. A **60**, 4635 (1999); V. Venturi, I.B. Whittingham, and J.F. Babb, e-print physics/0011072.
[9] H.F. Hess, Phys. Rev. B **34**, 3476 (1986).
[10] F. Bardou, O. Emile, J.M. Courty, C.I. Westbrook, and A. Aspect, Europhys. Lett. **20**, 681 (1992).
[11] H.C. Mastwijk, J.W. Thomsen, P. van der Straten, and A. Niehaus, Phys. Rev. Lett. **80**, 5516 (1998).
[12] P.J.J. Tol, N. Herschbach, E.A. Hessels, W. Hogervorst, and W. Vassen, Phys. Rev. A **60**, 761 (1999).
[13] M. Kumakura and N. Morita, Phys. Rev. Lett. **82**, 2848 (1999).
[14] A. Browaeys *et al.*, Eur. Phys. J. D **8**, 199 (2000).
[15] F. Pereira Dos Santos, F. Perales, J. Léonard, A. Sinatra, Junmin Wang, F.S. Pavone, E. Rasel, C.S. Unnikrishnan, and M. Leduc, Eur. Phys. J. D **14**, 15 (2001).
[16] J.C. Hill, L.L. Hatfield, N.D. Stockwell, and G.K. Walters, Phys. Rev. A **5**, 189 (1972).
[17] S. Nowak, A. Browaeys, J. Poupard, A. Robert, D. Boiron, C.I. Westbrook, and A. Aspect, Appl. Phys. B: Lasers Opt. **70**, 455 (2000).
[18] N. Herschbach, P.J.J. Tol, W. Hogervorst, and W. Vassen, Phys. Rev. A **61**, 050702(R) (2000).
[19] C.R. Monroe, E.A. Cornell, C.A. Sackett, C.J. Myatt, and C.E. Wieman, Phys. Rev. Lett. **70**, 414 (1993).
[20] K.B. Davis, M.O. Mewes, M.A. Joffe, M.R. Andrews, and W. Ketterle, Phys. Rev. Lett. **74**, 5202 (1995).
[21] M. Arndt, M. Ben Dahan, D. Guéry-Odelin, M.W. Reynolds, and J. Dalibard, Phys. Rev. Lett. **79**, 625 (1997).
[22] D.W. Snoke and J.P. Wolfe, Phys. Rev. B **39**, 4030 (1989).
[23] M.O. Mewes, M.R. Andrews, N.J. van Druten, D.M. Kurn, D.S. Durfee, and W. Ketterle, Phys. Rev. Lett. **77**, 416 (1996).
[24] A.G. Martin, K. Helmerson, V.S. Bagnato, G.P. Lafyatis, and D.E. Pritchard, Phys. Rev. Lett. **61**, 2431 (1988).
[25] O.J. Luiten, M.W. Reynolds, and J.T.M. Walraven, Phys. Rev. Lett. **53**, 382 (1996).
[26] This hypothesis is legitimate in $\mathcal{E}_-$ because it is true at $t=0$ and because only few particles will leave this region; one can find indications in [22] that this hypothesis is not too strong in $\mathcal{E}_+$.
[27] D. Boiron *et al.* (unpublished).
[28] M. Leduc (private communication).

VOLUME 93, NUMBER 9 PHYSICAL REVIEW LETTERS week ending 27 AUGUST 2004

Getting the Elastic Scattering Length by Observing Inelastic Collisions in Ultracold Metastable Helium Atoms

S. Seidelin, J. Viana Gomes,* R. Hoppeler, O. Sirjean, D. Boiron, A. Aspect, and C. I. Westbrook

Laboratoire Charles Fabry de l'Institut d'Optique, UMR 8501 du CNRS, F-91403 Orsay Cedex, France

(Received 13 January 2004; published 27 August 2004)

We report an experiment measuring simultaneously the temperature and the flux of ions produced by a cloud of triplet metastable helium atoms at the Bose-Einstein critical temperature. The onset of condensation is revealed by a sharp increase of the ion flux during evaporative cooling. Combining our measurements with previous measurements of ionization in a pure Bose-Einstein condensate, we extract an improved value of the scattering length $a = 11.3^{+2.5}_{-1.0}$ nm. The analysis includes corrections that take into account the effect of atomic interactions on the critical temperature, and thus an independent measurement of the scattering length would allow a new test of these calculations.

DOI: 10.1103/PhysRevLett.93.090409 PACS numbers: 03.75.Hh, 34.50.–s, 67.65.+z

Understanding and testing the role of interparticle interactions in dilute Bose-Einstein condensates (BEC) is an exciting area of current research. Although measurements of the interaction energy and the spectrum of excitations of a BEC have confirmed the validity of the Gross-Pitaevskii equation [1], there are still relatively few quantitative tests of other aspects, such as the effect of interactions on the value of the critical temperature (T_c) or the condensed fraction [2,3]. The success in condensing metastable helium atoms (He*) [4,5] was greeted with interest in the community partly because the metastability offers new detection strategies unavailable with other species. To fully use these strategies, however, we are still missing an accurate value of the s-wave scattering length a, the atomic parameter which determines all elastic scattering behavior at low energies. An accurate value of a would also be useful to help clarify some puzzling results concerning measurements of He* in the hydrodynamic regime, in which two different ways of measuring the elastic scattering rate appeared to be in contradiction [6]. Also, because He is a relatively simple atom, theoretical predictions of a are already in a rather narrow range [7,8] and these calculations should be tested.

A straightforward method to determine a is to use ballistic expansion of a BEC to measure the chemical potential for a known atom number. This was done in Refs. [4,5], but the measurements were limited by the calibration of the number of atoms. The reported values for a are 20 ± 10 and 16 ± 8 nm, respectively. A recent estimate, limited by similar effects, is $a = 10 \pm 5$ nm [9]. In this Letter, we report a new measurement of a which makes extensive use of a unique feature of He*, spontaneous Penning ionization within the sample.

We exploit two specific situations in which the absolute atom number N is simply related to a and measured quantities: (i) for a pure BEC, the number is deduced directly from the chemical potential μ and a, and (ii) for a cloud at the BEC threshold, it is simply related to T_c. Both μ and T_c are accurately deduced from time of flight (TOF) measurements. Comparison of ion rates from a pure BEC of known chemical potential and from a cloud at T_c allows us to extract a and the ionization rate constants. The deduced value of a is independent of the absolute ion detection efficiency, assuming that this efficiency is the same in the two measurements. The ion signal is also used in another novel way: since it provides a real-time observation of the onset of BEC [10], we use it to reliably produce a cloud at threshold.

A dense cloud of He* produces a steady flux of ions due to various ionization processes. Density losses due uniquely to *ionizing* collisions depend on the local density n according to $(dn/dt)_{\text{ionizing}} = -(n/\tau_i) - \beta n^2 - Ln^3$, with τ_i the lifetime due to ionizing collisions with the background gas and β and L the 2-body and 3-body ionization rate constants defined for a thermal cloud. The total ion rate from a thermal cloud is given by

$$\Phi = \frac{N}{\tau_i} + \frac{1}{2}\beta \int n^2 d\mathbf{r} + \frac{1}{3}L \int n^3 d\mathbf{r}. \qquad (1)$$

The numerical factors reflect the fact that although two (three) atoms are lost in 2-body (3-body) collisions, only one ion is produced. Ionization measurements on a pure BEC were reported in Ref. [11], and, as a was not precisely known, β and L were given in terms of a.

For a precise measurement of a, corrections due to interactions must be taken into account. In the mean-field approach, the density is given by [1]

$$n(\mathbf{r}) = \frac{1}{\lambda^3(T)} g_{3/2}\left[\exp\left(-\frac{1}{k_B T}[V(\mathbf{r}) + 2gn(\mathbf{r}) - \mu]\right)\right], \qquad (2)$$

with $\lambda(T)$ the thermal de Broglie wavelength, T the temperature k_B the Boltzmann constant, V the trapping potential $g = 4\pi\hbar^2 a/m$ the interaction constant, μ the chemical potential, and $g_\alpha(x) = \sum_{i=1}^{\infty} x^i/i^\alpha$.

The ion rate at the phase transition Φ_c can be derived from Eq. (2) by a first order perturbation theory similar to Ref. [12] but with a fixed temperature rather than a fixed atom number. We use the chemical potential of a gas in a harmonic potential at the BEC transition:

0031-9007/04/93(9)/090409(4)$22.50

$$\mu_c/k_BT_c = \frac{3}{2}\frac{\tilde{\omega}}{\omega_c} + 4g_{3/2}(1)\frac{a}{\lambda_c}. \tag{3}$$

This gives

$$\begin{aligned}\Phi_c = \left(\frac{\omega_c}{\overline{\omega}}\right)^3\Bigg[&\frac{1}{\tau_i}\left(1.20 + 2.48\frac{\tilde{\omega}}{\omega_c} + 12.35\frac{a}{\lambda_c}\right)\\ &+ \frac{\beta}{\lambda_c^3}\left(0.33 + 1.81\frac{\tilde{\omega}}{\omega_c} + 6.75\frac{a}{\lambda_c}\right)\\ &+ \frac{L}{\lambda_c^6}\left(0.22 + 2.21\frac{\tilde{\omega}}{\omega_c} + 6.50\frac{a}{\lambda_c}\right)\Bigg],\end{aligned} \tag{4}$$

with $\tilde{\omega} = (2\omega_\perp + \omega_\parallel)/3$, $\overline{\omega} = (\omega_\parallel \omega_\perp^2)^{1/3}$, $\omega_c = k_BT_c/\hbar$, and $\lambda_c = \lambda(T_c)$. The numerical values come from the calculation of arithmetic series and are independent of any parameters of the cloud. The terms proportional to a/λ_c account for the atomic interactions, while the corrections proportional to $\tilde{\omega}/\omega_c$ take into account the effect of finite sample size. For the typical parameters ($T_c \sim 2\ \mu$K and $a = 12$ nm) we have $a/\lambda_c \simeq \tilde{\omega}/\omega_c \simeq 0.02$, corresponding to an interaction correction of 20%, 40%, and 60% in the three successive terms in Eq. (4). Even though the first order corrections are large, we find, using an approach similar to Ref. [13], that the second order corrections are negligible: -4%, 1.8%, and -3%, respectively. Note that finite size corrections are always smaller than those due to interactions.

Our setup has been described in Ref. [11]. Briefly, we trap up to 2×10^8 atoms at 1 mK in an Ioffe-Pritchard cloverleaf trap with τ_i estimated to be >500 s. In a typical run, forced evaporation for 30 s cools a cloud to a temperature near the phase transition. At this point, the rf-knife frequency is decreasing at a rate of 400 kHz/s. The axial and radial oscillation frequencies in the harmonic trapping potential are $\omega_\parallel/2\pi = 47 \pm 3$ Hz and $\omega_\perp/2\pi = 1225 \pm 20$ Hz, respectively. A 2-stage, single anode microchannel plate detector (MCP) is placed 5 cm below the trapping region. Two grids above the MCP allow us either to repel positive ions and detect only the He* atoms or to attract and detect positive ions produced in the trapped cloud. As explained in Ref. [11], to detect the ion flux, the MCP is used in counting mode, whereas we record the TOF signal at low gain (analog mode) to avoid saturation. As explained in Ref. [4], the TOF signal is due to atoms in the $m = 0$ state which are insensitive to the magnetic field. However, atoms in magnetic field sensitive states are still present, and their trajectories are affected by uncontrolled residual fields. Therefore, during the time of flight, we apply a magnetic gradient in order to push these atoms away from the detector. The ratio between the detected atoms in the $m = 0$ state and the initial number of atoms in the cloud is not well known [10], so we use the TOF only to get the temperature.

The crux of the experiment is to obtain a cloud of atoms at the phase transition. To identify the BEC threshold point, we monitor the ion signal. We have shown in Ref. [10] that the onset of BEC is heralded by a sudden increase of the ion rate associated with the increased density of the condensate. More precisely, the BEC threshold corresponds to the rapid change in slope of the ion rate vs time or the maximum of the 2nd derivative [14]. Figure 1 shows a series of such ionization rates during evaporation through the BEC transition. From these curves we can determine an empirical relation between the time of the onset of condensation and the ion rate preceding it. This relation stays valid only as long as we keep the same evaporation ramp and bias field. We will refer to this as the "threshold curve." Because of fluctuations of the bias field, we observe fluctuations of the time of BEC onset from run to run. These correspond to approximately ±60 ms in time or ±25 kHz in frequency, a value which agrees with independent measurements of the fluctuations of the bias field.

Having established this relation, we can interrupt an evaporation sequence very close to the BEC threshold and record the instantaneous ion rate as well as the corresponding TOF signal. Only runs closer than ±60 ms to the threshold curve are used in the analysis.

We fit the associated TOF spectrum to determine the temperature (Fig. 2). We use Eq. (2) together with μ_c given in Eq. (3) for the initial atomic density and then assume purely ballistic expansion of the cloud after the switching off of the trap. We refer to this fit as the Bose fit. The fits are weighted by an estimated uncertainty in each point of the TOF curve. To make this estimate, we chose a set of TOF spectra which appeared to show no systematic deviation from their fits and used them to estimate the amplitude of the noise. This noise varies as the square root of the amplitude of the signal, indicating that we are limited by the shot noise of the atom detection. Our procedure is only an approximate indicator of the error bars. The chi square per degree of freedom χ^2 for the fits

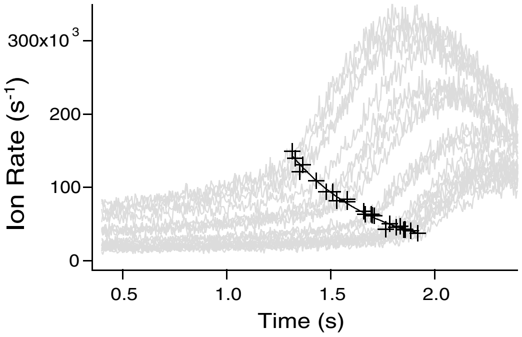

FIG. 1. Variation of the ion rate as the atomic cloud is cooled through the phase transition for various initial densities (gray curves). The rf-knife frequency at $t = 0$ is 2 MHz. The sudden increase of the ion rate (crosses) occurs at the BEC transition. The solid line passing through the transition points constitutes our empirical relation, named threshold curve.

deduced in this way ranges from 0.8 to 3. We then exclude a successively larger window (up to the rms of the TOF signal) from the fit (see Fig. 2). For all runs, we observe a variation of less than 5% and in most cases less than 3% of the temperature as the excluded window is increased.

In Fig. 2, we show an example of a typical TOF spectrum where the wings are fitted by a Gaussian and the Bose function described above. The ability of the Bose function to reproduce the center of the distribution without including it in the fit, unlike the Gaussian, confirms that the cloud is indeed close to the BEC threshold. In the following, we use the temperature given by the fit with an excluded window of half the rms width of the TOF signal in order to avoid the possibility of a small condensate component or other high density effects distorting our analysis.

Before plotting the ion rate as a function of the critical temperature, we correct the observed temperature to account for the hydrodynamic expansion of the cloud (see [2] and references therein). This is done in the spirit of Ref. [15], which uses the Boltzmann equation approach to take into account collisions during the expansion. The collision rate in Ref. [15] is calculated using a Gaussian density profile. We rather use the value calculated for an ideal Bose gas [16], which we have adapted to take interactions into account. This correction depends on the scattering length but the effect on the final value of a is only of order 0.3 nm for a ranging from 10 to 14 nm. We therefore simply assume $a = 12$ nm for this correction in the following. Due to the additional anisotropy of the expanding cloud in the horizontal (detector) plane, the fitting function should be modified; but a simulation of this effect shows that the correction to the temperature is less than 0.1%.

Finally, we correct the detected ion rate $\Phi_{\mathrm{c,det}}$ to account for the detection efficiency α such that $\Phi_{\mathrm{c}} = \Phi_{\mathrm{c,det}}/\alpha$. It should be noted that the rate constants were obtained by ion rate measurements [11]. This means that they were also corrected: $\beta = \beta_{\mathrm{det}}/\alpha'$ and $L = L_{\mathrm{det}}/\alpha'$. Equation (4) shows that, as long as $\alpha = \alpha'$, the detection efficiency cancels out and does not have any impact on the determination of a. We have checked experimentally that $\alpha = \alpha'$. To allow comparison with figures in earlier publications, all the figures have been corrected using the same α as earlier, namely, $\alpha = 0.42$ [10,11].

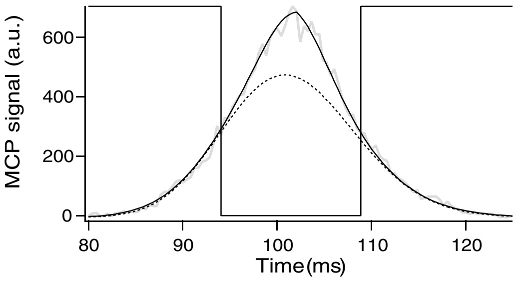

FIG. 2. Time of flight signal corresponding to a cloud released from the trap (at $t = 0$) when its ion rate is on the threshold curve. Here we have fitted the data with an excluded window indicated by the vertical lines (width equal to the rms width of the TOF signal). A Gaussian function (dotted line) does not describe the central part of the data well, while the Bose function as defined in the text (solid line) does, indicating that the cloud is close to threshold.

The results are plotted in Fig. 3. Curves corresponding to the expected variation for three values of the scattering length are also shown. We see that a large fraction of the data falls between $a = 10$ and 14 nm. The points at the highest temperatures, however, show a tendency to fall near the theoretical curve for $a = 10$ nm, while those at lower temperatures fall near $a = 14$ nm. To analyze this tendency further, we examine the TOF fits more closely using the χ^2 value as an indicator of the confidence level of each measurement. A large χ^2 could mean that the Bose function with μ imposed to μ_{c} is not the right fit function and, therefore, that the cloud is not sufficiently close to T_{c}. As shown in Fig. 3, outliers tend to be correlated with a large χ^2. Note, however, that the remaining scatter in the data is too large to be accounted for by our *a priori* estimates of the uncertainties in our ion rate or temperature measurements. We presume that it is due to fluctuations in the determination of the BEC threshold.

To determine the scattering length, we fit the black points in Fig. 3 with a as a free parameter and using β and L parametrized by a as in Ref. [11]. The fit gives (all points are given equal weight) $a = 11.3$ nm. Our chief estimated uncertainty stems from the fact that our data show a systematic tendency to fall above the best fit at low temperature and below it at high temperature. To estimate this uncertainty, we fit the data (including gray points) separately for T_{c} below and above 2 μK. We find $a = 13.8$ nm for the low temperature data and $a = 10.4$ nm for the high temperature data. The uncertainties in the measurements of β and L also contribute to the uncertainty in Eq. (4) used for fitting. In fact, the uncertainties in β and L are highly correlated [11] and their contribution to the uncertainty is less than 0.5 nm.

The error bars are obtained by summing quadratically the sources of uncertainties. Our final result for the scattering length is thus $a = 11.3^{+2.5}_{-1.0}$ nm. This result may be compared with the calculation in Ref. [8]. This work leads to $a = 8$ nm using the potential curves of Ref. [17]. From Ref. [8] one also finds that a 0.5% shift of the repulsive part of that potential would bring the theoretical value into agreement with our result. This 0.5% shift corresponds to the estimated uncertainty in the potential of Ref. [17]. Another theoretical treatment [7] gives a scattering length between 8 and 12 nm, also consistent with our results.

Our result also allows one to give values for the 2- and 3-body ionization rate constants. The error bars of Ref. [11] are modified to take into account the uncertainty

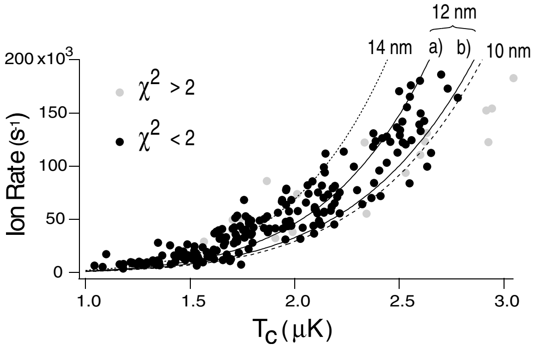

FIG. 3. Ion rate versus critical temperature. The points correspond to the results of 280 runs for which the ion rate was deemed sufficiently close to the condensation threshold. Gray indicates runs for which χ^2 in the TOF fits was above 2. The dashed line is the theoretical estimate for $a = 10$ nm, the dotted line for $a = 14$ nm [both including interaction corrections of Eq. (4)]. The two solid lines correspond to $a = 12$ nm, (*a*) with interactions and (*b*) without interactions, and illustrate the size of their effect.

of a. The uncertainty in the ion detection efficiency also contributes to the uncertainty in the rate constants. As discussed in Ref. [11], we will assume $\alpha = 0.42$ to get the central values of the rate constants. We will include a one-sided contribution to the error bars to account for the possibility, also discussed in [11], that α could be a factor of 2 smaller. We finally get $\beta = 0.9^{+1.7}_{-0.8} \times 10^{-14}$ cm^3/s and $L = 2.5^{+4.5}_{-1.7} \times 10^{-27}$ cm^6/s. The rate constants are in good agreement with theoretical predictions [8,18].

As shown in Fig. 3, curves a and b, our value of a is significantly shifted by the nonideal gas corrections of Eq. (4). Thus, when an independent measurement of the scattering length becomes available, our results can be used as a test of these corrections [19]. Note, however, that corrections to the critical temperature beyond mean-field theory [20] are small when one parametrizes the critical point in terms of an average density [13]. But an examination of the critical density measured in a local way, by imaging the ions from a cloud, for example, is sensitive to critical fluctuation phenomena which go beyond mean-field theory similar to the homogenous case [20]. Thus, refinements of the ionization measurements described here promise to continue to provide new tests of BEC physics.

This work is supported by EU Grants No. IST-2001-38863 and No. HPRN-CT-2000-00125 and by the INTAS Project No. 01-0855. S. S. is supported by the Danish Research Agency and J. V. G. by the Portuguese Foundation for Science and Technology.

*Permanent address: Departamento de Fisica, Universidade do Minho, Campus de Gualtar, 4710-057 Braga, Portugal.

[1] F. Dalfovo, S. Giorgini, L. P. Pitaevskii, and S. Stringari, Rev. Mod. Phys. **71**, 463 (1999).
[2] F. Gerbier, J. H. Thywissen, S. Richard, M. Hugbart, P. Bouyer, and A. Aspect, Phys. Rev. Lett. **92**, 030405 (2004).
[3] J. R. Ensher, D. S. Jin, M. R. Matthews, C. E. Wiemann, and E. A. Cornell, Phys. Rev. Lett. **77**, 4984 (1996).
[4] A. Robert, O. Sirjean, A. Browaeys, J. Poupard, S. Nowak, D. Boiron, C. I. Westbrook, and A. Aspect, Science **292**, 461 (2001).
[5] F. Pereira Dos Santos, J. Léonard, Junmin Wang, C. J. Barrelet, F. Perales, E. Rasel, C. S. Unnikrishnan, M. Leduc, and C. Cohen-Tannoudji, Phys. Rev. Lett. **86**, 3459 (2001).
[6] M. Leduc, J. Léonard, F. P. Dos Santos, E. Jahier, S. Schwarz, and C. Cohen-Tannoudji, Acta Phys. Pol. B **33**, 2213 (2002).
[7] A. S. Dickinson, F. X. Gadéa, and T. Leininger, J. Phys. B **37**, 587 (2004).
[8] P. Leo, V. Venturi, I. Whittingham, and J. Babb, Phys. Rev. A **64**, 042710 (2001).
[9] P. J. J. Tol, W. Hogervorst, and W. Vassen, Phys. Rev. A **70**, 013404 (2004).
[10] S. Seidelin, O. Sirjean, J. Viana Gomes, D. Boiron, C. I. Westbrook, and A. Aspect, J. Opt. B **5**, 112 (2003).
[11] O. Sirjean, S. Seidelin, J. Viana Gomes, D. Boiron, C. I. Westbrook, A. Aspect, and G. V. Shlyapnikov, Phys. Rev. Lett. **89**, 220406 (2002).
[12] S. Giorgini, L. P. Pitaevskii, and S. Stringari, Phys. Rev. A **54**, R4633 (1996).
[13] P. Arnold and B. Tomàšik, Phys. Rev. A **64**, 053609 (2001).
[14] O. Sirjean, Ph.D. thesis, Université Paris XI, 2003, available at http://tel.ccsd.cnrs.fr/documents/archives0/00/00/30/88
[15] P. Pedri, D. Guéry-Odelin, and S. Stringari, Phys. Rev. A **68**, 043608 (2003).
[16] G. M. Kavoulakis, C. J. Pethick, and H. Smith, Phys. Rev. A **61**, 053603 (2000).
[17] J. Stärck and W. Meyer, Chem. Phys. Lett. **225**, 229 (1994).
[18] G. V. Shlyapnikov, J. T. M. Walraven, U. M. Rahmanov, and M. W. Reynolds, Phys. Rev. Lett. **73**, 3247 (1994); P. O. Fedichev, M. W. Reynolds, and G. V. Shlyapnikov, Phys. Rev. Lett. **77**, 2921 (1996); P. F. Bedaque, E. Braaten, and H. W. Hammer, Phys. Rev. Lett. **85**, 908 (2000).
[19] A measurement using photoassociation spectroscopy is in progress at the Ecole Normale Supérieure in Paris [M. Leduc (private communication)].
[20] M. Holzmann, J. N. Fuchs, G. Baym, J. P. Blaizot, and F. Laloë, C. R. Phys. **5**, 21 (2004); N. Prokof'ev, O. Ruebenacker, and B. Svistunov, Phys. Rev. A **69**, 053625 (2004), and references therein.

INSTITUTE OF PHYSICS PUBLISHING JOURNAL OF OPTICS B: QUANTUM AND SEMICLASSICAL OPTICS
J. Opt. B: Quantum Semiclass. Opt. **5** (2003) S112–S118 PII: S1464-4266(03)55547-1

Using ion production to monitor the birth and death of a metastable helium Bose–Einstein condensate

S Seidelin[1], O Sirjean, J Viana Gomes[2], D Boiron, C I Westbrook and A Aspect

Laboratoire Charles Fabry de l'Institut d'Optique, UMR 8501 du CNRS,
F-91403 Orsay Cedex, France

E-mail: signe.seidelin@iota.u-psud.fr

Received 29 October 2002
Published 2 April 2003
Online at stacks.iop.org/JOptB/5/S112

Abstract
We discuss observations of the ion flux from a cloud of trapped 2 $^3S_1$ metastable helium atoms. Both Bose–Einstein condensates (BEC) and thermal clouds were investigated. The ion flux is compared with time-of-flight observations of the expanded cloud. We show data concerning BEC formation and decay, as well as measurements of two- and three-body ionization rate constants. We also discuss possible improvements and extensions of our results.

Keywords: Cold atoms, Bose–Einstein condensate, metastable helium, condensate formation, Penning collisions

1. Introduction

Metastable helium (He*) has recently joined the list of atomic species for which Bose–Einstein condensates (BEC) have been realized [1, 2]. Its major feature is the 20 eV internal energy of the metastable state. Although this metastability leads to additional possible loss channels, it has been shown that these are not a serious problem. Indeed, ionizing collisions are a benefit because their low rate is nevertheless easily detectable. Ion detection is thus a new, 'non-destructive' and real-time observation tool for studies of the phenomenon of BEC formation kinetics [3–7]. In this paper we will describe our progress toward rendering the ion signal quantitative.

Several loss mechanisms are specific to the metastable state. First, collisions with the background gas lead to Penning ionization of the background gas:

$$X + He^* \rightarrow X^+ + He + e^- .$$

The positive ion X^+ thus produced can be easily detected and if this is the dominant ion production mechanism, as it is for a dilute sample (for a density $n \lesssim 10^{10}$ cm^{-3}), the corresponding flux is proportional to the number of trapped He* atoms. So for example we can easily measure the lifetime of a dilute, trapped sample. This linearity no longer holds when the density of the trapped cloud becomes high. Collisions between atoms in the cloud must be taken into account. The relevant ionization mechanisms involve both two-body processes:

$$He^* + He^* \rightarrow \begin{cases} He^+ + He(1S) + e^- \\ He_2^+ + e^- \end{cases} \tag{1}$$

and a three-body process:

$$\begin{aligned} He^* + He^* + He^* \quad &\rightarrow \quad He_2^* \quad + He^*(\sim 1\ \mathrm{mK}) \\ &\hookrightarrow \quad He^+ + He(1S) + e^- . \end{aligned} \tag{2}$$

When these processes are present, the ion flux is related to the spatial integral of n^2 and n^3. At BEC densities, the two- and three-body processes dominate the background gas ionization, and so detecting the ion flux in this case amounts to monitoring the atomic density.

In this paper, after a brief description of our experimental set-up, we present observations, via the ion flux, of the formation and the decay of a He* BEC. The observations are mainly qualitative, but we discuss some of the requirements for making them quantitative. We then discuss our measurements of the two- and three-body ionization rate constants both in a BEC [8] and in a thermal cloud. We discuss some of the systematic errors in these measurements and conclude with some ideas for avoiding these errors.

---

[1] Author to whom any correspondence should be addressed.

[2] Permanent address: Departamento de Fisica, Universidade do Minho, Campus de Gualtar, 4710-057 Braga, Portugal.

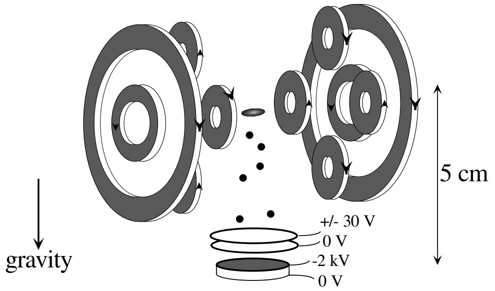

Figure 1. Experimental set-up. The cold atoms are trapped in a cloverleaf type magnetic trap. A special feature of our set-up is the MCP placed below the trapping region. Two grids above the MCP allow us either to repel positive ions and detect only the He* atoms suddenly released from the trap (TOF measurements), or to attract and detect the positive ions produced in the trapped cloud (ion rate measurements).

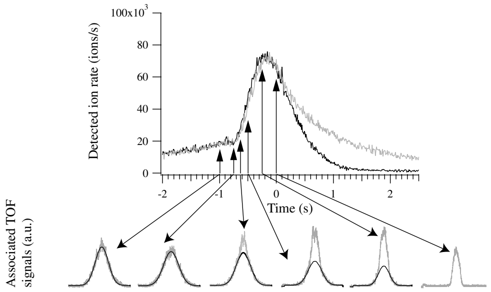

Figure 2. Single-shot measurements of the ion rate versus time and the corresponding TOF signals. Forced evaporative cooling takes place until $t = 0$ (only the last 2 s of the rf ramp are shown: from 1400 to 1000 kHz). The upper, lighter, ion curve corresponds to the case where we keep an rf shield on during the decay, while the lower, darker, decay curve is recorded without. The arrows indicate the time the trap was switched off to record the TOF. The dark curves superimposed on the TOF signals are Gaussian fits to the wings of the TOF.

2. Set-up and experimental procedure

Our set-up has been described previously [1, 8, 9]. Briefly, we trap up to 2×10^8 atoms at 1 mK in a Ioffe–Pritchard trap with a lifetime (τ) of 90 s. We use a 'cloverleaf' configuration (figure 1) [10] with a bias field $B_0 = 300$ mG. The axial and radial oscillation frequencies in the harmonic trapping potential are typically $\nu_\parallel = 47 \pm 3$ Hz and $\nu_\perp = 1200 \pm 50$ Hz respectively ($\varpi/2\pi = (\nu_\parallel \nu_\perp^2)^{1/3} = 408$ Hz). In a typical run, forced evaporative cooling takes place for 40 s and is divided into four linear ramps. The last ramp lasts for 5 s and the frequency decreases from 2000 kHz to a value between 1500 and 1000 kHz, depending on the condensed fraction wanted. A frequency of 1000 kHz (which is about 50 kHz above the minimum of the trapping potential) corresponds to the formation of a pure condensate.

A special feature of our set-up is the detection scheme, based on a two-stage, single-anode microchannel plate detector (MCP) placed 5 cm below the trapping region (figure 1). Two grids above the MCP allow us either to repel positive ions and detect only the He* atoms, or to attract and detect positive ions produced in the trapped cloud. To detect the ion flux, the MCP is used in counting mode [8]: the anode pulses from each ion are amplified, and processed by a counter which records the time delay between successive events. We can also use the MCP to record a time-of-flight (TOF) signal of the atoms released from the trap. Because the width of the TOF distribution is small (about 5 ms for a BEC) compared with the mean arrival time (100 ms), all of the atoms hit the detector with nearly the same final velocity of 1 m s^{-1}. The TOF spectra are then proportional to the spatial distribution along the vertical direction, integrated over the two horizontal directions. To record the TOF we use the MCP in analogue mode to avoid saturation due to the very high instantaneous flux [8].

3. Monitoring the evolution of a He* cloud

To monitor the evolution of an atomic cloud, one usually releases the cloud and measures the TOF signal. Such a technique is destructive, and one must repeat the cooling sequence for each measurement. The TOF signals are thus subject to fluctuations in the initial number of atoms. In our case, we have a supplementary signal: the ion rate. We can thus minimize these fluctuations, by selecting runs having identical ion rates from the time between the beginning of the last rf ramp until release.

Another type of observation is possible, however. We can use the evolution of the *value* of the ion rate, which is obtained in a single run, independent of any initial fluctuations. When the density is close to the density for BEC formation (i.e. $n \gtrsim 10^{12}$ cm^{-3}), two- and three-body collisions within the cloud dominate the ion production. Thus the ion rate is related to the density of the cloud via the two- and three-body rate constants. Under some conditions (see appendix A) a record of the ion rate followed by a TOF measurement at the end of the formation of the BEC allows one to monitor the evolution of all the parameters of the cloud. In such an observation, knowledge of the two- and three-body rate constants is essential. This is the aim of the experiments described in section 4.

3.1. Observation of condensate formation during the evaporation ramp

Before trying to do a quantitative experiment on BEC formation from of a non-equilibrium uncondensed cloud [3, 4], we can explore qualitatively what happens during our standard evaporation ramp. We show in figure 2 the evolution of the ion rate from 2 s before the end of the rf ramp to 2.5 s after it. In addition we show the TOF signals corresponding to various times before the end of the ramp, selected using their initial ion rate. Between times $t = -2$ and 0 s, the rf was ramped down linearly from 1.4 to 1 MHz. At $t = 0$ a pure condensate is formed. The comparison of the TOF and ion data first shows that the appearance of a narrow structure in the TOF spectrum corresponds, as closely as we can observe it, to an abrupt change in the slope of the ion signal. Thus, not only is the ion signal a reliable indicator of the presence of a BEC, but also a precise measure of the time of its appearance.

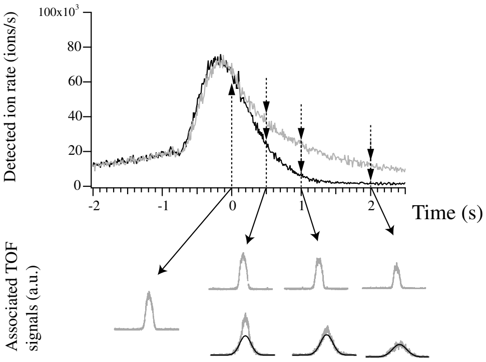

Figure 3. Same as in figure 2 except that we examine the decay of the ion signal after $t = 0$. The upper TOF curves correspond to the upper (lighter) ion decay curve (rf shield present). The lower TOF curves correspond to the lower (darker) ion curve (without rf shield). This shows that the rf shield is maintaining a quasi-pure BEC during the decay, and that in the absence of an rf shield the condensate rapidly heats up, causing the ion rate to drop even faster.

One's first reaction in looking at the ion rate signal is to assume that the higher the ion signal, the larger the BEC and the smaller the thermal cloud. Figure 2 shows, however, that this is not quite the case: the maximum in the ion signal arrives before the achievement of a pure BEC. In fact, computing the value of the ion signal is rather complex. First, as was discussed in [11, 12], as well as below, the indistinguishability of the atoms in the BEC renders the effective two- and three-body collision rate constants smaller than in the thermal cloud by factors of $1/2!$ and $1/3!$ respectively. Collisions between condensed and non-condensed atoms must also be taken into account [11] and the degree of overlap between the two clouds must be calculated. Thus it might be conceivable that the ion rate goes down when a BEC is formed. We show, however, in appendix A that for a fixed total number of atoms, the ion rate increases monotonically as a BEC becomes more and more pure. The observation in figure 2 is explained by the fact that, up until $t = 0$ in figure 2, the atoms are being evaporatively cooled as well as undergoing ionizing collisions and thus the total number of atoms must be decreasing. An explicit calculation including the atom loss is given in appendix A and agrees qualitatively with our observations.

3.2. Observing the decay of the condensate

Figure 3 shows a series of TOF spectra taken after the end of the rf ramp. Two situations are shown. In one case (upper, lighter ion curve) the rf knife was held on at the frequency corresponding to the end of the ramp. In the other case (lower, darker ion curve) the rf power was turned off completely at the end of the ramp. The data show that the condensate remains pure with the rf knife kept on. In the absence of the rf knife, the ion rate decays much faster and one sees that the sample rapidly acquires a thermal component. Since the total number of trapped atoms in the presence of a knife must be smaller than or equal to that in the absence of rf knife, we conclude that the rapid decline in ion rate is due to a loss of sample density and not of the total number of atoms. This conclusion is confirmed by a fit to the thermal wings, which reveals a heating as shown in figure 4.

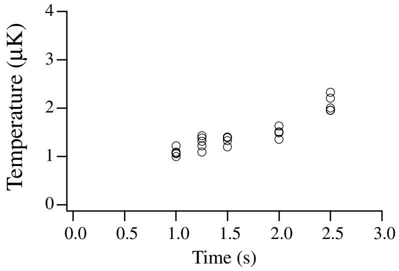

Figure 4. Heating of the condensate in the absence of an rf shield. The temperature increases from 1.1 to 2.2 μK in 1.5 s. The time $t = 0$ is the same as in figures 2 and 3. For each different time, four different TOFs have been acquired and fitted.

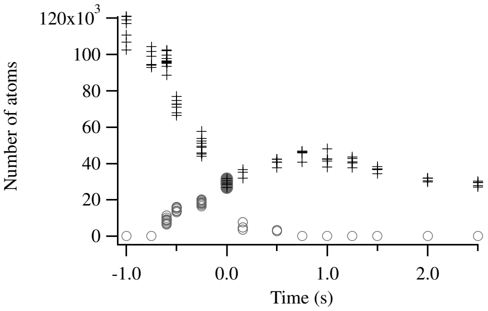

Figure 5. The measured number of atoms as a function of time. Crosses represent the total atom number, circles represent the number of atoms in the condensed part. The data come from the fits of the TOFs presented in figures 2 and 3 and correspond to the case where the rf knife is absent. The time scale indicated is the same as in figures 2 and 3. The increase in the total number after $t = 0$ is spurious (see text).

3.3. Measuring the total number of atoms

An attempt to measure the total number of atoms as a function of time is shown in figure 5. Both the total number and the condensed number as derived from fits to the TOF signals of figures 2 and 3 are plotted. Surprisingly the total number of atoms appears to increase between $t = 0$ and 1 s. There must be a systematic error, which we can account for by recalling that in our apparatus we only detect atoms which make non-adiabatic transitions to the (field insensitive) $m = 0$ state during the turn-off of the magnetic trap [1]. The fraction we observe is of the order of 10%. It is quite possible that this non-adiabatic transition does not occur with equal probability at every point in the trap. Thus clouds with different spatial distributions may be converted to the $m = 0$ state with different efficiencies. This could explain why atoms in the thermal cloud are observed with a higher efficiency than condensed atoms, as indicated in figure 5.

We conclude that our measurements of the absolute number of atoms contain uncontrolled systematic errors of the order of a factor of two. So, even if we know the ionization rate constants, we cannot use the ion rate to study condensate growth kinetics because we need the absolute value of the initial number of atoms. It would also be useful to measure the variation in the number of atoms during formation. Such a study will have to wait for a more reliable method of releasing the atoms from the trap (see conclusion). However, the measurement of the ionization rate constants is a first step. For a BEC, we can circumvent the systematic error on the detection efficiency of the atoms to make a measurement of the ionization rate constants. This has been described in [8] and will be summarized in the following section. Afterwards, we will investigate the effect of this systematic error on the measurement for a thermal cloud.

4. Rate constants of ionizing collisions

The usual method of measuring the inelastic rate constants relies on fits to a non-exponential decay of the number of atoms. This method has some practical problems if the sample heats during the measurement: the density changes which complicates the fitting procedure. A way to avoid this heating is to apply an rf shield, but this causes atom losses, which are not due to collisions. What is even more inconvenient in our case is that what is measured in this kind of experiment is a decreasing atom number due to losses, which can be due to ionizing as well as non-ionizing collisions. We want to relate the ion rate to the density of the cloud, so what we need is the rate constants for *ionizing* two- and three-body collisions. We therefore use another method which consists of directly observing the products of the collisions, namely the number of ions, as a function of the density of the cloud.

As we have seen in section 3, there is a systematic error on the measurement of the number of atoms and thus of the density of the cloud. But we will see that we can circumvent it in the case of the BEC. Let us then assume first that we are able to measure the number of atoms accurately.

We use the MCP to detect both the ions and the TOF signal. In a single run we record the ion rate during the last seconds of the ramp until we switch off the magnetic trap and record the TOF signal (to obtain the atom number N and the density). The very last value of the ion rate recorded corresponds to ions produced by the cloud observed with the TOF signal. We repeat this sequence many times with different numbers of atoms in the cloud. The way to vary this number is to keep the atoms in the trap with an rf shield kept on. In this way we reduce the atom number and keep the temperature of the cloud constant. As explained in appendix A, the relation between ion rate and density is quite complex in the case of the presence of collisions between atoms in the condensed part and atoms in the thermal part. We therefore only examine the case of a pure BEC *or* a pure thermal cloud. In that case we can write the ion rate per atom Γ as follows:

$$\frac{\text{ion rate}}{N} = \Gamma = \frac{1}{\tau'} + \frac{1}{2}\kappa_2\beta\langle n\rangle + \frac{1}{3}\kappa_3 L\langle n^2\rangle \qquad (3)$$

where $\langle n\rangle = \frac{1}{N}\int n^2\,\mathrm{d}\boldsymbol{r}$ and $\langle n^2\rangle = \frac{1}{N}\int n^3\,\mathrm{d}\boldsymbol{r}$, n being the local density. We have also introduced the two- and three-body ionizing collision rate constants, β and L respectively, defined according to their effect on the density loss in a thermal gas[3]: $(\frac{\mathrm{d}n}{\mathrm{d}t})_{ionization} = -\frac{n}{\tau'} - \beta n^2 - Ln^3$. The effective lifetime $\tau' \geqslant \tau$ is due to *ionizing* collisions with the background gas. The numerical factors come from the fact that although two or three atoms are lost in each type of collision, only one ion is produced. The factors κ_2 and κ_3 take into account the fact that the two-and three-particle local correlation functions are different depending on whether it is a BEC or a thermal cloud. For the thermal cloud $\kappa_2 = \kappa_3 = 1$, while for a dilute BEC, one has $\kappa_2 = 1/2!$ and $\kappa_3 = 1/3!$ [11, 12]. When the sample is very dense, quantum depletion must be taken into account, which modifies these factors [11]. A measurement of β and L would allow us to test experimentally the theoretical values of κ_2 and κ_3 [8].

4.1. Rate constants for a BEC

To determine the ionizing collision rate constants β and L, we need an absolute calibration of the number of atoms in the condensate, N_0, and the peak density, n_0, in order to calculate $\langle n\rangle$ and $\langle n^2\rangle$. As discussed above, we do not have a good calibration of these quantities. In the case of a BEC, however, the measurement of the chemical potential μ obtained by a fit of the TOF signal gives an accurate value for the product $n_0 a = \mu \mathrm{m}/4\pi\hbar^2$, a being the scattering length. With the value of $\overline{\omega}$ we also obtain the product $N_0 a = (1/15)(\hbar/m\overline{\omega})^{1/2}\,(2\mu/\hbar\overline{\omega})^{5/2}$. Experimentally we confirm that $\mu \propto N_d^{2/5}$ where N_d is the number of detected atoms [8]. This is a good indication that our detector is linear and that the detection efficiency for a BEC is indeed independent of μ. Assuming a value of the scattering length ($a = 20$ nm), we therefore have an accurate measurement of n_0 and N_0. We have measured the rate constants β and L for a condensate [8]. We obtain by a fit to equation (3) (having corrected for the effect of quantum depletion and the fact that the BEC also contains a small thermal fraction) $\beta = 2.9(\pm 2.0) \times 10^{-14}$ cm^3 s^{-1} and $L = 1.2(\pm 0.7) \times 10^{-26}$ cm^6 s^{-1}. These values agree with the theoretical estimates [13, 14]. The scattering length is not well known [1, 2], so we have also given β and L for different values of a [8].

4.2. Rate constants for a thermal cloud

To determine the rate constants for a thermal cloud we need, as before, to determine the atom number and density. We cannot use the same trick as in section 4.1 to avoid systematic errors in the detection efficiency. If we want to use the above experimental method for a thermal cloud we must rely on a fit of the TOF to find the atom number and the temperature T. In appendix B, we propose a method to determine the rate constants which is independent of an absolute detection efficiency, but at this stage we will concentrate on the same technique as used for a BEC.

As we have shown above, the detection efficiency is expected to be different for a thermal cloud and we can investigate the effect of this systematic error on these measurements. We repeat the above described experiment, this time with a pure thermal cloud. To begin with, we assume that the detection efficiency is the same for a BEC and a thermal cloud. We

---

[3] Collision rate constants are sometimes defined directly for a BEC ($\beta' = \beta/2$ and $L' = L/6$).

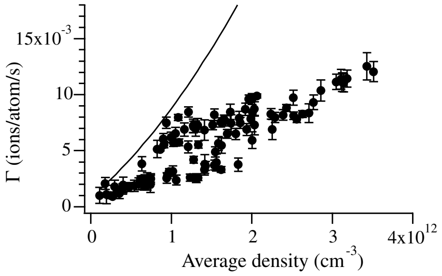

Figure 6. Ion rate per trapped atom (Γ) in a thermal cloud versus average density. The full curve corresponds to the value of β and L deduced from the condensate measurements.

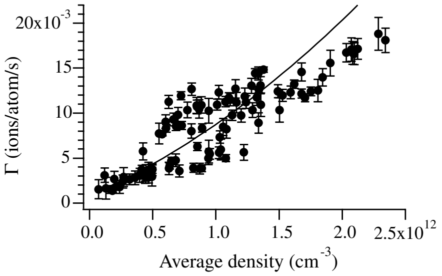

Figure 7. Same as figure 6 but assuming a detection efficiency of the thermal cloud a factor of 1.5 higher relative to the BEC. The data have simply been rescaled along both axes; the full curve is the same as in figure 6.

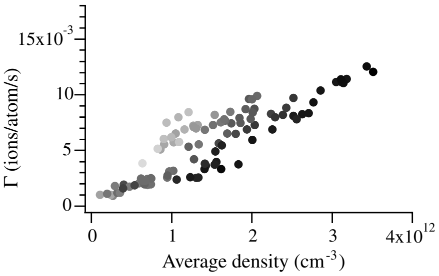

Figure 8. Same data as in figure 6 but with the different temperatures indicated. The lighter circles correspond to the point with higher temperatures (the maximum temperature is 5.5 μK), the darker circles with lower temperatures (minimum temperature 1.8 μK).

plot the ion rate per atom as a function of $\langle n\rangle$ in figure 6. We can extrapolate the data to obtain the vertical intercept, which corresponds to $1/\tau'$. For densities corresponding to the moment of formation of BEC, the corresponding ion rate N/τ' is negligible compared with the total ionization rate, meaning that we are dominated by two- and three-body processes (see figures 2 and 5). To compare with the results obtained for the BEC, we have also plotted the curve we would expect using the above values of β and L. It is clear that the data do not agree with this curve. Moreover, no possible pair of β and L taken within their error bars (see [8]) can transform the curve so that it agrees with the data. Nor can assuming a different scattering length. What *can* make the curve agree with the data is assuming a different detection efficiency for atoms in the thermal cloud. If we assume for example that the detection efficiency is a factor of 1.5 higher for a thermal cloud relative to a BEC (which is consistent with figure 5), the curve agrees better with the data as shown in figure 7.

The dispersion of the data points is quite large. This dispersion can be understood by examining figure 8 in which we have plotted the same data as in figure 6, but now indicating the temperature corresponding to each different point on the graph. There is a clear systematic variation with temperature. One possible explanation is that the detection efficiency is temperature dependent. This agrees with the above idea that the efficiency depends on the spatial extent of the cloud which is indeed related to the temperature. We do not know the form of the detection efficiency as a function of temperature, but comparing these data (indicating that cold atoms are better detected) with the fact that a thermal cloud is better detected than a BEC, leads us to conclude that there exists a certain temperature giving a maximal detection efficiency. Therefore the correction to the detection efficiency for thermal atoms is not just a simple factor, but rather a function of temperature. Without knowing this correction, we cannot use this method to determine the collision constants for a thermal cloud. Still, these results are a consistency check on the rate constants measured using a BEC.

5. Conclusion

We have seen that the benefits of ion detection are twofold. First, the ion rate can be used to select BECs with very similar parameters out of a sample with large fluctuations. Second, the ion rate itself can give information on the condensate on a single-shot basis. Quantitatively, we still have some difficulties interpreting the data due to systematic errors in the detection calibration.

One way to overcome this problem is to release the atoms from the trap by the mean of Raman transitions. It should be possible to transfer close to 100% of the atoms into the $m = 0$ state. This will eliminate the temperature dependence of the detection efficiency and allow us to obtain more precise measurements of β and L, both for the BEC by improving the value of the scattering length and for the thermal cloud by making the detection efficiency temperature independent.

Acknowledgments

We thank A Villing and F Moron for their assistance with the electronics. This work is supported by the European Union under grants IST-1999-11055 and HPRN-CT-2000-00125, and by the DGA grant 00.34.025. JVG thanks Fundação para a Ciência e a Tecnologia and SS acknowledges Danish Research Training Council and Danish Research Agency for financial support.

Appendix A. Predictions of the ion rate during the formation of the BEC

The two- and three-body ion rates (I_{2b} and I_{3b} respectively) in a sample containing both a BEC and a thermal cloud are given by [11]:

$$I_{2b} = \frac{1}{2}\frac{\beta}{2!}\int \mathrm{d}\boldsymbol{r}\,[n_0^2(\boldsymbol{r}) + 4n_0(\boldsymbol{r})n_{th}(\boldsymbol{r}) + 2n_{th}^2(\boldsymbol{r})] \tag{A.1}$$

$$I_{3b} = \frac{1}{3}\frac{L}{3!}\int \mathrm{d}\boldsymbol{r}\,[n_0^3(\boldsymbol{r}) + 9n_0^2(\boldsymbol{r})n_{th}(\boldsymbol{r}) + 18n_0(\boldsymbol{r})n_{th}^2(\boldsymbol{r}) + 6n_{th}^3(\boldsymbol{r})] \tag{A.2}$$

where $n_0(\boldsymbol{r})$ is the local density of the BEC and $n_{th}(\boldsymbol{r})$ is the local density of the thermal cloud. Here we have taken into account the symmetrization factors, but neglected quantum depletion.

Four parameters are needed to determine the densities of the two clouds: N_0, μ, N_{th} and T_{th}. In the Thomas–Fermi approximation, however, the BEC density depends only on μ:

$$n_0(\boldsymbol{r}) = \max\left[0, \frac{\mu - U(\boldsymbol{r})}{g}\right] \tag{A.3}$$

with $U(\boldsymbol{r})$ the harmonic trapping potential and $g = 4\pi\hbar^2 a/m$ the interaction strength. The density of the thermal cloud depends on two parameters. But, if thermodynamic equilibrium is reached, taking into account the interactions between the BEC and the thermal cloud (and neglecting the interaction energy of the thermal cloud), we can write:

$$n_{th}(\boldsymbol{r}) = \frac{1}{\lambda_{dB}^3} g_{3/2}\left(\exp\left(-\frac{1}{k_B T}(U(\boldsymbol{r}) + 2gn_0(\boldsymbol{r}) - \mu)\right)\right) \tag{A.4}$$

where λ_{dB} is the thermal de Broglie wavelength and $g_{3/2}(x) = \sum_{n=1}^{+\infty} \frac{x^n}{n^{3/2}}$. In that case, given μ, n_{th} only depends on one additional parameter.

A.1. Comparison between the ion rates created by a thermal cloud at $T = T_C$ and a pure BEC

Before trying to calculate the ion rate for any T, which requires numerical calculation, let us first examine the ion rate created by a thermal cloud at $T = T_C$ with a number of atoms N and that created by a pure BEC ($T = 0$) with a number of atoms ηN ($\eta < 1$).

In the case of two-body collisions, the ratio R_{2b} of the ion rates created by a pure BEC (I^{BEC}) and by a thermal cloud (I^{th}) is related to the ratio of the peak densities. For three-body collisions the ratio (R_{3b}) is related to the square of that ratio. Using the above equations we find:

$$\left(\frac{n_0}{n_{th}}\right) = C_0 \eta^{2/5} N^{-1/10} \left(\frac{\overline{\sigma}}{a}\right)^{3/5} \tag{A.5}$$

$$R_{2b} = \frac{I_{2b}^{BEC}}{I_{2b}^{th}} = C_2 \eta^{7/5} N^{-1/10} \left(\frac{\overline{\sigma}}{a}\right)^{3/5} \tag{A.6}$$

$$R_{3b} = \frac{I_{3b}^{BEC}}{I_{3b}^{th}} = C_3 \eta^{9/5} N^{-2/10} \left(\frac{\overline{\sigma}}{a}\right)^{6/5} \tag{A.7}$$

where $\overline{\sigma} = \sqrt{\frac{\hbar}{m\overline{\omega}}}$. The numerical factors $C_0 \simeq 0.78$, $C_2 \simeq 1.05$ and $C_3 \simeq 0.49$ are independent of the atom considered and only assume that the cloud is trapped in a 3D harmonic trap. The maximum ratios are reached in the case of no loss ($\eta = 1$). Using the typical values of our experiment ($a \simeq 20$ nm, $N \simeq 4 \times 10^5$ and $\overline{\omega} \simeq 2\pi \times 408$ Hz), we find $(\frac{n_0}{n_{th}})_{max} \simeq 4$, $(R_{2b})_{max} \simeq 5$ and $(R_{3b})_{max} \simeq 12$.

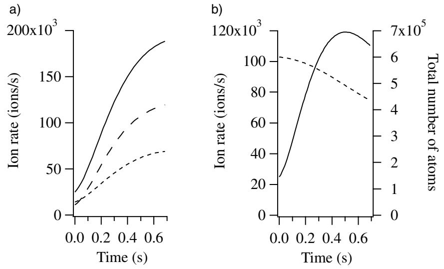

Figure A.1. Evolution of the ion rate with time. In (a) the total number of atoms is constant. We show the different contributions to the total ion rate (continuous curve) of the ion rate created by two-body collisions (short dashed curve) and three-body collisions (long dashed curve). In (b) the total number of atoms (dashed curve) decreases due to ionizing collisions. Here the ion rate exhibits a maximum before the formation of a pure BEC. For both graphs, the initial number of atoms is 6×10^5 and a linear evolution of the temperature between T_C and 0 is imposed. The rates have been calculated with the values of rate constants measured in [8].

If the total number of atoms decreases during the formation of the BEC, these ratios rapidly fall. For instance, if the number of atoms decreases by a factor of 3.5 during the last 750 ms of evaporation as shown in figure 5, we would not have seen an increase of ionization rate but roughly the same ion rate at $t = -750$ and 0 ms! This is an additional evidence of the difference of neutral atom detection efficiency for a thermal cloud and BEC (i.e. the total number of atoms decreased by less than 3.5).

A.2. Evolution of the ion rate between $T = T_C$ and $T = 0$

Using equations (A.1) and (A.2), we have numerically calculated the ion rates for all temperatures. If the cloud is at thermodynamic equilibrium all the parameters of the cloud are deduced from two parameters, for example the total number of atoms and the temperature. To simulate a time evolution of the ion rate we thus need a model for the variation of these parameters. In this appendix we will assume a linear evolution of the temperature between $T = T_C$ and 0 in 0.7 s. This is of course a simplification, but given the linearity of the evaporative cooling ramp, it is quite a good approximation.

In figure A.1(a) we show the evolution of the ion rates assuming a constant total number of atoms. The ion rate increases monotonically. We also see that the number of ions produced and thus also the number of lost atoms is not necessarily negligible compared with the total.

We can attempt to take into account these losses in our model. In the experiments described in the text, the losses are not only due to the ionizing collisions but also to the rf knife. In addition, losses not only lead to a decrease in the total number of atoms but also to a change in the temperature because these collisions change the condensed fraction. Thus, modelling the ion rate can be quite complicated. Here we wish simply to illustrate the effect of loss, so we assume that losses are only due to ionizing collisions, and we will neglect losses due to the rf knife. Figure A.1(b) shows the results. The atom number decreases by only 30% and the ion rate reaches a local maximum before the formation of the pure BEC, as in our experiment. Extensions of our model to include losses due to the rf knife would allow one to monitor all the parameters of the cloud using the ion signal.

Appendix B. Proposed measurement of rate constants independent of absolute neutral atom detection efficiency

We will assume in this section that the absolute ion detection efficiency is known, and that two- and three-body losses are ionizing collisions [13]. The idea behind this method is that two TOF signals separated by a given time can measure the relative atom loss during this time, while the ion rate can measure the absolute atom loss. These data allow one to extract the rate constants without relying on an absolute calibration of the neutral atom detection efficiency. The method works if the neutral detection efficiency is unknown but independent of temperature. Otherwise, we must also assume that the cloud does not heat during the measurement or that we know the variation of detection efficiency with temperature.

To simplify the discussion we will neglect three-body reactions and assume that the sample does not heat during the measurement. This will allow us to derive analytical expressions, but the results are easily generalized to include heating as well as three-body reactions. We can then write the ion rate $I(t)$ as:

$$I(t) = \frac{\epsilon N(t)}{\tau'} + \frac{\beta\epsilon}{2V_{eff}} N(t)^2 \tag{B.1}$$

with τ' the lifetime due to ionizing collisions, $N(t)$ the absolute atom number, V_{eff} defined by $\langle n \rangle = N/V_{eff}$ and ϵ the ion detection efficiency. We write $N_d(t) = \alpha N(t)$ where $N_d(t)$ is the number of atoms detected and α is the neutral atom detection efficiency. Then

$$I(t) = \frac{\epsilon N_d(t)}{\alpha\tau'} + \frac{\epsilon\beta}{\alpha^2 2V_{eff}} N_d(t)^2. \tag{B.2}$$

We can also write an equation for the atom number

$$\frac{\mathrm{d}N(t)}{\mathrm{d}t} = -\frac{N(t)}{\tau} - \frac{\beta}{V_{eff}} N(t)^2 \tag{B.3}$$

with τ the total lifetime of the sample that we can measure independently at lowest density. The solution is:

$$\frac{N(t)}{N(t_0)} = \frac{1}{\left(1 + \frac{\beta}{V_{eff}} N(t_0)\tau\right) \mathrm{e}^{(t-t_0)/\tau} - \frac{\beta}{V_{eff}} N(t_0)\tau}. \tag{B.4}$$

Substituting again $N_d(t) = \alpha N(t)$ we have:

$$\frac{N_d(t)}{N_d(t_0)} = \frac{1}{\left(1 + \frac{\beta}{\alpha V_{eff}} N_d(t_0)\tau\right) \mathrm{e}^{(t-t_0)/\tau} - \frac{\beta}{\alpha V_{eff}} N_d(t_0)\tau}. \tag{B.5}$$

Thus we can measure an initial ion rate and the corresponding detected atom number $N_d(t_0)$ by a TOF signal, let the system evolve for a certain time and then again measure the ion rate and the atom number $N_d(t)$. With the evolution of the ion rate, we can deduce $\epsilon/\alpha\tau'$ and $\epsilon\beta/\alpha^2 V_{eff}$ from equation (B.1), and from the evolution of the atom number we can deduce $\beta/\alpha V_{eff}$ using equation (B.5). With the value of V_{eff} and ϵ, we can obtain the value β. We can also obtain the detection efficiency α.

If we allow for three-body reactions, the method can still be used but (B.4) is no longer analytical and must be integrated numerically. If the sample heats during the measurement, we only have to recalculate the volume V_{eff} for each TOF measurement.

The reason why we have not yet been able to apply this method is, as indicated above, that the sample is heating so that the detection efficiency changes during the measurement. As we have not been able to measure the temperature dependence of $\alpha(T)$ the above equations cannot be solved. We hope to render the detection efficiency temperature independent in the near future by using Raman transitions as mentioned in the conclusion.

References

[1] Robert A, Sirjean O, Browaeys A, Poupard J, Nowak S, Boiron D, Westbrook C I and Aspect A 2001 *Science* **292** 461

[2] Pereira D S F, Léonard J, Junmin W, Barrelet C J, Perales F, Rasel E, Unnikrishnan C S, Leduc M and Cohen-Tannoudji C 2001 *Phys. Rev. Lett.* **86** 3459

[3] Miesner H J, Stamper-Kurn D M, Andrews M R, Durfee D S, Inouye S and Ketterle W 1998 *Science* **270** 1005

[4] Köhl M, Hänsch T W and Esslinger T 2002 *Phys. Rev. Lett.* **88** 080402

[5] Kagan Yu M, Svistunov B V and Shlyapnikov G V 1992 *Sov. Phys.–JETP* **75** 387

[6] Gardiner C W, Zoller P, Ballagh R J and Davis M J 1997 *Phys. Rev. Lett.* **79** 1793

[7] Bijlsma M J, Zaremba E and Stoof H T C 2000 *Phys. Rev.* A **62** 063609-1

[8] Sirjean O, Seidelin S, Viana Gomes J, Boiron D, Westbrook C I, Aspect A and Shlyapnikov G V 2002 *Phys. Rev. Lett.* **89** 220406

[9] Browaeys A 2000 Thèse de l'Université Paris-Sud available at http://ccsd.cnrs.fr/

[10] Mewes M O, Andrews M R, van Druten N J, Kurn D M, Durfee D S and Ketterle W 1996 *Phys. Rev. Lett.* **77** 416

[11] Kagan Yu M, Svistunov B V and Shlyapnikov G V 1985 *JETP Lett.* **42** 209

[12] Burt E A, Ghrist R W, Myatt C J, Holland M J, Cornell E A and Wieman C E 1997 *Phys. Rev. Lett.* **79** 337

[13] Shlyapnikov G V, Walraven J T M, Rahmanov U M and Reynolds M W 1994 *Phys. Rev. Lett.* **73** 3247
Fedichev P O, Reynolds M W, Rahmanov U M and Shlyapnikov G V 1996 *Phys. Rev.* A **53** 1447

[14] Venturi V, Whittingham I B, Leo P J and Peach G 1999 *Phys. Rev.* A **60** 4635
Venturi V and Whittingham I B 2000 *Phys. Rev.* A **61** 060703(R)

VOLUME 89, NUMBER 22 PHYSICAL REVIEW LETTERS 25 NOVEMBER 2002

Ionization Rates in a Bose-Einstein Condensate of Metastable Helium

O. Sirjean, S. Seidelin, J. Viana Gomes,* D. Boiron, C. I. Westbrook, and A. Aspect
Laboratoire Charles Fabry de l'Institut d'Optique, UMR 8501 du CNRS, F-91403 Orsay Cedex, France

G.V. Shlyapnikov
FOM Institute for Atomic and Molecular Physics, Kruislaan 407, 1098 SJ Amsterdam, The Netherlands
and Russian Research Center Kurchatov Institute, Kurchatov Square, 123182 Moscow, Russia

(Received 5 August 2002; published 12 November 2002)

We have studied ionizing collisions in a BEC of metastable He. Measurements of the ion production rate combined with measurements of the density and number of atoms for the same sample allow us to estimate both the two- and three-body contributions to this rate. A comparison with the decay of the atom number indicates that ionizing collisions are largely or wholly responsible for the loss. Quantum depletion makes a substantial correction to the three-body rate constant.

DOI: 10.1103/PhysRevLett.89.220406 PACS numbers: 34.50.–s, 05.30.–d, 67.65.+z, 82.20.Pm

The observation of Bose-Einstein condensation (BEC) of metastable helium (He in the 2^3S_1 state, denoted He*) [1,2] constituted a pleasant surprise for experimentalists although the possibility had been predicted theoretically [3]. Success hinged, among other things, on a strong suppression of Penning ionization in the spin-polarized, magnetically trapped gas. Too high a rate of ionization would have prevented the accumulation of sufficient density to achieve evaporative cooling. The ionization rate is not completely suppressed however, and when the atomic density gets high enough, a magnetically trapped sample of He* does produce a detectable flux of ions. As shown in [1], this signal can even be used as a signature of BEC. The observation of ions from the condensate opens the possibility of monitoring in real time the growth kinetics of a condensate [4]. This is an exciting prospect, but to quantitatively interpret the ion rate, one needs the contributions of two- and three-body collisions.

In this paper we use the unique features of metastable atoms to detect, in a single realization, the ionization rate, the density, and the atom number. This allows us to extract two- and three-body rate constants without relying on fits to nonexponential decay of the atom number, which require good experimental reproducibility [5–7] and are difficult to interpret quantitatively [5]. After estimating the ionization rate constants, a comparison with the decay of the atom number reveals no evidence for collisional avalanche processes. Thus, by contrast with ^{87}Rb [8], He* seems to be a good candidate for studying the "hydrodynamic" regime [9], as well as the effects of quantum depletion, i.e., a departure from the Gross-Pitaevskii wave function in the Bogoliubov theory, due to atomic interactions [10]. Indeed in our analysis of the three-body ionization process, quantum depletion makes a substantial correction [11].

Much theoretical [3,12] and experimental [1,2,13,14] work has already been devoted to estimating inelastic decay rates in He*. The dominant two-body decay mechanisms, called Penning ionization,

$$\mathrm{He}^* + \mathrm{He}^* \rightarrow \begin{cases} \mathrm{He}^+ + \mathrm{He}(1S) + e^- \\ \mathrm{He}_2^+ + e^- \end{cases} \tag{1}$$

are known to be suppressed by at least 3 orders of magnitude in a spin-polarized sample, but the total rate constant has not yet been measured. The three-body reaction,

$$\begin{aligned} \mathrm{He}^* + \mathrm{He}^* + \mathrm{He}^* &\rightarrow \mathrm{He}_2^* + \mathrm{He}^*(\sim 1\ \mathrm{mK}) \\ &\hookrightarrow \mathrm{He}^+ + \mathrm{He}(1S) + e^- \end{aligned} \tag{2}$$

proceeds via three-body recombination followed by autoionization of the excited molecule. Both reactions yield one positive ion which is easily detected. We define collision rate constants according to the density loss in a thermal cloud: $\frac{dn}{dt} = -\frac{n}{\tau} - \beta n^2 - Ln^3$ with n the local density, τ the (background gas limited) lifetime of the sample, and β and L the two-body and three-body ionization rate constants defined for a thermal cloud [15]. The theoretical estimates of the rate constants at 1 μK are $\beta \sim 2 \times 10^{-14}\ \mathrm{cm}^3\,\mathrm{s}^{-1}$ [3,12] and $L \sim 10^{-26}\ \mathrm{cm}^6\,\mathrm{s}^{-1}$ [16], and the experimental upper limits were [1,2] $\beta \leq 8.4 \times 10^{-14}\ \mathrm{cm}^3\,\mathrm{s}^{-1}$ and $L \leq 1.7 \times 10^{-26}\ \mathrm{cm}^6\,\mathrm{s}^{-1}$.

For a pure BEC, in the Thomas-Fermi regime with a number of atoms N_0, and a peak density n_0, one can calculate the expected ionization rate per trapped atom:

$$\Gamma = \frac{\text{ion rate}}{N_0} = \frac{1}{\tau'} + \frac{2}{7}\kappa_2\beta n_0 + \frac{8}{63}\kappa_3 L n_0^2. \tag{3}$$

The numerical factors come from the integration over the parabolic spatial profile and the fact that although two or three atoms are lost in each type of collision, only one ion is produced. The effective lifetime $\tau' \geq \tau$ is due to *ionizing* collisions with the background gas. The factors κ_i take into account the fact that the two- and three-particle local correlation functions are smaller than those of a thermal cloud. For a dilute BEC $\kappa_2 = 1/2!$ and $\kappa_3 = 1/3!$ [7,11]. Because the He* scattering length (a) is so large, quantum depletion ($\sim \sqrt{n_0 a^3}$) leads to significant corrections [11] to the κ's as we discuss below.

Much of our setup has been described previously [1,17,18]. Briefly, we trap up to 2×10^8 atoms at 1 mK in a Ioffe-Pritchard trap with a lifetime (τ) of 90 s. We use a "cloverleaf" configuration [19] with a bias field $B_0 =$ 150 mG. The axial and radial oscillation frequencies in the harmonic trapping potential are $\nu_\parallel = 47 \pm 3$ Hz and $\nu_\perp = 1800 \pm 50$ Hz, respectively $[\overline{\omega}/2\pi = (\nu_\parallel \nu_\perp^2)^{1/3} =$ 534 Hz]. A crucial feature of our setup is the detection scheme, based on a two stage, single anode microchannel plate detector (MCP) placed below the trapping region. Two grids above the MCP allow us either to repel positive ions and detect only the He* atoms, or to attract and detect positive ions produced in the trapped cloud.

To detect the ion flux, the MCP is used in counting mode: the anode pulses from each ion are amplified, discriminated with a 600 ns dead time and processed by a counter which records the time delay between successive events. Typical count rates around BEC transition are between 10^2 and 10^5 s^{-1}. We have checked that the correlation function of the count rate is flat, indicating that there is no double counting nor any significant time correlation in the ion production. The dark count rate is of order 1 s^{-1}. By changing the sign of the grid voltage, we have checked that while counting ions, the neutral He* detection rate is negligible compared to the ion rate (less than 5%) even when the radio frequency (rf) shield is on. The intrinsic ion detection efficiency of the MCP for 2 keV He^+ ions is close to the open area ratio (60%) [20]. To estimate the total ion detection efficiency, we then multiply by the geometric transmission of the two grids $(0.84)^2$. Based on Refs. [20,21], we assume this (0.42) is an upper limit on our detection efficiency.

To find the values of N_0 and n_0 corresponding to the measured ion rate, we use the MCP to observe the time-of-flight (TOF) signal of the He* atoms released from the rapidly switched off trap. The instantaneous count rate can be as high as 10^6 s^{-1}, and the MCP saturates when used in counting mode. To avoid this problem, we lower the MCP gain, and record the TOF signal in analog mode with a time constant of 400 μs. Several tests were performed to verify the linearity of the detector.

In a typical run, evaporative cooling takes place for 40 s, down to an rf-knife frequency about 50 kHz above the minimum of the trapping potential. Near the end of the ramp, the ion rate increases sharply, signaling the appearance of a BEC (Fig. 4 in [1]). After reaching the final value, the rf knife is held on at that frequency. This constitutes an rf shield which eliminates hot atoms and maintains a quasipure BEC for up to 15 s (see Fig. 3). By quasipure we mean that we see no thermal wings in signals such as shown in the inset of Fig. 1. From tests of our fitting procedure, we estimate that the smallest thermal fraction we can distinguish is about 20%, with a temperature on the order of the chemical potential. Runs with visible thermal wings were discarded.

To acquire the TOF signals corresponding to a given ion rate, we turn off the rf shield, wait 50 ms, and then turn off the magnetic trap and switch the MCP to analog mode. To be sure that the rf has no influence on the ion rate, we use only the number of ions observed during the 50 ms delay to get the rate. We fit the TOF signals to an inverted parabola squared as expected for a pure BEC in the Thomas-Fermi regime and for a TOF width ($\sim$ 5 ms) narrow compared to the mean arrival time (100 ms) [1]. Under these assumptions, the chemical potential μ depends only on the TOF width, the atomic mass, and the acceleration of gravity [22], and thus can be measured quite accurately. Figure 1 shows that μ varies as expected as $N_d^{2/5}$ with N_d the number of detected atoms in the quasipure BEC. A fit on a log-log plot gives a slope of 0.39. Residuals from the linear fit do not show any systematic variation which is a good indication of the detection linearity and of the proportionality between N_d and N_0.

To determine the collision rate constants β and L, we need an absolute calibration of the number of atoms and the density. As discussed in Ref. [1], all the atoms are not detected, and the direct calibration has a 50% uncertainty which is responsible for the large uncertainty in the scattering length a. In fact the measurement of the chemical potential gives an accurate value for the product $n_0 a = \mu m/4\pi\hbar^2$, and with the value of $\overline{\omega}$ gives the product $N_0 a = (1/15)(\hbar/m\overline{\omega})^{1/2}(2\mu/\hbar\overline{\omega})^{5/2}$ as well. Therefore, in the hopes that the He* scattering length will be measured more accurately in the future, we shall express N_0 and n_0 in terms of a. In this paper, unless stated otherwise, we suppose that $a = 20$ nm, and in our conclusions we shall discuss how our results depend on a.

Figure 2 shows the ion rate per atom Γ versus the peak density. The densest sample corresponds to $N_0 = 2 \times 10^5$

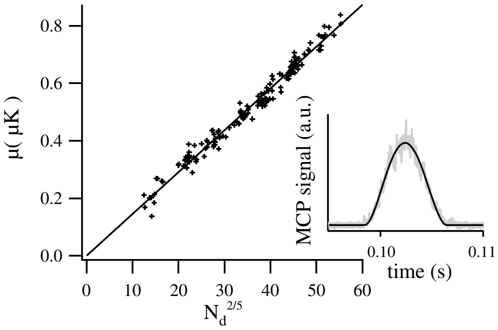

FIG. 1. Chemical potential versus number of detected atoms to the power $\frac{2}{5}$ and its linear fit. Data are for quasipure BEC. The inset shows a typical TOF signal and its inverted parabola squared fit.

atoms and $n_0 = 2.5 \times 10^{13}$ cm^{-3}. The corresponding Thomas-Fermi radii are $r_\perp \simeq 5$ μm and $r_\parallel \simeq 200$ μm. The vertical intercept in Fig. 2 corresponds to ionizing collisions with the background gas $(1/\tau')$. We have independently estimated this rate using trapped thermal clouds at 1 mK and 5 μK and found $1/\tau' \lesssim 5 \times 10^{-3}$ s^{-1}. This value is negligible at the scale of the figure.

The curvature in Fig. 2 shows that three-body ionizing collisions are significant. Before fitting the data to get β and L, we must take into account several effects. First, for three-body collisions, quantum depletion is important. For $T = 0$, on the basis of Ref. [11], we obtain a multiplicative correction to the factor κ_3 of $(1 + \epsilon) = (1 + 23.2 \times \sqrt{n_0 a^3})$ [23]. At our highest density $\epsilon \simeq 0.35$. Two-body collisions are subject to an analogous correction but approximately 3 times smaller. The fits in Fig. 2 include the density dependence of $\kappa_{2,3}$, associated with quantum depletion. The $n_0^{3/2}$ dependence introduced for two-body collisions is far too small to explain the curvature in the data. The density dependence of $\kappa_{2,3}$ does not improve the quality of the fit, but it significantly reduces the value of the fitted value of L (by 30%).

In addition, the fact that the sample probably contains a small thermal component means that collisions between the condensed and the thermal parts must be taken into account [6,11]. Assuming a 10% thermal population $(\frac{\mu}{k_B T} \simeq 1.5)$, we find $\kappa_3 = \frac{1}{6}(1 + \epsilon + \epsilon')$, with an additional correction $\epsilon' \simeq 0.11$ for the densest sample [24].

Taking into account all these corrections, and assuming an ion detection efficiency of 0.42, the fitted values of the collision rate constants [15] are $\beta_{20} = 2.9(\pm 2.0) \times 10^{-14}$ cm^3 sec^{-1} and $L_{20} = 1.2(\pm 0.7) \times 10^{-26}$ cm^6 sec^{-1}, where the subscripts refer to the assumed value of a. These values are in good agreement with the theoretical estimates. The error bars are estimated as follows. We fix either β or L and use the other as a fit parameter. We repeat this procedure for different values of the fixed parameter and take the range over which we can get a converging and physically reasonable fit (i.e., no negative rate constants) as the uncertainty in the fixed parameter. These error bars are highly correlated since if β is increased, L must be decreased and vice versa. The error bars do not include the uncertainty in the absolute ion detection efficiency (see below).

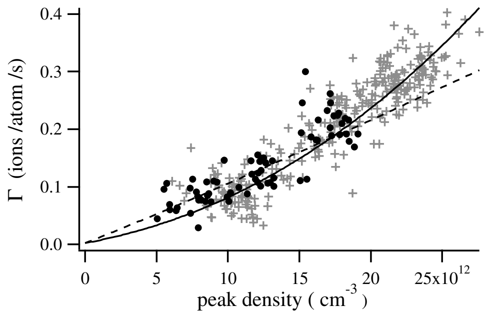

FIG. 2. Ion rate per trapped atom versus peak density for 350 different quasipure BEC's. Atom number and density are deduced from μ , $\overline{\omega}$, and a (here 20 nm). Data were taken for two different bias fields corresponding to $\nu_\perp = 1800$ Hz (crosses) and $\nu_\perp = 1200$ Hz (circles). The dashed line corresponds to the best fit involving only two-body collisions. The solid line is a fit to two- and three-body processes.

Until now we have assumed $a = 20$ nm, but current experiments give a range from 8 to 30 nm [1,2]. Using Eq. (3) and our parametrization of n_0 and N_0 in terms of a, one can see that, in the absence of quantum depletion, the values of β and L extracted from our analysis would be proportional to a^2 and a^3, respectively. Taking quantum depletion into account, no simple analytical dependence exists, but one can numerically evaluate β and L vs a and fit the results to expansions with leading terms in a^2 and a^3, respectively. The effect of quantum depletion is negligible for β $[\beta_a \approx \beta_{20}(\frac{a}{20})^2]$. For L, we find $L_a \approx L_{20}(\frac{a}{20})^3[1 - 0.21\frac{a-20}{20}]$ with a in nm.

To test the consistency of our measurements, we plot the decay of the atom number (Fig. 3). To acquire these data, we held the BEC in the trap in the presence of the rf shield for varying times. This study involves multiple BEC realizations, which typically exhibit large fluctuations in the initial atom number. We have been able to reduce this noise by using the ion signal to select only data corresponding to the same ion rate 500 ms after the end of the ramp. This time corresponds to $t = 0$ in the figure. We also plot the predicted decay curve (solid line) corresponding to ionization only. This curve results from a numerical integration of the atom loss due to ionization processes, calculated from the fitted values β_{20} and L_{20}. The fact that the error bars on β and L are correlated

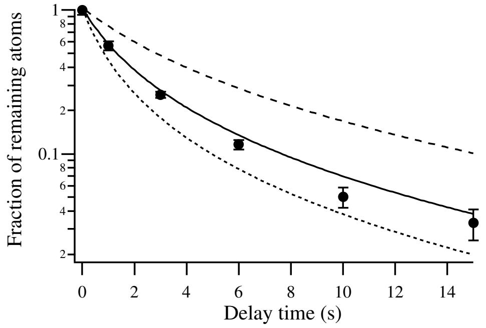

FIG. 3. Fraction of remaining atoms measured by TOF as a function of time. The rf shield is on and the cloud remains a quasipure condensate during the decay. The lines correspond to the predicted atom decay according to Eq. (3) with the fitted value of the two- and three-body rate constants for $a = 10$ nm (dashed line), $a = 20$ nm (solid line), and $a = 30$ nm (dotted line). The case of $a = 10$ nm is not necessarily excluded because other, nonionizing losses could be present.

leads to a small uncertainty on the solid curve that happens to be of the same order of magnitude as the typical error bars on the data. The observed decay agrees fairly well with the solid curve, and ionization apparently accounts for most of the loss. If the ion detection efficiency were actually lower than we assume, the predicted decay would be faster than the observed decay which is unphysical (assuming $a = 20$ nm). We conclude that our estimate of the ion detection efficiency is reasonable and does not lead to an additional uncertainty in β and L.

We also plot the curves obtained from the same analysis but with scattering lengths of 10 and 30 nm, assuming a detection efficiency of 0.42. The curve corresponding to $a = 30$ nm lies below the data points. Based on our analysis, this means that $a = 30$ nm is excluded. A scattering length of 25 nm is the largest one consistent with our data. In contrast, the decay predicted for an analysis with $a = 10$ nm is slower than the observed decay. This would mean that there are additional nonionizing losses (contributing up to half of the total loss), and/or that we have overestimated the ion detection efficiency by a factor as large as 2. In the latter case, β and L should be multiplied by the same factor. This results for $a = 10$ nm in a supplementary systematic uncertainty on β and L of a factor as large as 2.

In the event that our upper limit on the ion detection efficiency is too low, the rate constants β and L should be reduced by a factor as large as 2.4 ($= 0.42^{-1}$). In that case, our data would not exclude $a = 30$ nm and nonionizing losses could significantly contribute to the total loss.

Even though the peak densities of our BEC are small compared to those in alkalis, the elastic collision rate is high because of the large scattering length, and one must consider the possibility of collisional avalanches. For $a = 20$ nm our densest cloud has a mean free path of 7 μm and using the definition of [8] the collisional opacity is 0.8. With Rb atoms this would result in much increased loss due to avalanches [8]. Here we have to consider secondary collisions leading to both ion production and atom loss. However, for secondary ionization, mean free paths are at least 2 orders of magnitude larger than $r_{\|}$. Hence secondary ionization is unimportant. This conclusion is supported by our observation of no correlation in the time distribution of detected ions.

The good agreement between the data and the curve in Fig. 3 indicates that losses due to nonionizing collisional avalanches are not taking place either. This is in agreement with data on elastic collisions with He^+, He_2^+, and He(1S), which have small cross sections [25]. Collisions with hot He* atoms from the reaction of Eq. (2) are more likely to play a role, but due to the higher velocity, the elastic cross section for these atoms is smaller. In Rb the situation is different because a d-wave resonance increases the total cross section [8].

The theoretical analysis shows that quantum depletion strongly affects the measured three-body rate constant. One way to experimentally demonstrate this effect would be to compare with similar measurements with thermal clouds. Absolute calibration of ion and atom detection efficiency should play no role in this comparison, if one could prove that they are the same for both situations.

We thank F. Gerbier for stimulating discussions. This work was supported by the European Union under Grants No. IST-1999-11055 and No. HPRN-CT-2000-00125, and by the DGA Grant No. 00.34.025.

---

*Permanent address: Departamento de Fisica, Universidade do Minho, Campus de Gualtar, 4710-057 Braga, Portugal.

[1] A. Robert *et al.*, Science **292**, 461 (2001).
[2] F. Pereira Dos Santos *et al.*, Phys. Rev. Lett. **86**, 3459 (2001); F. Pereira Dos Santos *et al.*, Eur. Phys. J. D **19**, 103 (2002).
[3] G.V. Shlyapnikov *et al.*, Phys. Rev. Lett. **73**, 3247 (1994); P.O. Fedichev *et al.*, Phys. Rev. A **53**, 1447 (1996).
[4] H.J. Miesner *et al.*, Science **270**, 1005 (1998); M. Köhl *et al.*, Phys. Rev. Lett. **88**, 080402 (2002).
[5] J.L. Roberts *et al.*, Phys. Rev. Lett. **85**, 728 (2000).
[6] J. Söding *et al.*, Appl. Phys. B **69**, 257 (1999).
[7] E.A. Burt *et al.*, Phys. Rev. Lett. **79**, 337 (1997).
[8] J. Schuster *et al.*, Phys. Rev. Lett. **87**, 170404 (2001).
[9] M. Leduc *et al.*, Acta Phys. Pol. B **33**, 2213 (2002).
[10] F. Dalfovo *et al.*, Rev. Mod. Phys. **71**, 463 (1999).
[11] Y. Kagan, B.V. Svistunov, and G.V. Shlyapnikov, JETP Lett. **42**, 209 (1985).
[12] V. Venturi *et al.*, Phys. Rev. A **60**, 4635 (1999); V. Venturi and I.B. Whittingham, Phys. Rev. A **61**, 060703(R) (2000).
[13] J.C. Hill *et al.*, Phys. Rev. A **5**, 189 (1972).
[14] N. Herschbach *et al.*, Phys. Rev. A **61**, 50 702 (2000).
[15] Collision rate constants are sometimes defined directly for a BEC ($\beta' = \beta/2$ and $L' = L/6$).
[16] P.O. Fedichev, M.W. Reynolds, and G.V. Shlyapnikov, Phys. Rev. Lett. **77**, 2921 (1996); P.F. Bedaque, E. Braaten, and H.W. Hammer, Phys. Rev. Lett. **85**, 908 (2000).
[17] A. Browaeys *et al.*, Phys. Rev. A **64**, 034703 (2001).
[18] S. Nowak *et al.*, Appl. Phys. B **70**, 455 (2000).
[19] M.O. Mewes *et al.*, Phys. Rev. Lett. **77**, 416 (1996).
[20] R.S. Gao *et al.*, Rev. Sci. Instrum. **55**, 1756 (1984).
[21] B. Deconihout *et al.*, Appl. Surf. Sci. **94/95**, 422 (1996).
[22] Y. Castin and R. Dum, Phys. Rev. Lett. **77**, 5315 (1996); Y. Kagan, E.L. Surkov, and G.V. Shlyapnikov, Phys. Rev. A **54**, R1753 (1996).
[23] The numerical factor $64/\sqrt{\pi}$ of [11] changes to 23.2 for a trapped bose gas.
[24] We have $\epsilon' = (\langle\langle 3n_0^2(n' + \alpha)\rangle\rangle + \langle 3n_0^2\langle n' + \alpha\rangle\rangle) \times \langle\langle n_0^3\rangle\rangle^{-1}$. The symbol $\langle\cdots\rangle$ denotes the integration over the condensate spatial region. The thermal part of the noncondensed density, n', and that of the anomalous average, α, are obtained in the local density approximation. This gives $\epsilon' = 7.7 \times \sqrt{n_0 a^3}$ for $(\mu/k_B T) = 1.5$.
[25] H.C.W. Beijerinck *et al.*, Phys. Rev. A **61**, 23 607 (2000).

REPORTS

Hanbury Brown Twiss Effect for Ultracold Quantum Gases

M. Schellekens,[1] R. Hoppeler,[1] A. Perrin,[1] J. Viana Gomes,[1,2]
D. Boiron,[1] A. Aspect,[1] C. I. Westbrook[1]*

We have studied two-body correlations of atoms in an expanding cloud above and below the Bose-Einstein condensation threshold. The observed correlation function for a thermal cloud shows a bunching behavior, whereas the correlation is flat for a coherent sample. These quantum correlations are the atomic analog of the Hanbury Brown Twiss effect. We observed the effect in three dimensions and studied its dependence on cloud size.

Nearly half a century ago, Hanbury Brown and Twiss (HBT) performed a landmark experiment on light from a gaseous discharge (*1*). The experiment demonstrated strong correlations in the intensity fluctuations at two nearby points in space despite the random or chaotic nature of the source. Although the effect was easily understood in the context of classical statistical wave optics, the result was surprising when viewed in terms of the quantum theory. It implied that photons coming from widely separated points in a source such as a star were "bunched." On the other hand, photons in a laser were not bunched (*2*, *3*). The quest to understand the observations stimulated the birth of modern quantum optics (*4*). The HBT effect has since found applications in many other fields from particle physics (*5*) to fluid dynamics (*6*).

Atom or photon bunching can be understood as a two-particle interference effect (*7*). Experimentally, one measures the joint probability for two particles emitted from two separated source points, *A* and *B*, to be detected at two detection points, *C* and *D*. One must consider the quantum mechanical amplitude for the process *A*→*C* and *B*→*D* as well as that for *A*→*D* and *B*→*C*. If the two processes are indistinguishable, the amplitudes interfere. For bosons, the interference is constructive, resulting in a joint detection probability that is enhanced compared with that of two statistically independent detection events, whereas for fermions the joint probability is lowered. As the detector separation is increased, the phase difference between the two amplitudes grows large enough that an average over all possible source points *A* and *B* washes out the interference, and one recovers the sit-

---

[1] Laboratoire Charles Fabry de l'Institut d'Optique, UMR 8501 du CNRS, Centre Scientifique d'Orsay, Bâtiment 503, 91403 Orsay CEDEX, France. [2] Departimento de Fisica, Universidade do Minho, 4710-057 Braga, Portugal.

*To whom correspondence should be addressed. E-mail: christoph.westbrook@iota.u-psud.fr

uation for uncorrelated detection events. This fact was used by HBT to measure the angular size of a star (*8*), but another major consequence of the observation was to draw attention to the importance of two-photon amplitudes and how their interference can lead to surprising effects. These quantum amplitudes must not be confused with classical electromagnetic field amplitudes (*3*). Two-photon states subsequently led to many other striking examples of "quantum weirdness" (*9*). In contrast to a chaotic source, all photons in a single mode laser are in the same quantum state. Hence, there is only one physical process and no bunching effect. A similar effect is expected for atoms in a Bose-Einstein condensate (BEC).

Two-particle correlations have been observed both for cold neutral atoms (*10*–*12*) and for electrons (*13*–*15*), and three-particle correlations (*16*–*18*) at zero distance have also been used to study atomic gases. But the full three-dimensional effect and its dependence on the size and degeneracy of a sample has yet to be demonstrated for massive particles. Here, we demonstrate the effect for a trapped cloud of atoms close to the BEC transition temperature released onto a detector capable of individual particle detection. We extract, for varying cloud sizes, a three-dimensional picture of the correlations between identical particles produced by quantum interference. We also show that a BEC shows no such correlations. The results are in agreement with an ideal gas model and show the power of single particle detection techniques applied to the study of degenerate quantum gases.

The calculation of the phase difference of the possible two-particle detection amplitudes given in (*7*) can be adapted to the case of particles of mass m traveling to a detector in a time t. One can show that the correlation length observed at the detectors, that is, the typical detector separation for which interference survives, is $l_i = \frac{\hbar t}{m s_i}$, where s_i is the source size along the direction i, $\hbar$ is the reduced Planck's constant, and we have assumed that the size of the cloud at the detector is much larger than the initial size. The optical analog of this expression, for a source of size s and wavelength λ at a distance L from the observation plane, is $l = L\lambda/2\pi s$. This is the length scale of the associated speckle pattern. The formula can be recovered for the case of atoms traveling at constant velocity v toward a detector at distance L if one identifies h/mv with the deBroglie wavelength corresponding to velocity v. The formula we give is also valid for atoms accelerated by gravity, and the interpretation of l as the atomic speckle size remains valid. A pioneering experiment on atom correlations used a continuous beam of atoms (*10*). For a continuous beam, the correlation time, or equivalently, the longitudinal correlation length, depends on the velocity width of the source and not on the source size. Thus, the longitudinal and transverse directions are qualitatively different. By contrast, our measurements are performed on a cloud of atoms released suddenly from a magnetic trap. In this case, the three dimensions can all be treated equivalently, and the relation above applies in all three. Because the trap is anisotropic, the correlation function is as well, with an inverted ellipticity. Our sample is a magnetically trapped cloud of metastable helium atoms evaporatively cooled close to the BEC transition temperature (*19*) (about 0.5 μK for our conditions). Our source is thus very small, and together with a long time of flight (308 ms) and helium's small mass, we achieve a large speckle size or correlation volume (30 μm by 800 μm by 800 μm), which simplifies the detection problem. For example, the observations are much less sensitive to the tilt of the detector than in (*10*).

To detect the atoms, we use an 8-cm-diameter microchannel plate detector (MCP). It is placed 47 cm below the center of the magnetic trap. A delay line anode permits position-sensitive detection of individual particles in the plane of the detector (*20*) (Fig. 1). Atoms are released from the trap by suddenly turning off the magnetic field. About 10% of these atoms are transferred to the magnetic field–insensitive $m = 0$ state by nonadiabatic transitions (*19*) and fall freely to the detector. The remaining atoms are removed by applying additional magnetic field gradients during the time of flight. For each detected atom, we record the in-plane coordinates x and y and the time of detection t. The atoms hit the detector at 3 m/s with a velocity spread below 1%, and so we convert t into a vertical position z. The observed root mean square (rms) resolution is $d \sim 250$ μm in x and y and 2 nm in z. These data allow us to construct a three-dimensional histogram of pair separations (Δx, Δy, and Δz) for all particles detected in a single cloud. The histograms are summed over the entire atomic distribution and over many shots, typically 1000 (*21*).

Because of our good resolution along z, we begin by concentrating on the correlation function along this axis. Normalized correlation functions for various experimental conditions are shown in Fig. 2A. To compute the normalized correlation function, we divide the pair separation histogram by the autoconvolution of the average single particle distribution along z. We also normalize the correlation function to unity for large separations. This amounts to dividing, for each elementary pixel of our detector, the joint detection probability by the product of the individual detection probabilities at the two pixels. This gives us the usual normalized correlation function $g^{(2)}(\Delta x = 0, \Delta y = 0, \Delta z)$. The HBT bunching effect corresponds to the bump in the top three graphs of Fig. 2A. The fourth graph shows the result for a BEC. No correlation is observed. [A detector saturation effect in the BEC data required a modified analysis procedure (*21*).] We have also recorded data for a cloud with a 2-mm radius and 1-mK temperature for which the correlation length is so small that the bunching effect is washed out by the in-plane detector resolution. Experimentally, the normalized correlation function in this case is indeed flat to within less than 1%.

We plot (Fig. 2B) the normalized correlation functions in the $\Delta x - \Delta y$ plane and for $\Delta z = 0$ for the same three data sets. The data in Fig. 2B show the asymmetry in the correlation function arising from the difference in the two transverse dimensions of the trapped cloud. The long axis of the correlation function is orthogonal to that of the magnetic trap.

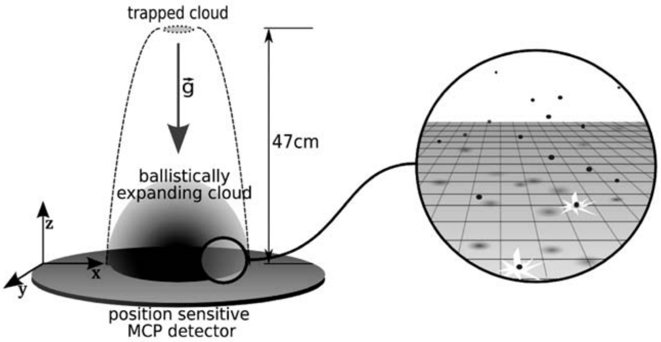

Fig. 1. Schematic of the apparatus. The trapped cloud has a cylindrical symmetry with oscillation frequencies of $\omega_x/2\pi = 47$ Hz and $\omega_y/2\pi = \omega_z/2\pi = 1150$ Hz. During its free fall toward the detector, a thermal cloud acquires a spherical shape. A 1-μK temperature yields a cloud with an rms radius of about 3 cm at the detector. Single particle detection of the neutral atoms is possible because of each atom's 20-eV internal energy that is released at contact with the MCP. Position sensitivity is obtained through a delay-line anode at the rear side of the MCP.

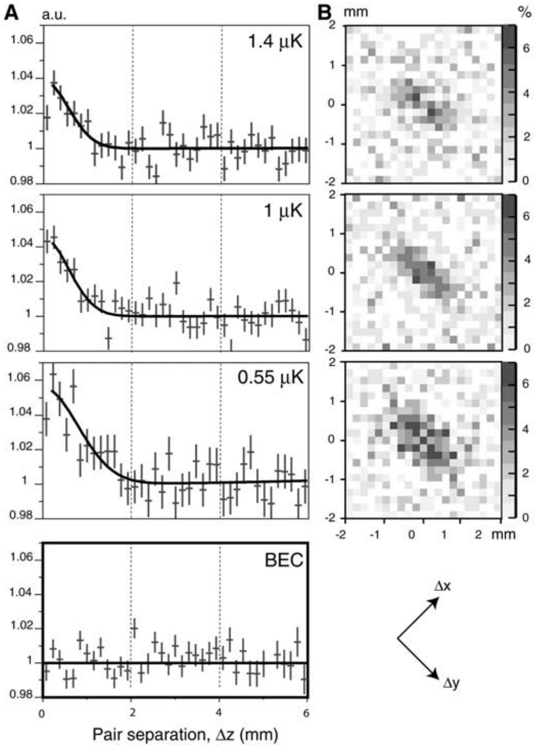

Fig. 2. (**A**) Normalized correlation functions along the vertical (*z*) axis for thermal gases at three different temperatures and for a BEC. For the thermal clouds, each plot corresponds to the average of a large number of clouds at the same temperature. Error bars correspond to the square root of the number of pairs. a.u., arbitrary units. (**B**) Normalized correlation functions in the $\Delta x - \Delta y$ plane for the three thermal gas runs. The arrows at the bottom show the 45° rotation of our coordinate system with respect to the axes of the detector. The inverted ellipticity of the correlation function relative to the trapped cloud is visible.

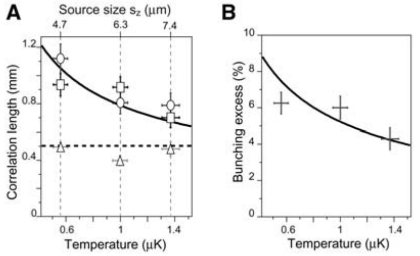

Fig. 3. Results of fits to the data in Fig. 2, A and B. (**A**) Fitted correlation lengths l_x, l_y, and l_z along the three axes (triangles, squares, and circles) as a function of temperature. The upper axis shows the corresponding source size s_z. Vertical error bars are from the fits. Horizontal error bars correspond to the standard deviation of the measured temperature. Along the *x* axis, the measurement is entirely limited by the detector resolution. The dotted horizontal line is the result of an independent estimate of the resolution. The result for the *y* axis has been corrected for the finite detector resolution as characterized by the fitted value of l_x. The *z* axis suffers from no such resolution limit. The solid curve corresponds to $\hbar t/ms_z$. (**B**) Fitted contrast η of the correlation function for the three temperatures used. The solid line corresponds to the same noninteracting gas model as the line in (A) (*21*) and includes the finite detector resolution.

We expect the experimental normalized correlation function for a thermal bosonic gas to be described by

$$g^{(2)}_{\text{th}}(\Delta x, \Delta y, \Delta z) = 1 + \eta \exp\left(-\left[\left(\frac{\Delta x}{l_x}\right)^2 + \left(\frac{\Delta y}{l_y}\right)^2 + \left(\frac{\Delta z}{l_z}\right)^2\right]\right) \tag{1}$$

We have assumed here that the gas is noninteracting and that the velocity and density distribution remain roughly Gaussian even close to the BEC transition temperature. Numerical simulations indicate that this is a good approximation when the correlation function is averaged over the entire cloud (*22*). As discussed above, the correlation lengths should be inversely proportional to the sizes, s_i, of the sample. In a harmonic trap with trapping frequency ω_i along the *i* direction, one has $s_i = \sqrt{\frac{k_B T}{m\omega_i^2}}$, where k_B is Boltzmann's constant and *T* is the temperature of the atoms. Because *T* is derived directly from the time of flight spectrum, we shall plot our data as a function of *T* rather than of *s*. The parameter η would be unity for a detector whose resolution width *d* is small compared with the correlation length. Our *d* is smaller than l_y but larger than l_x, and in this case the convolution by the detector resolution results in an η given roughly by $l_x/2d \sim 5\%$. We use Eq. 1 to fit the data by using η and the l_i as fit parameters and compare the results to the ideal gas model (*21*).

The results for l_x, l_y, and l_z for our three temperatures are plotted in Fig. 3A. The fitted values of l_x are ~450 μm and are determined by the detector resolution rather than the true coherence length along *x*. The value of l_y has been corrected for the finite spatial resolution of the detector. The fitted value of l_z requires no correction, because in the vertical direction the resolution of the detector is much better. l_y and l_z are consistent and agree with the prediction using the known trap frequencies and temperatures. Figure 3B shows the fitted value of η versus temperature, along with the prediction of the same ideal gas model as in Fig. 3A, using the measured detector resolution. The data are in reasonable agreement with the model, although we may be seeing too little contrast at the lowest temperature. The run at 0.55 μK was above, but very close to, the BEC transition temperature. (We know this because, when taking data at 0.55 μK, about one-third of the shots contained small BECs; these runs were eliminated before plotting Fig. 2.) Future work will include examining whether the effect of the repulsive interactions between atoms or finite atom number must be taken into account.

The results reported here show the power of single particle detection in the study of quantum gases. The correlations we have observed are among the simplest that should be present. Two recent experiments have shown correlations in a Mott insulator (*11*) as well as in atoms produced from the breakup of molecules near a Feshbach resonance (*12*). Improved observations of these effects may be possible with individual particle detection. Other atom pair production mechanisms, such as four-wave mixing (*23*, *24*), can be investigated. A fermionic analog to this experiment using ^{3}He would also be (*25*) of great interest.

References and Notes

1. R. Hanbury Brown, R. Q. Twiss, *Nature* **177**, 27 (1956).
2. F. T. Arecchi, E. Gatti, A. Sona, *Phys. Lett.* **20**, 27 (1966).
3. R. J. Glauber, *Phys. Rev. Lett.* **10**, 84 (1963).
4. R. J. Glauber, *Quantum Optics and Electronics*, C. DeWitt, A. Blandin, C. Cohen-Tannoudji, Eds. (Gordon and Breach, New York, 1965), p. 63.
5. G. Baym, *Acta Phys. Pol. B* **29**, 1839 (1998).
6. B. Berne, R. Pecora, *Dynamic Light Scattering* (Dover, New York, 2000).
7. U. Fano, *Am. J. Phys.* **29**, 539 (1961).
8. R. Hanbury Brown, R. Twiss, *Nature* **178**, 1046 (1956).
9. J. S. Bell, *Speakable and Unspeakable in Quantum Mechanics* (Cambridge Univ. Press, Cambridge, ed. 2, 2004).
10. M. Yasuda, F. Shimizu, *Phys. Rev. Lett.* **77**, 3090 (1996).
11. S. Fölling *et al.*, *Nature* **434**, 481 (2005).

12. M. Greiner, C. A. Regal, J. T. Stewart, D. S. Jin, *Phys. Rev. Lett.* **94**, 110401 (2005).
13. M. Henny *et al.*, *Science* **284**, 296 (1999).
14. W. D. Oliver, J. Kim, R. C. Liu, Y. Yamamoto, *Science* **284**, 299 (1999).
15. H. Kiesel, A. Renz, F. Hasselbach, *Nature* **418**, 392 (2002).
16. Y. Kagan, B. V. Svistunov, G. V. Shlyapnikov, *Sov. Phys. JETP* **42**, 209 (1985).
17. E. A. Burt *et al.*, *Phys. Rev. Lett.* **79**, 337 (1997).
18. B. Laburthe Tolra *et al.*, *Phys. Rev. Lett.* **92**, 190401 (2004).
19. A. Robert *et al.*, *Science* **292**, 461 (2001); published online 22 March 2001 (10.1126/science.1060622).
20. O. Jagutzki *et al.*, *Nucl. Instrum. Methods Phys. Res. A* **477**, 244 (2004).
21. See supporting online materials on *Science* Online for details.
22. M. Naraschewski, R. Glauber, *Phys. Rev. A* **59**, 4595 (1999).
23. L. Deng *et al.*, *Nature* **398**, 218 (1999).
24. J. Vogels, K. Xu, W. Ketterle, *Phys. Rev. Lett.* **89**, 020401 (2002).
25. R. Stas, J. McNamara, W. Hogervorst, W. Vassen, *Phys. Rev. Lett.* **93**, 053001 (2004).
26. A. Öttl, S. Ritter, M. Köhl, T. Esslinger, *Phys. Rev. Lett.* **95**, 090404 (2005).
27. After submission of this manuscript, we became aware of a related experiment concerning atom correlations in an atom laser (*26*). We thank R. Sellem of the Détection Temps, Position Image Technology Division (supported by the Mission Ressources et Compétences Technologiques–CNRS Federation FR2764 and by the Université Paris-Sud) for a decisive role in the development of the time-to-digital converter, and O. Jagutzki for advice on delay lines.

Supporting Online Material
www.sciencemag.org/cgi/content/full/1118024/DC1
SOM Text

27 July 2005; accepted 5 September 2005
Published online 15 September 2005;
10.1126/science.1118024
Include this information when citing this paper.

Eur. Phys. J. D **41**, 157–162 (2006)
DOI: 10.1140/epjd/e2006-00197-8

THE EUROPEAN PHYSICAL JOURNAL D

Atomic density of a harmonically trapped ideal gas near Bose-Einstein transition temperature

R. Hoppeler[1], J. Viana Gomes[1,a], and D. Boiron[1,b]

Laboratoire Charles Fabry de l'Institut d'Optique, UMR 8501 du CNRS, 91403 Orsay Cedex, France

Received 19 August 2005 / Received in final form 20 May 2006

Abstract. We have studied the atomic density of a cloud confined in an isotropic harmonic trap at the vicinity of the Bose-Einstein transition temperature. We show that, for a non-interacting gas and near this temperature, the ground-state density has the same order of magnitude as the excited states density at the centre of the trap. This holds in a range of temperatures where the ground-state population is negligible compared to the total atom number. We compare the exact calculations, available in a harmonic trap, to semi-classical approximations. We show that these latter should include the ground-state contribution to be accurate.

PACS. 03.75.Hh Static properties of condensates; thermodynamical, statistical, and structural properties – 03.65.Sq Semiclassical theories and applications – 05.30.Jp Boson systems

The phenomenon of Bose-Einstein condensation (BEC) is a phase transition. Below the critical temperature T_c, the ground-state population, which is the order parameter, becomes macroscopic. This phenomenon, that happens strictly speaking only at the thermodynamic limit, is usually illustrated in textbooks with a homogeneous gas. Experimentally, the Bose-Einstein condensation of dilute gases has been observed since 1995 with atoms confined in a harmonic trap [1]. These stimulating experimental data have quickly pointed out that two effects had to be taken into account: the interatomic interactions and the finite number of atoms [2]. Several papers, as the present one, have studied harmonically trapped ideal gases containing a finite number of atoms. Two quantities have been investigated in detail: the atom number [3,4,6–9] and the specific heat [5,7,9]. For a finite but large (typically 10^6) number of atoms, the properties of the atomic cloud change abruptly at a characteristic temperature we will name the transition temperature T^*. This temperature is shifted compared to T_c, but by a small amount, typically of few percent for atom numbers around 10^6. There is also a characteristic temperature for the specific heat; it is different from the previous one but still close to T_c [5,9].

Surprisingly, less attention has been paid on the atomic density of an ideal gas [10]. In a homogeneous gas it is obviously equivalent to the atom number but this is no more the case in a spatially varying potential. It becomes the good parameter of the theory, in particular to perform local density approximations. This quantity is then particularly important for the study of the shift of the critical temperature by the interatomic interactions, both within the mean-field approximation [6] and beyond this approximation [11]. We will show, in the case of an isotropic harmonic trapping and for a finite atom number, that the ground-state density at the centre of the trap increases much more sharply than its population as the temperature decreases. This leads to the fact that near the Bose-Einstein transition temperature the density is already dominated by the ground-state contribution. This holds whatever the atom number is, and is a remanence of the infinite compressibility of an ideal gas at the thermodynamic limit [12]. Usual semi-classical approximations do not take into account the ground-state contribution and then fail in the vicinity of the Bose-Einstein transition temperature. This is not a finite size effect in the sense that it is not related to the discretization of the excited states energy levels. We will compare the exact results with semi-classical approximations. The addition of the ground-state contribution on the latter ones improves their accuracy. We will finally show that the influence of the ground-state is smaller if the measured quantity is the density integrated over at least one dimension. It is still large for typical experimental parameters.

We will perform our calculations in the grand canonical ensemble (GCE). Then, the Bose-Einstein distribution gives the population N_i of a given energy level ϵ_i: $N_i = (e^{\beta(\epsilon_i-\mu)}-1)^{-1}$ with $\sum_{i=0}^{\infty} N_i = N$. Here $\beta = 1/k_BT$ with

---

[a] *Permanent address:* Departamento de Fisica, Universidade do Minho, Campus de Gualtar, 4710-057 Braga, Portugal.

[b] e-mail: `denis.boiron@iota.u-psud.fr`

k_B the Boltzmann's constant, μ the chemical potential and N the total atom number. The equivalence between GCE and the canonical or microcanonical ensemble, these latter being probably more appropriate descriptions, is generally not guaranteed, especially for systems that are not at the thermodynamic limit. For instance, it is well-known that the GCE predicts unphysical large fluctuations of the condensate population at low temperature [13]. However, the authors of references [10,14,15] have shown that the occupation numbers N_i in GCE are very close to the ones in the canonical ensemble. The difference is more pronounced for small atom number and anisotropic clouds. As a result and because GCE enables to give analytic expressions on contrary to the other ensembles, we will use GCE in the following.

For a fixed atom number, the chemical potential increases as the temperature decreases. As μ has to be smaller than ϵ_0, the ground-state energy, the excited states population will saturate when μ approaches ϵ_0 whereas N_0 is still increasing: $N - N_0 = \sum\limits_{i=1}^{\infty} N_i(\mu, T) \leq \sum\limits_{i=1}^{\infty} N_i(\epsilon_0, T)$. As in references [2,16], we will define the transition temperature T^* as the temperature for which the excited states saturated population is equal to the total atom number:

$$\sum_{i=1}^{\infty} N_i(\epsilon_0, T^*) = N. \tag{1}$$

As pointed out in the introduction, there is not a unique definition of the transition temperature for a finite atom number. Other definitions use, for instance, a change in the slope for the condensate fraction in function of temperature (more explicitly $d^3(N_0/N)/dT^3 = 0$) [17], a change in the power dependence on the condensate fraction in function of the atom number [9], which are also pertinent. We have checked that these various definitions affect marginally the value of T^* and do not modify our conclusions [18]. In the following we will then use equation (1) to define T^*. Note that the chemical potential μ^* at the transition temperature is close but not equal to the ground-state energy; it is determined by the constraint

$$\sum_{i=0}^{\infty} N_i(\mu^*, T^*) = N. \tag{2}$$

There are only a few examples of trapping potentials where the eigen-energies and the eigen-functions are known exactly. Semi-classical approximations give usually accurate enough results and are suited to include interatomic interactions, at least perturbatively. We will derive various type of semi-classical approximations in the following and test their accuracy because the harmonic potential is an exactly solvable potential.

We will first examine the situation where $\hbar\omega \ll k_B T$ with ω the oscillation frequency of the isotropic harmonic trap. This corresponds to the large atom number limit and semi-classical approximations should work. Replacing the discrete energy spectrum by a continuous one and neglecting the ground-state energy ϵ_0, the density is $\rho(r) = \frac{1}{\lambda^3} g_{\frac{3}{2}}[z \exp(-\frac{\tau}{2}(r/\sigma)^2]$ with $z = e^{\beta\mu}$ the fugacity, $\tau = \hbar\omega/k_B T$ and $g_{\frac{3}{2}}(\ )$ a Bose function [19]. With the above notation, the thermal de Broglie wavelength is $\lambda = \sigma\sqrt{2\pi\tau}$ and the size of the cloud is $\sqrt{k_B T/m\omega^2} = \sigma/\sqrt{\tau}$. Similarly, the atom number is $N = g_3(z)/\tau^3$. Equation (1) leads then to $N = \zeta(3)/\tau^{*3}$, with τ^* the value of τ at $T = T^*$. The above expressions for the density and atom number are in fact approximations for the excited states and do not contain the ground-state contribution. Then μ^* defined by equation (2) is equal to 0 and $z^* = 1$. The transition temperature defined here corresponds to the critical temperature T_c. The peak density at the transition temperature is then given by $\rho(0)\lambda^3 = g_{\frac{3}{2}}(z^*) = \zeta(3/2) \approx 2.612$. For temperatures below T_c, the excited states population is given by $\zeta(3)/\tau^3$. Then, the ground-state population fraction is $N_0/N = 0$ for $T > T_c$ and $N_0/N = 1 - (T/T_c)^3$ for $T < T_c$. This fraction will be plotted in Figure 1, labelled with sc_∞.

These approximations are too crude and give inaccurate results for the atomic density, however. The reason is that the ground-state contribution cannot be neglected. A better expression is $\rho(r) = \frac{1}{\lambda^3} g_{\frac{3}{2}}[z e^{-\frac{\tau}{2}(r/\sigma)^2}] + \rho_0(r)$ and similarly $N = \frac{1}{\tau^3} g_3(z) + N_0$ with $\rho_0(r) = [N_0/(\sqrt{\pi}\sigma)^3] e^{-(r/\sigma)^2}$ and $N_0 = z/(1-z)$. The value of T^* is unchanged as it is defined by the excited states saturation, but z^* is now different from 1. Using $g_3(z^*) \approx \zeta(3) - \zeta(2)x^*$ with $z^* = e^{-x^*}$ $(x = \beta(\epsilon_0 - \mu) > 0)$, one finds using equation (2) that $x^* \approx \tau^{*3/2}/\sqrt{\zeta(2)}$ [9]. The ground-state population is $\sim 1/x^*$ and, as expected, is vanishingly small as $\tau^* \to 0$ compared to the excited-state population $\zeta(3)/\tau^{*3}$. The ground-state peak density is $\sim 1/(\sqrt{\pi}\sigma)^3 x^*$ whereas the excited state peak density is $\zeta(3/2)/\lambda^{*3}$. As $\lambda^* = \sigma\sqrt{2\pi\tau^*}$, the two quantities have the same order of magnitude! The above high-N analysis predicts then that the degeneracy parameter at the transition temperature

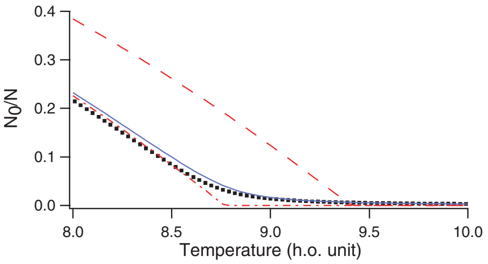

Fig. 1. Ground-state population fraction in function of the temperature in $\hbar\omega/k_B$ unit for a cloud of 10^3 atoms. The dotted curve corresponds to the exact result given by model *ex*. The solid, dot-dashed and dashed lines correspond respectively to the semi-classical models *sc*, sc_0 and sc_∞. The last two neglect the ground-state contribution above their corresponding transition temperature and the first two take into account finite size effects. The model *sc* is the closest to *ex* near Bose-Einstein transition.

is $\rho(0)\lambda^3 = \zeta(3/2) + 2\sqrt{2\zeta(2)} \approx 6.24$ and not 2.612. The ground-state population is extremely small but the size of its wave-function is also extremely small compared to the atomic cloud size. For a harmonic trap both depend on the same small parameter, raised to the same power. So, even for very large atom number, the traditional criterion for BEC should be modified. This effect is linked to the pathological behaviour of the ground-state density at the thermodynamic limit, i.e. the infinite compressibility of an ideal gas [12]. This limit means $N \to \infty$ with $N\omega^3 \to$ constant. The ground-state size being $\sigma = \sqrt{\hbar/m\omega}$, the density of that state behaves as $\sqrt{N}$ below threshold and is then infinite at the thermodynamic limit whereas the density above T_c is finite.

We will now address the case of atom numbers in the accessible experimental range, 10^3–10^6. It is well-known that the transition temperature will be shifted compared to T_c [3,4,7]. A better approximation, which takes into account the ground-state energy to first order, is $\rho(r) = \frac{1}{\lambda^3}\{g_{\frac{3}{2}}[\tilde{z}(r)] + \frac{3\tau}{2} g_{\frac{1}{2}}[\tilde{z}(r)]\}$ where $\tilde{z}(r) = ze^{-\frac{\tau}{2}(r/\sigma)^2}$. Then $N = \frac{1}{\tau^3}[g_3(z) + \frac{3\tau}{2} g_2(z)]$. The corresponding transition temperature is T^*_{sc} such that $N = \frac{1}{\tau^{*3}_{sc}}[\zeta(3) + \frac{3}{2}\zeta(2)\tau^*_{sc}]$. This is the usual semi-classical approximation found in the literature. The ground-state population fraction is then $N_0/N = 0 \quad \text{for} \quad T > T^*_{sc}$ and

$$N_0/N = 1 - \left(\frac{T}{T^*_{sc}}\right)^3 \frac{\zeta(3) + \dfrac{3\tau}{2}\zeta(2)}{\zeta(3) + \dfrac{3\tau^*_{sc}}{2}\zeta(2)}$$

for $T < T^*_{sc}$. This fraction, also plotted in Figure 1, will be labelled with sc_0. Note that $g_{\frac{1}{2}}(z)$ diverges at $z = 1$ [20], meaning that this approximation is intrinsically inaccurate near the centre of the trap and near the transition temperature. This divergence is however weak, and any spatial integration would give a finite result. We can still cure this pathology by adding, as before, the ground-state contribution. We obtain then

$$\begin{cases} \rho_{sc}(r) = \dfrac{1}{\lambda^3}\{g_{\frac{3}{2}}[\tilde{z}(r)] + \dfrac{3\tau}{2} g_{\frac{1}{2}}[\tilde{z}(r)]\} + \dfrac{z}{1-z}\dfrac{e^{-(\frac{r}{\sigma})^2}}{(\sqrt{\pi}\sigma)^3} \\ N = \dfrac{1}{\tau^3}[g_3(z) + \dfrac{3}{2}\tau g_2(z)] + \dfrac{z}{1-z} \\ T^*_{sc} \text{ such that } N = \dfrac{1}{\tau^{*3}_{sc}}[\zeta(3) + \dfrac{3}{2}\zeta(2)\tau^*_{sc}] \end{cases} . \tag{3}$$

This semi-classical approximation will be labelled with sc in the following. The comparison of T^*_{sc} with the value given by the exact model (see below) can be used to check the finite size correction. Even so, this comparison is useless to check the contribution coming from the ground state since it does not depend on it (same transition temperature as sc_0).

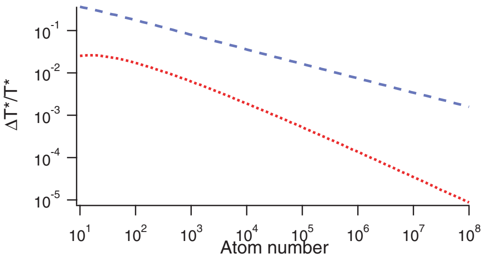

Fig. 2. Relative shift of the semi-classical transition temperatures T_c (dashed line) and T^*_{sc} (dotted line) to T^*_{ex} (see text) in function of the atom number. Both temperatures converge for high atom numbers. The critical temperature at thermodynamic limit, T_c, deviates by less than 1% for $N > 5 \times 10^5$. The semi-classical transition temperature defined for a finite atom number, T^*_{sc}, is much more accurate and deviates by less than 1% for $N > 400$.

We can now test these semi-classical approximations for a harmonically trapped gas. As we referred before, for this case, the eigen-energies and the eigen-functions are known exactly. The corresponding expressions of the atomic density and atom number [13], labelled with ex in the following, are:

$$\begin{cases} \rho_{ex}(r) = \dfrac{1}{(\sqrt{\pi}\sigma)^3}\sum\limits_{l=1}^{\infty} \dfrac{z^l}{(1-e^{-2\tau l})^{3/2}}\, e^{-\tanh(\frac{\tau l}{2})(\frac{r}{\sigma})^2} \\ N = \sum\limits_{l=1}^{\infty} \dfrac{z^l}{(1-e^{-\tau l})^3} \\ T^*_{ex} \text{ such that } N = \sum\limits_{l=1}^{\infty}\left(\dfrac{1}{(1-e^{-\tau^*_{ex} l})^3} - 1\right) \end{cases}$$

where, here $z = e^{\beta(\mu-\epsilon_0)}$. The semi-classical model corresponds to a Taylor expansion in τ of these last expressions.

In Figure 1 we plot the ground-state population fraction in function of the temperature for the various models described above. When the number of atoms is only 10^3, finite size effects are large. The prediction of model sc_∞ is clearly wrong compared to the exact model prediction. On contrary models sc_0 and sc give a result close to the one of ex [21]. Figure 2 shows the relative deviations of T_c and T^*_{sc} from T^*_{ex} in function of the atom number. As expected the different values are similar but, as above, the model sc give a closer result to ex than sc_∞. The value T^*_{sc} deviates less than 1% for $N > 400$ and the relative shift is $\sim 10^{-4}$ for typical experimental atom numbers. This is well below actual experimental uncertainties. The thermodynamic value T_c deviates more, typically 1% but is still close to T^*_{ex} [3,4,7,9]. The discrepancy with T_c would have been more pronounced for an anisotropic trap (see below).

This two figures illustrate what is called finite size effects, the fact that the energy level spacing is not negligible compared to the temperature. What we are interested in is the role of the ground-state. For this, the transition temperature and the condensate population fraction are not the best observables. It is nevertheless already clear from Figure 1 that sc is a significant improved model to describe semi-classically a cloud near degeneracy compared to sc_0. The high-N model predicts that the ground-state influence should be much more pronounced on the peak density. We will now focus our attention on that observable,

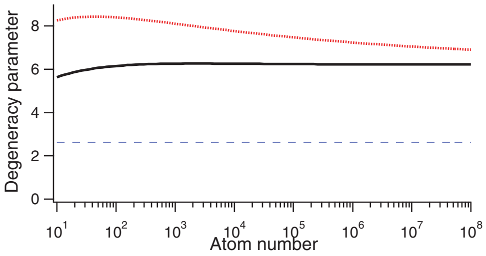

Fig. 3. Degeneracy parameter $\rho(0)\lambda^3$ in function of the atom number N for clouds at the transition temperature. The dotted line corresponds to the semi-classical model *sc* at $T = T^*_{sc}$ and the solid line to model *ex* at $T = T^*_{ex}$. Even if the degeneracy parameters are somewhat different, they both differ significantly to the usual value of 2.612 (dashed horizontal line). This deviation is due to an under-estimation of the ground-state density. The actual values are close to our high-N prediction of 6.24 (see text).

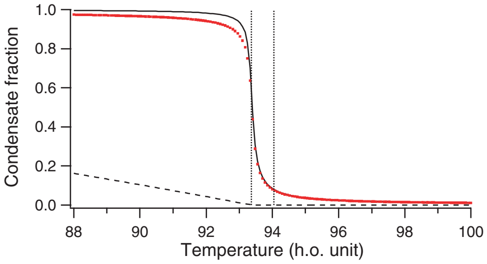

Fig. 4. Condensate atom number fraction N_0/N (dashed line) and peak density fraction $\rho_0(0)/\rho(0)$ (solid line) in function of the temperature in harmonic oscillator unit $\hbar\omega/k_B$, using model *ex*. The cloud contains 10^6 atoms. The transition temperature is $T^*_{ex} = 93.37\hbar\omega/k_B$ and the asymptotic thermodynamic temperature is $T_c = 94.05\hbar\omega/k_B$. The positions of these temperatures are shown as vertical lines in the figure. The ground-state peak density increases much more sharply than the ground-state population around the transition temperature. The former has also a significant value above T^*_{ex}. The model *sc* is indistinguishable for N_0/N, but is slightly different for $\rho_0(0)/\rho(0)$ (dotted line).

only in the more pertinent comparison between the models *sc* and *ex*.

This is first illustrated in Figure 3 where the degeneracy parameter $\rho(0)\lambda^3$ is plotted in function of the atom number for clouds at $T = T^*$. We plot this number for the semi-classical approximation *sc* and for the exact model, *ex*. The two curves are higher than 2.612. This highlights the inaccuracy of the standard semi-classical models (sc_0 or sc_∞) that do not take into account the ground-state contribution. It confirms also the calculation developed above. The degeneracy parameter is astonishingly constant till 10^3 atoms and does not differ much even for smaller atom numbers. Models *sc* and *ex*, which have almost the same transition temperature, have the same asymptotic value of the degeneracy parameter. This value, 6.24, is the one predicted by our high-N analysis. The model *sc* is significantly higher than this value for experimentally accessible atom numbers. This is because our first analysis does not take into account the $\frac{3}{2}\tau$ term of model *sc*. To first order [19],

$$x^*_{sc} \approx \frac{(\tau^*_{sc})^{\frac{3}{2}}}{\sqrt{\zeta(2)}}\left(1 + \frac{9}{8\zeta(2)}\tau^*_{sc}\ln\tau^*_{sc}\right)$$

and is then slightly smaller than $(\tau^*_{sc})^{3/2}/\sqrt{\zeta(2)}$. Consequently the ground-state peak density is bigger at T^*_{sc} using model *sc* than at T_c using the high-N model. The excited states peak density is also higher in model *sc* because of this $\frac{3}{2}\tau g_{\frac{1}{2}}$ term.

The next three figures deal with the cloud properties around the Bose-Einstein threshold. Figures 4 and 5 show the evolution of the condensate fraction N_0/N and the condensate peak density fraction in function of T for two different atom numbers, 10^6 and 10^3. Figure 6 shows the

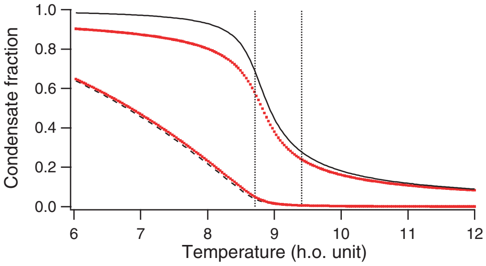

Fig. 5. Same as in Figure 4 but with 10^3 atoms. The transition temperature is $T^*_{ex} = 8.71\hbar\omega/k_B$ and the asymptotic thermodynamic temperature is $T_c = 9.41\hbar\omega/k_B$. Since the number of populated states is considerably reduced compared to Figure 4, the discrepancy between *sc* (dotted lines) and *ex* is more pronounced. This also explains why the increase of the condensate peak density is slower.

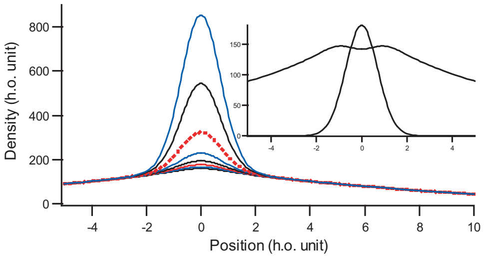

Fig. 6. Atomic density ρ_{ex} in function of r/σ where σ is the size of the harmonic oscillator ground-state. The temperature is $T = 93.37\hbar\omega/k_B$ and the atom number N spans from 0.990×10^6 to 1.004×10^6 by step of 2000 atoms. The curve at threshold is in dotted line and corresponds to 10^6 atoms. The inset shows the excited states and ground state density profile at threshold. The dip around $r = 0$ is mainly due to the first excited state population.

density profile of clouds near degeneracy. What prevails in Figure 4 is the sharp increase of the condensate peak density compared to the condensate population. Moreover the models sc and ex give very close results validating our analysis on the ground-state contribution near degeneracy. This means that the peak density is a much better marker of the Bose-Einstein threshold than the atom number. This feature is in fact used experimentally: the appearance of a small peak over a broad distribution is the usual criterion to distinguish clouds above or below the transition temperature. This sharpness also explains why the value of the peak density is very sensitive to the value of the temperature (cf. Fig. 3). Figure 4 shows also that, above threshold, the ground-state peak density fraction decays slowly. This is even more pronounced in Figure 5 where $N = 10^3$ instead of 10^6. It comes from the fact that the number of populated states is not macroscopic anymore ($k_B T < 10\hbar\omega$) and then the transition is smoother for smaller atom number. Once again, the density is a better marker of degeneracy than the atom number. This figure shows also that the $\frac{3}{2}\tau$ term and the ground-state contribution make the model sc still very close to model ex, respecting the density and population fractions, even for 10^3 atoms.

The above analysis is focused on the peak density i. e. at the centre of the cloud. Figure 6 shows the total density profile of clouds, all at the same temperature, but containing different numbers of atoms around N^*_{ex}, the number of atoms for which $T = T^*_{ex}$ ($N = N^*_{ex}$ corresponds to the dotted line). This figure simulates somehow an experimental observation of BEC threshold. Only the central part is sensitive to the atom number; this corresponds to the condensate growing as the number of atoms is increased and to the fact that the excited states are already saturated for these atom numbers. Moreover, by looking at the graph, one would rather think that the Bose-Einstein transition occurs for a smaller atom number. This points out that the definition on the transition temperature based on an atom number criterion does not fully correspond to the one based on the atomic density which would be more connected to experiments. The inset shows the excited states and ground state density profiles at threshold. The excited states density exhibits a dip in the centre of the cloud, obviously not present in semi-classical models (monotonic functions). We check that the height of the dip is proportional to $1/\tau$ and can almost be totally attributed to the first excited state population. The aim of this paper is to show the importance of the ground-state in the study of non-interacting clouds close to threshold. The inset reveals that the first excited state density is also largely under-estimated; it represents ~10% of the peak density whereas it contributes only to ~0.1% of the population.

We have shown results on the atomic density at the vicinity of the transition temperature. Detection techniques consist rather on 1D-integrated density, corresponding to 2D absorption images, or 2D-integrated density [23]. One can show that, at threshold, the 1D and 2D-integrated peak density of the ground-state are vanishingly small for large atom numbers on contrary to the non-integrated case. The peak 1D-integrated density fraction behaves at threshold as $\sqrt{\tau}$ and the 2D-integrated peak density as τ. For typical atom number this is nevertheless not negligible. This is illustrated in Figure 7 where is plotted the condensate peak density fraction for 3D, 2D and 1D images of clouds at threshold. The calculations use the model ex. At the transition temperature T^*_{ex}, the ground-state contributes to more than 10% for $N < 2500$ atoms in 1D images and for $N < 8 \times 10^6$ atoms for 2D images. It means that, even with the conventional technique of absorption images, the effect should be experimentally observable if interactions could be switched off using, for instance, the magnetic tunability of the scattering length close to a Feshbach resonance [24].

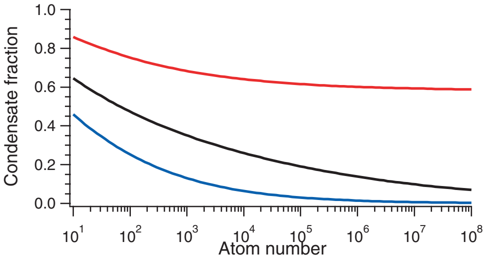

Fig. 7. Contribution of the ground-state on the peak density for, from bottom to top, 1D, 2D and 3D images in function of the number of trapped atoms. The clouds are at the transition temperature T^*_{ex} and the calculations use model ex. A 3D image would give the density in all three dimensions of space [25] whereas a 2D (resp. 1D) image corresponds to the density integrated over one (resp. 2) dimension. For $N = 10^4$ atoms the ground-state contributes to ~26% in 2D images and ~6% in 1D images. In contrast to 3D image, the ground-state contribution is very small for large atom number; it is not for typical atom numbers accessible in experiments.

Apart from the atomic density, two- and three-body inelastic loss rates will also be affected and could be 20 to 30% higher than predicted by model sc_0 around the transition temperature for typical atom numbers. Finally, in most experimental set-ups, the trapping potential is anisotropic and finite size effects are then stronger. Indeed the term $\frac{3}{2}\tau$ in equation (3) should be replaced by $\frac{3}{2}\frac{\tilde{\omega}}{\bar{\omega}}\tau$, with $\bar{\omega} = (\prod_i \omega_i)^{1/3}$ the geometric mean and $\tilde{\omega} = \frac{1}{3}\sum_i \omega_i$ the arithmetic mean [3]. Whatever the anisotropy is, $\tilde{\omega}$ is always larger than ω, making the finite size contribution stronger. To first order and if $k_B T^*_{ex} \gg \hbar\omega_i$ for $i = x, y$ and z, the ground-state contribution should be the same since our high-N analysis does not depend on any anisotropy.

In conclusion, we have shown that the density of an ideal atomic gas is dominated by the ground-state contribution near the transition temperature. The inter-atomic interactions have been neglected in our analysis and will modify our conclusions. With repulsive interactions, the clouds tends to decrease its density at the centre of the cloud whereas it tends to increase it with attractive interactions. Previous calculations have treated separately finite size and interactions effects, both corrections being finally added [6]. Since the ground-state has a nonperturbative effect on the density, our analysis tends to prove that both effects have to be investigated together. The approach of reference [10] could in this respect provide helpful informations. Feshbach resonances, which enable to tune the interactions strength, constitute a powerful tool to check the accuracy of the different theoretical models. Moreover, a full three-dimensional density measurement would also be valuable; this type of measurement is at the edge to be available in our experiment on metastable helium in Orsay [25].

We thank S. Giorgini for stimulating discussions. The Atom Optics group of LCFIO is member of the Institut Francilien de Recherche sur les Atomes Froids (IFRAF).

References

1. *Proceedings of the International School of Physics "Enrico Fermi"*, Course CXL, edited by M. Inguscio, S. Stringari, C.E. Wieman (IOS Press, Amsterdam, 1999)
2. F. Dalfovo, S. Giorgini, L.P. Pitaeskii, S. Stringari, Rev. Mod. Phys. **71**, 463 (1999)
3. S. Grossmann, M. Holthaus, Z. Naturforsch. A **50**, 921 (1995)
4. W. Ketterle, N.J. van Druten, Phys. Rev. A **54**, 656 (1996)
5. K. Kirsten, D.J. Toms, Phys. Rev. A **54**, 4188 (1996)
6. S. Giorgini, L.P. Pitaevskii, S. Stringari, Phys. Rev. A **54**, R4633 (1996)
7. H. Haugerud, T. Haugest, F. Ravndal, Phys. Lett. A **225**, 18 (1997)
8. S. Giorgini, L.P. Pitaevskii, S. Stringari, J. Low Temp. Phys. **109**, 309 (1997)
9. R.K. Pathria, Phys. Rev. A **58**, 1490 (1998)
10. W. Krauth, Phys. Rev. Lett. **77**, 3695 (1996)
11. P. Arnold, B. Tomàšik, Phys. Rev. A **64**, 053609 (2001)
12. K. Huang, *Statistical Mechanics* (Wiley, 1987)
13. L.D. Landau, E.M. Liftshiz, *Statistical Physics* (Butterworths, 1996)
14. H.D. Politzer, Phys. Rev. A **54**, 5048 (1996)
15. C. Herzog, M. Olshanii, Phys. Rev. A **55**, 3254 (1997)
16. Y. Castin, lecture note in *"Coherent atomic matter waves"*, Les Houches, Session LXXII, edited by R. Kaiser, C.I. Westbrook, F. David (Springer, 2001)
17. T. Bergeman, D.L. Feder, N.L. Balazs, B.I. Schneider, Phys. Rev. A **61**, 063605 (2000)
18. In reference [9], the transition temperature was indeed T_{sc} (see later in the text). The transition temperature defined by the maximum of the second derivative of the condensate fraction has been calculated for atom number in the range 10^3–10^8; the relative deviation is below $\sim 10^{-3}$ on the transition temperature and $\sim 10^{-2}$ on the condensate peak density fraction
19. We use the usual definition of Bose functions $g_a(x) = \sum_{l=1}^{\infty} x^l/l^a$. We remind that $g_a(1) = \zeta(a)$ with $\zeta(\ )$ the Riemann Zeta function. Note that $g_1(x) = -\ln(1-x)$ and $dg_a/dx(x) = g_{a-1}(x)/x$
20. After submission of this article, we have been aware of a different type of semi-classical approximations which does not give rise to divergences. See V.I. Yukalov, Phys. Rev. A **72**, 033608 (2005)
21. We use the result of reference [22] for the calculation of the Bose functions near the transition temperature. For the series in model *ex*, the convergence is very slow but can easily be accelerated. For instance, it is much better to write $N = \frac{z}{1-z} + \sum_{l=1}^{\infty} z^l \left(\frac{1}{1-e^{-\tau l}} - 1\right)$ because the second term converges for large l because of the z^l part *and* because of the $\left(\frac{1}{1-e^{-\tau l}} - 1\right)$ part
22. J.E. Robinson, Phys. Rev. **83**, 678 (1951)
23. A. Robert, O. Sirjean, A. Browaeys, J. Poupard, S. Nowak, D. Boiron, C.I. Westbrook, A. Aspect, Science **292**, 461 (2001); published online 22 march 2001 `(10.1126/science.1060622)`
24. V. Vuletic, A.J. Kerman, C. Chin, S. Chu, Phys. Rev. Lett. **82**, 1406 (1999)
25. M. Schellekens, R. Hoppeler, A. Perrin, J. Viana Gomes, D. Boiron, A. Aspect, C.I. Westbrook, Science **310**, 648 (2005); published online 15 september 2005 `(10.1126/science.1118024)`

PHYSICAL REVIEW A **74**, 053607 (2006)

Theory for a Hanbury Brown Twiss experiment with a ballistically expanding cloud of cold atoms

J. Viana Gomes,[1,2] A. Perrin,[1] M. Schellekens,[1] D. Boiron,[1,*] C. I. Westbrook,[1] and M. Belsley[2]
[1]*Laboratoire Charles Fabry de l'Institut d'Optique, UMR 8501 du CNRS et Université Paris 11, 91403 Orsay Cedex, France*
[2]*Departamento de Fisica, Universidade do Minho, Campus de Gualtar, 4710-057 Braga, Portugal*

(Received 19 June 2006; published 7 November 2006)

We have studied one-body and two-body correlation functions in a ballistically expanding, noninteracting atomic cloud in the presence of gravity. We find that the correlation functions are equivalent to those at thermal equilibrium in the trap with an appropriate rescaling of the coordinates. We derive simple expressions for the correlation lengths and give some physical interpretations. Finally a simple model to take into account finite detector resolution is discussed.

DOI: 10.1103/PhysRevA.74.053607 PACS number(s): 03.75.Hh, 05.30.Jp

I. INTRODUCTION

Whether a source emits photons or massive particles, if it is to be used in an interferometric experiment, an essential property is its coherence. The study of coherence in optics has shown that more than one kind of coherence can be defined [1]. The most familiar type of coherence is known as first order coherence and is related to the visibility of interference fringes in an interferometer. It is proportional to the value of the correlation function of the associated field. Second order coherence is less intuitive and corresponds to the correlation function of the intensity or squared modulus of the field. From a particle point of view, second order coherence is a way of quantifying density correlations and is related to the probability of finding one particle at a certain location given that another particle is present at some other location. Particle correlations can arise simply from exchange symmetry effects and exist even when there is no interaction between the particles. This fact was clearly demonstrated in the celebrated Hanbury Brown Twiss experiment which showed a second order correlation for photons coming from widely separated points in a thermal source such as a star [2].

Analogous correlations in massive particles have also been studied, particularly in the field of nuclear physics [3–7]. Spatial correlations using low energy electrons have also been studied [8,9]. The advent of laser and evaporative cooling techniques has also made it possible to look for correlations between neutral atoms and recently a wide variety of different situations have been studied [10–16]. Correlation phenomena are generally richer when using massive particles because they can be either bosons or fermions, they often have a more complex internal structure and a large range of possible interactions with each other. In the field of ultracold atoms, the many theoretical papers to date have included treatments of bosons in a simple three-dimensional (3D) harmonic trap [17,18], a one-dimensional (1D) bosonic cloud in the Thomas-Fermi regime and Tonks-Girardeau limit [19–21], the Mott insulator or superfluid phase for atoms trapped in optical lattices [22] and the two-dimensional (2D) gas [23].

Almost all these theoretical treatments have dealt with atomic clouds at thermal equilibrium. On the other hand, all the experiments so far except Ref. [16] have measured correlations in clouds released from a trap which expand under the influence of gravity and possibly interatomic interactions. It is generally not trivial to know how the correlation properties evolve during expansion. Moreover, matter waves have different dispersion characteristics than light. All this raises interesting questions concerning the value of the correlation lengths during the atomic cloud expansion. In particular we would like to know how to use the results of Ref. [17] to analyze the experimental results of Ref. [15], a conceptually simple experiment in which second order correlations were measured in a freely expanding cloud of metastable helium atoms. The correlation length was defined as the characteristic length of the normalized second order correlation function. We will use the same definition in this paper (see Sec. II A for details).

To illustrate a more general question that comes up in thinking about the coherence of de Broglie waves, consider a beam of particles with mean velocity v hitting a detector. Two obvious length scales come immediately to mind, the de Broglie wavelength $\hbar/(m\Delta v)$ associated with the velocity spread Δv and the length associated with the inverse of the energy spread of the source $\hbar v/m(\Delta v)^2$. These two scales are obviously very different if v is large compared to the velocity spread. In this paper, we will show that in an experiment such as Ref. [15], the correlation length corresponds to neither of the above length scales, although they can be relevant in other situations. We find that the correlation length after an expansion time t of a cloud of initial size s is $\hbar t/ms$. This result is the atom optical analog of the van Cittert-Zernike theorem [24]. It has also been stated in a different form in Ref. [25]. For the special case of an ideal gas in a harmonic trap of oscillation frequency ω, the correlation length can be recast as $\lambda\omega t$ where λ is the thermal de Broglie wavelength. Hence the correlation length after expansion is simply dilated compared to that at equilibrium with the same scaling factor as the spatial extent of the cloud itself.

We will confine ourselves here to the case of a cloud of noninteracting atoms released suddenly from a harmonic

---

[*] Electronic address: denis.boiron@institutoptique.fr; http://www.atomoptic.fr

trap. The paper is organized as follows. We will begin in Sec. II with some simple definitions and general results about the correlation properties of a noninteracting cloud both at thermal equilibrium in a trapping potential and after a ballistic expansion. Without making any assumptions about the form of the trapping potential, we can only find simple analytical results in the limit of a nondegenerate gas. Next we will make a more exact and careful treatment by specializing to the very important case of a harmonic potential. We introduce the flux operator [26] involved in the experimental electronic detection with metastable helium and then calculate the correlation function of the flux. We will summarize the results and give a physical interpretation in Sec. IV. This interpretation will allow us to comment on the rather different case of a continuous beam as in the experiments of Refs. [7,10,14]. In Sec. V we will use our results to analyze the experimentally important problem of finite detector resolution. Finally, the Appendix adds some detailed calculations concerning the expressions found in Sec. III B.

II. GENERAL RESULTS ON CORRELATION FUNCTIONS OF NONINTERACTING GASES

Here we recall some basic results concerning the density and first and second order correlation functions for a cloud of noninteracting bosons at thermal equilibrium. A more detailed analysis can be found in Ref. [17]. Theoretical treatments that take into account interatomic interactions can be found in Refs. [17,18,27]. We also give some approximate results for a noninteracting gas after it has expanded from a trap.

A. Definitions

Consider a cloud of N atoms at thermal equilibrium at a temperature T, confined in a trapping potential. This potential is characterized by $\{\epsilon_{\mathbf{j}}, \psi^0_{\mathbf{j}}(\mathbf{r})\}$ the energy and wave function of level $\mathbf{j}$ (here supposed nondegenerate for simplicity). In second quantization, one defines the field operators

$$\hat{\Psi}^\dagger(\mathbf{r}) = \sum_{\mathbf{j}} \psi^*_{\mathbf{j}}(\mathbf{r})\hat{a}^\dagger_{\mathbf{j}}, \quad \hat{\Psi}(\mathbf{r}) = \sum_{\mathbf{j}} \psi_{\mathbf{j}}(\mathbf{r})\hat{a}_{\mathbf{j}}.$$

The operator $\hat{a}^\dagger_{\mathbf{j}}$ creates and $\hat{a}_{\mathbf{j}}$ annihilates one particle in state $|\psi_{\mathbf{j}}\rangle$ whereas $\hat{\Psi}^\dagger(\mathbf{r})$ creates and $\hat{\Psi}(\mathbf{r})$ annihilates a particle at position $\mathbf{r}$.

Correlation functions and the atomic density are statistical averages of such field operators. We use the Bose-Einstein distribution, $\langle\hat{a}^\dagger_{\mathbf{j}}\hat{a}_{\mathbf{k}}\rangle = \delta_{\mathbf{jk}}(e^{\beta(\epsilon_{\mathbf{j}}-\mu)}-1)^{-1}$ where $\beta = 1/(k_BT)$, k_B is the Boltzmann constant and μ is the chemical potential. The value of μ ensures the normalization $\Sigma_{\mathbf{j}}\langle\hat{a}^\dagger_{\mathbf{j}}\hat{a}_{\mathbf{j}}\rangle = N$. We can then define

(a) the first order correlation function $G^{(1)}(\mathbf{r},\mathbf{r}') = \langle\hat{\Psi}^\dagger(\mathbf{r})\hat{\Psi}(\mathbf{r}')\rangle$,

(b) the second order correlation function $G^{(2)}(\mathbf{r},\mathbf{r}') = \langle\hat{\Psi}^\dagger(\mathbf{r})\hat{\Psi}(\mathbf{r})\hat{\Psi}^\dagger(\mathbf{r}')\hat{\Psi}(\mathbf{r}')\rangle$,

(c) and the density $\rho_{\mathrm{eq}}(\mathbf{r}) = \langle\hat{\Psi}^\dagger(\mathbf{r})\hat{\Psi}(\mathbf{r})\rangle = G^{(1)}(\mathbf{r},\mathbf{r})$.

Several other first and second order correlation functions can be defined (see below) but these are the most common ones. The first order correlation function appears in interference experiments whereas second order correlation functions are related to intensity interference or density fluctuation. First and second order correlation functions are connected for thermal noninteracting atomic clouds. The $G^{(2)}$ function contains a statistical average of the type $\langle\hat{a}^\dagger_{\mathbf{j}}\hat{a}_{\mathbf{k}}\hat{a}^\dagger_{\mathbf{l}}\hat{a}_{\mathbf{n}}\rangle$ which can be calculated through the thermal averaging procedure (Wick theorem [28]). One finds $\langle\hat{a}^\dagger_{\mathbf{j}}\hat{a}_{\mathbf{k}}\hat{a}^\dagger_{\mathbf{l}}\hat{a}_{\mathbf{n}}\rangle = \langle\hat{a}^\dagger_{\mathbf{j}}\hat{a}_{\mathbf{j}}\rangle\langle\hat{a}^\dagger_{\mathbf{k}}\hat{a}_{\mathbf{k}}\rangle \times(\delta_{\mathbf{jl}}\delta_{\mathbf{kn}} + \delta_{\mathbf{jn}}\delta_{\mathbf{kl}}) + \langle\hat{a}^\dagger_{\mathbf{j}}\hat{a}_{\mathbf{j}}\rangle\delta_{\mathbf{kl}}\delta_{\mathbf{jn}}$, which leads to

$$G^{(2)}(\mathbf{r},\mathbf{r}') = \rho_{\mathrm{eq}}(\mathbf{r})\rho_{\mathrm{eq}}(\mathbf{r}') + |G^{(1)}(\mathbf{r},\mathbf{r}')|^2 + \rho_{\mathrm{eq}}(\mathbf{r})\delta(\mathbf{r}-\mathbf{r}').$$

The last term is the so-called shot-noise term. It will be neglected in the following because it is proportional to N whereas the others are proportional to N^2.

It is convenient to define a normalized second order correlation function

$$g^{(2)}(\mathbf{r},\mathbf{r}') = \frac{G^{(2)}(\mathbf{r},\mathbf{r}')}{\rho_{\mathrm{eq}}(\mathbf{r})\rho_{\mathrm{eq}}(\mathbf{r}')}.$$

If the cloud has a finite correlation length, then for distances larger than this length the first order correlation function vanishes. Then $g^{(2)}(\mathbf{r},\mathbf{r}) = 2$ and $g^{(2)}(\mathbf{r},\mathbf{r}') \to 1$ when $|\mathbf{r}-\mathbf{r}'| \to \infty$. This means that the probability of finding two particles close to each other is enhanced by a factor of 2, compared to the situation where they are far apart. This is the famous bunching effect first observed by Hanbury Brown and Twiss with light [2].

The above expression of the $G^{(2)}$ function cannot be applied in the vicinity and below the Bose-Einstein transition temperature. The calculation of $\langle\hat{a}^\dagger_{\mathbf{j}}\hat{a}_{\mathbf{k}}\hat{a}^\dagger_{\mathbf{l}}\hat{a}_{\mathbf{n}}\rangle$ is performed in the grand canonical ensemble which assumes the existence of a particle reservoir that does not exist for the condensate. It is well known [29] that this gives unphysically large fluctuations of the condensate at low enough temperature. This pathology disappears at the thermodynamic limit if there is an interatomic interaction [29]. It has also been shown that it cancels for a finite number of noninteracting particles if one uses the more realistic canonical ensemble [30]. One way to keep using the grand canonical ensemble is to add the canonical result for the ground state [17]. This approach is validated by the results in Ref. [30] and will be used in the following. The largest deviation is expected to occur near the transition temperature [30]. The contribution of the ground state is $-\langle\hat{a}^\dagger_{\mathbf{0}}\hat{a}_{\mathbf{0}}\rangle^2\delta_{\mathbf{j0}}\delta_{\mathbf{k0}}\delta_{\mathbf{l0}}\delta_{\mathbf{n0}}$. Then, with ρ_0 the ground-state density, it follows that,

$$G^{(2)}(\mathbf{r},\mathbf{r}') = \rho_{\mathrm{eq}}(\mathbf{r})\rho_{\mathrm{eq}}(\mathbf{r}') + |G^{(1)}(\mathbf{r},\mathbf{r}')|^2 - \rho_0(\mathbf{r})\rho_0(\mathbf{r}'). \tag{1}$$

The normalized second-order then becomes

$$g^{(2)}(\mathbf{r},\mathbf{r}') = 1 + \frac{|G^{(1)}(\mathbf{r},\mathbf{r}')|^2}{\rho_{\mathrm{eq}}(\mathbf{r})\rho_{\mathrm{eq}}(\mathbf{r}')} - \frac{\rho_0(\mathbf{r})\rho_0(\mathbf{r}')}{\rho_{\mathrm{eq}}(\mathbf{r})\rho_{\mathrm{eq}}(\mathbf{r}')}.$$

Because the ground state density is negligible for a thermal cloud, the normalized correlation function $g^{(2)}(\mathbf{r},\mathbf{r}')$ still goes from 2 to 1 as the separation of $\mathbf{r}$ and $\mathbf{r}'$ increases. On the other hand, for a BEC at $T=0$, only the ground state is occupied. Then $|G^{(1)}(\mathbf{r},\mathbf{r}')|2 = \rho_{\mathrm{eq}}(\mathbf{r})\rho_{\mathrm{eq}}(\mathbf{r}') = \rho_0(\mathbf{r})\rho_0(\mathbf{r}')$ and

$g^{(2)}(\mathbf{r},\mathbf{r}')=1$. The amount of particle bunching present in the second order correlation function can be quantified as $g^{(2)}(\mathbf{r},\mathbf{r}')-1$ and this typically decays exponentially as the modulus squared of the separation between the two points increases. We define the correlation length to be the characteristic length over which the amount of particle bunching decays, that is the distance over which $g^{(2)}(\mathbf{r},\mathbf{r}')-1$ decays to $1/e$ of its maximum value. The correlation length of a BEC is infinite. Such a system is said to exhibit bunching at high temperature over the correlation length and no bunching in the condensed phase.

B. Correlations in an expanding cloud

In most experiments, particle correlations and other characteristics are not directly measured in the atom cloud, (Ref. [16] is an exception). Rather, the cloud is released from a trap and allowed to expand during a "time of flight" before detection. For a sufficiently long time of flight, and neglecting interactions between the atoms, the positions one measures at a detector reflect the initial momenta of the particles. The results of Sec. II A concerning the correlation functions in position space all have analogs in momentum space. In fact the correlation functions in the two reciprocal spaces are closely related. At equilibrium, i.e., inside the trap, the following relationships can be easily derived:

$$\int d\mathbf{p}G^{(1)}(\mathbf{p},\mathbf{p})e^{-i\mathbf{p}\cdot\mathbf{r}/\hbar} = \int d\mathbf{R}G^{(1)}(\mathbf{R}-\mathbf{r}/2,\mathbf{R}+\mathbf{r}/2),$$

$$\int d\mathbf{r}G^{(1)}(\mathbf{r},\mathbf{r})e^{i\mathbf{q}\cdot\mathbf{r}/\hbar} = \int d\mathbf{P}G^{(1)}(\mathbf{P}-\mathbf{q}/2,\mathbf{P}+\mathbf{q}/2).$$

In other words, the spatial correlation length is related to the width of the momentum distribution and the momentum correlation length is related to the width of the spatial distribution, i.e., the size of the cloud. No equally simple and general relationship holds for the second order correlation functions. This is because, close to the BEC transition temperature, and at points where the ground state wave function is not negligible, the special contribution of the ground state, the last term in Eq. (1) must be included, and this contribution depends on the details of the confining potential. On the other hand, for an ideal gas far from the transition temperature one can neglect the ground state density, make the approximation that the correlation length is very short, neglect commutators such as $[\hat{\mathbf{r}},\hat{\mathbf{p}}]$, and then write the thermal density operator as $\hat{\sigma}=e^{-\beta(\hat{\mathbf{P}}^2/2m)}e^{-\beta V(\hat{\mathbf{r}})}$. These approximations lead to

$$G^{(2)}(\mathbf{p},\mathbf{p}') = \rho_{\mathrm{eq}}(\mathbf{p})\rho_{\mathrm{eq}}(\mathbf{p}') + |G^{(1)}(\mathbf{p},\mathbf{p}')|^2$$

and

$$G^{(1)}(\mathbf{P}-\mathbf{q}/2,\mathbf{P}+\mathbf{q}/2) \sim e^{-\beta(\mathbf{P}^2/2m)}\int d\mathbf{r}e^{-\beta V(\mathbf{r})}e^{i\mathbf{q}\cdot\mathbf{r}/\hbar}.$$

One sees that in this limit, the interesting part of $G^{(2)}$ in momentum space is proportional to the square of the Fourier transform of the density distribution and independent of the mean momentum $\mathbf{P}$. This result is the analog of the van Cittert-Zernike theorem [24]. For a trapped cloud of size s_α in the α direction, one has a momentum correlation "length" given by

$$p_\alpha^{(\mathrm{coh})} = \frac{\hbar}{s_\alpha}. \tag{2}$$

If atoms are suddenly released from a trap and allowed to freely evolve for a sufficiently long time t, the positions of the particles reflect their initial momenta and the spatial correlation length at a detector is given by

$$l_\alpha^{(d)} = \frac{p_\alpha^{(\mathrm{coh})}}{m}t = \frac{\hbar t}{ms_\alpha}. \tag{3}$$

The normalized second order correlation function is then a Gaussian of rms width $l^{(d)}/\sqrt{2}$. This result was experimentally confirmed in Ref. [15]. One wonders however, to what extent the approximations we have made are valid. The clouds used in Ref. [15] were in fact very close to the transition temperature so that effects due to the Bose nature of the density matrix may be important. Although the time of flight was very long, it is useful to quantify the extent to which identifying the momentum correlation length in the trap with the spatial correlation length at the detector is accurate. Finally, the effect of gravity on the falling atoms never appears in the above approximate treatment, and we would like to clarify the role it plays. In order to answer these questions we undertake a more careful calculation. We will confine ourselves to atoms initially confined in a harmonic trap, a good approximation to the potential used in most experiments, and happily, one for which the eigenstates and energies are known exactly.

III. DENSITY AND CORRELATION FUNCTIONS FOR A HARMONIC TRAP

A. At equilibrium in the trap

The eigenfunctions for a three-dimensional harmonic potential of oscillation frequency ω_α in the α direction, are given by

$$\psi_{\mathbf{j}}^0(\mathbf{r}) = \prod_{\alpha=x,y,z} A_{j_\alpha}e^{-r_\alpha^2/2\sigma_\alpha^2}H_{j_\alpha}(r_\alpha/\sigma_\alpha).$$

Here $\sigma_\alpha=\sqrt{\hbar/m\omega_\alpha}$ is the harmonic oscillator ground-state size, H_{j_α} is the Hermite polynomial of order j_α and $A_{j_\alpha}=[\sqrt{\pi}\sigma_\alpha 2^{j_\alpha}(j_\alpha)!]^{-1/2}$. The eigenenergies are given by $\epsilon_{\mathbf{j}}=\Sigma_{\alpha=x,y,z}\hbar\omega_\alpha(j_\alpha+1/2)$. Then [17,29], with $\tau_\alpha=\beta\hbar\omega_\alpha$ and $\tilde{\mu}=\mu-\hbar\Sigma\omega_\alpha/2$, one finds

$$\rho_{\mathrm{eq}}(\mathbf{r}) = \frac{1}{\pi^{3/2}}\sum_{l=1}^{\infty} e^{\beta l\tilde{\mu}}\prod_\alpha \frac{1}{\sigma_\alpha\sqrt{1-e^{-2\tau_\alpha l}}}e^{-\tanh(\tau_\alpha l/2)(r_\alpha^2/\sigma_\alpha^2)}$$

and

$$G^{(1)}(\mathbf{r},\mathbf{r}') = \frac{1}{\pi^{3/2}}\sum_{l=1}^{\infty} e^{\beta l\tilde{\mu}}\prod_{\alpha}\frac{1}{\sigma_\alpha\sqrt{1-e^{-2\tau_\alpha l}}}\exp\left[-\tanh\left(\frac{\tau_\alpha l}{2}\right)\right. \\ \left.\times\left(\frac{r_\alpha + r'_\alpha}{2\sigma_\alpha}\right)^2 - \coth\left(\frac{\tau_\alpha l}{2}\right)\left(\frac{r_\alpha - r'_\alpha}{2\sigma_\alpha}\right)^2\right].$$

The above expressions can be transformed into more familiar forms in limiting cases:

(i) For high temperature, $\mu\rightarrow-\infty$ and one recovers the Maxwell-Boltzmann distribution. The density is $\rho_{\mathrm{eq}}(\mathbf{r}) = \frac{N}{\lambda^3}\Pi_\alpha \tau_\alpha e^{-(\tau_\alpha/2)(r_\alpha^2/\sigma_\alpha^2)}$ with $\lambda = \hbar\sqrt{2\pi}/\sqrt{mk_BT}$ the thermal de Broglie wavelength. The size of the cloud is $s_\alpha = \sigma_\alpha/\sqrt{\tau_\alpha} = \sqrt{k_BT/m\omega_\alpha^2}$. The first order correlation function is

$$G^{(1)}(\mathbf{r},\mathbf{r}') = \frac{N}{\lambda^3}\prod_\alpha \tau_\alpha e^{-(\tau_\alpha/2)((\mathbf{r}_\alpha + \mathbf{r}'_\alpha)/2\sigma_\alpha)^2} e^{-\pi((\mathbf{r}_\alpha - \mathbf{r}'_\alpha)/\lambda)^2}. \tag{4}$$

Using our definition, the correlation length is $l^{(t)} = \lambda/\sqrt{2\pi}$.

(ii) For a temperature close to but above the Bose-Einstein transition temperature, one must keep the summation over the index l. The density is $\rho_{\mathrm{eq}}(\mathbf{r}) = \frac{1}{\lambda^3}g_{3/2}(e^{\beta\tilde{\mu}}\Pi_\alpha e^{-(\tau_\alpha/2)(r_\alpha^2/\sigma_\alpha^2)})$, where $g_a(x) = \Sigma_{l=1}^{\infty} x^l/l^a$ is a Bose function. The first order correlation function is

$$G^{(1)}(\mathbf{r},\mathbf{r}') = \frac{1}{\lambda^3}\sum_{l=1}^{\infty}\frac{e^{l\beta\tilde{\mu}}}{l^{3/2}} \\ \times\prod_\alpha e^{-(\tau_\alpha l/2)((\mathbf{r}_\alpha + \mathbf{r}'_\alpha)/2\sigma_\alpha)^2} e^{-(\pi/l)((\mathbf{r}_\alpha - \mathbf{r}'_\alpha)/\lambda)^2}.$$

As the temperature decreases, the number of values of l that contribute significantly to the sum increases. It is then clear from the above expression for $G^{(1)}$ that the correlation length near the center of the trap will increase and that the normalized correlation function is no longer Gaussian. Far from the center, only the $l=1$ term is important and the correlation function remains Gaussian. Thus close to degeneracy the correlation length is position dependent (for an explicit example see Sec. III B 5).

(iii) Near and below the transition temperature, the second order correlation function is given by Eq. (1) with $\rho_0(\mathbf{r}) = \frac{e^{\beta\tilde{\mu}}}{1-e^{\beta\tilde{\mu}}}\Pi_\alpha \frac{e^{-r_\alpha^2/\sigma_\alpha^2}}{(\sqrt{\pi}\sigma_\alpha)^3}$. As the temperature decreases, the correlation at zero distance, $g^{(2)}(0,0)$ decreases from 2 to 1 and the correlation length increases. Around the transition temperature, $g^{(2)}(0,0)$ is already significantly different from 2 since the condensate peak density is already very large for a noninteracting harmonically trapped cloud [31]. At $T=0$, the correlation length is infinite and $g^{(2)}(\mathbf{r},\mathbf{r}')=1$.

B. Correlations in a harmonically trapped cloud after expansion

Here we consider the cloud after expansion. First we discuss two classes of detection methods which must be distinguished before calculating correlation functions.

1. Detection

We assume that the trapping potential is switched off instantaneously at $t=0$. The cloud expands and falls due to gravity. Two types of detection can be performed:

(a) *Snap shot*. An image is taken of the entire cloud at $t=t_0$. We have then access to

$$G_{im}^{(2)}(\mathbf{r},t_0;\mathbf{r}',t_0) = \langle\hat{\Psi}^\dagger(\mathbf{r},t_0)\hat{\Psi}(\mathbf{r},t_0)\hat{\Psi}^\dagger(\mathbf{r}',t_0)\hat{\Psi}(\mathbf{r}',t_0)\rangle.$$

The usual imaging technique is absorption, and so one has access to the above correlation functions integrated along the imaging beam axis. This was used for the experiments of Refs. [12,13].

(b) *Flux measurement*. The atoms are detected when they cross a given plane. We will only consider the situation in which this plane is horizontal at $z=H$. One has access to

$$G_{fl}^{(2)}(\mathbf{r}=\{x,y,z=H\},t;\mathbf{r}'=\{x',y',z'=H\},t') \\ = \langle\hat{I}(\mathbf{r},t)\hat{I}(\mathbf{r}',t')\rangle,$$

where $\hat{I}$ is the flux operator defined below. The detection systems required for such experiments correspond most closely to those of Refs. [10,15], in which a microchannel plate, situated below the trapped cloud, recorded the arrival times and in one case the positions of the atoms. It also corresponds closely to imaging a cloud that crosses a thin sheet of light [32], or to the experiment of Ref. [14], in which the transmission of a high finesse optical cavity records atoms as they cross the beam.

These two correlation functions are different, but if the detection is performed after a long time of flight, they are in fact nearly equivalent. This equivalence will be discussed in the following.

The flux operator is defined quantum mechanically by

$$\hat{I}(\mathbf{r},t) = \frac{\hbar}{m}\,\mathrm{Im}[\hat{\Psi}^\dagger(\mathbf{r},t)\partial_z\hat{\Psi}(\mathbf{r},t)] = \frac{\hbar}{2mi}[\hat{\Psi}^\dagger(\mathbf{r},t)\partial_z\hat{\Psi}(\mathbf{r},t) \\ - \partial_z\hat{\Psi}^\dagger(\mathbf{r},t)\hat{\Psi}(\mathbf{r},t)].$$

The flux has thus the dimensions of a density times a velocity. We will give the explicit expression of this velocity in the Sec. III B 4. Here, the atomic field operators $\hat{\Psi}(\mathbf{r},t)$ depend on space coordinates as well as on time. They represent the time evolution of the atomic field during the flight of the atoms, falling from the trap. The field operators for the falling cloud can be easily derived if we assume that there are no interactions between the atoms and that the occupation number in each mode is constant (as in free expansion). In this case, these operators can be defined as

$$\hat{\Psi}^\dagger(\mathbf{r},t) = \sum_{\mathbf{j}}\psi_{\mathbf{j}}^*(\mathbf{r},t)\hat{a}_{\mathbf{j}}^\dagger, \quad \hat{\Psi}(\mathbf{r},t) = \sum_{\mathbf{j}}\psi_{\mathbf{j}}(\mathbf{r},t)\hat{a}_{\mathbf{j}},$$

where the spatiotemporal dependence is carried by the wave function and the statistical occupation by the creation and annihilation operators.

2. Ballistic expansion of a harmonic oscillator stationary state

After switching off the trap, the harmonic oscillator wave functions noted $\psi_{\mathbf{j}}^0$ are no longer stationary states. There are two ways to calculate the correlation after expansion: propagation of wave functions or propagation of the density matrix (the Schrödinger or the Heisenberg picture). In the following we will use the first approach which is physically more transparent (see Ref. [33] for the Heisenberg picture).

The ballistic expansion of a cloud is easy to calculate with the appropriate Green function. The Green function K is defined as

$$\psi_{\mathbf{j}}(\mathbf{r},t) = \int_{-\infty}^{\infty} \mathbf{d}r_0 K(\mathbf{r},t;\mathbf{r}_0,t_0)\psi^0_{\mathbf{j}}(\mathbf{r}_0,t_0).$$

As the $\psi^0_{\mathbf{j}}$ functions are stationary states for $t<0$, we can take $t_0=0$ in the following. The Green function for particles in an arbitrarily time-varying quadratic potential is known [34]. After expansion, the potential is only due to gravity and the Green function is then

$$K(\mathbf{r},t;\mathbf{r}_0) = \left(\frac{m}{2i\pi\hbar t}\right)^{3/2} e^{ia(\mathbf{r}-\mathbf{r}_0)^2} e^{ib(z+z_0)} e^{-ic}$$

with $a=\frac{m}{2\hbar t}$, $b=\frac{mgt}{2\hbar}$, and $c=\frac{mg^2t^3}{24\hbar}$.

One can then derive an analytical expression of $\psi_{\mathbf{j}}(\mathbf{r},t)$ [35,36],

$$\psi_{\mathbf{j}}(\mathbf{r},t) = e^{i\phi(\mathbf{r},t)}\prod_{\alpha}\frac{e^{ij_\alpha(\delta_\alpha+3\pi/2)}}{\sqrt{\omega_\alpha t - i}}\psi^0_{\mathbf{j}}(\tilde{\mathbf{r}}), \tag{5}$$

where $\delta_\alpha = \tan^{-1}\left(\frac{1}{\omega_\alpha t}\right)$,

$$\phi(\mathbf{r},t) = \frac{m}{2\hbar t}\left[(\tilde{x}\omega_x t)^2 + (\tilde{y}\omega_y t)^2 + (\tilde{z}\omega_z t)^2 + 2gt^2\left(z - \frac{1}{8}gt^2\right)\right] - c - \frac{3\pi}{4} \tag{6}$$

and, with $\tilde{\mathbf{r}}=\{\tilde{x},\tilde{y},\tilde{z}\}$,

$$\tilde{x} = \frac{x}{\sqrt{1+\omega_x^2t^2}}, \quad \tilde{y} = \frac{y}{\sqrt{1+\omega_y^2t^2}}, \quad \tilde{z} = \frac{H - \frac{1}{2}gt^2}{\sqrt{1+\omega_z^2t^2}}. \tag{7}$$

In the case of flux measurement, the position of the detector is fixed at $z=H$. The phase $\phi(\tilde{x},\tilde{y},t)$ is global as it does not depend on the index $\mathbf{j}$; it will cancel in second order correlation measurements. This is in contrast to interferometric measurements where it is this phase that gives rise to fringes. The above results show that after release, the wave function is identical to that in the trap except for a phase factor and a scaling factor in the positions [37]. This scaling is obviously a property of a harmonic potential, and it considerably simplifies the expression of the correlation functions as we will see below.

3. Flux operator

Using $\partial_z H_n(z) = 2nH_{n-1}(z)$, the spatial derivative of the wave function can be written

$$\partial_z\psi_{\mathbf{j}}(\mathbf{r},t) = \frac{m}{\hbar}[(iv_2 - v_1)\psi_{j_z}(z,t) - iv_3\sqrt{j_z}\psi_{j_z-1}(z,t)]\psi_{j_x}(x,t)\psi_{j_y}(y,t),$$

where the velocities v_1, v_2, and v_3 are time dependent and are given by

$$v_1(t) = \omega_z\frac{H - \frac{1}{2}gt^2}{1+\omega_z^2t^2}, \tag{8}$$

$$v_2(t) = \frac{1}{t}\left(H + \frac{1}{2}gt^2 - \frac{H - \frac{1}{2}gt^2}{1+\omega_z^2t^2}\right), \tag{9}$$

$$v_3(t) = \frac{\sqrt{2}\omega_z\sigma_z}{\sqrt{1+\omega_z^2t^2}}e^{i\delta_z}. \tag{10}$$

The velocity v_2 is usually much larger than the other two and will give the dominant contribution for the mean flux and the second order correlation function. An atom with zero initial velocity will acquire after a time t a velocity gt which is close to $v_2(t)$. The flux operator is

$$\hat{I}(\mathbf{r},t) = \sum_{\mathbf{j},\mathbf{k}}\left(v_2\psi^*_{\mathbf{j}}\psi_{\mathbf{k}} - \frac{1}{2}(v_3\sqrt{k}\psi^*_{\mathbf{j}}\psi_{\mathbf{k}-1_{\mathbf{z}}} + v_3^*\sqrt{j}\psi^*_{\mathbf{j}-1_{\mathbf{z}}}\psi_{\mathbf{k}})\right)\hat{a}^\dagger_{\mathbf{j}}\hat{a}_{\mathbf{k}}, \tag{11}$$

where $\mathbf{j}-\mathbf{1_z}$ is the vector (j_x,j_y,j_z-1) and where we write $\psi=\psi(\mathbf{r},t)$.

4. Mean density and mean flux

We will first calculate the mean density $\rho(\mathbf{r},t) = \langle\hat{\Psi}^\dagger(\mathbf{r},t)\hat{\Psi}(\mathbf{r},t)\rangle$. Using Eq. (5), one finds easily that $\rho(\mathbf{r},t) = \frac{1}{\prod_\alpha\sqrt{1+\omega_\alpha^2t^2}}\rho_{\text{eq}}(\tilde{\mathbf{r}})$. This means that the density has the same form during expansion up to an anisotropic scale factor given by Eq. (7) [37,38]. The statistical average of Eq. (11) leads to

$$\langle\hat{I}(\mathbf{r},t)\rangle = \sum_{\mathbf{j}}\left(v_2|\psi_{\mathbf{j}}|^2 - \frac{\sqrt{j_z}}{2}(v_3\psi^*_{j_z}\psi_{j_z-1} + v_3^*\psi_{j_z}\psi^*_{j_z-1})|\psi_{j_x}\psi_{j_y}|^2\right) \times\langle\hat{a}^\dagger_{\mathbf{j}}\hat{a}_{\mathbf{j}}\rangle.$$

Because $v_3\psi^*_{j_z}\psi_{j_z-1} = i\frac{|v_3|}{\sqrt{1+\omega_z^2t^2}}\psi^0_{j_z}(\tilde{z})\psi^0_{j_z-1}(\tilde{z}) = -v_3^*\psi_{j_z}\psi^*_{j_z-1}$, the second term cancels out. Then, without any approximation,

$$\langle\hat{I}(\mathbf{r},t)\rangle = \frac{v_2(t)}{\prod_\alpha\sqrt{1+\omega_\alpha^2t^2}}\rho_{\text{eq}}(\tilde{\mathbf{r}}) = v_2(t)\rho(\mathbf{r},t).$$

The flux is proportional to the density of a cloud at thermal equilibrium with rescaled coordinates. This means that the mean flux of an expanding noninteracting cloud is proportional to the atomic density without any approximation. This result holds with and without gravity taken into account.

5. Second order correlation

Here we calculate the correlation functions. A discussion is given in the next section. The snap-shot correlation function is

$$G_{im}^{(2)}(\mathbf{r},t;\mathbf{r}',t) = \sum_{\mathbf{j},\mathbf{k},\mathbf{l},\mathbf{n}} \psi_{\mathbf{j}}^{*}\psi_{\mathbf{k}}\psi_{\mathbf{l}}'^{*}\psi_{\mathbf{n}}'\langle \hat{a}_{\mathbf{j}}^{\dagger}\hat{a}_{\mathbf{k}}\hat{a}_{\mathbf{l}}^{\dagger}\hat{a}_{\mathbf{n}}\rangle.$$

Using Eq. (5), one finds, without any approximation (except the neglect of the shot-noise term):

$$G_{im}^{(2)}(\mathbf{r},t;\mathbf{r}',t) = \frac{1}{\prod_{\alpha}(1+\omega_{\alpha}^{2}t^{2})} \times[\rho_{\mathrm{eq}}(\tilde{\mathbf{r}})\rho_{\mathrm{eq}}(\tilde{\mathbf{r}}') + |G^{(1)}(\tilde{\mathbf{r}},\tilde{\mathbf{r}}')|^{2} - \rho_{0}(\tilde{\mathbf{r}})\rho_{0}(\tilde{\mathbf{r}}')].$$

As in the case of the mean density, the snap-shot correlation function has the same form as in the trap except for an anisotropic scale factor.

The calculation of $G_{fl}^{(2)}$ is similar,

$$\langle \hat{I}(\mathbf{r},t)\hat{I}(\mathbf{r}',t')\rangle = -\left(\frac{\hbar}{2m}\right)^{2} \sum_{\mathbf{j},\mathbf{k},\mathbf{l},\mathbf{n}} [\psi_{\mathbf{j}}^{*}(\partial_{z}\psi_{\mathbf{k}}) - (\partial_{z}\psi_{\mathbf{j}}^{*})\psi_{\mathbf{k}}] \times[\psi_{\mathbf{l}}'^{*}(\partial_{z}\psi_{\mathbf{n}}') - (\partial_{z}\psi_{\mathbf{l}}'^{*})\psi_{\mathbf{n}}']\langle \hat{a}_{\mathbf{j}}^{\dagger}\hat{a}_{\mathbf{k}}\hat{a}_{\mathbf{l}}^{\dagger}\hat{a}_{\mathbf{n}}\rangle.$$

Two major differences appear compared to the mean flux calculation: the terms in v_3 and the phase factor $\delta_{\alpha}+3\pi/2$ in Eq. (5) do not cancel. This makes the exact calculation very tedious. It is postponed to the Appendix.

Experiments are usually performed in situations satisfying two conditions: (1) the width of the cloud after expansion is much larger than that of the trapped cloud, and (2) the mean velocity acquired during free fall is much larger than the velocity spread of the trapped cloud. The first condition means that $\omega_{\alpha}t \gg 1$ and the second one that $gt \gg \sqrt{k_B T/m}$. The latter condition also means that the mean arrival time, $t_0 = \sqrt{2H/g}$, is much larger than the time width $\sqrt{k_B T/mg^2}$ of the expanding cloud. With these approximations the scale factors become quite simple. $\tilde{x} \sim \frac{x}{\omega_x t_0}$, $\tilde{y} \sim \frac{y}{\omega_y t_0}$ and $\tilde{z} \sim \frac{H-(1/2)gt^2}{\omega_z t_0} \sim \frac{g(t_0-t)}{\omega_z}$. In particular, the coordinate $\tilde{z}$ is proportional to the arrival time t. This means that in experiments that measure arrival times, the results have the same form when expressed as a function of vertical position.

In the correlation function of the flux, the above approximations also lead to $v_2 \approx \sqrt{2gH}$ and $|\sqrt{j_z}v_3/v_2| \approx \sqrt{\frac{k_B T}{\hbar\omega_z}}\frac{\sigma_z}{\sqrt{2H}} = \frac{s_z}{\sqrt{2H}}$ where s_z is the width of the cloud inside the trap and where the typical value of the occupied trap level, j_z, is $\sim\frac{k_B T}{\hbar\omega_z}$. The term containing v_3 is then very small compared to the one proportional v_2. In Ref. [15] for instance the above ratio is $\sim 10^{-5}$. We will neglect terms containing v_3 in the following. The phase factors δ_{α} in Eq. (5) are also very small since $\omega_{\alpha}t \gg 1$ and can be neglected (see the Appendix).

Under all these approximations, one finds

$$G_{fl}^{(2)}(\mathbf{r},t;\mathbf{r}',t') = \frac{v_2 v_2'}{\prod_{\alpha}\sqrt{(1+\omega_{\alpha}^{2}t^{2})(1+\omega_{\alpha}^{2}t'^{2})}}[\rho_{\mathrm{eq}}(\tilde{\mathbf{r}})\rho_{\mathrm{eq}}(\tilde{\mathbf{r}}') + |G^{(1)}(\tilde{\mathbf{r}},\tilde{\mathbf{r}}')|^{2} - \rho_{0}(\tilde{\mathbf{r}})\rho_{0}(\tilde{\mathbf{r}}')].$$

We again find the same correlation function as in the trap, rescaled by a slightly different factor compared to $G_{im}^{(2)}$. This factor simply reflects the expansion of the cloud between the times t and t'.

The scaling laws for the harmonic potential result in a very simple expression for the correlation lengths at the detector,

$$l_{\alpha}^{(d)} = l^{(t)}\sqrt{1+(\omega_{\alpha}t)^{2}}. \tag{12}$$

Where $l_{\alpha}^{(d)}$ is the correlation length along the α direction at the detector and $l_{\alpha}^{(t)}$ is the correlation length in the trap. If the gas is far from degeneracy $l^{(t)}=\frac{\lambda}{\sqrt{2\pi}}$, and we recover the result of Eq. (3). Close to degeneracy the correlation length is position dependent. In the case of a pulse of atoms as in Ref. [15], this formula applies along all three space axes. In addition, when making a flux measurement, one often expresses the longitudinal correlation length as a correlation time. For a pulse of atoms from a harmonic trap, with a mean velocity v at the detector, the correlation time is

$$t^{(\mathrm{coh})} = \frac{l_{z}^{(d)}}{v} = l^{(t)}\frac{\omega_z}{g}. \tag{13}$$

It is independent of the propagation time as long as $\omega_z t \gg 1$.

These calculations are illustrated in the following figures. For simplicity we have used an isotropic trapping potential. As pointed out above, the normalized second-order correlation functions $g_{im}^{(2)}$ and $g_{fl}^{(2)}$ are virtually identical with typical parameters (see the Appendix) and we will use the shorter notation $g^{(2)}$. In Fig. 1 we show the normalized correlation function $g^{(2)}(\tilde{r},0)$ as a function of $\tilde{r} \sim r/\omega t$ for various temperatures in the vicinity the Bose-Einstein phase transition T^{*}. We use the saturation of the excited state population to define T^{*} [31]. This is the correlation function *at the center of the cloud.* One sees that at $T=T^{*}$ (the thick dashed line in the figure), the correlation function at zero distance is already significantly diminished compared to higher temperatures. The correlation length, on the other hand, is larger than $\lambda\omega t/\sqrt{2\pi}$. Also, one sees that the correlation function is almost flat for temperatures a few percent below T^{*}.

In many experiments of course, one does not measure the local correlation function, but the correlation function averaged over all points in the sample [15]. The effect of this averaging is shown in Fig. 2. We plot $g_{m}^{(2)}(\tilde{r}) = \frac{\int d\mathbf{R}G^{(2)}(\mathbf{R}+\tilde{r}\mathbf{e},\mathbf{R})}{\int d\mathbf{R}G^{(1)}(\mathbf{R}+\tilde{r}\mathbf{e},\mathbf{R}+\tilde{r}\mathbf{e})G^{(1)}(\mathbf{R},\mathbf{R})}$, where the vector $\mathbf{e}$ is a unit vector in some direction. One sees that the amplitude of the correlation function decreases more slowly, and that after averaging, the correlation length hardly varies as one passes T^{*}.

To illustrate how local the effects which distinguish Figs. 1 and 2 are, we also plot in Fig. 3 the value of $g^{(2)}(\tilde{r},\tilde{r})$, the zero distance correlation function as a function of $\tilde{r}$ in the vicinity of the cloud center. One sees that even below T^{*}, the

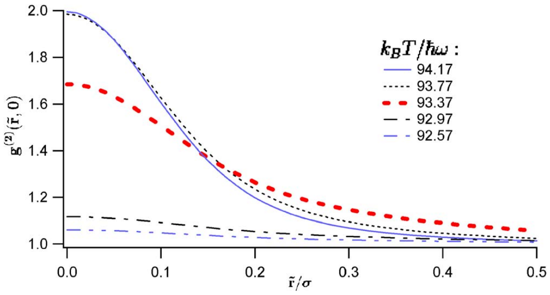

FIG. 1. (Color online) Two-body normalized correlation function at the trap center, $g^{(2)}(\tilde{r},0)$ for 10^6 atoms as a function of the position $\tilde{r}=r/\omega t$ for various temperatures around transition temperature. The horizontal axis is labelled in units of the size of the harmonic oscillator wave function σ. The thick dashed line corresponds to the transition temperature T^* defined in Ref. [31] and is $93.37\hbar\omega/k_B$ for 10^6 atoms. The temperature step is $0.4\hbar\omega/k_B$. The thermal de Broglie wavelength is $\sim 0.26\sigma$. The effect of the ground state population is clearly visible in the reduction of $g^{(2)}(0,0)$, and in the rapid flattening out of the correlation function slightly below T^*.

correlator is close to 2 at a rescaled distance of a few times the harmonic oscillator length scale. We can simply interpret this effect by observing that at $\tilde{r}$ the effective chemical potential is $\mu - V(\tilde{r})$. Away from the center, the effective chemical potential is small and this part of the cloud can be described as a Boltzmann cloud.

Before interpreting these results further, we recall some of our assumptions and their possible violation. First, we obtain Eq. (12) if we make a semiclassical approximation assuming that k_BT greatly exceeds the energy spacing in the trap in each dimension of space. In an anisotropic trap, this condition can be violated in one or two dimensions and then correlation length along these directions will be larger and can become infinite for a small enough temperature. Second, we have assumed a noninteracting gas throughout.

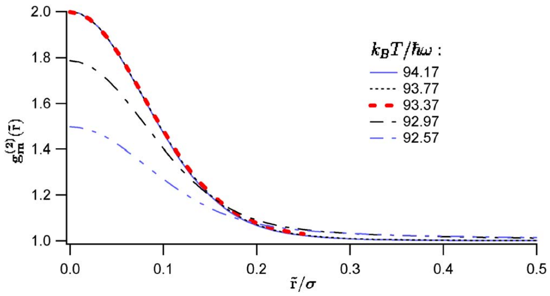

FIG. 2. (Color online) Two-body normalized correlation function $g_m^{(2)}(\tilde{r})$ for 10^6 atoms as a function of $\tilde{r}$. This function is an average of the two-body correlation function over the cloud. The conditions are the same conditions as for Fig. 1. Unlike Fig. 1, the shape is always almost Gaussian and converges more slowly to a flat correlation for low temperatures. This is because only a small region around $\tilde{r}=0$ is fully sensitive to the quantum atomic distribution.

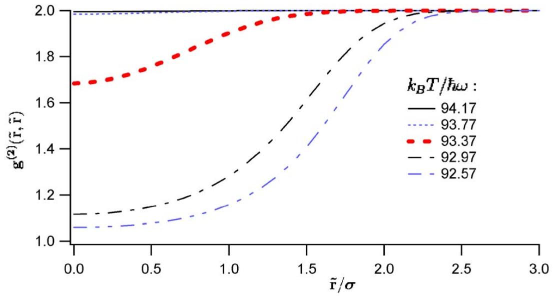

FIG. 3. (Color online) Two-body normalized correlation function $g^{(2)}(\tilde{r},\tilde{r})$ for 10^6 atoms as a function of $\tilde{r}$. The conditions are the same as for Fig. 1. Even for $T<T^*$ the correlation goes to 2 far from the center. This is due to the finite spatial extent of the condensate. It can also be understood in terms of the chemical potential $\mu(\tilde{r})$ which, in a local density approximation, decreases as $\tilde{r}$ increases and thus the correlation is equivalent to that of a hotter cloud.

Repulsive interactions inflate the trapped cloud, and thus reduce the length $l^{(d)}$ at the detector. We expect this to be the main effect for atomic clouds above the Bose-Einstein transition threshold, where the effects of atomic interactions are typically small. The reduction is typically a few percent. Even slightly below T^*, the condensate density is quite high, expelling the thermal atoms from the center of the trap. The effects of interactions inside the trap and during the cloud's expansion cannot be neglected. Taking them into account is then complex and beyond the scope of this paper.

IV. PHYSICAL INTERPRETATIONS

The main result of this paper is that in an experiment which averages over a detector in the sense of Fig. 2, even at $T=T^*$, the correlation lengths at the detector are well approximated by

$$l_\alpha^{(d)} = l^{(t)}\omega_\alpha t.$$

The correlation length increases linearly with the time of flight. A simple way to understand this result is to consider the analogy with optical speckle. Increasing the time of flight corresponds to increasing the propagation distance to the observation plane in the optical analog. The speckle size, i.e., the correlation length, obviously increases linearly with the propagation distance. Another way to understand the time dependence is to remark that after release, the atomic cloud is free and the phase space density should be constant. Since the density decreases with time as $\Pi_\alpha(\omega_\alpha t)$ and the spread of the velocity distribution is constant, the correlation volume must increase by the same factor [25].

Yet another way to look at the correlation length is to observe that, far from degeneracy, the correlation length inside the trap is the thermal de Broglie wavelength, that is, $\frac{\lambda}{\sqrt{2\pi}}=\hbar/\Delta p$ where $\Delta p=m\Delta v$ is the momentum width of the cloud. By analogy, after expansion, the correlation length is $\hbar/(\Delta p)_{\text{loc}}$, where $(\Delta p)_{\text{loc}}$ is the "local" width of the momentum distribution. As the pulse of atoms propagates, fast and slow atoms separate, so that at a given point in space the width in momentum is reduced by a factor $\frac{s_\alpha}{\Delta v t}$.

For a continuous beam, the formula (12) only applies in the transverse directions. In the longitudinal direction, an argument in terms of a local thermal de Broglie wavelength can be used to find the coherence length or time. If the atoms travel at velocity v without acceleration, the momentum spread and correlation length remain constant. Defining the energy width of the beam as $\Delta E = mv\Delta v$, one finds a correlation time $\lambda / v = \hbar / \Delta E$ [7]. In the presence of an acceleration such as gravity, the momentum spread of the beam decreases (the energy spread at any point ΔE is constant), which increases the correlation length. The correlation time, however, remains $\hbar / \Delta E$ [10].

The result that the coherence length of a cloud of atoms can vary with the distance of propagation, is in apparent contradiction with the results of Refs. [39,40]. Those papers give convincing reasons, both experimental and theoretical, for why the dispersion associated with the propagation of massive particles should *not* result in an increase of the coherence length. The contradiction is resolved by noting that the Mach-Zender interferometer considered in that work is sensitive to the function $f(\mathbf{r},t) = \int d\mathbf{R} G^{(1)}(\mathbf{R},t;\mathbf{R}+\mathbf{r},t)$. If the Hamiltonian commutes with the momentum operator, i.e., if plane waves are stationary states, one can easily demonstrate that the function f and hence its width are independent of the time t. The experiments we analyze are sensitive to the *modulus of* $G^{(1)}$ whose width will always increase with time. Thus the coherence length can depend on the interferometer as well as the source.

The role of the acceleration of gravity in these experiments is minor. It governs the propagation time and the speed of the particles when they reach the detector. In a pulsed beam, gravity has no effect on the correlation length, although it does affect the correlation time. It also renders the rescaling of the z coordinate linear for large times so that the correlation function in position z and time have the same form. Without gravity (cancellation with a magnetic field gradient for example), a pulse of atoms would take longer to reach the detector, thereby giving the correlation length more time to dilate, and in addition they would hit the detector at a lower velocity. The correlation time would then increase with time and its order of magnitude would be $\frac{\lambda \omega t_0}{v_T} = \frac{\hbar\omega}{k_B T} t_0$ where $v_T = \sqrt{k_B T / m}$ is the thermal velocity and $t_0 = v_T / H$ is the time of flight to the detector.

V. EFFECT OF FINITE DETECTOR RESOLUTION

In the preceding sections, the detector was considered ideal, i.e., with arbitrarily good spatial and temporal resolution. Here we will consider a model of a more realistic detector, in which we suppose that the spatial resolution in the x-y plane is Gaussian. This is often the case due to smearing in pixels [13,16] and is also approximately true in Ref. [15]. To simplify the discussion we will restrict our analysis to the case $T \gg T^*$ and use a Maxwell-Boltzmann distribution rather than Bose-Einstein distribution. In this case, each direction of space is independent and we will only consider one direction at a time in the following.

There are three different scales in the problem: the size of the cloud at the detector $s(t) \approx \sqrt{\frac{k_B T}{m}} t$, the correlation length at the detector $l^{(d)}$ and the rms width of the detector resolution function d. The definition of the resolution function is that for a density $\rho(x) = A e^{-x^2/2s(t)^2}$, the observed density is given by a convolution

$$\rho_{\mathrm{obs}}(x) = \int dx_0 \rho(x_0) \frac{e^{-(1/2)[(x-x_0)/d]^2}}{\sqrt{2\pi} d}$$

$$= \frac{A}{\sqrt{1 + d^2/s(t)^2}} e^{-\{x^2/2[s(t)^2+d^2]\}}.$$

Similarly if $G^{(1)}(x,x') = A e^{i\phi} e^{-(x+x')^2/2(2s)^2} e^{-(x-x')^2/2(l^{(d)})^2}$ is the first order correlation function and $G^{(1)}_{\mathrm{obs}}(x,x')$ the observed one, we have

$$|G^{(1)}_{\mathrm{obs}}(x,x')|^2 = \int dx_0 dx'_0 |G^{(1)}(x_0,x'_0)|^2 \times \frac{e^{-(1/2)[(x-x_0)/d]^2}}{\sqrt{2\pi} d} \frac{e^{-(1/2)[(x'-x'_0)/d]^2}}{\sqrt{2\pi} d} \tag{14}$$

$$= \frac{|A|^2}{\sqrt{[1 + d^2/s^2(t)][1 + 4d^2/(l^{(d)})^2]}} \times e^{-\{(x+x')^2/4[s(t)^2+d^2]\}} e^{-\{(x-x')^2/[l^{(d)}]^2+4d^2\}} \tag{15}$$

Consequently, with $\alpha = x, y$ and z:

(i) The amplitude of the normalized correlation function becomes

$$g^{(2)}_{\mathrm{obs}}(\mathbf{0},\mathbf{0}) = \left(\frac{G^{(1)}_{\mathrm{obs}}(\mathbf{0},\mathbf{0})}{\rho_{\mathrm{obs}}(\mathbf{0})} \right)^2 = 1 + \prod_\alpha \sqrt{\frac{1 + d_\alpha^2/s_\alpha^2(t)}{1 + 4d_\alpha^2/(l_\alpha^{(d)})^2}}.$$

(ii) The observed widths of the cloud are $s_\alpha(t) \to \sqrt{s_\alpha^2(t) + d_\alpha^2}$.

(iii) The observed correlation lengths are $l_\alpha^{(d)} \to \sqrt{(l_\alpha^{(d)})^2 + (2d_\alpha)^2}$. The factor 2 can be understood as $\sqrt{2} \times \sqrt{2}$ where the first term comes from the fact that d_α is defined for one particle and not for a pair of particles and the second one comes from the fact that the correlation length is not defined as an rms width.

In the experiment of Ref. [15] the trapped cloud had a cigar shape. At the detector the cloud was spherical but the correlation volume was anisotropic with $l_x^{(d)} \ll d \approx l_y^{(d)}/4$. In the third (vertical) direction, the resolution width was much smaller than any other length scale. The observed contrast of the correlation function was therefore approximately, $\frac{l_x^{(d)}}{2d}$.

VI. CONCLUSION

The most important conclusion of this paper is that the expansion of a noninteracting cloud from a harmonic trap in thermal equilibrium, admits a rather simple, analytical treatment of the time variation of the density and the correlation functions. In such a pulse of atoms, correlation lengths scale in the same way as the size of the density profile. The agreement with experiment indicates that the neglect of interactions is a good approximation above the BEC transition temperature. An important next step however, is to examine interaction effects so that the next generation of experiments, which will be more precise and better resolved, can be fully interpreted.

ACKNOWLEDGMENTS

The Atom Optics group of LCFIO is member of the Institut Francilien de Recherche sur les Atomes Froids (IFRAF) and of the Fédération LUMAT of the CNRS (FR2764). This work is supported by the PESSOA Program 07988NJ, by the Atom Chips network MCRTN-CT-2003-505032, and the ANR under Contract No. 05-NANO-008-01.

APPENDIX

Explicit expression of the flux correlation function

We found in Sec. III B, the following expression for the flux operator:

$$\hat{I}(\mathbf{r},t)=\sum_{\mathbf{j},\mathbf{k}}\left(v_2\psi_{\mathbf{j}}^{*}\psi_{\mathbf{k}}-\frac{1}{2}(v_3\sqrt{k}\psi_{\mathbf{j}}^{*}\psi_{\mathbf{k}-1_{\mathbf{z}}}+v_3^{*}\sqrt{j}\psi_{\mathbf{j}-1_{\mathbf{z}}}^{*}\psi_{\mathbf{k}})\right)\hat{a}_{\mathbf{j}}^{\dagger}\hat{a}_{\mathbf{k}},$$

where $\mathbf{j}-1_{\mathbf{z}}$ is the vector (j_x,j_y,j_z-1) and where we write $\psi=\psi(\mathbf{r},t)$.

The second order correlation function for the flux is then,

$$\begin{aligned}\langle\hat{I}(\mathbf{r},t)\hat{I}(\mathbf{r}',t')\rangle=\sum_{\mathbf{j},\mathbf{k},\mathbf{l},\mathbf{n}}&\left(v_2\psi_{\mathbf{j}}^{*}\psi_{\mathbf{k}}-\frac{1}{2}(v_3\sqrt{k_z}\psi_{\mathbf{j}}^{*}\psi_{\mathbf{k}-1_{\mathbf{z}}}\right.\\&\left.+v_3^{*}\sqrt{j_z}\psi_{\mathbf{j}-1_{\mathbf{z}}}^{*}\psi_{\mathbf{k}})\right)\\&\times\left(v_2'\psi'^{*}_{\mathbf{l}}\psi'_{\mathbf{n}}-\frac{1}{2}(v_3'\sqrt{n_z}\psi'^{*}_{\mathbf{l}}\psi'_{\mathbf{n}-1_{\mathbf{z}}}\right.\\&\left.+v'^{*}_3\sqrt{l_z}\psi'^{*}_{\mathbf{l}-1_{\mathbf{z}}}\psi'_{\mathbf{n}})\right)\\&\times\langle\hat{a}_{\mathbf{j}}^{\dagger}\hat{a}_{\mathbf{k}}\hat{a}_{\mathbf{l}}^{\dagger}\hat{a}_{\mathbf{n}}\rangle.\end{aligned}$$

Neglecting the shot-noise and ground-state contributions, this leads to

$$\langle\hat{I}(\mathbf{r},t)\hat{I}(\mathbf{r}',t')\rangle=\langle\hat{I}(\mathbf{r},t)\rangle\langle\hat{I}(\mathbf{r}',t')\rangle+\mathrm{Re}(A)$$

with

$$\begin{aligned}A=\sum_{\mathbf{j},\mathbf{l}}&\left(v_2v_2'\psi_{\mathbf{j}}^{*}\psi_{\mathbf{j}}'\psi_{\mathbf{l}}\psi'^{*}_{\mathbf{l}}+\frac{1}{2}v_3v_3'\sqrt{j_zl_z}\psi_{\mathbf{j}}^{*}\psi'_{\mathbf{j}-1_{\mathbf{z}}}\psi_{\mathbf{l}-1_{\mathbf{z}}}\psi'^{*}_{\mathbf{l}}\right.\\&+\frac{1}{2}v_3v'^{*}_3l_z\psi_{\mathbf{j}}^{*}\psi_{\mathbf{j}}'\psi_{\mathbf{l}-1_{\mathbf{z}}}\psi'^{*}_{\mathbf{l}-1_{\mathbf{z}}}-v_2v_3'\sqrt{j_z}\psi_{\mathbf{j}}^{*}\psi'_{\mathbf{j}-1_{\mathbf{z}}}\psi_{\mathbf{l}}\psi'^{*}_{\mathbf{l}}\\&\left.-v_2'v_3\sqrt{l_z}\psi_{\mathbf{j}}^{*}\psi_{\mathbf{j}}'\psi_{\mathbf{l}-1_{\mathbf{z}}}\psi'^{*}_{\mathbf{l}}\right)\langle\hat{a}_{\mathbf{j}}^{\dagger}\hat{a}_{\mathbf{j}}\rangle\langle\hat{a}_{\mathbf{l}}^{\dagger}\hat{a}_{\mathbf{l}}\rangle.\end{aligned}$$

We write $A=\Sigma_{i=1}^{5}T_i$ where the T_i terms can be recast, using $\tan\delta_\alpha=1/\omega_\alpha t$, $\tan\delta'_\alpha=1/\omega_\alpha t'$, $\Delta_\alpha=\delta'_\alpha-\delta_\alpha$, $\Sigma_\alpha j_\alpha(\delta'_\alpha-\delta_\alpha)=\mathbf{j}\cdot\boldsymbol{\Delta}$, $\psi_{\mathbf{l}}^{0}=\psi_{\mathbf{l}}^{0}(\tilde{\mathbf{r}})$, and $\psi_{\mathbf{l}}'^{0}=\psi_{\mathbf{l}}^{0}(\tilde{\mathbf{r}}')$,

$$\begin{aligned}T_1&=v_2v_2'\sum_{\mathbf{j},\mathbf{l}}\psi_{\mathbf{j}}^{*}\psi_{\mathbf{j}}'\psi_{\mathbf{l}}\psi'^{*}_{\mathbf{l}}\langle\hat{a}_{\mathbf{j}}^{\dagger}\hat{a}_{\mathbf{j}}\rangle\langle\hat{a}_{\mathbf{l}}^{\dagger}\hat{a}_{\mathbf{l}}\rangle=\frac{v_2v_2'}{\prod_\alpha\sqrt{(1+\omega_\alpha^2t^2)(1+\omega_\alpha^2t'^2)}}\sum_{\mathbf{j},\mathbf{l}}\psi_{\mathbf{j}}^{0}\psi'^{0}_{\mathbf{j}}\psi_{\mathbf{l}}^{0}\psi'^{0}_{\mathbf{l}}e^{i\Sigma_\alpha(j_\alpha-l_\alpha)(\delta'_\alpha-\delta_\alpha)}\langle\hat{a}_{\mathbf{j}}^{\dagger}\hat{a}_{\mathbf{j}}\rangle\langle\hat{a}_{\mathbf{l}}^{\dagger}\hat{a}_{\mathbf{l}}\rangle\\&=\frac{v_2v_2'}{\prod_\alpha\sqrt{(1+\omega_\alpha^2t^2)(1+\omega_\alpha^2t'^2)}}\left|\sum_{\mathbf{j}}\psi_{\mathbf{j}}^{0}\psi'^{0}_{\mathbf{j}}e^{i\mathbf{j}\cdot\boldsymbol{\Delta}}\langle\hat{a}_{\mathbf{j}}^{\dagger}\hat{a}_{\mathbf{j}}\rangle\right|^{2},\end{aligned}$$

$$\begin{aligned}T_2&=\frac{1}{2}v_3v_3'\sum_{\mathbf{j},\mathbf{l}}\sqrt{j_zl_z}\psi_{\mathbf{j}}^{*}\psi'_{\mathbf{j}-1_{\mathbf{z}}}\psi_{\mathbf{l}-1_{\mathbf{z}}}\psi'^{*}_{\mathbf{l}}\langle\hat{a}_{\mathbf{j}}^{\dagger}\hat{a}_{\mathbf{j}}\rangle\langle\hat{a}_{\mathbf{l}}^{\dagger}\hat{a}_{\mathbf{l}}\rangle=\\&-\frac{1}{2}\frac{|v_3v_3'|}{\prod_\alpha\sqrt{(1+\omega_\alpha^2t^2)(1+\omega_\alpha^2t'^2)}\left(\sum_{\mathbf{j}}\sqrt{j_z}\psi_{\mathbf{j}}^{0}\psi'^{0}_{\mathbf{j}-1_{\mathbf{z}}}e^{i\mathbf{j}\cdot\boldsymbol{\Delta}}\langle\hat{a}_{\mathbf{j}}^{\dagger}\hat{a}_{\mathbf{j}}\rangle\right)\left(\sum_{\mathbf{l}}\sqrt{l_z}\psi_{\mathbf{l}-1_{\mathbf{z}}}^{0}\psi'^{0}_{\mathbf{l}}e^{-i\mathbf{l}\cdot\boldsymbol{\Delta}}\langle\hat{a}_{\mathbf{l}}^{\dagger}\hat{a}_{\mathbf{l}}\rangle\right)},\end{aligned}$$

$$T_3=\frac{1}{2}v_3v'^{*}_3\sum_{\mathbf{j},\mathbf{l}}l_z\psi_{\mathbf{j}}^{*}\psi_{\mathbf{j}}'\psi_{\mathbf{l}-1_{\mathbf{z}}}\psi'^{*}_{\mathbf{l}-1_{\mathbf{z}}}\langle\hat{a}_{\mathbf{j}}^{\dagger}\hat{a}_{\mathbf{j}}\rangle\langle\hat{a}_{\mathbf{l}}^{\dagger}\hat{a}_{\mathbf{l}}\rangle=\frac{1}{2}\frac{|v_3v_3'|}{\prod_\alpha\sqrt{(1+\omega_\alpha^2t^2)(1+\omega_\alpha^2t'^2)}}\left(\sum_{\mathbf{j}}\psi_{\mathbf{j}}^{0}\psi'^{0}_{\mathbf{j}}e^{i\mathbf{j}\cdot\boldsymbol{\Delta}}\langle\hat{a}_{\mathbf{j}}^{\dagger}\hat{a}_{\mathbf{j}}\rangle\right)\left(\sum_{\mathbf{l}}l_z\psi_{\mathbf{l}-1_{\mathbf{z}}}^{0}\psi'^{0}_{\mathbf{l}-1_{\mathbf{z}}}e^{-i\mathbf{l}\cdot\boldsymbol{\Delta}}\langle\hat{a}_{\mathbf{l}}^{\dagger}\hat{a}_{\mathbf{l}}\rangle\right),$$

$$T_4=-v_2v_3'\sum_{\mathbf{j},\mathbf{l}}\sqrt{j_z}\psi_{\mathbf{j}}^{*}\psi'_{\mathbf{j}-1_{\mathbf{z}}}\psi_{\mathbf{l}}\psi'^{*}_{\mathbf{l}}\langle\hat{a}_{\mathbf{j}}^{\dagger}\hat{a}_{\mathbf{j}}\rangle\langle\hat{a}_{\mathbf{l}}^{\dagger}\hat{a}_{\mathbf{l}}\rangle=-i\frac{v_2|v_3'|}{\prod_\alpha\sqrt{(1+\omega_\alpha^2t^2)(1+\omega_\alpha^2t'^2)}}\left(\sum_{\mathbf{j}}\sqrt{j_z}\psi_{\mathbf{j}}^{0}\psi'^{0}_{\mathbf{j}-1_{\mathbf{z}}}e^{i\mathbf{j}\cdot\boldsymbol{\Delta}}\langle\hat{a}_{\mathbf{j}}^{\dagger}\hat{a}_{\mathbf{j}}\rangle\right)\left(\sum_{\mathbf{l}}\psi_{\mathbf{l}}^{0}\psi'^{0}_{\mathbf{l}}e^{-i\mathbf{l}\cdot\boldsymbol{\Delta}}\langle\hat{a}_{\mathbf{l}}^{\dagger}\hat{a}_{\mathbf{l}}\rangle\right),$$

$$T_5 = -v_2' v_3 \sum_{\mathbf{j},\mathbf{l}} \sqrt{l_z}\,\psi_{\mathbf{j}}^{*}\psi_{\mathbf{j}}'\,\psi_{\mathbf{l}-1_{\mathbf{z}}}\psi'^{*}_{\mathbf{l}}\langle \hat{a}_{\mathbf{j}}^{\dagger}\hat{a}_{\mathbf{j}}\rangle\langle \hat{a}_{\mathbf{l}}^{\dagger}\hat{a}_{\mathbf{l}}\rangle = -i\frac{v_2'|v_3|}{\prod_{\alpha}\sqrt{(1+\omega_\alpha^2 t^2)(1+\omega_\alpha^2 t'^2)}}\left(\sum_{\mathbf{j}} \psi_{\mathbf{j}}^{0}\psi'^{0}_{\mathbf{j}}e^{i\mathbf{j}\cdot\boldsymbol{\Delta}}\langle \hat{a}_{\mathbf{j}}^{\dagger}\hat{a}_{\mathbf{j}}\rangle\right)\left(\sum_{\mathbf{l}} \sqrt{l_z}\,\psi_{\mathbf{l}-1_{\mathbf{z}}}^{0}\psi'^{0}_{\mathbf{l}}e^{-i\mathbf{l}\cdot\boldsymbol{\Delta}}\langle \hat{a}_{\mathbf{l}}^{\dagger}\hat{a}_{\mathbf{l}}\rangle\right).$$

The term T_1 is a real number which is not the case for T_2, T_3, T_4, and T_5.

Calculation for harmonic oscillator stationary states

All the above terms can be calculated analytically. All the series are identical in the direction x and y. We are then left with the calculation of three series in only one direction,

$$\sum_{n=0}^{\infty} \sqrt{n}\,\psi_{n-1}^{0}(\tilde{z})\psi_{n}^{0}(\tilde{z}')e^{-nu},$$

$$\sum_{n=0}^{\infty} \sqrt{n}\,\psi_{n}^{0}(\tilde{z})\psi_{n-1}^{0}(\tilde{z}')e^{-nu},$$

$$\sum_{n=0}^{\infty} n\,\psi_{n-1}^{0}(\tilde{z})\psi_{n-1}^{0}(\tilde{z}')e^{-nu}.$$

The function $g_u(\tilde{z},\tilde{z}') = \Sigma_{n=0}^{\infty}\psi_n^0(\tilde{z})\psi_n^0(\tilde{z}')e^{-nu}$ is known [17,29] and its expression is

$$g_u(\tilde{z},\tilde{z}') = \frac{1}{\sigma\sqrt{\pi(1-e^{-2u})}}\exp\left[-\tanh\left(\frac{u}{2}\right)\left(\frac{\tilde{z}+\tilde{z}'}{2\sigma}\right)^2 - \coth\left(\frac{u}{2}\right)\left(\frac{\tilde{z}-\tilde{z}'}{2\sigma}\right)^2\right].$$

Using

$$\tilde{z}\psi_n^0(\tilde{z}) = \tfrac{\sigma}{\sqrt{2}}\langle \tilde{z}|\hat{a}+\hat{a}^{\dagger}|\psi_n^0\rangle = \tfrac{\sigma}{\sqrt{2}}[\sqrt{n}\,\psi_{n-1}^0(\tilde{z}) + \sqrt{n+1}\,\psi_{n+1}^0(\tilde{z})],$$

one finds

$$\tilde{z}g_u(\tilde{z},\tilde{z}') = \frac{\sigma}{\sqrt{2}}\Big(\sum \sqrt{n}\,\psi_{n-1}^0(\tilde{z})\psi_n^0(\tilde{z}')e^{-nu} + e^{u}\sum \sqrt{n}\,\psi_n^0(\tilde{z})\psi_{n-1}^0(\tilde{z}')e^{-nu}\Big).$$

It follows easily that

$$\sum_{n=0}^{\infty} \sqrt{n}\,\psi_{n-1}^{0}(\tilde{z})\psi_{n}^{0}(\tilde{z}')e^{-nu} = \frac{\sqrt{2}}{\sigma}\frac{\tilde{z}-e^{u}\tilde{z}'}{1-e^{2u}}g_u(\tilde{z},\tilde{z}'),$$

$$\sum_{n=0}^{\infty} \sqrt{n}\,\psi_{n}^{0}(\tilde{z})\psi_{n-1}^{0}(\tilde{z}')e^{-nu} = \frac{\sqrt{2}}{\sigma}\frac{\tilde{z}'-e^{u}\tilde{z}}{1-e^{2u}}g_u(\tilde{z},\tilde{z}').$$

Moreover,

$$\Sigma_{n=0}^{\infty}\, n\,\psi_{n-1}^{0}(\tilde{z})\psi_{n-1}^{0}(\tilde{z}')e^{-nu} = e^{-u}[g_u(\tilde{z},\tilde{z}') - \partial_u g_u(\tilde{z},\tilde{z}')].$$

Then,

$$\sum_{n=0}^{\infty} n\,\psi_{n-1}^{0}(\tilde{z})\psi_{n-1}^{0}(\tilde{z}')e^{-nu} = \left[\frac{1}{1-e^{-2u}} + \frac{1}{2}\left(\frac{\tilde{z}+\tilde{z}'}{2\sigma\cosh\frac{u}{2}}\right)^2 - \frac{1}{2}\left(\frac{\tilde{z}-\tilde{z}'}{2\sigma\sinh\frac{u}{2}}\right)^2\right]e^{-u}g_u(\tilde{z},\tilde{z}').$$

Explicit expression of the flux correlation function—Part II

We define $G_B^{(1)}(\mathbf{r},\mathbf{r}',\mathbf{u}) = \Sigma_{\mathbf{n}}^{\infty}\psi_{\mathbf{n}}^0(\mathbf{r})\psi_{\mathbf{n}}^0(\mathbf{r}')e^{-\mathbf{nu}}$. This function, the 3D equivalent of the function g_u, is connected to the one-body correlation function by $G^{(1)}(\mathbf{r},\mathbf{r}') = \Sigma_{l=1}^{\infty}e^{\beta l\tilde{\mu}}G_B^{(1)}(\mathbf{r},\mathbf{r}',l\boldsymbol{\tau})$ with $\tau_\alpha = \beta\hbar\omega_\alpha$.

Then,

$$T_1 = \frac{v_2 v_2'}{\prod_{\alpha}\sqrt{(1+\omega_\alpha^2 t^2)(1+\omega_\alpha^2 t'^2)}}\left|\sum_{l} e^{\beta l\tilde{\mu}}G_B^{(1)}(\tilde{\mathbf{r}},\tilde{\mathbf{r}}',l\boldsymbol{\tau}-i\boldsymbol{\Delta})\right|^2,$$

$$T_2 = -\frac{1}{2}\frac{|v_3 v_3'|}{\prod_{\alpha}\sqrt{(1+\omega_\alpha^2 t^2)(1+\omega_\alpha^2 t'^2)}}\left(\sum_{l} e^{\beta l\tilde{\mu}}\frac{\sqrt{2}}{\sigma}\frac{\tilde{z}-e^{l\tau_z-i\Delta_z}\tilde{z}'}{1-e^{2(l\tau_z-i\Delta_z)}}G_B^{(1)}(\tilde{\mathbf{r}},\tilde{\mathbf{r}}',l\boldsymbol{\tau}-i\boldsymbol{\Delta})\right) \times\left(\sum_{k} e^{\beta k\tilde{\mu}}\frac{\sqrt{2}}{\sigma}\frac{\tilde{z}'-e^{k\tau_z+i\Delta_z}\tilde{z}}{1-e^{2(k\tau_z+i\Delta_z)}}G_B^{(1)}(\tilde{\mathbf{r}},\tilde{\mathbf{r}}',k\boldsymbol{\tau}+i\boldsymbol{\Delta})\right),$$

$$T_3 = \frac{1}{2}\frac{|v_3 v_3'|}{\prod_\alpha \sqrt{(1+\omega_\alpha^2 t^2)(1+\omega_\alpha^2 t'^2)}}\left(\sum_l e^{\beta l\tilde{\mu}} G_B^{(1)}(\tilde{\mathbf{r}},\tilde{\mathbf{r}}',l\boldsymbol{\tau}-i\boldsymbol{\Delta})\right)\times\left\{\sum_k e^{\beta k\tilde{\mu}}\left[\frac{1}{1-e^{-2(k\tau_z+i\Delta_z)}}+\frac{1}{2}\left(\frac{\tilde{z}+\tilde{z}'}{2\sigma\cosh\frac{k\tau_z+i\Delta_z}{2}}\right)^2 - \frac{1}{2}\left(\frac{\tilde{z}-\tilde{z}'}{2\sigma\sinh\frac{k\tau_z+i\Delta_z}{2}}\right)^2\right]e^{-(k\tau_z+i\boldsymbol{\Delta}_z)}G_B^{(1)}(\tilde{\mathbf{r}},\tilde{\mathbf{r}}',k\boldsymbol{\tau}+i\boldsymbol{\Delta})\right\},$$

$$T_4 = -i\frac{v_2|v_3'|}{\prod_\alpha \sqrt{(1+\omega_\alpha^2 t^2)(1+\omega_\alpha^2 t'^2)}}\left(\sum_l e^{\beta l\tilde{\mu}}\frac{\sqrt{2}}{\sigma}\frac{\tilde{z}-e^{l\tau_z-i\Delta_z}\tilde{z}'}{1-e^{2(l\tau_z-i\Delta_z)}}G_B^{(1)}(\tilde{\mathbf{r}},\tilde{\mathbf{r}}',l\boldsymbol{\tau}-i\boldsymbol{\Delta})\right)\times\left(\sum_k e^{\beta k\tilde{\mu}}G_B^{(1)}(\tilde{\mathbf{r}},\tilde{\mathbf{r}}',k\boldsymbol{\tau}+i\boldsymbol{\Delta})\right),$$

$$T_5 = -i\frac{|v_3|v_2'}{\prod_\alpha \sqrt{(1+\omega_\alpha^2 t^2)(1+\omega_\alpha^2 t'^2)}}\left(\sum_l e^{\beta l\tilde{\mu}}G_B^{(1)}(\tilde{\mathbf{r}},\tilde{\mathbf{r}}',l\tau-i\boldsymbol{\Delta})\right)\times\left(\sum_k e^{\beta k\tilde{\mu}}\frac{\sqrt{2}}{\sigma}\frac{\tilde{z}'-e^{k\tau_z+i\boldsymbol{\Delta}_z}\tilde{z}}{1-e^{2(k\tau_z+i\boldsymbol{\Delta}_z)}}G_B^{(1)}(\tilde{\mathbf{r}},\tilde{\mathbf{r}}',k\tau+i\boldsymbol{\Delta})\right).$$

The dominant term is T_1 and is the one used in Sec. III B 5.

Contribution of neglected terms in the correlation of the flux

Here we evaluate the neglected terms T_2 to T_5 and the shot-noise contribution. They will be evaluated in the case of clouds far above BEC threshold. Under this assumption, all the functions are separable in the variables x, y, and t and the summation over the index l in the preceding equations reduces to the single term $l=1$.

Shot-noise contribution

Using the above analysis one can show that the main term is still proportional to $v_2 v_2'$. The additional term is then,

$$\frac{v_2 v_2'}{\prod_\alpha \sqrt{(1+\omega_\alpha^2 t^2)(1+\omega_\alpha^2 t'^2)}}e^{\beta\tilde{\mu}}G_B^{(1)}(\tilde{\mathbf{r}},\tilde{\mathbf{r}}',\boldsymbol{\tau}-i\boldsymbol{\Delta})G_B^{(1)}(\tilde{\mathbf{r}},\tilde{\mathbf{r}}',i\boldsymbol{\Delta}).$$

For $t=t'$, $\boldsymbol{\Delta}=\mathbf{0}$ and $G_B^{(1)}(\tilde{\mathbf{r}},\tilde{\mathbf{r}}',\mathbf{0})=\delta(\tilde{\mathbf{r}}-\tilde{\mathbf{r}}')$. The shot-noise term is then

$$\frac{v_2^2}{\prod_\alpha (1+\omega_\alpha^2 t^2)}\rho_{\text{eq}}(\tilde{\mathbf{r}})\delta(\tilde{\mathbf{r}}-\tilde{\mathbf{r}}').$$

As expected, this term corresponds also to the one at equilibrium with rescaled coordinates.

T_2–T_5 contribution

We have $G_{fl.}^{(2)}(\mathbf{r},t;\mathbf{r}',t')=\langle\hat{I}(\mathbf{r},t)\hat{I}(\mathbf{r}',t')\rangle=\langle\hat{I}(\mathbf{r},t)\rangle\times\langle\hat{I}(\mathbf{r}',t')\rangle+\text{Re}(A)$ where $A=\Sigma_{i=1}^5 T_i$.

Case $t=t'$:

(a) $\boldsymbol{\Delta}=\mathbf{0}$, then $T_1=\frac{v_2 v_2'}{\prod_\alpha\sqrt{(1+\omega_\alpha^2 t^2)(1+\omega_\alpha^2 t'^2)}}|G^{(1)}(\tilde{\mathbf{r}},\tilde{\mathbf{r}}')|^2$, T_2 and T_3 are real number and $\text{Re}(T_4)=\text{Re}(T_5)=0$.

(b) One finds, to leading orders, $g^{(2)}(0,0,t;0,0,t)-2 \approx \frac{1}{8}\left(\frac{s_z}{H}\right)^2\left(1-2\frac{t-t_0}{t_0}\right)\left(1-\frac{\tau_z^2}{6}\right)$ where s_z is the initial size of the cloud in the vertical direction and $t_0=\sqrt{2H/g}$.

(c) The deviation from 2 is extremely small in the experimental conditions of Ref. [15] ($\sim 10^{-11}$) but shows that the bunching is strictly speaking not 2 at the center. This behavior is expected for any flux correlation function of dispersive waves [41].

(d) The correlation lengths at the detector are not modified by the additional terms.

Case $t \neq t'$:

(a) The correlation function can be written as

$$g^{(2)}(0,0,t;0,0,t') = 1 + \frac{|G_B^{(1)}(\tilde{\mathbf{r}},\tilde{\mathbf{r}}',\boldsymbol{\tau}+i\boldsymbol{\Delta})|^2}{G_B^{(1)}(\tilde{\mathbf{r}},\tilde{\mathbf{r}},\boldsymbol{\tau})G_B^{(1)}(\tilde{\mathbf{r}}',\tilde{\mathbf{r}}',\boldsymbol{\tau})}(1+\epsilon).$$

(b) where

$$\frac{|G_B^{(1)}(\tilde{\mathbf{r}},\tilde{\mathbf{r}}',\boldsymbol{\tau}+i\boldsymbol{\Delta})|^2}{G_B^{(1)}(\tilde{\mathbf{r}},\tilde{\mathbf{r}},\boldsymbol{\tau})G_B^{(1)}(\tilde{\mathbf{r}}',\tilde{\mathbf{r}}',\boldsymbol{\tau})} \approx e^{-[(t-t')/t^{(\text{coh})}]^2[1-(\tau_z^2)/6]1-[(t+t'-2t_0)/t_0]}$$

and

(c)

$$\epsilon \approx \frac{1}{8}\left(\frac{w_z}{H}\right)^2\left[1-\left(\frac{t+t'-2t_0}{t_0}\right)\right]\left(1-\frac{\tau_z^2}{6}\right) - \frac{3}{2(\omega_z t_0 \tau_z)^2}\left(\frac{t-t'}{t_0}\right)^2\left(1+\frac{\tau_z}{3}\right).$$

We have neglected terms in $\tau_z, (t-t_0)^3, (t'-t_0)^3, (t-t_0)^2(t'-t_0), (t-t_0)(t'-t_0)^2$, and higher orders.

(d) The value of ϵ is extremely small ($\sim 10^{-10}$) using Ref. [15]. The deviation from $e^{-[(t-t')/t^{(\text{coh})}]^2}$ is mainly due to the mean time $(t+t')/2$ contribution and changes the value of the correlation time in the wings of the time of flight by $\sim 3\%$. The effect of the phase factor $\boldsymbol{\Delta}$ is negligible.

[1] L. Mandel and E. Wolf, *Optical Coherence and Quantum Optics* (Cambridge University Press, Cambridge, 1995).
[2] R. Hanbury Brown and R. Q. Twiss, Nature (London) **177**, 27 (1956).
[3] G. Baym, Acta Phys. Pol. B **29**, 1839 (1998).
[4] D. H. Boal, C.-K. Gelbke, and B. K. Jennings, Rev. Mod. Phys. **62**, 553 (1990).
[5] U. Heinz and B. V. Jacak, Annu. Rev. Nucl. Part. Sci. **49**, 529 (1999).
[6] C.-Y. Wong, *Introduction to High-Energy Heavy-Ion Collisions* (World Scientific, Singapore, 1994).
[7] M. Iannuzzi, A. Orecchini, F. Sacchetti, P. Facchi, and S. Pascazio, Phys. Rev. Lett. **96**, 080402 (2006).
[8] M. Henny, S. Oberholzer, C. Strunk, T. Heinzel, K. Ensslin, M. Holland, and C. Schonenberger, Science **284**, 296 (1999).
[9] W. D. Oliver, J. Kim, R. C. Liu, and Y. Yamamoto, Science **284**, 299 (1999).
[10] M. Yasuda and F. Shimizu, Phys. Rev. Lett. **77**, 3090 (1996).
[11] D. Hellweg, L. Cacciapuoti, M. Kottke, T. Schulte, K. Sengstock, W. Ertmer, and J. J. Arlt, Phys. Rev. Lett. **91**, 010406 (2003).
[12] M. Greiner, C. A. Regal, J. T. Stewart, and D. S. Jin, Phys. Rev. Lett. **94**, 110401 (2005).
[13] S. Fölling, F. Gerbier, A. Widera, O. Mandel, T. Gericke, and I. Bloch, Nature (London) **434**, 481 (2005).
[14] A. Öttl, S. Ritter, M. Köhl, and T. Esslinger, Phys. Rev. Lett. **95**, 090404 (2005).
[15] M. Schellekens, R. Hoppeler, A. Perrin, J. Viana Gomes, D. Boiron, A. Aspect, and C. I. Westbrook, Science **310**, 648 (2005).
[16] J. Esteve, J.-B. Trebbia, T. Schumm, A. Aspect, C. I. Westbrook, and I. Bouchoule, Phys. Rev. Lett. **96**, 130403 (2006).
[17] M. Naraschewski and R. J. Glauber, Phys. Rev. A **59**, 4595 (1999).
[18] M. Holzmann and Y. Castin, Eur. Phys. J. D **7**, 425 (1999).
[19] K. V. Kheruntsyan, D. M. Gangardt, P. D. Drummond, and G. V. Shlyapnikov, Phys. Rev. Lett. **91**, 040403 (2003).
[20] C. Mora and Y. Castin, Phys. Rev. A **67**, 053615 (2003).
[21] M. A. Cazalilla, J. Phys. B **37**, 1 (2004).
[22] E. Altman, E. Demler, and M. D. Lukin, Phys. Rev. A **70**, 013603 (2004).
[23] C. Gies and D. A. W. Hutchinson, Phys. Rev. A **70**, 043606 (2004).
[24] M. Born and E. Wolf, *Optics*, 6th ed. (Pergamon, Oxford 1980), Chap. 10.4.
[25] D. E. Miller, J. R. Anglin, J. R. Abo-Shaeer, K. Xu, J. K. Chin, and W. Ketterle, Phys. Rev. A **71**, 043615 (2005).
[26] N. K. Whitlock, S. M. Barnett, and J. Jeffers, J. Phys. B **36**, 1273 (2003).
[27] W. Krauth, Phys. Rev. Lett. **77**, 3695 (1996).
[28] W. H. Louisell, *Quantum Statistical Properties of Radiation* (Wiley, New York, 1973).
[29] L. D. Landau and E. M. Liftshiz, *Statistical Physics* (Butterworth, London, 1996).
[30] H. D. Politzer, Phys. Rev. A **54**, 5048 (1996).
[31] R. Hoppeler, J. C. Viana Gomes, and D. Boiron, Eur. Phys. J. D (to be published).
[32] A. G. Sinclair and M. A. Kasevich, Rev. Sci. Instrum. **68**, 1657 (1997).
[33] C. Cohen-Tannoudji, lecture notes at the Collège de France (1992) available at http://www.phys.ens.fr/cours/college-de-france/1992-93/1992-93.htm
[34] R. P. Feynmann and A. R. Hibbs, *Quantum Mechanics and Path Integrals* (McGraw-Hill, New York, 1965).
[35] I. S Gradshteyn and I. M. Ryzhik, *Table of Integrals, Series, and Products* (Academic, London, 1980).
[36] M. Naraschewski, H. Wallis, A. Schenzle, J. I. Cirac, and P. Zoller, Phys. Rev. A **54**, 2185 (1996).
[37] Y. Castin and R. Dum, Phys. Rev. Lett. **77**, 5315 (1996).
[38] Y. Kagan, E. L. Surkov, and G. V. Shlyapnikov, Phys. Rev. A **54**, R1753 (1996).
[39] H. Kaiser, S. A. Werner, and E. A. George, Phys. Rev. Lett. **50**, 560 (1983).
[40] A. G. Klein, G. I. Opat, and W. A. Hamilton, Phys. Rev. Lett. **50**, 563 (1983).
[41] A. Perrin, D. Boiron, and M. Belsley (unpublished).

nature
Vol 445|25 January 2007|doi:10.1038/nature05513

LETTERS

Comparison of the Hanbury Brown–Twiss effect for bosons and fermions

T. Jeltes[1], J. M. McNamara[1], W. Hogervorst[1], W. Vassen[1], V. Krachmalnicoff[2], M. Schellekens[2], A. Perrin[2], H. Chang[2], D. Boiron[2], A. Aspect[2] & C. I. Westbrook[2]

Fifty years ago, Hanbury Brown and Twiss (HBT) discovered photon bunching in light emitted by a chaotic source[1], highlighting the importance of two-photon correlations[2] and stimulating the development of modern quantum optics[3]. The quantum interpretation of bunching relies on the constructive interference between amplitudes involving two indistinguishable photons, and its additive character is intimately linked to the Bose nature of photons. Advances in atom cooling and detection have led to the observation and full characterization of the atomic analogue of the HBT effect with bosonic atoms[4–6]. By contrast, fermions should reveal an antibunching effect (a tendency to avoid each other). Antibunching of fermions is associated with destructive two-particle interference, and is related to the Pauli principle forbidding more than one identical fermion to occupy the same quantum state. Here we report an experimental comparison of the fermionic and bosonic HBT effects in the same apparatus, using two different isotopes of helium: ^{3}He (a fermion) and ^{4}He (a boson). Ordinary attractive or repulsive interactions between atoms are negligible; therefore, the contrasting bunching and antibunching behaviour that we observe can be fully attributed to the different quantum statistics of each atomic species. Our results show how atom–atom correlation measurements can be used to reveal details in the spatial density[7,8] or momentum correlations[9] in an atomic ensemble. They also enable the direct observation of phase effects linked to the quantum statistics of a many-body system, which may facilitate the study of more exotic situations[10].

Two-particle correlation analysis is an increasingly important method for studying complex quantum phases of ultracold atoms[7–13]. It goes back to the discovery, by Hanbury Brown and Twiss[1], that photons emitted by a chaotic (incoherent) light source tend to be bunched: the joint detection probability is enhanced, compared to that of statistically independent particles, when the two detectors are close together. Although the effect is easily understood in the context of classical wave optics[14], it took some time to find a clear quantum interpretation[3,15]. The explanation relies on interference between the quantum amplitude for two particles, emitted from two source points S_1 and S_2, to be detected at two detection points D_1 and D_2 (see Fig. 1). For bosons, the two amplitudes $\langle D_1|S_1\rangle\langle D_2|S_2\rangle$ and $\langle D_1|S_2\rangle\langle D_2|S_1\rangle$ must be added, which yields a factor of 2 excess in the joint detection probability, if the two amplitudes have the same phase. The sum over all pairs (S_1,S_2) of source points washes out the interference, unless the distance between the detectors is small enough that the phase difference between the amplitudes is less than one radian, or equivalently if the two detectors are separated by a distance less than the coherence length. Study of the joint detection rates versus detector separation along the i direction then reveals a 'bump' whose width l_i is the coherence length along that axis[1,5,16–19]. For a source size s_i (defined as the half width at $e^{-1/2}$ of a gaussian density profile) along the i direction, the bump has a half width at e^{-1} of $l_i = ht/(2\pi m s_i)$, where m is the mass of the particle, t the time of flight from the source to the detector, and h Planck's constant. This formula is the analogue of the formula $l_i = L\lambda/(2\pi s_i)$ for photons, if $\lambda = h/(mv)$ is identified with the de Broglie wavelength for particles travelling at velocity $v = L/t$ from the source to the detector.

For indistinguishable fermions, the two-body wavefunction is antisymmetric, and the two amplitudes must be subtracted, yielding a null probability for joint detection in the same coherence volume. In the language of particles, it means that two fermions cannot have momenta and positions belonging to the same elementary cell of

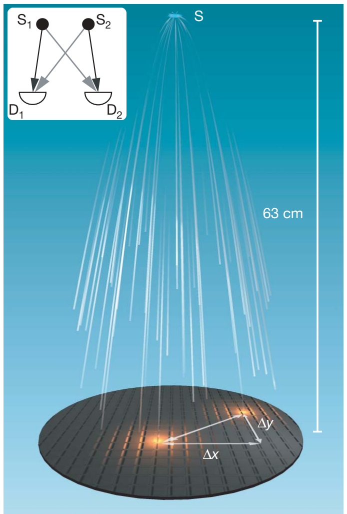

Figure 1 | The experimental set-up. A cold cloud of metastable helium atoms is released at the switch-off of a magnetic trap. The cloud expands and falls under the effect of gravity onto a time-resolved and position-sensitive detector (microchannel plate and delay-line anode) that detects single atoms. The horizontal components of the pair separation Δr are denoted Δx and Δy. The inset shows conceptually the two 2-particle amplitudes (in black or grey) that interfere to give bunching or antibunching: S_1 and S_2 refer to the initial positions of two identical atoms jointly detected at D_1 and D_2.

---

[1] Laser Centre Vrije Universiteit, De Boelelaan 1081, 1081 HV Amsterdam, The Netherlands. [2] Laboratoire Charles Fabry de l'Institut d'Optique, CNRS, Univ. Paris-sud, Campus Polytechnique RD 128, 91127 Palaiseau Cedex, France.

phase space. As a result, for fermions the joint detection rate versus detector separation is expected to exhibit a dip around the null separation. Such a dip for a fermion ensemble must not be confused with the antibunching dip that one can observe with a single particle (boson or fermion) quantum state—for example, resonance fluorescence photons emitted by an individual quantum emitter[20]. In contrast to the HBT effect for bosons, the fermion analogue cannot be interpreted by any classical model, either wave or particle, and extensive efforts have been directed towards an experimental demonstration. Experiments have been performed with electrons in solids[21,22] and in a free beam[23], and with a beam of neutrons[24], but none has allowed a detailed study and a comparison of the pure fermionic and bosonic HBT effects for an ideal gas. A recent experiment using fermions in an optical lattice[25], however, does permit such a study and is closely related to our work.

Here we present an experiment in which we study the fermionic HBT effect for a sample of polarized, metastable ^{3}He atoms (^{3}He*), and we compare it to the bosonic HBT effect for a sample of polarized, but not Bose condensed, metastable ^{4}He atoms (^{4}He*) produced in the same apparatus at the same temperature. We have combined the position- and time-resolved detector, previously used[5,26] for ^{4}He*, with an apparatus with which ultracold samples of ^{3}He* or ^{4}He* have recently been produced[27]. Fermions or bosons at thermal equilibrium in a magnetic trap are released onto the detector, which counts individual atoms (see Fig. 1) with an efficiency of approximately 10%. The detector allows us to construct the normalized correlation function $g^{(2)}(\Delta\mathbf{r})$, that is, the probability of joint detection at two points separated by $\Delta\mathbf{r}$, divided by the product of the single detection probabilities at each point. Statistically independent detection events result in a value of 1 for $g^{(2)}(\Delta\mathbf{r})$. A value larger than 1 indicates bunching, while a value less than 1 is evidence of antibunching.

We produce gases of pure ^{3}He* or pure ^{4}He* by a combination of evaporative and sympathetic cooling in an anisotropic magnetic trap (see Methods). Both isotopes are in pure magnetic substates, with nearly identical magnetic moments and therefore nearly identical trapping potentials, so that trapped non-degenerate and non-interacting samples have the same size at the same temperature. The temperatures of the samples yielding the results of Fig. 2, as measured by the spectrum of flight times to the detector, are $0.53 \pm 0.03\,\mu$K and $0.52 \pm 0.05\,\mu$K for ^{3}He* and ^{4}He*, respectively. The uncertainties correspond to the standard deviation of each ensemble. In a single realization, we typically produce 7×10^4 atoms of both ^{3}He* and ^{4}He*. The atom number permits an estimate of the Fermi and Bose–Einstein condensation temperatures of approximately 0.9 μK and 0.4 μK, respectively. Consequently, Fermi pressure in the trapped ^{3}He* sample has a negligible (3%) effect on the trap size, and repulsive interactions in the ^{4}He* sample have a similarly small effect. The trapped samples are therefore approximately gaussian ellipsoids elongated along the x axis with an r.m.s. size of about $110 \times 12 \times 12\,\mu\mathrm{m}^3$. To release the atoms, we turn off the current in the trapping coils and atoms fall under the influence of gravity. The detector, placed 63 cm below the trap centre (see Fig. 1), then records the x–y position and arrival time of each detected atom.

The normalized correlation functions $g^{(2)}(0,0,\Delta z)$ along the z (vertical) axis, for ^{3}He* and ^{4}He* gases at the same temperature, are shown in Fig. 2. Each correlation function is obtained by analysing the data from about 1,000 separate clouds for each isotope (see Methods). Results analogous to those of Fig. 2 are obtained for correlation functions along the y axis, but the resolution of the detector in the x–y plane (about 500 μm half width at e^{-1} for pair separation) broadens the signals. Along the x axis (the long axis of the trapped clouds), the expected widths of the HBT structures are one order of magnitude smaller than the resolution of the detector and are therefore not resolved.

Figure 2 shows clearly the contrasting behaviours of bosons and fermions. In both cases we observe a clear departure from statistical independence at small separation. Around zero separation, the fermion signal is lower than unity (antibunching) while the boson signal is higher (bunching). Because the sizes of the ^{3}He* and ^{4}He* clouds at the same temperature are the same, as are the times of flight (pure free fall), the ratio of the correlation lengths is expected to be equal to the inverse of the mass ratio, 4/3. The observed ratio of the correlation lengths along the z axis in the data shown is 1.3 ± 0.2. The individual correlation lengths are also in good agreement with the formula $l_z = ht/(2\pi m s_z)$, where s_z is the source size along z. Owing to the finite resolution, the contrast in the signal, which should ideally go to 0 or 2, is reduced by a factor of order ten. The amount of contrast reduction is slightly different for bosons and fermions, and the ratio should be about 1.5. The measured ratio is 2.4 ± 0.2. This discrepancy has several possible explanations. First, the magnetic field switch-off is not sudden (timescale ~1 ms), and this could affect bosons and fermions differently. Second, systematic errors may be present in our estimate of the resolution function. The resolution, however, does not affect the widths of the observed correlation functions along z, and thus we place the strongest emphasis on this ratio as a test of our understanding of boson and fermion correlations in an ideal gas. More information on uncertainties and systematic errors, as well as a more complete summary of the data, are given in Supplementary Information.

Improved detector resolution would allow a more detailed study of the correlation function, and is thus highly desirable. The effect of the resolution could be circumvented by using a diverging atom lens to demagnify the source[4]. According to the formula $l = ht/(2\pi ms)$, a smaller effective source size gives a larger correlation length. We have tried such a scheme by creating an atomic lens with a blue-detuned, vertically propagating, laser beam, forcing the atoms away from its axis (see Methods). The laser waist was not large compared to the cloud size, and therefore our 'lens' suffered from strong aberrations, but a crude estimate of the demagnification, neglecting aberrations, gives about 2 in the x–y plane. Figure 3 shows a comparison of

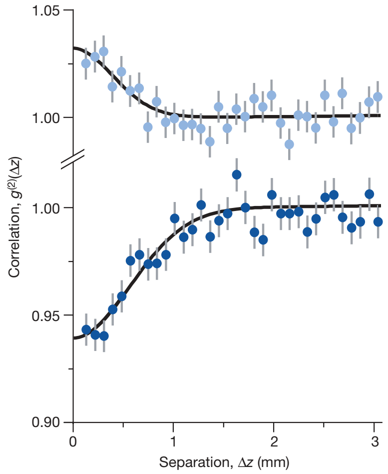

Figure 2 | Normalized correlation functions for ^{4}He* (bosons) in the upper plot, and ^{3}He* (fermions) in the lower plot. Both functions are measured at the same cloud temperature (0.5 μK), and with identical trap parameters. Error bars correspond to the square root of the number of pairs in each bin. The line is a fit to a gaussian function. The bosons show a bunching effect, and the fermions show antibunching. The correlation length for ^{3}He* is expected to be 33% larger than that for ^{4}He* owing to the smaller mass. We find 1/e values for the correlation lengths of 0.75 ± 0.07 mm and 0.56 ± 0.08 mm for fermions and bosons, respectively.

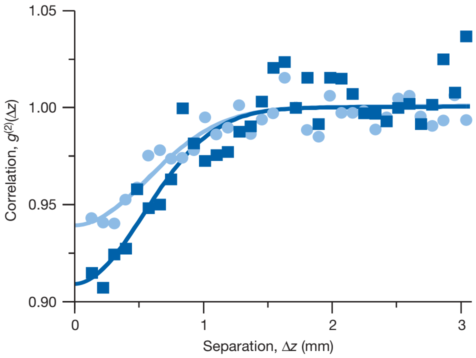

Figure 3 | Effect of demagnifying the source size. We show normalized correlation functions along the z (vertical) axis for ^{3}He*, with (dark blue squares) and without (light blue circles) a diverging atomic lens in the x–y plane. The dip is deeper with the lens, because the increase of the correlation lengths in the x–y plane leads to less reduction of contrast when convolved with the resolution function in that plane.

$g^{(2)}(\Delta z)$ for fermions with and without the defocusing lens. We clearly see a greater antibunching depth, consistent with larger correlation lengths in the x–y plane (we have checked that l_y is indeed increased) and therefore yielding a smaller reduction of the contrast when convolved with the detector resolution function. As expected, the correlation length in the z direction is unaffected by the lens in the x–y plane. Although our atomic lens was far from ideal, the experiment shows that it is possible to modify the HBT signal by optical means.

To conclude, we emphasize that we have used samples of neutral atoms at a moderate density in which interactions do not play any significant role. Care was taken to manipulate bosons and fermions in conditions as similar as possible. Thus the observed differences can be understood as a purely quantum effect associated with the exchange symmetries of wavefunctions of indistinguishable particles.

The possibility of having access to the sign of phase factors in a many-body wavefunction opens fascinating perspectives for the investigation of intriguing analogues of condensed-matter systems, which can now be realized with cold atoms. For instance, one could compare the many-body state of cold fermions and that of 'fermionized' bosons in a one-dimensional sample[28,29]. Our successful manipulation of the HBT signal by interaction with a laser suggests that other lens configurations could allow measurements in position space (by forming an image of the cloud at the detector) or in any combination of momentum and spatial coordinates.

METHODS

Experimental sequence. Clouds of cold ^{4}He* are produced by evaporative cooling of a pure ^{4}He* sample, loaded into a Ioffe–Pritchard magnetic trap[30]. The trapped state is 2^3S_1, $m_J = 1$, and the trap frequency values are 47 Hz and 440 Hz for axial and radial confinement, respectively. The bias field is 0.75 G, corresponding to a frequency of 2.1 MHz for a transition between the $m_J = 1$ and $m_J = 0$ states at the bottom of the trap. After evaporative cooling, we keep the radio frequency evaporation field ('r.f. knife') on at constant frequency for 500 ms, then wait for 100 ms before switching off the trap. In contrast to the experiments of ref. 5, atoms are released in a magnetic-field-sensitive state.

To prepare ^{3}He* clouds, we simultaneously load ^{3}He* and ^{4}He* atoms in the magnetic trap[27]. The trapping state for ^{3}He* is 2^3S_1, $F = 3/2$, $m_F = 3/2$, and axial and radial trap frequencies are 54 Hz and 506 Hz—the difference compared to ^{4}He* is only due to the mass. The two gases are in thermal equilibrium in the trap, so that ^{3}He* is sympathetically cooled with ^{4}He* during the evaporative cooling stage. Once the desired temperature is reached, we selectively eliminate ^{4}He* atoms from the trap using the r.f. knife. The gyromagnetic ratios for ^{4}He* and ^{3}He* are 2 and 4/3 respectively, so that the resonant frequency of the $m = 1$ to $m = 0$ transition for ^{4}He* is 3/2 times larger than the $m = 3/2$ to $m = 1/2$ transition for ^{3}He*. An r.f. ramp from 3 MHz to 1.9 MHz expels all the ^{4}He* atoms from the trap without affecting ^{3}He*. We then use the same trap switch-off procedure to release the ^{3}He* atoms (also in a magnetic-field-sensitive state) onto the detector. We can apply magnetic field gradients to check the degree of spin polarization of either species.

Correlation function. The detailed procedure leading to this correlation is given in ref. 5. Briefly, we convert arrival times to z positions, and then use the three-dimensional positions of each atom to construct a histogram of pair separations $\Delta\mathbf{r}$ in a particular cloud. We then sum the pair distribution histograms for 1,000 successive runs at the same temperature. For separations much larger than the correlation length, this histogram reflects the gaussian spatial distribution of the cloud. To remove this large-scale shape and obtain the normalized correlation function, we divide the histogram by the autoconvolution of the sum of the 1,000 single-particle distributions.

Atom lens experiment. A 300 mW laser beam with an elliptical waist of approximately $100 \times 150\,\mu\text{m}^2$ propagates vertically through the trap. The laser frequency is detuned by 300 GHz from the 2^3S_1 to 2^3P_2 transition. After turning off the magnetic trap, and waiting 500 µs for magnetic transients to die away, the defocusing laser is turned on for 500 µs.

Received 15 November; accepted 7 December 2006.

1. Hanbury Brown, R. & Twiss, R. Q. Correlation between photons in two coherent beams of light. *Nature* **177,** 27–29 (1956).
2. Scully, M. O. & Zubairy, M. S. *Quantum Optics* (Cambridge Univ. Press, Cambridge, UK, 1997).
3. Glauber, R. J. in *Quantum Optics and Electronics* (eds DeWitt, C., Blandin, A. & Cohen-Tannoudji, C.) 63–185 (Gordon and Breach, New York, 1965).
4. Yasuda, M. & Shimizu, F. Observation of two-atom correlation of an ultracold neon atomic beam. *Phys. Rev. Lett.* **77,** 3090–3093 (1996).
5. Schellekens, M. *et al.* Hanbury Brown Twiss effect for ultracold quantum gases. *Science* 310, 648–651 (2005); published online 15 September 2005 (doi:10.1126/science.1118024).
6. Öttl, A., Ritter, S., Köhl, M. & Esslinger, T. Correlations and counting statistics on an atom laser. *Phys. Rev. Lett.* **95,** 090404 (2005).
7. Fölling, S. *et al.* Spatial quantum noise interferometry in expanding condensates. *Nature* **434,** 481–484 (2005).
8. Spielman, I. B., Phillips, W. D. & Porto, J. V. The Mott insulator transition in two dimensions. Preprint at ⟨http://arxiv.org/cond-mat/0606216⟩ (2006).
9. Greiner, M., Regal, C. A., Stewart, J. T. & Jin, D. S. Probing pair-correlated fermionic atoms through correlations in atom shot noise. *Phys. Rev. Lett.* **94,** 110401 (2005).
10. Altman, E., Demler, E. & Lukin, M. D. Probing many-body states of ultracold atoms via noise correlations. *Phys. Rev. A* **70,** 013603 (2004).
11. Grondalski, J., Alsing, P. M. & Deutsch, I. H. Spatial correlation diagnostics for atoms in optical lattices. *Opt. Express* **5,** 249–261 (1999).
12. Hellweg, D. *et al.* Measurement of the spatial correlation function of phase fluctuating Bose-Einstein condensates. *Phys. Rev. Lett.* **91,** 010406 (2003).
13. Estève, J. *et al.* Observations of density fluctuations in an elongated Bose gas: ideal gas and quasicondensate regimes. *Phys. Rev. Lett.* **96,** 130403 (2006).
14. Loudon, R. *The Quantum Theory of Light* 3rd edn (Oxford Univ. Press, Oxford, 2000).
15. Fano, U. Quantum theory of interference effects in the mixing of light from phase independent sources. *Am. J. Phys.* **29,** 539–545 (1961).
16. Hanbury Brown, R. & Twiss, R. Q. A test of a new stellar interferometer on Sirius. *Nature* **178,** 1046–1048 (1956).
17. Baym, G. The physics of Hanbury Brown-Twiss intensity interferometry: From stars to nuclear collisions. *Acta Phys. Pol. B* **29,** 1839–1884 (1998).
18. Boal, D. H., Gelbke, C.-K. & Jennings, B. K. Intensity interferometry in subatomic physics. *Rev. Mod. Phys.* **62,** 553–602 (1990).
19. Viana Gomes, J. *et al.* Theory for a Hanbury Brown Twiss experiment with a ballistically expanding cloud of cold atoms. *Phys. Rev. A* **74,** 053607 (2006).
20. Kimble, H. J., Dagenais, M. & Mandel, L. Photon antibunching in resonance fluorescence. *Phys. Rev. Lett.* **39,** 691–695 (1978).
21. Henny, M. *et al.* The fermionic Hanbury Brown and Twiss experiment. *Science* **284,** 296–298 (1999).
22. Oliver, W. D., Kim, J., Liu, R. C. & Yamamoto, Y. Hanbury Brown and Twiss-type experiment with electrons. *Science* **284,** 299–301 (1999).
23. Kiesel, H., Renz, A. & Hasselbach, F. Observation of Hanbury Brown-Twiss anticorrelations for free electrons. *Nature* **418,** 392–394 (2002).
24. Iannuzzi, M., Orecchini, A., Sacchetti, F., Facchi, P. & Pascazio, S. Direct experimental evidence of free-fermion antibunching. *Phys. Rev. Lett.* **96,** 080402 (2006).
25. Rom, T. *et al.* Free fermion antibunching in a degenerate atomic Fermi gas released from an optical lattice. *Nature* **444,** 733–736 (2006).
26. Jagutzki, O. *et al.* A broad-application microchannel-plate detector system for advanced particle or photon detection tasks: Large area imaging, precise multi-hit timing information and high detection rate. *Nucl. Instrum. Methods Phys. Res. A* **477,** 244–249 (2002).

27. McNamara, J. M., Jeltes, T., Tychkov, A. S., Hogervorst, W. & Vassen, W. Degenerate Bose-Fermi mixture of metastable atoms. *Phys. Rev. Lett.* **97,** 080404 (2006).
28. Girardeau, M. Relationship between systems of impenetrable bosons and fermions in one dimension. *J. Math. Phys. (NY)* **1,** 516–523 (1960).
29. Olshanii, M. Atomic scattering in the presence of an external confinement and a gas of impenetrable bosons. *Phys. Rev. Lett.* **81,** 938–941 (1998).
30. Tychkov, A. S. *et al.* Metastable helium Bose-Einstein condensate with a large number of atoms. *Phys. Rev. A* **73,** 031603(R) (2006).

Supplementary Information is linked to the online version of the paper at www.nature.com/nature.

Acknowledgements This work was supported by the access programme of Laserlab Europe. The LCVU group in Amsterdam is supported by the 'Cold Atoms' programme of the Dutch Foundation for Fundamental Research on Matter (FOM) and by the Space Research Organization Netherlands (SRON). The Atom Optics group of LCFIO is a member of the IFRAF institute and of the Fédération LUMAT of the CNRS, and is supported by the French ANR and by the SCALA programme of the European Union.

Author Information Reprints and permissions information is available at www.nature.com/reprints. The authors declare no competing financial interests. Correspondence and requests for materials should be addressed to C.I.W. (christoph.westbrook@institutoptique.fr) or W.V. (w.vassen@few.vu.nl).

Observation of Atom Pairs in Spontaneous Four-Wave Mixing of Two Colliding Bose-Einstein Condensates

A. Perrin, H. Chang, V. Krachmalnicoff, M. Schellekens, D. Boiron, A. Aspect, and C. I. Westbrook*

Laboratoire Charles Fabry de l'Institut d'Optique, CNRS, Univ Paris-Sud, Campus Polytechnique, RD128, 91127 Palaiseau cedex, France

(Received 23 April 2007; published 12 October 2007)

We study atom scattering from two colliding Bose-Einstein condensates using a position sensitive, time resolved, single atom detector. In analogy to quantum optics, the process can also be thought of as spontaneous, degenerate four-wave mixing of de Broglie waves. We find a clear correlation between atoms with opposite momenta, demonstrating pair production in the scattering process. We also observe a Hanbury Brown–Twiss correlation for collinear momenta, which permits an independent measurement of the size of the pair production source and thus the size of the spatial mode. The back-to-back pairs occupy very nearly two oppositely directed spatial modes, a promising feature for future quantum optics experiments.

DOI: 10.1103/PhysRevLett.99.150405 PACS numbers: 03.75.Nt, 34.50.−s

Recent years have seen the emergence of "quantum atom optics", that is the extension of the many analogies between atom optics and traditional optics to the quantum optical domain in which phenomena like vacuum fluctuations and entanglement play a central role. In optics, the advent of correlated photon pairs [1] has provided a fruitful avenue of investigation, with examples including single photon sources and entangled states [2]. Partly inspired by this work, there have been many proposals concerning atom pairs, especially the production and observation of entanglement [3–7]. Many authors have also theoretically investigated other aspects of the pair production mechanism in both atomic collisions and in the breakup of diatomic molecules [7–13].

As emphasized in Ref. [4], pair production can be studied in two limits. If many atoms are created in a single mode, stimulated emission of atoms is important, and one can speak of two mode squeezing in analogy with Ref. [14]. The opposite limit, in which the occupation number of the modes is much less than unity, corresponds to the spontaneous production of atom pairs, entangled either in spin or momentum in analogy with Refs. [15,16]. Experiments on stimulated atomic four-wave mixing [17–19] and on parametric amplification in an optical lattice [20,21] are in the first limit, and pairs of "daughter BEC's" with opposite velocities have been clearly observed. Experiments in the regime of individual atom pairs include the many experiments investigating the scattered halo in collisions of cold atoms either in the s-wave regime [22–24] or for higher partial waves [25,26]. None of these experiments, however, has demonstrated correlated pairs. The only evidence of atom pair production with cold atoms has been reported in absorption images of atoms from the breakup of molecules near a Feshbach resonance [27].

Here, we report on the observation of individual atom pairs with opposite velocities produced in the collision of two condensates. A time and position resolved, single atom detector [28] permits us to reconstruct the three dimensional distribution of the scattered atoms: a spherical shell in velocity space. We also reconstruct the two-particle correlation function in 3D and find a strong correlation between atoms emitted back to back. This process can be interpreted as a spontaneous four-wave mixing process constrained by a phase matching condition as in the non linear optical analog which produces twin photons [2]. It can also be seen as the result of pairwise elastic collisions between atoms, constrained by momentum conservation. We measure the width of the velocity correlation function for a back to back atom pair and show that it corresponds very nearly to the uncertainty limited momentum spread of the colliding BECs.

This interpretation is confirmed by the observation of the velocity correlation function for two atoms scattered in the *same* direction. This latter effect, predicted in Refs. [7,10,13], is another manifestation of the Hanbury Brown–Twiss effect (HBT). As in high energy collisions [29], the effect allows us to measure the size of the collision volume.

The fact that the width of the HBT peak is close to that of the back-to-back correlation confirms that for a given atom on the collision sphere, its partner is scattered into a single mode of the matter wave field. This observation is crucial for future experiments in which one would like to bring pairs back together in order to confirm their entanglement in the spirit of Ref. [16] or observe other quantum effects [30].

We produce condensates of 10^4–10^5 atoms in the $m_x = 1$ sublevel of the 2^3S_1 state of metastable helium (He*). The condensates are stored in a cylindrically symmetric magnetic trap with axial and radial trapping frequencies of 47 and 1150 Hz, respectively. The bias field is 0.25 G in the x direction (see Fig. 1), and defines the quantization axis. The uncertainty limited velocity spread of the colliding

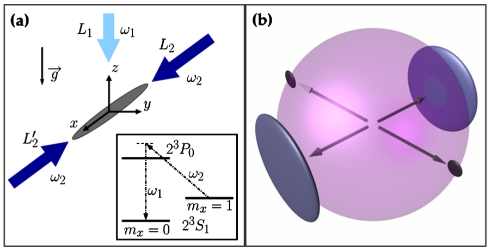

FIG. 1 (color online). (a) View of the magnetically trapped condensate (in the $m_x = 1$ state) and the three laser beams which create two cigar shaped counterpropagating free condensates (in the $m_x = 0$ state) by σ^-/π Raman transfers induced by $L_1 - L_2$ and $L_1 - L_2'$, respectively (see inset). L_1 is π-polarized (along x) while L_2 and L_2' are σ^--polarized. (b) Representation in velocity space of the expected atomic density after the collision. The scattered atoms are on a sphere and the remaining condensates, pancake-shaped after expansion, lie on the edge of the sphere along the x axis. A collision process involving an atom of each condensate is also represented. The shape of the scattering modes is related to the uncertainty limited momentum spread of the condensates.

atoms is thus anisotropic and we calculate it numerically using the Gross-Pitaevskii equation [31]. For a condensate with 3×10^4 atoms, we find rms axial and radial velocity spreads of $v_x^{\mathrm{rms}} = 0.0044 v_{\mathrm{rec}}$ and $v_{yz}^{\mathrm{rms}} = 0.091 v_{\mathrm{rec}}$, where $v_{\mathrm{rec}} = 9.2$ cm/s is the single photon recoil velocity, $\hbar k/m$ where k is the photon wave vector and m is the atomic mass. The spread in these values due to the spread in condensate number is about $\pm 20\%$.

To generate two colliding Bose-Einstein condensates, we use two stimulated Raman transitions with different momentum transfers, produced by phase coherent laser beams L_1, L_2, and L_2', as shown in Fig. 1 [31]. These transitions have two purposes: first they transfer atoms to the magnetic field insensitive state $m_x = 0$ so that they freely fall to the detector and second, they separate the condensate into two components with velocities $v_{\mathrm{rec}}(\mathbf{e_1} \pm \mathbf{e_2})$, where $\mathbf{e_1}$ and $\mathbf{e_2}$ are the unit vectors along the propagation axes of the laser beams L_1 and L_2 respectively. The beams are pulsed on for a duration of ~500 ns and couple about 60% of the atoms to the $m_x = 0$ state. We do not switch off the magnetic trap, therefore atoms remaining in $m_x = 1$ stay trapped. The two colliding condensates travel with a relative velocity of $2v_{\mathrm{rec}}$, at least 8 times larger than the speed of sound in the initial condensate. This ensures that elementary excitations of the condensate correspond to free particles. Since they are no longer trapped, the two colliding condensates expand radially, reducing the collision rate. A numerical model [8], assuming an expansion identical to that of a single condensate with the same total number of atoms, shows a roughly exponential decrease in the pair production rate with a time constant of ~150 μs.

After the collision, atoms fall onto a 8 cm microchannel plate detector placed 46.5 cm below the trap center. This detector measures the arrival time of the atoms and their positions in the x-y plane [28,32]. Figure 2 shows successive 2.4 ms time slices showing the atom positions as they cross the detector plane. The time of flight for the center of mass to reach the detector is 320 ms. Since this time of flight is large compared to the collision duration, and the observed patterns are large compared to the collision volume, the observed 3D atom positions accurately reflect the velocity distribution after collision. In the following, we will only refer to the velocities of the detected atoms.

In Fig. 2, one clearly sees a spherical shell of radius of v_{rec}, represented by circles of varying diameter [see also Fig. 1(b)]. In the midplane of the sphere one can see the unscattered, pancake-shaped condensates I, II which locally saturate the detector. Other features are also visible in Fig. 2. In frames (a),(b) one sees a condensate, III, which underwent no momentum transfer, possibly due to the imperfect polarization of the Raman beams which can produce an off resonant, single beam Raman transition [31]. A fourth condensate, IV, probably resulting from four-wave mixing [17] of condensate III and the main unscattered condensates I, II is visible in frames (h),(i). Frames (b),(c) show a collision sphere due to the collision of I with atoms remaining trapped in $m_x = 1$ and with condensate III. The two spots within the sphere in frames (d)–(f) are not understood.

To avoid effects of local saturation of the detector in our analysis, we exclude regions around the 4 condensates, representing about 40% of the sphere. On the remaining area of the sphere we detect between 30 and 300 atoms on

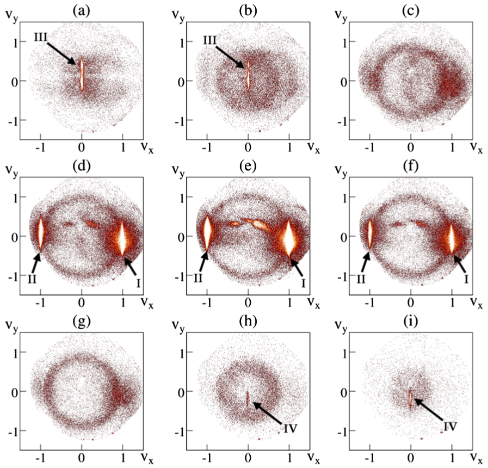

FIG. 2 (color online). (a)–(i) Images of the collision of two condensates. Each frame represents a 2.4 ms time slice of the atomic cloud as it passes the plane of the detector (x-y). 150 shots have been averaged to obtain these images. The two colliding condensates I, II and the collision sphere are clearly visible. Other features visible in the images are discussed in the text. The axes are marked in units of the recoil velocity.

each shot, with an average of about 100 per shot. Assuming a detection efficiency of 10% [32], this means that ~5% of the atoms are scattered from the two condensates. This number is consistent with the expected *s*-wave cross section [33] and the estimated evolution of the density during the collision.

We examine the pair correlation function for atoms in back to back directions by constructing, within the set of all the scattered atoms in one shot, a three-dimensional histogram containing all the pairs with a velocity sum $\mathbf{V} = \mathbf{V_1} + \mathbf{V_2}$ close to zero. We then sum the histograms over 1100 shots. Another histogram containing all the pairs of the sum of all shots gives the accidental coincidence rate for uncorrelated atoms and is used as a normalization. We thus recover the normalized second order correlation function, averaged over the sphere [31], $g^{(2)}(\mathbf{V})$ of the distribution of relative velocities of atom pairs on the sphere. Figure 3(a) shows the behavior of $g^{(2)}(\mathbf{V})$ around $\mathbf{V} = \mathbf{0}$ projected along the three space axes. The peak indicates that, given the detection of an atom on the sphere, there is an enhanced probability of detecting a second one on the opposite side. Cartesian coordinates are best suited to plotting the data because of the competing spherical symmetry of the scattering process and the cylindrical symmetry of the source.

To analyze these results further, we perform a three-dimensional Gaussian fit to the normalized histogram:

$$g^{(2)}(V_x, V_y, V_z) = 1 + \eta e^{-[(V_x^2/2\sigma_x^2)-(V_y+V_z)^2/(2\sigma_{yz}^2)]}. \qquad (1)$$

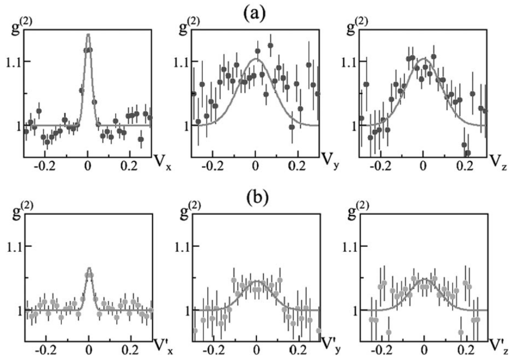

FIG. 3. Back-to-back [panel (a)] and collinear [panel (b)] correlation peaks. (a) Projection of $g^{(2)}(\mathbf{V} = \mathbf{V_1} + \mathbf{V_2})$ along the different axes of the experiment and around $\mathbf{V} = \mathbf{0}$. The projection consists in averaging the correlation in the two other directions over a surface equal to the products of the corresponding correlation lengths. This averaging makes the height smaller than the 3D fitted value $\eta^{\mathrm{BB}} = 0.19 \pm 0.02$. The peak is the signature for correlated atoms with opposite velocities. (b) Projection of $g^{(2)}(\mathbf{V}' = \mathbf{V_1} - \mathbf{V_2})$ along the different axes of the experiment. This peak is due to the Hanbury Brown–Twiss bunching effect. All velocities are expressed in units of the recoil velocity.

The fit gives $\eta^{\mathrm{BB}} = 0.19 \pm 0.02$, $\sigma_x^{\mathrm{BB}} = 0.017 \pm 0.002 v_{\mathrm{rec}}$, and $\sigma_{yz}^{\mathrm{BB}} = 0.081 \pm 0.004 v_{\mathrm{rec}}$. The observed width in the x direction is limited by the rms pair resolution of the detector, $0.14 v_{\mathrm{rec}}$ [31,36]. In the y and z directions, the observed width is close to the uncertainty limited velocity scale v_{yz}^{rms} discussed above. It is therefore reasonable to conclude that the anisotropy in the correlation function is closely related to the anisotropy of the momentum distribution in the source. Detailed modeling accounting accurately for this width is in progress, but for purposes of this Letter, we will simply compare the width with that of the correlation function for collinear atoms as described below.

The procedure to construct the correlation function for nearly collinear velocities (the HBT effect) is the same as that for the back-to-back correlation function. Defining the relative velocity $\mathbf{V}' = \mathbf{V_1} - \mathbf{V_2}$, we show in Fig. 3(b) the correlation function $g^{(2)}(\mathbf{V}')$ around $\mathbf{V}' = \mathbf{0}$. Using the fitting function, Eq. (1), we find: $\eta^{\mathrm{CL}} = 0.10 \pm 0.02$, $\sigma_x^{\mathrm{CL}} = 0.016 \pm 0.003 v_{\mathrm{rec}}$, and $\sigma_{yz}^{\mathrm{CL}} = 0.069 \pm 0.008 v_{\mathrm{rec}}$. As in the back to back case, the width in the x direction is limited by the resolution while in the y-z plane it is close to v_{yz}^{rms}. If we think of the HBT effect as giving a measure of the size of the pair production source, the width of the collinear correlation function defines the size of a mode of the scattered matter wave field. The fact that the back-to-back and collinear widths are so close, at least in the directions we can resolve, is further, strong evidence that, at least in the directions we resolve, the pairs we produce are in oppositely directed modes.

We now turn to the height of the peaks η. In the collinear case we expect the value of η^{CL} to be unity for a detector resolution much smaller than the peak width. Since in the x direction the width is clearly limited by the resolution, a crude estimate for η^{CL} is the ratio of the ideal width to the observed one: $\eta^{\mathrm{CL}} \approx v_x^{\mathrm{rms}}/\sigma_x = 0.3$. The discrepancy with the fitted value may have to do with our crude estimate of the effective source size along x and therefore of v_x^{rms}.

In the back-to-back case, the height of the peak is not limited to unity. A simple model of the peak height compares the number of true pairs to random coincidences in a volume ΔV defined by the widths observed in Fig. 3:

$$1 + \eta^{\mathrm{BB}} = \frac{\text{true} + \text{random}}{\text{random}} = 1 + \frac{V}{N\Delta V}. \qquad (2)$$

Here N is the number of atoms scattered on a single shot (but not necessarily detected) and V is the volume of the scattering shell. A rough estimate of $\Delta V/V$ is 1/1400. As mentioned above, we detect on average 100 atoms on the analyzed 60% of the sphere. Assuming again a quantum efficiency of 10%, a rough estimate of the average number N is 1700 so that we find $\eta^{\mathrm{BB}} \approx 0.8$ which gives the correct order of magnitude. We emphasize that ΔV is limited by the detector resolution in the x direction and is therefore about 10 times larger than the volume corresponding to a single mode. Thus, as stated in the introduc-

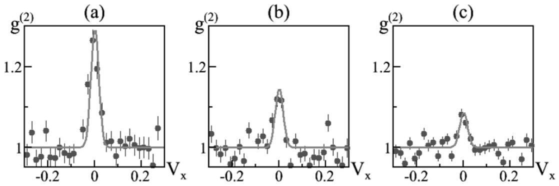

FIG. 4. Projections of $g^{(2)}(\mathbf{V})$ along the x axis and around $\mathbf{V} = \mathbf{0}$. Bin of mean number of detected atoms of (a) 50, (b) 125, and (c) 190.

tion, the number of scattered atoms per mode is small compared to unity, and we are in the separated entangled pair production regime. We can verify the $1/N$ dependence of Eq. (2) by binning the data according to the number of scattered atoms per shot. Dividing the 1100 shots into 3 bins of different atom numbers we do observe the expected trend as shown in Fig. 4.

A detailed model of the pair production process must include a more careful description of the collision geometry of colliding and expanding condensates as well as the effect of the condensates' mean field on the scattered atoms, something which is neglected in the above discussion. A rough estimate of the mean field effect is found by adding the chemical potential to the kinetic energy of a scattered atom. This gives an additional velocity broadening of order $0.03v_{\text{rec}}$, not entirely negligible compared to the observed widths. Several workers are developing such models. The correlation functions we observe lend themselves to an investigation of Cauchy-Schwartz inequalities [2]. A cross correlation (back-to-back) greater than an autocorrelation (collinear) violates a Cauchy-Schwartz inequality for classical fields. Sub-Poissonian number differences between opposite directions should also be present [7]. A future publication will discuss these aspects of the experiment.

We acknowledge valuable discussions with K. Kheruntsyan, K. Mølmer, and M. Trippenbach. Our group is a member of the IFRAF institute, and is supported by the french ANR, the QUDEDIS program, and the SCALA program of the European Union.

---

*christoph.westbrook@institutoptique.fr

[1] D. C. Burnham and D. L. Weinberg, Phys. Rev. Lett. **25**, 84 (1970).
[2] See, for example, D. Walls and G. Milburn, *Quantum Optics* (Springer, New York, 1991).
[3] H. Pu and P. Meystre, Phys. Rev. Lett. **85**, 3987 (2000).
[4] L.-M. Duan, A. Sørensen, J. I. Cirac, and P. Zoller, Phys. Rev. Lett. **85**, 3991 (2000).
[5] K. V. Kheruntsyan, M. K. Olsen, and P. D. Drummond, Phys. Rev. Lett. **95**, 150405 (2005).
[6] T. Opatrný and G. Kurizki, Phys. Rev. Lett. **86**, 3180 (2001).
[7] C. M. Savage, P. E. Schwenn, and K. V. Kheruntsyan, Phys. Rev. A **74**, 033620 (2006).
[8] Y. B. Band, M. Trippenbach, J. P. Burke, and P. S. Julienne, Phys. Rev. Lett. **84**, 5462 (2000).
[9] P. Naidon and F. Masnou-Seeuws, Phys. Rev. A **68**, 033612 (2003).
[10] P. Ziń *et al.*, Phys. Rev. Lett. **94**, 200401 (2005).
[11] P. Ziń, J. Chwedeńczuk, and M. Trippenbach, Phys. Rev. A **73**, 033602 (2006).
[12] A. A. Norrie, R. J. Ballagh, and C. W. Gardiner, Phys. Rev. A **73**, 043617 (2006).
[13] P. Deuar and P. D. Drummond, Phys. Rev. Lett. **98**, 120402 (2007).
[14] A. Heidmann *et al.*, Phys. Rev. Lett. **59**, 2555 (1987).
[15] Z. Y. Ou and L. Mandel, Phys. Rev. Lett. **61**, 50 (1988); Y. H. Shih and C. O. Alley, Phys. Rev. Lett. **61**, 2921 (1988).
[16] M. A. Horne, A. Shimony, and A. Zeilinger, Phys. Rev. Lett. **62**, 2209 (1989); J. G. Rarity and P. R. Tapster, Phys. Rev. Lett. **64**, 2495 (1990).
[17] L. Deng *et al.*, Nature (London) **398**, 218 (1999).
[18] J. M. Vogels, K. Xu, and W. Ketterle, Phys. Rev. Lett. **89**, 020401 (2002).
[19] J. M. Vogels, J. K. Chin, and W. Ketterle, Phys. Rev. Lett. **90**, 030403 (2003).
[20] N. Gemelke *et al.*, Phys. Rev. Lett. **95**, 170404 (2005).
[21] G. K. Campbell *et al.*, Phys. Rev. Lett. **96**, 020406 (2006).
[22] A. P. Chikkatur *et al.*, Phys. Rev. Lett. **85**, 483 (2000).
[23] K. Gibble, S. Chang, and R. Legere, Phys. Rev. Lett. **75**, 2666 (1995).
[24] N. Katz, E. Rowen, R. Ozeri, and N. Davidson, Phys. Rev. Lett. **95**, 220403 (2005).
[25] C. Buggle, J. Leonard, W. von Klitzing, and J. T. M. Walraven, Phys. Rev. Lett. **93**, 173202 (2004).
[26] N. R. Thomas, N. Kjærgaard, P. S. Julienne, and A. C. Wilson, Phys. Rev. Lett. **93**, 173201 (2004).
[27] M. Greiner, C. A. Regal, J. T. Stewart, and D. S. Jin, Phys. Rev. Lett. **94**, 110401 (2005).
[28] M. Schellekens *et al.*, Science **310**, 648 (2005).
[29] G. Baym, Acta Phys. Pol. B **29**, 1839 (1998).
[30] C. K. Hong, Z. Y. Ou, and L. Mandel, Phys. Rev. Lett. **59**, 2044 (1987).
[31] See EPAPS Document No. E-PRLTAO-99-043742 for the experimental details for interested readers. For more information on EPAPS, see http://www.aip.org/pubservs/epaps.html.
[32] T. Jeltes *et al.*, Nature (London) **445**, 402 (2007).
[33] We extrapolate from [34,35] a value of 5.3 nm for the scattering length between $m = 0$ atoms.
[34] S. Moal *et al.*, Phys. Rev. Lett. **96**, 023203 (2006).
[35] P. J. Leo, V. Venturi, I. B. Whittingham, and J. F. Babb, Phys. Rev. A **64**, 042710 (2001).
[36] J. Viana Gomes *et al.*, Phys. Rev. A **74**, 053607 (2006).

PHYSICAL REVIEW A **77**, 033601 (2008)

Hanbury Brown and Twiss correlations in atoms scattered from colliding condensates

Klaus Mølmer
Lundbeck Foundation Theoretical Center for Quantum System Research, Department of Physics and Astronomy, University of Aarhus, DK-8000 Århus C, Denmark

A. Perrin, V. Krachmalnicoff, V. Leung, D. Boiron, A. Aspect, and C. I. Westbrook
Laboratoire Charles Fabry de l'Institut d'Optique, CNRS, Université Paris-sud Campus Polytechnique, RD128, 91127 Palaiseau, France

(Received 1 October 2007; published 4 March 2008)

Low energy elastic scattering between clouds of Bose condensed atoms leads to the well known *s*-wave halo with atoms emerging in all directions from the collision zone. In this paper we discuss the emergence of Hanbury Brown and Twiss coincidences between atoms scattered in nearly parallel directions. We develop a simple model that explains the observations in terms of an interference involving two pairs of atoms each associated with the elementary *s*-wave scattering process.

DOI: 10.1103/PhysRevA.77.033601 PACS number(s): 03.75.Gg, 34.50.−s

I. INTRODUCTION

In a number of experiments, Bose-Einstein condensates have been prepared to collide with each other with well defined collision energies and momenta. At the microscopic level, when two particles with equal mass and opposite velocities collide in an *s*-wave collision, the collision partners will propagate away from each other with the same probability amplitude in all directions, but their individual momenta are correlated in opposite directions, as their total center-of-mass momentum is conserved in the collision process. In experiments with colliding condensates, the scattering into all directions has been clearly observed as a so-called *s*-wave halo of scattered particles [1]. The observation of pair correlations of particles leaving the collision region back-to-back (see Fig. 1), requires efficient detection of all momentum components of individual atoms, and this correlation has recently been observed as a significant coincidence signal in a collision experiment with Bose-Einstein condensates of metastable atomic helium [2]. The same experiment also observed an increased coincidence of particles scattered into *the same* direction. This phenomenon is due to the bosonic nature of the particles and to the fact that several independent scattering processes occur simultaneously.

We shall present a theoretical analysis of this Hanbury Brown and Twiss correlation phenomenon, aiming at a simple model which explains its qualitative and quantitative character in experiments. It is important to emphasize that the appearance of atoms moving in the same direction is not compatible with momentum conservation in a single collision process of two counterpropagating atoms, and our discussion will, indeed, refer to effects that rely on a many-body treatment of the collision of larger ensembles. In order to get physical insight, we will separate the problem in two: first, we treat independent pairwise collisions in which the collisional interaction gives rise to pairs of scattered atoms, and second, we treat the evolution of the many-body state describing the ensemble of scattered atoms neglecting the interactions in order to apply analytic methods. The validity of this separation and means to improve the theory, if necessary, will be discussed.

In Sec. II, we present a full second quantized description of the collision of a large number of identical bosons. We shall write down the second quantized many-body Hamiltonian, and discuss how the elementary processes of interest relate to the different terms in this Hamiltonian. We treat the case where all the atoms initially populate two counterpropagating single particle states which are only weakly depleted by the collisions, and which will hence serve as *c*-number field sources for creation of pairs. This is in analogy with the quantum optics treatment of spontaneous four-wave mixing, where photon pairs are generated from the interaction of two incident laser beams, described by classical electromagnetic waves. In Sec. III, we discuss the Bogoliubov transformation, which provides a very accurate approximation to the time evolution of the system. We shall not, however, apply this transformation in a quantitative treatment, but rather show that its formal structure already predicts the collinear [Hanbury Brown and Twiss (HBT)] correlation and motivates a quite general analytical Ansatz for the quantum state of the scattered atoms. In Sec. IV, we shall consider the leading two- and four-atom terms in an expansion of the quantum state of scattered atoms, and show that they hold the key to the observed Hanbury Brown and Twiss correla-

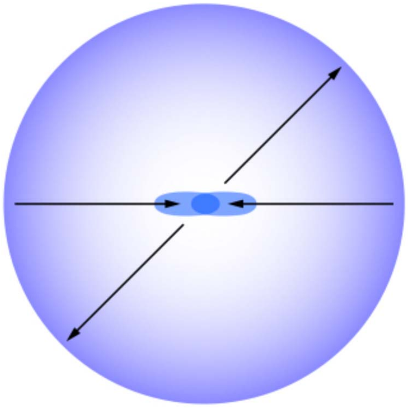

FIG. 1. (Color online) Diagrammatic representation of two condensates colliding and giving rise to an s-wave halo of scattered particles. Particles are scattered pairwise back-to-back.

tions. In Sec. V, we shall use energy conservation and phase matching considerations to motivate a simple analytical model, from which we show that the coincidence of scattered particles in the same direction, though a many-body effect, can be understood quantitatively from the properties of the simple two-atom scattering wave function. Section VI concludes the paper with a discussion of the insights offered by our analysis.

II. COLLIDING BOSE-EINSTEIN CONDENSATES

The Hamiltonian,

$$H=\int d\vec{r}\hat{\Psi}^{\dagger}(\vec{r})\left(-\frac{\hbar^{2}}{2m}\Delta+V(\vec{r})+\frac{g}{2}\hat{\Psi}^{\dagger}(\vec{r})\hat{\Psi}(\vec{r})\right)\hat{\Psi}(\vec{r}), \quad (1)$$

with field operators obeying the Bosonic commutator relations $[\Psi(\vec{r}),\Psi^{\dagger}(\vec{r}\,')]=\delta(\vec{r}-\vec{r}\,')$, gives a good description of bosons interacting at low collision energies via a short range potential. The interaction is represented by a delta-function interaction term with strength g, proportional to the s-wave scattering length. The atoms may be subject to a wide range of trapping or guiding potentials $V(\vec{r})$, or they may propagate freely ($V=0$), and the initial state of the system may be specified according to experimental preparation procedures to describe, for example, a single condensate or several macroscopically populated components. We are interested in the situation, in which two condensates with well defined momenta, and hence relatively large spatial extent, propagate toward each other. The conventional second quantized Hamiltonian fully describes the problem, and a Monte Carlo-type simulation of the dynamics [3–5], and perhaps even simpler simulation approaches based on truncated Wigner function expansions [6,7], may solve this problem in full generality by full three-dimensional (3D) propagation of stochastic Schrödinger-type equations.

We assume that elastic collisions occur with a sufficiently small cross section that the colliding condensates are only weakly depleted due to the collision term in Eq. (1). The Hamiltonian has terms describing the kinetic energy and the potential energy of atoms moving in the external potential and finally, a term describing the mean field repulsive or attractive potential due to the other atoms of the colliding condensates. But the product of two creation and two annihilation operators in the interaction term does not only read as density dependent correction to the potential energy in the Gross-Pitaevskii equation: the product of two creation operators may also cause the creation of a pair of atoms with momenta entirely different from the incident ones, extracted consistently from the condensates by the product of annihilation operators. The pairs of atoms "created" in the scattering process are the ones that are detected as the s-wave halo around the condensate collision region in Fig. 1.

We can think of each point in the collision zone as a point source for a pair of initially close atoms (atoms only collide at short range), which are subsequently separated by free propagation, perturbed by the interaction with the condensate components. This propagation, together with the coherent addition of pair amplitudes originating from the entire collision zone leads to a complicated many-body entangled state, but energy conservation, imposed after a sufficiently long interaction time, and momentum conservation, imposed by phase matching, serves to justify our simpler model, described below.

III. BOGOLIUBOV APPROXIMATION

If the original condensates are only weakly depleted by the scattering, we may follow Refs. [8–10] and expand the atomic field annihilation operator,

$$\hat{\Psi}(\vec{r},t)=\psi_{\vec{k}_0}(\vec{r},t)+\psi_{-\vec{k}_0}(\vec{r},t)+\hat{\Psi}'(\vec{r},t), \quad (2)$$

as a sum of mean field terms $\psi_{\pm\vec{k}_0}$ describing the incident wave packets, and noise terms $\hat{\Psi}'(\vec{r},t)$, describing field components of the initially unpopulated scattering modes. We shall assume that there is no active external potential during the collision, and for convenience we omit the prime on the noise operator terms in the following. The Bogoliubov approximation consists of applying the Gross-Pitaevskii equation to the propagation in time of the mean field part and of obtaining the Heisenberg equations of motion for the field operators from an expansion of the Hamiltonian (1) to second order in the noise operator terms.

These equations of motion are linear in the field creation and annihilation operators,

$$\begin{aligned} i\hbar\partial_t\hat{\Psi}(\vec{r},t)=&\left(-\frac{\hbar^{2}}{2m}\Delta+2g|\psi_{\vec{k}_0}(\vec{r},t)+\psi_{-\vec{k}_0}(\vec{r},t)|^{2}\right)\hat{\Psi}(\vec{r},t)\\ &+g[\psi_{\vec{k}_0}(\vec{r},t)+\psi_{-\vec{k}_0}(\vec{r},t)]^{2}\hat{\Psi}^{\dagger}(\vec{r},t). \end{aligned} \quad (3)$$

By expanding the operator solution to this equation as a formal Bogoliubov transformation,

$$\hat{\Psi}(\vec{r},t)=\int d\vec{r}\,'[f(\vec{r},\vec{r}\,',t)\hat{\Psi}(\vec{r}\,',0)+g(\vec{r},\vec{r}\,',t)\hat{\Psi}^{\dagger}(\vec{r}\,',0)], \quad (4)$$

the Heisenberg equations of motion (3) can be rewritten as partial differential equations for the c-number functions f and g, and the atomic annihilation operators are at any given time explicitly expressed as linear combinations of the annihilation and creation operators at time zero, where the initial state is assumed to be known (incident condensate wave functions, no scattered atoms). The mean atom number and any higher order correlation function of the field can therefore be expressed algebraically in terms of the expansion coefficients of the Bogoliubov transformation and the known vacuum expectation values of field operator products. Although obviously related, the use of the Bogoliubov transformation here is different from the Bogoliubov approximation used to identify low-lying, collective excitation modes in a condensate. The analysis rather follows the philosophy of squeezed light generation with optical parametric oscillators in quantum optics, where the Bogoliubov method is used to diagonalize a multimode Hamiltonian with pair creation and annihilation operators [11] (see also [12,13]). By use of the Bogoliubov approximation, the full many-body problem has been reduced to partial differential equations of a complexity comparable to the single particle Schrödinger equation, and one only has to solve time dependent wave equations in three spatial dimensions as done in Refs. [8–10].

Here we shall demonstrate some properties of the solution that follow by purely analytical arguments, i.e., without access to the precise solution. Since the initial state of the atomic scattering modes (momentum components) of interest is the vacuum state, which has a Gaussian (Wigner) probability distribution for the multimode field variables, and the Bogoliubov transformation is linear in field operators, the state will, independently of the precise form of the transformation, at all later times be a Gaussian with vanishing mean field expectation value [14]. If we restrict the analysis to a single final momentum state (mode), by a partial trace over all other modes, the state of this mode is also a Gaussian state with vanishing mean amplitude. It is thus fully characterized by the second moments of the Hermitian linear combinations $q_{\vec{k}} \equiv (\hat{\Psi}^\dagger(\vec{k}) + \hat{\Psi}(\vec{k}))/\sqrt{2}$, $p_{\vec{k}} = i(\hat{\Psi}^\dagger(\vec{k}) - \hat{\Psi}(\vec{k}))/\sqrt{2}$ of the field operators. We now wish to establish that our Gaussian distribution is symmetric, i.e., $\mathrm{Var}(q_{\vec{k}}) = \mathrm{Var}(p_{\vec{k}})$. This indeed follows if the "anomalous" moments $\langle \hat{\Psi}^\dagger(\vec{k})^2 \rangle = \langle \hat{\Psi}(\vec{k})^2 \rangle = 0$, i.e., if there is no coherence between states differing by two atoms propagating in the given direction. We now apply the physical argument, that the collisional Hamiltonian does not produce such coherence, since the collision process can only produce pairs of atoms propagating in opposite directions, and states, e.g., with zero and two atoms with momentum $\vec{k}$ must also contain zero and two atoms with momentum around $-\vec{k}$. The anomalous moments vanish due to the orthogonality of these parts of the wave function.

It is well known in quantum optics, that a symmetric Gaussian state is equivalent to an incoherent mixture of number states with exponential number distribution, also known as a thermal state with the density matrix [11],

$$\rho_1 = (1 - |t|^2) \sum |t^2|^n |n\rangle\langle n|. \tag{5}$$

The state conditioned upon detection, and annihilation, of a single particle reads,

$$\rho_c = \nu \hat{a} \rho_1 \hat{a}^\dagger = \frac{(1 - |t|^2)^2}{|t|^2} \sum_n |t^2|^n n |n-1\rangle\langle n-1|, \tag{6}$$

where ν is a normalization constant. A straightforward calculation shows that this state has precisely twice as many bosons on average as (5), and hence that the probability to detect two bosons by a low efficiency detector is twice the square of the single quantum detection probability. It thus follows that the coincidence counting rate for observing two atoms leaving the collision zone in the same, narrowly defined, direction, $\langle \hat{\Psi}^\dagger(\vec{k}) \hat{\Psi}^\dagger(\vec{k}) \hat{\Psi}(\vec{k}) \hat{\Psi}(\vec{k}) \rangle$ is twice the square of the mean counting rate, and twice the coincidence rate for seeing atoms in two unrelated directions.

Without performing any calculations, we therefore understand qualitatively the observed coincidences observed in the experiments [2] as the direct consequence of the thermal counting statistics (Gaussian quadrature distribution) of the output flux in all scattering directions. This is the famous Hanbury Brown and Twiss effect [17–20] observed originally as photon bunching in chaotic light resulting from the addition of the contributions of many incoherent emitters. We note that the factor n in the expansion (6) is a bosonic amplification factor stemming from the $\sqrt{n}$ coefficients accompanying the annihilation operator acting on the quantum state. The effects of this amplification factor are also observed in condensate formation [21] and matter wave amplification [22] experiments. In order to provide a natural estimate of the HBT momentum correlation function, one could develop the field correlations by solution of the linear Bogoliubov-de-Gennes equations for the problem [8–10] which by the corresponding linear transformation of operators provides the first and second order momentum correlation functions and hence the momentum range within which the bunching effect takes place. Here, we will rather keep track of the binary scattering states, and in particular of the counterpropagating partners, which will give us an alternative and very useful physical interpretation of the effect.

The Bogoliubov transformation of field operators is equivalent to a multimode unitary squeezing operation [11], which is indeed nothing but the time evolution operator of a Hamiltonian with quadratic terms in field creation and annihilation operators. Such an operator can be ordered as a product of three exponentials [15,16]: one involving a sum of products of pairs of creation operators, one involving a sum of products of creation and annihilation operators and one involving a sum of products of pairs of annihilation operators. When acting on the initial vacuum state vector, only the unit term of the series expansion of the latter two exponentials contribute, and the state can therefore be written in terms of a quadratic form of creation operators of atoms, e.g., in the momentum space representation,

$$|\Psi\rangle = N_\Psi \exp\left(\int d\vec{k}_1 d\vec{k}_2 \psi(\vec{k}_1, \vec{k}_2) \hat{\Psi}^\dagger(\vec{k}_1) \hat{\Psi}^\dagger(\vec{k}_2) \right) |\mathrm{vac}\rangle. \tag{7}$$

The function $\psi(\vec{k}_1, \vec{k}_2)$ generally depends in a complex manner on the dynamical evolution. It is of course related to the scattering wave function of a single pair of atoms, and we shall come back to this relationship in connection with the model studied in Sec. V of the paper. The use of second quantization automatically yields the bosonic symmetry of our state, but in addition we can require that the pair amplitude function obey the explicit exchange symmetry $\psi(\vec{k}_1, \vec{k}_2) = \psi(\vec{k}_2, \vec{k}_1)$. For now, let us assume, that the propensity for atoms to be scattered into opposite directions also implies that $\psi(\vec{k}_1, \vec{k}_2)$ takes nonvanishing values for all directions of the scattered particles, but only if $\vec{k}_1 \sim -\vec{k}_2$. The function $\psi(\vec{k}_1, \vec{k}_2)$ is not a normalized wave function: the larger its amplitude the more particle pairs are created, and higher order terms of the exponential play more and more important roles. The many-body state $|\Psi\rangle$ is normalized by the prefactor N_Ψ in (7).

We now proceed to determine the density-density correlations of atoms detected in two different directions, labeled by momentum states $(\vec{k},\vec{k}')$, i.e., the expectation value

$$F(\vec{k},\vec{k}') \propto \langle \hat{\Psi}^{\dagger}(\vec{k})\hat{\Psi}^{\dagger}(\vec{k}')\hat{\Psi}(\vec{k}')\hat{\Psi}(\vec{k})\rangle \tag{8}$$

The state (7) is a Gaussian state, and by Wick's theorem [23] this expectation value can be written down in terms of only pair-expectation values. We shall address the contribution from the four-atom component in the expansion of the exponential in (7), as this provides a straightforward interpretation of the origin and the behavior of the atomic Hanbury Brown and Twiss correlations.

IV. TWO-ATOM AND FOUR-ATOM STATES

The state (7) can be written explicitly,

$$|\Psi\rangle = N_{\Psi}\bigg(|\text{vac}\rangle + \int d\vec{k}_1 d\vec{k}_2 \psi(\vec{k}_1,\vec{k}_2)\hat{\Psi}^{\dagger}(\vec{k}_1)\hat{\Psi}^{\dagger}(\vec{k}_2)|\text{vac}\rangle + \frac{1}{2}\bigg(\int d\vec{k}_1 d\vec{k}_2 \psi(\vec{k}_1,\vec{k}_2)\hat{\Psi}^{\dagger}(\vec{k}_1)\hat{\Psi}^{\dagger}(\vec{k}_2)\bigg)^2|\text{vac}\rangle + \ldots\bigg). \tag{9}$$

The zero order term is the vacuum state. The first order term is a two-atom state of atoms propagating back-to-back, and the second order term of the series expansion of (7) is the four-atom state

$$|\Psi_4\rangle \equiv \bigg(\int d\vec{k}_1 d\vec{k}_2 \psi(\vec{k}_1,\vec{k}_2)\hat{\Psi}^{\dagger}(\vec{k}_1)\hat{\Psi}^{\dagger}(\vec{k}_2)\bigg)^2|\text{vac}\rangle, \tag{10}$$

which we will show accounts for the observed HBT effect. The squared pair creation operator in (10) can be expanded as a fourfold integral. To obtain the correlation function (8), we have to apply the product of the two annihilation operators on $|\Psi_4\rangle$ and determine the squared norm of the resulting state,

$$F(\vec{k},\vec{k}') \propto \|\hat{\Psi}(\vec{k})\hat{\Psi}(\vec{k}')|\Psi_4\rangle\|^2. \tag{11}$$

Using the field commutator relations, we can shift the annihilation operators to the right of all creation operators in (11). This yields a total of 12 terms, which by relabeling and use of the exchange symmetry can be reduced to a sum of three different contributions,

$$\begin{aligned}\hat{\Psi}(\vec{k})\hat{\Psi}(\vec{k}')|\Psi_4\rangle \propto \int d\vec{k}_1 d\vec{k}_2 \{&\psi(\vec{k}_1,\vec{k}_2)\psi(\vec{k},\vec{k}') \\ &+ \psi(\vec{k}_1,\vec{k})\psi(\vec{k}_2,\vec{k}') \\ &+ \psi(\vec{k}_1,\vec{k}')\psi(\vec{k}_2,\vec{k})\}\hat{\Psi}^{\dagger}(\vec{k}_1)\hat{\Psi}^{\dagger}(\vec{k}_2)|\text{vac}\rangle.\end{aligned} \tag{12}$$

and thus its squared norm:

$$\begin{aligned}F(\vec{k},\vec{k}') \propto \int d\vec{k}_1 d\vec{k}_2 |&\psi(\vec{k}_1,\vec{k}_2)\psi(\vec{k},\vec{k}') + \psi(\vec{k}_1,\vec{k})\psi(\vec{k}_2,\vec{k}') \\ &+ \psi(\vec{k}_1,\vec{k}')\psi(\vec{k}_2,\vec{k})|^2.\end{aligned} \tag{13}$$

This is the main result of the paper. Dealing explicitly with the four atom component it is easy to see what happens. In Fig. 2. we illustrate the case of detection of a particle pair in random directions. Because, as noted below Eq. (4), $\psi(\vec{k},\vec{k}')$ vanishes unless $\vec{k}$ and $\vec{k}'$ are anti-parallel, the first term in Eq. (10) only contributes if the detectors correspond to opposite directions. For opposite or random directions such as in Fig. 2, there is also no cross term between the second two terms because one vanishes whenever the other is finite. If $(\vec{k},\vec{k}')$ are nearly parallel, as illustrated in Fig. 3, the last two terms evaluate the two different ψ-terms at the detector directions and at the direction specified by the integration variables.

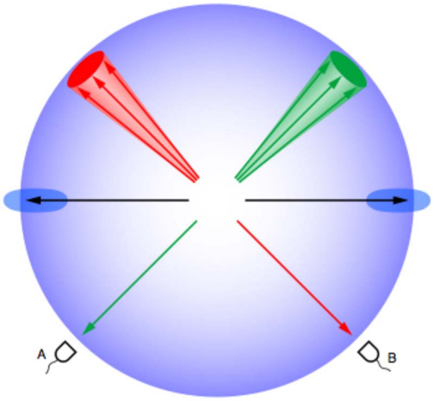

FIG. 2. (Color online) State of four atoms, scattered pairwise back-to-back. Atoms detected by detectors A and B in an arbitrary pair of directions have partners recoiling in the opposite directions within a certain width imposed by the uncertainty on total and relative momentum of the atoms. The quantum state of the detected pair is obtained by a partial trace over the recoiling momentum components, and the coincidence counting yield in the detectors is just the product of the single detector count signals

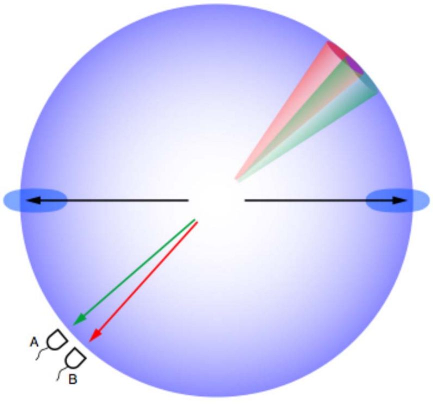

FIG. 3. (Color online) State of four atoms, with two atoms detected in nearly parallel directions. The detected atoms are not unambiguously identified with their recoiling partners if their momentum distributions are wide enough to overlap. This leads to an interference term in the coincidence counting yield in detectors A and B as expressed by the formal expression (13).

This means that values of the integration variables $\vec{k}_1,\vec{k}_2$ exist (opposite to the detector directions), where both of the last terms in (13) contribute, namely if $\vec{k}_1$ and $\vec{k}_2$ are within the "recoil cone" of both detection directions $\vec{k}$ and $\vec{k}'$. For identical $\vec{k}$ and $\vec{k}'$ this interference give precisely the factor 2 increase of coincidences compared to the case of random directions. We also note that the enhanced coincidences occur within a solid angle specified precisely by this "recoil cone". The next section develops our model one step further and carries out the calculation for the special choice of a Gaussian for the function $\psi(\vec{k}_1,\vec{k}_2)$.

V. RESULT FOR A SIMPLE ANSATZ FOR $\psi(\vec{k}_1,\vec{k}_2)$

As stated above, the Bogoliubov approximation to the actual state can be found numerically by solution of linear wave equations. In this section, we shall rather take a simpler approach by making an Ansatz for the shape of the function ψ by appealing to the dynamics and the conservation laws valid in the bipartite collision dynamics.

Energy conservation, which is effectively enforced during the temporal solution of the Schrödinger equation, suggests that the atomic pair state $\psi(\vec{k}_1,\vec{k}_2)$ describes particles with the same energy as the incident condensate particles. Momentum conservation suggests that they also have the same total momentum as the colliding pair. Due to the finite size of the colliding clouds, this does not strictly imply that the two atoms must have exactly opposite momenta. The finite size of the collision zone implies a quantum mechanical momentum uncertainty, and if contributions from small regions (with correspondingly large total momentum uncertainty) are added coherently the resulting phase matching condition is not sharp if the entire collision zone has finite size. There are therefore quantum fluctuations of both the modulus and direction of the momenta. When the particles escape from the collision zone as illustrated in Fig. 1, they are also repelled by the mean field interaction with the two condensate components. Here we will not try to describe accurately the effect of this interaction, which is in any case small when atoms leave a condensate after receiving an initial kinetic energy large compared to the chemical potential [24]. Note, however, that such mean field repulsion has in fact turned out to be tractable in the atom laser output from a condensate, where a generalized ABCD matrix formalism yields an analytical description of the propagation [25].

We define coordinates such that the nearly parallel $\vec{k},\vec{k}'$ of interest are close to the negative z-direction. Their partners at $\vec{k}_1,\vec{k}_2$ must both be close to the positive z-direction, and we shall assume the z-coordinates to be equal and opposite and only look at their x and y components. Their widths are related to the wave functions of the colliding condensates, both due to the amplitude of collisions out of these condensates and due to the mean field repulsion, and they are thus in general anisotropic. We restrict for simplicity the integration to one transverse coordinate (putting vector arrows on the arguments will yield the 2D result), and we assume that a single pair is described by a wave function, where the wave function amplitude for the recoiling partner has a bell shaped profile, that we for simplicity approximate by a Gaussian, centered at minus the coordinates of the detected particle. The width of this wave function is parametrized by a momentum width K which thus represents both the momentum width of the colliding condensate particles and the acceleration due to the mean field.

Assuming thus the last two terms in (13) to be of such Gaussian shape, and ignoring the first term which vanishes for the geometry studied, we can explicitly calculate the coincidence signal:

$$\begin{aligned} F(\vec{k},\vec{k}') &\propto \int dk_1 dk_2 |\exp\{-[(k_1+k)^2+(k_2+k')^2]/2K^2\} \\ &\quad + \exp\{-[(k_1+k')^2+(k_2+k)^2]/2K^2\}|^2 \\ &\propto 1+\exp[-(k-k')^2/2K^2], \end{aligned} \tag{14}$$

where we recall that k and k' here refer to (small) transverse coordinates of the detector directions with respect to a given axis, i.e., $(k-k')$ is the radial momentum of the outgoing particles multiplied with their mutual (small) angle in radians.

We recover the Hanbury Brown and Twiss correlations, and we observe that the correlations persist for final state momenta within a distance from each other of the order of the quantum mechanical uncertainty of the total momentum of the atom pair escaping the collision zone. This is in accord with our interpretation in terms of the interference between the indistinguishable components illustrated as the overlapping recoil cones in Fig. 1(c), that leads to the last term in (14) depending on both k and k', whereas the direct terms lose the k and k' dependence due to the Gaussian integrals.

It is interesting to note, that Eq. (14) follows from a two-state amplitude $\psi(k,k')\propto\exp(-(k+k')^2/2K^2)$ for transverse momentum components of atoms propagating in nearly opposite directions, and therefore the two atom component of Eq. (9) predicts a correlation of atoms in opposite directions with the dependence $|\psi(k,k')|^2\propto\exp(-(k+k')^2/K^2)$. The Hanbury Brown and Twiss bunching thus occurs within a Gaussian width that is $\sqrt{2}$ times larger than the range of correlation of recoiling atomic momenta. This prediction for the Gaussian wave functions has been verified by more detailed analysis of the full 3D propagation [5]. One way to understand the broadening is to recognize that the density dependence of the pair production mechanism results in a source which is spatially narrower than the condensates themselves.

Although we have based our analysis on the four-atom component of the full many body states, we have argued that a calculation based on the full state would yield the same results, and in particular that the HBT correlation amounts to a factor of two in parallel directions while the correlation in opposite directions is not limited by this factor. When multiple scattering is neglected, the complete many-body problem is solved by the Bogoliubov-de-Gennes equations, and the resulting Gaussian or thermal character of the many-body state is fully accounted for by the second moments. This does not imply, however, that one would get the same quantitative results for scattering of few and many atoms. If the normalized wave function for a single scattered pair in the case of a low scattering probability is denoted $\chi(\vec{k}_1,\vec{k}_2)$, it may be reasonable to describe the collision process by the effective Hamiltonian $H=\kappa\int d\vec{k}_1 d\vec{k}_2 \chi(\vec{k}_1,\vec{k}_2)\hat{\Psi}^\dagger(\vec{k}_1)\hat{\Psi}^\dagger(\vec{k}_2)$ $+$H.c., where κ is a coupling strength. The unitary time evolution operator is the exponential of this operator multiplied by $(t/i\hbar)$ or integrated over a suitable time interval. We note that this does not generally result in an expression for $\psi(\vec{k}_1,\vec{k}_2)$ in (7) which is proportional to $\chi(\vec{k}_1,\vec{k}_2)$. In the case of single mode squeezing, it is known that one must evaluate the hyperbolic tangent function of the squeezing parameter to convert the squeezing operator to the normal order form [11], and in our general multimode case, normal ordering is accomplished by evaluating the tanh function of a matrix argument [15,16]. For small arguments, in the perturbative regime of spontaneous four wave mixing, tanh is a linear function, and we get the same momentum dependence. Outside the perturbative regime, we retain the factor 2 bunching effect by our general argument, but the precise shape of the correlation peak may be modified.

VI. DISCUSSION

We have presented a simple interpretation of the observed Hanbury Brown and Twiss correlations observed in the elastic scattering of Bose-Einstein condensates. We emphasize, that in order to make quantitative predictions, it is necessary to make a more elaborate calculation of the pair formation and the propagation of the atoms both in free space and in the regions where the mean field of the condensate components act as a perturbing potential. Such a description is offered by the Bogoliubov theory in Refs. [8–10], and we note that [10] as well as [4] also provide numerical evidence for the density correlations discussed in the present paper. Our interpretation relies on the structural property of the solutions to the Bogoliubov theory (7), but it proceeds by applying a different physical reasoning which recognizes that the two detected particles are accompanied by collision partners propagating in the opposite directions, and we hence observe part of a four-atom state. This is an appealing picture, in particular because the prediction of the coincidence signal, and in particular its width, relates to the transverse spreading of the pair wave functions of oppositely propagating atoms after the bipartite collisions.

As we discussed in the text, when observed from only one direction, the reduced density matrix of the expanding atomic cloud is similar to a thermal state. This density matrix is sufficient to predict the outcome of any measurement on the observed part of the system, and it explains the experimental findings as an analog of the observed bunching of the photons from a thermal/chaotic light source. The optical Hanbury Brown and Twiss experiment has a characteristic transverse spatial scale over which the correlation falls to unity, related to the transverse momentum distribution of the photons impinging on the detector, and in a similar manner we have a finite transverse coherence length in the atomic scattering experiment. We discussed the isotropic s-wave scattering, with possible corrections due to anisotropy of the colliding clouds and spatial phase matching. In addition, one may apply a periodic background potential, which may alter the energy dependence on the momentum vector of moving atoms, and hence modify the scattering profile [26,27], and with confinement to one dimension, it may lead to highly selective population of specific momentum states with strong, observable quantum correlations [28,29].

It is interesting to recall that a mixed quantum state, i.e., a density matrix, can always be formally obtained as the reduced state of a larger quantum system which is in a pure state, and in particular any thermal quantum state of a bosonic degree of freedom can be modeled by a pure squeezed state in a doubled tensor space. This is known as the "thermofields" formulation [30], and for example the single mode thermal state (5) can be obtained as the trace over one of the modes of a non-degenerate two mode squeezed state, as obtained, e.g., from a non-degenerate optical parametric oscillator (OPO),

$$|\psi_{OPO}\rangle \propto \sum_n t^n |n,n\rangle. \tag{15}$$

In our four-atom analysis, the apparently thermal state arriving at nearby detectors is precisely part of such a larger system. The advantage of this insight is that the spatial scale of the extended state, in our case the probability distribution of the total momentum of scattered atoms, directly yields the density correlations in the reduced density matrix. More elaborate analyses [31] have shown how density-density correlations in the image of expanding gases can reveal a wide range of more complex many-body properties, as confirmed by experiments [32].

Finally, if the collision occurs between two different bosonic species, the same kind of correlations will occur for the density correlations of each species, but not for the cross correlation, where the recoiling atoms are distinguishable, and hence do not interfere. For collisions between bosons and fermions the situation is different. Electrons have been demonstrated to show antibunching related to their fermionic character [33], and antibunching has also been demonstrated for neutral fermionic atoms [34,35]. Collisions between a Bose condensate and a degenerate Fermi gas, where all fermions initially occupy orthogonal states, but where Pauli blocking forbids more than one atom ending up in the same final state should lead to observable antibunching effects in the scattered bosons.

ACKNOWLEDGMENTS

The authors gratefully acknowledge discussions with Karen Kheruntsyan and financial support from the European Union integrated project SCALA and the ESF cold atom network QUDEDIS. The Atom Optics group of LCFIO is a member of the IFRAF institute, and is supported by the French ANR and by the Atom Chips program of the European Union.

[1] K. Gibble, S. Chang, and R. Legere, Phys. Rev. Lett. **75**, 2666 (1995); A. P. Chikkatur, A. Görlitz, D. M. Stamper-Kurn, S. Inouye, S. Gupta, and W. Ketterle, *ibid.* **85**, 483 (2000); J. M. Vogels, K. Xu, and W. Ketterle, *ibid.* **89**, 020401 (2002); N. Katz, J. Steinhauer, R. Ozeri, and N. Davidson, *ibid.* **89**, 220401 (2002); C. Buggle, J. Leonard, W. von Klitzing, and J. T. M. Walraven, *ibid.* **93**, 173202 (2004); N. R. Thomas, N. Kjærgaard, P. S. Julienne, and A. C. Wilson, *ibid.* **93**, 173201 (2004).
[2] A. Perrin, H. Chang, V. Krachmalnicoff, M. Schellekens, D. Boiron, A. Aspect, and C. I. Westbrook, Phys. Rev. Lett. **99**, 150405 (2007).
[3] M. J. Steel, M. K. Olsen, L. I. Plimak, P. D. Drummond, S. M. Tan, M. J. Collett, D. F. Walls, and R. Graham, Phys. Rev. A **58**, 4824 (1998).
[4] P. Deuar and P. D. Drummond, Phys. Rev. Lett. **98**, 120402 (2007).
[5] A. Perrin, C. M. Savage, D. Boiron, V. Krachmalnicoff, C. I. Westbrook, and K. Kheruntsyan, e-print arXiv:0712.2145v1.
[6] A. Sinatra, C. Lobo, and Y. Castin, Phys. Rev. Lett. **87**, 210404 (2001).
[7] A. A. Norrie, R. J. Ballagh, and C. W. Gardiner, Phys. Rev. A **73**, 043617 (2006).
[8] P. Ziń, J. Chwedeńczuk, A. Veitia, K. Rzążewski, and M. Trippenbach, Phys. Rev. Lett. **94**, 200401 (2005).
[9] J. Chwedeńczuk, P. Ziń, K. Rzażewski, and M. Trippenbach, Phys. Rev. Lett. **97**, 170404 (2006).
[10] P. Ziń, J. Chwedeńczuk, and M. Trippenbach, Phys. Rev. A **73**, 033602 (2006).
[11] C. M. Caves and B. L. Schumaker, Phys. Rev. A **31**, 3068 (1985).
[12] U. V. Poulsen and K. Mølmer, Phys. Rev. A **63**, 023604 (2001).
[13] U. V. Poulsen and K. Mølmer, Phys. Rev. A **76**, 013614 (2007).
[14] A. K. Ekert and P. L. Knight, Phys. Rev. A **43**, 3934 (1991).
[15] C. F. Lo, Phys. Rev. A **51**, 1706 (1995).
[16] Hong-yi Fan, J. Opt. B: Quantum Semiclassical Opt. **5**, R147 (2003).
[17] R. Hanbury Brown and R. Q. Twiss, Nature (London) **178**, 1046 (1956).
[18] R. Q. Twiss, A. G. Little, and R. Hanbury Brown, Nature (London) **180**, 324 (1957).
[19] G. A. Rebka and R. V. Pound, Nature (London) **180**, 1035 (1957).
[20] B. L. Morgan and L. Mandel, Phys. Rev. Lett. **16**, 1012 (1966).
[21] H.-J. Miesner, D. M. Stamper-Kurn, M. R. Andrews, D. S. Durfee, S. Inouye, and W. Ketterle, Science **279**, 1005 (1998).
[22] S. Inouye, T. Pfau, S. Gupta, A. P. Chikkatur, A. Görlitz, D. E. Pritchard, and W. Ketterle, Nature (London) **402**, 641 (1999).
[23] W. H. Louisell, *Quantum Statistical Properties of Radiation* (John Wiley and Sons, New York, 1973).
[24] N. P. Robins, C. Figl, S. A. Haine, A. K. Morrison, M. Jeppesen, J. J. Hope, and J. D. Close, Phys. Rev. Lett. **96**, 140403 (2006).
[25] Y. Le Coq, J. H. Thywissen, S. A. Rangwala, F. Gerbier, S. Richard, G. Delannoy, P. Bouyer, and A. Aspect, Phys. Rev. Lett. **87**, 170403 (2001); J.-F. Riou, W. Guerin, Y. Le Coq, M. Fauquembergue, V. Josse, P. Bouyer, and A. Aspect, *ibid.* **96**, 070404 (2006).
[26] N. Katz, E. Rowen, R. Ozeri, and N. Davidson, Phys. Rev. Lett. **95**, 220403 (2005).
[27] K. Mølmer, New J. Phys. **8**, 170 (2006).
[28] K. M. Hilligsøe and K. Mølmer, Phys. Rev. A **71**, 041602(R) (2005).
[29] G. K. Campbell, J. Mun, M. Boyd, E. W. Streed, W. Ketterle, and D. E. Pritchard, Phys. Rev. Lett. **96**, 020406 (2006).
[30] S. M. Barnett and P. L. Knight, J. Opt. Soc. Am. B **2**, 467 (1985).
[31] E. Altman, E. Demler, and M. D. Lukin, Phys. Rev. A **70**, 013603 (2004); J. Grondalski, P. Alsing, and I. Deutsch, Opt. Express **5**, 249 (1999); J. Viana Gomes, A. Perrin, M. Schellekens, D. Boiron, C. I. Westbrook, and M. Belsley, Phys. Rev. A **74**, 053607 (2006).
[32] S. Fölling, F. Gerbier, A. Widera, O. Mandel, T. Gericke, and I. Bloch, Nature (London) **434**, 481 (2005); M. Schellekens, R. Hoppeler, A. Perrin, J. Viana Gomes, D. Boiron, A. Aspect, and C. I. Westbrook, Science **310**, 648 (2005).
[33] H. Kiesel, A. Renz, and F. Hasselbach, Nature (London) **418**, 392 (2002).
[34] T. Jeltes, J. M. McNamara, W. Hogervorst, W. Vassen, V. Krachmalnicoff, M. Schellekens, A. Perrin, H. Chang, D. Boiron, A. Aspect, and C. I. Westbrook, Nature (London) **445**, 402 (2007).
[35] T. Rom, Th. Best, D. van Oosten, U. Schneider, S. Fölling, B. Paredes, and I. Bloch, Nature (London) **444**, 733 (2006).

PHYSICAL REVIEW A **77**, 026101 (2008)

Comment on "Quantum time-of-flight distribution for cold trapped atoms"

J. Viana Gomes,[1,*] M. Belsley,[1] and D. Boiron[2]
[1]*Departamento de Fisica, Universidade do Minho, Campus de Gualtar, 4710-057 Braga, Portugal*
[2]*Laboratoire Charles Fabry de l'Institut d'Optique, CNRS, Univ Paris-Sud, Campus Polytechnique, RD128, 91127 Palaiseau cedex, France*

(Received 6 July 2007; revised manuscript received 8 November 2007; published 21 February 2008)

Ali *et al.* [Phys. Rev. A **75**, 042110 (2007)] have claimed that empirically testable differences exist between the quantum and semiclassical time of flight distribution for cold trapped atoms. We believe these claims to be misleading. For the particular case of noninteracting bosonic particles released from a harmonic trapping potential, we show that the quantum and semiclassical calculations for the time-of-flight distribution are equivalent, provided one is not too close to the quantum degeneracy point.

DOI: 10.1103/PhysRevA.77.026101 PACS number(s): 03.65.Ta, 03.65.Xp, 37.10.De

Empirical fits to the time-of-flight (TOF) signals that are observed when a cold atomic cloud expands following the switch-off of the trapping potential are commonly used to infer the thermal and quantum characteristics of the sample. Ali and co-workers [1] claim that the result of a "quantum calculation" for the TOF differs in an "empirically testable way" from the commonly used semiclassical description of the TOF signal. In particular they present results portraying striking differences for the TOF signal as the "size" of the initially trapped atomic cloud is varied. These results clearly differ from the semiclassical description which predicts that for a sufficiently long time of flight, the size of the expanding cloud is determined solely by the initial temperature of the sample. We believe, however, that the deviations from the semiclassical description predicted by Ali and co-workers are manifest only in extreme limits, when the simple thermal averaging they employed is not appropriate. The purpose of this comment is to point out several subtle yet important points that we believe were neglected by Ali and co-workers in their development.

The calculation of Ali *et al.* is performed on noninteracting particles and is based on the quantum mechanical flux (which they call the "probability current"). Restricted to the one-dimensional case, the proposed model starts by describing each atom in the cloud as a Gaussian wave packet centered at $z=0$ and moving with a group velocity v, such that $\psi(z,t=0)=(2\pi\sigma_0^2)^{-1/4}\exp\left(-\frac{z^2}{4\sigma_0^2}\right)\exp\left(i\frac{mv}{\hbar}z\right)$. The ballistic expansion is accomplished by computing the time evolution of the wave packets with the appropriate propagator for free fall under the influence of a constant gravitational field. Carrying this out, a v-dependent amplitude term appears in the evolved wave function $\psi(z,t)$. This term allows Ali and co-workers to compute a thermal average of the particle's flux $\hbar/m\,\mathrm{Im}[\psi^*(z,t)\partial_z\psi(z,t)]$, with v distributed according to a Maxwell-Boltzmann factor. The resulting TOF distribution is characterized by a width and a velocity of the center of the cloud. For a long propagation time, the width is given in their model by

$$\sigma_{(\text{Ali } et\ al.)}=\sqrt{\left(\frac{\hbar}{2m\sigma_0}\right)^2+\frac{k_BT}{m}}\,t. \tag{1}$$

This result is in contradiction with the semiclassical model [2]. Provided that the localization induced by trapping potential does not significantly alter the thermal velocity distribution, one can estimate the initial momentum distribution of a cloud at temperature T using the equipartition theorem $\langle\hat{p}^2\rangle/2m=k_BT/2$, yielding $\sigma_p=\sqrt{\langle\hat{p}^2\rangle}=\sqrt{mk_BT}$. Using Maxwell-Boltzmann statistics, the semiclassical approximation states thus that the size at large enough time t is

$$\sigma_{(\text{sc})}=\sqrt{\frac{k_BT}{m}}\,t.$$

The discrepancy, illustrated in Fig. 4 of Ref. [1], happens when the term $\hbar/2m\sigma_0$ is comparable or larger than $\sqrt{k_BT/m}$. In their model Ali *et al.* seem to be assuming that each velocity class of the atomic cloud starts out in a kind of minimum uncertainty wave packet of size σ_0. Very little is said about this size and it is treated by the authors as a free parameter which is independent of the temperature. The first term in Eq. (1) is simply the momentum spread, due to the uncertainly principle. Hence, differences appear only when the characteristic energy associated with the strong uniform localization assumed by Ali *et al.* is comparable to the thermal energy. This would seem to place them below the quantum degeneracy point for any realizable smoothly varying trapping potential with a reasonable number of atoms. At such an extreme initial localization, their use of a continuous Maxwell-Boltzmann velocity distribution to carry out the thermal averaging appears inadequate.

One of the most common trapping potentials is the harmonic potential for which a fully quantum mechanical calculation can be carried out for the time of flight signal resulting from an initially thermalized cloud of noninteracting Bose atoms [3]. In this case the TOF signal mimics the original density distribution in the trap provided a rescaling of the coordinate is performed. Using the results of Sec. B.4 of Ref. [3], the root mean square value of the TOF signal can be written as

---

[*] zgomes@fisica.uminho.pt

$$\sigma^2_{(Q)} = (1+\omega^2 t^2)\frac{\sigma^2}{2}\frac{\sum_{l=1}^{\infty}\frac{e^{\beta l\tilde{\mu}}}{(1-e^{-\tau l})^3}\frac{1}{\tanh(\tau l/2)}}{\sum_{l=1}^{\infty}\frac{e^{\beta l\tilde{\mu}}}{(1-e^{-\tau l})^3}}$$

with $\sigma=\sqrt{\hbar/m\omega}$, $\tau=\hbar\omega/k_BT$, $\beta=1/k_BT$, and $\tilde{\mu}=\mu-3\hbar\omega/2$ where μ is the chemical potential and ω the trap oscillation frequency. For simplicity we have considered an isotropic harmonic potential. Using Bose-Einstein statistics, an improved semiclassical calculation valid close to degeneracy could be obtained under the approximation $\tau \ll 1$ and would give

$$\sigma^2_{(\mathrm{sc\ imp.})} = (1+\omega^2 t^2)\frac{\sigma^2}{\tau}\frac{g_4(e^{\beta\tilde{\mu}})}{g_3(e^{\beta\tilde{\mu}})},$$

$$\sigma_{(\mathrm{sc\ imp.})} = \sqrt{\frac{g_4(e^{\beta\tilde{\mu}})}{g_3(e^{\beta\tilde{\mu}})}}\sqrt{\frac{k_BT}{m}}t,$$

where in the last line, only for simplicity and to clarify the final result, we have also made the approximation $\sqrt{1+\omega^2t^2} = \omega t$. In this expression we have also used the definition of the so-called Bose function $g_i(x)=\Sigma_{l=1}^{\infty}\frac{x^l}{l^i}$. The results are plotted in Fig. 1. For temperatures well above the quantum degeneracy $\sigma_{(Q)}$ coincides with $\sigma_{(\mathrm{sc})}$ and $\sigma_{(\mathrm{scimp})}$ and is still very close to $\sigma_{(\mathrm{scimp})}$ near the degeneracy. Therefore, at least for the important case of a harmonic trapping potential, semiclassical approximations lead to accurate descriptions of TOF signals provided one is not too close or below quantum degeneracy.

We note that for temperatures close to, but above quantum degeneracy, the cloud released from a harmonic trapping potential tends to expand slightly less rapidly than the semiclassical prediction. This reflects the tendency of Bose-Einstein statistics to favor higher populations in the lower energy levels of the trapping potential in comparison to Maxwell-Boltzmann statistics, resulting in somewhat less ballistic spreading upon release. These results are in marked contrast to the calculations of Ali *et al.*, which always predict an increase in the clouds width due to the quantum localization effects.

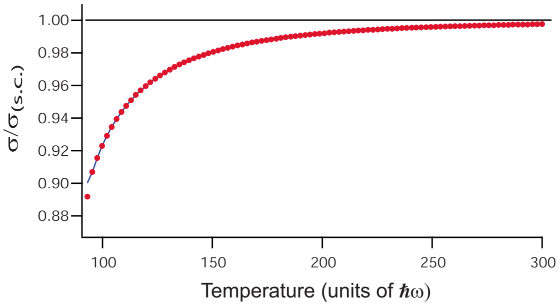

FIG. 1. (Color online) Width of the time of flight signal in function of the temperature (in units of $\hbar\omega$) for a expanding cloud initially confined in a harmonic potential of $N=10^6$ atoms. The widths are normalized by $\sigma_{(\mathrm{sc})}$. The full quantum result (dots) is very close to the improved semiclassical results (solid line) above quantum degeneracy ($k_BT_c \approx 94\hbar\omega$). Both tend to $\sigma_{(\mathrm{sc})}$ at high temperature.

Finally we would like to mention that even for a noninteracting atomic cloud trapped within a harmonic potential typical semiclassical calculations can lead to results that deviate significantly from the quantum description above Bose-Einstein degeneracy. An interesting example is the calculation of the atomic degeneracy parameter at the trap center [4]. Although the number of atoms in the ground-state energy level may be a small fraction of the total number of atoms, their density can still be comparable to that of the excited states population density due to the strong localization of the ground-state wave function. Since semiclassical calculations usually neglect the ground state near to but above the quantum degeneracy temperature these models will fail to adequately describe the gas in this region.

The Atom Optics group of LCFIO is member of the Institut Francilien de Recherche sur les Atomes Froids (IFRAF) and of the Fédération LUMAT of the CNRS Grant No. (FR2764). This work was supported by the PESSOA Program No. 07988NJ, by the Atom Chips network Grant No. MCRTN-CT-2003-505032, and the ANR under Contract No. 05-NANO-008-01.

[1] Md. Manirul Ali, Dipankar Home, A. S. Majumdar, and Alok K. Pan, Phys. Rev. A **75**, 042110 (2007).
[2] I. Yavin, M. Weel, A. Andreyuk, and A. Kumarakrishnana, Am. J. Phys. **70**, 149 (2002).
[3] J. Viana Gomes, A. Perrin, M. Schellekens, D. Boiron, C. I. Westbrook, and M. Belsley, Phys. Rev. A **74**, 053607 (2006).
[4] R. Hoppeler, J. Viana Gomes, and D. Boiron, Eur. Phys. J. D **41**, 157 (2007).

New Journal of Physics
The open-access journal for physics

Atomic four-wave mixing via condensate collisions

A Perrin[1], **C M Savage**[2], **D Boiron**[1], **V Krachmalnicoff**[1],
C I Westbrook[1] **and K V Kheruntsyan**[3,4]
[1] Laboratoire Charles Fabry de l'Institut d'Optique, CNRS, Univ Paris-Sud,
Campus Polytechnique, RD128, 91127 Palaiseau Cedex, France
[2] ARC Centre of Excellence for Quantum-Atom Optics, Department of Physics,
Australian National University, Canberra ACT 0200, Australia
[3] ARC Centre of Excellence for Quantum-Atom Optics,
School of Physical Sciences, University of Queensland, Brisbane,
QLD 4072, Australia
E-mail: christoph.westbrook@institutoptique.fr and
karen.kheruntsyan@uq.edu.au

New Journal of Physics **10** (2008) 045021 (26pp)
Received 11 December 2007
Published 30 April 2008
Online at http://www.njp.org/
doi:10.1088/1367-2630/10/4/045021

Abstract. We perform a theoretical analysis of atomic four-wave mixing via a collision of two Bose–Einstein condensates of metastable helium atoms, and compare the results to a recent experiment. We calculate atom–atom pair correlations within the scattering halo produced spontaneously during the collision. We also examine the expected relative number squeezing of atoms on the sphere. The analysis includes first-principles quantum simulations using the positive P-representation method. We develop a unified description of the experimental and simulation results.

---

[4] Author to whom any correspondence should be addressed.

New Journal of Physics **10** (2008) 045021
1367-2630/08/045021+26$30.00

Contents

1. Introduction

Recent years have seen the introduction of powerful new tools for studying degenerate quantum gases. For example, on the experimental side correlation measurements offer a new experimental probe of many-body effects [1]–[11]. On the theoretical side, the challenges posed by the new experimental techniques are being met by quantum dynamical simulations of large numbers of interacting particles in realistic parameter regimes. These are becoming possible due to the advances in computational power and improvements in numerical algorithms (for recent examples, see [12]–[15]).

In this paper, we study metastable helium (^{4}He*), which is currently unique in *quantum atom optics* in that it permits a comparison of experimentally measured [16] and theoretically calculated quantum correlations. This is one of the first examples in which experimental measurements can be considered in the context of first-principles calculations. Our goal in this paper is to confront a theoretical analysis with the results of recent experiments on atomic four-wave mixing via a collision of two Bose–Einstein condensates (BECs) of metastable ^{4}He* atoms [16]. Figure 1 is a schematic momentum space diagram of these experiments. Two condensates, whose atoms have approximately equal but opposite momenta, $\mathbf{k}_1$ and $\mathbf{k}_2 \simeq -\mathbf{k}_1$,

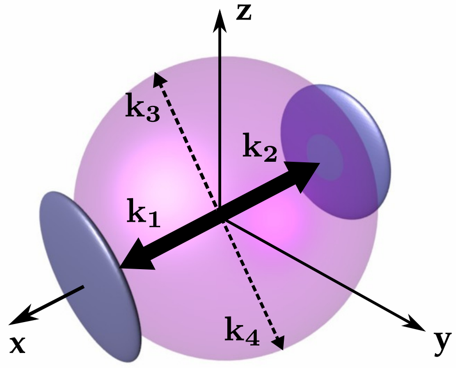

Figure 1. Schematic momentum space diagram of the atomic four-wave mixing interaction. Optical Raman pulses generate untrapped condensates with momenta $\mathbf{k}_1$ and $\mathbf{k}_2 = -\mathbf{k}_1$ parallel to the x-axis (dark disks). These undergo a four-wave mixing interaction to produce correlated atomic pairs on a spherical shell of radius k_1.

interact by four-wave mixing, while they spatially overlap, to produce correlated atomic pairs with approximately equal but opposite momenta, $\mathbf{k}_3$ and $\mathbf{k}_4$, satisfying momentum conservation, $\mathbf{k}_1 + \mathbf{k}_2 = \mathbf{k}_3 + \mathbf{k}_4$. Figure 1 corresponds to the experimental data shown in figure 2 of [16], since after time-of-flight expansion, atomic momentum is mapped into atomic position.

We perform first-principles quantum simulations of the collision dynamics using the positive P-representation method [17]–[20]. The advantage of this method is that given the Hamiltonian of the interacting many-body system, no additional approximations are imposed to simulate the quantum dynamics governed by the Hamiltonian. The drawback on the other hand, is that it usually suffers from large sampling errors and the boundary term problem [21] as the simulation time t_{sim} increases, eventually leading to diverging results.

An empirically estimated upper bound for the positive-P simulation time (beyond which the stochastic trajectories start to make large excursions in phase space, leading to boundary term problem and uncontrollable sampling errors [21]) for the evolution of condensates with s-wave scattering interactions is given approximately by [22]

$$t_{\mathrm{sim}} \lesssim 2.5m(\Delta V)^{1/3}/[4\pi\hbar a \rho_0^{2/3}], \qquad (1)$$

where m is the atom mass, a is the s-wave scattering length, ρ_0 is the condensate peak density, and $\Delta V = \Delta x \Delta y \Delta z$ is the volume of the elementary cell of the computational lattice, with lattice spacings of Δx, Δy and Δz. Applying this formula to metastable helium, we see that this is a particularly challenging case among commonly condensed atoms due to its small atomic mass and relatively large scattering length. Our simulations are restricted to short interaction times (typically $\lesssim 25\,\mu$s), which are about six times shorter than the experimental interaction time of [16]. Despite this, our positive-P simulations provide useful insights into the experimental observations; in addition, they can serve as benchmarks for approximate theoretical methods (such as the Hartree–Fock–Bogoliubov method [23]–[26] or the truncated Wigner method [12, 13]) to establish the range of their validity.

We note that the simulations of BEC collisions of [12, 13] using the truncated Wigner method are in a different regime than the ones carried out here using the positive-P method. More specifically, the authors of [12, 13] simulate condensates at much higher densities, for which the approximations of the method [13, 27] are satisfied. The advantage of the Wigner method over the positive-P is that it does not suffer from boundary term problem and can be used to simulate condensate collisions for longer durations.

In the present paper, we calculate atom pair correlations within the scattering halo produced spontaneously during the collision (see figure 1). The scattering halo is a spherical shell in momentum space. In the limit of small occupation of the scattered modes, the s-wave nature of the collisions ensures an approximately uniform atom population over the halo. We consider the strength and the width of the correlation signal, as well as the momentum width of the halo. We also analyze relative atom number squeezing and the violation of the classical Cauchy–Schwartz inequality.

In section 2 of this paper, we will summarize the experimental results we wish to analyze. In section 3, we discuss order of magnitude estimates. In section 4, we describe simulations using the positive P-representation method, and in section 5, we discuss the results of our simulations. Section 6 summarizes our work.

2. Summary of experimental results

2.1. *Overview of the experiment*

The starting point of the experiment is a $^4\mathrm{He}^*$ condensate of 10^4–10^5 atoms confined in a magnetic trap whose frequencies are: $\omega_x/2\pi = 47\,\mathrm{Hz}$ and $\omega_y/2\pi = \omega_z/2\pi = 1150\,\mathrm{Hz}$. A sudden Raman outcoupling drives the trapped $^4\mathrm{He}^*$ from the $m_x = 1$ Zeeman sublevel into the magnetic field insensitive state $m_x = 0$ [16]. The Raman transition also splits the initial ($m_x = 1$) condensate into two roughly equally populated condensates with opposite velocities along the x-direction. The magnitude of each velocity is equal to the recoil velocity $v_r = 9.2\,\mathrm{cm\,s^{-1}}$, defined by the momentum of the photons used to create the colliding condensates $\hbar k_r$, $k_r = 5.8\times 10^6\,\mathrm{m^{-1}}$. The relative velocity $2v_r$ of the two condensates is about eight times higher than the speed of sound $c_s = \sqrt{\mu/m}$ of the initial condensate, ensuring that the relevant elementary excitations of the condensates correspond to free particles.

During the separation of the condensates, elastic collisions occurring between atoms with opposite velocities scatter a small fraction (5%) of the total initial atom number into the halo. The system is shown in three dimensions (3D) in an accompanying video of the experimental results after a 320 ms time of flight[5]. For the purposes of this paper, the experiment consists in the acquisition of the 3D positions of the particles scattered into the collision halo after the time of flight. This information permits the reconstruction of the 3D momentum vectors of the individual particles after they have ceased interacting with each other.

---

[5] A 3D, animated rendition of the atomic positions 320 ms after release from the trap, available from stacks.iop.org/NJP/10/045021/mmedia. The vertical positions are derived from the arrival times as described in [16]. Each point corresponds to the detection of one atom and the animation shows the sum of 50 separate runs. The ellipsoids at the sides are the colliding condensates. The ellipsoids at the top and bottom result from imperfect Raman polarizations and stimulated atomic four-wave mixing (see [16]). The four condensates are excluded from the analysis given in the text.

2.2. Main results

Knowledge of the momentum vectors in turn permits the construction of two-particle correlation functions in momentum space. The correlation function shows features for particles traveling both back-to-back (BB) and collinearly. The BB correlation results from binary, elastic collisions between atoms, whereas the collinear (CL) correlation is a two particle interference effect involving members of two different pairs: a Hanbury Brown–Twiss correlation [28]. Both correlation functions are anisotropic because of the anisotropy of the initial colliding condensates.

To quantify these correlations, we first introduce the unnormalized normally-ordered second-order correlation function between the densities at two points in momentum space,

$$G^{(2)}(\mathbf{k}_1,\mathbf{k}_2)=\langle:\hat{n}(\mathbf{k}_1)\hat{n}(\mathbf{k}_2):\rangle. \tag{2}$$

Here, $\hat{n}(\mathbf{k})=\hat{a}^{\dagger}(\mathbf{k})\hat{a}(\mathbf{k})$ is the momentum density operator, $\hat{a}^{\dagger}(\mathbf{k})$ and $\hat{a}(\mathbf{k})$ are the Fourier transforms of the field creation and annihilation operators $\hat{\Psi}^{\dagger}(\mathbf{x})$ and $\hat{\Psi}(\mathbf{x})$, and the colons :: stand for normal ordering of the operators according to which all creation operators stand to the left of the annihilation operators, so that

$$\langle:\hat{n}(\mathbf{k}_1)\hat{n}(\mathbf{k}_2):\rangle=\langle\hat{a}^{\dagger}(\mathbf{k}_1)\hat{a}^{\dagger}(\mathbf{k}_2)\hat{a}(\mathbf{k}_2)\hat{a}(\mathbf{k}_1)\rangle. \tag{3}$$

Because of a low data rate, the correlation measurements must be averaged over the entire collision sphere to get statistically significant results. The average CL second-order correlation as a function of the relative displacement Δk_i in the k_i-direction ($i=x,y,z$) is defined as

$$g^{(2)}_{\mathrm{CL}}(\Delta k_i)=\frac{\int_{\mathcal{D}}\mathrm{d}^3\mathbf{k}\,G^{(2)}(\mathbf{k},\mathbf{k}+\mathbf{e}_i\Delta k_i)}{\int_{\mathcal{D}}\mathrm{d}^3\mathbf{k}\langle\hat{n}(\mathbf{k})\rangle\langle\hat{n}(\mathbf{k}+\mathbf{e}_i\Delta k_i)\rangle}, \tag{4}$$

where $\mathbf{e}_i$ is the unit vector in the k_i-direction. The normalization of $g^{(2)}_{\mathrm{CL}}(\Delta k_i)$ ensures that for uncorrelated densities $g^{(2)}_{\mathrm{CL}}(\Delta k_i)=1$. The integration domain $\mathcal{D}$ in (4) selects a certain region of interest in momentum space and can be defined, for example, to contain only a narrow spherical shell and to eliminate the initial colliding condensates. Due to the averaging, the dependence of the correlation functions on the direction **k** is lost.

The average BB correlation function $g^{(2)}_{\mathrm{BB}}(\Delta k_i)$ between two diametrically opposite points, one of which is additionally displaced by Δk_i in the k_i-direction, is defined similarly to $g^{(2)}_{\mathrm{CL}}(\Delta k_i)$:

$$g^{(2)}_{\mathrm{BB}}(\Delta k_i)=\frac{\int_{\mathcal{D}}\mathrm{d}^3\mathbf{k}\,G^{(2)}(\mathbf{k},-\mathbf{k}+\mathbf{e}_i\Delta k_i)}{\int_{\mathcal{D}}\mathrm{d}^3\mathbf{k}\langle\hat{n}(\mathbf{k})\rangle\langle\hat{n}(-\mathbf{k}+\mathbf{e}_i\Delta k_i)\rangle}. \tag{5}$$

The experimental observations can be summarized as follows. The width of both correlation functions along the axial direction of the condensate, the x-axis, is limited by the resolution of the detector and hence contains little information about the collision. In the radial direction (with respect to the symmetry of the colliding condensates), one observes a peak which can be fitted to a Gaussian function with rms widths $\sigma^{\mathrm{CL}}_{y,z}$ and $\sigma^{\mathrm{BB}}_{y,z}$ for the CL and BB cases, respectively. The experimental results are summarized in the following table

$\sigma^{\mathrm{BB}}_{y,z}/k_r$	$\sigma^{\mathrm{CL}}_{y,z}/k_r$	$\sigma^{\mathrm{CL}}_{y,z}/\sigma^{\mathrm{BB}}_{y,z}$
0.081 ± 0.004	0.069 ± 0.008	0.85 ± 0.15

(6)

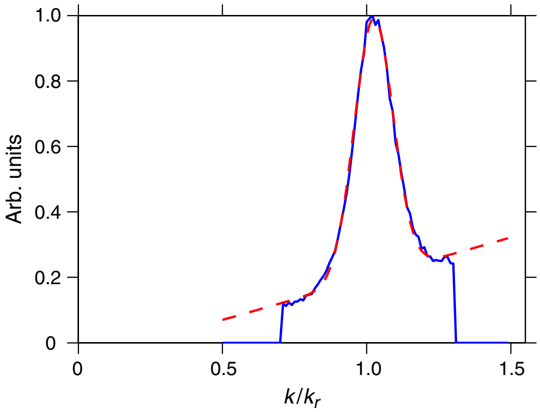

Figure 2. Cross-section of the scattering halo. A sloped background is present due to thermal atoms in the trap. This background has been fitted to a straight line and subtracted in order to estimate the rms width, $\delta k \simeq 0.067k_r$.

One can also use the data to deduce the averaged radial width δk of the scattering halo. Figure 2 shows a cross-section of the halo, averaged over all accessible scattering angles. The presence of the unscattered condensates prevents observation of the shell along the x-axis, but along the accessible directions we find $\delta k \simeq 0.067k_r$.

3. Qualitative analysis

In this section, we discuss some simple, analytical estimates of the measured quantities. In later sections, we will do more precise, numerical calculations which will verify the results of this section.

3.1. Width of the pair correlation functions

As discussed in [16], the width of the BB and CL correlation functions should be on the order of the momentum width of the initial condensate, which in turn is proportional to the inverse width of its spatial profile. For a Gaussian density profile of the initial condensate in position space $\rho(\mathbf{x}) = \langle \hat{\Psi}^\dagger(\mathbf{x})\hat{\Psi}(\mathbf{x})\rangle = \rho_0 \exp[-\sum_{i=x,y,z} r_i^2/(2w_i^2)]$, and therefore a Gaussian density distribution in momentum space, $n(\mathbf{k}) = \langle \hat{n}(\mathbf{k})\rangle \propto \exp[-\sum_{i=x,y,z} k_i^2/(2\sigma_i^2)]$, with $\sigma_i = 1/2w_i$, an approximate theoretical treatment based on a simple ansatz for the pair wavefunction predicts a Gaussian dependence of the BB and CL correlation functions on the relative wavevectors Δk_i [28]:

$$G^{(2)}(\mathbf{k}, -\mathbf{k}+\mathbf{n}_i\Delta k_i) \propto \exp\left(-\frac{\Delta k_i^2}{2(\sigma_i^{\mathrm{BB}})^2}\right), \tag{7}$$

$$G^{(2)}(\mathbf{k}, \mathbf{k}+\mathbf{n}_i\Delta k_i) \propto \exp\left(-\frac{\Delta k_i^2}{2(\sigma_i^{\mathrm{CL}})^2}\right). \tag{8}$$

The widths of the BB (σ_i^{BB}) and CL (σ_i^{CL}) correlations are related to the momentum-space width σ_i of the initial (source) condensate via [28]

$$\sigma_i^{\mathrm{BB}}/\sigma_i=\sqrt{2}, \tag{9}$$

$$\sigma_i^{\mathrm{CL}}/\sigma_i=2, \tag{10}$$

and therefore the width of the BB correlation is $\sqrt{2}$ times smaller than the width of the CL correlation. Similar predictions of correlation widths have been made and discussed in [13, 24].

In section 5.1, the initial momentum-space widths are found to be $\sigma_x=0.0025k_r$ and $\sigma_{y,z}=0.055k_r$, assuming $N=9.84\times10^4$ atoms. Expressing the experimentally measured widths in units of $\sigma_{y,z}$, we can rewrite (6) as

$\sigma_{y,z}^{\mathrm{BB}}/\sigma_{y,z}$	$\sigma_{y,z}^{\mathrm{CL}}/\sigma_{y,z}$	$\sigma_{y,z}^{\mathrm{CL}}/\sigma_{y,z}^{\mathrm{BB}}$
1.47 ± 0.07	1.25 ± 0.15	0.85 ± 0.15

(11)

and therefore, equation (9) is in agreement with the measured width of the radial BB correlation function, whereas (10) overestimates the width of the CL correlation function by almost 60%. As we show below, first-principles simulations using the positive-P method and incorporating atom–atom interactions result in widths which are closer to the experimental values.

The discrepancy between the two theoretical approaches (which apparently is larger for the CL correlations than for the BB ones) comes mostly from the fact that the above calculation is made for a Gaussian shape of the initial BEC density profile, whereas in practice and in the positive-P simulations the spatial density of a harmonically trapped condensate is closer to an inverted parabola (as in the Thomas–Fermi limit) rather than to a Gaussian. An alternative theoretical model [29], based on the undepleted source condensate approximation and a numerical solution to the linear operator equations of motion for scattered atoms, also confirms that for short times the momentum-space correlation widths are narrower if the source condensate has a parabolic spatial density profile, compared to the case of a Gaussian density profile.

3.2. Width of the scattered halo

A second, experimentally accessible quantity in a BEC collision is the width $\hbar\delta k_i$ in momentum space of the halo on which the scattered atoms are found. Clearly the momentum spread σ_i (in $i=x$-, y- or z-direction) of the colliding condensates imposes a minimum width

$$\delta k_i \gtrsim \sigma_i. \tag{12}$$

This limit suggests that the halo could be anisotropic. As noted above, however, the experiment in [16] is not highly sensitive to such an anisotropy, and measures the width chiefly in the y- and z-directions.

Other physical considerations also affect this width, and suggest that the halo should rather be isotropic, in which case we can drop the index from δk. Here, we discuss two mechanisms that impose a finite radial width on the halo.

If the pairs are produced during a finite time interval Δt, the total energy of the pair is necessarily broadened by $\hbar/\Delta t$. This is true even if the relative momentum is well defined.

For a mean k-vector k_r, the finite interaction time between the colliding BECs results in a broadening of

$$\delta k \simeq \frac{m}{\hbar k_r \Delta t}, \tag{13}$$

where we assumed $\delta k/k_r \ll 1$. In the experiment, the collision time is sufficiently long that the above effect does not impose a limitation on the width of the sphere. In the positive-P simulations, however, numerical stability problems limit the maximum collision time that can be simulated, as discussed in section 5, and this time does indeed impose a width on the halo. For short collision times, where the scattering is in the spontaneous regime, our numerical results for the width δk are in good agreement with the simple estimate of equation (13).

For long collision times, it can happen that so many atoms are scattered that Bose enhancement and stimulated effects become important. In this case, the width of the scattering shell can be estimated by a slightly more involved approximate approach based on analytic solutions for the uniform system within the undepleted ‘pump’ (source condensate) approximation [30]. Under this approximation, the present system is equivalent to the dissociation of a condensate of molecular dimers studied in detail in [14, 31, 32]. The latter system in turn is analogous to parametric down-conversion in optics [33]. The details of the approximate solutions, common to condensate collisions and molecular dissociation, and the relationship between them are given in appendix C. The resulting width of the halo found from this approach is

$$\delta k \simeq \frac{4\pi a \rho_0}{k_r}. \tag{14}$$

We see that in this regime, the width is proportional to the scattering length a and the peak density ρ_0, but it no longer depends on the collision duration.

The physical interpretation of equation (14) is that with the stronger effective coupling (or nonlinearity) $a\rho_0$, one can excite and amplify spectral components that are further detuned from the exact resonance condition $\hbar\Delta_k = 0$ (or further ‘phase mismatched’). The inverse dependence on collision momentum k_r can be understood via the quadratic dependence of the energy on momentum k: to get the same excitation at a given energy offset $\hbar\Delta_k$, (C.3), one requires smaller absolute momentum offset δk at larger k_r than at small k_r.

Positive-P simulations covering the transition from the spontaneous to stimulated regimes are available for ^{23}Na condensate collisions as in [15]. The numerical results in this case are in agreement with the simple analytic estimate of equation (14). More specifically, we find that for collision durations between 300 and 640 μs the actual numerical results for the width of the spherical halo vary, respectively, between $\delta k/k_r \simeq 0.13$ and $\delta k/k_r \simeq 0.087$, whereas equation (14) predicts $\delta k/k_r \simeq 0.096$.

For ^{4}He*, on the other hand, the small mass and the larger scattering length of ^{4}He* atoms limit the maximum simulation time to $t_{\mathrm{sim}} \lesssim 25\,\mu$s. This is far from the stimulated regime, and therefore we do not have a direct comparison of the numerical results with equation (14). The experiment is also not in the stimulated regime. We are nevertheless tempted by the numerical ^{23}Na result to extrapolate equation (14) to ^{4}He* BEC collisions in the long time limit and we obtain $\delta k/k_r \simeq 0.05$. Adding this width in quadrature to the momentum width of the initial condensate, $\sigma_{y,z} \simeq 0.055 k_r$, gives $\sqrt{(0.05k_r)^2 + (0.055k_r)^2} = 0.074k_r$, not far from the experimentally observed radial momentum width of $\delta k \simeq 0.067k_r$. We thus suggest that the mechanism leading to equation (14) may play a role in the experiment.

4. Model

The effective field theory Hamiltonian governing the dynamics of the collision of BECs is given by

$$\hat{H} = \int \mathrm{d}\mathbf{x}\left\{\frac{\hbar^2}{2m}|\nabla\hat{\Psi}|^2 + \frac{\hbar U_0}{2}\hat{\Psi}^\dagger\hat{\Psi}^\dagger\hat{\Psi}\hat{\Psi}\right\}, \tag{15}$$

where $\hat{\Psi}(\mathbf{x},t)$ is the field operator with the usual commutation relation $[\hat{\Psi}(\mathbf{x},t), \hat{\Psi}^\dagger(\mathbf{x}',t)] = \delta^{(3)}(\mathbf{x}-\mathbf{x}')$, m is the atomic mass, the first term is the kinetic energy, and the second term describes the s-wave scattering interactions between the atoms. The trapping potential for preparing the initial condensate before the collision is omitted since we are only modeling the dynamics of the outcoupled condensates in free space. The use of the effective delta function interaction potential $U(x-y) = U_0\delta(x-y)$ assumes a UV momentum cutoff k^{max}. In our numerical simulations, the momentum cutoff is imposed explicitly via the finite computational lattice. If the lattice spacings (Δx, Δy and Δz) in each spatial dimension are chosen to be much larger than the s-wave scattering length a, then the respective momentum cutoffs satisfy $k^{\mathrm{max}}_{x,y,z} \ll 1/a$. In this case the coupling constant U_0 is given by the familiar expression $U_0 \simeq 4\pi\hbar a/m$ [34] without the need for explicit renormalization.

To model the dynamics of quantum fields describing the collision of two BECs, we use the positive P-representation approach [17]. In this approach, the quantum field operators $\hat{\Psi}(\mathbf{x},t)$ and $\hat{\Psi}^\dagger(\mathbf{x},t)$ are represented by two complex stochastic c-number fields $\Psi(\mathbf{x},t)$ and $\tilde{\Psi}(\mathbf{x},t)$ whose dynamics is governed by the following stochastic differential equations [15]:

$$\frac{\partial\Psi(\mathbf{x},t)}{\partial t} = \frac{\mathrm{i}\hbar}{2m}\nabla^2\Psi - \mathrm{i}U_0\tilde{\Psi}\Psi\Psi + \sqrt{-\mathrm{i}U_0\Psi^2}\,\zeta_1(\mathbf{x},t), \tag{16a}$$

$$\frac{\partial\tilde{\Psi}(\mathbf{x},t)}{\partial t} = -\frac{\mathrm{i}\hbar}{2m}\nabla^2\tilde{\Psi} + \mathrm{i}U_0\Psi\tilde{\Psi}\tilde{\Psi} + \sqrt{\mathrm{i}U_0\tilde{\Psi}^2}\,\zeta_2(\mathbf{x},t). \tag{16b}$$

Here, $\zeta_1(\mathbf{x},t)$ and $\zeta_2(\mathbf{x},t)$ are real independent noise sources with zero mean, $\langle\zeta_j(\mathbf{x},t)\rangle = 0$, and the following non-zero correlation:

$$\langle\zeta_j(\mathbf{x},t)\zeta_k(\mathbf{x}',t')\rangle = \delta_{jk}\delta^{(3)}(\mathbf{x}-\mathbf{x}')\delta(t-t'). \tag{17}$$

The stochastic fields $\Psi(\mathbf{x},t)$ and $\tilde{\Psi}(\mathbf{x},t)$ are independent of each other $[\tilde{\Psi}(\mathbf{x},t) \neq \Psi^*(\mathbf{x},t)]$ except in the mean, $\langle\tilde{\Psi}(\mathbf{x},t)\rangle = \langle\Psi^*(\mathbf{x},t)\rangle$, where the brackets $\langle\ldots\rangle$ refer to stochastic averages with respect to the positive P-distribution function. In numerical realizations, this is represented by an ensemble average over a large number of stochastic realizations (trajectories). Observables described by quantum mechanical ensemble averages over normally ordered operator products have an exact correspondence with stochastic averages over the fields $\Psi(\mathbf{x},t)$ and $\tilde{\Psi}(\mathbf{x},t)$:

$$\langle[\hat{\Psi}^\dagger(\mathbf{x},t)]^m[\hat{\Psi}(\mathbf{x}',t)]^n\rangle = \langle[\tilde{\Psi}(\mathbf{x},t)]^m[\Psi(\mathbf{x}',t)]^n\rangle. \tag{18}$$

The initial condition for our simulations is a coherent state of a trapped condensate, modulated with a standing wave that imparts initial momenta $\pm k_r$ (where $k_r = mv_r/\hbar$ and v_r is the collision velocity) in the x-direction,

$$\Psi(\mathbf{x},0) = \langle\hat{\Psi}(\mathbf{x},0)\rangle = \sqrt{\rho_0(\mathbf{x})/2}\left(\mathrm{e}^{\mathrm{i}k_r x} + \mathrm{e}^{-\mathrm{i}k_r x}\right), \tag{19}$$

with $\tilde{\Psi}(\mathbf{x},0) = \Psi^*(\mathbf{x},0)$. Here, $\rho_0(\mathbf{x})$ is the density profile given by the ground state solution to the Gross–Pitaevskii equation in imaginary time. The above initial condition models a sudden

Raman outcoupling of a BEC of trapped ^{4}He* atoms in the $m_x = 1$ sublevel into the magnetic field insensitive state $m_x = 0$, using two horizontally counter-propagating lasers and a third vertical laser [16]. In this geometry, the Raman transitions split the initial ($m_x = 1$) condensate into two equally populated condensates and simultaneously impart velocities of $\pm v_r$ onto the two halves. As a result, the two outcoupled condensates undergo a collision and expand in free space. Accordingly, in our dynamical simulations, the field $\hat{\Psi}(\mathbf{x}, t)$ represents the atoms in the untrapped state $m_x = 0$, having the s-wave scattering length of $a_{00} = 5.3\,\mathrm{nm}$ ([16] and references therein), while the initial density profile $\rho_0(\mathbf{x})$ refers to that of the trapped atoms in the $m_x = 1$ state having the scattering length of $a_{11} = 7.51\,\mathrm{nm}$ [35]. The same distinction in terms of the scattering length in question applies to the definition of the interaction strength $U_0 \simeq 4\pi\hbar a/m$, in which a has to be understood as a_{11} for the trapped condensate or as a_{00} for the outcoupled cloud.

In our simulations, we assume for simplicity that the outcoupling from the trapped $m_x = 1$ state is 100% efficient, in which case the entire population is transferred into the $m_x = 0$ state and therefore we have only to model s-wave scattering interactions between the atoms in the $m_x = 0$ state. In the experiment, on the other hand, the transfer efficiency is only about 60% and therefore the collisions between the atoms in the $m_x = 0$ and $m_x = 1$ are not completely negligible and may be responsible for some of the deviations between the present theoretical results and the experimental observations.

5. Results and discussion

5.1. Main numerical example

Here, we present the results of positive-P numerical simulations of collisions of two condensates of ^{4}He* atoms ($m \simeq 6.65 \times 10^{-27}\,\mathrm{kg}$) as in the experiment of [16]. The key parameters in our main numerical example are the collision velocity, $v_r = 9.2\,\mathrm{cm\,s^{-1}}$, and the peak density of the initial trapped condensate, $\rho_0 = 2.5 \times 10^{19}\,\mathrm{m^{-3}}$. The trap frequencies are matched exactly with the experimental values, $\omega_x/2\pi = 47\,\mathrm{Hz}$ and $\omega_y/2\pi = \omega_z/2\pi = 1150\,\mathrm{Hz}$. The s-wave scattering length for the magnetically trapped atoms in the $m_x = 1$ sublevel is $a_{11} = 7.5\,\mathrm{nm}$; the s-wave scattering length for the outcoupled atoms in the $m_x = 0$ sublevel is $a_{00} = 5.3\,\mathrm{nm}$. Other simulation parameters are given in appendix D.

The initial state of the trapped condensate is found via the solution of the Gross–Pitaevskii equation in imaginary time. Given the above trap frequencies and the peak density as a target, we find that the total number of atoms in the main example is $N = 9.84 \times 10^4$. With these parameters, the average kinetic energy of colliding atoms is $E_{\mathrm{kin}}/k_{\mathrm{B}} = m v_r^2/2k_{\mathrm{B}} \simeq 2.0 \times 10^{-6}\,\mathrm{K}$, which is about 7.4 times larger than the mean-field energy of the initial condensate $E_{\mathrm{MF}}/k_{\mathrm{B}} = 4\pi\hbar^2 a_{11}\rho_0/m k_{\mathrm{B}} \simeq 2.7 \times 10^{-7}\,\mathrm{K}$.

The duration of simulation in the main example is $t_f = 25\,\mu\mathrm{s}$. This is considerably smaller than the estimated duration of collision in the experiment, 140 μs (see appendix A). The number of scattered atoms in our numerically simulated example at $t_f = 25\,\mu\mathrm{s}$ is $\sim$1750, representing $\sim$1.8% of the total number of atoms in the initial BEC. Operationally, the fraction of scattered atoms is determined as the total number of atoms contained within the scattering halo (see figure 3 showing two orthogonal slices through the momentum density distribution) after eliminating the regions of momentum space occupied by the two colliding condensates. We implement the elimination by simply discarding the data points corresponding to $|k_x| > 0.99k_r$,

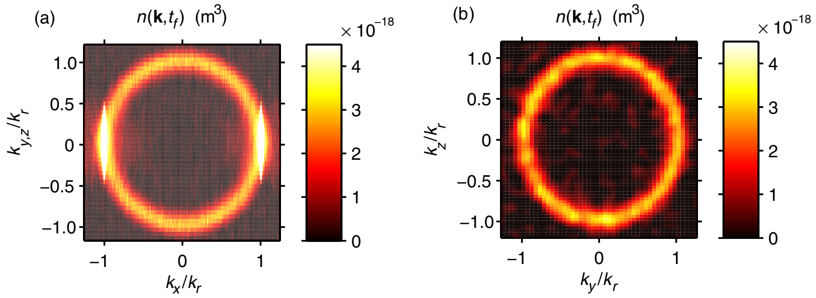

Figure 3. Slices through $k_z = 0$ (a) and $k_x = 0$ (b) of the 3D atomic density distribution in momentum space $n(\mathbf{k}, t_f)$ after $t_f = 25\,\mu$s collision time. Due to the symmetry in the transverse direction (orthogonal to x), the average density through $k_y = 0$ coincides with that of $k_z = 0$. The color scale is chosen to clearly show the halo of spontaneously scattered atoms and cuts off the high-density peaks of the two colliding condensates (shown in white on the left panel).

which fully contain the colliding condensates. This cuts off a small fraction of the scattered atoms as well, but the procedure is simple to implement operationally and is unambiguous.

In order to compare our calculated fraction of scattered atoms at $t_f = 25\,\mu$s with the experimentally measured fraction of 5% at the end of collision at $\sim 140\,\mu$s, we first note that these timescales are relatively short and correspond to the regime of spontaneous scattering. The number of scattered atoms increases approximately linearly with time, therefore our calculated fraction of 1.8% can be extrapolated to about 10% to correspond to the expected fraction at $\sim 140\ \mu$s. Next, one has to scale this value by a factor 0.6^2 to account for the fact that in the experiment only 60% of the initial number of atoms was transferred to the $m_x = 0$ state of the colliding condensates. Accordingly, our theoretical estimate of 10% should be proportionally scaled down to 4% conversion, in good agreement with the experimentally estimated fraction of 5% (see also appendix A).

In figure 4, we plot the radial momentum distribution of scattered atoms (solid line), obtained after angle averaging of the full 3D distribution within the region $|k_x| \leqslant 0.8k_r$. The numerical result is fitted with a Gaussian $\propto \exp[-(k-k_0)^2/(2\delta k^2)]$ (dashed line), centered at $k_0 = 0.98k_r$ and having the radial width of $\delta k = 0.10k_r \simeq 5.8 \times 10^5\,\mathrm{m}^{-1}$, where $k = |\mathbf{k}|$. The fitted radial width of $\delta k = 0.10k_r$ of the numerical simulation is in reasonable agreement with the simple estimate of equation (13), which gives $\delta k \simeq 0.075k_r$ for $\Delta t = 25\,\mu$s.

Figure 5 shows the numerical results for the BB and CL correlations (solid lines with circles), defined in equations (4) and (5). Due to the symmetry of the y- and z-directions, the results in these directions are practically the same. In order to verify the hypothesis that the shape and therefore the width of the pair correlation functions is governed by the width of the momentum distribution of the source condensate, we also plot the actual initial momentum distributions of the source condensate in the two orthogonal directions (with the understanding that the horizontal axis Δk_i now refers to the actual wavevector component k_i). The actual data points for the correlation functions and for the momentum distribution of the source are shown by the circles and squares, respectively, and are fitted with Gaussian curves for simplicity and

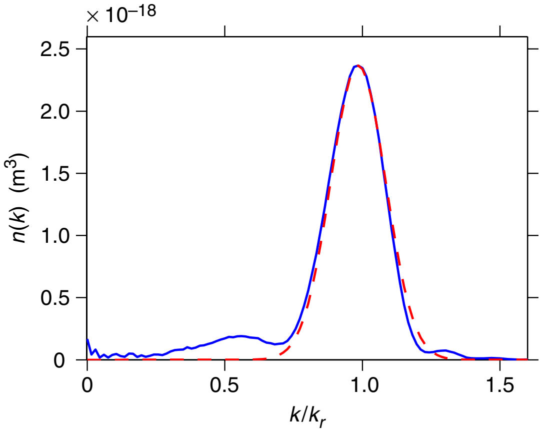

Figure 4. Angle averaged (radial) momentum distribution $n(k)$ of the scattered atoms (solid line) and a simple Gaussian fit (dashed line) used to define the radial width $\delta k = 0.10k_r$ of the halo around the peak momentum $k_0 = 0.98k_r$ (see text).

to guide the eye. The Gaussian fits for the correlation functions (solid lines) give:

$$g^{(2)}_{\mathrm{BB}}(\Delta k_i) - 1 = 9.2 \exp\{-\Delta k_i^2/[2(\sigma_i^{\mathrm{BB}})^2]\}, \tag{20}$$

$$g^{(2)}_{\mathrm{CL}}(\Delta k_i) - 1 = \exp\{-\Delta k_i^2/[2(\sigma_i^{\mathrm{CL}})^2]\}, \tag{21}$$

where the correlation widths σ_i^{BB} and σ_i^{CL} are shown in the table (22) below. The Gaussian fits (dashed lines) for the slices of the initial momentum distribution $n_0(k_i) \propto \exp\{-k_i^2/[2(\sigma_i)^2]\}$ are scaled to the same peak value as $g^{(2)}_{\mathrm{BB/CL}}(0) - 1$ and have $\sigma_x = 0.0025k_r$ and $\sigma_{y,z} = 0.055k_r$.

By comparing the solid and the dashed lines, we see that the shape of the correlation functions indeed closely follow the shape of the momentum distribution of the source. More specifically, we find that the following results provide the best fit to our numerical data:

$\sigma_x^{\mathrm{BB}}/\sigma_x$	$\sigma_{y,z}^{\mathrm{BB}}/\sigma_{y,z}$	$\sigma_x^{\mathrm{CL}}/\sigma_x$	$\sigma_{y,z}^{\mathrm{CL}}/\sigma_{yz}$
1.18	1.39	1.27	1.57

(22)

The ratios between the CL and BB correlation widths are $\sigma_x^{\mathrm{CL}}/\sigma_x^{\mathrm{BB}} \simeq 1.08$ and $\sigma_{y,z}^{\mathrm{CL}}/\sigma_{y,z}^{\mathrm{BB}} \simeq 1.13$. The errors due to stochastic sampling on all quoted values of the correlation widths are smaller than 3%.

The values for $\sigma_{y,z}^{\mathrm{CL}}/\sigma_{y,z}$ and $\sigma_{y,z}^{\mathrm{BB}}/\sigma_{y,z}$ can be compared with the respective experimentally measured values of table (11) and we see reasonably good agreement, even though the numerical data are for a much shorter collision time. The remaining discrepancy between the numerical data at $t_f = 25\,\mu$s and the experimentally measured values after a ~140 μs interaction time may be due to the evolution of the condensates past 25 μs, not attainable within the positive-P method. The above numerical results for the correlation widths can also be compared with the simple analytic estimate based on the Gaussian ansatz treatment of equations (9) and (10). We find that the approximate analytic results overestimate the BB and CL widths by ~20 and 40%, respectively, in the present example.

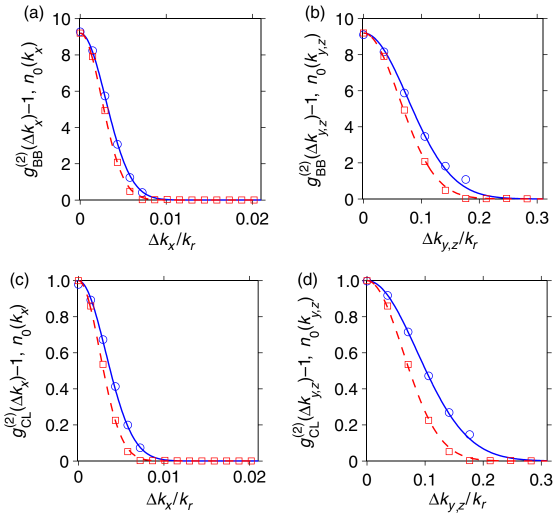

Figure 5. BB and CL atom–atom pair correlation, $g^{(2)}_{\mathrm{BB/CL}}(\Delta k_i)-1$ as a function of the displacement Δk_i ($i = x, y$ and z) in units of the collision momentum k_r, after $t_f = 25\,\mu$s collision time. The circles are the numerical results, angle-averaged over the halo of scattered atoms after elimination of the regions occupied by the two colliding condensates; the solid lines are simple Gaussian fits to guide the eye (see text). For comparison, we also plot the initial momentum distribution $n_0(k_i)$ of the colliding condensates; the actual data points are shown by the squares and are fitted by a dashed-line Gaussian.

The amplitude of the correlation functions can also be inferred by simple models. In fact, the CL correlation function is a manifestation of the Hanbury Brown and Twiss effect since it involves pairs from two independent spontaneous scattering events and we expect an amplitude of $g^{(2)}_{\mathrm{CL}}(0) = 2$ [28]. This is in agreement with the positive-P simulations. The BB correlation amplitude, on the other hand, can be substantially higher and display super-bunching ($g^{(2)}_{\mathrm{BB}}(0) \gg 1$) [14, 24] since the origin of this correlation is a simultaneous creation of a pair of particles in a single scattering event.

In a simple qualitative model [16], the amplitude of the BB correlation can be linked to the inverse population of the atomic modes on the halo. As we show in appendix B, this model follows the trends observed in our first-principles numerical simulations.

5.2. Shorter collision time

Here, we present the results of numerical simulation for the same parameters as in our main numerical example from section 5.1, except that the data are analyzed at $t_f = 12.5\,\mu$s, which is half the previous interaction time. We found in section 5.1 that $\sigma^{\mathrm{BB}}_{yz}$, $\sigma^{\mathrm{CL}}_{yz}$ and the width of the halo δk are all nearly the same. In section 3, however, we argue that the widths of the correlation functions and the halo are governed by different limits (equations (9), (10) and (13) or (14), respectively). The example in this section illustrates this point.

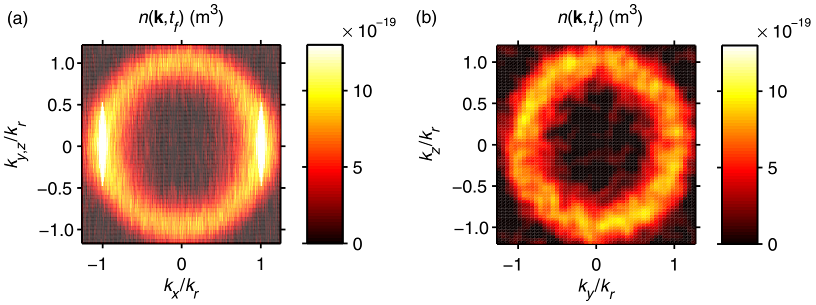

Figure 6. Same as in figure 3, except for $t_f = 12.5\,\mu$s collision time.

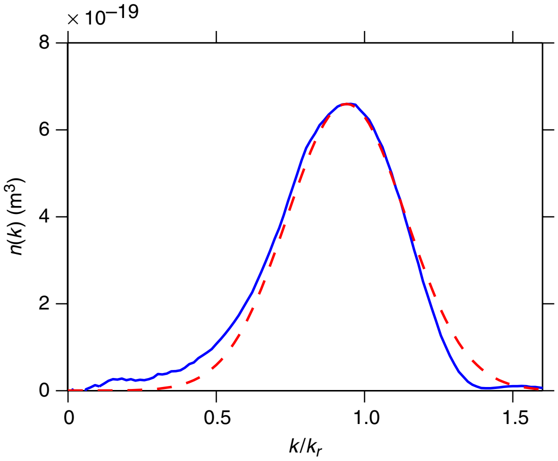

Figure 7. Same as in figure 4, except for $t_f = 12.5\,\mu$s collision time. The width and the peak of the fitted Gaussian here are: $\delta k = 0.20k_r$ and $k_0 = 0.95k_r$.

Figure 6 shows two orthogonal slices of the s-wave scattering sphere in momentum space (cf figure 3), whereas figure 7 is the corresponding radial distribution after angle averaging. The most obvious feature of the distribution is that it is broader than at $t_f = 25\,\mu$s and the fitted Gaussian gives the radial width of $\delta k = 0.20k_r$. This is precisely twice the width in figure 4 and is in agreement with the simple qualitative estimate of equation (13).

The BB and CL correlation functions after $t_f = 12.5\,\mu$s collision time are qualitatively very similar to those shown in figure 5, except that the Gaussian fits are

$$g^{(2)}_{\mathrm{BB}}(\Delta k_i) - 1 = 35.6\,\exp\{-\Delta k_i^2/[2(\sigma_i^{\mathrm{BB}})^2]\}, \tag{23}$$

$$g^{(2)}_{\mathrm{CL}}(\Delta k_i) - 1 = \exp\{-\Delta k_i^2/[2(\sigma_i^{\mathrm{CL}})^2]\}, \tag{24}$$

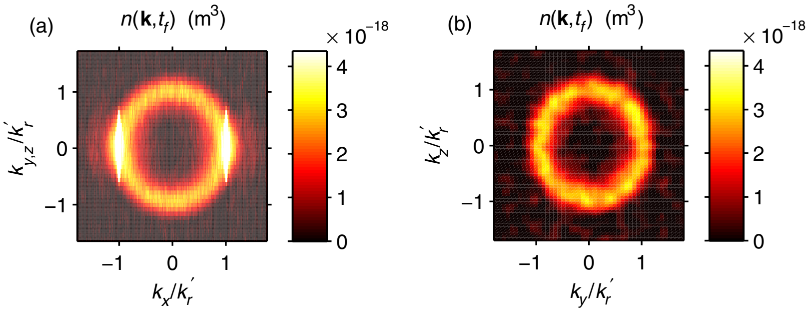

Figure 8. Same as in figure 3, except for $\sqrt{2}$ times smaller collision velocity, $v_r' = 6.46\,\mathrm{cm\,s^{-1}}$ ($k_r' = 4.09 \times 10^6\,\mathrm{m^{-1}}$). The axes for the momentum components k_i ($i = x, y$ and z) are in units of smaller recoil momentum than in figure 3, and therefore the absolute radius of the s-wave scattering sphere is smaller in the present example.

with the correlation widths given by

$\sigma_x^{\mathrm{BB}}/\sigma_x$	$\sigma_{y,z}^{\mathrm{BB}}/\sigma_{y,z}$	$\sigma_x^{\mathrm{CL}}/\sigma_x$	$\sigma_{y,z}^{\mathrm{CL}}/\sigma_{yz}$
1.16	1.28	1.27	1.48

(25)

The ratios between the widths are $\sigma_x^{\mathrm{CL}}/\sigma_x^{\mathrm{BB}} \simeq 1.09$ and $\sigma_{y,z}^{\mathrm{CL}}/\sigma_{y,z}^{\mathrm{BB}} \simeq 1.16$.

For the correlation functions, the main difference compared to the case for $25\,\mu\mathrm{s}$ is that the peak value of the BB correlation is now larger, reflecting the lower atomic density on the scattering halo. The correlation widths, on the other hand, are practically unchanged, at least within the numerical sampling errors of the positive-P simulations; the errors are at the level of the third significant digit in the quoted values, which we suppress. The number of scattered atoms in this example is about 850, which is approximately half the number at $25\,\mu\mathrm{s}$, confirming the approximately linear dependence on time in the spontaneous scattering regime.

5.3. Smaller collision velocity

In this example, we present the results of simulations in which the collision velocity is smaller by a factor $\sqrt{2}$ than before, $v_r' = 6.5\,\mathrm{cm\,s^{-1}}$ ($k_r' = 4.1 \times 10^6\,\mathrm{m^{-1}}$), while all other parameters are unchanged. In practice, this can be achieved by changing the propagation directions of the Raman lasers that outcouple the atoms from the trapped state. As in the previous example, the halo width illustrates equation (13).

The results of positive-P simulations for the momentum density distribution at $t_f = 25\,\mu\mathrm{s}$ are shown in figures 8 and 9. The most obvious feature of the distribution is again the fact that it is now broader than in our main example of section 5.1. The width of the Gaussian function fitted to the numerically calculated radial momentum distribution is given by $\delta k = 0.21 k_r'$. This is again in excellent agreement with the simple analytic estimate of equation (13), which predicts the broadening to be inversely proportional to the collision velocity. We also note that the peak momentum (relative to k_r') in the present example is slightly shifted towards the center of the

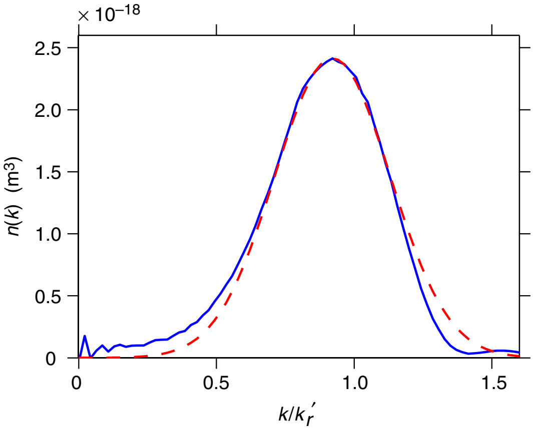

Figure 9. Same as in figure 4 except for $\sqrt{2}$ times smaller collision velocity v_r' ($k_r' = 4.1 \times 10^6\,\mathrm{m}^{-1}$). The width and the peak of the fitted Gaussian are $\delta k = 0.21k_r' = 8.6 \times 10^5\,\mathrm{m}^{-1}$ and $k_0 = 0.92k_r'$.

halo, $k_0 = 0.92k_r'$, which is a feature predicted in [30] to occur when the ratio of the kinetic energy to the interaction energy per particle is reduced.

The BB and CL correlation functions in this example are again qualitatively very similar to those shown in figure 5, except that the Gaussian fits are

$$g^{(2)}_{\mathrm{BB}}(\Delta k_i) - 1 = 9.0 \exp\{-\Delta k_i^2/[2(\sigma_i^{\mathrm{BB}})^2]\}, \tag{26}$$

$$g^{(2)}_{\mathrm{CL}}(\Delta k_i) - 1 = \exp\{-\Delta k_i^2/[2(\sigma_i^{\mathrm{CL}})^2]\}, \tag{27}$$

with the correlation widths given by

$\sigma_x^{\mathrm{BB}}/\sigma_x$	$\sigma_{y,z}^{\mathrm{BB}}/\sigma_{y,z}$	$\sigma_x^{\mathrm{CL}}/\sigma_x$	$\sigma_{y,z}^{\mathrm{CL}}/\sigma_{y,z}$
1.16	1.35	1.31	1.51

(28)

where $\sigma_x/k_r' \simeq 0.0035$ and $\sigma_x/k_r' \simeq 0.078$. The ratios between the CL and BB correlation widths are $\sigma_x^{\mathrm{CL}}/\sigma_x^{\mathrm{BB}} \simeq 1.13$ and $\sigma_{y,z}^{\mathrm{CL}}/\sigma_{y,z}^{\mathrm{BB}} \simeq 1.12$.

As we see from these results, the absolute widths of the correlation functions are practically unchanged compared to the main numerical example (22). This provides further evidence that, at least for short collision times, the correlation widths are governed by the momentum width of the source condensate, which is unchanged in the present example compared to the case of section 5.1.

The number of scattered atoms in this example is about 1270, which is approximately $\sqrt{2}$ times smaller than in section 5.1 and corresponds to ~1.3% conversion. This scaling is in agreement with the rate equation approach [24], according to which the number of scattered atoms is proportional to the square root of the collision energy and hence to the collision momentum, which is $\sqrt{2}$ times smaller here.

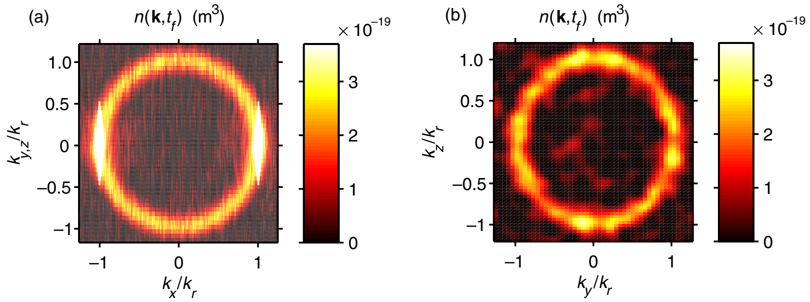

Figure 10. Same as in figure 3 except for the scattering lengths of $a_{00} = 2.65$ nm and $a_{11} = 3.75$ nm, which are twice as small as before.

5.4. Smaller scattering length

Finally, we present the results of numerical simulations for the same parameters as in our main numerical example from section 5.1, except that the scattering lengths a_{11} and a_{00} are artificially halved, i.e. $a_{00} = 2.65$ nm and $a_{11} = 3.75$ nm. The trap frequencies are unchanged and we modify the chemical potential to arrive at the same peak density of the initial BEC in the trap, $\rho_0 \simeq 2.5 \times 10^{19}\,\mathrm{m}^{-3}$. The total number of atoms is now smaller, $N \simeq 3.5 \times 10^4$. One effect of changing the scattering length is that it changes the size and shape of the trapped cloud, and therefore also its momentum distribution. The shape is slightly closer to a Gaussian and therefore also to the treatment in [28].

Due to the smaller scattering length, the density distribution in position space of the initial trapped condensate is now narrower and conversely the momentum distribution of the colliding condensates is broader. On the other hand, the width of the halo (see figures 10 and 11 at $t_f = 25\,\mu$s) of scattered atoms is practically unchanged compared to the example of figure 4, as it is governed by the energy–time uncertainty consideration (13), for the spontaneous scattering regime. The only quantitative difference is the lower peak density on the scattering sphere, which is due to the weaker strength of atom–atom interactions resulting in a slower scattering rate. The number of scattered atoms at 25 μs is ∼180, corresponding to 0.51% conversion of the initial total number $N \simeq 3.5 \times 10^4$. The fraction 0.51% itself corresponds approximately to a scaling law of $\sim a^{3/2}$, which is the same as the scaling of the total initial number of trapped atoms in the Thomas–Fermi limit for a fixed peak density.

Since the widths of the correlation functions are governed by the width of the momentum distribution of the initial colliding condensates, we expect corresponding broadening of the correlation functions as well (see figure 12). To quantify this effect, we fit the momentum distribution of the initial BEC by a Gaussian $\propto \exp\{-k_i^2/[2(\sigma_i)^2]\}$, where $\sigma_x = 0.0036k_r$ and $\sigma_{y,z} = 0.068k_r$ (cf with $\sigma_x = 0.0025k_r$ and $\sigma_{y,z} = 0.055k_r$ in figure 5, which are $\sim\sqrt{2}$ smaller). The Gaussian fits to the correlation functions in figure 12 are

$$g^{(2)}_{\mathrm{BB}}(\Delta k_i) - 1 = 49 \exp\{\Delta k_i^2/[2(\sigma_i^{\mathrm{BB}})^2]\}, \qquad (29)$$

$$g^{(2)}_{\mathrm{CL}}(\Delta k_i) - 1 = 0.94 \exp\{\Delta k_i^2/[2(\sigma_i^{\mathrm{CL}})^2]\}, \qquad (30)$$

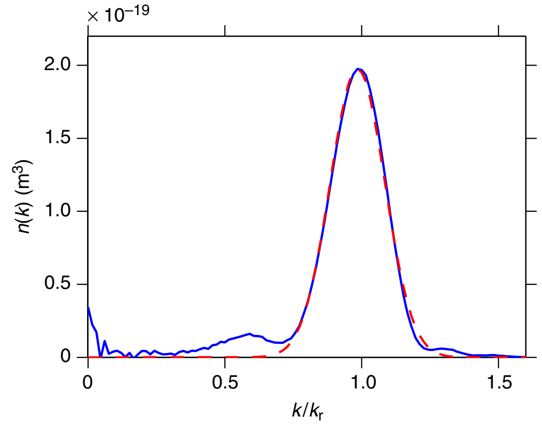

Figure 11. Same as in figure 4 except for twice as small values of the scattering lengths a_{00} and a_{11}. The width and the peak of the fitted Gaussian are $\delta k = 0.10k_r$ and $k_0 = 0.98k_r$, which are the same as in figure 4.

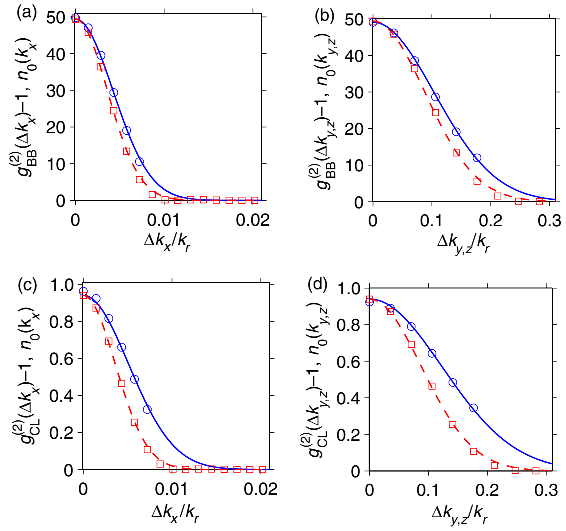

Figure 12. Same as in figure 5 except for twice as small s-wave scattering lengths a_{11} and a_{00}.

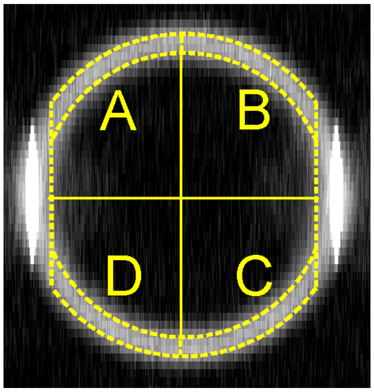

Figure 13. Illustration of the four regions of the momentum space density, forming the quadrants A, B, C and D on the s-wave scattering sphere, on which we analyze the data for relative number squeezing.

where the widths σ_i^{BB} and σ_i^{CL} are given by

$\sigma_x^{\mathrm{BB}}/\sigma_x$	$\sigma_{y,z}^{\mathrm{BB}}/\sigma_{y,z}$	$\sigma_x^{\mathrm{CL}}/\sigma_x$	$\sigma_{y,z}^{\mathrm{CL}}/\sigma_{y,z}$
1.18	1.53	1.42	1.81

(31)

We see that the relative widths are practically unchanged, implying that the absolute widths are broadened. The ratios between the CL and BB correlation widths are slightly increased and are given by $\sigma_x^{\mathrm{CL}}/\sigma_x^{\mathrm{BB}} \simeq 1.20$ and $\sigma_{y,z}^{\mathrm{CL}}/\sigma_{y,z}^{\mathrm{BB}} \simeq 1.18$.

These numerical results make the present example—with the diminished role of atom–atom interactions—somewhat closer to the simple analytic predictions of equations (9) and (10) based on a Gaussian ansatz for non-interacting condensates.

5.5. *Relative number squeezing and violation of Cauchy–Schwartz inequality*

Another useful measure of atom–atom correlations is the normalized variance of the relative number fluctuations between atom numbers $\hat{N}_i$ and $\hat{N}_j$ in a pair of counting volume elements denoted via i and j,

$$V_{i-j} = \frac{\langle [\Delta(\hat{N}_i - \hat{N}_j)]^2 \rangle}{\langle \hat{N}_i \rangle + \langle \hat{N}_j \rangle} = 1 + \frac{\langle : [\Delta(\hat{N}_i - \hat{N}_j)]^2 : \rangle}{\langle \hat{N}_i \rangle + \langle \hat{N}_j \rangle}, \tag{32}$$

where $\Delta\hat{X} = \hat{X} - \langle \hat{X} \rangle$ is the fluctuation. This definition uses the conventional normalization with respect to the shot-noise level characteristic of Poissonian statistics, such as for a coherent state, $\langle \hat{N}_i \rangle + \langle \hat{N}_i \rangle$. In this case, the variance $V_{i-j} = 1$, which corresponds to the level of fluctuations in the absence of any correlation between $\hat{N}_i$ and $\hat{N}_j$. Variance smaller than one, $V_{i-j} < 1$, implies reduction (or squeezing) of fluctuations below the shot-noise level and is due to quantum correlation between the particle number fluctuations in $\hat{N}_i$ and $\hat{N}_j$. Perfect (100%) squeezing of the relative number fluctuations corresponds to $V_{i-j} = 0$.

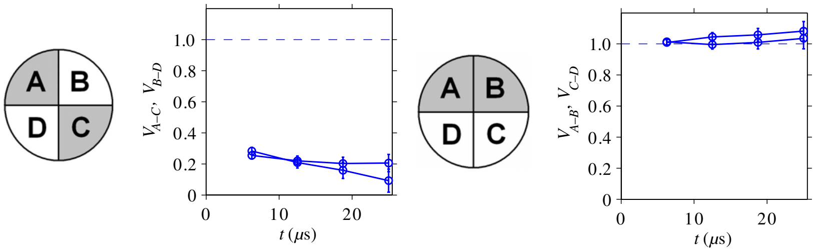

Figure 14. Relative number variance in the diametrically opposite and neighboring quadrants, $V_{A-C/B-D}$ and $V_{A-B/C-D}$, as a function of time.

In the context of the present model for the BEC collision experiment and possible correlation measurements between atom number fluctuations on diametrically opposite sides of the s-wave scattering sphere, we assign the indices $i, j = A, B, C$ and D in equation (32) to one of the four quadrants as illustrated in figure 13. The total atom number operator $\hat{N}_i$ in each quadrant $\mathcal{D}_i$ within the s-wave scattering sphere is defined after elimination of the regions in momentum space occupied by the two colliding condensates

$$\hat{N}_i(t) = \int_{\mathcal{D}_i} \mathrm{d}k_x \mathrm{d}k_y \int_{-\infty}^{+\infty} \mathrm{d}k_z \hat{n}(\mathbf{k}, t). \tag{33}$$

Operationally, this is implemented by discarding the data points beyond $|k_x| > 0.8k_r$. In addition, the quadrants $\mathcal{D}_i$ are defined on a 2D plane after integrating the momentum distribution along the z-direction, which in turn only takes into account the 3D data points satisfying $|1 - k^2/k_r^2| < 0.28$, i.e. lying in the narrow spherical shell $k_r \pm \delta k$ with $\delta k \simeq 0.14k_r$. The elimination of the inner and outer regions of the halo is done to minimize the sampling error in our simulations, since these regions have vanishingly small population and produce large noise in the stochastic simulations.

The choice of the quadrants as above is a particular implementation of the procedure of binning, known to result in a stronger correlation signal and larger relative number squeezing [11, 36]. Due to strong BB pair correlations, we expect the relative number fluctuations in the diametrically opposite quadrants to be squeezed, $V_{A-C}, V_{B-D} < 1$, while the relative number variance in the neighboring quadrants, such as V_{A-B} and V_{C-D}, is expected to be larger than or equal to one. The positive-P simulations confirm these expectations and are shown in figure 14, where we see strong (∼80%) relative number squeezing for the diametrically opposite quadrants, $V_{A-C,B-D} \simeq 1 - 0.8 = 0.2$.

These results assume a uniform detection efficiency of $\eta = 1$, whereas if the efficiency is less than 100% ($\eta < 1$), then the second term in equation (32) should be multiplied by η. This implies, that for $\eta = 0.1$ as an example, the above prediction of ∼80% relative number squeezing will be degraded down to a much smaller but still measurable value of ∼ 8% squeezing ($V_{A-C,B-D} \simeq 1 - 0.08 = 0.92$). Even with perfect detection efficiency, our simulations do not lead to ideal (100%) squeezing. This can be understood in terms of a small fraction of collisions that take place with a center-of-mass momentum offset that is (nearly) parallel to one of the borders between the quadrants. As a result, the respective scattered pairs fail to appear in diametrically opposite quadrants during the (finite) propagation time (see also [36]).

For the symmetric case with $\langle \hat{N}_i \rangle = \langle \hat{N}_j \rangle$ and $\langle \hat{N}_i^2 \rangle = \langle \hat{N}_j^2 \rangle$, the variance V_{i-j} can be rewritten as

$$V_{i-j} = 1 + \langle \hat{N}_i \rangle [g_{ii}^{(2)} - g_{ij}^{(2)}], \tag{34}$$

where the second-order correlation function $g_{ij}^{(2)}$ is defined according to

$$g_{ij}^{(2)} = \frac{\langle : \hat{N}_i \hat{N}_j : \rangle}{\langle \hat{N}_i \rangle \langle \hat{N}_j \rangle}. \tag{35}$$

Equation (34) helps to relate the relative number squeezing, $V_{i-j} < 1$, to the violation of the classical Cauchy–Schwartz inequality $g_{12}^{(2)} > g_{11}^{(2)}$, studied extensively in quantum optics with photons [33, 37]. The analysis presented here (see also [36] on molecular dissociation) shows that the Cauchy–Schwartz inequality, and its violation, is a promising area of study in *quantum atom optics* as well.

6. Summary

An important conclusion that we can draw from the numerical simulations is that the predicted widths of the correlation functions are remarkably robust against the parameter variations we were able to explore (in section 5.1 through 4). This gives us confidence in our physical interpretation of the width as being chiefly due to the initial momentum width of the condensate. The discrepancy with the analytical calculation of [28] seems to be primarily due to the different cloud shapes used. The width of the halo varies with the parameters we tested in a predictable way and also confirms the discussion in section 3.

As for comparison with the experiment, the numerically calculated widths of the scattering halo and the correlation functions coincide with the experimental ones to within better than 20% in most cases. The main discrepancy with the experiment is in the *ratio* of the BB and CL correlation widths. From the experimental point of view, these ratios are more significant than the individual widths since some sources of uncertainty, such as the number of atoms and the size of the condensates, cancel. The discrepancy may mean that the CL correlations are not sufficient to characterize the size and momentum distribution in the source at this level of accuracy. The discrepancies may of course also be due to the numerous experimental imperfections, especially the fact that the Raman outcoupling was only 60% efficient, and therefore an appreciable trapped $m_x = 1$ condensate was left behind. This defect may be remedied in future experiments. On the other hand, the current simulations neglect the unavoidable interaction of the scattered atoms with unscattered, $m_x = 0$ condensates as they leave the interaction region. This interaction could alter the trajectories of the scattered atoms in a minor, but complicated way. Future numerical work must examine this possibility further.

Still, the overall message of this work is that a first principles quantum field theory approach can quantitatively account for experimental observations of atomic four-wave mixing experiments. This work represents the first time that this sort of numerical simulation has been carefully confronted with an experiment. An interesting extension would be to examine the regime of stimulated scattering. It has been predicted that a highly anisotropic BEC could lead to an anisotropic population of the scattering halo [38, 39]. This effect would be a kind of atomic analogue of superradiance observed when off-resonant light is shone on a condensate [40, 41]. In addition, our results may be useful beyond the cold atom community: theoretical descriptions of correlation measurements in heavy ion collisions [42] may benefit from some of our insights.

Acknowledgments

We acknowledge stimulating discussions with A Aspect, K Mølmer, M Trippenbach, P Deuar and M Davis, and thank the developers of the XMDS software [43]. CS and KK acknowledge support from the Australian Research Council and the Queensland State Government. Part of this work was done at the Institut Henri Poincaré—Centre Emile Borel; KK thanks the institute for hospitality and support. The atom optics group is supported by the SCALA program of the EU and by the IFRAF institute.

Appendix A. Duration of the collision

In order to estimate the collision duration one can consider a simple classical model of the collision [24]. Denoting by $\rho_1(\mathbf{x}, t)$ and $\rho_2(\mathbf{x}, t)$ the density distributions of the two condensates, the number of scattered atoms $N_{\mathrm{sc}}(t)$ at a given time can be written

$$N_{\mathrm{sc}}(t) = 2\int_0^t \mathrm{d}t' \int \mathrm{d}^3\mathbf{x}\, 2\sigma_0 v_r \rho_1(\mathbf{x}, t')\rho_2(\mathbf{x}, t'), \tag{A.1}$$

where $\sigma_0 = 8\pi a_{00}^2$ is the cross-section for a collision of two particles. In this latter formula $a_{00} \simeq 5.3\,\mathrm{nm}$ is the scattering length between $m_x = 0$ atoms [16].

The time-dependent density of the two condensates can be calculated from the expansion of a condensate in the Thomas–Fermi regime described in [44]. This approach suggests two different timescales for the collision duration. First, the separation of the two condensates occurs in a time defined by the ratio of the longitudinal size of the condensates and their relative velocity $t_{\mathrm{sep}} = R_x/v_r$. Taking for R_x the Thomas–Fermi radius of the initial condensate, one can show that t_{sep} is on the order of 1 ms. At the same time, the condensates expand during their separation on a timescale $t_{\mathrm{exp}} = 1/\omega_y = 1/\omega_z \simeq 140\,\mu\mathrm{s}$. This latter effect appears to be predominant in the evaluation of equation (A.1) and t_{exp} can be taken as a definition of the collision duration Δt. The numerical evaluation of equation (A.1) gives $N_{\mathrm{sc}}(\Delta t) \simeq 0.66 N_{\mathrm{sc}}(\infty)$ and the estimated total number of scattered atoms corresponds to the experimentally observed 5% of the initial total number of atoms in the trapped condensate.

Appendix B. Occupation number of the scattering modes and amplitude of the BB correlation

In order to estimate the occupation number of the scattering modes one needs to compare the number of scattered atoms N_{sc} to the number of scattering modes N_m. To achieve this one has to first consider the volume of a scattering mode V_m, given by the first-order coherence volume (also dubbed ‘phase grain’ in [12, 15]). Such a volume corresponds in fact to the coherence volume of the source condensate, and in practice it can also be deduced from the measurement of the width of the CL correlation function $g^{(2)}_{\mathrm{CL}}(\Delta k_i)$ as one expects in a Hanbury Brown–Twiss experiment. For simplicity, we match the scattering mode volume V_m to the coherence volume of the source condensate in momentum space,

$$V_m \simeq \beta\sigma_x(\sigma_{yz})^2, \tag{B.1}$$

where β is a geometrical factor which depends on the geometry of the modes. Approximating the source condensate in momentum space by a Gaussian $\propto \exp[-x^2/(2\sigma_x^2) - (y^2 + z^2)/(2\sigma_{y,z}^2)]$, one has $\beta = (2\pi)^{3/2}$.

The number of scattering modes N_m can in turn be estimated from knowledge of the total volume of the scattering shell V,

$$N_m = \frac{V}{V_m}, \tag{B.2}$$

where the volume V is determined from the value of the width of the scattering shell δk:

$$\begin{aligned} V &= \int \mathrm{d}^3\mathbf{k}\ \exp[-(k-k_r)^2/(2\delta k^2)] \\ &\simeq 4\pi\sqrt{2\pi}k_r^2\delta k, \end{aligned} \tag{B.3}$$

for $\delta k \ll k_r$. If we apply this estimate to the results of the main numerical example (see section 5.1), we find $N_m \simeq 26\,400$. As $N_{\mathrm{sc}} = 1750$, this implies an occupation number per mode of $N_{\mathrm{sc}}/N_m \simeq 0.066$. Such an estimate confirms that the system is indeed in the spontaneous regime and that bosonic stimulation effects are negligible.

The simple model of [16] for the BB correlation predicts that its height is given by

$$g_{\mathrm{BB}}^{(2)}(0) = 1 + N_m/N_{\mathrm{sc}}. \tag{B.4}$$

Using the above estimate of N_m and the actual value of N_{sc} found from the numerical simulations, we obtain that the height of the BB correlation peak should be approximately given by ∼ 16. This compares favorably with the actual numerical result of 10.2. Similarly, we obtain the BB correlation peak of: ∼62 in the example with the shorter collision time (compare with the numerical result of 36.6); ∼18 in the example with the smaller collision velocity (compare with 10); and ∼70 in the example with the smaller scattering length (compare with 50).

Appendix C. Width of the s-wave scattering sphere in the undepleted ‘pump’ approximation

To estimate the width of the halo of scattered atoms beyond the spontaneous regime we use the analytic solutions for a uniform system in the so-called undepleted ‘pump’ approximation in which the number of atoms in the colliding condensates are assumed constant. This approximation is applicable to short collision times. Nevertheless, it formally describes the regime of stimulated scattering and can be used to estimate the width of the s-wave scattering sphere as we show here.

The problem of BEC collisions in the undepleted ‘pump’ approximation was studied in [30]; the solutions for the momentum distribution of the s-wave scattered atoms are formally equivalent to those obtained for dissociation of a BEC of molecular dimers in the undepleted molecular condensate approximation [14, 31]. For a uniform system with periodic boundary conditions, one has the following analytic solution for momentum mode occupation numbers:

$$n_{\mathbf{k}}(t) = \frac{\bar{g}^2}{\bar{g}^2 - \Delta_k^2}\sinh^2\left(\sqrt{\bar{g}^2 - \Delta_k^2}\,t\right). \tag{C.1}$$

Here, the constant $\bar{g}$ is given by

$$\bar{g} = 2U_0\rho_0 = \frac{8\pi\hbar a_{00}\rho_0}{m}, \tag{C.2}$$

where $U_0 = 4\pi\hbar a_{00}/m$ corresponds to the coupling constant $g/\hbar$ of [30], and we note that the results of [30] contain typographical errors and have to be corrected as follows [45]: given the Hamiltonian of (1), with $g = 4\pi\hbar^2 a/m$, the coupling g in (2), (7), (9) and (10), as well as in the definition of $\Delta(p)$ after (9), should be replaced by $2g$. In the problem of molecular dissociation, the constant $\bar{g}$ corresponds to $\bar{g} = \chi\sqrt{\rho_0}$ [14], where χ is the atom–molecule coupling and ρ_0 is the molecular BEC density.

The parameter Δ_k in equation (C.1) corresponds to the energy offset from the resonance condition

$$\hbar\Delta_k \equiv \frac{\hbar^2 k^2}{2m} - \frac{\hbar^2 k_r^2}{2m}, \tag{C.3}$$

where $\hbar k_r$ is the collision momentum; in molecular dissociation, $\hbar^2 k_r^2/m$ corresponds to the effective dissociation energy $2\hbar|\Delta_{\mathrm{eff}}|$, using the notation of [14].

From equation (C.1), we see that modes with $\bar{g}^2 - \Delta_k^2 > 0$ experience Bose enhancement and grow exponentially with time, whereas the modes with $\bar{g}^2 - \Delta_k^2 < 0$ oscillate at the spontaneous noise level. The absolute momenta of the exponentially growing modes lie near the resonant momentum $\hbar k_r$, and therefore we can use the condition $\bar{g}^2 - \Delta_k^2 = 0$ to define the approximate width of the s-wave scattering sphere. First, we write $k = k_r + \Delta k$ and assume for simplicity that k_r is large enough so that $\Delta k \ll k_r$. Then the condition $\bar{g}^2 - \Delta_k^2 = 0$ can be approximated by

$$1 - \left(\frac{\hbar k_r \Delta k}{m\bar{g}}\right)^2 \simeq 0. \tag{C.4}$$

This can be solved for Δk and used to define the width $\delta k = \Delta k/2$ of the s-wave scattering sphere as

$$\frac{\delta k}{k_r} \simeq \frac{m\bar{g}}{2\hbar k_r^2} = \frac{4\pi a_{00}\rho_0}{k_r^2}. \tag{C.5}$$

The reason for defining it as half of Δk is to make δk closer in definition to the half-width at half maximum and to the rms width around k_r.

The above simple analytic estimate (C.5) gives $\delta k/k_r \simeq 0.05$ for the present $^4\mathrm{He}^*$ parameters. For comparison, the actual width of the analytic result (C.1) varies between $\delta k/k_r \simeq 0.12$ and $\delta k/k_r \simeq 0.027$ for durations between $\bar{g}t = 1$ and $\bar{g}t = 7$, corresponding, respectively, to $t \simeq 20\,\mu$s and $t \simeq 140\,\mu$s in the present $^4\mathrm{He}^*$ example.

Appendix D. Positive-P simulation parameters

The positive-P simulations in our main numerical example of section 5 are performed on a computational lattice with $1400 \times 50 \times 70$ points in the (x, y, z)-directions, respectively. The length of the quantization box along each dimension is $L_x = 252\,\mu$m, $L_y = 20.52\,\mu$m and $L_z = 30.76\,\mu$m. The computational lattice in momentum space is reciprocal to the position space lattice and has the lattice spacing of $\Delta k_i = 2\pi/L_i$, giving $\Delta k_x = 2.49 \times 10^4\,\mathrm{m}^{-1}$,

$\Delta k_y = 3.06 \times 10^5\,\mathrm{m}^{-1}$ and $\Delta k_z = 2.04 \times 10^5\,\mathrm{m}^{-1}$. The momentum cutoffs are $k_x^{(\max)} = 1.75 \times 10^7\,\mathrm{m}^{-1}$, $k_y^{(\max)} = 7.66 \times 10^6\,\mathrm{m}^{-1}$ and $k_z^{(\max)} = 7.15 \times 10^6\,\mathrm{m}^{-1}$.

The momentum cutoff in the collision direction, $k_x^{(\max)}$, is more than 3 times larger than the collision momentum k_r, and hence it captures all relevant scattering processes of interest, including the energy non-conserving scatterings $(k_r) + (k_r) \to (3k_r) + (-k_r)$ and $(-k_r) + (-k_r) \to (-3k_r) + (k_r)$ [15]. In all our figures, the regions of momentum space covering $k_x \simeq \pm 3k_r$ are not shown for the clarity of presentation of the main halo. These scattering processes, which produce a weak but not negligible signal at $k_x \simeq \pm 3k_r$, i.e. outside the main halo, are enhanced by Bose stimulation due to the large population of the colliding condensate components at $k_x \simeq \mp k_r$, respectively. In the remaining y- and z-directions, such processes are absent and therefore the number of lattice points and the momentum cutoffs can be smaller.

Since the momentum distribution of the initial condensate is narrowest in the k_x-direction, one may question whether the resolution of $\Delta k_x = 2.49 \times 10^4\,\mathrm{m}^{-1}$ with 1400 lattice points is sufficient. We check this by repeating the simulations with $4200 \times 40 \times 40$ lattice points and quantization lengths of $L_x = 753\,\mu\mathrm{m}$ and $L_y = L_z = 15.4\,\mu\mathrm{m}$, which give smaller lattice spacing $\Delta k_x = 8.24 \times 10^3\,\mathrm{m}^{-1}$, together with $\Delta k_y = \Delta k_z = 4.08 \times 10^5\,\mathrm{m}^{-1}$, $k_x^{(\max)} = 1.75 \times 10^7\,\mathrm{m}^{-1}$ and $k_y^{(\max)} = k_z^{(\max)} = 8.16 \times 10^6\,\mathrm{m}^{-1}$. Our results on the new lattice reproduce the previous ones, within the sampling errors of the stochastic simulations. We typically average over 2800 stochastic trajectories, and take 128 time steps in the simulations over 25 μs collision time. A typical simulation of this size takes about 100 h on 7 CPUs running in parallel at 3.6 GHz clock speed.

References

[1] Jeltes T *et al* 2007 *Nature* **445** 402

[2] Hellweg D, Cacciapuoti L, Kottke M, Schulte T, Sengstock K, Ertmer W and Arlt J J 2003 *Phys. Rev. Lett.* **91** 010406

[3] Esteve J, Trebbia J B, Schumm T, Aspect A, Westbrook C I and Bouchoule I 2006 *Phys. Rev. Lett.* **96** 130403

[4] Rom T, Best T, van Oosten D, Schneider U, Fölling S, Paredes B and Bloch I 2006 *Nature* **444** 733

[5] Öttl A, Ritter S, Köhl M and Esslinger T 2005 *Phys. Rev. Lett.* **95** 090404

[6] Ritter S, Öttl A, Donner T, Bourdel T, Köhl M and Esslinger T 2007 *Phys. Rev. Lett.* **98** 090402

[7] Hofferberth S, Lesanovsky I, Schumm T, Schmiedmayer J, Imambekov A, Gritsev V and Demler E 2007 *Preprint* 0710.1575

[8] Schellekens M, Hoppeler R, Perrin A, Viana Gomes J, Boiron D, Westbrook C I and Aspect A 2005 *Science* **310** 648

[9] Yasuda M and Shimizu F 1996 *Phys. Rev. Lett.* **77** 3090

[10] Fölling S, Gerbier F, Widera A, Mandel O, Gerike T and Bloch I 2005 *Nature* **434** 481

[11] Greiner M, Regal C A, Stewart J T and Jin D S 2005 *Phys. Rev. Lett.* **94** 110401

[12] Norrie A A, Ballagh R J and Gardiner C W 2005 *Phys. Rev. Lett.* **94** 040401

[13] Norrie A A, Ballagh R J and Gardiner C W 2006 *Phys. Rev.* A **73** 043617

[14] Savage C M, Schwenn P E and Kheruntsyan K V 2006 *Phys. Rev.* A **74** 033620

[15] Deuar P and Drummond P D 2007 *Phys. Rev. Lett.* **98** 120402

[16] Perrin A, Chang H, Krachmalnicoff V, Schellekens M, Boiron D, Aspect A and Westbrook C I 2007 *Phys. Rev. Lett.* **99** 150405

[17] Drummond P D and Gardiner C W 1980 *J. Phys. A: Math. Gen.* **13** 2353

[18] Gardiner C W and Zoller P 2000 *Quantum Noise* (Berlin: Springer)

[19] Steel M J, Olsen M K, Plimak L I, Drummond P D, Tan S M, Collett M J, Walls D F and Graham R 1998 *Phys. Rev.* A **58** 4824

[20] Drummond P D and Corney J F 1999 *Phys. Rev.* A **60** R2661

[21] Gilchrist A, Gardiner C W and Drummond P D 1997 *Phys. Rev.* A **55** 3014

[22] Deuar P and Drummond P D 2006 *J. Phys. A: Math. Gen.* **39** 1163

[23] Ziń P, Chwedeńczuk J, Veitia A, Rzażewski K and Trippenbach M 2005 *Phys. Rev. Lett.* **94** 200401

[24] Ziń P, Chwedeńczuk J and Trippenbach M 2006 *Phys. Rev.* A **73** 033602

[25] Morgan S A, Rusch M, Hutchinson D A W and Burnett K 2003 *Phys. Rev. Lett.* **91** 250403

[26] Yurovsky V A 2002 *Phys. Rev.* A **65** 033605

[27] Sinatra A, Lobo C and Castin I 2002 *J. Phys. B: At. Mol. Opt. Phys.* **35** 3599

[28] Molmer K, Perrin A, Krachmalnicoff V, Leung V, Boiron D, Aspect A and Westbrook C I 2008 *Phys. Rev.* A **77** 033601

[29] Ögren H M and Kheruntsyan K V (unpublished)

[30] Bach R, Trippenbach M and Rzażewski K 2002 *Phys. Rev.* A **65** 063605

[31] Kheruntsyan K V and Drummond P D 2002 *Phys. Rev.* A **66** 031602

[32] Davis M J, Thwaite S J, Olsen M K and Kheruntsyan K V 2008 *Phys. Rev.* A **77** 023617

[33] Walls D and Milburn G 1991 *Quantum Optics* (New York: Springer)

[34] Abrikosov A A, Gorkov L P and Dzyaloshinski I E 1963 *Methods of Quantum Field Theory in Statistical Physics* (New York: Springer)

[35] Moal S, Portier M, Kim J, Dugué J, Rapol U D, Leduc M and Cohen-Tannoudji C 2006 *Phys. Rev. Lett.* **96** 023203

[36] Savage C M and Kheruntsyan K V 2007 *Phys. Rev. Lett.* **99** 220404

[37] Zou X, Wang L and Mandel L 1991 *Opt. Commun.* **84** 351

[38] Vardi A and Moore M G 2002 *Phys. Rev. Lett.* **89** 090403

[39] Pu H and Meystre P 2000 *Phys. Rev. Lett.* **85** 3987

[40] Inouye S, Chikkatur A, Stamper-Kurn D M, Stenger J, Pritchard D and Ketterle W 1999 *Science* **285** 571

[41] Gross M and Haroche S 1982 *Phys. Rep.* **93** 301

[42] Wong C Y and Zhang W N 2007 *Phys. Rev.* C **76** 034905

[43] Collecut G R and Drummond P D 2001 *Comput. Phys. Commun.* **142** 219

[44] Castin Y and Dum R 1996 *Phys. Rev. Lett.* **77** 5315

[45] Trippenbach M, private communication

PHYSICAL REVIEW A **78**, 053605 (2008)

Pair correlations of scattered atoms from two colliding Bose-Einstein condensates: Perturbative approach

J. Chwedeńczuk,[1] P. Ziń,[2] M. Trippenbach,[1,2] A. Perrin,[3,4] V. Leung,[3] D. Boiron,[3] and C. I. Westbrook[3]
[1]*Institute of Theoretical Physics, Physics Department, Warsaw University, Hoża 69, PL-00-681 Warsaw, Poland*
[2]*The Andrzej Sołtan Institute for Nuclear Studies, Warsaw University, Hoża 69, PL-00-681 Warsaw, Poland*
[3]*Laboratoire Charles Fabry de l'Institut d'Optique, CNRS, Univ Paris-Sud, Campus Polytechnique, RD128, 91127 Palaiseau cedex, France*
[4]*Atominstitut der Österreichischen Universitäten, TU-Wien, Stadionallee 2, A-1020 Vienna, Austria*
(Received 22 July 2008; published 4 November 2008)

We apply an analytical model for anisotropic, colliding Bose-Einstein condensates in a spontaneous four-wave-mixing geometry to evaluate the second-order correlation function of the field of scattered atoms. Our approach uses quantized scattering modes and the equivalent of a classical, undepleted pump approximation. Results to lowest order in perturbation theory are compared with a recent experiment and with other theoretical approaches.

DOI: 10.1103/PhysRevA.78.053605 PACS number(s): 03.75.Nt, 34.50.Cx

I. INTRODUCTION

The analog of correlated photon pair production [1] has recently been demonstrated using atoms. Both molecular dissociation [2] and four-wave mixing of de Broglie waves [3] have shown correlation peaks. As in quantum optics, such atom pairs lend themselves to investigations into nonclassical correlation phenomena such as entanglement of massive particles [4–7] and spontaneous directionality or superradiant effects [5,8]. From the point of view of the outgoing atoms, the underlying physics is very similar and thus theoretical descriptions should be applicable to both processes. The experiment using four-wave mixing of metastable helium atoms in particular has yielded detailed information about the atomic pair correlations. Efforts to treat the experimental situations are therefore highly desirable.

Theoretically, a description of condensate collisions in the spontaneous scattering regime requires a formulation that extends beyond the mean-field model [9,10]. In previous work on spherical Gaussian wave packets, within a perturbative approach, we have given analytical formulas for the correlation functions [11,12].

In this paper we extend our method to anisotropic condensates to give an analytic description of the correlation properties of spontaneously emitted atom pairs in a geometry much closer to and in good agreement with the experiment [3]. Numerical approaches using the truncated Wigner method [13,14] and positive-*P* method [15–17] have also been used, in particular to give insight into the stimulation regime where bosonic enhancement comes to play.

Here, we use the model of colliding condensates to examine two types of correlations. First, we shall focus on atom pairs originating from the same two-body scattering event. These consequently have nearly opposite momenta. Thus we analyze the opposite-momenta correlations of atom pairs. Second, we examine two-body correlations between atoms scattered with nearly collinear momenta, a manifestation of the Hanbury Brown-Twiss (HBT) effect [11,15,16,18]. In both cases, the demonstration of a two-particle correlation requires a measurement of the conditional probability of detecting a particle at position $\mathbf{r}_1$ given that a particle was detected at $\mathbf{r}_2$. This probability is proportional to the second-order correlation function $G^{(2)}(\mathbf{r}_1,\mathbf{r}_2)$ of the field $\hat{\delta}$ of atoms: i.e.,

$$G^{(2)}(\mathbf{r}_1,\mathbf{r}_2) = \langle \hat{\delta}^{\dagger}(\mathbf{r}_1)\hat{\delta}^{\dagger}(\mathbf{r}_2)\hat{\delta}(\mathbf{r}_2)\hat{\delta}(\mathbf{r}_1)\rangle .$$

We shall pay particular attention to correlations in momentum space and compare these results with experimental data of [3]. A careful comparison of a numerical treatment based on the positive-*P* method [17] with the experiment [3] indicated reasonable agreement, but one of the limitations of the method, the short collision duration which could be simulated, left some unresolved questions. In particular, energy conservation is a less stringent constraint for short collision times, and thus one can wonder about the role this constraint plays in the experiment. The treatment given here is not subject to this limitation and also agrees fairly well with the experiment for most of the experimentally accessible observables. One observable quantity, however—the averaged width of the collinear correlation function in a direction orthogonal to the symmetry axis—disagrees with the experiment and with Ref. [17]. In our treatment, it is precisely the requirement of energy conservation that is at the origin of the difference. At the end of the paper we shall discuss possible explanations of this discrepancy.

Let us first describe the experiment in which a collision of two Bose-Einstein condensates of metastable helium produces a cloud of scattered atoms. A condensate of approximately 10^4–10^5 He* atoms is created in a cigar-shaped magnetic trap with axial and radial trapping frequencies of $\omega_z = 2\pi\times 47$ Hz and $\omega_r = 2\pi\times 1150$ Hz, respectively. Three laser beams are used to transfer the atoms into two counterpropagating wave packets by a Raman process, with a transfer efficiency of about 60%. As the wave packets counterpropagate with a relative velocity of $2v_{\text{rec}} = 18.4$ cm/s, atoms from the two clouds collide via *s*-wave scattering, populating a spherical shell in momentum space often referred to as the "halo" [19–21] (see Fig. 1). In the experiment, about 5% of the atoms are scattered. In addition

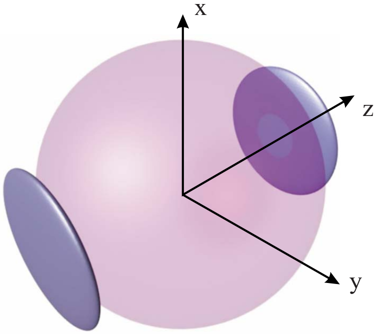

FIG. 1. (Color online) Velocity space representation of the pair production experiment. Raman pulses generate counterpropagating condensates which collide and expand into disk-shaped clouds along the z axis. Atoms scattered during the collision expand to form a spherical shell of correlated pairs. Note that the orientation of the axes in this article differs from Ref. [3]

to splitting the condensate, the Raman transition transfers the atoms into an untrapped magnetic substate. The transferred atoms thus expand freely, falling onto a microchannel plate (MCP) detector that allows the three-dimensional reconstruction of the position of single atoms with an estimated efficiency of 10% [22,23]. Knowing the positions of individual atoms, the initial momenta and the second-order momentum correlation function of the cloud of scattered particles can be computed. The precision of the measurement is limited by the finite resolution of the MCP. This factor will be taken into account in our comparison between the theoretical estimates and the experimental results.

II. MODEL FOR SCATTERING

To make the comparison, we introduce a simplified model for atom scattering during a collision of two Bose-Einstein condensate wave packets. In this model we assume that two counterpropagating wave packets constitute a classical undepleted source for the process of scattering. This concept is introduced in analogy to examples in quantum optics, where a strong coherent laser field is treated as a classical wave and its depletion is neglected [24]. We shall simplify the model further on. Since we assume that the two colliding condensates remain undepleted, the population of the $\hat{\delta}$ field of scattered atoms should be small, as compared to the number of atoms in the condensates. In such a regime, a Bogoliubov approximation is often used [25,26], leading to linearized equations of motion for the quantum fields. In our case, the $\hat{\delta}$ field of scattered atoms satisfies the Heisenberg equation (for details of the derivation, see [11,12])

$$i\hbar\partial_t\hat{\delta}(\mathbf{r},t) = -\frac{\hbar^2\nabla^2}{2m}\hat{\delta}(\mathbf{r},t) + 2g\psi_Q(\mathbf{r},t)\psi_{-Q}(\mathbf{r},t)\hat{\delta}^{\dagger}(\mathbf{r},t). \tag{1}$$

Here $\psi_{\pm Q}(\mathbf{r},t)$ is the c-number wave function of the colliding condensates with mean momentum per atom equal to $\pm\hbar Q$. Moreover, the coupling constant $g=\frac{4\pi\hbar^2 a}{m}$ is related to the atomic mass m and s-wave scattering length a of He*.

To permit analytic calculations, we model the condensate wave functions $\psi_{\pm Q}(x,y,z,t)$ as Gaussians:

$$\psi_{\pm Q} = \sqrt{\frac{N}{2\pi^{3/2}\sigma_r^2\sigma_z}}\exp\left(\mp iQz - \frac{i\hbar Q^2 t}{2m}\right)$$
$$\times\exp\left[-\frac{1}{2\sigma_r^2}(x^2+y^2) - \frac{1}{2\sigma_z^2}\left(z \mp \frac{\hbar Q t}{m}\right)^2\right], \tag{2}$$

where N is the total number of particles in both wave packets. The radial (σ_r) and axial (σ_z) width of the Gaussians are extracted from the initial condensate wave function Ψ_0 which is calculated numerically from the Gross-Pitaevski equation using an imaginary-time method. In practice, we fit $\int dv_x\int dv_y|\Psi_0(\mathbf{v})|^2$ with a Gaussian function $\propto\exp(-v_z^2/\chi_z^2)$ and then use $\sigma_z=\hbar/(m\chi_z)$. We define σ_r similarly. Here, for simplicity, we neglect the spread of the condensates during the collision. This assumption seems reasonable because most of the atom collisions take place before the two clouds have had time to expand.

It is useful to change variables and rescale the field operator

$$\frac{\hbar Q}{m\sigma_z}t \to t, \quad \mathbf{r}/\sigma_z \to \mathbf{r}, \quad \frac{1}{\sigma_z^{3/2}}\hat{\delta}(\mathbf{r},t) \to \hat{\delta}(\mathbf{r},t),$$

which simplifies the equation of motion (1): i.e.,

$$i\beta\partial_t\hat{\delta}(\mathbf{r},t) = -\frac{1}{2}\nabla^2\hat{\delta}(\mathbf{r},t) + \alpha e^{-(x^2+y^2)/\gamma^2-z^2}e^{-i\beta t-t^2}\hat{\delta}^{\dagger}(\mathbf{r},t), \tag{3}$$

where $\alpha=\frac{4Na\sigma_z}{\sigma_r^2\sqrt{\pi}}$, $\beta=Q\sigma_z$, and $\gamma=\frac{\sigma_r}{\sigma_z}$.

The condensate density in momentum space then reads

$$|\Psi_0(\mathbf{k})|^2 = \frac{N\beta^3}{\sqrt{\pi^3}\gamma^2}\exp[-\beta^2(k_z^2+\gamma^2k_r^2)]. \tag{4}$$

The three parameters α, β, and γ fully determine the dynamics of the field of scattered atoms. For $N=10^4$ and $\hbar Q=mv_{\text{rec}}$ we have $\alpha=1652$, $\beta=227$, and $\gamma=0.05$.

We also find $\chi_z=0.004v_{\text{rec}}$, $\sigma_z=39\ \mu\text{m}$, $\chi_r=0.0870v_{\text{rec}}$, and $\sigma_r=2\ \mu\text{m}$. The parameter α is a measure of the strength of the interactions between particles. As such, it governs the fraction of atoms scattered into the halo. As a consistency check, in Appendix A we give an alternate estimate of α in the experiment using the observed fraction of scattered atoms.

In Sec. III we derive an analytical expression for the second-order correlation function in the perturbative regime. It is still an open question whether, for these parameters, the perturbative approach applies. We tackle this issue after the evaluation of the $G^{(2)}$ function is Sec. III C. In Sec. IV we compare the perturbative results with the experimental data of [3].

III. DERIVATION OF $G^{(2)}$ IN THE PERTURBATIVE REGIME

We shall begin the analytical calculations with a definition of the Fourier transform of the $\hat{\delta}$ operator:

$$\hat{\delta}(\mathbf{r},t) = \left(\frac{\beta}{2\pi}\right)^{3/2} \int d\mathbf{k} e^{i\beta\mathbf{k}\cdot\mathbf{r} - i\beta k^2 t/2} \hat{\delta}(\mathbf{k},t). \tag{5}$$

This particular form of the Fourier transformation "incorporates" the free evolution of the field. Substitution of Eq. (5) into Eq. (3) gives

$$\partial_t \hat{\delta}(\mathbf{k},t) = \mathcal{A} e^{-i\beta t} e^{-t^2} \int d\mathbf{k}' e^{(i\beta/2)(k^2+k'^2)t} \times \exp\left(-\frac{\gamma^2\beta^2}{4}(\mathbf{k}_r+\mathbf{k}'_r)^2 - \frac{\beta^2}{4}(k_z+k'_z)^2\right)\hat{\delta}^{\dagger}(\mathbf{k}',t),$$

where $\mathcal{A} = -i\frac{\alpha\beta^2\gamma^2}{8\pi^{3/2}}$, $\mathbf{k}_r = k_x\mathbf{e}_x + k_y\mathbf{e}_y$, and $\mathbf{e}_i$ is a unit vector in i direction. The above can be integrated formally, giving

$$\hat{\delta}(\mathbf{k},t) = \mathcal{A}\int_0^t d\tau e^{-i\beta\tau} e^{-\tau^2} \int d\mathbf{k}' e^{(i\beta/2)(k^2+k'^2)\tau} \times \exp\left(-\frac{\gamma^2\beta^2}{4}(\mathbf{k}_r+\mathbf{k}'_r)^2 - \frac{\beta^2}{4}(k_z+k'_z)^2\right)\hat{\delta}^{\dagger}(\mathbf{k}',\tau).$$

Since in the Heisenberg picture the scattered field remains in its initial vacuum state and the evolution of the $\hat{\delta}$ field is linear, the second-order correlation function $G^{(2)}(\mathbf{k}_1,\mathbf{k}_2)$ decomposes into

$$\begin{aligned} G^{(2)}(\mathbf{k}_1,\mathbf{k}_2;t) &= \langle \hat{\delta}^{\dagger}(\mathbf{k}_1,t)\hat{\delta}^{\dagger}(\mathbf{k}_2,t)\hat{\delta}(\mathbf{k}_2,t)\hat{\delta}(\mathbf{k}_1,t)\rangle \\ &= G^{(1)}(\mathbf{k}_1,\mathbf{k}_1;t)\cdot G^{(1)}(\mathbf{k}_2,\mathbf{k}_2;t) \\ &\quad + |G^{(1)}(\mathbf{k}_1,\mathbf{k}_2;t)|^2 + |M(\mathbf{k}_1,\mathbf{k}_2;t)|^2, \end{aligned} \tag{6}$$

where $M(\mathbf{k}_1,\mathbf{k}_2;t) = \langle\hat{\delta}(\mathbf{k}_1,t)\hat{\delta}(\mathbf{k}_2,t)\rangle$ is the anomalous density and $G^{(1)}(\mathbf{k}_1,\mathbf{k}_2;t) = \langle\hat{\delta}^{\dagger}(\mathbf{k}_1,t)\hat{\delta}(\mathbf{k}_2,t)\rangle$ is the first-order correlation function. Below we calculate these two functions in the lowest order and for a time $t=\infty$ because all the measurements are made long after the collision has finished. We expand $\hat{\delta}$ in a series of perturbative solutions,

$$\hat{\delta}(\mathbf{k},t=\infty) = \sum_{i=0}^{\infty}\hat{\delta}^{(i)}(\mathbf{k}),$$

where to the lowest order we get

$$\hat{\delta}^{(1)}(\mathbf{k}) = \mathcal{A}\int_0^{\infty} d\tau e^{-i\beta\tau}e^{-\tau^2}\int d\mathbf{k}' e^{(i\beta/2)(k^2+k'^2)\tau} \times \exp\left(-\frac{\gamma^2\beta^2}{4}(\mathbf{k}_r+\mathbf{k}'_r)^2 - \frac{\beta^2}{4}(k_z+k'_z)^2\right)\hat{\delta}^{(0)\dagger}(\mathbf{k}'). \tag{7}$$

A. Anomalous density: $\mathbf{k}_1 \simeq -\mathbf{k}_2$ correlations

The anomalous density to the first order is expressed as

$$M(\mathbf{k}_1,\mathbf{k}_2) = \langle\hat{\delta}^{(0)}(\mathbf{k}_1)\hat{\delta}^{(1)}(\mathbf{k}_2)\rangle.$$

Using Eq. (7) we get

$$\begin{aligned} M(\mathbf{k}_1,\mathbf{k}_2) &= \mathcal{A}\exp\left(-\frac{\gamma^2\beta^2}{4}(\mathbf{k}_{1,r}+\mathbf{k}_{2,r})^2\right) \\ &\quad\times\exp\left(-\frac{\beta^2}{4}(k_{1,z}+k_{1,z})^2\right) \\ &\quad\times\int_0^{\infty} d\tau\exp(-i\beta\Delta\tau - \tau^2), \end{aligned}$$

where $\Delta = \beta(1-\frac{k_1^2+k_2^2}{2})$. This gives

$$\begin{aligned} M(\mathbf{k}_1,\mathbf{k}_2) = &-i\frac{\alpha\beta^2\gamma^2}{16\pi}\exp\left(-\frac{\beta^2}{4}(k_{1,z}+k_{2,z})^2\right) \\ &\times\exp\left(-\frac{\gamma^2\beta^2}{4}(\mathbf{k}_{1,r}+\mathbf{k}_{2,r})^2 - \frac{\Delta^2}{4}\right)\left[1-\mathrm{erf}\left(\frac{i\Delta}{2}\right)\right]. \end{aligned} \tag{8}$$

This expression shows that the anomalous density describes the correlations of atoms with opposite momenta. In other words, it is non-negligible only when $\mathbf{k}_1 \simeq -\mathbf{k}_2$. If this condition is not satisfied, the exponential functions drop quickly. Comparing this expression to Eq. (4), we find that the widths of the anomalous density have the same anisotropy and are 2 times larger than the condensate density. Moreover, this expression shows that this function is also non-negligible only for $\Delta \lesssim 1$. As β is large, $\Delta \sim 1$ only when $k_1 \simeq 1$ and $k_2 \simeq 1$. This requirement expresses the conservation of energy in the collision of two atoms.

B. First-order correlation function: $\mathbf{k}_1 \simeq \mathbf{k}_2$ correlations

To the lowest order we have

$$G^{(1)}(\mathbf{k}_1,\mathbf{k}_2) = \langle\hat{\delta}^{(1)\dagger}(\mathbf{k}_1)\hat{\delta}^{(1)}(\mathbf{k}_2)\rangle.$$

Using Eq. (7) and $\langle\hat{\delta}^{(0)}(\mathbf{k}_1)\hat{\delta}^{(0)\dagger}(\mathbf{k}_2)\rangle = \delta^{(3)}(\mathbf{k}_1-\mathbf{k}_2)$ we get

$$\begin{aligned} G^{(1)}(\mathbf{k}_1,\mathbf{k}_2) = |\mathcal{A}|^2 &\int_0^{\infty} d\tau\int_0^{\infty} d\tau' \exp[-\tau^2-\tau'^2+i\beta(\tau-\tau')] \\ &\times\int d\mathbf{k}\exp\left[-\frac{\gamma^2\beta^2}{4}[(\mathbf{k}_{1,r}+\mathbf{k}_r)^2 \right.\\ &\left.+(\mathbf{k}_{2,r}+\mathbf{k}_r)^2]\right] \\ &\times\exp\left[-\frac{\beta^2}{4}[(k_{1,z}+k_z)^2+(k_{2,z}+k_z)^2]\right] \\ &\times\exp\left[i\frac{\beta}{2}(k^2+k_2^2)\tau' - i\frac{\beta}{2}(k^2+k_1^2)\tau\right]. \end{aligned}$$

In Appendix B we show that if the following three conditions are satisfied,

$$\beta \gg 1, \quad \frac{\gamma}{|\mathbf{u}_r|} \ll 1, \quad \frac{1}{|\mathbf{u}_r|\beta\gamma} \ll 1, \tag{9}$$

where $\mathbf{u}=(\mathbf{k}_1+\mathbf{k}_2)/|\mathbf{k}_1+\mathbf{k}_2|$ and $\mathbf{u}_r=(\mathbf{k}_{1,r}+\mathbf{k}_{2,r})/|\mathbf{k}_1+\mathbf{k}_2|$ refers to the radial component of $\mathbf{u}$, then the atomic density is given by

$$G^{(1)}(\mathbf{k},\mathbf{k}) = \frac{\alpha^2\beta\gamma^3}{32\sqrt{2\pi}|\mathbf{u}_r} \exp\left[-\frac{2\beta^2\gamma^2(k-1)^2}{|\mathbf{u}_r|^2}\right] \tag{10}$$

and the first-order correlation function by

$$\begin{aligned} G^{(1)}(\mathbf{k}_1,\mathbf{k}_2) = {} & \frac{\alpha^2\beta\gamma^3}{32\sqrt{2\pi}|\mathbf{u}_r|} \exp\left[-\frac{\gamma^2\beta^2}{8}\Delta k_r^2 - \frac{\beta^2}{8}\Delta k_z^2\right] \\ & \times \exp\left(-\frac{\beta^2}{8}(\mathbf{u}\Delta\mathbf{k})^2\right)\left[1-\operatorname{erf}\left(\frac{i\beta\mathbf{u}\Delta\mathbf{k}}{2\sqrt{2}}\right)\right] \\ & \times \exp\left(-\frac{2\beta^2\gamma^2\Delta K^2}{\mathbf{u}_r^2}\right). \end{aligned} \tag{11}$$

We have introduced $\frac{|\mathbf{k}_1+\mathbf{k}_2|}{2}=1+\Delta K$, $\Delta\mathbf{k}=\mathbf{k}_1-\mathbf{k}_2$ and assumed $|\Delta\mathbf{k}|$ is small.

The conditions (9) are fulfilled in the experiment of Ref. [3] because the region $u_r \sim 0$ corresponds to the location of the two condensates and has been excluded from the analysis. The density of the scattered particles is peaked around $k=1$ with a width of $\frac{|\mathbf{u}_r|}{\beta\gamma} \ll 1$. We thus expect an anisotropic halo thickness, but the anisotropy is only strong around $u_r \sim 0$, a direction which was inaccessible in the experiment of Ref. [3]

As in the case of the anomalous density M, we can decompose $G^{(1)}(\mathbf{k}_1,\mathbf{k}_2)$ into factors expressing momentum conservation [first line of Eq. (11)] and energy conservation [second line of Eq. (11)]. We find that the widths of the momentum contribution are $\sqrt{2}$ larger than the corresponding ones for $M(\mathbf{k}_1,\mathbf{k}_2)$ [12,18]. As discussed in Refs. [17,18], the $\sqrt{2}$ is due to the assumption of a Gaussian density profile. The energy contribution happens to be much more constraining than for $M(\mathbf{k}_1,\mathbf{k}_2)$ because of the term $\mathbf{u}\Delta\mathbf{k}$. If $\mathbf{u}\Delta\mathbf{k}=0$, meaning $k_1=k_2$, the width of $G^{(1)}(\mathbf{k}_1,\mathbf{k}_2)$ is given by the momentum contribution. But if $\mathbf{u}\Delta\mathbf{k}\neq 0$ and, for instance, if $\mathbf{u}$ is parallel to $\Delta\mathbf{k}$, its width is $\propto 1/\beta$ even in the radial plane, in contradiction with the simple model developed in Ref. [3].

C. Applicability of perturbation theory

Perturbation theory is valid provided the scattering of atoms is spontaneous. When bosonic enhancement comes in to play, the perturbative approach fails. Here we give a simple estimate for parameters such as the number of scattered atoms and the dimensionless parameter β for which the perturbation is small and the above first-order results can be used. Note that, usually, to verify whether the perturbation is small, one has to calculate the physical quantities up to second order. Then, comparison of the two lowest orders would give an answer to the question if the perturbation theory can be used. Moreover, such an approach would yield an expansion parameter in the perturbative series. However, we were unable to evaluate the physical quantities to second order in this case. Thus below we provide an alternative method for verification of whether for these parameters α, β, and γ the perturbative approach applies.

A coherence volume can be attributed to each scattered atom. It is a volume in momentum space in which the atom is first-order coherent. In other words, if we choose a scattered atom with momentum $\mathbf{k}$, the volume set by all the wave vectors $\mathbf{k}_1$ for which $|G^{(1)}(\mathbf{k},\mathbf{k}_1)|$ is not negligible is the coherence volume. If two bosons scatter in such a way that their coherence volumes overlap, their joint detection amplitude is enhanced by an interference effect. In other words, scattering into an already occupied mode is stimulated. The function $G^{(1)}$ permits an estimate of both the number of scattered atoms and their associated coherence volumes. If the number of scattered atoms is small, coherence volumes are unlikely to overlap and stimulated scattering is negligible. In this situation we expect our perturbative solution to be valid.

The above argument was used in the case of the collision of two spherically symmetric ($\gamma=1$) Gaussian wave packets [12] and, in comparisons with numerical solutions of the equation for the field $\hat{\delta}$, proved to be correct. Here we apply an analogous reasoning for the case $\gamma\neq 1$. A conservative estimate for the maximum number of scattered atoms for which the perturbative approach applies is $N_{\text{crit}}=V/V_c$, where V is a lower bound on the k-space volume into which atoms are scattered and V_c is an upper bound on the coherence volume of an individual atom.

In the comparison with the experiment (Sec. IV) we analyze a k-space volume Ω which excludes angles θ smaller than $\pi/4$. From Eq. (10) one sees that the density of scattered atoms is peaked around $k=1$ with an rms width of $\sin\theta/\gamma\beta$. In the volume Ω, the minimum rms width of the shell is $(\gamma\beta\sqrt{2})^{-1}$. Taking twice this minimum rms as the thickness of the shell, we find a lower limit on the volume of $V>4\pi/\gamma\beta$.

The analysis of Eq. (11) shows that V_c reaches its maximum in Ω for $\theta\simeq\pi/4$ (or $\theta\simeq 3\pi/4$, but due to symmetry we will focus on one of these values). If we set $\theta=\pi/4+\delta\theta$, $\varphi=\delta\varphi$, and $k_1=k_2=1$, we find

$$G^{(1)}(\theta,\varphi) \propto \exp\left(-\frac{\beta^2(\delta\theta)^2}{16} - \frac{\beta^2\gamma^2(\delta\varphi)^2}{16}\right).$$

This gives an angular area of coherence approximately equal to $8\pi/\gamma\beta^2$. Now we need to find the coherence width in the radial direction. Setting $\mathbf{k}_1=(1+\delta k/2)\mathbf{k}/k$ and $\mathbf{k}_2=(1-\delta k/2)\mathbf{k}/k$ we get

$$G^{(1)}(\delta k) \propto \exp\left(-\frac{\beta^2\delta k^2}{8}\right).$$

The limit on the coherence volume is therefore $V_c<64\pi/3\gamma\beta^3$.

Combining the estimates of V and V_c, we find that the critical number of atoms is given by $N_{\text{crit}}=\frac{3\beta^2}{16}$. For $\beta=227$ we get $N_{\text{crit}}\approx 10^4$. In the experimental realization, the number of atoms detected in Ω varied from 30 to 300. Assuming 10% detection efficiency this gives a maximum of 3000 scattered atoms. Thus the experiment should be in the perturbative regime. A similar argument is given in Ref. [17] leading to a similar value of N_{crit}.

IV. COMPARISON WITH EXPERIMENT

The formulas (8) and (11) cannot be directly compared with experimental data. This is due to an extra step which is made during the measurements: the joint probabilities measured in experiment are averaged over a region of interest Ω which excludes the unscattered condensates. We approximate Ω by $\theta \in [\frac{\pi}{4}, \frac{3\pi}{4}]$ and $\varphi \in [0, 2\pi]$ [where $\mathbf{u} = (\sin\theta\cos\varphi, \sin\theta\sin\varphi, \cos\theta)$].

In case of local momentum correlations, the normalization procedure is done by choosing $\mathbf{k}_1$ and $\mathbf{k}_2$ almost equal: $\mathbf{k}_1 - \mathbf{k}_2 = \delta\mathbf{k}$, where $\delta\mathbf{k}$ is small. So we set $\mathbf{k}_1 = \mathbf{k} + \delta\mathbf{k}/2$ and $\mathbf{k}_2 = \mathbf{k} - \delta\mathbf{k}/2$. The averaging corresponds to calculation of an integral

$$\langle |G^{(1)}(\delta\mathbf{k})|^2 \rangle = \int_\Omega d\mathbf{k} |G^{(1)}(\mathbf{k}_1,\mathbf{k}_2)|^2. \tag{12}$$

Then, this function is normalized by

$$\int_\Omega d\mathbf{k} G^{(1)}(\mathbf{k}_1,\mathbf{k}_1) \cdot G^{(1)}(\mathbf{k}_2,\mathbf{k}_2). \tag{13}$$

Let us denote the resulting normalized function by $\langle |g^{(1)}(\delta\mathbf{k})|^2 \rangle$. As the anomalous density vanishes for local correlations, Eq. (6) gives

$$g^{(2)}(\delta\mathbf{k}) = 1 + \langle |g^{(1)}(\delta\mathbf{k})|^2 \rangle.$$

For $\delta\mathbf{k} = 0$ we get $g^{(2)}(0) = 2$ [18].

In the case of back-to-back momentum correlations, in analogy we have $\mathbf{k}_1$ and $\mathbf{k}_2$ almost opposite: $\mathbf{k}_1 + \mathbf{k}_2 = \delta\mathbf{k}$. We set $\mathbf{k}_1 = \mathbf{k} + \delta\mathbf{k}/2$ and $\mathbf{k}_2 = -\mathbf{k} + \delta\mathbf{k}/2$. Once again, the averaging corresponds to

$$\langle |M(\delta\mathbf{k})|^2 \rangle = \int_\Omega d\mathbf{k} |M(\mathbf{k}_1,\mathbf{k}_2)|^2.$$

After normalization by the function (13) we obtain $\langle |m(\delta\mathbf{k})|^2 \rangle$. For the opposite momentum correlations, $G^{(1)}$ vanishes; thus,

$$g^{(2)}(\delta\mathbf{k}) = 1 + \langle |m(\delta\mathbf{k})|^2 \rangle.$$

Let us now calculate the normalization function from (13), as is common for both local- and opposite-momentum correlations. From Eq. (11) we have

$$G^{(1)}(\mathbf{k}_{1,2}) = \frac{\alpha^2 \beta \gamma^3 \sqrt{\pi}}{32\pi\sqrt{2}|\mathbf{u}_{1,2r}|} \exp\left[-\frac{\beta^2\gamma^2(k_{1,2}^2 - 1)^2}{2|\mathbf{u}_{1,2r}|^2}\right].$$

Now, in spherical coordinates, $|\mathbf{u}_{1,2r}| = |\sin\theta_{1,2}|$, where $\theta_{1,2}$ is an angle between the vector $\mathbf{k}_{1,2}$ and z axis. Since $\frac{1}{2}\delta\mathbf{k}$ is much smaller than $\mathbf{k}$, we can approximate $\sin\theta_{1,2} \simeq \sin\theta$, where θ is an angle between the vector $\mathbf{k}$ and z axis and drop higher-order terms in $\delta\mathbf{k}$ in the exponentials. We end up with the approximate expression

$$\int_\Omega d\mathbf{k} G^{(1)}(\mathbf{k}_1,\mathbf{k}_1) \cdot G^{(1)}(\mathbf{k}_2,\mathbf{k}_2) \simeq \frac{\alpha^4\beta^2\gamma^6}{2^{11}\pi\sin^2\theta} \int_\Omega d\mathbf{k} \exp\left[-\frac{\beta^2\gamma^2(k^2-1)^2}{\sin^2\theta} - \frac{\beta^2\gamma^2(\mathbf{k}\cdot\delta\mathbf{k})^2}{\sin^2\theta}\right].$$

If $\delta\mathbf{k} = \delta k \cdot \mathbf{e}_x$, $\mathbf{k}\cdot\delta\mathbf{k} = k\delta k \sin\theta\cos\phi$, and if $\delta\mathbf{k} = \delta k \cdot \mathbf{e}_z$, $\mathbf{k}\cdot\delta\mathbf{k} = k\delta k\cos\theta$. The resulting integrals are calculated numerically.

A. Back-to-back momentum correlations

As discussed above, we set $\mathbf{k}_1 = \mathbf{k} + \delta\mathbf{k}/2$ and $\mathbf{k}_2 = -\mathbf{k} + \delta\mathbf{k}/2$. Using Eq. (8),

$$|M(\mathbf{k}_1,\mathbf{k}_2)|^2 = \frac{\alpha^2\beta^4\gamma^4}{256\pi^2} \exp\left(-\frac{\gamma^2\beta^2}{2}\delta k_r^2 - \frac{\beta^2}{2}\delta k_z^2 - \frac{\Delta^2}{4}\right) \times \left[1 + \mathrm{erfi}^2\left(\frac{\Delta}{2}\right)\right].$$

Here, $\Delta = \beta(1 - k^2 - \frac{\delta k^2}{4})$. The averaging over Ω is equivalent to

$$\langle |M(\delta\mathbf{k})|^2 \rangle = \int_\Omega d\mathbf{k} |M(\mathbf{k}_1,\mathbf{k}_2)|^2 = \frac{\alpha^2\beta^4\gamma^4}{256\pi^2} e^{-(\gamma^2\beta^2/2)\delta k_r^2} e^{-\beta^2/2\,\delta k_z^2} \times \int_\Omega d\mathbf{k} e^{-\Delta^2/4}\left[1 + \mathrm{erfi}^2\left(\frac{\Delta}{2}\right)\right].$$

Numerical evaluation of this integral (for parameters β and γ as defined above) shows that the averaged anomalous density can be well approximated by

$$\langle |M(\delta\mathbf{k})|^2 \rangle \propto \exp\left(-\frac{\gamma^2\beta^2}{2}\delta k_r^2 - \frac{\beta^2}{2}\delta k_z^2\right).$$

As we see, the width of $\langle |M(\delta\mathbf{k})|^2 \rangle$ is primarily determined by the momentum conservation constraint, but the analysis shows that energy conservation plays a role, decreasing the predicted width in the xy plane by the order of 10%. We normalize the second-order correlation function by (13) and introduce an empirical parameter η_{bb} to normalize the height of the calculated correlation function to that of the data. We recall that the experimentally observed heights involve complex issues such as detector resolution, and we refer the reader to Ref. [3] for more information. It is not our purpose to account for the heights here; thus, our empirical parameter is simply a means to compare experimental and theoretical widths.

We find

$$g^{(2)}(\delta\mathbf{k}) = 1 + \eta_{\mathrm{bb}} \langle |m(\delta\mathbf{k})|^2 \rangle.$$

This function is plotted in Fig. 2, using the value $\eta_{\mathrm{bb}} = 0.032$. We find good agreement with the experimental data

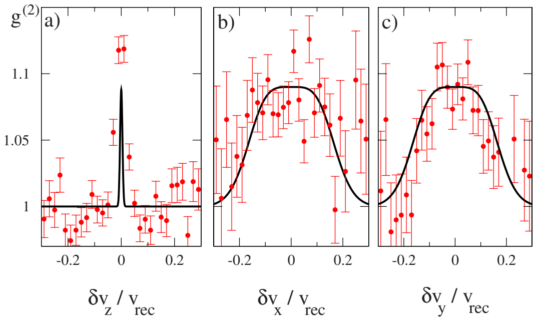

FIG. 2. (Color online) Normalized opposite-momentum correlations calculated in perturbative regime as compared with experimental data. Three plots correspond to three different directions. Here, $\delta v_i = (\hbar/m)\delta k_i$ and $v_{\mathrm{rec}} = (\hbar/m)Q$.

in the x and y directions. In the z direction, the width of the experimental peak is dominated by the detector resolution which is larger than the calculated width.

B. Local momentum correlations

For the collinear correlation function we choose $\mathbf{k}_1 = \mathbf{k} + \delta\mathbf{k}/2$ and $\mathbf{k}_2 = \mathbf{k} - \delta\mathbf{k}/2$. Using Eq. (11) and the definition from Eq. (12) we have

$$\langle |G^{(1)}(\delta\mathbf{k})|^2\rangle = \int_\Omega d\mathbf{k} \frac{\alpha^4\beta^2\gamma^6}{2^{11}\pi|\mathbf{u}_r|^2} \exp\left(-\frac{\beta^2}{4}(\mathbf{u}\,\delta\mathbf{k})^2\right) \times \exp\left[-\frac{\gamma^2\beta^2}{4}\delta k_r^2 - \frac{\beta^2}{4}\delta k_z^2\right] \times \left[1 + \mathrm{erfi}^2\left(\frac{\beta}{2\sqrt{2}}\mathbf{u}\,\delta\mathbf{k}\right)\right] \times \exp\left(-\frac{4\beta^2\gamma^2(k-1)^2}{\mathbf{u}_r^2}\right).$$

Let us now consider two separate cases.

Let us set $\delta\mathbf{k} = \delta k_x \mathbf{e}_x$. Then, $\mathbf{u}\,\delta\mathbf{k} = \delta k \sin\theta\cos\varphi$. Integration over the region Ω consists of an angular and a radial integral. The radial one is

$$I_r = \int_0^\infty k^2 dk \exp\left(-\frac{4\beta^2\gamma^2(k-1)^2}{\mathbf{u}_r^2}\right).$$

The width of this Gaussian function is so small that we can set $k^2 dk \sim dk$. Setting $k = 1 + dk$ and extending the lower limit of the integral to $-\infty$ gives $I_r \propto |\mathbf{u}_r|$. Thus

$$\langle |G^{(1)}(\delta k_x)|^2\rangle \propto e^{-(\gamma^2\beta^2/4)\delta k_x^2} \int_0^{2\pi} d\varphi \int_{\pi/4}^{3/4\pi} d\theta \times \exp\left(-\frac{\beta^2}{4}\delta k_x^2 u^2(\theta,\varphi)\right) \times \left[1 + \mathrm{erfi}^2\left(\frac{\beta\delta k_x}{2\sqrt{2}}u(\theta,\varphi)\right)\right],$$

where $u(\theta,\varphi) = \sin\theta\cos\varphi$. This integral is calculated numerically, and we obtain

$$\langle g^{(2)}(\delta k_x)\rangle = 1 + \langle |g^{(1)}(\delta k_x)|^2\rangle.$$

The result is again rescaled by the parameter η_{cl}, although it need not be identical to the back-to-back case:

$$\langle g^{(2)}(\delta k_x)\rangle = 1 + \eta_{cl}\langle |g^{(1)}(\delta k_x)|^2\rangle.$$

As $\langle |g^{(1)}(0)|^2\rangle = 1$, we deduce the value of $\eta_{\mathrm{cl}} = 0.05$.

Now we set $\delta\mathbf{k} = \delta k_z \mathbf{e}_z$, and therefore $\mathbf{u}\,\delta\mathbf{k} = \delta k_z \cos\theta$. The radial integral is the same as in the previous case, and we find

$$\langle |G^{(1)}(\delta k_z)|^2\rangle \propto \exp\left[-\frac{\beta^2}{4}(\delta k_z)^2\right] \times \int_{\pi/4}^{3/4\pi} d\theta \exp\left(-\frac{\beta^2}{4}(\delta k_z)^2\cos^2\theta\right) \times \left[1 + \mathrm{erfi}^2\left(\frac{\beta\delta k_z}{2\sqrt{2}}\cos\theta\right)\right].$$

Numerically we find

$$\langle g^{(2)}(\delta k_z)\rangle = 1 + \eta_{\mathrm{cl}}\langle |g^{(1)}(\delta k_z)|^2\rangle.$$

We find that choosing $\eta_{\mathrm{cl}} = 0.05$ makes the observed heights match.

Once again, because of the detector resolution, we find that the calculated peak is much narrower than the observed one in the z direction. What is more surprising is that the widths of the correlation functions in the x and y directions are also narrower than those in the experiment. As can be seen from the discussion following Eq. (11), the peak width along the direction of the outgoing atoms is strongly constrained by the energy conservation requirement. This means that for scattering far from the z axis (θ large), the x and y components of the correlation function are narrower than they would be taking momentum conservation alone into account. This result contradicts the simple reasoning of Ref. [3].

In the next section we speculate about why the above width for the correlation function is in agreement with neither the experiment nor the positive-P simulations.

V. CONCLUSIONS

The perturbative result we have presented here, while rather complex, has the virtue that the results are analytic and permit identification of the physical processes involved in the pair formation process. In particular, the roles of energy and momentum conservation are clearly identified. Our results for the back-to-back correlation are in good agreement with the experiment. On the other hand, the collinear correlation function, as shown in Fig. 3, is in apparent contradiction with both the experiment and with the calculation of Ref. [17]. The perturbative correlation function given in this work is narrower. This discrepancy clearly needs more attention, both theoretical and experimental, but we wish to make some comments about possible causes. First, as discussed in

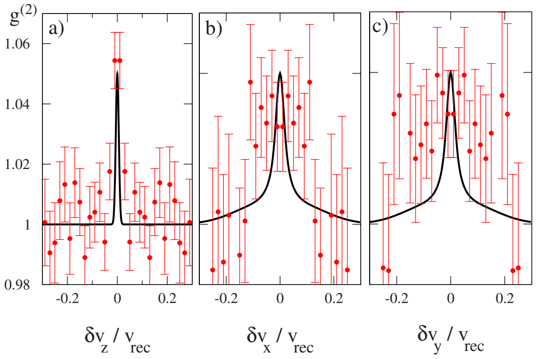

FIG. 3. (Color online) Normalized collinear correlations calculated in the perturbative regime as compared with experimental data. Three plots correspond to three different directions. Due to cylindrical symmetry of the colliding condensates, theoretical results preserve this symmetry. Here, $\delta v_i = (\hbar/m)\delta k_i$ and $v_{\mathrm{rec}} = (\hbar/m)Q$.

Ref. [17], the calculations using the positive-*P* representation are not able to simulate the entire duration of the collision; indeed, only about 20% of the collision time can be simulated. Thus, energy conservation is not as strictly enforced, leading to additional broadening in the calculations of Ref. [17]. Although this effect was discussed in that reference, the problem requires further scrutiny; it is not entirely clear to us which widths are most affected by a short collision time. Second, the experimental observations are also subject to effects not treated here. It was briefly mentioned in Ref. [3] that the mean-field interaction between the escaping atoms and the remaining condensates may not be negligible. It is therefore important to undertake an analysis of their effect on the correlation functions. Finally, an important simplification in the present treatment is the assumption that the condensates do not expand during the collision. This assumption seems reasonable because most of the atom collisions take place before the clouds have had time to expand. Still, a quantitative estimate of the influence of the condensate expansion is another avenue for future analysis.

Clarifying these questions may have ramifications beyond atom optics. Conceptually similar experiments involving collisions between heavy ions have also uncovered discrepancies between observations and simple models [27,28], the so-called “HBT puzzle.” We hope that the work presented here will continue to stimulate careful thought about the four-wave-mixing process of matter waves.

ACKNOWLEDGMENTS

We acknowledge the support of the CIGMA project of the Eurocores program of ESF, the SCALA project of the EU, and the Institut Francilien pour la Recherche en Atomes Froids. P.Z. and J.Ch. acknowledge the support of a Polish Government scientific grant.

APPENDIX A: DETERMINATION OF α

When we introduced α, it was simply defined in terms of the number of atoms, the condensate size, and the scattering length. Here we give a complementary estimate of α which provides a consistency check. The result essentially shows that our treatment is able to predict, to within experimental uncertainties, the number of scattered atoms. We start from Eq. (10). The integration of this equation over Ω gives the number of scattered atoms to first order. This result, being a function of α, can be compared with the number of scattered atoms in the experiment. Knowing this number, we can evaluate α. First, using Eq. (10), the number of scattered atoms in Ω is given by

$$\mathcal{N}_\Omega = \frac{\alpha^2\beta\gamma^3}{32\sqrt{2\pi}|\mathbf{u}_r|}\int_\Omega d\mathbf{k}\,\exp\left[-\frac{\beta^2\gamma^2(k^2-1)^2}{2|\mathbf{u}_r|^2}\right].$$

Let us focus for a moment on the radial part of the above integral:

$$I_{\mathrm{rad}} = \frac{\alpha^2\beta\gamma^3}{32\sqrt{2\pi}|\mathbf{u}_r|}\int_0^\infty k^2 dk\,\exp\left[-\frac{\beta^2\gamma^2(k^2-1)^2}{2|\mathbf{u}_r|^2}\right].$$

First, as the integrand is strongly peaked around $k=1$, the measured volume can be dropped; i.e., $k^2\sim 1$. Then, introducing $k=1+\delta k$ and assuming δk is small we get

$$I_{\mathrm{rad}} \simeq \frac{\alpha^2\beta\gamma^3}{32\sqrt{2\pi}|\mathbf{u}_r|}\int_{-1}^\infty d(\delta k)\exp\left[-\frac{2\beta^2\gamma^2(\delta k)^2}{|\mathbf{u}_r|^2}\right].$$

The lower limit can be extended to $-\infty$, giving

$$I_{\mathrm{rad}} \simeq \frac{\alpha^2\beta\gamma^3}{32\sqrt{2\pi}|\mathbf{u}_r|}\int_{-\infty}^\infty d(\delta k)\exp\left[-\frac{2\beta^2\gamma^2(\delta k)^2}{|\mathbf{u}_r|^2}\right] = \frac{\alpha^2\gamma^2}{64}.$$

Integration over the angular variables gives a factor of $2\sqrt{2\pi}$ and

$$\mathcal{N}_\Omega = \frac{\pi\sqrt{2}}{32}\alpha^2\gamma^2.$$

From the experimental data we know that the number of scattered atoms varies from 300 to 3000. For $N_\Omega=300$ we get $\alpha=930$, and for $N_\Omega=3000$ we get $\alpha=2940$. Thus the value of $\alpha=1652$ calculated from the model of colliding Gaussians lies somewhere in between. This result confirms that the choice of parameters such as σ_r and σ_z is reasonable.

APPENDIX B: FIRST-ORDER CORRELATION FUNCTION: $\mathbf{k}_1\simeq\mathbf{k}_2$ CORRELATIONS

To first order the $G^{(1)}$ function is

$$G^{(1)}(\mathbf{k}_1,\mathbf{k}_2) = |\mathcal{A}|^2\int_0^\infty d\tau\int_0^\infty d\tau'\,\exp[-\tau^2-\tau'^2+i\beta(\tau-\tau')]$$
$$\times\int d\mathbf{k}\,\exp\left[-\frac{\gamma^2\beta^2}{4}[(\mathbf{k}_{1,r}+\mathbf{k}_r)^2 + (\mathbf{k}_{2,r}+\mathbf{k}_r)^2]\right]$$

$$\times\exp\left[-\frac{\beta^2}{4}[(k_{1,z}+k_z)^2+(k_{2,z}+k_z)^2]\right]$$
$$\times\exp\left[i\frac{\beta}{2}(k^2+k_2^2)\tau'-i\frac{\beta}{2}(k^2+k_1^2)\tau\right].$$

Thus, in contrast to the anomalous density, we must perform a two fold time as well as a three-dimensional space integral. The space integral can be evaluated analytically. Then, introducing $x=\frac{\tau+\tau'}{\sqrt{2}}$ and $y=\frac{\tau-\tau'}{\sqrt{2}}$ the first-order correlation function is

$$G^{(1)}(\mathbf{k}_1,\mathbf{k}_2)=\frac{\alpha^2\beta\gamma^2}{16\pi^{3/2}\sqrt{2}}\exp\left[-\frac{\gamma^2\beta^2}{8}|\mathbf{k}_{1,r}-\mathbf{k}_{2,r}|^2-\frac{\beta^2}{8}|k_{1,z}-k_{2,z}|^2\right]\int_0^\infty dx\int_{-x}^{x}dy\,\exp\left[-x^2+i\frac{\beta}{2\sqrt{2}}x(k_2^2-k_1^2)\right]$$
$$\times\exp\left[-y^2\left(1+\frac{\mathbf{u}_r^2}{\gamma^2}+\mathbf{u}_z^2\right)+i\beta\sqrt{2}y\left(1-\frac{k_1^2+k_2^2}{4}-\frac{(\mathbf{k}_1+\mathbf{k}_2)^2}{8}\right)\right]\exp\left[i\sqrt{2}y\frac{(\mathbf{k}_{1,r}+\mathbf{k}_{2,r})^2}{4}\frac{y^2}{\gamma^2(\beta\gamma^2)}\frac{1}{1+2y^2/(\beta\gamma^2)^2}\right]$$
$$\times\exp\left[\frac{y^2}{\gamma^2}\left(\mathbf{u}_r^2-\frac{(\mathbf{k}_{1,r}+\mathbf{k}_{2,r})^2}{4[1+2y^2/(\beta\gamma^2)^2]}\right)\right]\exp\left[i\sqrt{2}y\frac{(k_{1,z}+k_{2,z})^2}{4}\frac{y^2}{\beta}\frac{1}{1+2y^2/\beta^2}\right]$$
$$\times\exp\left[y^2\left(\mathbf{u}_z^2-\frac{(\mathbf{k}_{1,r}+\mathbf{k}_{2,r})^2}{4(1+2y^2/\beta^2)}\right)\right]\frac{1}{1+i\sqrt{2}y/(\beta\gamma^2)}\frac{1}{\sqrt{1+i\sqrt{2}y/\beta}},$$

where $\mathbf{u}=\mathbf{u}_r+\mathbf{u}_z$ is a vector of unit length and direction $\mathbf{k}_1+\mathbf{k}_2$. As the scattering of atoms conserves energy and momentum, we expect that the density of atoms should be centered around $|\mathbf{k}|=1$ (which corresponds to $|\mathbf{k}|=Q$ in physical units). Moreover, from the factor $\exp[-y^2(1+\frac{\mathbf{u}_r^2}{\gamma^2}+\mathbf{u}_z^2)]$, we deduce that the characteristic width of variable y is $1/\sqrt{1+\frac{\mathbf{u}_r^2}{\gamma^2}+\mathbf{u}_z^2}$.

Using the second of conditions (9) we have

$$\exp\left[-y^2\left(1+\frac{\mathbf{u}_r^2}{\gamma^2}+\mathbf{u}_z^2\right)\right]\simeq\exp\left[-y^2\frac{\mathbf{u}_r^2}{\gamma^2}\right].$$

Since the characteristic range of y is $\gamma/|\mathbf{u}_r|$, all the terms proportional to y/β and $y/\beta\gamma^2$ can be dropped. This gives

$$G^{(1)}(\mathbf{k}_1,\mathbf{k}_2)=\frac{\alpha^2\beta\gamma^2}{16\pi^{3/2}\sqrt{2}}$$
$$\times\exp\left[-\frac{\gamma^2\beta^2}{8}|\mathbf{k}_{1,r}-\mathbf{k}_{2,r}|^2-\frac{\beta^2}{8}|k_{1,z}-k_{2,z}|^2\right]$$
$$\times\int_0^\infty dx\int_{-x}^{x}dy\,\exp\left[-x^2+i\frac{\beta}{2\sqrt{2}}x(k_2^2-k_1^2)\right]$$
$$\times\exp\left[-\frac{y^2}{\gamma^2}\mathbf{u}_r^2+i\beta\sqrt{2}y\left(1-\frac{k_1^2+k_2^2}{4}\right.\right.$$
$$\left.\left.-\frac{(\mathbf{k}_1+\mathbf{k}_2)^2}{8}\right)+\frac{y^2}{\gamma^2}\left(\mathbf{u}_r^2-\frac{(\mathbf{k}_{1,r}+\mathbf{k}_{2,r})^2}{4}\right)\right].\tag{B1}$$

Now, by letting $\mathbf{k}_1=\mathbf{k}_2=\mathbf{k}$ in Eq. (B1) let us focus on the momentum density of scattered atoms:

$$G^{(1)}(\mathbf{k},\mathbf{k})=\frac{\alpha^2\beta\gamma^2}{16\pi^{3/2}\sqrt{2}}\int_0^\infty dx\,\exp[-x^2]\int_{-x}^{x}dy\,\exp\left[-\frac{y^2}{\gamma^2}\mathbf{u}_r^2\right.$$
$$\left.+i\beta\sqrt{2}y(1-k^2)\right]\exp\left[\frac{y^2}{\gamma^2}\mathbf{u}_r^2(1-k^2)\right].$$

From the above we deduce that the characteristic width of x is 1, which is much larger that the characteristic width of y. This allows another approximation—the limits of y integral can be expanded up from $-\infty$ to ∞. The variables y and x effectively decouple, giving

$$G^{(1)}(\mathbf{k},\mathbf{k})=\frac{\alpha^2\beta\gamma^2}{32\pi\sqrt{2}}\int_{-\infty}^{\infty}\exp\left[-\frac{y^2}{\gamma^2}\mathbf{u}_r^2+i\beta\sqrt{2}y(1-k^2)\right]$$
$$\times\exp\left[\frac{y^2}{\gamma^2}\mathbf{u}_r^2(1-k^2)\right]dy.$$

After integration over y and with $k\sim 1$, one obtains

$$G^{(1)}(\mathbf{k},\mathbf{k})=\frac{\alpha^2\beta\gamma^3}{32\sqrt{2\pi}|\mathbf{u}_r|}\exp\left[-\frac{2\beta^2\gamma^2(k-1)^2}{|\mathbf{u}_r|^2}\right].$$

Equation (B1) can be rewritten in the form

$$G^{(1)}(\mathbf{k}_1,\mathbf{k}_2)=\frac{\alpha^2\beta\gamma^2}{16\pi^{3/2}\sqrt{2}}$$
$$\times\exp\left[-\frac{\gamma^2\beta^2}{8}|\mathbf{k}_{1,r}-\mathbf{k}_{2,r}|^2-\frac{\beta^2}{8}|k_{1,z}-k_{2,z}|^2\right]$$
$$\times\int_0^\infty dx\int_{-x}^{x}dy\,\exp\left[-x^2+i\frac{\beta}{2\sqrt{2}}x(k_2^2-k_1^2)\right]$$
$$\times\exp\left[-\frac{y^2}{\gamma^2}\mathbf{u}_r^2+i\beta\sqrt{2}y\left(1-\frac{k_1^2+k_2^2}{4}\right.\right.$$

$$-\frac{(\mathbf{k}_1+\mathbf{k}_2)^2}{8}\Bigg)+\frac{y^2}{\gamma^2}\left(\mathbf{u}_r^2-\frac{(\mathbf{k}_{1,r}+\mathbf{k}_{2,r})^2}{4}\right)\Bigg].$$

Introducing $\frac{|\mathbf{k}_1+\mathbf{k}_2|}{2}=1+\Delta K$ and $\Delta\mathbf{k}=\mathbf{k}_1-\mathbf{k}_2$, where $|\Delta\mathbf{k}|$ is small, we obtain

$$G^{(1)}(\mathbf{k}_1,\mathbf{k}_2)=\frac{\alpha^2\beta\gamma^3}{32\sqrt{2\pi}|\mathbf{u}_r|}\exp\left[-\frac{\gamma^2\beta^2}{8}\Delta\mathbf{k}_r^2-\frac{\beta^2}{8}\Delta k_z^2\right]\times\exp\left(-\frac{\beta^2}{8}(\mathbf{u}\Delta\mathbf{k})^2-\frac{2\beta^2\gamma^2\Delta K^2}{\mathbf{u}_r^2}\right)\times\left[1-\mathrm{erf}\left(\frac{i\beta\mathbf{u}\Delta\mathbf{k}}{2\sqrt{2}}\right)\right].$$

[1] D. C. Burnham and D. L. Weinberg, Phys. Rev. Lett. **25**, 84 (1970).
[2] M. Greiner, C. A. Regal, J. T. Stewart, and D. S. Jin, Phys. Rev. Lett. **94**, 110401 (2005).
[3] A. Perrin, H. Chang, V. Krachmalnicoff, M. Schellekens, D. Boiron, A. Aspect, and C. I. Westbrook, Phys. Rev. Lett. **99**, 150405 (2007).
[4] L.-M. Duan, A. Sørensen, J. I. Cirac, and P. Zoller, Phys. Rev. Lett. **85**, 3991 (2000).
[5] H. Pu and P. Meystre, Phys. Rev. Lett. **85**, 3987 (2000).
[6] T. Opatrný and G. Kurizki, Phys. Rev. Lett. **86**, 3180 (2001).
[7] K. V. Kheruntsyan, M. K. Olsen, and P. D. Drummond, Phys. Rev. Lett. **95**, 150405 (2005).
[8] A. Vardi and M. G. Moore, Phys. Rev. Lett. **89**, 090403 (2002).
[9] R. Bach, M. Trippenbach, and K. Rzążewski, Phys. Rev. A **65**, 063605 (2002).
[10] V. A. Yurovsky, Phys. Rev. A **65**, 033605 (2002).
[11] P. Ziń, J. Chwedeńczuk, A. Veitia, K. Rzążewski, and M. Trippenbach, Phys. Rev. Lett. **94**, 200401 (2005).
[12] P. Ziń, J. Chwedeńczuk, and M. Trippenbach, Phys. Rev. A **73**, 033602 (2006).
[13] A. A. Norrie, R. J. Ballagh, and C. W. Gardiner, Phys. Rev. Lett. **94**, 040401 (2005).
[14] A. A. Norrie, R. J. Ballagh, and C. W. Gardiner, Phys. Rev. A **73**, 043617 (2006).
[15] C. M. Savage, P. E. Schwenn, and K. V. Kheruntsyan, Phys. Rev. A **74**, 033620 (2006).
[16] P. Deuar and P. D. Drummond, Phys. Rev. Lett. **98**, 120402 (2007).
[17] A. Perrin, C. M. Savage, D. Boiron, V. Krachmalnicoff, C. I. Westbrook, and K. V. Kheruntsyan, New J. Phys. **10**, 045021 (2008).
[18] K. Mølmer, A. Perrin, V. Krachmalnicoff, V. Leung, D. Boiron, A. Aspect, and C. I. Westbrook, Phys. Rev. A **77**, 033601 (2008).
[19] A. P. Chikkatur, A. Görlitz, D. M. Stamper-Kurn, S. Inouye, S. Gupta, and W. Ketterle, Phys. Rev. Lett. **85**, 483 (2000).
[20] K. Gibble, S. Chang, and R. Legere, Phys. Rev. Lett. **75**, 2666 (1995).
[21] N. Katz, E. Rowen, R. Ozeri, and N. Davidson, Phys. Rev. Lett. **95**, 220403 (2005).
[22] M. Schellekens, R. Hoppeler, A. Perrin, J. Viana Gomes, D. Boiron, C. I. Westbrook, and A. Aspect, Science **310**, 648 (2005).
[23] T. Jeltes, J. M. McNamara, W. Hogervorst, W. Vassen, V. Krachmalnicoff, M. Schellekens, A. Perrin, H. Chang, D. Boiron, A. Aspect *et al.*, Nature (London) **445**, 402 (2007).
[24] M. O. Scully and M. S. Zubairy, *Quantum Optics*, 1st ed. (Cambridge University Press, Cambridge, England, 1997).
[25] E. M. Lifshitz and L. P. Pitaevskii, *Statistical Physics* (Pergamon Press, Oxford, 1980), Pt. 2.
[26] P. Öhberg, E. L. Surkov, I. Tittonen, S. Stenholm, M. Wilkens, and G. V. Shlyapnikov, Phys. Rev. A **56**, R3346 (1997).
[27] M. Lisa, S. Pratt, R. Stoltz, and U. Wiedemann, Annu. Rev. Nucl. Part. Sci. **55**, 357 (2005).
[28] C.-Y. Wong and W.-N. Zhang, Phys. Rev. C **76**, 034905 (2007).

Bibliographie

[1] J. Dalibard, J.-M. Raimond, and J. Zinn-Justin, *Fundamental systems in quantum optics, Proceedings of the Les Houches Summer School, Session LIII* (North Holland, Amsterdam, 1992).

[2] H. Metcalf and P. van der Straten, *Laser cooling and trapping* (Springer Verlag, New York, 1999).

[3] D. E. Pritchard, "Cooling Neutral Atoms in a Magnetic Trap for Precision Spectroscopy", *Phys. Rev. Lett.* **51**, 1336 (1983).

[4] P. O. Schmidt, S. Hensler, J. Werner, T. Binhammer, A. Görlitz, and T. Pfau, "Doppler cooling of an optically dense cloud of magnetically trapped atoms", *J. Opt. Soc. Amer. B* **20**, 960 (2003).

[5] J. I. Cirac, M. Lewenstein, and P. Zoller, "Collective laser cooling of trapped atoms", *Europhys. lett.* **35**, 647 (1996).

[6] D. Boiron, C. Triché, D. R. Meacher, P. Verkerk, and G. Grynberg, "Three-dimensional cooling of cesium atoms in four-beam gray optical molasses", *Phys. Rev. A* **52**, R3425 (1995).

[7] C. Triché, D. Boiron, S. Guibal, D. R. Meacher, P. Verkerk, and G. Grynberg, "Cesium atoms in grey optical lattices. Study of temperature and capture efficiency", *Opt. Comm* **126**, 49 (1996).

[8] D. Boiron, A. Michaud, P. Lemonde, Y. Castin, C. Salomon, S. Weyers, K. Szymaniec, L. Cognet, and A. Clairon, "Laser cooling of cesium atoms in gray optical molasses down to 1.1 μK", *Phys. Rev. A* **53**, R3734 (1996).

[9] D. Boiron, A. Michaud, J. M. Fournier, L. Simard, M. Sprenger, G. Grynberg, and C. Salomon, "Cold and dense cesium clouds in far-detuned dipole traps", *Phys. Rev. A* **57**, R4106 (1998).

[10] F. Bardou, O. Emile, J.-M. Courty, C. I. Westbrook, and A. Aspect, "Magnetooptical trapping of metastable helium - collisions in the presence of resonant light", *Europhys. Lett.* **20**, 681 (1992).

[11] A. Browaeys, A. Robert, O. Sirjean, J. Poupard, S. Nowak, D. Boiron, C. I. Westbrook, and A. Aspect, "Thermalization of magnetically trapped metastable helium", *Phys. Rev. A* **64**, 034703 (2001).

[12] A. Robert, O. Sirjean, A. Browaeys, J. Poupard, S. Nowak, D. Boiron, C. I. Westbrook, and A. Aspect, "A Bose-Einstein condensate of metastable atoms", *Science* **292**, 461 (2001).

[13] A. Robert, *Réalisation d'un condensat de Bose-Einstein d'Hélium métastable*, Ph.D. thesis, Université Paris-Sud, 2001.

[14] O. Sirjean, S. Seidelin, J. V. Gomes, D. Boiron, C. I. Westbrook, A. Aspect, and G. V. Shlyapnikov, "Ionization Rates in a Bose-Einstein Condensate of Metastable Helium", *Phys. Rev. Lett.* **89**, 220406 (2002).

[15] O. Sirjean, *Collisions ionisantes : un nouveau diagnostic pour les condensats de Bose-Einstein d'hélium métastable*, Ph.D. thesis, Université Paris-Sud, 2003.

[16] S. Seidelin, *Collisions dans un gaz d'hélium métastable au voisinage de la dégénérescence quantique*, Ph.D. thesis, Université Paris-Sud, 2004.

[17] S. Seidelin, J. V. Gomes, R. Hoppeler, O. Sirjean, D. Boiron, A. Aspect, and C. I. Westbrook, "Getting the Elastic Scattering Length by Observing Inelastic Collisions in Ultracold Metastable Helium Atoms", *Phys. Rev. Lett.* **93**, 090409 (2004).

[18] O. Jagutzki, V. Mergel, K. Ullmann-Pfleger, L. Spielberger, U. Spillmann, R. Dörner, and H. Schmidt-Böking, "A Broad-Application Microchannel-Plate Detector System for Advanced Particle or Photon Detection Tasks : Large Area Imaging, Precise Multi-Hit Timing Information and High Detection Rate", *Nucl. Inst. & Meth. in Phys. Res. A* **477**, 244 (2004).

[19] R. Hoppeler, *De la condensation de Bose-Einstein à l'effet Hanbury Brown & Twiss atomique de l'hélium métastable*, Ph.D. thesis, Université Paris-Sud, 2004.

[20] M. Schellekens, *The Hanbury Brown and Twiss Effect for Cold Atoms*, Ph.D. thesis, Université Paris-Sud, 2007.

[21] M. Schellekens, R. Hoppeler, A. Perrin, J. Viana Gomes, D. Boiron, C. I. Westbrook, and A. Aspect, "Hanbury Brown Twiss Effect for Ultracold Quantum Gases", *Science* **310**, 648 (2005).

[22] J. V. Gomes, A. Perrin, M. Schellekens, D. Boiron, C. I. Westbrook, and M. Belsley, "Theory for a Hanbury Brown Twiss experiment with a ballistically expanding cloud of cold atoms", *Phys. Rev. A* **74**, 053607 (2006).

[23] T. Jeltes, J. M. McNamara, W. Hogervorst, W. Vassen, V. Krachmalnicoff, M. Schellekens, A. Perrin, H. Chang, D. Boiron, A. Aspect, and C. I. Westbrook, "Comparison of the Hanbury Brown-Twiss effect for bosons and fermions", *Nature* **445**, 402 (2007).

[24] A. Perrin, *Observation de paires d'atomes corrélés au travers de la collision de deux condensats de Bose-Einstein*, Ph.D. thesis, Université Paris et Marie Curie, 2007.

[25] A. Perrin, H. Chang, V. Krachmalnicoff, M. Schellekens, D. Boiron, A. Aspect, and C. I. Westbrook, "Observation of Atom Pairs in Spontaneous Four-Wave Mixing of Two Colliding Bose-Einstein Condensates", *Phys. Rev. Lett.* **99**, 150405 (2007).

[26] M. H. Anderson, J. R. Ensher, M. R. Matthews, C. E. Wieman, and E. A. Cornell, "Observation of Bose-Einstein Condensation in a Dilute Atomic Vapor", *Science* **269**, 198 (1995).

[27] C. C. Bradley, C. A. Sackett, J. J. Tollett, and R. G. Hulet, "Evidence of Bose-Einstein Condensation in an Atomic Gas with Attractive Interactions", *Phys. Rev. Lett.* **75**, 1687 (1995).

[28] K. B. Davis, M. O. Mewes, M. R. Andrews, N. J. van Druten, D. S. Durfee, D. M. Kurn, and W. Ketterle, "Bose-Einstein Condensation in a Gas of Sodium Atoms", *Phys. Rev. Lett.* **75**, 3969 (1995).

[29] B. Desruelle, V. Boyer, S. G. Murdoch, G. Delannoy, P. Bouyer, A. Aspect, and M. Lécrivain, "Interrupted evaporative cooling of ^{87}Rb atoms trapped in a high magnetic field", *Phys. Rev. A* **60**, R1759 (1999).

[30] D. S. Jin, J. R. Ensher, M. R. Matthews, C. E. Wieman, and E. A. Cornell, "Collective Excitations of a Bose-Einstein Condensate in a Dilute Gas", *Phys. Rev. Lett.* **77**, 420 (1996).

[31] D. S. Jin, M. R. Matthews, J. R. Ensher, C. E. Wieman, and E. A. Cornell, "Temperature-Dependent Damping and Frequency Shifts in Collective Excitations of a Dilute Bose-Einstein Condensate", *Phys. Rev. Lett.* **78**, 764 (1997).

[32] M.-O. Mewes, M. R. Andrews, N. J. van Druten, D. M. Kurn, D. S. Durfee, C. G. Townsend, and W. Ketterle, "Collective Excitations of a Bose-Einstein Condensate in a Magnetic Trap", *Phys. Rev. Lett.* **77**, 988 (1996).

[33] M. R. Andrews, C. G. Townsend, H.-G. Miesner, D. S. Durfee, D. M. Kurn, and W. Ketterle, "Observation of Interference Between Two Bose-Einstein Condensates", *Science* **275**, 637 (1997).

[34] M.-O. Mewes, M. R. Andrews, D. M. Kurn, D. S. Durfee, C. G. Townsend, and W. Ketterle, "Output Coupler for Bose-Einstein Condensed Atoms", *Phys. Rev. Lett.* **78**, 582 (1997).

[35] I. Bloch, T. W. Hänsch, and T. Esslinger, "Atom Laser with a cw Output Coupler", *Phys. Rev. Lett.* **82**, 3008 (1999).

[36] J. Stenger, S. Inouye, D. M. Stamper-Kurn, H. J. Miesner, A. P. Chikkatur, and W. Ketterle, "Spin domains in ground-state Bose-Einstein condensates", *Nature* **396**, 345 (1998).

[37] F. Dalfovo, S. Giorgini, L. P. Pitaevskii, and S. Stringari, "Theory of Bose-Einstein condensation in trapped gases", *Rev. Mod. Phys.* **71**, 463 (1999).

[38] Y. Castin, in *Coherent atomic matter waves, Lecture Notes of Les Houches Summer School*, EDITED BY R. Kaiser, C. I. Westbrook, and F. David (Springer-Verlag, Berlin / Heidelberg, 2001).

[39] D. S. Hall, "Resource letter : BEC-1 : Bose-Einstein condensates in trapped dilute gases", *Am. J. Phys.* **71**, 649 (2003).

[40] I. Bloch, J. Dalibard, and W. Zwerger, "Many-body physics with ultracold gases", *Rev. Mod. Phys.* **80**, 885 (2008).

[41] M. Inguscio, S. Stringari, and C. E. Wieman, *Proceedings of the Enrico Fermi International Summer School on Bose-Einstein Condensation in Atomic Gases* (IOS Press, Washington, 1999).

[42] C. J. Pethick and H. Smith, *Bose-Einstein Condensation in Dilute Gases* (Cambridge University Press, Cambridge, Great Brittain, 2002).

[43] A. Browaeys, *Piégeage magnétique d'un gaz d'Hélium métastable : vers la condensation de Bose-Einstein*, Ph.D. thesis, Université Paris-Sud, 2000.

[44] J. C. Viana Gomes, *Thermométrie et propriétés de cohérence d'un gaz ultra-froid d'hélium métastable*, Ph.D. thesis, Université Paris-Sud, 2007.

[45] P. C. Pastor, G. Giusfredi, P. D. Natale, G. Hagel, C. de Mauro, and M. Inguscio, "Absolute Frequency Measurements of the $2\ {}^3S_1 \rightarrow 2\ {}^3P_{0,1,2}$ Atomic Helium Transitions around 1083 nm", *Phys. Rev. Lett.* **92**, 023001 (2004).

[46] T. Zelevinsky, D. Farkas, and G. Gabrielse, "Precision Measurement of the Three $2\ {}^3P_J$ Helium Fine Structure Intervals", *Phys. Rev. Lett.* **95**, 203001 (2005).

[47] K. Pachucki, "Improved Theory of Helium Fine Structure", *Phys. Rev. Lett.* **97**, 013002 (2006).

[48] G. W. F. Drake, W. Nortershauser, and Z. C. Yan, "Isotope shifts and nuclear radius measurements for helium and lithium", *Can. J. Phys.* **83**, 311 (2005).

[49] C. D. Lin, W. R. Johnson, and A. Dalgarno, "Radiative decays of the $n = 2$ states of He-like ions", *Phys. Rev. A* **15**, 154 (1977).

[50] G. W. F. Drake, "Theory of Relativistic Magnetic Dipole Transitions : Lifetime of the Metastable 2^3S State of the Heliumlike Ions", *Phys. Rev. A* **3**, 908 (1971).

[51] G. Łach and K. Pachucki, "Forbidden transitions in the helium atom", *Phys. Rev. A* **64**, 042510 (2001).

[52] Y. Harada, S. Masuda, and H. Ozaki, "Electron spectroscopy using metastable atoms as probes for solid surfaces", *Chem. Rev.* **97**, 1897 (1997).

[53] F. B. Dunning, A. C. H. Smith, and R. F. Stebbings, "Secondary electron ejection from metal surfaces by metastable atoms. I. Measurement of secondary emission coefficients using a crossed beam method", *J. Phys. B : At. Mol. Phys.* **4**, 1683 (1971).

[54] R. D. Rundel, F. B. Dunning, J. S. Howard, J. P. Riola, and R. F. Stebbings, "A Gas Cell Method for the Measurement of Secondary Electron Ejection Coefficients for Metastable Atoms on Metal Surfaces", *Rev. Sci. Instr.* **44**, 60 (1973).

[55] F. B. Dunning, R. D. Rundel, and R. F. Stebbings, "Determination of secondary electron ejection coefficients for rare gas metastable atoms", *Rev. Sci. Instr.* **46**, 697 (1975).

[56] J. Wiza, "Microchannel plate detectors", *Nucl. Instr. and Meth.* **162**, 587 (1979).

[57] M. Yasuda and F. Shimizu, "Observation of Two-Atom Correlation of an Ultracold Neon Atomic Beam", *Phys. Rev. Lett.* **77**, 3090 (1996).

[58] R. S. Gao, P. S. Gibner, J. H. Newman, K. A. Smith, and R. F. Stebbings, "Absolute and angular efficiencies of a microchannel-plate position-sensitive detector", *Rev. Sci. Instr.* **55**, 1756 (1984).

[59] B. Deconihout, F. Vurpillot, M. Bouet, and L. Renaud, "Improved ion detection efficiency of microchannel plate detectors", *Rev. Sci. Instr.* **73**, 1734 (2002).

[60] S. Seidelin, O. Sirjean, J. V. Gomes, D. Boiron, C. I. Westbrook, and A. Aspect, “Using ion production to monitor the birth and death of a metastable helium Bose-Einstein condensate”, *J. Opt. B : Quantum Semiclass. Opt.* **5**, 112 (2003).

[61] Y. Castin and R. Dum, “Bose-Einstein Condensates in Time Dependent Traps”, *Phys. Rev. Lett.* **77**, 5315 (1996).

[62] Y. Kagan, E. L. Surkov, and G. V. Shlyapnikov, “Evolution of a Bose gas in anisotropic time-dependent traps”, *Phys. Rev. A* **55**, R18 (1997).

[63] O. H. Siegmund, J. V. Vallerga, A. S. Tremsin, J. Mcphate, and B. Feller, “High spatial resolution neutron sensing microchannel plate detectors”, *Nucl. Inst. & Meth. in Phys. Res. A* **576**, 178 (2007).

[64] C. Firmani, E. Ruiz, C. W. Carlson, M. Lampton, and F. Paresce, “High-resolution imaging with a two-dimensional resistive anode photon counter”, *Rev. Sci. Instrum.* **53**, 570 (1982).

[65] J. S. Lapington, B. Sanderson, L. B. C. Worth, and J. A. Tandy, “Imaging achievements with the Vernier readout”, *Nucl. Inst. & Meth. in Phys. Res. A* **477**, 250 (2002).

[66] D. Ceolin, G. Chaplier, M. Lemonnier, G. A. Garcia, C. Miron, L. Nahon, M. Simon, N. Leclercq, and P. Morin, “High spatial resolution two-dimensional position sensitive detector for the performance of coincidence experiments”, *Rev. Sci. Instr.* **76**, 043302 (2005).

[67] S. Kraft, A. Günther, J. Fortágh, and C. Zimmermann, “Spatially resolved photoionization of ultracold atoms on an atom chip”, *Phys. Rev. A* **75**, 063605 (2007).

[68] A. Stibor, S. Kraft, T. Campey, D. Komma, A. Günther, J. Fortágh, C. J. Vale, H. Rubinsztein-Dunlop, and C. Zimmermann, “Calibration of a single-atom detector for atomic microchips”, *Phys. Rev. A* **76**, 033614 (2007).

[69] T. Gericke, P. Würtz, D. Reitz, C. Utfeld, and H. Ott, “All-optical formation of a Bose-Einstein condensate for applications in scanning electron microscopy”, *Appl. Phys. B* **89**, 447 (2007).

[70] T. Gericke, P. Würtz, D. Reitz, T. Langen, and H. Ott, “High Resolution Imaging of Single Atoms in a Quantum Gas”, *Nature Phys.* **4**, 949 (2008).

[71] T. P. Meyrath, F. Schreck, J. L. Hanssen, C.-S. Chuu, and M. G. Raizen, “Bose-Einstein condensate in a box”, *Phys. Rev. A* **71**, 041604 (2005).

[72] H. L. Bethlem, F. M. H. Crompvoets, R. T. Jongma, S. Y. T. van de Meerakker, and G. Meijer, “Deceleration and trapping of ammonia using time-varying electric fields”, *Phys. Rev. A* **65**, 053416 (2002).

[73] J. M. Doyle, B. Friedrich, J. Kim, and D. Patterson, “Buffer-gas loading of atoms and molecules into a magnetic trap”, *Phys. Rev. A* **52**, R2515 (1995).

[74] S. V. Nguyen, S. C. Doret, C. B. Connolly, R. A. Michniak, W. Ketterle, and J. M. Doyle, “Evaporative cooling of metastable helium in the multi-partial-wave regime”, *Phys. Rev. A* **72**, 060703 (2005).

[75] S. Nowak, A. Browaeys, J. Poupard, A. Robert, D. Boiron, C. I. Westbrook, and A. Aspect, "Magnetic trapping of metastable helium atoms", *Appl. Phys. B* **70**, 455 (2000).

[76] M.-O. Mewes, M. R. Andrews, N. J. van Druten, D. M. Kurn, D. S. Durfee, and W. Ketterle, "Bose-Einstein Condensation in a Tightly Confining dc Magnetic Trap", *Phys. Rev. Lett.* **77**, 416 (1996).

[77] W. Petrich, M. H. Anderson, J. R. Ensher, and E. A. Cornell, "Stable, Tightly Confining Magnetic Trap for Evaporative Cooling of Neutral Atoms", *Phys. Rev. Lett.* **74**, 3352 (1995).

[78] J. Fortagh and C. Zimmermann, "Magnetic microtraps for ultracold atoms", *Rev. Mod. Phys.* **79**, 235 (2007).

[79] H. F. Hess, "Evaporative cooling of magnetically trapped and compressed spin-polarized hydrogen", *Phys. Rev. B* **34**, 3476 (1986).

[80] O. J. Luiten, M. W. Reynolds, and J. T. M. Walraven, "Kinetic theory of the evaporative cooling of a trapped gas", *Phys. Rev. A* **53**, 381 (1996).

[81] M. W. Müller, A. Merz, M. W. Ruf, H. Hotop, W. Meyer, and M. Movre, "Experimental and theoretical studies of the bi-excited collision systemes He* (2 ^{3}S) + He*(2 ^{3}S, 2 ^{1}S) at thermal and subthermal kinetic energies", *Z. Phys. D* **21**, 89 (1991).

[82] P. S. Julienne and F. H. Mies, "Collisions of ultracold trapped atoms", *J. Opt. Soc. Am. B* **6**, 2257 (1989).

[83] P. S. Julienne, A. M. Smith, and K. Burnett, "Theory of collisions between laser cooled atoms", *Adv. At. Mol. Opt. Phys.* **30**, 141 (1993).

[84] V. Venturi and I. B. Whittingham, "Close-coupled calculation of field-free collisions of cold metastable helium atoms", *Phys. Rev. A* **61**, 060703 (2000).

[85] H. C. Mastwijk, J. W. Thomsen, P. van der Straten, and A. Niehaus, "Optical Collisions of Cold, Metastable Helium Atoms", *Phys. Rev. Lett.* **80**, 5516 (1998).

[86] H. C. Mastwijk, M. van Rijnbach, J. W. Thomsen, P. van der Straten, and A. Niehaus, "Photo induced collisions with laser cooled He* atoms", *Eur. J. Phys. D* **4**, 131 (1998).

[87] M. Kumakura and N. Morita, "Laser Trapping of Metastable ^{3}He Atoms : Isotopic Difference in Cold Penning Collisions", *Phys. Rev. Lett.* **82**, 2848 (1999).

[88] P. J. J. Tol, N. Herschbach, E. A. Hessels, W. Hogervorst, and W. Vassen, "Large numbers of cold metastable helium atoms in a magneto-optical trap", *Phys. Rev. A* **60**, R761 (1999).

[89] R. J. W. Stas, J. M. McNamara, W. Hogervorst, and W. Vassen, "Homonuclear ionizing collisions of laser-cooled metastable helium atoms", *Phys. Rev. A* **73**, 032713 (2006).

[90] A. Browaeys, J. Poupard, A. Robert, S. Nowak, W. Rooijakkers, E. Arimondo, L. Marcassa, D. Boiron, C. I. Westbrook, and A. Aspect, "Two

body loss rate in a magneto-optical trap of metastable He", *Eur. Phys. J. D* **8**, 199 (2000).

[91] F. Pereira Dos Santos, F. Perales, J. Léonard, A. Sinatra, J. M. Wang, F. S. Pavone, E. Rasel, C. S. Unnikrishnan, and M. Leduc, "Penning collisions of laser-cooled metastable helium atoms", *Eur. Phys. J. D* **14**, 15 (2001).

[92] J. stärck and W. Meyer, "Long-range interaction potential of the $^5\Sigma_g^+$ state of He_2", *Chem. Phys. lett.* **225**, 229 (1994).

[93] G. V. Shlyapnikov, J. T. M. Walraven, U. M. Rahmanov, and M. W. Reynolds, "Decay Kinetics and Bose Condensation in a Gas of Spin-Polarized Triplet Helium", *Phys. Rev. Lett.* **73**, 3247 (1994).

[94] P. O. Fedichev, M. W. Reynolds, U. M. Rahmanov, and G. V. Shlyapnikov, "Inelastic decay processes in a gas of spin-polarized triplet helium", *Phys. Rev. A* **53**, 1447 (1996).

[95] V. Venturi, I. B. Whittingham, P. J. Leo, and G. Peach, "Close-coupled calculation of collisions of magnetostatically trapped metastable helium atoms", *Phys. Rev. A* **60**, 4635 (1999).

[96] P. J. Leo, V. Venturi, I. B. Whittingham, and J. F. Babb, "Ultracold collisions of metastable helium atoms", *Phys. Rev. A* **64**, 042710 (2001).

[97] P. O. Fedichev, M. W. Reynolds, and G. V. Shlyapnikov, "Three-Body Recombination of Ultracold Atoms to a Weakly Bound s Level", *Phys. Rev. Lett.* **77**, 2921 (1996).

[98] P. F. Bedaque, E. Braaten, and H.-W. Hammer, "Three-body Recombination in Bose Gases with Large Scattering Length", *Phys. Rev. Lett.* **85**, 908 (2000).

[99] Y. Kagan, B. V. Svistunov, and G. V. Shlyapnikov, "Effect of Bose condensation on inelastic processes in gases", *JETP Lett.* **42**, 209 (1985).

[100] F. Pereira Dos Santos, J. Léonard, J. Wang, C. J. Barrelet, F. Perales, E. Rasel, C. S. Unnikrishnan, M. Leduc, and C. Cohen-Tannoudji, "Bose-Einstein Condensation of Metastable Helium", *Phys. Rev. Lett.* **86**, 3459 (2001).

[101] A. S. Tychkov, T. Jeltes, J. M. McNamara, P. J. J. Tol, N. Herschbach, W. Hogervorst, and W. Vassen, "Metastable helium Bose-Einstein condensate with a large number of atoms", *Phys. Rev. A* **73**, 031603 (2006).

[102] B. D. Esry, C. H. Greene, and J. P. Burke, "Recombination of Three Atoms in the Ultracold Limit", *Phys. Rev. Lett.* **83**, 1751 (1999).

[103] C. R. Monroe, E. A. Cornell, C. A. Sackett, C. J. Myatt, and C. E. Wieman, "Measurement of Cs-Cs elastic scattering at $T = 30\ \mu$K", *Phys. Rev. Lett.* **70**, 414 (1993).

[104] H. Wu and C. J. Foot, "Direct simulation of evaporative cooling", *J. Phys. B- At. Mol. Opt. Phys.* **29**, L321 (1996).

[105] M. Arndt, M. Ben Dahan, D. Guéry-Odelin, M. W. Reynolds, and J. Dalibard, "Observation of a Zero-Energy Resonance in Cs-Cs Collisions", *Phys. Rev. Lett.* **79**, 625 (1997).

[106] F. X. Gadea, T. Leininger, and A. S. Dickinson, “Calculated scattering length for spin-polarized metastable helium”, *J. Chem. Phys.* **117**, 7122 (2002).

[107] A. S. Dickinson, F. X. Gadea, and T. Leininger, “Scattering lengths for spin-polarized metastable helium-3 and helium-4”, *J. Phys. B-At. Mol. Opt. Phys.* **37**, 587 (2004).

[108] M. Przybytek and B. Jeziorski, “Bounds for the scattering length of spin-polarized helium from high-accuracy electronic structure calculations”, *J. Chem. Phys.* **123**, 134315 (2005).

[109] J. Kim, S. Moal, M. Portier, J. Dugué, M. Leduc, and C. Cohen-Tannoudji, “Frequency shifts of photoassociative spectra of ultracold metastable helium atoms : A new measurement of the s-wave scattering length”, *Europhys. Lett.* **72**, 548 (2005).

[110] S. Moal, M. Portier, J. Kim, J. Dugué, U. D. Rapol, M. Leduc, and C. Cohen-Tannoudji, “Accurate Determination of the Scattering Length of Metastable Helium Atoms Using Dark Resonances between Atoms and Exotic Molecules”, *Phys. Rev. Lett.* **96**, 023203 (2006).

[111] M. R. Matthews, B. P. Anderson, P. C. Haljan, D. S. Hall, C. E. Wieman, and E. A. Cornell, “Vortices in a Bose-Einstein Condensate”, *Phys. Rev. Lett.* **83**, 2498 (1999).

[112] F. Chevy, K. W. Madison, and J. Dalibard, “Measurement of the Angular Momentum of a Rotating Bose-Einstein Condensate”, *Phys. Rev. Lett.* **85**, 2223 (2000).

[113] J. R. Abo-Shaeer, C. Raman, J. M. Vogels, and W. Ketterle, “Observation of Vortex Lattices in Bose-Einstein Condensates”, *Science* **292**, 476 (2001).

[114] S. Burger, K. Bongs, S. Dettmer, W. Ertmer, K. Sengstock, A. Sanpera, G. V. Shlyapnikov, and M. Lewenstein, “Dark Solitons in Bose-Einstein Condensates”, *Phys. Rev. Lett.* **83**, 5198 (1999).

[115] L. Khaykovich, F. Schreck, G. Ferrari, T. Bourdel, J. Cubizolles, L. D. Carr, Y. Castin, and C. Salomon, “Formation of a Matter-Wave Bright Soliton”, *Science* **296**, 1290 (2002).

[116] K. E. Strecker, G. B. Partridge, A. G. Truscott, and R. Hulet, “Formation and propagation of matter-wave soliton trains”, *Nature* **417**, 150 (2002).

[117] S. Jochim, M. Bartenstein, A. Altmeyer, G. Hendl, S. Riedl, C. Chin, J. H. Denschlag, and R. Grimm, “Bose-Einstein condensation of molecules”, *Science* **302**, 2101 (2003).

[118] M. W. Zwierlein, C. A. Stan, C. H. Schunck, S. M. F. Raupach, S. Gupta, Z. Hadzibabic, and W. Ketterle, “Observation of Bose-Einstein Condensation of Molecules”, *Phys. Rev. Lett.* **91**, 250401 (2003).

[119] M. Greiner, C. A. Regal, and D. S. Jin, “Emergence of a molecular Bose-Einstein condensate from a Fermi gas”, *Nature* **426**, 537 (2003).

[120] D. S. Petrov, C. Salomon, and G. V. Shlyapnikov, “Weakly Bound Dimers of Fermionic Atoms”, *Phys. Rev. Lett.* **93**, 090404 (2004).

[121] S. Dettmer, D. Hellweg, P. Ryytty, J. J. Arlt, W. Ertmer, K. Sengstock, D. S. Petrov, G. V. Shlyapnikov, H. Kreutzmann, L. Santos, and M. Lewenstein, "Observation of Phase Fluctuations in Elongated Bose-Einstein Condensates", *Phys. Rev. Lett.* **87**, 160406 (2001).

[122] B. Paredes, A. Widera, V. Murg, O. Mandel, S. Fölling, I. Cirac, G. V. Shlyapnikov, T. W. Hänsch, and I. Bloch, "Tonks-Girardeau gas of ultracold atoms in an optical lattice", *Nature* **429**, 277 (2004).

[123] Z. Hadzibabic, P. Kruger, M. Cheneau, B. Battelier, and J. Dalibard, "Berezinskii-Kosterlitz-Thouless Crossover in a Trapped Atomic Gas", *Nature* **441**, 1118 (2007).

[124] M. Greiner, O. Mandel, T. Esslinger, T. W. Hänsch, and I. Bloch, "Quantum phase transition from a superfluid to a Mott insulator in a gas of ultracold atoms", *Nature* **415**, 39 (2002).

[125] L. Deng, E. Hagley, J. Wen, M. Trippenbach, Y. Band, P. Julienne, J. Simsarian, K. Helmerson, S. Rolston, and W. Phillips, "Four wave mixing with matter waves", *Nature* **398**, 218 (1999).

[126] J. M. Vogels, K. Xu, and W. Ketterle, "Generation of Macroscopic Pair-Correlated Atomic Beams by Four-Wave Mixing in Bose-Einstein Condensates", *Phys. Rev. Lett.* **89**, 020401 (2002).

[127] S. L. Cornish, N. R. Claussen, J. L. Roberts, E. A. Cornell, and C. E. Wieman, "Stable ^{85}Rb Bose-Einstein Condensates with Widely Tunable Interactions", *Phys. Rev. Lett.* **85**, 1795 (2000).

[128] T. Weber, J. Herbig, M. Mark, H.-C. N¨agerl, and R. Grimm, "Bose-Einstein Condensation of Cesium", *Science* **299**, 232 (2003).

[129] A. Griesmaier, J. Werner, S. Hensler, J. Stuhler, and T. Pfau, "Bose-Einstein Condensation of Chromium", *Phys. Rev. Lett.* **94**, 160401 (2005).

[130] Y. Takasu, K. Maki, K. Komori, T. Takano, K. Honda, M. Kumakura, T. Yabuzaki, and Y. Takahashi, "Spin-Singlet Bose-Einstein Condensation of Two-Electron Atoms", *Phys. Rev. Lett.* **91**, 040404 (2003).

[131] G. Modugno, G. Ferrari, G. Roati, R. J. Brecha, A. Simoni, and M. Inguscio, "Bose-Einstein Condensation of Potassium Atoms by Sympathetic Cooling", *Science* **294**, 1320 (2001).

[132] E. Mandonnet, A. Minguzzi, R. Dum, I. Carusotto, Y. Castin, and J. Dalibard, "Evaporative cooling of an atomic beam", *Eur. Phys. J. D* **10**, 9 (2000).

[133] T. Lahaye, J. M. Vogels, K. J. Günter, Z. Wang, J. Dalibard, and D. Guéry-Odelin, "Realization of a Magnetically Guided Atomic Beam in the Collisional Regime", *Phys. Rev. Lett.* **93**, 093003 (2004).

[134] C.-H. Cheng and S.-K. Yip, "Anisotropic Fermi Superfluid via p-Wave Feshbach Resonance", *Phys. Rev. Lett.* **95**, 070404 (2005).

[135] A. G. Truscott, K. E. Strecker, W. I. McAlexander, G. B. Partridge, and R. G. Hulet, "Observation of Fermi Pressure in a Gas of Trapped Atoms", *Science* **291**, 2570 (2001).

[136] F. Schreck, G. Ferrari, K. L. Corwin, J. Cubizolles, L. Khaykovich, M.-O. Mewes, and C. Salomon, "Sympathetic cooling of bosonic and fermionic lithium gases towards quantum degeneracy", *Phys. Rev. A* **64**, 011402 (2001).

[137] F. Schreck, L. Khaykovich, K. L. Corwin, G. Ferrari, T. Bourdel, J. Cubizolles, and C. Salomon, "Quasipure Bose-Einstein Condensate Immersed in a Fermi Sea", *Phys. Rev. Lett.* **87**, 080403 (2001).

[138] C. Chin, M. Bartenstein, A. Altmeyer, S. Riedl, S. Jochim, J. H. Denschlag, and R. Grimm, "Observation of the pairing gap in a strongly interacting Fermi gas", *Science* **305**, 1128 (2004).

[139] M. W. Zwierlein, J. R. Abo-Shaeer, A. Schirotzek, C. H. Schunck, and W. Ketterle, "Vortices and superfluidity in a strongly interacting Fermi gas", *Nature* **435**, 1047 (2005).

[140] M. Bartenstein, A. Altmeyer, S. Riedl, S. Jochim, C. Chin, J. H. Denschlag, and R. Grimm, "Crossover from a Molecular Bose-Einstein Condensate to a Degenerate Fermi Gas", *Phys. Rev. Lett.* **92**, 120401 (2004).

[141] T. Bourdel, L. Khaykovich, J. Cubizolles, J. Zhang, F. Chevy, M. Teichmann, L. Tarruell, S. J. J. M. F. Kokkelmans, and C. Salomon, "Experimental Study of the BEC-BCS Crossover Region in Lithium 6", *Phys. Rev. Lett.* **93**, 050401 (2004).

[142] R. G. Dall and A. G. Truscott, "Bose-Einstein condensation of metastable helium in a bi-planar quadrupole Ioffe configuration trap", *Opt. Comm.* **270**, 255 (2007).

[143] J. Léonard, M. Walhout, A. P. Mosk, T. Müller, M. Leduc, and C. Cohen-Tannoudji, "Giant Helium Dimers Produced by Photoassociation of Ultracold Metastable Atoms", *Phys. Rev. Lett.* **91**, 073203 (2003).

[144] J. Léonard, A. P. Mosk, M. Walhout, P. van der Straten, M. Leduc, and C. Cohen-Tannoudji, "Analysis of photoassociation spectra for giant helium dimers", *Phys. Rev. A* **69**, 032702 (2004).

[145] S. Moal, M. Portier, N. Zahzam, and M. Leduc, "Lifetime of weakly bound dimers of ultracold metastable helium studied by photoassociation", *Phys. Rev. A* **75**, 033415 (2007).

[146] R. J. W. Stas, J. M. McNamara, W. Hogervorst, and W. Vassen, "Simultaneous Magneto-Optical Trapping of a Boson-Fermion Mixture of Metastable Helium Atoms", *Phys. Rev. Lett.* **93**, 053001 (2004).

[147] J. M. McNamara, T. Jeltes, A. S. Tychkov, W. Hogervorst, and W. Vassen, "Degenerate Bose-Fermi Mixture of Metastable Atoms", *Phys. Rev. Lett.* **97**, 080404 (2006).

[148] R. G. Dall, L. J. Byron, A. G. Truscott, G. R. Dennis, M. T. Johnsson, M. Jeppesen, and J. J. Hope, "Observation of transverse interference fringes on an atom laser beam", *Opt. Express* **15**, 17673 (2007).

[149] R. Hoppeler, J. V. Gomes, and D. Boiron, "Atomic density of a harmonically trapped ideal gas near Bose-Einstein transition temperature", *Eur. Phys. J. D* **41**, 157 (2007).

[150] E. Tiesinga, B. J. Verhaar, and H. T. C. Stoof, "Threshold and resonance phenomena in ultracold ground-state collisions", *Phys. Rev. A* **47**, 4114 (1993).

[151] S. Inouye, M. R. Andrews, J. Stenger, H. J. Miesner, D. M. Stamper-Kurn, and W. Ketterle, "Observation of Feshbach resonances in a Bose-Einstein condensate", *Nature* **392**, 151 (1998).

[152] E. Tiesinga, A. J. Moerdijk, B. J. Verhaar, and H. T. C. Stoof, "Conditions for Bose-Einstein condensation in magnetically trapped atomic cesium", *Phys. Rev. A* **46**, R1167 (1992).

[153] T. Weber, J. Herbig, M. Mark, H.-C. Nägerl, and R. Grimm, "Three-Body Recombination at Large Scattering Lengths in an Ultracold Atomic Gas", *Phys. Rev. Lett.* **91**, 123201 (2003).

[154] T. Kraemer, M. Mark, P. Waldburger, J. G. Danzl, C. Chin, B. Engeser, A. D. Lange, K. Pilch, A. Jaakkola, H. C. Nagerl, and R. Grimm, "Evidence for Efimov quantum states in an ultracold gas of caesium atoms", *Nature* **440**, 315 (2006).

[155] P. O. Fedichev, Y. Kagan, G. V. Shlyapnikov, and J. T. M. Walraven, "Influence of Nearly Resonant Light on the Scattering Length in Low-Temperature Atomic Gases", *Phys. Rev. Lett.* **77**, 2913 (1996).

[156] J. L. Bohn and P. S. Julienne, "Prospects for influencing scattering lengths with far-off-resonant light", *Phys. Rev. A* **56**, 1486 (1997).

[157] J. L. Bohn and P. S. Julienne, "Semianalytic theory of laser-assisted resonant cold collisions", *Phys. Rev. A* **60**, 414 (1999).

[158] F. K. Fatemi, K. M. Jones, and P. D. Lett, "Observation of Optically Induced Feshbach Resonances in Collisions of Cold Atoms", *Phys. Rev. Lett.* **85**, 4462 (2000).

[159] M. Theis, G. Thalhammer, K. Winkler, M. Hellwig, G. Ruff, R. Grimm, and J. H. Denschlag, "Tuning the Scattering Length with an Optically Induced Feshbach Resonance", *Phys. Rev. Lett.* **93**, 123001 (2004).

[160] G. Thalhammer, M. Theis, K. Winkler, R. Grimm, and J. H. Denschlag, "Inducing an optical Feshbach resonance via stimulated Raman coupling", *Phys. Rev. A* **71**, 033403 (2005).

[161] K. Enomoto, K. Kasa, M. Kitagawa, and Y. Takahashi, "Optical Feshbach Resonance Using the Intercombination Transition", *Phys. Rev. Lett.* **101**, 203201 (2008).

[162] J. C. J. Koelemeij and M. Leduc, "Prospects for measurement and control of the scattering length of metastable helium using photoassociation techniques", *Eur. Phys. J. D* **31**, 263 (2004).

[163] G. Peach, I. B. Whittingham, and T. J. Beams, "Ultracold atomic collisions in tight harmonic traps : Quantum-defect model and application to metastable helium atoms", *Phys. Rev. A* **70**, 032713 (2004).

[164] T. J. Beams, I. B. Whittingham, and G. Peach, "Autoionization of spin-polarized metastable helium in tight anisotropic harmonic traps", *Phys. Rev. A* **76**, 062707 (2007).

[165] P. Bouyer and M. A. Kasevich, “Heisenberg-limited spectroscopy with degenerate Bose-Einstein gases”, *Phys. Rev. A* **56**, R1083 (1997).

[166] A. Luis, “Nonlinear transformations and the Heisenberg limit”, *Phys. Lett. A* **329**, 8 (2004).

[167] S. Boixo, S. T. Flammia, C. M. Caves, and J. Geremia, “Generalized Limits for Single-Parameter Quantum Estimation”, *Phys. Rev. Lett.* **98**, 090401 (2007).

[168] A. M. Rey, L. Jiang, and M. D. Lukin, “Quantum-limited measurements of atomic scattering properties”, *Phys. Rev. A* **76**, 053617 (2007).

[169] S. Choi and B. Sundaram, “Bose-Einstein condensate as a nonlinear Ramsey interferometer operating beyond the Heisenberg limit”, *Phys. Rev. A* **77**, 053613 (2008).

[170] R. Loudon, *The Quantum Theory of Light, 3rd Ed.* (Oxford University Press, Oxford, Great Brittain, 2000).

[171] R. Hanbury Brown and R. Q. Twiss, “Correlation between photons in two coherent beams of light”, *Nature* **177**, 27 (1956).

[172] R. Hanbury Brown and R. Q. Twiss, “A test of a new type of stellar interferometer on Sirius”, *Nature* **178**, 1046 (1956).

[173] U. Fano, “Quantum theory of interference effects in the mixing of light from phase independent sources”, *Am. J. Phys.* **29**, 539 (1961).

[174] R. J. Glauber, “The Quantum Theory of Optical Coherence”, *Phys. Rev.* **130**, 2529 (1963).

[175] R. J. Glauber, “Coherent and Incoherent States of the Radiation Field”, *Phys. Rev.* **131**, 2766 (1963).

[176] R. J. Glauber, in *Quantum Optics and Electronics*, edited by C. de Witt, A. Blandin, and C. Cohen-Tannoudji (Gordon and Breach, New York, 1965).

[177] R. J. Glauber, “Nobel Lecture : One hundred years of light quanta”, *Rev. Mod. Phys.* **78**, 1267 (2006).

[178] H. J. Kimble, M. Dagenais, and L. Mandel, “Photon Antibunching in Resonance Fluorescence”, *Phys. Rev. Lett.* **39**, 691 (1977).

[179] M. Born and E. Wolf, *Principle of Optics* (Pergamon Press, London, 1959).

[180] A. Sørensen, L.-M. Duan, J. Cirac, and P. Zoller, “Many-particle entanglement with Bose-Einstein condensates”, *Nature* **409**, 63 (2001).

[181] M. Naraschewski and R. J. Glauber, “Spatial coherence and density correlations of trapped Bose gases”, *Phys. Rev. A* **59**, 4595 (1999).

[182] M. Holzmann and Y. Castin, “Pair correlation function of an inhomogeneous interacting Bose-Einstein condensate”, *Eur. Phys. J. D* **7**, 425 (1999).

[183] K. Xu, Y. Liu, D. E. Miller, J. K. Chin, W. Setiawan, and W. Ketterle, “Observation of Strong Quantum Depletion in a Gaseous Bose-Einstein Condensate”, *Phys. Rev. Lett.* **96**, 180405 (2006).

[184] S. Ritter, A. Öttl, T. Donner, T. Bourdel, M. Kohl, and T. Esslinger, “Observing the Formation of Long-Range Order during Bose-Einstein Condensation”, *Phys. Rev. Lett.* **98**, 090402 (2007).

[185] T. E. Judd, R. G. Scott, and T. M. Fromhold, "Atom-chip diffraction of Bose-Einstein condensates : The role of interatomic interactions", *Phys. Rev. A* **78**, 053623 (2008).

[186] M. Henny, S. Oberholzer, C. Strunk, T. Heinzel, K. Ensslin, M. Holland, and C. Schönenberger, "The fermionic Hanbury Brown and Twiss experiment", *Science* **284**, 296 (1999).

[187] W. D. Oliver, J. Kim, R. C. Liu, and Y. Yamamoto, "Hanbury Brown and Twiss-type experiment with electrons", *Science* **284**, 299 (1999).

[188] H. Kiesel, A. Renz, and F. Hasselbach, "Observation of Hanbury Brown-Twiss anticorrelations for free electrons", *Nature* **418**, 392 (2002).

[189] M. Iannuzzi, A. Orecchini, F. Sacchetti, P. Facchi, and S. Pascazio, "Direct Experimental Evidence of Free-Fermion Antibunching", *Phys. Rev. Lett.* **96**, 080402 (2006).

[190] D. H. Boal, C.-K. Gelbke, and B. K. Jennings, "Intensity interferometry in subatomic physics", *Rev. Mod. Phys.* **62**, 553 (1990).

[191] C.-Y. Wong, *Introduction to High-Energy Heavy-Ion Collisions* (World Scientific, Singapore, 1994).

[192] G. Baym, "The physics of Hanbury Brown-Twiss intensity interferometry : From stars to nuclear collisions", *Act. Phys. Pol. B* **29**, 1839 (1998).

[193] U. Heinz and B. V. Jacak, "Two-Particle Correlations in Relativistic Heavy-Ion Collisions", *Nucl. Part. Sci.* **49**, 529 (1999).

[194] D. Hellweg, L. Cacciapuoti, M. Kottke, T. Schulte, K. Sengstock, W. Ertmer, and J. J. Arlt, "Measurement of the Spatial Correlation Function of Phase Fluctuating Bose-Einstein Condensates", *Phys. Rev. Lett.* **91**, 010406 (2003).

[195] J. Esteve, J.-B. Trebbia, T. Schumm, A. Aspect, C. I. Westbrook, and I. Bouchoule, "Observations of Density Fluctuations in an Elongated Bose Gas : Ideal Gas and Quasicondensate Regimes", *Phys. Rev. Lett.* **96**, 130403 (2006).

[196] S. Fölling, F. Gerbier, A. Widera, O. Mandel, T. Gerike, and I. Bloch, "Spatial quantum noise interferometry in expanding condensates", *Nature* **434**, 481 (2005).

[197] T. Rom, T. Best, D. van Oosten, U. Schneider, S. Fölling, B. Paredes, and I. Bloch, "Free fermion antibunching in a degenerate atomic Fermi gas released from an optical lattice", *Nature* **444**, 733 (2006).

[198] I. B. Spielman, W. D. Phillips, and J. V. Porto, "Mott-Insulator Transition in a Two-Dimensional Atomic Bose Gas", *Phys. Rev. Lett.* **98**, 080404 (2007).

[199] A. Öttl, S. Ritter, M. Köhl, and T. Esslinger, "Correlations and Counting Statistics of an Atom Laser", *Phys. Rev. Lett.* **95**, 090404 (2005).

[200] E. A. Burt, R. W. Ghrist, C. J. Myatt, M. J. Holland, E. A. Cornell, and C. E. Wieman, "Coherence, Correlations, and Collisions : What One Learns about Bose-Einstein Condensates from Their Decay", *Phys. Rev. Lett.* **79**, 337 (1997).

[201] B. L. Tolra, K. M. O'Hara, J. H. Huckans, W. D. Phillips, S. L. Rolston, and J. V. Porto, "Observation of Reduced Three-Body Recombination in a Correlated 1D Degenerate Bose Gas", *Phys. Rev. Lett.* **92**, 190401 (2004).

[202] T. Kinoshita, T. Wenger, and D. S. Weiss, "Local Pair Correlations in One-Dimensional Bose Gases", *Phys. Rev. Lett.* **95**, 190406 (2005).

[203] E. Altman, E. Demler, and M. D. Lukin, "Probing many-body states of ultracold atoms via noise correlations", *Phys. Rev. A* **70**, 013603 (2004).

[204] S. Hofferberth, I. Lesanovsky, T. Schumm, J. Schmiedmayer, A. Imambekov, V. Gritsev, and E. Demler, "Probing quantum and thermal noise in an interacting many-body system", *Nature Phys.* **4**, 489 (2008).

[205] M. Greiner, C. A. Regal, J. T. Stewart, and D. S. Jin, "Probing Pair-Correlated Fermionic Atoms through Correlations in Atom Shot Noise", *Phys. Rev. Lett.* **94**, 110401 (2005).

[206] M. A. Cazalilla, "Low-energy properties of a one-dimensional system of interacting bosons with boundaries", *Europhys. Lett.* **59**, 793 (2002).

[207] K. V. Kheruntsyan, D. M. Gangardt, P. D. Drummond, and G. V. Shlyapnikov, "Pair Correlations in a Finite-Temperature 1D Bose Gas", *Phys. Rev. Lett.* **91**, 040403 (2003).

[208] C. Mora and Y. Castin, "Extension of Bogoliubov theory to quasicondensates", *Phys. Rev. A* **67**, 053615 (2003).

[209] N. K. Wilkin and J. M. F. Gunn, "Condensation of "Composite Bosons" in a Rotating BEC", *Phys. Rev. Lett.* **84**, 6 (2000).

[210] A. S. Sørensen, E. Demler, and M. D. Lukin, "Fractional Quantum Hall States of Atoms in Optical Lattices", *Phys. Rev. Lett.* **94**, 086803 (2005).

[211] K. Mølmer, A. Perrin, V. Krachmalnicoff, V. Leung, D. Boiron, A. Aspect, and C. I. Westbrook, "Hanbury Brown and Twiss correlations in atoms scattered from colliding condensates", *Phys. Rev. A* **77**, 033601 (2008).

[212] A. Perrin, C. M. Savage, D. Boiron, V. Krachmalnicoff, C. I. Westbrook, and K. Kheruntsyan, "Atomic four-wave mixing via condensate collisions", *N. J. Phys.* **10**, 045021 (2008).

[213] J. Chwedeńczuk, P. Ziń, M. Trippenbach, A. Perrin, V. Leung, D. Boiron, and C. I. Westbrook, "Pair correlations of scattered atoms from two colliding Bose-Einstein Condensates : Perturbative Approach", *Phys. Rev. A* **78**, 053605 (2008).

[214] D. C. Burnham and D. L. Weinberg, "Observation of Simultaneity in Parametric Production of Optical Photon Pairs", *Phys. Rev. Lett.* **25**, 84 (1970).

[215] S. Friberg, C. K. Hong, and L. Mandel, "Measurement of Time Delays in the Parametric Production of Photon Pairs", *Phys. Rev. Lett.* **54**, 2011 (1985).

[216] J. G. Rarity, P. R. Tapster, E. Jakeman, T. Larchuk, R. A. Campos, M. C. Teich, and B. E. A. Saleh, "Two-photon interference in a Mach-Zehnder interferometer", *Phys. Rev. Lett.* **65**, 1348 (1990).

[217] S. J. FREEDMAN and J. F. CLAUSER, "Experimental Test of Local Hidden-Variable Theories", *Phys. Rev. Lett.* **28**, 938 (1972).

[218] A. ASPECT, P. GRANGIER, and G. ROGER, "Experimental Tests of Realistic Local Theories via Bell's Theorem", *Phys. Rev. Lett.* **47**, 460 (1981).

[219] A. ASPECT, P. GRANGIER, and G. ROGER, "Experimental Realization of Einstein-Podolsky-Rosen-Bohm Gedankenexperiment : A New Violation of Bell's Inequalities", *Phys. Rev. Lett.* **49**, 91 (1982).

[220] A. ASPECT, J. DALIBARD, and G. ROGER, "Experimental Test of Bell's Inequalities Using Time- Varying Analyzers", *Phys. Rev. Lett.* **49**, 1804 (1982).

[221] J. G. RARITY and P. R. TAPSTER, "Experimental violation of Bell's inequality based on phase and momentum", *Phys. Rev. Lett.* **64**, 2495 (1990).

[222] C. K. HONG, Z. Y. OU, and L. MANDEL, "Measurement of subpicosecond time intervals between two photons by interference", *Phys. Rev. Lett.* **59**, 2044 (1987).

[223] A. JOOBEUR, B. E. A. SALEH, T. S. LARCHUK, and M. C. TEICH, "Coherence properties of entangled light beams generated by parametric down-conversion : Theory and experiment", *Phys. Rev. A* **53**, 4360 (1996).

[224] D. WALLS and G. MILBURN, *Quantum Optics* (Springer, New York, 1991).

[225] A. EINSTEIN, B. PODOLSKY, and N. ROSEN, "Can Quantum-Mechanical Description of Physical Reality Be Considered Complete ?", *Phys. Rev.* **47**, 777 (1935).

[226] B. L. SCHUMAKER and C. M. CAVES, "New formalism for two-photon quantum optics. II. Mathematical foundation and compact notation", *Phys. Rev. A* **31**, 3093 (1985).

[227] C. F. LO, "Normal ordering of the SU(1,1) and SU(2) squeeze operators", *Phys. Rev. A* **51**, 1706 (1995).

[228] H. Y. FAN, "Operator ordering in quantum optics theory and the development of Dirac's symbolic method", *J. Opt. B* **5**, R147 (2003).

[229] A. HEIDMANN, R. J. HOROWICZ, S. REYNAUD, E. GIACOBINO, C. FABRE, and G. CAMY, "Observation of Quantum Noise Reduction on Twin Laser Beams", *Phys. Rev. Lett.* **59**, 2555 (1987).

[230] J. M. RAIMOND, M. BRUNE, and S. HAROCHE, "Manipulating quantum entanglement with atoms and photons in a cavity", *Rev. Mod. Phys.* **73**, 565 (2001).

[231] S. HAROCHE and J.-M. RAIMOND, *Exploring the Quantum : Atoms, Cavities and Photons* (Oxford University Press, Oxford, 2006).

[232] C. KURTSIEFER, O. DROSS, D. VOIGT, C. R. EKSTROM, T. PFAU, and J. MLYNEK, "Observation of correlated atom-photon pairs on the single-particle level", *Phys. Rev. A* **55**, R2539 (1997).

[233] M. A. ROWE, D. KIELPINSKI, V. MEYER, C. A. SACKETT, W. M. ITANO, C. MONROE, and D. J. WINELAND, "Experimental violation of a Bell's inequality with efficient detection", *Nature* **409**, 791 (2001).

[234] R. BLATT and D. WINELAND, "Entangled states of trapped atomic ions", *Nature* **453**, 1008 (2008).

[235] J. I. CIRAC and P. ZOLLER, "Quantum Computations with Cold Trapped Ions", *Phys. Rev. Lett.* **74**, 4091 (1995).

[236] F. SCHMIDT-KALER, H. HAFFNER, M. RIEBE, S. GULDE, G. P. T. LANCASTER, T. DEUSCHLE, C. BECHER, C. F. ROOS, J. ESCHNER, and R. BLATT, "Realization of the Cirac-Zoller controlled-NOT quantum gate", *Nature* **422**, 408 (2003).

[237] D. LEIBFRIED, E. KNILL, S. SEIDELIN, J. BRITTON, R. B. BLAKESTAD, J. CHIAVERINI, D. B. HUME, W. M. ITANO, J. D. JOST, C. LANGER, R. OZERI, R. REICHLE, and D. J. WINELAND, "Creation of a six-atom 'Schrodinger cat' state", *Nature* **438**, 639 (2005).

[238] E. HAGLEY, X. MAÎTRE, G. NOGUES, C. WUNDERLICH, M. BRUNE, J. M. RAIMOND, and S. HAROCHE, "Generation of Einstein-Podolsky-Rosen Pairs of Atoms", *Phys. Rev. Lett.* **79**, 1 (1997).

[239] D. N. MATSUKEVICH, T. CHANELIÈRE, S. D. JENKINS, S.-Y. LAN, T. A. B. KENNEDY, and A. KUZMICH, "Entanglement of Remote Atomic Qubits", *Phys. Rev. Lett.* **96**, 030405 (2006).

[240] C.-W. CHOU, J. LAURAT, H. DENG, K. S. CHOI, H. DE RIEDMATTEN, D. FELINTO, and H. J. KIMBLE, "Functional Quantum Nodes for Entanglement Distribution over Scalable Quantum Networks", *Science* **316**, 1316 (2007).

[241] D. N. MATSUKEVICH, P. MAUNZ, D. L. MOEHRING, S. OLMSCHENK, and C. MONROE, "Bell Inequality Violation with Two Remote Atomic Qubits", *Phys. Rev. Lett.* **100**, 150404 (2008).

[242] M. LAMEHI-RACHTI and W. MITTIG, "Quantum mechanics and hidden variables : A test of Bell's inequality by the measurement of the spin correlation in low-energy proton-proton scattering", *Phys. Rev. D* **14**, 2543 (1976).

[243] Y. HASEGAWA, R. LOIDL, G. BADUREK, M. BARON, and H. RAUCH, "Violation of a Bell-like inequality in single-neutron interferometry", *Nature* **425**, 45 (2003).

[244] H. SAKAI *et al.*, "Spin Correlations of Strongly Interacting Massive Fermion Pairs as a Test of Bell's Inequality", *Phys. Rev. Lett.* **97**, 150405 (2006).

[245] M. TRIPPENBACH, Y. B. BAND, and P. S. JULIENNE, "Theory of four-wave mixing of matter waves from a Bose-Einstein condensate", *Phys. Rev. A* **62**, 023608 (2000).

[246] H. PU and P. MEYSTRE, "Creating Macroscopic Atomic Einstein-Podolsky-Rosen States from Bose-Einstein Condensates", *Phys. Rev. Lett.* **85**, 3987 (2000).

[247] V. A. YUROVSKY, "Quantum effects on dynamics of instabilities in Bose-Einstein condensates", *Phys. Rev. A* **65**, 033605 (2002).

[248] A. VARDI and M. G. MOORE, "Directional "Superradiant" Collisions : Bosonic Amplification of Atom Pairs Emitted from an Elongated Bose-Einstein Condensate", *Phys. Rev. Lett.* **89**, 090403 (2002).

[249] R. BACH, M. TRIPPENBACH, and K. RZĄŻEWSKI, "Spontaneous emission of atoms via collisions of Bose-Einstein condensates", *Phys. Rev. A* **65**, 063605 (2002).

[250] P. ZIŃ, J. CHWEDEŃCZUK, A. VEITIA, K. RZĄŻEWSKI, and M. TRIPPENBACH, "Quantum Multimode Model of Elastic Scattering from Bose-Einstein Condensates", *Phys. Rev. Lett.* **94**, 200401 (2005).

[251] A. A. Norrie, R. J. Ballagh, and C. W. Gardiner, "Quantum Turbulence in Condensate Collisions : An Application of the Classical Field Method", *Phys. Rev. Lett.* **94**, 040401 (2005).

[252] K. V. Kheruntsyan, M. K. Olsen, and P. D. Drummond, "Einstein-Podolsky-Rosen Correlations via Dissociation of a Molecular Bose-Einstein Condensate", *Phys. Rev. Lett.* **95**, 150405 (2005).

[253] J. M. Vogels, J. K. Chin, and W. Ketterle, "Coherent Collisions between Bose-Einstein Condensates", *Phys. Rev. Lett.* **90**, 030403 (2003).

[254] A. P. Chikkatur, A. Görlitz, D. M. Stamper-Kurn, S. Inouye, S. Gupta, and W. Ketterle, "Suppression and Enhancement of Impurity Scattering in a Bose-Einstein Condensate", *Phys. Rev. Lett.* **85**, 483 (2000).

[255] K. V. Kheruntsyan and P. D. Drummond, "Quantum correlated twin atomic beams via photodissociation of a molecular Bose-Einstein condensate", *Phys. Rev. A* **66**, 031602 (2002).

[256] P. Ziń, Chwedeńczuk, and M. Trippenbach, "Elastic scattering losses from colliding Bose-Einstein condensates", *Phys. Rev. A* **73**, 033602 (2006).

[257] A. A. Norrie, R. J. Ballagh, and C. W. Gardiner, "Quantum turbulence and correlations in Bose-Einstein condensate collisions", *Phys. Rev. A* **73**, 043617 (2006).

[258] P. Drummond and C. Gardiner, "Generalised P-representations in quantum optics", *J. Phys. A* **13**, 2353 (1980).

[259] P. Deuar and P. D. Drummond, "First-principles quantum dynamics in interacting Bose gases : I. The positive P representation", *J. Phys. A* **39**, 1163 (2006).

[260] H. Pu, W. Zhang, and P. Meystre, "Wave Mixing of Optical Pulses and Bose-Einstein Condensates", *Phys. Rev. Lett.* **91**, 150407 (2003).

[261] M. Gross and S. Haroche, "Superradiance : An essay on the theory of collective spontaneous emission", *Phys. Rep.* **93**, 301 (1982).

[262] K. Tordrup, A. Negretti, and K. M. lmer, "Holographic Quantum Computing", *Phys. Rev. Lett.* **101**, 040501 (2008).

[263] M. D. Reid and D. F. Walls, "Violations of classical inequalities in quantum optics", *Phys. Rev. A* **34**, 1260 (1986).

[264] P. Deuar and P. D. Drummond, "Correlations in a BEC Collision : First-Principles Quantum Dynamics with 150 000 Atoms", *Phys. Rev. Lett.* **98**, 120402 (2007).

[265] C. M. Savage and K. V. Kheruntsyan, "Spatial Pair Correlations of Atoms in Molecular Dissociation", *Phys. Rev. Lett.* **99**, 220404 (2007).

[266] T. Opatrný and G. Kurizki, "Matter-Wave Entanglement and Teleportation by Molecular Dissociation and Collisions", *Phys. Rev. Lett.* **86**, 3180 (2001).

[267] L.-M. Duan, G. Giedke, J. I. Cirac, and P. Zoller, "Inseparability Criterion for Continuous Variable Systems", *Phys. Rev. Lett.* **84**, 2722 (2000).

[268] D. V. Strekalov, A. V. Sergienko, D. N. Klyshko, and Y. H. Shih, "Observation of Two-Photon "Ghost" Interference and Diffraction", *Phys. Rev. Lett.* **74**, 3600 (1995).

[269] M. D'Angelo, Y.-H. Kim, S. P. Kulik, and Y. Shih, "Identifying Entanglement Using Quantum Ghost Interference and Imaging", *Phys. Rev. Lett.* **92**, 233601 (2004).

[270] K. Helmerson and L. You, "Creating Massive Entanglement of Bose-Einstein Condensed Atoms", *Phys. Rev. Lett.* **87**, 170402 (2001).

[271] P. Naidon and F. Masnou-Seeuws, "Photoassociation and optical Feshbach resonances in an atomic Bose-Einstein condensate : Treatment of correlation effects", *Phys. Rev. A* **73**, 043611 (2006).

[272] P. Naidon, E. Tiesinga, and P. S. Julienne, "Two-Body Transients in Coupled Atomic-Molecular Bose-Einstein Condensates", *Phys. Rev. Lett.* **100**, 093001 (2008).

[273] D. Schneble, Y. Torii, M. Boyd, E. W. Streed, D. E. Pritchard, and W. Ketterle, "The Onset of Matter-Wave Amplification in a Superradiant Bose-Einstein Condensate", *Science* **300**, 475 (2003).

[274] K. M. Hilligsøe and K. Mølmer, "Phase-matched four wave mixing and quantum beam splitting of matter waves in a periodic potential", *Phys. Rev. A* **71**, 041602 (2005).

[275] G. K. Campbell, J. Mun, M. Boyd, E. W. Streed, W. Ketterle, and D. E. Pritchard, "Parametric Amplification of Scattered Atom Pairs", *Phys. Rev. Lett.* **96**, 020406 (2006).

[276] R. H. Dicke, "Coherence in Spontaneous Radiation Processes", *Phys. Rev.* **93**, 99 (1954).

[277] N. E. Rehler and J. H. Eberly, "Superradiance", *Phys. Rev. A* **3**, 1735 (1971).

[278] S. Inouye, A. P. Chikkatur, D. M. Stamper-Kurn, J. Stenger, D. E. Pritchard, and W. Ketterle, "Superradiant Rayleigh Scattering from a Bose-Einstein Condensate", *Science* **285**, 571 (1999).

[279] Y. Yoshikawa, T. Sugiura, Y. Torii, and T. Kuga, "Observation of superradiant Raman scattering in a Bose-Einstein condensate", *Phys. Rev. A* **69**, 041603 (2004).

[280] Y. Yoshikawa, Y. Torii, and T. Kuga, "Superradiant Light Scattering from Thermal Atomic Vapors", *Phys. Rev. Lett.* **94**, 083602 (2005).

[281] M. Kozuma, Y. Suzuki, Y. Torii, T. Sugiura, T. Kuga, E. W. Hagley, and L. Deng, "Phase-coherent amplification of matter waves", *Science* **286**, 2309 (1999).

[282] S. Inouye, T. Pfau, S. Gupta, A. P. Chikkatur, G. A., D. E. Pritchard, and W. Ketterle, "Phase-coherent amplification of atomic matter waves", *Nature* **402**, 641 (1999).